NNT/NL : 2021AIXM0055/008ED352

THÈSE DE DOCTORAT

Soutenue à Aix-Marseille Université
le 26 février 2021 par

Paul ADAMCZYK

Asymmetries and anisotropies in the cold gas random motions in nearby spiral galaxies

Discipline
Physique et Sciences de la Matière

Spécialité
Astrophysique et Cosmologie

École doctorale
ED 352

Laboratoire
Laboratoire d'Astrophysique de Marseille

Composition du jury

Françoise COMBES Astronome, Professeure au Collège de France, Observatoire de Paris	Rapporteure
Claudia MENDES DE OLIVEIRA Professeure, Universidade de São Paulo	Rapporteure
Véronique BUAT Professeure, Aix-Marseille Univ.	Examinatrice
Laurent CHEMIN Professeur Associé, Universidad de Antofagasta	Examinateur
Philippe AMRAM Professeur, Aix-Marseille Univ.	Directeur de thèse
Benoît EPINAT Astronome-adjoint, Aix-Marseille Univ.	Co-Directeur de thèse

Je soussigné, Paul Adamczyk, déclare par la présente que le travail présenté dans ce manuscrit est mon propre travail, réalisé sous la direction scientifique de Philippe Amram et Benoît Epinat, dans le respect des principes d'honnêteté, d'intégrité et de responsabilité inhérents à la mission de recherche. Les travaux de recherche et la rédaction de ce manuscrit ont été réalisées dans le respect à la fois de la charte nationale de déontologie des métiers de la recherche et de la charte d'Aix-Marseille Université relative à la lutte contre le plagiat.

Ce travail n'a pas été précédemment soumis en France ou à l'étranger dans une version identique ou similaire à un organisme examinateur.

Fait à Marseille le 12 janvier 2021

Résumé

Le coeur de cette thèse porte sur l'étude des asymétries et des anisotropies dans les distributions de dispersion de vitesses radiales du gaz neutre dans un échantillon de galaxies spirales proches. Dans un premier temps, afin d'extraire des courbes de rotation de manière homogène du sondage HI WHISP, j'ai constitué un échantillon de 313 galaxies spirales et irrégulières. J'ai ensuite utilisé l'algorithme ^{3D}Barolo permettant de calculer les courbes de rotation en ajustant un modèle dit d'anneaux inclinés sur chaque cube de données et non pas sur les champs de vitesses. Cette méthode novatrice, comparée aux méthodes utilisées traditionnellement, permet de s'affranchir d'effets instrumentaux bien connus liés à la résolution spatiale finie des observations. Dans un second temps, j'ai réalisé la toute première étude systématique des mouvements aléatoires du gaz froid sur un échantillon soigneusement sélectionné de 15 galaxies spirales extraites de l'échantillon HI THINGS et de 15 autres galaxies spirales de l'échantillon HI WHISP. Cette étude est motivée par la recherche systématique d'anisotropies dans les champs de dispersions de vitesses, comme cela a été découvert dans la galaxie Messier 33 (M33). Cette anisotropie indiquerait que le gaz neutre et froid du milieu interstellaire serait distribué en amas dense et qu'il serait par conséquent moins sujet aux collisions qu'escompté, ce qui limiterait la dissipation de son énergie. Je montre dans cette thèse que le résultat découvert dans M33 n'est pas confirmé pour d'autres galaxies de même nature et que cette particularité de M33 est probablement liée à un effet de projection. Néanmoins, en analysant ces champs de dispersion de vitesse à l'aide de transformées de Fourier, j'ai découvert la présence d'un signal d'ordre 4, présentant un alignement systématique de $\pi/4$ par rapport au grand axe. A travers deux différentes méthodes, je confirme la réalité physique de ce signal, et je propose différentes pistes pour l'interpréter. Parmi celles-ci, une discussion sur les effets instrumentaux est détaillée, ainsi qu'une possible explication par des effets d'anisotropies d'une nature différente.

Mots clés : galaxies : paramètres fondamentaux ; galaxies : cinématique et dynamique ; galaxies : spirale ; galaxies : structure ; galaxies : milieu interstellaire ; galaxies : HI ;

Abstract

The core of this thesis concerns the study of asymmetries and anisotropies in the radial velocity dispersion distributions of neutral gas in a sample of nearby spiral galaxies. First, in order to extract rotation curves in a homogeneous way from the HI WHISP survey, I constituted a sample of 313 spiral and irregular galaxies. I then used the ^{3D}Barolo algorithm to calculate the rotation curves by fitting a model called tilted-ring on each data-cube and not on the velocity fields. This innovative method, compared to the methods traditionally used, accounts for the well-known instrumental effects linked to the finite spatial resolution of the observations. Secondly, I carried out the very first systematic study of the random movements of cold gas on a carefully selected sample of 15 spiral galaxies extracted from the sample HI THINGS and 15 other spiral galaxies from the sample HI WHISP. This study is motivated by the systematic search for anisotropies in the velocity dispersions fields, as was discovered in the galaxy Messier 33 (M33). This anisotropy would indicate that the neutral and cold gas of the interstellar medium would be distributed in dense clusters and that it would therefore be less subject to collisions than expected, which would limit the dissipation of its energy. I show in this thesis that the result discovered in M33 is not confirmed for other galaxies of the same nature and that this particularity of M33 is probably linked to a projection effect. However, by analyzing these velocity dispersion fields using Fourier transforms, I discovered the presence of a 4th order signal, exhibiting a systematic alignment of $\pi/4$ with respect to the major axis . Through two different methods, I confirm the physical reality of this signal, and I suggest different ways to interpret it. Among these, a discussion of instrumental effects is detailed, as well as a possible explanation by anisotropy effects of a different nature.

Keywords: galaxies: fundamental parameters; galaxies: kinematics and dynamics; galaxies: spiral; galaxies: structure; galaxies: interstellar medium; galaxies: HI;

Remerciements

Je tiens à remercier mes directeurs de thèse, Philippe Amram, et Benoit Epinat, pour m'avoir fait confiance pour cette thèse, pour leur écoute et leur aide, pour les conseils ainsi que pour la liberté que j'ai eu pour m'écarter du sujet initial afin de mener cette étude sur les dispersions de vitesse du gaz dans les galaxies. Merci également de m'avoir permis de prendre part aux programmes d'observation GHASP, à l'OHP, qui furent des délicieux moments de détente (et de fatigue) dans un environnement sain et en compagnie de techniciens passionants ! Merci pour les nombreuses relectures du manuscrit ainsi que les commentaires sur les slides pour la soutenance.

Un grand merci également à Laurent Chemin, avec qui j'ai eu la chance d'aller travailler durant quelques semaines au Chili, à l'Université d'Antofagasta. Son accueil, sa gentillesse et son professionalisme ont été très important pour construire et développer ce projet de thèse, et surtout pour le mener à son terme.

J'aimerais aussi remercier Samuel Boissier pour nos nombreuses discussions qui m'ont aidées à rester motivé durant ces 3 années qui n'ont pas toujours été faciles.

Merci à Françoise Maxant, le coeur vivant du laboratoire, dont l'implication et l'investissement n'ont pas d'égal. Jamais je n'ai rencontré une personne dans l'administration avec une telle envie de bien faire et d'aider au mieux chaque personne. Chaque discussion était un grand moment de plaisir.

Merci à tous les doctorants que j'ai eu la chance de rencontrer, Mathieu, Grégoire, Abhi, Siju, Romain, Vincent, Minerva, etc... et avec qui j'ai pu passé de très bons moments.

Merci aux membres du jury pour leur lecture attentive du manuscrit et leurs commentaires très gratifiant à la fois dans le rapport écrit et à l'issue de la soutenance.

Un grand merci à ma famille, mes cousin(e)s, mes tantes, mes oncles, mon parrain, à mes grands-parents, avec une pensée émue pour mon grand-père qui est décédé durant cette thèse et qui aurait été on ne peut plus fier de son petit fils.

Et merci évidemment à mes parents pour leur soutien infaillible tout au long de ma vie.

Contents

Résumé **3**

Abstract **4**

Remerciements **5**

Contents **6**

List of Figures **9**

List of Tables **15**

1 Introduction **16**
1.1 Scientific context 16
1.2 The structure of dark matter halos 17
1.3 HI observations with aperture synthesis interferometers 20
1.4 Anisotropies and asymmetries of galaxies HI distributions 22
1.5 Velocity dispersion anisotropies and asymmetries 25

2 Samples **27**
2.1 WHISP 27
2.1.1 Motivations for large HI surveys 27
2.1.2 Sample properties 28
2.1.3 Definition of the working sample 29
2.1.4 Important results obtained with WHISP data 32
2.1.5 $H\alpha$ follow-up of WHISP : GHASP 34
2.2 THINGS 36
2.2.1 Motivations for a high-resolution HI survey 36
2.2.2 Sample properties 36
2.2.3 Important results obtained with THINGS data 36
2.2.4 Definition of the working sample 38
2.2.5 $H\alpha$ follow-up of the SINGS survey 38
2.3 Connecting samples 39

3 Revisiting the WHISP analysis **41**
3.1 ^{3D}Barolo 42
3.1.1 Description of the algorithm 44

3.1.2 Methodology . . . 45
3.1.3 Checking results . . . 46
3.2 Results and comparison with literature . . . 47
3.3 Lopsidedness study . . . 48
3.4 Mass distributions in nearby galaxies . . . 51
3.4.1 Outlines . . . 51
3.4.2 Correcting from distance effect . . . 51
3.4.3 Computing dark matter halo mass . . . 53

4 Velocity dispersion study : framework and methodology **55**
4.1 Geometrical and mathematical framework . . . 55
4.2 Discussion of the mathematical framework . . . 59
4.3 Fast Fourier Transform (FFT) . . . 65
4.4 Systematic biases . . . 66
4.4.1 Beam smearing effect . . . 66
4.4.2 Noise in the FFT . . . 72

5 Anisotropy in the HI random motions **77**
5.1 Physical motivations . . . 77
5.2 Anisotropy study of the THINGS sample . . . 79
5.3 Anisotropy study of the WHISP sample . . . 82
5.3.1 From THINGS to WHISP : impact of beam smearing . . . 82
5.3.2 Analysis of the WHISP subsample . . . 86
5.4 Conclusion . . . 89

6 Asymmetries in the HI random motions **91**
6.1 Physical motivations . . . 91
6.2 Asymmetry of the THINGS sample . . . 92
6.2.1 Method 1 : Rings study . . . 92
6.2.2 Method 2 : stacked galaxy . . . 96
6.2.3 Method 3 : Median values of radial distributions . . . 107
6.3 Extension to the WHISP sample . . . 108
6.4 Discussion . . . 110
6.4.1 Uncertainty in the beam shape . . . 110
6.4.2 Beam smearing and σ_4 . . . 112
6.4.3 Multiple components and moments method compare with Gaussian fit . . . 123
6.4.4 Validity of the model and interpretation . . . 124
6.5 Conclusion . . . 127

Conclusion **132**

ANNEXES **140**

A Publication to be submitted January 6th, 2021. 140

B Parameters of the WHISP sample presented in the thesis 172

C Comparison with the literature 180

D Outputs from ^{3D}Barolo 183

E Anisotropy result for the THINGS sample 236

F Anisotropy result for the WHISP sample 242

G Asymmetry results for the THINGS sample 248

H Detail of individual galaxy 254

I THINGS maps superposed with B-band contours 270

List of Figures

1.1 Mass modeling for UGC6537 in Korsaga et al. (2019). On the left, fit of the pseudo-isothermal sphere model and on the right the NFW model. Blue and red points represent respectively the approaching and receding sides of $H\alpha$ data and black points are the HI points. The disk is the dark blue curve, the bulge the red one, the light blue represents the gas component and the dark matter halo is in green. 20
1.2 Karl Jansky's antenna. Credit: NRAO/AUI/NSF 21
1.3 Example of symmetric warp : HI map of NGC4013 superposed to the optical disk (white contours), published in Bottema (1996), left panel. Example of asymmetric warp : NGC4565 from Sancisi (1976), right panel. 23
1.4 Example of lopsidedness : galaxy M101, HI map at 23" x 29" resolution (left) and the corresponding integrated HI profile (right). Images adapted from Kamphuis (1993) 24

2.1 Characteristic of the sample of 313 galaxies from the WHISP survey used in this thesis. 30
2.2 Beam ratio Bmaj/Bmin vs declination at full resolution (left panel) and 30" resolution (right panel). Beam shape information is shown with blue symbols, and the inverse of the sine of the declination with red symbols. 31
2.3 Beam ratio Bmin/Bmaj at 30" (left) and 60"(right) vs beam ratio full resolution for a subsample consisting in galaxies observed before 1995. The color code indicates the declination of each object. 31

3.1 Tilted-ring model of M83 as presented in Rogstad et al. (1974) 43
3.2 Operational scheme of ^{3D}Barolo, from Di Teodoro & Fraternali (2015) 45
3.3 Comparison of the flux computed using the mask define before with the one from N05. The solid line correspond to the 1-1 relation. 47
3.4 Comparison of the rotation curves obtained using ^{3D}Barolo with HI data and $H\alpha$ data available in the literature. 48
3.5 Figure from van Eymeren et al. (2011a). The five typical kinematic behaviour based on the rotation curves from the approaching and receding sides. 50
3.6 Comparison of the χ^2 values for the best fit model of the ISO and NFW dark matter halos (left) and comparison of the dark matter halo mass computed using $H\alpha$ only or HI only, compared to the hybrid data. . . 54

4.1 Velocity ellipsoid, in cylindrical coordinates. To the left, illustration of a group of stars or gaseous clouds travelling along an orbit in the mid-plane ($z = 0$) at mean radial and rotational velocities V_R and V_θ, and with a r.m.s. planar velocity of V and random motion σ. The blue dashed circle corresponds to an orbit of purely circular motions. To the right, the 3 components of the random motion describe the so-called velocity ellipsoid. 57
4.2 Mock σ_{los} galaxy to illustrate the different case : isotropic and symmetric (top left), isotropic and asymmetric (top right), anisotropic and symmetric (bottom left), anisotropic and asymmetric (bottom right). 63
4.3 Mock σ_{los} galaxy to illustrate the different case : isotropic and symmetric (top left), isotropic and asymmetric (top right), anisotropic and symmetric (bottom left), anisotropic and asymmetric (bottom right). 64
4.4 Fraction of missing values in each of the 883 rings of the 15 THINGS galaxies. 66
4.5 Observed radial velocity map of NGC5055 from SINGS (Fig. from Daigle et al. 2006, top panel), radial velocity map modeled using Courteau rotation curves from SINGS data (middle panel), and radial velocity map observed with THINGS (bottom panel). Black rectangle on the middle and bottom panel indicates the size of the galaxy in $H\alpha$. 69
4.6 Beam smearing modeling using SINGS (top panel) and THINGS data of NGC5055. We overplot contours at 1-2-5-10 km/s in gray to highlight the fast decrease of the beam smearing effect in the outer part of the galaxy. 71
4.7 Mean difference between the input $\sigma_{k,in}$ of the toy model and the FFT output $\sigma_{k,out}$ following the relation $y_k = \sqrt{\frac{\sum(\sigma_{k,out}-\sigma_{k,in})^2}{M}}$, where M is the number of iterations of the noise, as a function of $\sigma_{k,in}$. Errorbars are the 1σ uncertainties of the distributions. Each quadrant shows an order of the FFT. Left/right column represents models with $\sigma_0 = 10/20$ km s^{-1} and $\sigma_{Gauss} = 20/40$ km s^{-1}. 74
4.8 Noise on the dispersion amplitude for orders 1 to 4 of the FFT vs σ_0 for two distinct values of $d\sigma$ (top panel : $d\sigma = 1$ km/s, bottom panel : $d\sigma = 4$ km/s) and various number of points in the FFT N. The dashed lines correspond to Eq. 4.21, each curve corresponding to a different value of N (from top to bottom : 1000, 2000, 4000 and 10000). Dots corresponds to different orders (order 1 : green, order 2 : red, order 3 : black, order 4 : magenta). The similar behaviour of orders leads to superposed points. 75

5.1 Example of asymmetric velocity dispersion in the HI gas of the Messier 33 galaxy. Top panel : azimuth-velocity dispersion diagram at $R = 5.7$ kpc, with filled symbols corresponding to the observed dispersions and the red solid line to the results of the model of Eq. 4.9 at this radius. Bottom panel : velocity anisotropy parameter in the disk plane. From Chemin et al. (2020). 78

5.2 Example of fit of the azimuthal variations in the case $\sigma_R > \sigma_\theta$ (left, NGC 2403 at R = 564") and in the case $\sigma_\theta > \sigma_R$ (right, NGC 3521 at R = 150"). 81

5.3 Radial variation of the dispersion ellipsoid and anisotropy parameter β_θ of the galaxy NGC2403. 81

5.4 Mock dispersion maps with beam smearing correction of NGC2403 at different spatial resolutions. Left : beam smearing correction map ; middle : observed velocity dispersion in presence of beam smearing ; right : corrected velocity dispersion map. 84

5.5 Anisotropy for NGC2403, NGC2841, NGC2903 at different resolution on the beam smearing uncorrected (left column) and corrected (right column) dispersion maps. 85

5.6 Example of beam smearing modelisation for UGC7766 (first line) and UGC4325 (second second). On the left column, we have the beam smearing modelisation, on the middle one, the raw dispersion maps extracted with CAMEL and on the the right column the quadratical subtraction of the raw maps with the beam smearing model. Coordinates are given in pixels to give an idea of the number of pixels to sample the galaxy. 88

5.7 Dispersion ellipsoid and anisotropy parameter β_θ calculated on the dispersion map corrected from the beam smearing of the galaxy UGC7766. 89

6.1 Radial profiles of the FFT parameters for NGC3198. Top panel shows amplitudes σ_k while lower panel shows phases ϕ_k/π as a function of radius for modes 1 to 4. 93

6.2 Amplitude (left column) and phase (right column) distribution of the Fourier modes 1 to 4 in the 883 rings of the study. Phases are normalized such that 0.5 is the half period of the mode, and 1 is the full period. The period of the mode k is $\frac{2\pi}{k}$. 94

6.3 Number of rings (top) and number of pixels (bottom) for each galaxy of our sample. Galaxies are sorted with decreasing number of radius. . . 96

6.4 Velocity dispersion squared σ^2 vs the angular sector θ for each galaxy. A bin step 5 degrees has been selected for each sector θ. (Upper left panel) For the whole sample of 15 galaxies. (Upper right panel) Same as the left panel but without galaxies NGC2841 (light blue curve), NGC3627 (red curve) and NGC3521(dark blue curve). (Bottom left panel) Stacked-galaxy computed using the mean velocity dispersion squared for each angular sector. (Bottom right) Stacked-galaxy using the median value instead of the mean. . . . 98
6.5 THINGS dispersion map of NGC2841 (top left panel), projected result of the term of order 2 from the FFT (top right panel), azimuthal map (bottom left) and projected result of the FFT containing orders 0 to 4 (bottom right panel). . . . 99
6.6 σ vs θ (top panel) and σ^2 vs θ (bottom panel). Continuous black line with the black dots are the data points. Dashed black line is the FFT model of the data. Colored continuous lines represents individual orders 1 to 4. . . . 100
6.7 The sample is randomly divided into 2 subsamples, in order to see if the trend observed in the global sample is due to a bias from some galaxies. 102
6.8 Distribution of the order of the FFT for 500 iterations of the mock sample THINGS. The vertical lines corresponds to the reference value of the THINGS sample. . . . 104
6.9 σ^2 vs θ for the "super-galaxy" with various azimuthal bins sizes : 20 deg (top left), 10 deg (top right), 5 deg (bottom left), 2 deg (bottom right). . 105
6.10 Median phase ϕ_k vs velocity dispersion σ_k issued from FFT analysis of individual galaxies. Each point represents the median value of the radial distribution of the FFT parameters for a galaxy. Dashed horizontal line represents the minor (black) and major axis (blue) of galaxies. 108
6.11 Amplitude (left column) and phase (right column) distribution of the Fourier modes 1 to 4 in the 154 rings from the WHISP sample. Phases are normalized such that 0.5 is the half period of the mode, and 1 is the full period. The period of the mode k is $\frac{2\pi}{k}$. . . . 109
6.12 Amplitude (left column) and phase (right column) distribution of the Fourier modes 1 to 4 in the (883 + 154) rings from the THINGS (blue) and WHISP (green) samples respectively. Phases are normalized such that 0.5 is the half period of the mode, and 1 is the full period. The period of the mode k is $\frac{2\pi}{k}$. . . . 110
6.13 Beam smearing modelisation of NGC5055 with the actual beam from THINGS(top left panel) and the corresponding FFT of this map reduced to a single radius (top right panel). Same plot with a circular beam of 10 arcsec^2 (middle row) and orders 2 (bottom left) and 4 (bottom right) of the FFT from top panel. . . . 113
6.14 Variations of the parameters of the FFT with the radius, amplitudes on top panel and phases on bottom panel. . . . 114

6.15 Variations of the parameters of the FFT with the radius, amplitudes on top panel and phases on bottom panel. 115
6.16 Beam smearing model and corresponding FFT at different inclinations : 30°, 50° and 70° for the top, middle and bottom panel respectively. . . 117
6.17 Total signal and FFT orders superposed for the different cases mentioned before. a) top left, b) top right, c) bottom left, d) bottom right. . . 119
6.18 Total signal and FFT orders superposed for the different cases mentioned before. a) top left, b) top right, c) bottom left, d) bottom right. . . 122
6.19 Amplitude (left column) and phase (right column) distribution of the Fourier modes 1 to 4 in the 664 rings of the THINGS subsample, after exclusion of the 4 most inclined THINGS galaxies. Phases are normalized such that 0.5 is the half period of the mode, and 1 is the full period. The period of the mode k is $\frac{2\pi}{k}$. 123
6.20 Example of multiple components in the profiles of NGC2841 (left) and corresponding region in the dispersion map (right) indicated with the black square. 124
6.21 Radial variation of the azimuthally averaged velocity dispersion in galaxies from the THINGS sample. The black circles represents the Gaussian fit and the green one the second-order moments. Figure from Mogotsi et al. (2016). 125
6.22 Multiple plots of NGC2841 126

C.0 Comparison of the rotation curves obtained using ^{3D}Barolo with HI data and $H\alpha$ data available in the literature. 181

E.0 Radial variation of the dispersion ellipsoid (left) and β_θ (right) 237

F.0 Radial variation of the dispersion ellipsoid (left) and β_θ (right) 243

G.0 Radial variation of the FFT parameters : amplitudes on the left panel, and angle phases on the right panel. 249

H.1 Overview of NGC925 255
H.2 Overview of NGC2403 256
H.3 Overview of NGC2841 257
H.4 Overview of NGC2903 258
H.5 Overview of NGC2976 259
H.6 Overview of NGC3031 260
H.7 Overview of NGC3198 261
H.8 Overview of NGC3521 262
H.9 Overview of NGC3621 263
H.10 Overview of NGC3627 264
H.11 Overview of NGC4736 265
H.12 Overview of NGC5055 266

H.13 Overview of NGC6946 267
H.14 Overview of NGC7331 268
H.15 Overview of NGC7793 269

I.0 Flux map from THINGS with B-band contours superposed in gray (left), and dispersion maps from THINGS superposed with the flux contours (right). The blue ellipse corresponds to the last radius of each galaxy. . 271

List of Tables

2.1 Subsample of THINGS data use in this thesis 39

4.1 Beam parameters for the THINGS data 72
4.2 SINGS parameters to model the beam smearing effect 73

5.1 Main properties of the 3 galaxies studied 82
5.2 Properties of the WHISP subsample used for the study of random motions. 87

6.1 Properties of the distributions of Fourier amplitudes in the 883 rings of the sample. 95
6.2 FFT parameters for the 30 subsamples 103
6.3 FFT parameters of NGC5055 obtained using 4 different methods : the first column corresponds to the mean value of the FFT distributions among the 100 rings, the second one the median value of these distributions. Column 3 and 4 corresponds to the FFT parameters of the single radius velocity dispersion, before and after this dispersion within angular sector. 106
6.4 FFT parameters for the beam smearing model of NGC5055 at different inclinations. 116
6.5 FFT parameters for the total signal obtained in the 4 configurations describe in section 6.4.2. 119
6.6 FFT parameters for the total signal obtained in the 4 configurations mentioned above. 121

B.1 Properties of the WHISP subsample used in this thesis 179

1. Introduction

Sommaire

1.1 Scientific context 16
1.2 The structure of dark matter halos 17
1.3 HI observations with aperture synthesis interferometers 20
1.4 Anisotropies and asymmetries of galaxies HI distributions 22
1.5 Velocity dispersion anisotropies and asymmetries 25

1.1. Scientific context

The current most accepted scenario to explain the cosmic evolution and the structure of the Universe is the ΛCold Dark Matter (CDM) paradigm. It describes a late Universe energy budget dominated by Dark Energy at the level of 68.3% (Planck Collaboration et al. 2020), which accounts for the acceleration of the Universe expansion, a phenomenon perhaps associated with the cosmological constant Λ from the early works of Albert Einstein. Cold Dark Matter is the second main component, accounting for 26.6% of the energy of the Universe (Planck Collaboration et al. 2020). It is called Dark Matter (DM) because no electromagnetic light has ever been observed from this component, at any wavelength, and Cold because the hierarchical growth of structures in the Universe implies that dark matter particles have non-relativistic velocities, by opposition with Hot DM and Warm DM models in which particles have lower mass and velocities closer to the speed of light. It does not interact with ordinary matter, or only weakly, and its exotic nature still remains unknown, as of 2020. Its presence has been inferred from the gravitational effects it exerts on baryonic matter, which contributes to the remaining 5.1% of the Universe energy (Planck Collaboration et al. 2020). Baryonic matter is the ordinary matter we are made of. It is mostly composed of gas, stars and black holes in galaxies, and in the intergalactic medium. In practice, less than half of the total baryonic matter predicted by the Big Bang Nucleosynthesis has been observed through electromagnetic radiation. The missing baryons to be detected by telescopes should reside in large amounts of cold and hot gas inside and around galaxies and in galaxy clusters but mainly in the intergalactic medium.

Historically, DM was hypothesized by Oort (1932), through a study of the vertical motions of stars in the Solar neighborhood. It resulted that only 50% of the surface density was due to the observable matter, suggesting that half of the surface density was associated with non-visible matter. This discovery led to numerous debates and finally it appeared that DM is not dominant in the galactic disk of the Milky Way. So the first observably indisputable evidence for the presence of missing matter was reported in 1933 by Zwicky, who observed surprisingly high velocity dispersion in the Coma cluster (Zwicky 1933). When applying the virial theorem, Zwicky found that the average mass density in the cluster was 400 times higher than the one deduced from visible matter (the total stellar mass of the galaxies). The same behaviour was observed in the Virgo cluster (Smith 1936), again suggesting that most of matter in galaxy clusters was not visible.

A way to probe dark matter in galaxies is to study rotation curves, the radial variation of the rotational velocity. In a regular disk galaxy, with stars rotating around the center of the galaxy, the velocity should decrease as $R^{-1/2}$ at large radius (roughly following the Keplerian law). Nevertheless, observations of galaxies show flat or even rising rotation curves (Bosma 1978), pointing out the need for a hidden component to explain the difference with the expected Keplerian fall of the velocity at large radius. However, Kalnajs (1983) and Kent (1986) argued that with appropriate mass-to-light ratios for the stellar components (bulge and disk), the shape of optical rotation curves could be explained by luminous baryons only. Nevertheless, confirmations of the necessity for such important amount of hidden matter in outer galaxy regions were further obtained (Carignan & Freeman 1985; van Albada et al. 1985; Begeman 1987). The study of mass distribution of galactic disks is indeed very sensitive to the disk extent, which is better probed through radio observations of the neutral atomic gas than optical spectroscopy of the inner disk of ionized gas.

1.2. The structure of dark matter halos

Following these results, the next steps were to study the shape of mass profiles of galaxies, that is the structure of DM halos, the total amount of DM, and the possible relations with luminous baryons. In particular, a key question has been to investigate if the gravitational potential of DM dominates at all radii, or only in the outer parts of galaxies.

A powerful tool to study the dynamics of galactic disks and the properties of DM halos is the modeling of the mass distribution underlying rotation curves. To derive a mass model, we assume that the rotation curve, which is the ordered motion of gas or stars in the azimuthal direction (V_θ, considering a disk aligned with a cylindrical frame R, θ, z), is a proxy of the circular motion V_c. This assumption is justified as non-circular motions are generally negligible in front of V_θ, on average. Given that the total gravitational potential Φ is the linear sum of individual contributions from the luminous and dark matter, and that $V_c^2 = R\frac{d\Phi}{dR}$, we can then decompose the observed (quadratic) rotation curve into individual components that account for the distribution of the gaseous, stellar and dark masses:

$$V_\theta^2 = V_{\text{gas}}^2 + \Gamma_{\text{star}} V_{\text{star}}^2 + V_{\text{DM}}^2, \tag{1.1}$$

where Γ_{star} is the mass-to-light ratio of the stellar component(s). To derive the structure of DM halos, we thus need in a first place to know how the luminous baryons are distributed. Let us consider first the stellar component. Stars can be thought of as black or gray bodies that radiate. The luminosity of a star is directly linked to its mass, $L \propto M^{3.5}$, and the higher the luminosity, the shorter the life of a star. Then, massive stars tend to be young and hot, thus emitting in UV and at the smallest wavelengths from the visible electromagnetic spectrum. Blue photometric bands are thus mostly sensitive to younger, massive stars. On the other hand, cooler and low mass stars can live billions of years, and emit mostly at near-infrared wavelengths. Through the Initial Mass Function (IMF), we can have an idea of the ratio of the numbers of massive stars to low mass stars (Kroupa 2001; Chabrier 2003). Many more low mass stars are produced than high-mass ones therefore, despite the difference in mass, the stellar mass budget in a galaxy is dominated by that of old stars. To convert the observed stellar luminosity profile into a stellar mass profile, we use Γ_{star}. This ratio is given in solar units. If a galaxy was filled by stars of Solar type only, then one would expect an average mass-to-light ratio of 1. Nevertheless, a galaxy is composed by multiple stellar populations. In the visible bands, $\Gamma_{\text{star}} > 1 M_\odot / L_\odot$ while in near-infrared $\Gamma_{\text{star}} \lesssim 1 M_\odot / L_\odot$. Due to the large scatter of Γ_{star}, and the not perfect knowledge of the IMF at low and high mass, the mass-to-light ratio is generally a source of uncertainty in mass distribution models of galaxies. For a more detailed discussion of this point, see e.g. Portinari et al. (2004) and van der Kruit & Freeman (2011).

Then, the velocity contribution of the gas component is derived from the HI surface density profile, scaled by a factor of ~ 1.4 to account for the contribution of the atomic Helium gas that comes from primordial nuclear synthesis, and heavier atoms. A mass model should also consider a contribution from the molecular gas, mainly H2. However, in nearby galaxies, the total gaseous mass is usually dominated by that of the atoms (e.g. Kam et al. 2017, by a factor of 10), so that authors often neglect the molecular gas contribution, which is by the way often poorly known.

Once the luminous matter is constrained, it should be scaled by mass-to-light ratio and the velocity contribution of the DM halo can be fitted directly to the rotation curve. It makes it possible to derive the structural parameters of the DM mass density profile, generally the scale density and size of the halo. One of the most appropriate model for DM halo density to fit observed rotation curves, is the pseudo-isothermal sphere (e.g. Blais-Ouellette et al. 2001, hereafter noted ISO), described by a volume density distribution:

$$\rho_{\text{ISO}}(R) = \frac{\rho_0}{1 + (R/R_c)^2}, \tag{1.2}$$

where ρ_0 the central density, and R_c the core radius of the halo. This model is thus characterised by its constant density $\rho \sim \rho_0$ for $R \to 0$, and is usually referred as the "cored" density distribution. For $R >> 0$, such distribution implies $\rho \propto R^{-2}$, and the asymptotic velocity agrees well with the rise or flatness of rotation curves. An important point to note here is that the DM mass profile accounts for both non-baryonic and baryonic hidden matter.

Another model of DM distribution is that inferred from cosmological simulations. The ΛCDM model has great success to explain the large-scale structures of the Universe. In the numerical simulations, the shape of DM profiles is seen independent on the halo mass (i.e. "universal", from the smallest to the largest cosmological scales), and given by the so-called Navarro-Frenk-White profile (Navarro et al. 1996, 1997):

$$\rho_{\mathrm{NFW}}(R) = \frac{\rho_i}{(R/R_S)(1+R/R_S)^2} \tag{1.3}$$

with ρ_i a scale density proportional to the critical density for closure of the Universe, and R_S, the scale radius of the halo. The NFW profile is thus cuspy in the halo central regions ($\rho \propto R^{-1}$).

The difference between the cuspy inner DM density predicted by simulations, and the observed cored DM halos is known as the cusp-core controversy. It represents a major challenge for the ΛCDM model. For detailed reviews about this discrepancy, see de Blok (2010) and Bosma (2017). To explain the controversy, it has been proposed that the process of feedback from strong SN events could suppress part of the central cusp, turning it into cored DM distributions, as found in cosmological simulations combined with hydrodynamics of gas, and star formation (Governato et al. 2010, 2012). This result seems to depend strongly on the way feedback and star formation are implemented in the simulations, however, and is not seen in other cosmological simulations (e.g. Oman et al. 2019).

In observations, one of the key point to fit the structure of DM halos is the accuracy on the inner rising part of rotation curves (Blais-Ouellette et al. 2001). The inner disk regions are subject to the beam smearing effect. Due to the limiting size of the synthesized beam in radio interferometry (or the seeing at optical and near-infrared frequencies), a galaxy cannot be observed with infinite angular resolution. Therefore, a radio beam mixes the signal arising from different regions in a galaxy. This can generate artificial changes in the shape of rotation curves, particularly in regions where velocity gradient are not negligible. Therefore, in the outer parts of galactic disks, as V_θ is roughly constant, the beam smearing effect is not so much an issue. However, this is no more the case in inner regions, and the smearing of signal from contiguous pixels in data cubes can severely bias velocity maps. In particular, the beam smearing effect tends to lower the inner slopes of rotation curves, and thus the results in mass models. This is the reason why it is recommended to perform mass distribution models from hybrid rotation curves, i.e those where V_θ is given by high-resolution optical kinematics of ionized gas in the inner disk, and lower resolution HI kinematics in outer regions. An example of results from the modeling of the mass distribution of a spiral galaxy with the ISO and NFW forms is shown in Fig. 1.1, where we show the difference between a pseudo-isothermal sphere model and a NFW model

(Korsaga et al. 2019).

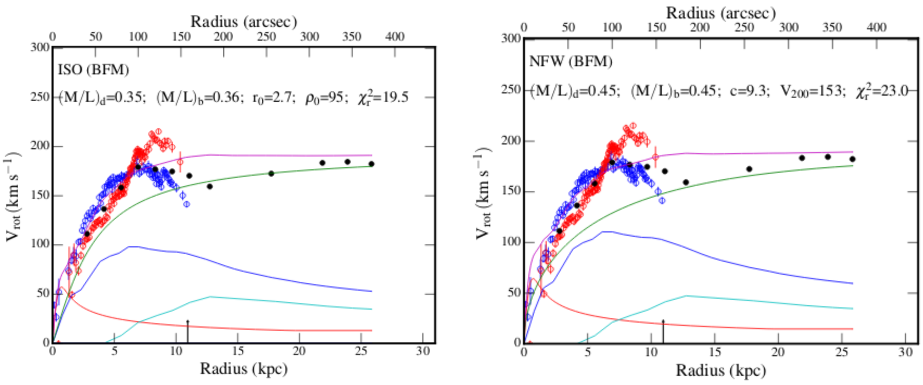

(a) ISO (b) NFW

Figure 1.1. – Mass modeling for UGC6537 in Korsaga et al. (2019). On the left, fit of the pseudo-isothermal sphere model and on the right the NFW model. Blue and red points represent respectively the approaching and receding sides of $H\alpha$ data and black points are the HI points. The disk is the dark blue curve, the bulge the red one, the light blue represents the gas component and the dark matter halo is in green.

1.3. HI observations with aperture synthesis interferometers

Let us go back in time for a moment, at the time of the first developments in radio astronomy, which today allow the observation of neutral gas with a spatial resolution which approaches that commonly used in optics. Radio astronomy started when Karl Jansky discovered the radio emission of the Milky Way in the early 1930s (Jansky 1933). This first discovery was followed by huge technological progress during Second World War which led to the first observation of the 21-cm emission line (the HI line) in 1951 Ewen & Purcell (1951). Atoms of Hydrogen are made of an electron orbiting around a proton. Orbits of the electron correspond to different energy states of the atom. At low temperature and low density, the probability density for the electron of being in the ground state is close to unity. In that ground state, there exists an hyperfine structure, depending on the spin of the proton and the electron. When both spins are parallel, the energy level is higher than when both spins are anti-parallel. Thus, when transiting from parallel to anti-parallel spins, the atom emits a photon with an energy of ≈ 5.87 μev, which corresponds to a wavelength of 21.106 cm, and a frequency of 1420 MHz. The intrinsic width of this line is small, thus the observed broadening is due to Doppler effects and the large scale motions of gas, allowing to measure the line-of-sight gas velocity and velocity dispersion through galaxies. Let's note here that the first mention of the 21-cm line came from a prediction made in 1945 (van de Hulst 1957), and the first measurement of its frequency in laboratory was made in 1947. The first radio observations were performed using a single antenna (Fig 1.2, Reber 1940, Appleton 1945).

The Rayleigh criterion gives the angular resolution $\theta_{\rm min}$ as a function of the wavelength λ and for a circular telescope of diameter D:

$$\theta_{\rm min} = 1.22\lambda/D \tag{1.4}$$

For a dish of 100 meter diameter, like the Green Bank Telescope, at 21 cm, the angular resolution is low, $\sim 9' \times 9'$. This type of observation is powerful to obtain accurate integrated HI profiles and mass estimates (e.g. Hindman et al. 1963), and for galaxies of angular size close to that of the beam size. To study with more details the HI distribution, one needs to observe galaxies with an angular size at least 2 or 3 times greater than the size of the beam. Nevertheless, to identify radio sources like quasars (e.g. Blandford & Königl 1979) or pulsars (Hewish et al. 1968), the angular resolution needs to be as close as possible as the one at optical wavelength (roughly $\approx 0.5''$ due to the perturbation of the atmosphere, on a good observing site, without any adaptive optics).

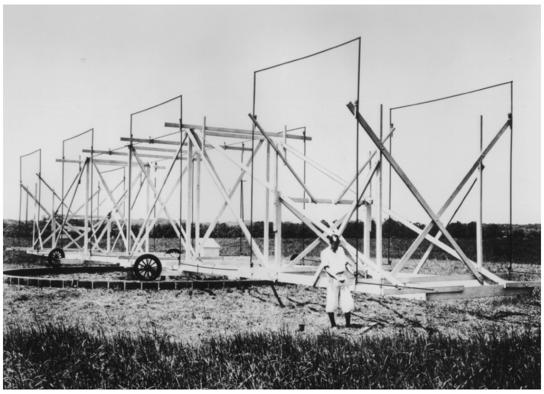

Figure 1.2. – Karl Jansky's antenna. Credit: NRAO/AUI/NSF

Such high resolution can be achieved by means of radio interferometry. For a detailed description of radio interferometry, see (Thompson et al. 2017). Since one antenna is not enough to obtain a high angular resolution, coherent observations using multiple radio receivers increase drastically the resolution, which is no more proportional to $1/D$, but to $1/B$, B being the baseline, i.e. the maximum spacing between antennas. Another strong advantage of interferometry is the sensitivity increase. Since the noise received in different antennas is not correlated, the cross-correlation of the signal lowers the noise level. The first radio interferometer was built by Ryle in 1946, and observed the signal emitted by the Sun Ryle & Vonberg (1946). In the 1960s, the first images of the Cambridge One-Mile telescope have shown a high level of details and features in the strong radio continuum sources Cassiopeia

A and Cygnus A (Ryle et al. 1965), and led to the development of large synthesis array observatories. In the early 1970s, a few interferometers were operational, like the Owens Valley Two-Element Interferometer (Rogstad & Shostak 1971), the Five Kilometers Radio Telescope in Cambridge (Ryle 1972), the Westerbork Synthesis Radio Telescope (WSRT) in the Netherlands (Baars et al. 1973), and later, the Very Large Array (VLA) in the state of New Mexico in USA (Thompson et al. 1980).

As we briefly mentioned, the first 21-cm observations were focused on the Milky Way (Muller & Oort 1951; Christiansen & Hindman 1952; van de Hulst et al. 1954; Muller & Westerhout 1957). All these observations led to the discovery and the confirmation of the presence of spiral arms in the outer part of the Milky Way. At the same time, in 1954, the first HI extragalactic sources were observed: the Magellanic Clouds (Kerr et al. 1954). Later with the development of instruments with better angular resolution, more and more galaxies were observed, and their HI distribution and kinematics mapped (Roberts 1967; Rogstad & Shostak 1972), thus showing flat HI rotation curves in outer regions of galactic disks (Bosma 1978; Faber & Gallagher 1979; Begeman 1987).

1.4. Anisotropies and asymmetries of galaxies HI distributions

Hydrogen is present in the interstellar medium in 3 different forms. In star forming regions, hot stars produces high energy photons which ionised the surrounding gas, creating HII regions. In those regions, observable in UV or in blue bands, the temperature is around 10^4K. In the coldest regions, the most present molecule is the molecular hydrogen H_2. Due to symmetries, this molecule has no dipole moments and is therefore hard to observe through infrared and radio observations. To probe this H_2 regions, the molecule CO is often used, because the ratio of CO luminosity and H_2 mass is supposed constant. Nevertheless, in the outermost part of galaxies, there are no CO anymore, and we can not probe the H_2 anymore. Finally, the last phase of the hydrogen in the interstellar medium is the neutral hydrogen HI , which is the topic of this thesis.

One of the most interesting property of HI distributions is the large extent of disks, generally at least twice the scale of stellar distributions, and which helped to probe more properly the DM halo. HI disks were also found to exhibit different geometries than stellar disks, with a distribution that can be twisted, bent, or warped (Sancisi 1976). Of course, signatures like spiral arms or bars, observed in the early 20's in optical, are also present in the neutral gas distribution.

Warps consist in a misalignment of the geometry of two parts of the disk. Due to projection effect, they can be observed directly in edge-on galaxies. Sancisi (1976) studied a sample of 5 edge-on galaxies and found significant deviations from a single plane in 4 of them. In Fig. 1.3 we present an example of an important warp in the galaxy NGC4013. In the inner part of the galaxy, the stellar disk and the HI disk have similar geometry, while at the end of the stellar distribution, the HI distribution is bent. Warps are mainly observed in HI , and stellar disk rarely exhibits prominent warps more than few degrees (Reshetnikov & Combes 1999). Initially thought to be isolated events, observations have shown that warped HI distributions were actually frequent, as common as spiral arms (Kuijken & Garcia-Ruiz 2001). In a statistical study of warps Bosma (1981b) found that at least half of the galaxies are warped, and linked these warps with the core radii of the DM halo. García-Ruiz et al. (2002) confirmed that most of the galaxies are warped, at all morphological types and found that the richer the environment the larger and the more asymmetric the warp, similarly to what was observed for stellar disk in Reshetnikov & Combes (1998).

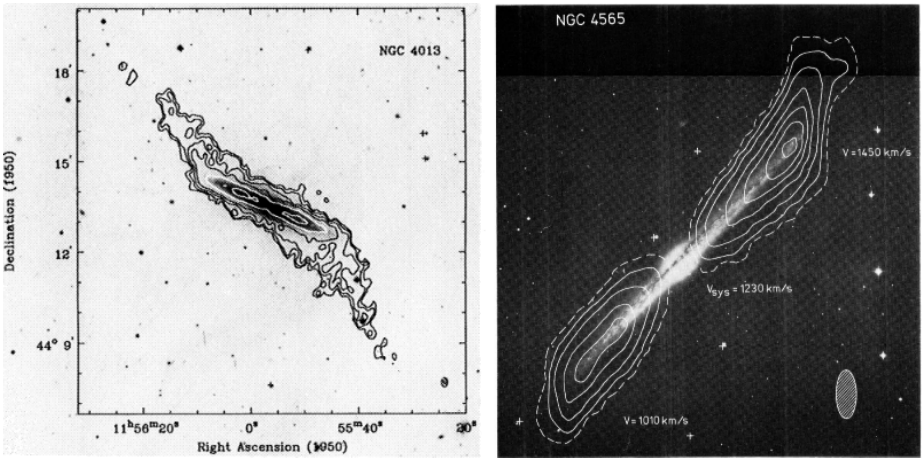

Figure 1.3. – Example of symmetric warp : HI map of NGC4013 superposed to the optical disk (white contours), published in Bottema (1996), left panel. Example of asymmetric warp : NGC4565 from Sancisi (1976), right panel.

Warps can be symmetric, such as in Fig. 1.3, left panel, but can also be asymmetric with only one side of the disk being warped (right panel). Indeed, asymmetries in the neutral hydrogen distribution are also very common (e.g. Baldwin et al. 1980) and understanding the sources of these asymmetries is crucial for galaxy evolution model and for dynamics. A proxy used to estimate the level of asymmetry in the HI distribution is the global profile of a galaxy. An asymmetric global profile is the result of large-scale asymmetries in the galaxy (Fig. 1.4). Richter & Sancisi (1994) studied a sample of 1700 HI integrated profiles of disc galaxies and concluded that more than 50% of galaxies have asymmetric neutral hydrogen distribution. Nevertheless the global profile of a galaxy is determined not only by the HI distribution but also by the disc kinematic, and establishing a link between those is not straightforward. Indeed, by comparing asymmetries in the morphology and kinematics of nine spiral galaxies, Kornreich et al. (2000) found no correlation between the morphological lopsidedness and the kinematic one. The term lopsidedness was used for the first time in Baldwin et al. (1980), and is used to describe a galaxy for which the spatial distribution is non-axisymmetric and displays a global mode m = 1 (Jog & Combes 2009). This lopsidedness is also present in the stellar disc, and systematic studies of Rix & Zaritsky (1995) and Zaritsky & Rix (1997) have shown that at least 30% of stellar discs are significantly lopsided.

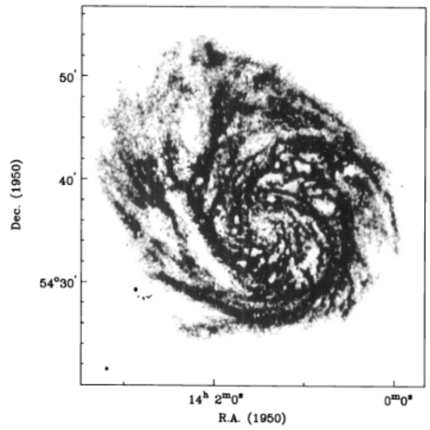

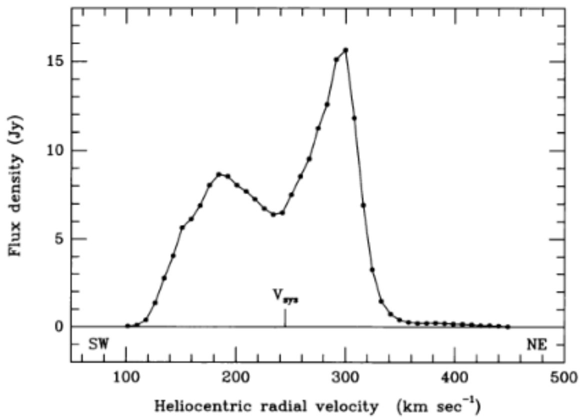

Figure 1.4. – Example of lopsidedness : galaxy M101, HI map at 23" x 29" resolution (left) and the corresponding integrated HI profile (right). Images adapted from Kamphuis (1993)

.

To probe asymmetries described above, a frequently used technique is the Fourier decomposition. This method was used early to study spiral arms (Kalnajs 1975; Considere & Athanassoula 1982) and bars (Ohta et al. 1990; Aguerri et al. 1998), which are typical of a mode m = 2 due to their bisymmetric pattern. Through a Fourier analysis of the surface brightness distribution, Rix & Zaritsky (1995) and Zaritsky & Rix (1997) characterised lopsidedness using the ratio A_1/A_0 of the first and zeroth order amplitudes respectively. Various applications exists such as the determination of spiral pitch angle (Davis et al. 2012), the study of bars strength (Garcia-Gómez et al. 2017), or the evaluation of non-circular motion in velocity fields (Trachternach et al. 2008).

My goal in this thesis is to go beyond the study of the surface brightness map or velocity map and to study the velocity dispersion of the neutral gas component of galaxies. The velocity dispersion, i.e. the random motions of gas particles, is a crucial point for many studies. For instance, in a previous part we described DM halos as spherical object, but in reality they are not perfectly spherical, and thus it is possible to define a flattening parameter for the halo. This flattening parameter is linked with the vertical velocity dispersion of the gaseous disk, and therefore studying the velocity dispersion allows to probe the DM halo shape (O'Brien et al. 2010; Olling 1995). Besides, asymmetric drift is a phenomenon that occurs when the mean tangential velocity of the particles is lower than the circular velocity at this radius. This asymmetric drift is linked with the radial velocity dispersion. A better knowledge of the velocity dispersion would led to a better understanding of radial flows in disks.

1.5. Velocity dispersion anisotropies and asymmetries

Due to degeneracies, it is hard to deproject the observed velocity dispersion into a vertical, a radial and a tangential velocity dispersion. Therefore, an hypothesis of isotropy is often assumed, implying that all the components mentioned above are considered equal. Is this hypothesis valid ? We clearly see that the vertical velocity dispersion and the radial one are linked with dynamical processes that are different, and therefore the equality of those component is not obvious. Furthermore, the presence of asymmetries change the local dynamic and affects the random motions of the neutral gas.

Due to the lack of spatial resolution, systematic study of asymmetries and anisotropies in the dispersion maps have not been performed yet. Only one galaxy was studied, M33 by Chemin et al. (2020) using Fourier decomposition. They found an important mode m = 2 with an angle phase aligned with the minor axis of M33, a signal which is expected in the case of an anisotropic velocity dispersion. Such anisotropy is also observed in numerical simulations of galaxies (Agertz et al. 2009; Kretschmer et al. 2020).

In this thesis we will focus on asymmetries and anisotropies in the cold gas component of spiral galaxies. Since each galaxy underwent its own evolution in its unique surroundings, a systematic study of asymmetry and anisotropy requires a large number of galaxies, to add statistical information to the result and to avoid bias due atypical galaxies. On the other hand, studying the velocity dispersion of the neutral gas is new, and therefore a special care is needed to understand its modeling. Therefore, using galaxies observed at high resolution, for which geometrical modeling already exists is necessary. For this purpose we use two distinct but complementary HI samples available from the literature and the archives : a first one called THINGS characterised by the high spatial resolution of the observation (150 to 800 pc) for a sample of 34 galaxies and a second one refereed as WHISP with a larger number of galaxies but a lower spatial resolution. Those two samples, as well as their optical counterpart are described in detail in the first chapter of the thesis.

In the second chapter, we present a new method to analyse data for the WHISP sample, in order to extract rotation curves, density profiles, and to study the lopsidedness for the sample. For this purpose, we perform a tilted-ring model analysis of the sample WHISP that contains more than 300 galaxies to recompute the rotation curves of the WHISP sample directly from the data-cube and not from the velocity fields. To achieve this goal, we use a recent tool, ^{3D}Barolo, which fits tilted-ring model on data-cube directly, allowing to account for the beam smearing effect.

In the next three chapters, we start the study of the anisotropies and asymmetries of velocity dispersion maps of a sample of 15 galaxies from the THINGS sample to which we add, in a second step, a subsample of WHISP.
In chapter 3, a mathematical introduction is presented, to describe the framework and the goals of this study. In particular, we introduce notions that are necessary to present the different case scenario of isotropy/anisotropy and symmetry/asymmetry. In a second step, we discuss the general methodology for the study and highlight the biases that can affect our study, whether they are physical or technical.

Chapter 4 is devoted to the anisotropy study of our sample. We describe the physical motivations and the specific methodology used in the case of a symmetric and anisotropic model. After presenting the results of this study, we test the limits due to spatial resolutions, in order to increase the number of galaxies using galaxies from the WHISP sample.

Finally in chapter 5 we present the asymmetry study of the HI velocity dispersion maps, using various methodology to avoid bias inherent to each methods. Finding a systematic behaviour of asymmetries could be a strong evidence for the presence of anisotropy of the random motion of the gas. In a first time we present the results for the THINGS data, and in a second time we present the result using a combination of galaxies from THINGS and WHISP to have more statistics. Finally, an extensive discussion about the influence of beam smearing on the results is presented.

Last, Chapter 6 presents the conclusions and perspective of my PhD thesis work.

2. Samples

Sommaire

2.1 WHISP 27
2.1.1 Motivations for large HI surveys 27
2.1.2 Sample properties 28
2.1.3 Definition of the working sample 29
2.1.4 Important results obtained with WHISP data 32
2.1.5 $H\alpha$ follow-up of WHISP : GHASP 34
2.1.5.1 Motivations for the GHASP survey 35
2.1.5.2 Sample properties 35
2.1.5.3 Observational status 35
2.2 THINGS 36
2.2.1 Motivations for a high-resolution HI survey 36
2.2.2 Sample properties 36
2.2.3 Important results obtained with THINGS data 36
2.2.4 Definition of the working sample 38
2.2.5 $H\alpha$ follow-up of the SINGS survey 38
2.3 Connecting samples 39

The main objective of this chapter is to present the different samples used in this thesis. We describe the purpose of each survey, the targets as well as technical information linked to the observations. We also highlight the main scientific results obtained with these datasets. In a final part, we underline the scientific complementarity of these data, and introduce briefly the studies performed in later chapters.

2.1. WHISP

2.1.1. Motivations for large HI surveys

At the end of the 70s and the early 1980's, studies of physical properties of the HI gas in galaxies were based on small samples (basically, less than ten galaxies, see e.g. Bosma 1978; Sancisi 1976; Bosma 1981a,b). Therefore, the need of larger HI samples spanning different morphologies, luminosities, and environments gave birth to the Westerbork HI Survey of Spiral and Irregular Galaxies (WHISP) (Kamphuis et al. 1996; van der Hulst et al. 2001). The aim of this survey was to map the HI emission in 500 to

1000 spiral and irregular galaxies, making it possible to perform statistical studies on a scale larger than in previous works, in order to address particularly two scientific objectives. A first goal was the study of the properties of the HI gas in galaxies : content, distribution, kinematics, asymmetries and perturbations (such as lopsidedness, warps or extraplanar structures). As the kinematics of the HI gas is a tracer of the gravitational potential of galaxies, a second immediate goal of WHISP was to provide the necessary material to studies of galactic dynamics, mass distribution models, and structure of dark matter haloes, through HI mass surface density profiles and rotation curves.

2.1.2. Sample properties

Observations were done at the Westerbork Synthesis Radio Telescope (WSRT) from 1992 to 2005. Galaxies were selected from the UGC catalogue (Nilson 1973). The WSRT is an East-West (E-W) array of 14 steerable antennas, located in Westerbork, Netherlands. The duration of an observation is 12h to have a full coverage of the uv plane (Thompson et al. 2017). To avoid synthesized beams with a too prominent elliptical shape, as well as images of lower quality, WHISP selected targets at declination larger than at 20°. Indeed the angular resolution in declination varies with the position on the sky and scales as $\frac{1}{\sin\delta}$ (Hogbom & Brouw 1974). In order to ensure sufficient linear resolution and resolve features in the moment maps, WHISP also adopted 1.5′ as lower limit for the length of the photometric major axis of galaxies (in the blue band). Finally, as last criterion, WHISP only focuses on galaxies with HI flux densities greater than 100 mJy, in order to provide data with sufficient signal-to-noise ratio. As the HI content depends on the morphological type, the early WHISP observations, those between 1992 and 1998, were biased towards gas-rich galaxies (i.e types mostly later than Sc galaxies). Due to a sensitivity improvement of a factor 2 of the WSRT in 1998, which allowed to observe fainter galaxies, the main targets of observations were chosen to be earlier types than Sc in order to have a more uniform distribution of galaxies versus the morphological types.

Observational data are reduced through a pipeline available on the WHISP homepage (http://www.astro.rug.nl/~whisp). The first step is to calibrate and flag the raw uv data, in order to create fits maps at three different resolutions (full, 30" and 60") and antenna patterns for each data-cube. The second step is the cleaning of these raw maps, which consists in subtracting the continuum by fitting a first order polynomial to the channel maps without HI emission, masking the regions with HI emission on Hanning-smoothed data at 60", and cleaning the data using the masks. Cleaned data are thus used again to refine the masks. The final mask is used for the three different resolutions.

This pipeline produces data cubes at 3 different resolutions : full resolution with a 14" × 14"/ sin(δ) beam size, where δ is the galaxy declination, 30" × 30", and 60" × 60" beams. Beam shape will be discussed in detail in the next section. HI flux densities are given in Westerbork Unit (W.U.), with 1 W.U. = 5 mJy/beam. The pixel scale is equal to about one third of the spatial resolution (i.e 20"/pixel for 60", 10"/pixel for 30" and

5"/pixel for the full resolution). For more details about the observations and reduction techniques, see van der Hulst et al. (2001) and Swaters et al. (2002). All the data are available for download on the website http://wow.astron.nl/

2.1.3. Definition of the working sample

The catalog of observed galaxies that is available on the WHISP homepage contains 383 entries. As WHISP galaxies were selected from the UGC catalogue, they are listed by their UGC number. Among the 375 galaxies with reduced data, about 40 of them are referred as being galactic companions, with no UGC number. Thus, the main WHISP galaxy sample is made of 342 galaxies. Furthermore, not all galaxies have referenced WSRT data, therefore a first step was to identify individually the data cube in which a galaxy appears. Since the data cubes are named using the main observation target, finding the corresponding data cube for a given galaxy is not straightforward. I started the process to identify one-by-one every galaxy from their equatorial coordinates. After this primary step, I have identified data for ~ 300 galaxies. The data for the remaining ~ 40 galaxies were missing, either because the cubes were not available in the WHISP database, or that we had cubes at one resolution only, or that there were some issues with the retrieved FITS files. Pr. Van der Hulst from Kapteyn Institute, who I warmly thank, was able to recover some of the missing data cubes. Other data were nevertheless unfortunately considered as lost. In the end, the working sample for my PhD is made of 313 galaxies from the original WHISP list. In Fig. 2.1 we show the distribution of our sample galaxies over different parameters : morphological type, systemic velocity, absolute $B-$band magnitude, inclination and characteristic optical diameter ($\log D_{25}$). A table listing physical and observational properties for each galaxy is given in Appendix 1.

General properties of the defined sample

The survey aimed at observing spiral and irregular galaxies. In my sample, the number of spiral galaxies presents a uniform distribution between 0 (S0a) and 8 (Sdm), with an excess of Sc galaxies. Irregular galaxies represent ≈ 25% of the total number of galaxies in the sample. We used the systemic velocity of galaxies as a proxy of their distance D, from the Hubble relation $V_{sys} = H_0 D$, assuming a Hubble constant $H_0 = 70$ km/s/Mpc. Top right panel of Fig. 2.1 indicates that 2/3 of galaxies of the sample have a distance lower than 30 Mpc, thus that 1/3 are located beyond 30 Mpc which corresponds to a systemic velocity of ~ 2000 km/s. At a distance of 30 Mpc, it implies that a FWHM beam resolution of 30" corresponds to a linear scale of 4.3 kpc. The galaxies span a broad range of absolute $B-$magnitude, from −12 to −23, with a distribution centered on −20. We observe a relatively low number of galaxies with a low inclination (< 30°). Most of galaxies have typical inclinations between 50° and 70°, and ~ 20% of them are more inclined than ~ 80°. Finally, for the optical galaxy sizes, we observe a wide distribution, with a scaling factor of 100 between the smallest and the largest ones.

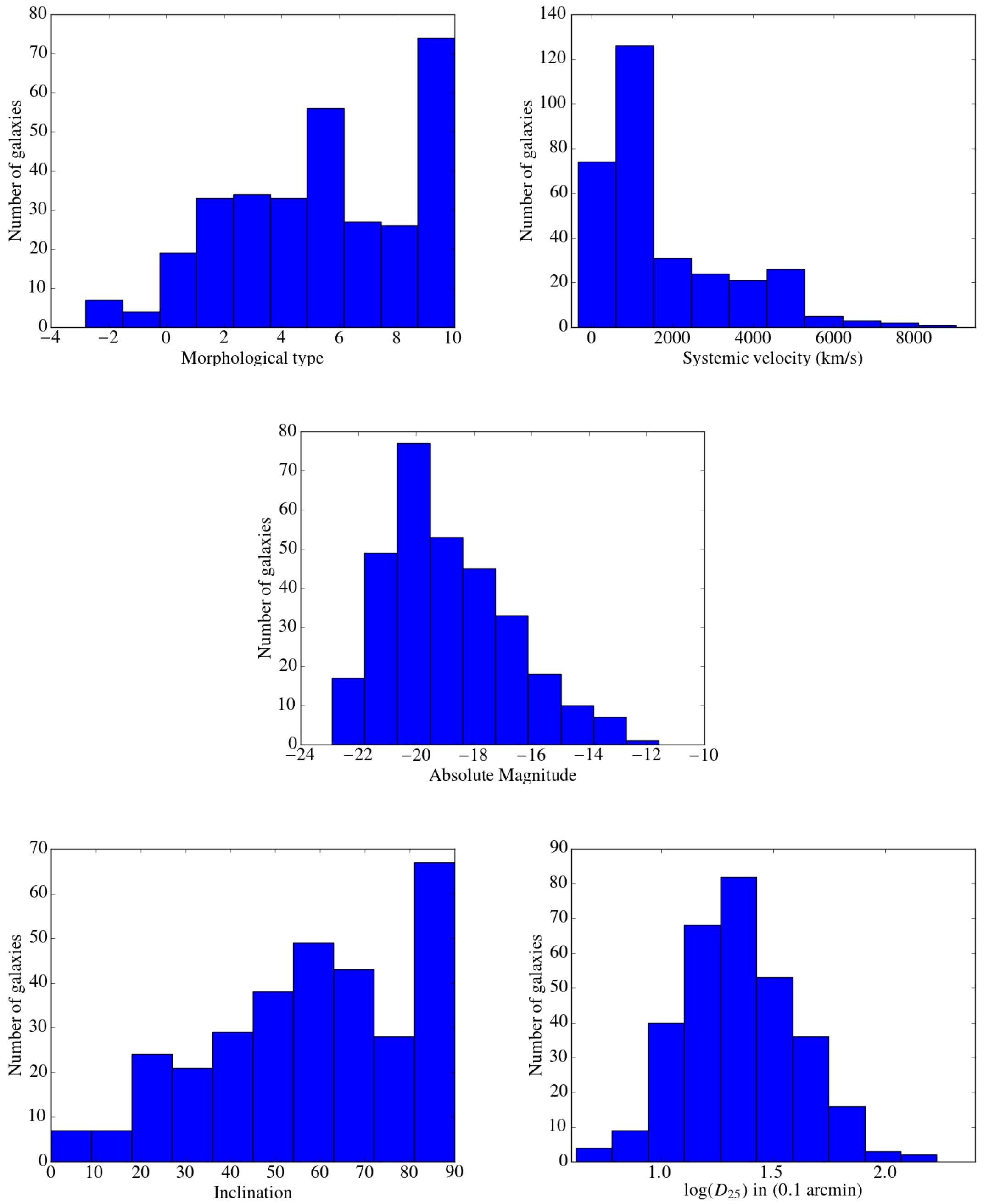

FIGURE 2.1. – Characteristic of the sample of 313 galaxies from the WHISP survey used in this thesis.

On the beam shape parameters in the data cubes

Another information that is crucial for the work presented in this thesis is the synthesized beam shape. This is provided in FITS files header with keywords : Bmin, Bmaj and Bpa, which indicate respectively the minor and major axis half power beam width (HPBW) of the beam which is supposed to be elliptical, and the position angle of its major axis. For ≈ 50 galaxies (observed before 1995), these informations were missing in the data cubes at 30" and 60" resolution. The full resolution beam was always given in the WHISP homepage. I performed a study to understand how changes the beam from the full resolution to lower resolution for galaxies for which this information was available, in order to extrapolate to galaxies without this information. The main parameters investigated were the declination of the object, the date of the observation, and the shape of the beam.

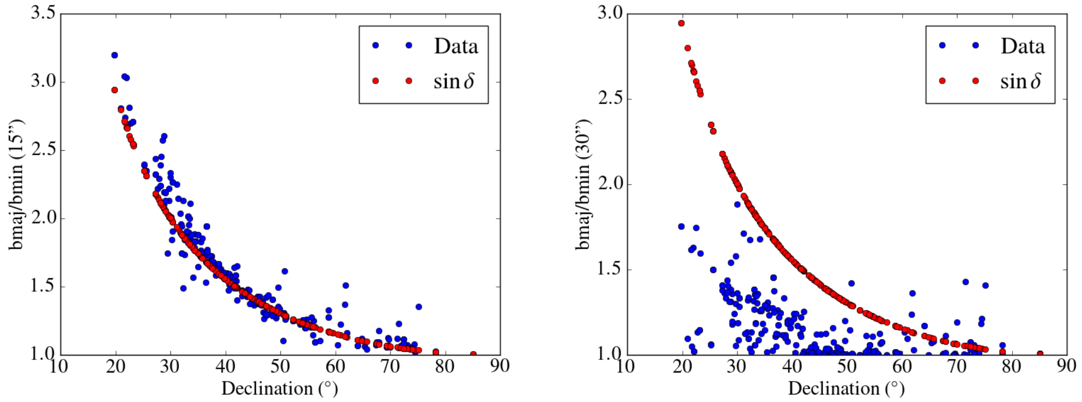

FIGURE 2.2. – Beam ratio Bmaj/Bmin vs declination at full resolution (left panel) and 30" resolution (right panel). Beam shape information is shown with blue symbols, and the inverse of the sine of the declination with red symbols.

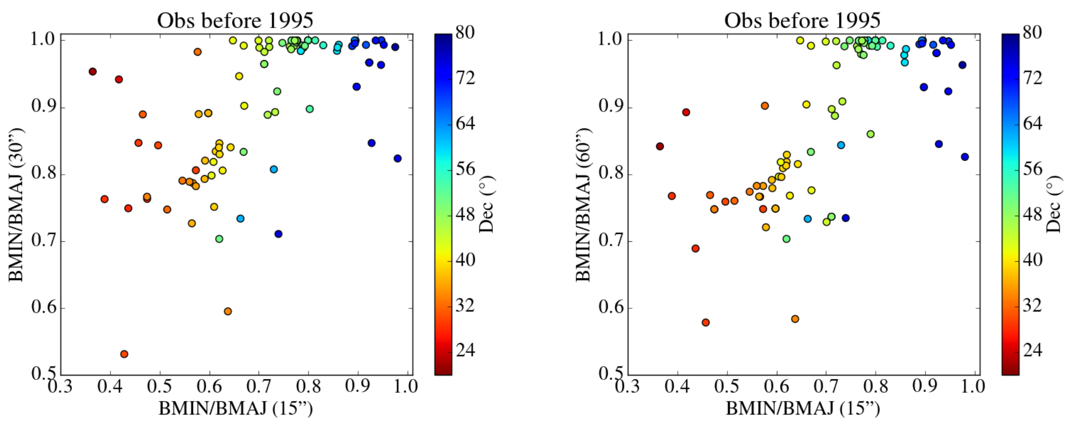

FIGURE 2.3. – Beam ratio Bmin/Bmaj at 30" (left) and 60"(right) vs beam ratio full resolution for a subsample consisting in galaxies observed before 1995. The color code indicates the declination of each object.

In Fig. 2.2, we show the ratio Bmaj/Bmin as a function of the declination of the galaxy, at full resolution 15" (left panel) and at 30" resolution (right panel). As we mentioned earlier, the EW configuration of the WSRT implies that the resolution in declination depends on the sky position and varies as $1/\sin\delta$. We thus overplot this scaling relation (red symbols). For the full resolution we observe that the beam ratio is matching the red curve perfectly, while at lower resolution the variation of the axis ratio of the beam with the declination is no longer observed, and with smaller Bmaj/Bmin than at full resolution.

Figure 2.3 shows the beam axis ratio Bmin/Bmaj at low resolution (30" and 60" in the left and right panels, respectively) as a function of the beam axis ratio at full resolution, but only for galaxies that were observed before 1995 and for which the beam parameters were available. Both plots are really similar. A general result is that for galaxies with declination $\delta \gtrsim 45°$, the beam at 30" and 60" is roundish in most cases. At lower declination, full resolution beams are very elliptical (with ratio Bmin/Bmaj spanning from 0.4 to 0.6), and lower resolution beam are not perfectly circular. It appeared that the weighting function applied to the visibilities at resolutions of 30" and 60" were done with a HPBW as close as possible to 30" and 60". In practice, this leads to beams that are almost round, with a beam area that is only within a few percent different from a perfectly circular beam (Pr. van der Hulst, private communication). This beam shape “circularization” is easier to perform when the initial beam is already almost circular (i.e. for galaxies at high declination). Pr. Van der Hulst kindly gave us the beam parameters for galaxies which were missing them.

2.1.4. Important results obtained with WHISP data

Various studies have been published from WHISP observations. I give here a brief overview of some of published results, by focusing on papers of interest for this thesis.

First of all, the kinematics of late-type dwarf galaxies was studied, yielding integrated and radially dependent properties (HI mass, surface density profiles) for 73 galaxies (Swaters et al. 2002), and rotation curves for 62 galaxies (Swaters et al. 2009). In the first article, the author measured the extent of the HI disc, and compared it to the optical one, and found a ratio 1.8 ± 0.8. This ratio is similar to values found for late-type spirals, though with a larger scatter. Most dwarf discs in their sample are gas rich, which corresponds to a ratio of the gas mass to $B-$band luminosity of $M_{HI}/L_B \sim 1.5$. They also observed that dwarf galaxy discs are lopsided and asymmetric, with half of the sample showing asymmetric global HI profiles, one third showing a lopsided spatial distribution of gas, and half having signatures of kinematic lopsidedness. In the second article, the authors adopted a new procedure to analyse the data, taking the effect of the beam smearing into account. After several comparisons with $H\alpha$ data to justify their methodology, these authors found similarities in the shape of rotation curves between late-type spirals and late-type dwarf galaxies, with a solid-body rotation in the inner part and a constant velocity in the outer part. More importantly, they deduced that the shape of the rotation curves does not depend on morphology and luminosity for galaxies fainter than $B = -19$ mag. Finally, they observed another similarity with spiral galaxies : the more concentrated the light in the center, the steeper the rotation curve rise in the inner region of discs. This implies that the baryonic mass still dominates in the central part of these galaxies.

A similar analysis was done for early morphological types of discs (from S0 to Sab) in Noordermeer et al. (2005) (68 galaxies), though without measuring the rotation curves. These authors measured similar extent of the HI disc compared to the optical one than in late-type disc galaxies. They also observed that the early-type discs with regular rotating discs all present a central hole in the HI distribution. Some of the galaxies exhibit a ring like structure, associated with an enhanced star formation. However, they also found that the HI density is too low to account for the enhanced star formation, implying that the mechanism responsible for the star formation at low densities remains to be identified in these galaxies. Finally, asymmetries and lopsidedness are often linked with interactions, accretions or mergers.

Another scientific interest of WHISP was the study of the physical properties of HI discs such as warps (García-Ruiz et al. 2002), and lopsidedness (van Eymeren et al. 2011a,b). García-Ruiz et al. (2002) performed a study on 26 edge-on galaxies from WHISP using HI and optical R-band data to study the HI disc morphologies. They found that 20 of the 26 galaxies are warped, and that all the galaxies with HI disc more extended than the optical disc are warped. Most of the warps are asymmetric, with amplitudes and shapes varying significantly within their sample, as well as from one side of discs to the other side. Galaxies in rich environment tend to exhibit larger and more asymmetric warps.

Then, van Eymeren et al. (2011a) and van Eymeren et al. (2011b) performed respectively a kinematical and a morphological analysis of the disc lopsidedness in 70 WHISP galaxies. For the kinematical analysis, these authors performed a tilted-ring analysis to obtain rotation curves, and compared the rotation curves from both disc halves. From the shapes of the curves of the two disc sides, they observed that the behaviour of both sides could be described into 5 different categories : symmetric (same behaviour for both sides), globally distorted (constant offset between both sides), locally distorted (same behaviour in the central region and large deviation in the outer part, and vice-versa), and distorted (two distincts behaviour and curves are crossing). In the second paper, the authors performed an harmonic decomposition of the surface density maps. They measured the ratio of the amplitude A_1 of the first order harmonics (lopsidedness) to A_0, the amplitude of the 0^{th} order (axisymmetric term), and found that, on average, $A_1/A_0 = 0.1$ in the optical disc, with a constant phase angle as a function of radius. This result tends to show that the lopsidedness is a common mode to the HI discs. In most galaxies, A_1 increases with radius, but also shows small-scales fluctuation which are thought to be due to swing amplification. Finally, early type galaxies are more lopsided than later ones, and no correlation was found between lopsidedness and the strength of interactions.

WHISP has been used to address questions about the environment of galaxies, and gas accretion from mergers. For example, Di Teodoro & Fraternali (2014) compared the star formation rate from IR data (1.29 $M_{\odot}\text{yr}^{-1}$) with an estimation of the maximum gas accretion from satellites galaxies (0.28 $M_{\odot}\text{yr}^{-1}$), finding that minor mergers can not sustain the process of star formation in spiral discs. In order to find correlations between the accretion rate and star formation processes, Yim & van der Hulst (2016) investigated the Kennicutt–Schmidt law in different types of galaxies to probe different environments : symmetric (quiescent galaxies), asymmetric (accreting) and interacting (tidally disturbed). They observed the confirmation of the link between the gas surface density and the star formation rate surface density. Interestingly, these authors did not observe significant differences between the three groups defined above.

Murugeshan et al. (2020) studied the relation between angular momentum, environment, star formation and morphology for 114 WHISP galaxies. They found an unbroken power-law between the specific angular momentum (j_b) and the baryonic mass (M_b) : $j_b \propto M_b^{0.55\pm0.02}$. They also studied the relation between the atomic gas fraction f_{atm} and the integrated atomic stability parameter q for galaxies with and without close neighbours. They showed that galaxies without close neighbours follow tightly the model prediction with an intrinsic scatter of 0.13 dex while galaxies with neighbours have a larger dispersion of 0.22 dex. This larger scatter is associated with past or present interactions of galaxies, and these galaxies exhibit higher star formation rates than galaxies without close neighbours. Finally, by using the bulge to total ratio (B/T) as a proxy of morphology, they found a relation between the atomic gas mass, the disc stability and the morphology, showing that galaxies with low q and f_{atm} tend to have higher B/T.

In chapter 3, I will focus on a new procedure to extract rotation curves from the data cubes of the WHISP sample, allowing to take the beam smearing effect into account. There are two main goals to perform this new analysis : firstly, obtain rotation curves which are not biased by instrumental effect to perform mass modeling similarly to Korsaga et al. (2019) with larger samples, secondly use these rotation curves to study the kinematic lopsidedness, by comparing the rotation curves from the approaching and receding sides. As I mentioned above, since all studies were based on small subsamples of WHISP, following methods that are not necessarily the same, an important objective of my work has been to perform a homogeneous analysis of the whole WHISP sample, following an improved methodology which takes into account the beam smearing effect (see section 2.1.5), providing less biased and updated mass density profiles and rotation curves.

2.1.5. $H\alpha$ follow-up of WHISP : GHASP

In the next chapters I will use the GHASP sample, a $H\alpha$ survey of galaxies, to model the beam smearing of WHISP galaxies. Furthermore, combining $H\alpha$ and HI data in mass modeling is of great importance to obtain robust results for the fit of DM halos. I also actively participated in the observations of targets from the WHISP sample.

2.1.5.1. Motivations for the GHASP survey

The Gassendi $H\alpha$ survey of SPirals (GHASP) is a project started in 1998 at Observatoire de Haute Provence (OHP), with a goal to study $H\alpha$ velocities in nearby spiral galaxies using Fabry-Perot interferometer (Garrido et al. 2002). At this time, large samples had been observed in $H\alpha$ (from few hundred to a thousand galaxies), but mostly with a slit spectroscopy technique, for rotation curves analysis. One of the main point of GHASP was to provide a large sample of 2D velocity fields. The first paper (Garrido et al. 2002) initially contained 23 galaxies, and in a series of paper the number increased to 203 galaxies (Garrido et al. 2003, 2004, 2005; Epinat et al. 2008a,b). A new data reduction procedure using adaptive binning techniques based on Voronoi tessellations was presented in Epinat et al. (2008a) to have an homogeneous reduction for the entire sample. Some of the key science questions to address with this survey are the following : study of kinematics in different environments, mass distribution models and structure of dark matter halos (Spano et al. 2008; Korsaga et al. 2019), modeling of non axisymmetric motion, derivation of the local Tully-Fisher relation (Torres-Flores et al. 2010), and study of relations between kinematic parameters of $H\alpha$ and physical properties such as the star formation rate.

2.1.5.2. Sample properties

As it was last published in Epinat et al. (2008a), the GHASP sample consisted in 203 nearby spiral galaxies. Those galaxies were selected from the initial WHISP target list, in order to have for each galaxy the $H\alpha$ and the HI kinematics. Nevertheless, not all galaxies have been observed from WHISP, leaving only ≈ 130 galaxies in common between both samples. Observations were performed at OHP on the 193cm telescope, with a Fabry-Perot interferometer and a 512 × 512 Imaging Photon Counting System (IPCS) with a pixel size of 0.68 arcsec, a field-of-view (FoV) of 5.8 arcmin^2. The angular resolution of the data is limited by the seeing at OHP, between 1.5 and 3 arcsec. The spectral resolution is ∼ 30 km/s (FWHM). The typical duration of an observation is 2 hours.

2.1.5.3. Observational status

In the last few years, Gómez-López et al. (2019) used the GHASP instrument to observe galaxies from the Hershel Reference Survey (HRS, Boselli et al. 2010)). 152 galaxies have been observed in 91 nights between February 2016 and April 2018 (Gómez-López et al. 2019). During these observing nights, when no HRS targets was observable, galaxies from the WHISP sample were then targeted, such that more than 50 galaxies were observed at this epoch. I took part in the observation run of 2018 for 15 nights. Later during autumn 2019 we had another observing time allocated at the OHP during which 15 galaxies were observed. Another observing session was planned in march 2020, which was supposed to take place during the week in which the lockdown has been established. The next observing run will take place during winter 2021. Observations performed since 2016 enhanced the common sample of WHISP and GHASP to around 200 galaxies. About 100 WHISP galaxies then remain to be observed.

2.2. THINGS

2.2.1. Motivations for a high-resolution HI survey

The goal of The HI Nearby Galaxy Survey (THINGS, Walter et al. 2008) was to map the atomic gas ISM in nearby galaxies at high resolution. The main scientific goal was to study the links between HI gas and dust, since THINGS is a complement to a NIR galaxy survey made with the Spitzer satellite, HI gas and star formation, the modeling of the mass distribution and the structure of dark matter halos. For this latter point, it is indeed crucial to observe the inner parts of rotation curves at high resolution to be able to discriminate between cuspy and core-dominated mass profiles.

2.2.2. Sample properties

Observations were realised with the Very Large Array (VLA) of the National Radio Astronomy Observatory. Targets were mostly selected from the Spitzer Infrared Nearby Galaxy Survey (SINGS, Kennicutt et al. 2003), an infrared imaging and spectroscopic survey of 75 galaxies. Distances for these galaxies are between 2 and 15 Mpc. At the angular resolution ~ 10", it corresponds linear resolutions between 150 and 800 pc. THINGS is the only survey to date made at such resolution for a few tens of galaxies. The resolution is close to the native data from the Spitzer Space Telescope at 24 µm (≈ 6") and GALEX in the near UV (≈ 5"), which is interesting for multi-wavelength studies.

THINGS contains 34 galaxies spanning different properties such as the morphological type, the star formation rate, and gas metallicity. It nonetheless does not contain early-type galaxies (E/S0, owing to expected extremely low HI densities in those systems), and edge-on discs (to avoid important projection effects). Observations are reduced following the procedure described in Walter et al. (2008). Outputs for each galaxy consist in a masked, flux re-scaled data cube, with 3 moment maps for the integrated HI emission (0th moment), line-of-sight velocity (1st moment) and velocity dispersion (2nd moment). The data are available in free access on `https://www2.mpia-hd.mpg.de/THINGS/Data.html`.

2.2.3. Important results obtained with THINGS data

In the same way as for the WHISP sample, I highlight some of scientific results obtained with THINGS data, focusing particularly on studies about the HI velocity dispersion, which is another main topic in this thesis.

de Blok et al. (2008) presented rotation curves and mass models for 19 of the 34 galaxies, as inferred from the tilted-ring model analysis. Non-circular motions in velocity fields were corrected following a method introduced in Trachternach et al. (2008). They did not observe steep declines of rotation curves. For some galaxies with curves previously identified as declining, the improvement in the PA and inclination trends make this velocity compatible with a flat one within the uncertainties in the rotation curve. For the mass distribution modeling, they found that the stellar mass-to-light ratios as inferred from fitting the model $V_{obs}^2 = V_{gas}^2 + \Gamma_{star} V_{star}^2 + V_{halo}^2$ to rotation curves, compare fairly well with those predicted by stellar population synthesis. In higher luminosity galaxies ($M_B > -19$), they found the NFW and ISO models fitting equally well the rotation curves, while in fainter galaxies, fits were found much better with the ISO model than the NFW cusp.

A similar study was performed specifically with dwarf galaxies from THINGS. de Blok et al. (2008) presented a new methodology dedicated to dwarf galaxies to extract the observed velocity from the HI cube. They compared their methodology (called bulk velocity field) with classical ones (i.e. intensity weighted mean) and found that the bulk velocity minimises the effect of small-scale random motions, making it more robust for kinematic studies. Their sample consisted in two galaxies only, IC 2574 and NGC 2366, for which they derived rotation curves and performed mass modeling using Spitzer 3,6 µm data. They found that, assuming a fixed stellar mass-to-light ratio, the dark matter distribution in both galaxies are inconsistent with the cuspy dark matter profiles seen in cosmological simulations. With seven dwarf disks from THINGS, Oh et al. (2011b) found a similar result.

At the same period, some cosmological simulations including hydrodynamical processes and strong feedback from supernovae events led to a closer match between observations and simulations (Governato et al. 2010). This result was confirmed by comparing simulations and observations of galaxies from some of the THINGS galaxies of Governato et al. (2012) and Oh et al. (2011a).

THINGS data have also been used to study the velocity dispersion of the gaseous component in galactic disc. For 11 galaxies, Tamburro et al. (2009) investigated the main processes driving the dispersion (2^{nd} order moment maps derived from the THINGS data cubes). They observe declining dispersion with radius in all galaxies, with a dispersion of 10 ± 2 km/s at R_{25}, the optical disc size. Inside $R = R_{25}$, they found that the line width is mostly driven by to the star formation activity, while at larger radii, the thermal broadening of the disc, heated by UV sources, can explain the observed dispersion.

Ianjamasimanana et al. (2012) investigated the HI profiles of THINGS galaxies. By creating super profiles, (i.e. shuffling and stacking of individual profiles with a signal-to-noise ratio greater than 3), they showed that those profiles are better reproduced by a double component Gaussian profile than by one emission line. These two components correspond respectively to the cold neutral medium, with a mean value of 6.5 ± 1.5km/s and the warm neutral medium with a mean value of 16.8 ± 4.3km/s. Ianjamasimanana et al. (2015) continued their work by comparing the results of the single

Gaussian fits with the double Gaussian fits. They found that the velocity dispersion as derived by the single Gaussian decreases less strongly than when it is derived by the two narrow and broad components. The flux ratio between the narrow and the broad components is correlated with the gas metallicity, star formation rate, and color index FUV-NUV, which the authors interpreted as the cold HI component associated with star formation. Moreover, the velocity dispersion from the single Gaussian tends to be closer to the one of the broad component, which indicates that the warm neutral medium dominates at high radii. Finally, the velocity dispersion they measured is globally lower than the values seen in 2nd moment maps. The comparison of velocity dispersions measured from the moment methods and the single Gaussian fit is shown in the Appendix of Mogotsi et al. (2016).

2.2.4. Definition of the working sample

My goal is to perform an exploratory study of asymmetries and anisotropies of THINGS HI velocity dispersions. To make the study possible, I need to have robust constraints on the geometrical parameters of the galaxies, namely the inclination and the position angle of the discs. That is why in this thesis I will focus only on the THINGS subsample described in de Blok et al. (2008), which yield these parameters as a function of the galactocentric radius. This subsample results from a selection of galaxies with inclinations between 40° and 80°, and which are dominated by rotation. These criteria exclude small galaxies, interacting and disturbed galaxies. Additionally, in my work, I discarded dwarf galactic discs, which will be studied in a future work. From the initial sample of de Blok et al. (2008), the galaxies NGC 2366, DDO 154, IC 2574 and NGC 4826 were thus excluded. A summary of general properties of the 15 galaxies from my THINGS working subsample is given in Tab. 2.1.

2.2.5. $H\alpha$ follow-up of the SINGS survey

The SINGS survey was designed to characterise the infrared emission in various types of galaxies and environment, to improve the understanding of the connection between star formation and interstellar medium. Some ancillary observations at multiwavelenght (from UV to HI) were also planned to provide images. Nevertheless, no optical kinematic data were available, and to fill this void, Daigle et al. (2006) and Dicaire et al. (2008) observed and published $H\alpha$ data for respectively 28 and 37 galaxies from the SINGS sample. Those observations were realised with a Fabry-Perot interferometer mainly at the Observatoire du mont Megantic, with 1.6m telescope and also at the Canada-France-Hawaii Telescope (CFHT) and at La Silla on 3.6m telescope.

For our study, it's a chance to have an $H\alpha$ counterpart of the THINGS sample. We saw in the introduction the importance of having $H\alpha$ and HI data available for studies of the structure of dark matter halos. Here the THINGS resolution is already good, then rotation curves are marginally affected by the beam smearing. Nevertheless, in the study, we will focus on 2D maps, not on rotation curves. As I will explain in Section 4.4.1, studying the beam smearing on rotation curves tends to minimize its effect. Then, on 2D maps we need to take into account for the beam smearing effect, and the higher $H\alpha$ resolution are very helpful to achieve this objective.

Galaxy name	α(J2000) (hh mm ss)	δ(J2000) (dd mm ss)	D Mpc	$\log(D_{25})$ log(0.1')	m_B mag	M_B mag	Incl deg	Δv km/s
NGC 925	02 27 16.5	+33 34 44	9.2	2.03	9.77	-20.04	66	2.6
NGC 2403	07 36 51.1	+65 36 03	3.2	2.20	8.11	-19.43	63	5.2
NGC 2841	09 22 02.6	+50 58 35	14.1	1.84	9.54	-21.21	74	5.2
NGC 2903	09 32 10.1	+21 30 04	8.9	2.07	8.82	-20.93	65	5.2
NGC 2976	09 47 15.3	+67 55 00	3.6	1.86	9.98	-17.78	65	5.2
NGC 3031	09 55 33.1	+69 03 55	3.6	2.33	7.07	-20.73	59	2.6
NGC 3198	10 19 55.0	+45 32 59	13.8	1.81	9.95	-20.75	72	5.2
NGC 3521	11 05 48.6	-00 02 09	10.7	1.92	9.21	-20.94	73	5.2
NGC 3621	11 18 16.5	-32 48 51	6.6	1.99	9.06	-20.05	65	5.2
NGC 3627	11 20 15.0	+12 59 30	9.3	2.01	9.09	-20.74	62	5.2
NGC 4736	12 50 53.0	+41 07 13	4.7	1.89	8.54	-19.80	41	5.2
NGC 5055	13 15 49.2	+42 01 45	10.1	2.07	8.90	-21.12	59	5.2
NGC 6946	20 34 52.2	+60 09 14	5.9	2.06	8.24	-20.61	33	1.3
NGC 7331	22 37 04.1	+34 24 57	14.7	1.96	9.17	-21.67	76	5.2
NGC 7793	23 57 49.7	-32 35 28	3.9	2.02	9.17	-18.79	50	2.6

Tableau 2.1. – Subsample of THINGS data use in this thesis

2.3. Connecting samples

After this presentation of the samples used in this work, we want to underline how complementary are WHISP and THINGS to address the scientific questions which were the guidelines of this thesis.

The initial goal of the thesis was to assemble a large sample of galaxies combining both $H\alpha$ (GHASP) and HI (WHISP)data in order to perform optimal kinematics studies, with a high resolution in the inner parts thanks to $H\alpha$ data and at large radius thanks to the HI data. Such a sample could, for instance, enable to study the structure of dark matter halos through mass modeling, as in Korsaga et al. (2019) for which I contributed, but on a much larger number of spiral galaxies. In the same perspective, those data can be used to perform 2D mass modeling of galaxies (Chemin et al. 2016). Such a method has not been fully implemented yet, in practice it would consist in fitting the dark matter halo directly on the 2D velocity field rather than on the rotation curve. In order to have a robust and homogeneous analysis, the first step was to derive rotation curves and mass density profiles for the largest part of the WHISP sample. In the same time, $H\alpha$ observations were planned to increase the number of common galaxies between WHISP and GHASP. This part is presented in the Chapter 3.

The second part of the thesis consists in modeling HI gas velocity dispersion maps of nearby galaxies (Chapter 3). Following the evidence of strongly asymmetric velocity random motions of the HI gas in the Local Group disc Messier 33, as possible hint of anisotropy in the gas velocity ellipsoid (Chemin et al. 2020), we want to perform the same analysis, but on a larger sample of nearby galaxies, in order to test the validity of anisotropic gas velocity dispersions. The first guess was to use the WHISP sample to have the largest sample possible, in order to have statistical information over a broad range of physical parameters (morphological types, gas mass). But since spatial resolution appears to be a crucial issue for this study, due to beam smearing effects (see Sect. 4.4.1) we decided to investigate first the HI velocity dispersion maps of galaxies from the THINGS sample. Working with those high resolution data allowed us to establish a robust methodology. THINGS was also used to estimate the limits in terms of linear resolution at which this type of study becomes meaningless, in order to extend the sample with WHISP galaxies.

3. Revisiting the WHISP analysis

Sommaire

3.1 ^{3D}Barolo 42
  3.1.1 Description of the algorithm 44
  3.1.2 Methodology 45
  3.1.3 Checking results 46
3.2 Results and comparison with literature 47
3.3 Lopsidedness study 48
3.4 Mass distributions in nearby galaxies 51
  3.4.1 Outlines 51
  3.4.2 Correcting from distance effect 51
  3.4.3 Computing dark matter halo mass 53

The goal of this chapter is to present a new rotation curve study we performed on the WHISP sample. As we mentioned in Chapter 1, only few WHISP sub-samples have been published, and only two papers (Swaters et al. 2009), (van Eymeren et al. 2011a) were providing rotation curves, for 62 and 70 galaxies respectively. In van Eymeren et al. (2011a) these curves where obtained by performing a tilted-ring model on velocity fields. To start this chapter we will describe the extraction of a rotation curve using this methodology, and point out its limitation. In Swaters et al. (2009), authors adopted a strategy to take the beam effect into account with a 2 steps procedure. In the first step they obtain initial guesses on rotation curve parameters, using mainly tilted-ring model on velocity fields. In the second step, they refine these parameters, and create a model data-cube from the rotation curves. Their goal is to adjust the rotation curves parameters to make the model data-cube as close as possible from the observed one. For this adjustments, they take the position-velocity plot (PV diagram) at 6 different position angles and adjust their model to make the best match on those PV plots. Finally, to have less subjective rotation curve, they perform a detailed modeling of the data. The rotation curve is used to build an axi-symmetric velocity field. A data-cube is created using this velocity field and the HI distribution at full resolution. This data-cube is convolved at 30" resolution and compared to the observed one using χ^2 values. This method is more powerful than the classic tilted-ring on velocity field used in van Eymeren et al. (2011a) and also more computationally expensive.

Here we perform an homogeneous analysis of the WHISP sample described in the previous section, using ^{3D}Barolo. The objective is to compare results obtained with 3D techniques to the previous rotation curves obtained using velocity fields, and to have an homogeneous set of rotation curve for the entire sample which can be used later for dark matter studies. Using the high number of galaxies present in the sample, we study asymmetries of the HI distributions by deriving rotation curves for both sides of the galaxy (approaching and receding) and comparing them. In the first part, we describe the algorithm of ^{3D}Barolo, and perform different tests to check the consistency of the results. Then in the next section, we present the outputs obtained (rotation curve, mass surface density, pv-plot,...) and compare with previous results published in earlier papers. In section 3, we present a study of asymmetry in the velocity maps that could be perform with the data provided in this work and finally in section 4 we present a paper I was involved in concerning the shape of dark matter halos using different tracers (HI only, $H\alpha$ only, HI + $H\alpha$, HI being the WHISP rotation curves).

3.1. ^{3D}Barolo

With the mean of radio synthesis observatories, it is possible to obtain spectra along each spatial pixel of a galaxy. These data products are referred as "3D data-cubes" due to the 2 spatial dimensions plus the spectral one which allows to trace kinematics of celestial objects. From this datacube, there exist a variety of methods to extract 2D maps such as line intensity, velocity maps and dispersion maps. A classical method is the study of the moments of the data-cube, which are given by :
Total flux intensity (0^{th} order moment of the datacube) :

$$\Sigma(x,y) = \int F(x,y,v)dv \tag{3.1}$$

Recession velocity (1^{st} moment) :

$$V(x,y) = \frac{\int vF(x,y,v)dv}{\Sigma(x,y)} \tag{3.2}$$

Velocity dispersion (2^{nd} moment) :

$$\sigma(x,y) = \left(\frac{\int (vF(x,y,v) - V(x,y))^2 dv}{\Sigma(x,y)}\right)^{1/2} \tag{3.3}$$

Since the spectral resolution is not infinite, the integrals over the spectral range becomes summations when applied to a data-cube. A second widely used method is to fit Gaussian function on each spectral profiles of the data-cube (Begeman 1987). Therefore the line intensity is given by the integral of the Gaussian, the recession velocity by the mean velocity of the Gaussian, and the dispersion velocity by its width. Depending on the spectral profiles of the galaxy, some variations of this techniques are used, such as the multiple Gaussian profile (Oh et al. 2008), including a skewness parameter (h_3 or h_4 Gauss-Hermite term, Ianjamasimanana et al. (2012), van der Marel & Franx (1993)). Various other techniques can exists such as the average intensity "median" velocity, the peak velocity method, envelope tracing (Sofue & Rubin 2001), Fourier quotient (Bender 1990), etc... Depending on the quality of the data (i.e. signal to noise ratio), the inclination angle or the morphological type of the targets, some methods are better suited than others.

In the last decades, rotation curves (i.e circular velocity against the galacto-centric radius) were computed based on the 2D velocity field, itself extracted from the 3D data-cube using astronomer's favourite technique. To obtain those circular velocities, galaxies are modeled by a tilted-ring disk, introduced for the study of M83 in Rogstad et al. (1974), which is a discretisation of a thin disk into a series of concentric annuli (Fig. 3.1). Using rings suppose a cylindrical symmetry, therefore all the parameters are dependant only on the galacto-centric radius. The circular velocity in those ring is assumed equal to the rotational velocities due to the thin disk approximation. Each ring is described by 4 geometrical parameters, the position of the center x_0 and y_0, the inclination i of the ring and its position angle PA, and 3 kinematical parameters,the systemic velocity V_{sys}, the projected circular velocity V_{rot} and the expansion (or radial) velocity V_{exp}. Each ring has its own set of parameters.

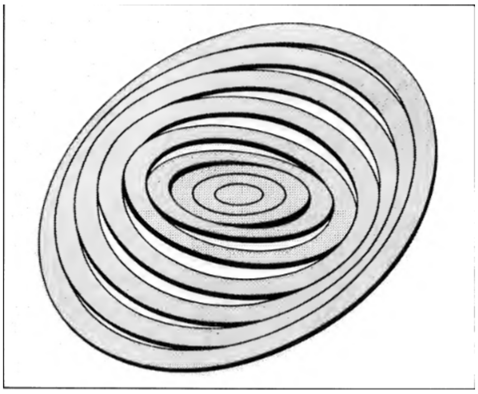

FIGURE 3.1. – Tilted-ring model of M83 as presented in Rogstad et al. (1974)

An harmonic decomposition of velocity fields, assuming that circular motions are dominant, leads to the following expression of the line-of-sight velocity (Franx et al. 1994) :

$$V_{los}(x, y) = V_{sys} + V_{rot}(R)\cos\theta\sin i + V_{exp}\sin\theta\sin i \tag{3.4}$$

with

$$\cos(\theta) = \frac{-(x - X_0)\sin PA + (y - Y_0)\cos PA}{R}$$
$$\sin(\theta) = \frac{-(x - X_0)\cos PA - (y - Y_0)\sin PA}{R\cos i}$$

with θ the azimuthal angle from the major axis of the galaxy in the disk plane and i its inclination angle, X_0 and Y_0 the position of the rotation center.

Therefore, the derivation of the rotation curve comes from the fit of Eq. 3.4 on each ring. Various programs perform this fit using non-linear least squares minimization. On high resolution data, results are reliable and give robust kinematics. This methods has two main drawbacks : the first one is that, for small and/or distant galaxies, kinematic might be dominated by beam smearing effect which is not taken into account in this modeling. The second issue comes from the derivation of velocity fields, which implies the extraction of a characteristic velocity in the line profile of each pixel. Obtaining this velocity might be tricky due to asymmetries of the line profile and therefore depending on the method used to derive the velocity field from the data-cube, the resulting velocity field might change a lot.

To improve the derivation of rotation curves, a recent method consists in fitting the tilted-ring model directly on the 3D data-cube. This technique implies a computational cost way heavier than a simple fit on a velocity field. Few programs perform this fit such as : TiRiFiC (Józsa et al. 2007), GalPack^{3D} (Bouché et al. 2015) and the one used here ^{3D}Barolo (or BBarolo) (Di Teodoro & Fraternali 2015).

3.1.1. Description of the algorithm

By opposition to 2D fit, the 3D modelisation doesn't have an analytical expression, therefore it makes use of a Monte-Carlo algorithm. The goal is to simulate observations, through a modelisation of the disk, and to compare them with the observations using a residuals minimization.

The tilted-ring model has 8 parameters for each ring :

1. Spatial coordinates of the center : XPOS and YPOS ;
2. Systemic velocity : VSYS ;
3. Inclination angle with respect to the observer : INC ;
4. Position angle of the major axis : PA ;
5. Rotational velocity : VROT ;
6. Dispersion velocity : VDISP ;
7. Face-on gas column density : DENS ;
8. Scale height of the disk : Z0 ;

Each parameter can vary from ring-to-ring. Using these parameters, the ring is randomly populated by emitting gaseous clouds. Once the ring is projected in the plane of the sky, it is possible to compute the observed velocity in the line-of-sight.
The second step consists in convolving this model with the instrumental PSF, or beam, of the observations. The beam is described by a 2D-Gaussian function, with 3 parameters : BMIN, the minor axis of the beam, BMAJ the major axis of the beam and BPA the position angle of the beam, measured anticlockwise from the vertical direction. After this step the model is at the same spatial resolution as the observation, and the next step consist in a pixel-by-pixel comparison of the model and the observed data-cube, to evaluate the quality of the modelisation. The residuals are computed for each pixel of the ring, and associated with a weighting function, it gives the goodness of the fit,

i.e. if the model converged or not. If it does, then the algorithm goes to the next ring, if it doesn't the parameters of the models are updated the loop restart. These processes are summarized in Fig 3.2.

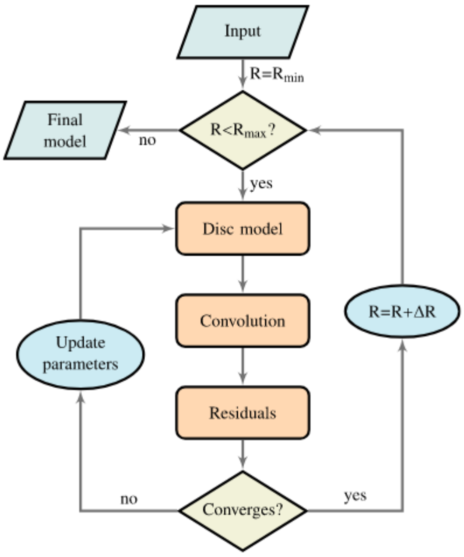

FIGURE 3.2. – Operational scheme of ^{3D}Barolo, from Di Teodoro & Fraternali (2015)

3.1.2. Methodology

As we described in the previous section, each annuli having is own set of parameters, which can vary from annulus to annulus. The parameters of a ring are the rotational velocity (VROT), the dispersion velocity (VDISP), the position angle (PA), the inclination (INC), the systemic velocity (VSYS), the position center of the ring (XPOS, YPOS) and the scale-height of the disk (Z0). In an ideal case, for high resolution data, high mass and extended galaxy one can let all parameters free for the fit. Nevertheless due to the diversity of WHISP galaxies, some galaxies are small, some have small gas mass, some are interacting of have been interacting in the past and then we have to reduce the number of parameters in the fit. Therefore, depending on the quality of the data, the set of parameters fitted changes, and for "good" galaxies we fit VROT, VDISP, INC and PA, while for smaller galaxy with patchy distributions we fit only VROT and VDISP. For each data-cube, we were, as a first guess, using value from the HyperLeda database, leaving almost all parameters free (VROT, VDISP, PA INC, VSYS, XPOS, YPOS). For some galaxies, due to the low signal, either BBarolo "couldn't run on this data-cube" or either the fit was not relevant. To add more constraints, we had to fix the position angle and the inclination in order to determine properly the center. Parameters for the center are the coordinate (XPOS, YPOS), as well as the systemic velocity. On the PV diagram, we checked by eye the position of the center. Then we fix the parameters VSYS, XPOS, YPOS and start the final fit. For each step we were fitting the model, updating the initial parameters and fitting again to improve the final results. Depending on the quality of the data, on the brightness and on the intrinsic velocity of the source, we might fix parameters INC and PA as well, in order to have smoother rotation curves.

For each galaxies, we launch BBarolo 9 times, 3 times for each resolution available (14" × 14"/ sin(δ), 30" and 60"). For each resolution we execute BBarolo first on both sides simultaneously, and then each sides separately, keeping the same parameters as for the fit of both sides. Performing a side-by-side analysis allows to access the asymmetries of the disk.

3.1.3. Checking results

Due to issues later associated with a version problem of ^{3D}Barolo, we initially found nonphysical results, in terms of mass densities especially. To understand the origin of the problem, I had to inspect the data and analyse them by myself, in a similar way as described in Swaters et al. (2002); Noordermeer et al. (2005).

The first step to study data-cubes is to create an efficient mask in order to isolate the region containing the emission of the galaxy. It allows to gain computational time and to trace better the kinematic of the galaxy. After few tests using the automatic masking from the software ending up being unsatisfactory, we decided to build our own mask.

To be able to get the extended low level emission, we smoothed the data-cube at twice the value of the resolution. Then we subtract the continuum, and we calculate the standard deviation. We kept only the signal that was above 2σ. This simple sigma-clipping discard most of the noisy regions in data-cubes. We compare our masks with those from Noordermeer et al. (2005)(N05), who used an additional step in their mask, in Fig. 3.3. This figure shows that the flux computed from both mask are really close, that's why we choose not to inspect each galaxy to mask the residual noise that can be left after the sigma-clipping.

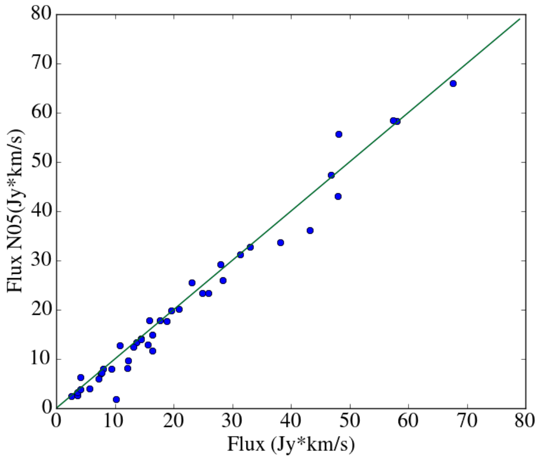

FIGURE 3.3. – Comparison of the flux computed using the mask define before with the one from N05. The solid line correspond to the 1-1 relation.

Using this mask, we compute the integrated global profiles for each galaxy by summing the spectral channels. Since the flux is given in units of W.U. (Westerbork Unit, 1 W.U. = 5 mJy/beam), we convert it into mJy. The total flux in mJy is the flux summed over all the pixels, divided by the number of pixel in a beam. For each galaxy we know the beam shape (see Sect. 2.1.3). By assuming a Gaussian beam, we calculate the value $\sigma_{\rm min}$ and $\sigma_{\rm maj}$ from the beam parameters BMIN and BMAJ :

$$\mathrm{FWHM} = 2\sigma\sqrt{2\ln 2} \tag{3.5}$$

which gives us the area of the beam in arcsec : $2\pi\sigma_{\rm min} * \sigma_{\rm maj}$. To obtain the number of pixel in a beam the last step is to divide the area (in arcsec) of the beam by the pixel scale (in arcsec/ pixel).

Using this short conversion, we are able to build integrated global profiles for each galaxy. The next step consists in computing the HI mass of the galaxy. The direct way is to use the formula that links the HI mass to the flux (in Jy × km/s) of the galaxy at a given distance D :

$$M_{HI} = 2.36 \times 10^5 D^2 \int F dv \tag{3.6}$$

To check the consistency of ^{3D}Barolo, a second method to compute the mass is to use the output mass density profiles. By summing the mass contribution of each annulus, we obtain the total mass as computed from the flux.

3.2. Results and comparison with literature

In Appendix C, we show the comparison of the HI and $H\alpha$ rotation curve available in the literature with the rotation curve derived with ^{3D}Barolo for 26 galaxies. Here we do not show the rotation curves at the highest 14" × 14"/ sin(δ) resolution which is often not computed due the bad quality of the data at such resolution. In Fig. 3.4 we show 2 examples for the galaxies UGC1913 and UGC2080.

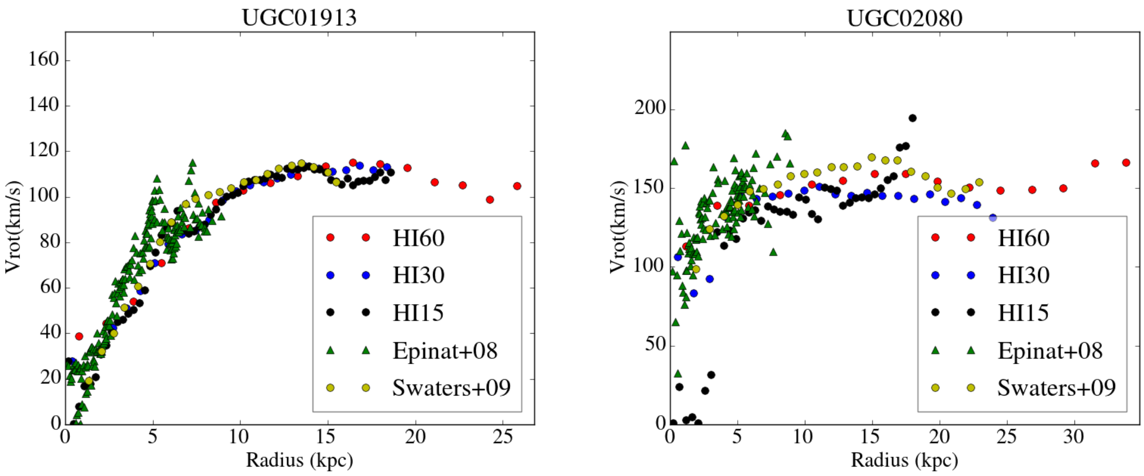

FIGURE 3.4. – Comparison of the rotation curves obtained using ^{3D}Barolo with HI data and $H\alpha$ data available in the literature.

A systematic comparison with the literature show a general agreement between the rotation curves extracted from ^{3D}Barolo and the one from the literature. Nevertheless, some galaxies exhibit significant differences : UGC4284, UGC8490, UGC9649, UGC10470. The largest differences are for the galaxy UGC8490, which is a prototype warped galaxy. This galaxy has been studied in Józsa (2007), in which a tilted-ring study is performed. The inclinations and the PA undergo a variations of respectively 20 and 50°. These variations are not detected using ^{3D}Barolo, explaining the differences observed.

In Appendix D, we present the result of the tilted-ring analysis for our sample. We chose to present only the data obtained with a resolution of 30" because it represents at highest resolution most of the small and far galaxies have low quality data on which the tilted-ring model was meaningless. On the left panel, we present the rotation curves modeled using both sides of the galaxy, in red, only the approaching side, in blue, and only the receding side, in green. On the middle panel we show the mass surface density profile in $M_\odot / pc^2$, and on the right panel the position-velocity diagram along the major axis of the galaxy.

3.3. Lopsidedness study

Using the rotation curves from the left panel, we can perform a similar work as presented in van Eymeren et al. (2011a) and extend their sample by a factor 4. Based on the difference between the rotation curves from the approaching and receding sides, they observed that the kinematic behaviour could be described by 5 typical configurations, shown in Fig. 3.5. We already described those ones in Sect. 2.1.4. Considering the Appendix D of the thesis, it is possible to classify the data for the 252 galaxies presented here into those 5 configurations. For a further analysis, one has to study the properties of the galaxies depending on their classifications. Indeed, galaxies from type 2 and type 5 are located in groups or have companions. Enhancing the statistic can improve the understanding on the origin of this lopsidedness.

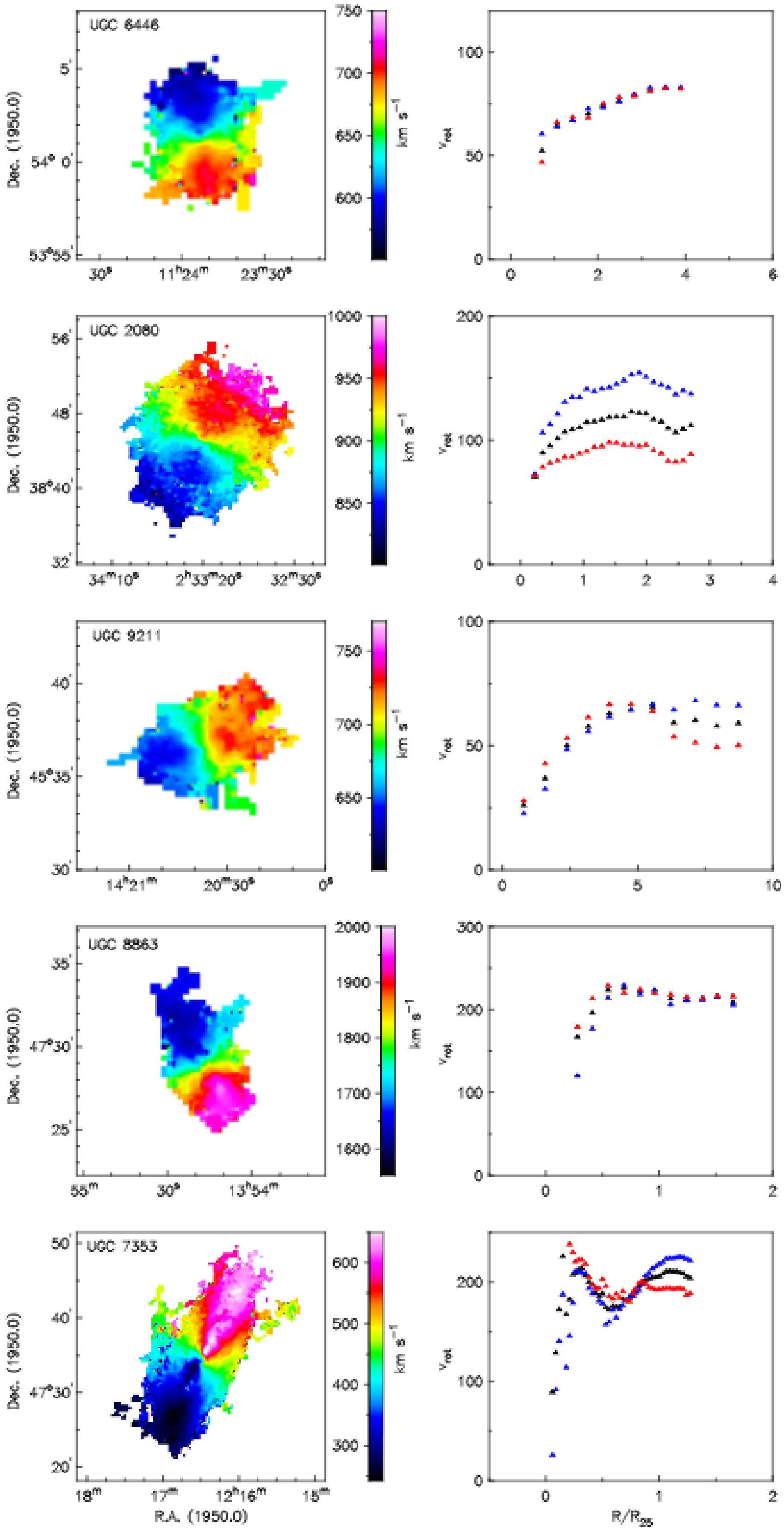

FIGURE 3.5. – Figure from van Eymeren et al. (2011a). The five typical kinematic behaviour based on the rotation curves from the approaching and receding sides.

3.4. Mass distributions in nearby galaxies

Following this work, I've been involved in a paper from Korsaga et al. (2019).

3.4.1. Outlines

The goal of this paper is to make a comparative study on the dark matter halo shape withing the optical radius depending on the tracer used and on the fitting procedures. We create different mass models, including or excluding some component (stars only using WISE 3,4µm or stars + gas), using different tracers ($H\alpha$ only from GHASP, HI only from WHISP, or an hybrid rotation curve $H\alpha + HI$). The two dark matter halos studied here are the pseudo-isothermal core halo (ISO) and the NFW cuspy halo. To fit these 2 models, we use 3 distinct procedures : the maximum disc model (MDM), which maximises the disk component (i.e. stars), the best fit model (BFM), which is a classical χ^2 minimization with all free parameters and finally a fix M/L (mass-to-light ratio) derived from $W_1 - W_2$ bands of WISE.

In this paper I had two separate jobs, the distance homogenisation of $H\alpha$ and HI data, and the computation of the dark matter halo masses.

3.4.2. Correcting from distance effect

As mentioned, we used a combination of $H\alpha$ and HI data. As the kinematics is different between those data, systemic velocity and then distances deduced from those datasets can be slightly different. But since distances are crucial to have proper estimate of the linear sizes in the galaxy, of the HI mass, we need, in order to compare $H\alpha$ and HI to adopt the same distance. Due to the homogeneity of the GHASP sample, we decided to use the distance computed with $H\alpha$ data, and therefore we had to adjust the HI data to the chosen distance. We have rotation curves and mass density profile calculated at a given distance D_1, what corrections do we have to apply if we consider an other distance D_2 ?

Linear size correction

The intrinsic radius of a galaxy depends on the distance following :

$$\tan\left(\frac{\theta}{2}\right) = \frac{R}{2D} \Rightarrow R = 2D \times \tan\left(\frac{\theta}{2}\right) \tag{3.7}$$

with θ the angular size of the galaxy, R the linear size and D the distance of the galaxy.

Pour θ fixe :

$$R_1 = 2D_1 \times \tan\left(\frac{\theta}{2}\right)$$
$$R_2 = 2D_2 \times \tan\left(\frac{\theta}{2}\right)$$

$$(1) \Rightarrow \frac{R_2}{R_1} = \frac{D_2}{D_1} \Rightarrow R_2 = R_1 \frac{D_2}{D_1} \tag{3.8}$$

To correct the radii, we simply have to multiply the radii (calculated at D_1) by the ratio of the distances D_2/D_1.

Mass correction

HI mass of a galaxy depends on flux and distances following :

$$M = 2.36 \times 10^5 D^2 \int F dv \tag{3.9}$$

with D the distance of the object in Mpc, $\int F dv$ the total flux in Jy × km × s^{-1} the mass in unit of solar mass $M_\odot$. We define $F_{tot} = \int F dv$, the total flux of the galaxy which is independent from the distance.

$$M_1 = 2.36 \times 10^5 D_1^2 F_{tot}$$
$$M_2 = 2.36 \times 10^5 D_2^2 F_{tot}$$

$$(2) \Rightarrow M_2 = M_1 \frac{D_2^2}{D_1^2} \tag{3.10}$$

To correct for the total mass, we need to multiply the mass by the ratio $(D_2/D_1)^2$.

Correction on the mass density profile

From the mass density profile of the object, the mass is calculated by summing contributions in each annulus :

$$dm(x, y) = \Sigma(x, y) dx dy \tag{3.11}$$

$$M(S) = \int_S dm(x, y) = \int_S \Sigma(x, y) dx dy \tag{3.12}$$

$$dm_1 = \Sigma_1 dr_1^2$$
$$dm_2 = \Sigma_2 dr_2^2$$

$$\Rightarrow \frac{\Sigma_1}{\Sigma_2} = \frac{dm_1}{dm_2} \times \frac{dr_2^2}{dr_1^2} = \frac{D_1^2}{D_2^2} \times \frac{D_2^2}{D_1^2} = 1 \tag{3.13}$$

Surface density is independent from the distance.

Velocity corrections For a spherical distribution of matter, velocity is given by :

$$V^2 \propto \frac{GM}{R} \tag{3.14}$$

$$D_1 : V_1^2 \propto \frac{GM_1}{R_1}$$
$$D_2 : V_2^2 \propto \frac{GM_2}{R_2}$$

$$\Rightarrow \frac{V_1^2}{V_2^2} = \frac{M_1}{M_2} \times \frac{R_2}{R_1} = \frac{D_1^2}{D_2^2} \times \frac{D_2}{D_1} = \frac{D_1}{D_2} \tag{3.15}$$

$$\Rightarrow V_2 = V_1 \sqrt{\frac{D_2}{D_1}} \tag{3.16}$$

To correct velocities, we need to multiply the velocity by the ratio $\sqrt{D_2/D_1}$.

3.4.3. Computing dark matter halo mass

In the paper we fit ISO and NFW dark matter halo using different procedures. For each halo, we fit two parameters, (r_0, ρ_0) which are respectively the characteristic radius and the central density of the ISO model and (c, V_{200}), the concentration parameter defined as $c = \frac{R_{200}}{r_0}$ and the virial velocity $V_{200} = \frac{H_0}{100} R_{200}$. The virial radius R_{200} corresponds to the radius where the mean density is 200 times the cosmological critical density. From the mass distribution given in Eq. 1.2, we can compute the dark matter halo mass :

- ISO dark matter halo mass :

$$M_{iso}(r) = 4\pi\rho_0 r_0^2 [r - r_0 \arctan\left(\frac{r}{r_0}\right)] \tag{3.17}$$

- NFW halo :

$$M_{nfw}(r) = 4\pi\rho_{crit}\delta_0 r_0^3 (\ln(1 + r/r_0) - \frac{r/r_0}{1 + r/r_0}) \tag{3.18}$$

which can be written in terms of c, R_{200}, V_{200} and $x = \frac{r}{R_{200}}$

$$M_{nfw}(r) = \frac{V_{200}^3}{Gh} \frac{\ln(1 + cx) - cx/(1 + cx)}{\ln(1 + c) - c/(1 + c)} \tag{3.19}$$

Given the parameters of the fit in each case (MDM, BFM and fix-M/L), I computed the dark matter halo mass, and different statistical information to perform a quantitative comparison between the different datasets, procedures and halo model. The result is given in Fig. 3.6.

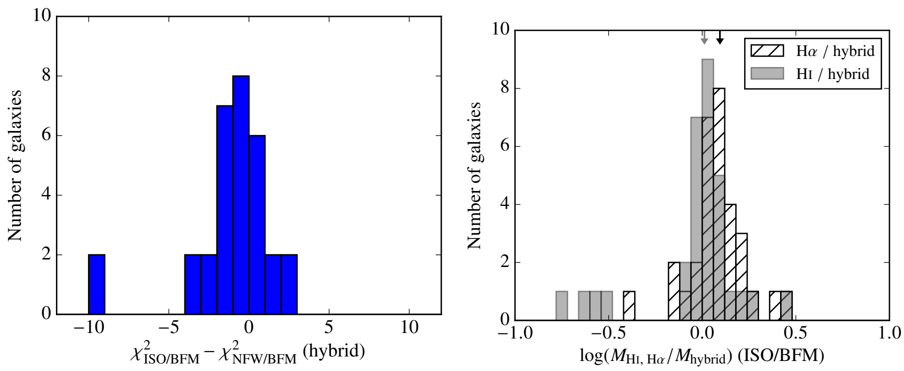

FIGURE 3.6. – Comparison of the χ^2 values for the best fit model of the ISO and NFW dark matter halos (left) and comparison of the dark matter halo mass computed using $H\alpha$ only or HI only, compared to the hybrid data.

In conclusion, my work provides rotation curves for an homogeneous sample of 313 galaxies, corrected from the beam smearing. Furthermore, $H\alpha$ observations were carried on during those years, increasing the number of common galaxies between WHISP and GHASP to more than 200. After the reduction process of the GHASP data, the combination of these data-sets will allow to perform a similar study on a sample seven times larger. Mass modeling on large samples is also a first step toward two mass modeling, which consist in fitting the dark matter halo directly on the 2D velocity fields.

4. Velocity dispersion study : framework and methodology

Sommaire

4.1 Geometrical and mathematical framework 55
4.2 Discussion of the mathematical framework 59
4.3 Fast Fourier Transform (FFT) 65
4.4 Systematic biases 66
4.4.1 Beam smearing effect 66
4.4.2 Noise in the FFT 72

In this chapter, we introduce the scientific context which motivates the study of asymmetries in the neutral gas velocity dispersion and the requested mathematical developments. Velocity dispersion is a second order moment, and therefore is a much more complex quantity to study than flux and radial velocity. In order to present properly the physical motivations of this work, it is necessary to first introduce and discuss the geometrical and mathematical framework used to study spatially resolved velocity dispersion.

4.1. Geometrical and mathematical framework

Due to its hydrodynamical properties, the gas lies inside a plane. The velocity vector in the frame of the galactic plane is described by two components lying in the plane of the galaxy, in the cylindrical frame :

1. V_θ : the tangential velocity, i.e. the rotation motion ;
2. V_R : the radial velocity, that is the inward or outward motion ;

and one component perpendicular to this plane :

3. V_z : the vertical velocity.

The observed velocity V_{los} (los for line-of-sight) is linked to the projection of V_θ, V_R and V_z along the line of sight through 5 additional parameters :

4. PA : the position angle of the major axis of the galaxy (measured counterclockwise from the North to the direction of receding side of the galaxy) ;
5. i : the inclination of the galactic disk with respect to the sky plane ;

6. $V_{\rm sys}$: the systemic velocity of the galaxy ;
7. x_c and y_c : coordinates of the rotation center in cartesian coordinates (sky projection)

through the following equation :

$$V_{\rm los} = V_{\rm sys} + V_\theta \cos\theta \sin i + V_R \sin\theta \sin i + V_z \cos i \tag{4.1}$$

Both the radial, tangential, and vertical components can vary with R and θ, which are the polar coordinates in the plane of the galaxy with respect to the center, choosing the major axis as reference $\theta = 0$. The azimuth in the plane of the galaxy, θ, is linked to the position angle PA, the inclination i, the position x (east-west),y (north-south) and center x_c, y_c in the sky by the set of equations 4.2 to 4.7 :

$$R\cos\theta = r\cos\psi \tag{4.2}$$

$$R\sin\theta = r\frac{\sin\psi}{\cos i} \tag{4.3}$$

$$\cos\psi = \frac{(y-y_c)\cos PA - (x-x_c)\sin PA}{r} \tag{4.4}$$

$$\sin\psi = -\frac{(x-x_c)\cos PA + (y-y_c)\sin PA}{r} \tag{4.5}$$

$$r = \sqrt{(x-x_c)^2 + (y-y_c)^2} \tag{4.6}$$

$$R = r\sqrt{\cos^2\psi + \frac{\sin^2\psi}{\cos^2 i}} \tag{4.7}$$

ψ being the counterclockwise angle in the plane of the sky from the North.

Using the same formalism, it is possible to define :

$$\sigma_{ab} = \overline{V_a V_b} - \overline{V_a}\,\overline{V_b} \tag{4.8}$$

where a and b denote the different coordinate direction : radial (r), azimuthal (θ) and vertical (z) and V_a and V_b gives the corresponding velocities. When $a \neq b$, the term is the covariance between V_a and V_b, whereas in the specific case of a = b, the term is the variance of V_a and we note $\sigma_{aa} = \sigma_a^2$. The line-of-sight velocity dispersion of a single particle is thus defined as in equation 4.1 by

$$\sigma_{\rm los}^2 = \overline{V_{\rm los}^2} - \overline{V_{\rm los}}^2$$

As $V_{\rm sys}$ is constant, we deduce that :

$$\begin{aligned}\sigma_{\rm los}^2 &= \sigma_\theta^2 \cos^2\theta \sin^2 i + \sigma_R^2 \sin^2\theta \sin^2 i + \sigma_z^2 \cos^2 i \\ &+2(\sigma_{R\theta}\cos\theta\sin\theta\sin^2 i + \sigma_{\theta z}\sin\theta\cos i\sin i + \sigma_{Rz}\cos\theta\cos i\sin i)\end{aligned} \tag{4.9}$$

where $\sigma_{R\theta}, \sigma_{Rz}, \sigma_{\theta z}$ are the covariance terms of Eq. 4.8. A null value $\sigma_{R\theta}$ is equivalent to state that σ_R and σ_θ are independent. This equation is the most generic form to express the velocity dispersion along the line-of-sight. Since we observe galaxies with a finite resolution, individual pixel/spaxels of 3D spectroscopy instruments observe at a given position the motions of hundreds or thousands of stars or tens of gaseous clouds, all of them following their own orbit with different radial, vertical and tangential velocities. The random motion thus describes the scatter of orbital motions in each direction at the given position, called the velocity dispersion ellipsoid (Fig. 4.1). It is characterized by the three axis ratios, $\sigma_\theta/\sigma_R, \sigma_\theta/\sigma_z, \sigma_z/\sigma_R$. For collisionless tracers, like stellar populations, the axis ratios are not equal. Indeed, stellar orbits are not perfectly circular, and the presence of large-scale asymmetries, like bars and spiral arms creates streaming and radial motions. The ellipsoid of stellar population generally shows $\sigma_R > \sigma_\theta > \sigma_z$.

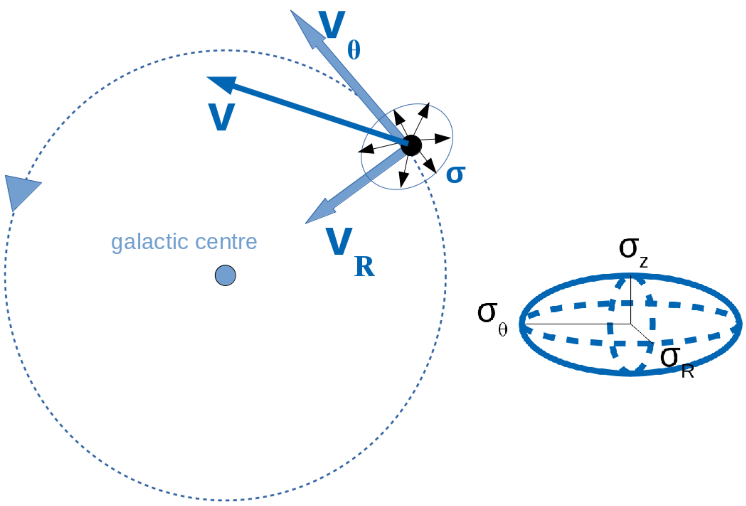

FIGURE 4.1. – Velocity ellipsoid, in cylindrical coordinates. To the left, illustration of a group of stars or gaseous clouds travelling along an orbit in the midplane ($z = 0$) at mean radial and rotational velocities V_R and V_θ, and with a r.m.s. planar velocity of V and random motion σ. The blue dashed circle corresponds to an orbit of purely circular motions. To the right, the 3 components of the random motion describe the so-called velocity ellipsoid.

We can recast the equation 4.9 in a sum of trigonometric polynomials of degree 2 :

$$\begin{aligned}\sigma_{\text{los}}^2 = &\left(\frac{\sigma_\theta^2 - \sigma_R^2}{2}\cos 2\theta + \sigma_{R\theta}\sin 2\theta\right)\sin^2 i \\ &+ (\sigma_{Rz}\cos\theta + \sigma_{\theta z}\sin\theta)\sin 2i \\ &+ \sigma_z^2\cos^2 i + \frac{\sigma_\theta^2 + \sigma_R^2}{2}\sin^2 i\end{aligned} \tag{4.10}$$

We can formulate differently this equation to match better the formalism introduced with Fourier Transforms (see Section 4.3). To do so, we write $a = \frac{\sigma_\theta^2 - \sigma_R^2}{2}$ and $b = \sigma_{R\theta}$, and define $\alpha_2 = \sin^2 i \sqrt{a^2+b^2}$, and ϕ_2 such that $\cos 2\phi_2 = a/\alpha_2$ and $\sin 2\phi_2 = b/\alpha_2$.
Hence, we get for the second degree term of Eq. 4.10 :

$$\left(\frac{\sigma_\theta^2 - \sigma_R^2}{2}\cos 2\theta + \sigma_{R\theta}\sin 2\theta\right)\sin^2 i = \alpha_2 \cos(2(\theta - \phi_2))$$

Similarly, we can introduce $\alpha_1 = \sin 2i\sqrt{\sigma_{Rz}^2 + \sigma_{\theta z}^2}$ and ϕ_1 such that $\cos\phi_1 = \sigma_{Rz}/\alpha_1$ and $\sin\phi_1 = \sigma_{\theta z}/\alpha_1$. We thus get for the term of degree 1 in Eq. 4.10 :

$$(\sigma_{Rz}\cos\theta + \sigma_{\theta z}\sin\theta)\sin 2i = \alpha_1 \cos(\theta - \phi_1)$$

Finally, defining $\alpha_0 = \sigma_z^2 \cos^2 i + \frac{\sigma_\theta^2 + \sigma_R^2}{2}\sin^2 i$ for the 0^{th} degree amplitude, which corresponds to the average value of $\sigma_{\rm los}^2$, we obtain :

$$\sigma_{\rm los}^2 = \alpha_0 + \alpha_1\cos(\theta - \phi_1) + \alpha_2\cos(2(\theta - \phi_2)) \tag{4.11}$$

As this relation is deduced from relation 4.1 and the conditions underlying its expression, these expressions are only valid for motions observed in the galactic plane. They are not valid for spheroidal objects, like stellar bulges or halos. As described before, terms α_0, α_1 and α_2 depend on $\sigma_R, \sigma_\theta, \sigma_z, \sigma_{R\theta}, \sigma_{Rz}, \sigma_{\theta z}$. In a general case, those parameters are dependent on the radius and the azimuth. Therefore, the azimuthal variations of $\sigma_{\rm los}$ are complex to analyse because $\alpha_0, \alpha_1, \alpha_2, \phi_1, \phi_2$ are all dependent on azimuth, combined with the variation in $\cos\theta$ and $\cos 2\theta$. In practice, for reasons of simplicity, in the following the cross-terms $\sigma_{R\theta}, \sigma_{Rz}, \sigma_{\theta z}$ are set to zero, implying $\alpha_1 = 0$. Nevertheless, the azimuthal dependence of Eq. 4.11 is still degenerated.

In practice, we do not observe directly $\sigma_{\rm los}$, because spectroscopic observations are a convolution of the physical dispersion with a Line Spread Function (LSF) with a finite instrumental resolution σ_{LSF}. Moreover, part of the physical dispersion is due to thermal processes in the gas. The observed velocity dispersion is thus given by :

$$\sigma_{\rm obs}^2 = \sigma_{\rm los}^2 + \sigma_{\rm LSF}^2 + \sigma_{\rm th}^2 \tag{4.12}$$

To express σ_{obs} following a similar polynomial decomposition as of Eq. 4.11, the term $\sigma_{\rm LSF}$ is a 0^{th} degree term, because the line spread function is roughly constant on the field. The thermal dispersion $\sigma_{\rm th}$ depends on the temperature of gas and is supposed isotropic. It therefore also fits in the 0^{th} degree. However, since it is linked to the temperature, and therefore to the local density of gas, which is clearly not axi-symmetric due to features like bars and spiral arms, it could contain a non axi-symmetric modulation. In the case of bars and 2 spiral arms, the asymmetric terms are dominated by the degree 2, they are anti-symmetric with respect to the minor axis (mirrored symmetry). Since the problem is highly degenerated, we assume a constant gas temperature on the galaxy. Indeed, random motions are due to different causes, mainly the thermic motions of the gas and the gravitational force exerted by the surroundings of the cloud. In this thesis we focus on the random motions caused by gravitational effects.

4.2. Discussion of the mathematical framework

Velocity ellipsoids and velocity dispersion ellipsoids formally introduced in equation 4.9, attempt to determining the shape and orientation of the three-dimensional distribution of velocities and velocity dispersions respectively from the point of view of the observer who is usually not located in the center of the system but who sees for instance a galaxy disk in projection under a certain inclination and position angle. Modelling in 3D the spatial distribution of velocities and velocity dispersion is a long-standing problem in galactic dynamics. Velocity ellipsoids comes up in the kinematics modelling of N-body systems. They are theoretical mathematical objects that must account for the velocity and velocity dispersion maps, that are observational quantities. Those ellipsoids model three-dimensional distributions whereas one-dimensional quantities only are observed, the line-of-sight velocities and line-of-sight velocity dispersions. The velocity dispersion tensor describes the local distribution of velocities at each point. This velocity ellipsoid is directly related to the symmetry and the shape of the galactic potential (e.g. Kuijken & Gilmore 1991). For instance, the stellar velocity ellipsoid of an axisymmetric disk galaxy is symmetric (e.g. Binney & Tremaine 2008). Non-axisymmetric structures such as bars and spiral arms in disk galaxies impact velocity ellipsoids, as shown by N-body simulations that indicate that the tilt of the stellar velocity ellipsoid is a signature of a bar in a disk (Saha et al. 2013).

Equation 4.9 or 4.10 show that six parameters are needed to describe this ellipsoid, $\sigma_R, \sigma_\theta, \sigma_z, \sigma_{R\theta}, \sigma_{Rz}, \sigma_{\theta z}$. Since we only have access to σ_{los}, all parameters are strongly degenerated and therefore some hypothesis are mandatory to simplify this issue. Some hypotheses concern the geometrical properties of the velocity ellipsoid components, i.e. hypothesis about symmetry and some others concerns the axis ratio of the ellipsoid, i.e. hypothesis about isotropy.

To clarify the terminology, we precise in these two paragraphs the notions of (a)symmetry and (an)isotropy. Symmetry refers to a system that is invariant under some transformations : translation, reflection, rotation, scaling, helical transformation, etc. The type of symmetry is determined by the type of the transformation. The overall shape is changed after a reflectional symmetry (or mirror symmetry), in that case, there exists an axis or a plane which divides the system into two pieces that are mirror images of each other. The overall shape does not change in case of :

(1) A translational symmetry.

(2) A scale symmetry when it is expanded or contracted.

(3) A rotational symmetry around a fixed point in the three angles defining any

rotation or about a line. Rotational symmetry around a point is also called central symmetry. A galaxy with a bar or an even number of spiral arms displays a rotational symmetry around an axis. It finds the same geometry/properties after a rotation of an angle π. Rotational symmetry based on comparing a source image with its rotated counterpart has been widely used in the literature (e.g. Abraham et al. 1996; Conselice et al. 2000).

(4) A cylindrical symmetry around an axis, that is also called axisymmetric, which is different from the rotational symmetry around an axis. In case of a cylindrical symmetry, the only dependence is radial, whatever the value of the azimuth angle, the system has the same properties at a given radius. For a planar system like the disk of a galaxy, this results in losing one of the two dimensions, the angular one. In the context of our study, axisymmetry is the symmetry that will hold our attention. When we mention a symmetric system, we mean an axisymmetric distribution, in which there are no azimuthal variations of the velocity dispersion components, while the asymmetric case describes all the distribution which deviates from axisymmetry. Structures like spiral arms or bars are rotationally symmetric but are not axisymmetric thus we consider them as asymmetric. A general tool for studying an ellipsoid is given by a cosine decomposition as the one given in relation 4.11 but harmonic decomposition will also be used later. So, by analogy we will call axisymmetric a symmetry of 0^{th} order while any symmetry of orders $m \geq 1$ is considered as an asymmetry.

Isotropy refers to a system that is invariant under all direction. For instance, around a point, which is for a galaxy its center of mass, at the same distance from that point, all the different directions are all equivalent and the potential energy at given distance is the same, as all directions are equivalent. More generally, a system is isotropic if none of its macroscopic properties have directional dependence. Links exist between isotropy and rotational symmetry : an isotropic system is rotationally symmetric and reciprocally. By consequence, anisotropy is the characteristic of a system in which certain physical properties vary with direction. An anisotropic medium has different properties depending on the direction in which it is studied.

If no further hypothesis is made, all those dispersion terms in equations 4.9 and 4.10 (σ_R, σ_θ, σ_z, $\sigma_{R\theta}$, σ_{Rz}, $\sigma_{\theta z}$) can vary with both radius (R) and azimuth (θ). This translates in terms α_i and ϕ_i also possibly varying with both coordinates in equation 4.11. This complex general case corresponds to the **anisotropic-asymmetric** case.

An assumption that can be made is the one where the ellipsoid is isotropic. This can be motivated by the fact that interstellar gas is a medium in which multi-directional collisions are thought to isotropize the gas velocity tensor. This is the reason why the ellipsoid of random motions of gas is often considered isotropic in galactic disks, equivalent to :

$$\begin{aligned} \sigma_{\mathrm{los}} = \sigma_R = \sigma_\theta = \sigma_z = \alpha_0 \\ \sigma_{R\theta} = \sigma_{Rz} = \sigma_{\theta z} = 0 \end{aligned} \tag{4.13}$$

In other words, in the isotropic case the velocity ellipsoid is locally spherical. There is no geometrical projection modulation anymore (and cross-terms are all null) and one thus does not need to deproject σ_{los} to study the random motions of gas. However, in the general **isotropic-non axi-symmetric** case, relation 4.13 is only valid locally, i.e. the isotropic dispersion amplitude itself can still vary as a function of position, with both R and θ. The amplitude of these variations with the azimuth θ quantifies in that case the degree of asymmetry, i.e. the deviation from axi-symmetry. One has to add an hypothesis of axi-symmetry of the system to remove the dependency with the azimuth. In that **isotropic-axi-symmetric** case, the line-of-sight dispersion can only vary with radius.

On the other side, non-collisional particles, which describe stellar systems, but eventually also gas if the collisional efficiency is smaller than unity, correspond to an **axisymmetric and anisotropic** velocity dispersion ellipsoid. In that case, the parameters of the ellipsoid do not longer depend on the azimuth and a single value could be used to model a axisymmetric ring at a given radius. A useful parameter to quantify the level of anisotropy in the plane of the galaxy is β_θ defined by :

$$\beta_\theta = 1 - \left(\frac{\sigma_\theta}{\sigma_R}\right)^2 \tag{4.14}$$

In the case of isotropy, $\sigma_\theta = \sigma_R$ leading to $\beta_\theta = 0$. In an anisotropic distribution of gas, this parameter can be negative, $\beta_\theta < 0$ corresponds to $\sigma_\theta > \sigma_R$ meaning that the gas particles move in tangential orbits or positive $\beta_\theta > 0$ because $\sigma_R > \sigma_\theta$, in other words orbits of the gas are more radial.

The terms α_0, α_1 and α_2 in equation 4.11 describe the order 0, 1 and 2 respectively. The 0^{th} order depends on the dispersion vector components σ_R, σ_θ and σ_z. The first order term is composed only by cross-terms σ_{Rz} and $\sigma_{\theta z}$. The second order term is composed by the difference $\sigma_\theta^2 - \sigma_R^2$ and a cross-term $\sigma_{R\theta}$. However, it is worth to notice that this problem remains degenerated, since only five independent parameters are necessary in relation 4.12. Within this assumption, some hypotheses can be made in order reduce the number of free parameters. By assuming a disk transparent and a symmetry with respect to the galactic plan, we can approximate that $\overline{V_z} = 0$. The assumption that rotation motions are preponderant is used to compute rotation curves and implies $\overline{V_r} = 0$.

However, the problem is more difficult for the velocity dispersion. For a stellar population distributed symmetrically, $\sigma_{R\theta}$ and σ_{Rz} are equal to zero (Shapiro et al. 2003). One solution to further reduce the number of free parameters is to constrain the ratio of planar component σ_R and σ_θ. This can be done by using the epicycle approximation :

$$\frac{\sigma_\theta^2}{\sigma_R^2} = \frac{1}{2}\left(1 + \frac{\partial \ln V_\theta}{\partial \ln R}\right) \tag{4.15}$$

R being the radius in the plane of the galaxy.

Within this approximation, the anisotropy parameter can be inferred at any radius. For a flat rotation curve, according to equation 4.15, $\sigma_R^2 = 2\sigma_\theta^2$ and $\beta_\theta = 0.5$, whereas for a solid body rotation curve $\sigma_R^2 = \sigma_\theta^2$ and $\beta_\theta = 0$. In absence of asymmetry, the dispersion component corresponding to vertical velocity dispersion does not depend on the azimuth. In face-on systems $\sigma_{\rm los} = \sigma_z$. Studies of such systems led to values of the vertical dispersion σ_z between 6 and 10 km/s (Combes & Becquaert 1997). Fixing σ_z to this value further enables to reduce the number of free parameters. If one only makes the assumption that the cross terms are null, we see from equation 4.10 that depending on the sign of $\sigma_\theta^2 - \sigma_R^2$, we have either a phase of 0 ($\sigma_\theta^2 - \sigma_R^2 > 0$) or $\pi/2$ ($\sigma_\theta^2 - \sigma_R^2 < 0$) for the line-of-sight dispersion as a function of the azimuth.

Making the distinction between isotropic-non-axi-symmetric and anisotropic-axi-symmetric cases is not trivial, especially if cross terms can differ from zero. However, in the anisotropic-symmetric case, only orders 0, 1 and 2 are expected for the azimuthal variations (i.e. Eq. 4.11), whereas asymmetries could be more complex. In practice, the study of the anisotropic-asymmetric case, which is not a simple task could eventually be achieved by making assumptions on the nature of the asymmetries. For instance, one could consider that along an asymmetric structure (e.g. a spiral arm), the amplitudes of the ellipsoid terms are constant. If the asymmetry has a shape that varies with both radius and azimuth, in theory, one could therefore deproject equation 4.9 along the asymmetry. This is beyond the scope of this thesis.

To illustrate the (an)isotropic and (a)symmetric considerations, we created a mock galaxy with controlled values $\sigma_R, \sigma_\theta, \sigma_z$, constant at all radii. The inclination is set to 60°, and the PA to 30°. All cross-terms are set equal to 0 in the following.

- In the first scenario, we create an isotropic symmetrical model (Fig. 4.2, top left). In the isotropic case $\sigma_{\rm los} = \sigma_R = \sigma_\theta = \sigma_z$, and we fix $\sigma_{los1} = 12$ km/s.
- The second scenario is an isotropic and asymmetrical model (Fig. 4.2, top right). We add an azimuthal modulation, with an arbitrary phase of 0.7π which could be associated with spiral arms features on a real galaxy : $\sigma_{los2}(\theta) = \sigma_{los1}(1 + 0.2\cos 2(\theta - 0.7\pi))$
- The third scenario is an anisotropic and axi-symmetrical model (Fig. 4.2, bottom left). In this case we compute the value σ_{los3} using Eq. 4.9. We fix the value $\sigma_{z3} = 6$ km/s, $\sigma_{\theta 3} = 12$ km/s and $\sigma_{R3} = 16$ km/s constant with the radius. We observe on the bottom left panel of Fig. 4.3 that the dispersion is maximum along the minor axis because of the sign of $\sigma_\theta - \sigma_R$ as it was discussed for Eq. 4.10.
- The last model is the most degenerated one, anisotropic and asymmetric (Fig. 4.2, bottom right). For this model we keep the same value σ_z and add the same modulation as in the second model for both planar terms $\sigma_{R4} = \sigma_{R3}(1+0.2\cos 2(\theta - 0.7\pi))$ and $\sigma_{\theta 4} = \sigma_{\theta 3}(1 + 0.2\cos 2(\theta - 0.7\pi))$. In that case the dispersion doesn't peak on the minor axis nor at a phase of 0.7π which is the maximum of the azimuthal modulation, but between those two values.

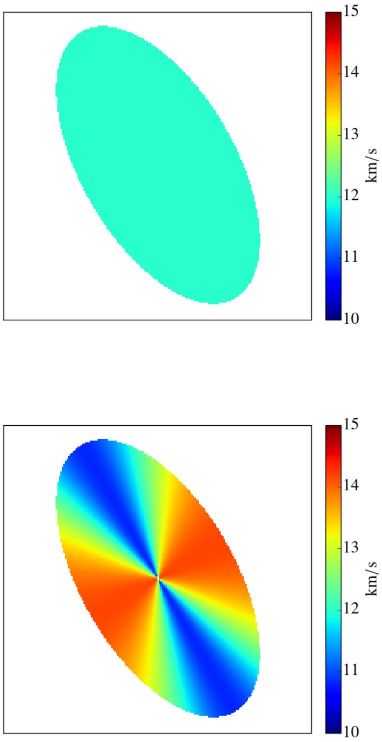

FIGURE 4.2. – Mock σ_{los} galaxy to illustrate the different case : isotropic and symmetric (top left), isotropic and asymmetric (top right), anisotropic and symmetric (bottom left), anisotropic and asymmetric (bottom right).

This previous set of models is very basic. In order to mimic the methodology that will be used in the next two chapters and to be closer from real galaxies, we perform a second set of models. Parameters σ_{los}, σ_R, σ_θ and σ_z are not constant anymore with the radius. We keep the same inclination and set the PA to 30°. All cross-terms are set to zero. To simulate a tilted-ring model, we decompose the galactic disk into 10 concentric rings.

— Isotropic and axi-symmetrical model (Fig. 4.3, top left) : like above, the isotropic case $\sigma_{\text{los}} = \sigma_R = \sigma_\theta = \sigma_z$ We set a radial decrease of σ_{los1} from 14 to 10 km/s. In a given ring, the value of the dispersion stays constant with the azimuth : $\sigma_{los1} = 14 - 0.4R$.

— Isotropic and non-axi-symmetrical model (Fig. 4.3, top right) : we keep the same radial decrease of σ_{los1} and add a second order modulation with an arbitrary phase, which could be associated with spiral arms features on a real galaxy : $\sigma_{los2}(R,\theta) = \sigma_{los1}(R)(1 + 0.2\cos 2(\theta - 0.7\pi))$

— Anisotropic and axi-symmetrical model (Fig. 4.3, bottom left) : in this case we compute the value σ_{los3} using Eq. 4.9. We fix the value $\sigma_z = 6$ km/s and keep it constant for all rings. This is a reasonable value that has been observed on face-on systems. Since the vertical dispersion is roughly constant in a galaxy, we use the previously described anisotropy parameter β_θ (Eq. 4.14). In our case we create a vector σ_R of dispersion with a radial decrease from 18 to 13 km/s, and a similar vector for σ_θ, with a faster decrease to increase the anisotropy with the radius : $\sigma_R = 18 - 0.5R$ and $\sigma_\theta = \sigma_R(1 - 0.05R)$. We observe on the bottom left panel of Fig. 4.3 that the dispersion is maximum along the minor axis because of the sign of $\sigma_\theta - \sigma_R$ as it was discussed for Eq. 4.10.

— Anisotropic and asymmetric model (Fig. 4.3, bottom right) : For this model we keep the same value of σ_z and same variation with radius of σ_θ and σ_r as for the anisotropic and axi-symmetric model for which we add the same modulation as in the second model. In that case the dispersion doesn't peak on the minor axis nor at a phase of 0.7π which is the maximum of the azimuthal modulation, but between those two values.

These figures illustrate the complexity of the problem and the difficulty to discriminate between the different model.

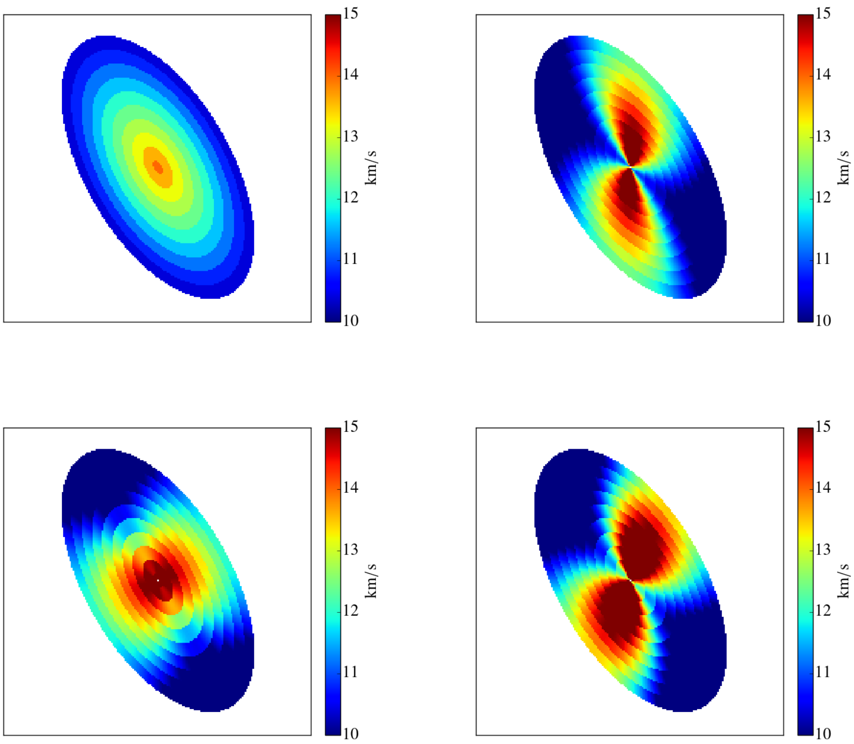

FIGURE 4.3. – Mock $\sigma_{\rm los}$ galaxy to illustrate the different case : isotropic and symmetric (top left), isotropic and asymmetric (top right), anisotropic and symmetric (bottom left), anisotropic and asymmetric (bottom right).

4.3. Fast Fourier Transform (FFT)

Fourier analysis are frequently used to probe spiral structures in galaxies (e.g. Puerari & Dottori 1992; Davis et al. 2012) and to study stellar bars (e.g. Combes & Sanders 1981; Combes et al. 1990; Garcia-Gómez et al. 2017). Harmonic expansion has been widely used to describe non-axisymmetry in velocity fields of galaxies (e.g. Franx et al. 1994; Schoenmakers et al. 1997; Wong et al. 2004; Trachternach et al. 2008), in particular with tools like kinemetry (Krajnović et al. 2006), which perform harmonic expansion of 2D maps of observed moments of the line-of-sight velocity distribution (surface brightness, velocity, velocity dispersion). The first harmonic decomposition of HI dispersion maps was performed on M33 by Chemin et al. (2020).

In this work, I study the following parametrisation of the line-of-sight velocity dispersion in order to investigate asymmetries of the dispersion maps :

$$\sigma_{obs}^2 = \sigma_0^2 + \sigma_1^2 \cos\big(\theta - \phi_1\big) + \sigma_2^2 \cos\big(2(\theta - \phi_2)\big) + \sigma_3^2 \cos\big(3(\theta - \phi_3)\big) + \sigma_4^2 \cos\big(4(\theta - \phi_4)\big) \tag{4.16}$$

This corresponds to the analytical expression of the FFT on σ^2 maps up to the fourth order. I use the dispersion squared, because it's easier to express the dispersion as a quadratic sum of the dispersion ellipsoid component(cf. Eq. 4.9) rather than a square root of quadratic terms.

In practice, I decompose the galactic disk in a series of concentric rings (we detail this in Sect. 6.2.1). For each ring, we have N pixels with associated values of the velocity dispersion σ^2 and azimuth θ. To make asymmetries more visible, we subtract the mean value of σ^2 in the corresponding ring which just centers values of σ^2 on 0. This affects only the 0^{th} order term of the FFT and does not change the asymmetries in the ring. We sort the velocity dispersion values with increasing values of azimuth and apply the FFT, using the routine scipy.fftpack.fft, leading to a decomposition with N/2 terms. Ordered values of azimuth at a given radius vary linearly whatever the inclination value, if no value is missing. A ring-by-ring study of the entire sample showed that missing values represents most of the time less than 1% of the total number of pixel in a ring as we can see on Fig. 4.4. We performed a similar study on WHISP data and observed that the result of the FFT is less robust when the number of missing values is important. Indeed, radius to radius, the phase is less continuous, we observe frequent phase jumps which are not physical. Even if it's not crucial here, we replaced the missing values by the average values in the ring, which is equivalent to adding zeros since we subtract by this mean value.

Because we only consider the five first terms of the FFT (from 0 to 4), each ring is described by 9 parameters : σ_0, σ_1, σ_2, σ_3, σ_4, ϕ_1, ϕ_2, ϕ_3, ϕ_4. We compute the FFT (i.e. Eq. 4.16) on each radius for each galaxy, obtaining the radial variation of these parameters.

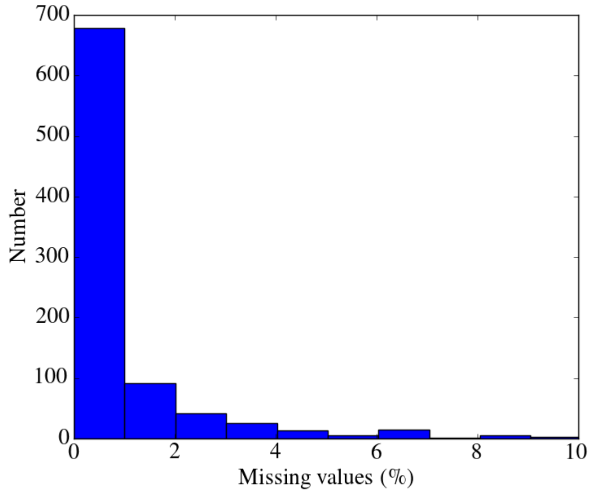

FIGURE 4.4. – Fraction of missing values in each of the 883 rings of the 15 THINGS galaxies.

To study asymmetries of the dispersion maps, Chemin et al. (2020) used both a least square fit and the FFT methodology described above, on the σ rather than σ^2 :

$$\sigma_{obs} = \sigma_0 + \sigma_1 \cos(\theta - \phi_1) + \sigma_2 \cos(2(\theta - \phi_2)) + \sigma_3 \cos(3(\theta - \phi_3)) + \sigma_4 \cos(4(\theta - \phi_4)) \tag{4.17}$$

Both methods turn out to give similar results for the four first orders. The main difference between the 2 methods is that the least square stops by construction at the order 4 while the FFT goes up to the order N/2 (N being the number of points) and is computationally faster. Another difference is that uncertainties are better handled in the least square fit. In addition, when some data is missing, the linearity between the index along the ring and the corresponding value of theta is partially lost, whereas the fit takes the sampling into account, as explained above. However, the work of Chemin et al. (2020) shows similar results between the two methods. In appendix H we show the residuals between the FFT containing all the orders minus the first 4 orders of the FFT and observe that higher orders are negligible.

4.4. Systematic biases

4.4.1. Beam smearing effect

The first systematic we need to get rid of is the beam smearing. We already presented several times this issue in the introduction and in the study of the WHISP sample. Beam smearing impacts the various kinematic maps extracted from datacubes (flux map, velocity field and velocity dispersion), but in a different way. de Blok et al. (2008) showed that the beam smearing is not important on THINGS data, by comparing an observed rotation curve derived from a cube smoothed at the THINGS resolution with a modeled rotation curve created using galaxy's parameters. Both curves behave similarly with differences below 1km/s except around two positions where they observed a more significant variation, but only due to the unrealistic shape of their model. They concluded that the beam smearing was not a serious problem. Nevertheless, the beam smearing pattern is not unidirectional : to derive the rotation curve, we focus mainly on positions close to the major axis, where the rotational velocity dominates, rather than on the minor axis where we expect more radial motions. This excludes or reduces the importance of velocities along the minor axis where the beam smearing can be important in 2D maps due to the azimuthal variations of the line-of-sight velocities (cf. equation 4.1), and due to the smaller apparent size of the minor axis. Therefore, using the rotation curve to evaluate the importance of beam smearing may minimize its impact. To avoid this, a 2D modeling is more appropriate, and in our case mandatory to determine the beam smearing component on velocity dispersion. Indeed, the beam smearing effect on the dispersion map is larger across the minor axis due to the strongest variation of $\cos(\theta)$ at a given rotation velocity. We thus need to take into account the 2D velocity field to compute the beam smearing induced on the dispersion map. Since we want to study azimuthal variations of the dispersion, we need to make a proper beam smearing correction. As we will show in the next sections, we observe a possible beam smearing remnant in the THINGS dispersion maps. For the moment let's focus on the methodology used for the modeling of the beam smearing effect.

To model the beam smearing effect on our data, we use the tool MocKing (Modeling Kinematics of Galaxies [1]) based on an analytical formula presented in Epinat et al. (2010) who derived the observed dispersion velocity in a galaxy in terms of the real dispersion and an instrumental dispersion (Eq. 4.18).

$$\sigma_1^2 = \sigma^2 + \frac{\int_{pix} \left[\overline{V}^2 M\right] \otimes_{xy} \mathrm{PSF}_{xy} dxy}{M_1} - \left(\frac{\int_{pix} \left[\overline{V} M\right] \otimes_{xy} \mathrm{PSF}_{xy} dxy}{M_1}\right)^2 \qquad (4.18)$$

with σ the local velocity dispersion, assumed constant to derive this equation. For the complete derivation of this equation, we refer the reader to the Appendices A3 and A4 of their paper. Using an appropriate velocity model, one can subtract quadratically the dispersion induced by the unresolved velocity gradients in the dispersion maps. MocKing handles velocity field and flux map at high resolution to compute this instrumental dispersion. It allows to define your own PSF, from a model or from a 2D map directly. MocKing also allows to compute velocity field from different rotation curve model already prepared, making the code very easy to adapt and use. We apply this method using two different approaches.

As we mentioned in section 2.2, THINGS targets were selected from the SINGS survey. Thus the THINGS survey also has a $H\alpha$ follow-up which allows us to have

1. https ://gitlab.lam.fr/bepinat/MocKinG

the kinematic of the ionised gas at really high resolution (Daigle et al. 2006; Dicaire et al. 2008). Thus, to model the beam smearing effect for our sample, we can use the data from SINGS or directly use the THINGS data. As we mentioned before, a flux map and a velocity field are needed to estimate the beam smearing contribution in the data. Using THINGS data is then really straightforward since we have those maps as well as the properties of the radio beam, given in Table 4.1. Using SINGS data for this purpose is more complex because we first need to compute a $H\alpha$ velocity field. Indeed, due to the holes in the observed velocity map of the SINGS data (see Fig. 4.5), we can't use them directly, and then we have to create a model map. We fit a Courteau model on the rotation velocities (Courteau 1997), and compute the 2D velocity field from this model, assuming the $H\alpha$ geometrical parameters listed in Table 4.2 are also valid for the HI gas, which may not be the case, in particular at large radii. A comparison of inclinations between optical and HI data (Table 4.2 and Table 4.1) show that on average the difference of inclination is less than 5 degrees. The most striking issue comes from galaxy NGC 925 for which HI inclination is 66 degrees, compared to the optical one which is 50 degrees. A modelisation using SINGS data would underestimate the beam smearing. Due to the higher resolution of the $H\alpha$ data, we have a better estimation of the correction in the inner part of the galaxy. The main drawback is that the 2D model is computed from a 1D rotation curve, and then does not contain any information on possible azimuthal deviations from axisymmetric rotation. Signatures like spiral arms and bars also induce beam smearing and are not taken into account with this method.

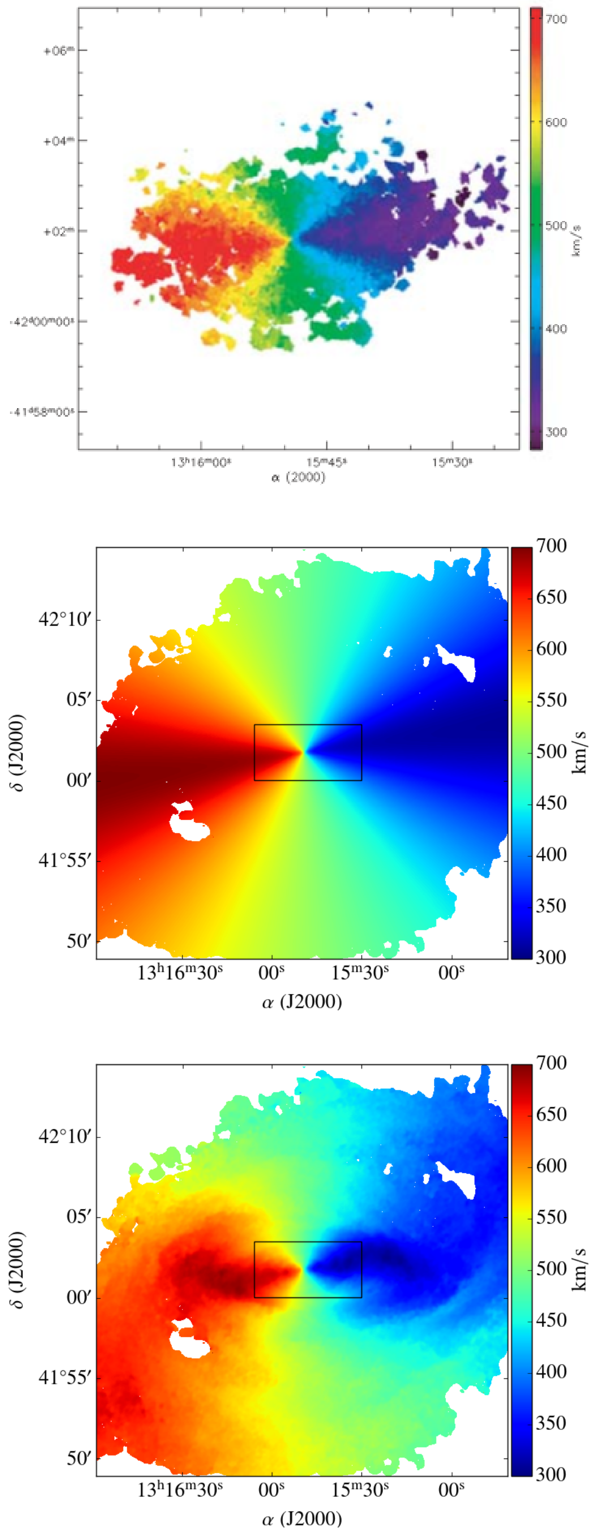

FIGURE 4.5. – Observed radial velocity map of NGC5055 from SINGS (Fig. from Daigle et al. 2006, top panel), radial velocity map modeled using Courteau rotation curves from SINGS data (middle panel), and radial velocity map observed with THINGS (bottom panel). Black rectangle on the middle and bottom panel indicates the size of the galaxy in $H\alpha$.

Fig 4.5 shows the difference between the observed radial velocity map from THINGS, the one from SINGS and the one modeled with SINGS for the galaxy NGC5055. We can observe that both maps are relatively close from each other on large scales, with a velocity model from $H\alpha$ data which is similar to the HI map from THINGS. Nevertheless, this galaxy seems to have a warp in HI. Our $H\alpha$ velocity model is constructed in excluding the possibility to have a warp, i.e. with fixed position angle and inclination for reasons explained in Epinat et al. (2008b), and thus in the outer part of the galaxy, we observe a discrepancy in the velocity fields. This is also due to the fact that the Courteau model at large radius is an extrapolation of the $H\alpha$ velocity field in the inner part. This is not crucial, because the beam smearing effect is dominant in the center, where both models are in agreement, and the beam smearing corrections in the outer part are negligible (see Fig. 4.6). Since the HI beam has a really complex shape, and we do not have any beam map from THINGS data, we approximate the beam by a 2D Gaussian function, created using parameters BMIN, BMAJ and BPA, which are respectively the minor and major axis and the orientation of the beam, showed in Table 4.1.

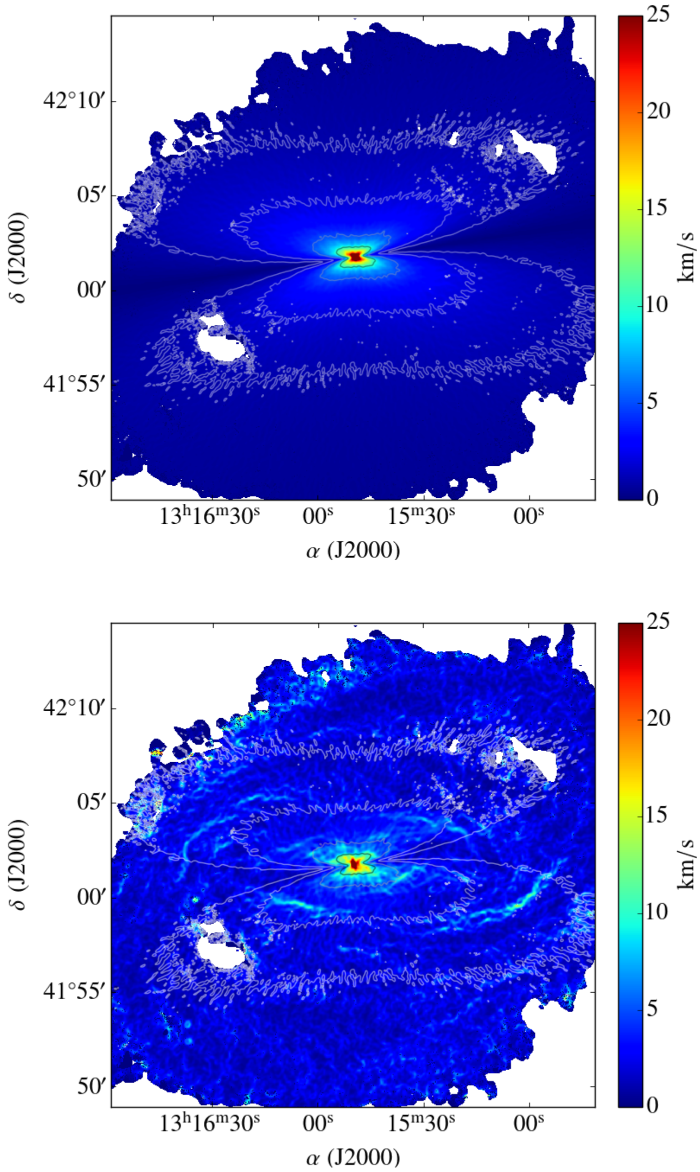

FIGURE 4.6. – Beam smearing modeling using SINGS (top panel) and THINGS data of NGC5055. We overplot contours at 1-2-5-10 km/s in gray to highlight the fast decrease of the beam smearing effect in the outer part of the galaxy.

Finally, the beam smearing modeling is shown in Fig 4.6 for NGC5055. A central peak and a X-shape pattern are the dominant features present in both maps. Fine structures are only present in the beam smearing map inferred from the THINGS velocity field and correspond to small scale deviations to rotation. In velocity fields, the impact of beam smearing is dominant in the center, which is not necessary the case for the dispersion. The amplitude of the central peak and the X-shape is slightly higher using SINGS data, due to the better resolution, but without a significant difference. Thus, we decided to use the model derived using THINGS data because we can account for local features at large radii and still having a robust description in the inner part of the galaxy.

Galaxy name	D Mpc	V_{sys} km/s	Incl deg	PA deg	B_{maj} arcsec	B_{min} arcsec	B_{pa} deg
NGC925	9.2	546.3	66.0	286.6	5.9	5.7	31
NGC2403	3.2	132.8	62.9	123.7	8.8	7.7	25
NGC2841	14.1	633.7	73.7	152.6	11.1	9.4	-12
NGC2903	8.9	555.6	65.2	204.3	15.3	13.3	-51
NGC2976	3.6	1.1	64.5	334.5	7.4	6.4	72
NGC3031	3.6	-39.8	59.0	330.2	12.9	12.4	80
NGC3198	13.8	660.7	71.5	215.0	13.0	11.6	-59
NGC3521	10.7	803.5	72.7	339.8	14.1	11.2	-62
NGC3621	6.6	728.5	64.7	345.4	15.9	10.2	4
NGC3627	9.3	708.2	61.8	173.0	10.6	8.9	-48
NGC4736	4.7	306.7	41.4	296.1	10.2	9.1	-23
NGC5055	10.1	496.8	59.0	101.8	10.1	8.7	-40
NGC6946	5.9	43.7	32.6	242.7	6.0	5.6	7
NGC7331	14.7	818.3	75.8	167.7	6.1	5.6	34
NGC7793	3.9	226.2	49.6	290.1	15.6	10.9	11

Tableau 4.1. – Beam parameters for the THINGS data

4.4.2. Noise in the FFT

Before applying FFT on real data, we need to understand in a first step how evolves the results of the FFT with the noise in the data, and to which limits we can recover the real signal. In other words, if the uncertainties on the dispersion are greater than the true signal, can we recover the true signal, and with which accuracy? To do so, we create a toy model from the equation 4.16, with phases $\phi_k = 0$ and in adding noise. The noise we add corresponds roughly to the uncertainties on the instrumental resolution that we will first estimate. The uncertainties on σ^2 are linked to the amplitude of the mean value σ_0 of the model and the intrinsic dispersion $d\sigma$ following the differential :

$$d(\sigma^2) = 2 \times \sigma_0 \times d\sigma \tag{4.19}$$

in which $\sigma = \sigma_0$ because in a ring all higher orders are on average zero and then $<\sigma>=\sigma_0$. Since we do not have uncertainty maps due to the processing techniques (moments method) on THINGS data, $d\sigma$ is not known precisely. By inspecting residual maps from WHISP, we estimate that the uncertainty on the dispersion velocity is

Galaxy name	α(J2000) (hh mm ss)	δ(J2000 (dd mm ss)	V_{sys} km/s	PA deg	Incl deg	V_{court} km/s	r_{court} arcsec	index
NGC0925	02 27 16.8	+33 34 41	554	105	50	132	187.0	5.13
NGC2403	07 36 54.5	+65 35 58	132	125	60	10000	0.3	0.10
NGC2841	09 22 02.6	+50 58 35	638	150	70	327	27.4	2.04
NGC2903	09 32 10.1	+21 30 04	556	212	64	197	79.2	299.70
NGC2976	09 47 15.4	+67 54 59	3	323.5	70.2	66	84.5	243.80
NGC3031	09 55 33.2	+69 03 55	-34	332.9	62.4	279	89.3	1.06
NGC3198	10 19 54.9	+45 33 09	660	33.9	69.8	170	50.5	1.54
NGC3521	11 05 48.6	-00 02 09	805	342	66.7	225	22.5	3.24
NGC3621	11 18 16.3	-32 48 45	727	342.5	65.2	10000	2.7	0.12
NGC3627	11 20 15.0	+12 59 30	727	170	65	1440	0.2	0.17
NGC4736	12 50 53.0	+41 07 14	308	292	36	169	0.0	1.88
NGC5055	13 15 49.3	+42 01 45	504	98.0	63	225	3.6	0.79
NGC6946	20 34 52.0	+60 09 15	46	239	38.4	223	7.7	0.50
NGC7331	22 37 04.1	+34 24 56	816	165	78.1	231	15.7	120.0
NGC7793	23 57 49.8	-32 35 28	230	277	47	287	39.9	0.42

Tableau 4.2. – SINGS parameters to model the beam smearing effect

typically $d\sigma = 1$ km/s. Thus, we define the noise δ on σ^2_{obs}, as a Gaussian distribution centered on 0 and with a standard deviation of $\sigma_{Gauss} = d\sigma^2$.

Finally, the equation of the toy model is given by :

$$\sigma^2_{obs} = \sigma^2_0 + \sigma^2_1 \cos(\theta) + \sigma^2_2 \cos(2\theta) + \sigma^2_3 \cos(3\theta) + \sigma^2_4 \cos(4\theta) + \delta \qquad (4.20)$$

With δ a random value in the noise distribution. In order to investigate the impact of the noise on the uncertainty of measured amplitudes $\sigma_{out,k}$, we first set the amplitude of one order $\sigma_{in,k}$ to 0, 1, 2 and 4 km s^{-1}, all other orders having their amplitude set to zero, except order zero. For each value of the amplitude $\sigma_{in,k}$, we realise $M = 1000$ iterations of the noise distribution and evaluate the FFT coefficients to measure the mean uncertainty on $\sigma_{out,k}$. We show the results in Fig. 4.7, with two values adopted for both σ_0 and σ_{Gauss}. This study clearly shows that the uncertainties do not depend on the order, nor on the amplitude of $\sigma_{in,k}$, and then, as expected, these uncertainties are proportional to σ_0. The difference between input and output amplitudes is larger when the amplitude is low, because amplitudes in the FFT decomposition cannot be negative.

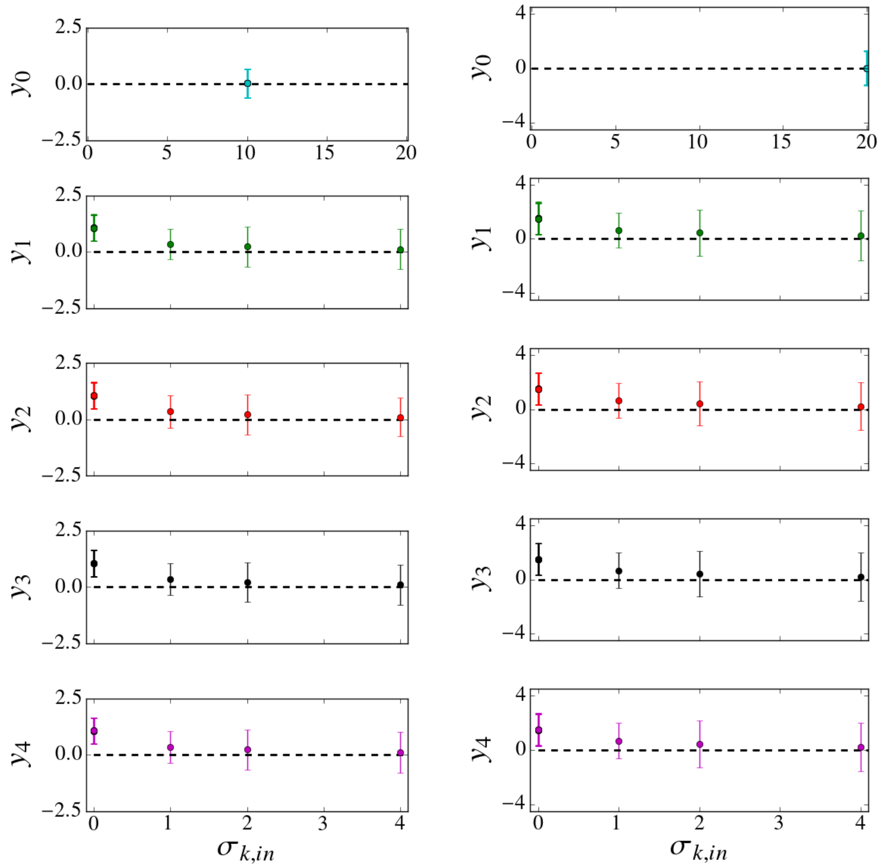

FIGURE 4.7. – Mean difference between the input $\sigma_{k,in}$ of the toy model and the FFT output $\sigma_{k,out}$ following the relation $y_k = \sqrt{\frac{\sum(\sigma_{k,out}-\sigma_{k,in})^2}{M}}$, where M is the number of iterations of the noise, as a function of $\sigma_{k,in}$. Errorbars are the 1σ uncertainties of the distributions. Each quadrant shows an order of the FFT. Left/right column represents models with $\sigma_0 = 10/20$ km s^{-1} and $\sigma_{Gauss} = 20/40$ km s^{-1}.

We then create toy models with $\sigma_{in,k} = 0$ except for $k = 0$, and input a noise δ by spanning different values for $d\sigma$, in order to find a function that describes the uncertainties depending on the main parameters : σ_0, $d\sigma$ and N the number of points in the FFT. Indeed, N varies from one ring to another and from one galaxy to another. We do 1000 iterations of the FFT and analyse the amplitudes for orders 1 to 4, which are 0 in our model (see Fig. 4.8). By varying parameters defined before, we observe that amplitudes of order $\sigma_k, k = 1, ..., 4$ vary with $\sqrt{2\sigma_0 d\sigma}$ and with $N^{-1/4}$, as expected, since the noise is supposed to vary as $N^{-1/2}$ on σ_k^2, and because we provide here the result on σ_k. That gives us the following equation for the noise :

$$d\sigma_{out,k}(\sigma_0, d\sigma, N) = \frac{\sqrt{2\sigma_0 d\sigma}}{0.75N^{1/4}} \tag{4.21}$$

The coefficient 0.75 was necessary to scale correctly the curves.

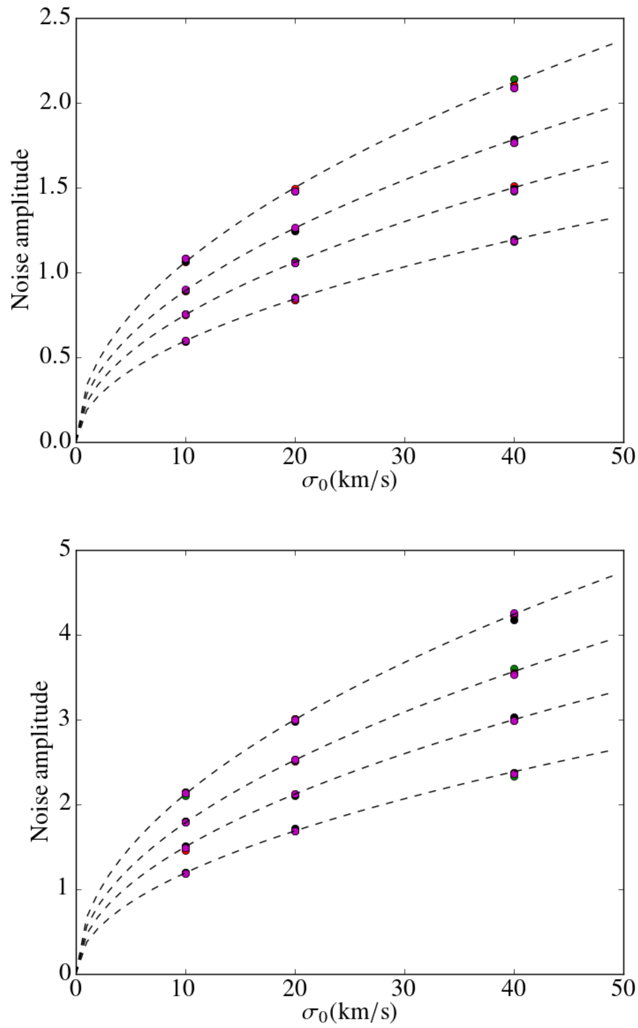

FIGURE 4.8. – Noise on the dispersion amplitude for orders 1 to 4 of the FFT vs σ_0 for two distinct values of $d\sigma$ (top panel : $d\sigma$ = 1 km/s, bottom panel : $d\sigma$ = 4 km/s) and various number of points in the FFT N. The dashed lines correspond to Eq. 4.21, each curve corresponding to a different value of N (from top to bottom : 1000, 2000, 4000 and 10000). Dots corresponds to different orders (order 1 : green, order 2 : red, order 3 : black, order 4 : magenta). The similar behaviour of orders leads to superposed points.

This formula (Eq. 4.21) allows us to have a robust estimation of the noise in a ring containing N pixels and with an average dispersion σ_0.

5. Anisotropy in the HI random motions

Sommaire

5.1 Physical motivations 77
5.2 Anisotropy study of the THINGS sample 79
5.3 Anisotropy study of the WHISP sample 82
  5.3.1 From THINGS to WHISP : impact of beam smearing 82
  5.3.2 Analysis of the WHISP subsample 86
5.4 Conclusion 89

5.1. Physical motivations

One can question the collisional or collisionless nature of interstellar gas. If the rate of collisions is low in a clumpy medium, asymmetries in velocity dispersion like those observed in gas velocity dispersion maps of galactic disks could be hints of anisotropic motions in a gaseous collisionless medium. Indeed, in presence of anisotropy, assuming null covariance terms, Equation 4.11 implies that $\sigma_{\rm los}$ maps should exhibit a bisymmetric pattern, with greater dispersions near one of the minor or major axes and lower near the other axis. The sign of $\sigma_\theta^2 - \sigma_R^2$ rules the orientation of the pattern, with greater values (smaller, respectively) near the minor axis (major axis) for $\sigma_\theta < \sigma_R$ ($\sigma_\theta > \sigma_R$) as described in the bottom left panel of Fig. 4.3.

This strong prediction for the shape of $\sigma_{\rm los}$ has been tested only once with the Local Group spiral galaxy Messier 33 (Chemin et al. 2020). This was the first attempt to study the properties of asymmetries in maps of HI and CO gas random motions, and the shape of the gas velocity ellipsoid in the mid-plane. This study showed that HI gas random motions are highly asymmetric, dominated by a large-scale bisymmetry aligned with the disk minor axis at almost every radii (Fig. 5.1, top). From an anisotropy viewpoint, this bisymmetry corresponds to an ellipsoid with $\sigma_\theta < \sigma_R$, thus an anisotropy parameter $\beta_\theta = 1 - (\sigma_\theta/\sigma_R)^2 > 0$ (Fig. 5.1, bottom). The β_θ profile differs strongly from the value expected from the isotropic configuration ($\beta_\theta = 0$). This implies that orbits of gas are more radial in the mid-plane (e.g. Binney & Tremaine 2008), a result reminiscent of the stellar kinematics in the Milky Way disk (e.g. Gaia Collaboration et al. 2018). Since the dispersion bisymmetry coincides with the presence of a gaseous spiral structure in Messier 33, radially biased orbits could perhaps be caused by elliptical motions inferred by the spiral potential.

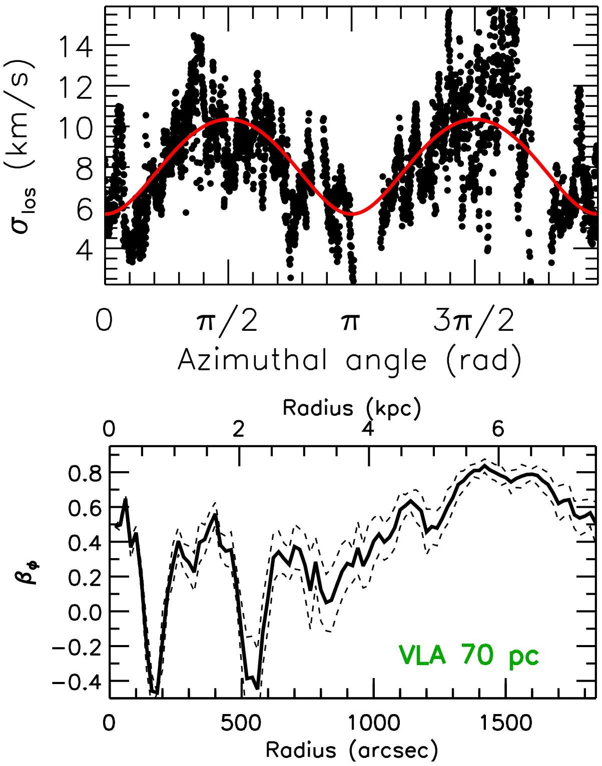

FIGURE 5.1. – Example of asymmetric velocity dispersion in the HI gas of the Messier 33 galaxy. Top panel : azimuth-velocity dispersion diagram at $R = 5.7$ kpc, with filled symbols corresponding to the observed dispersions and the red solid line to the results of the model of Eq. 4.9 at this radius. Bottom panel : velocity anisotropy parameter in the disk plane. From Chemin et al. (2020).

An eventual finding of anisotropy, indicating that part of the gas can behave like collisionless stars would have important implications in galactic dynamics. $\sigma_{\rm los}$ would no longer be the reference from which the velocity tensor can be measured directly, and models of the above equation would be necessary. For example, it would impact the study of the disk vertical equilibrium, which depends on σ_z, that is related to the history of the disk heating via secular and hierarchical processes, and to the mass distribution in the disk (Combes & Becquaert 1997; Koyama & Ostriker 2009; Bershady et al. 2010; Martinsson et al. 2013) or the study of the stability criterion, linearly depending on σ_r, which drives the possibility of star formation via the equilibrium of gas clouds against gravitational collapse (Leroy et al. 2008). Of particular interest for this study, it would also impact the study of the gas radial pressure support (also called 'gas asymmetric drift'), which depends on σ_r and on the radial derivative of σ_r. The radial pressure modifies the circular velocity curve into shallower velocity profiles (Dalcanton & Stilp 2010). Given that $\sigma_R > \sigma_{\rm los}$ and $d\sigma_R > d\sigma_{\rm los}$ in Messier 33, the isotropy assumption of $\sigma_R = \sigma_{\rm los}$ possibly underestimates the gas radial pressure in the disk, thus the inner slope of the gas rotation curve and the mass density profile.

Therefore, the modeling of gas random motions is important for the study of the collisional/collisionless nature of the gaseous medium, the structure of gas orbits in the mid-plane and the physical conditions in the gas. This problem has now to be investigated on a sample of different galaxies. In this chapter and in the next one, we will address this question by performing the first large-scale study of random motions of gas in nearby galaxies from high-quality HI data.

This chapter is dedicated to the anisotropy study of the velocity dispersion maps of the THINGS and WHISP samples in the simple case of axisymmetric systems. In that perspective, the azimuthal variations of the dispersion velocity are associated with anisotropy.

5.2. Anisotropy study of the THINGS sample

Tilted-ring models on 2D velocity fields have been performed by de Blok et al. (2008) for 19 of the 34 THINGS galaxies. Among the different methods to obtain the velocity field from the data-cube (i.e. intensity-weighted mean velocity, peak velocity field, Gaussian profiles, multiple Gaussian profiles, Hermite h3 polynomials), they have chosen to use the last one, especially due to the stability of the method in low S/N regions. All velocity profiles of the galaxy are fitted with the Hermite h3 polynomials. To filter low-quality regions of the galaxy, a mask was applied on the velocity field. Profiles for which : 1- the fitted maximum intensity is lower than $3\sigma_{ch}$, with σ_{ch} being the average noise in the profile out of the line region, 2- the dispersion of the fitted function is lower than the channel separation, were not kept in the velocity fields. They added a second mask using a sigma-clipping on the HI column density maps to suppress noise pixels. This mask is mainly excluding regions outside r_{min} and r_{max} which are respectively the innermost and outermost radii of the tilted-ring model they have fitted on the final velocity fields to obtain a rotation curve. The sampling of the rotation curve has then been fixed at 2 points per beam. These final velocity fields were then fitted with a tilted-ring model. In the present work, we used the same method to build the mask. Nevertheless, we note that for some galaxies like NGC3031 (Fig H.6), NGC3627 (Fig H.10), it seems from the velocity model that the model could extend further away. To be conservative and consistent with their analysis, we chose to keep the parameters of the tilted-ring model determined by de Blok et al. (2008).

To calculate the deprojected cylindrical coordinate on the dispersion maps we use the tilted-ring model described above and values are reported in Table 2.1. Knowing the radial variation of the position angle and inclination allows to take the warp into account. In our study we considered only one data-point per beam to minimize the correlation between adjacent rings. Indeed, due to the beam size, there is an overlap between rings and to avoid this redundant information we only use one point per beam.

We aim at measuring anisotropy directly at the local annulus scale. For this purpose each galaxy is decomposed into rings, and the azimuthal variation of the dispersion velocity is fitted by the combination of Eq. 4.11 and Eq. 4.12 with cross-terms equal to zero :

$$\sigma^2_{\rm obs} = \sigma^2_\theta \cos^2\theta \sin^2 i + \sigma^2_R \sin^2\theta \sin^2 i + \sigma^2_z \cos^2 i + \sigma^2_{th} + \sigma^2_{LSF} \tag{5.1}$$

Components σ_{th} and σ_{LSF} are considered as fixed parameters in the fit. The interstellar neutral gas could be cold or warm. In the case of a cold component the temperature is around 100 K which leads to $\sigma_{th} < 1$ km/s while in the case of a warm component the temperature of the gas is around 5500 K leading to dispersion of 6-7 km/s (Field et al. 1969; Wolfire et al. 1995). In our study we consider a cold gas for which σ_{th} is negligible compared to the observed dispersion, thus we fix $\sigma_{th} = 0$ km/s. We already discussed in the previous chapter the degeneracy of the parameters $\sigma_R, \sigma_\theta, \sigma_z$. We probed different ways to reduce the number of free parameters :
- fixing $\sigma_z = 0.5\ (\sigma^2_R + \sigma^2_\theta)$.
- fixing σ_z to a fixed value spanning between 6 and 10 km/s.
- fixing $\sigma_z =< \sqrt{\sigma^2_{\rm los} - \sigma^2_{th} - \sigma^2_{LSF}} >$ on a ring.

The choice of reducing the degeneracy could artificially bias the result toward anisotropy, hence we focus here on the last configuration, which corresponds to the most isotropic configuration. With this model the only two free parameters of the fit are σ_R and σ_θ. For the fitting process we use the routine mpfit, a code which performs a Levenberg-Marquardt least-squares minimization. Results can be sensitive to the initial conditions. To obtain a robust results, we perform 1000 fits for each ring, starting with random values between 0 and 50 km/s for σ_R and σ_θ. The final values are chosen as the mean of the distributions of σ_R and σ_θ.

In Fig. 5.2, we show two examples of fit. On the left panel is presented the azimuthal variation of a ring of NGC 2403 at R = 564". We observe that the period of the cosine in the fit is $\pi/2$. By identification to Eq. 4.11, we conclude that we are in the case $\sigma_R > \sigma_\theta$, equivalent to $\beta_\theta > 0$. Let's remind that this equation shows that the period of the $\cos(2\theta)$ is ruled by the sign $\sigma^2_\theta - \sigma^2_R$. The right panel shows the fit of the ring at R = 150" for the galaxy NGC 3521. By opposition to the left panel, the period is π, indicating that $\sigma_\theta > \sigma_R$.

For each galaxy, we plot :

— the radial variation of the dispersion ellipsoid, $\sigma_R, \sigma_\theta, \sigma_z$, the mean value of $\sigma_{\rm los}$ in a ring, and the mean value $\sigma_{los,mod}$ of the modeled line-of-sight dispersion.

— the radial variation of the anisotropy parameter $\beta_\theta = 1 - (\frac{\sigma_\theta}{\sigma_R})^2$

An example is given for NGC2403 in Fig. 5.3, with the dispersion ellipsoid on the left panel, σ_R, σ_θ and the mean value of $\sigma_{\rm los}$ in the ring. σ_z is fixed equal to $< \sigma_{\rm los} >$ so we do not plot it. Errorbars correspond to the 1σ of the distributions from the 1000 results. On the right panel we have the corresponding anisotropy parameter, which is another way to visualize the first plot. In the inner 200 pc, in average β_θ is close to 0, and the isotropic configuration is consistent within the uncertainties if we look at

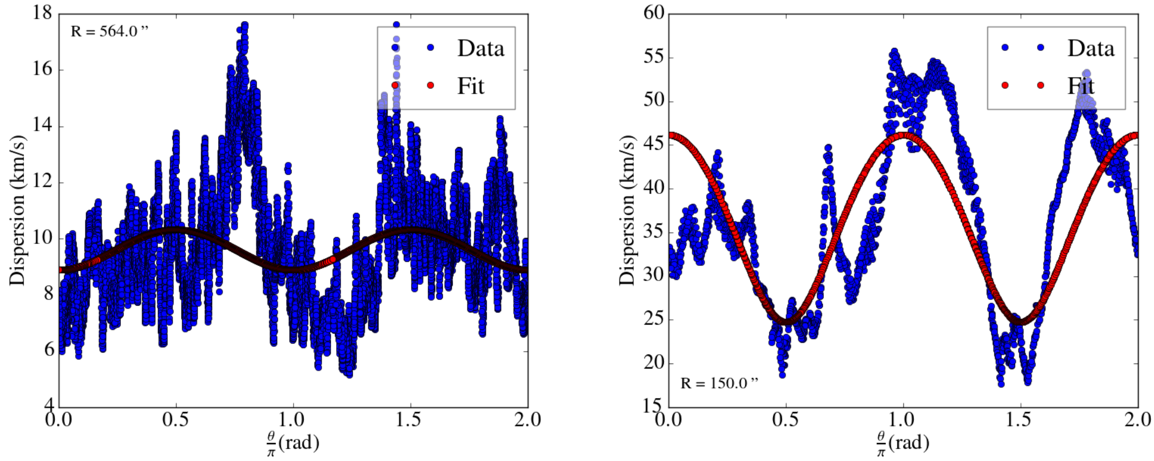

FIGURE 5.2. – Example of fit of the azimuthal variations in the case $\sigma_R > \sigma_\theta$ (left, NGC 2403 at R = 564") and in the case $\sigma_\theta > \sigma_R$ (right, NGC 3521 at R = 150").

the dispersion ellipsoid. At larger radii the radial component tends to dominate the azimuthal one, increasing the value of β_θ.

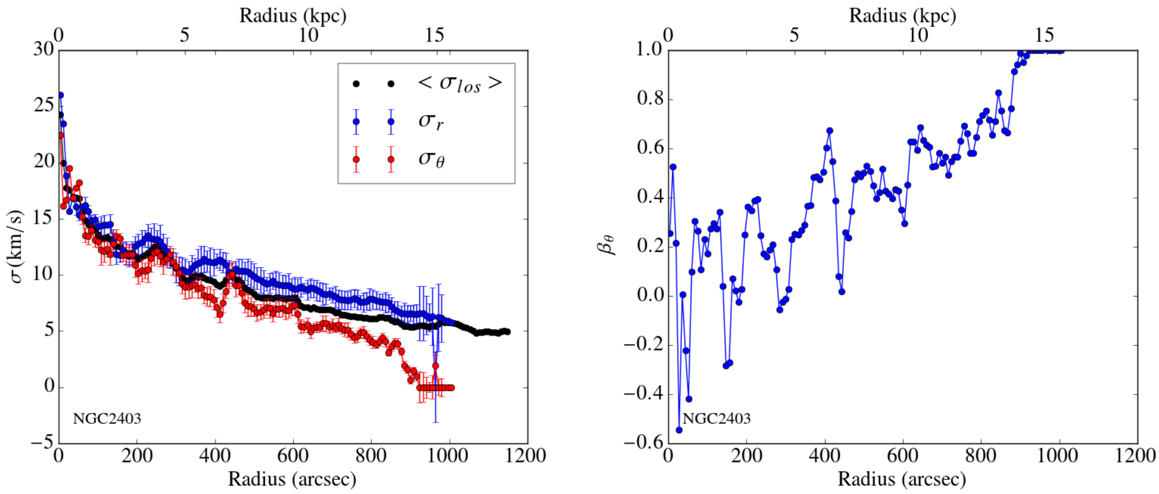

FIGURE 5.3. – Radial variation of the dispersion ellipsoid and anisotropy parameter β_θ of the galaxy NGC2403.

Results for the whole sample are presented in Appendix E. We note that the results obtained by the fit (for σ_R and σ_θ) are not reliable for most radii. It's a general result across a majority of the ring studied : the azimuthal variations at a given rings are often more complex than a simple function in $\cos 2\theta$. The strong order 2 aligned with the minor axis obtained in Chemin et al. (2020) is not found in other galaxies. Nevertheless half of the galaxies exhibits regions where the $\cos 2\theta$ seems to fit approximately the azimuthal variation, but with an angle phase different from $\pi/2$. In our model this fixed angle phase is due to the hypothesis that covariance terms $\sigma_{R\theta}, \sigma_{Rz}, \sigma_{\theta z}$ are null. Therefore, this hypothesis might be too restrictive.

5.3. Anisotropy study of the WHISP sample

5.3.1. From THINGS to WHISP : impact of beam smearing

Our initial goal was to perform this study on a much larger sample than THINGS, WHISP in order to have statistical constraints on the possible anisotropy with the morphological type for example. THINGS served as a test bench to implement the numerical code. Nevertheless, not all WHISP galaxies are suitable for this study. Indeed, the angular resolution of the observations is much lower with WHISP. In addition, the WHISP galaxies are more distant and contain a higher fraction of irregular galaxies; for those reasons, we suspect that some of them would be discarded. In this part, we investigate those effects and up to which limit we can measure asymmetries on galaxies. For this purpose, we use 3 typical galaxies from THINGS : NGC2403, NGC2841 and NGC2903, spanning different masses, distances and morphological types. The physical scale on these galaxies is much higher than the ones of WHISP galaxies, thus we degrade progressively the resolution of the THINGS data, to investigate the limit at which the anisotropy study becomes meaningless. Amongst the 252 WHISP galaxies for which we could obtain rotation curves with ^{3D}Barolo, the median physical scale of the beam is 1.43 kpc, and the spectral resolution varies, depending on the configuration of the observation between 3 and 20 km/s.

Galaxy	Type	D Mpc	v_{hel} km/s	inc deg	PA deg	M_{HI} $10^9 M_\odot$	Resolution pc	pixel arcsec	Δv kms^{-1}
NGC2403	Sc	3.2	132.8	62.9	123.7	2.58	135	1.0	5.2
NGC2841	Sb	14.1	635.2	74	153	8.58	750	1.5	5.2
NGC2903	Sbc	8.9	556.6	65	204	4.35	650	1.5	5.2

Tableau 5.1. – Main properties of the 3 galaxies studied

To avoid the noise inherent to observations, we model for each of the 3 galaxies a noise-free mock data-cube using Gaussian profiles. We use the flux, velocity and dispersion maps as well as the parameter of spectral resolution to build this data-cube. A visual comparison of the observed and modeled data-cube, as well as a comparison of the moment maps obtained via observations and modelisation shows that our mock data-cube reproduces very well the observed one.

In order to artificially lower the resolution, for each galaxy we smooth and bin this model data-cube. In Table 5.1, we have for each galaxy the size of the data-cube, the pixel size and the beam size. To lower the resolution, we create 4 mock data-cubes using oversampling parameters of 4, 8, 16 and 32. An oversampling of 4 means that the spatial dimensions are divided by 4, and the pixel size is multiplied by 4. In WHISP data, there is a factor 3 between the spatial resolution and the pixel size (i.e. the pixel size for maps smoothed at a resolution of 60" is 20", for 30" maps the pixel size is 10"). The resolution is thus given by 3 times the oversampling parameters times the pixel size. To obtain this resolution, we have to smooth the data-cube with a Gaussian function of resolution $\sqrt{(3 \times \mathrm{k} \times \mathrm{p})^2 - FWHM^2}$, with k the oversampling parameter, p the pixel size, and FWHM the size of the beam, we assume it round by taking the mean of Bmin and Bmaj. This step results in the creation of 4 binned and smoothed mock data-cubes for each galaxy.

The next step is the beam smearing modelisation of these data-cubes, with the same methodology as described in Sect. 4.4.1. To recall the basis, from a flux map and a velocity map at high resolution we can estimate the level on unresolved gradients in our data. For the modelisation of WHISP galaxies, we use the flux map from WHISP at a given resolution, and a modeled velocity field using GHASP $H\alpha$ data. Indeed, we do not have access to the flux distribution at a really high distribution. Therefore, to mimic the same conditions as for the WHISP galaxies, to model the beam smearing of our mocks data-cubes at low resolution, we use the velocity map from THINGS and the flux map smoothed at the resolution of the data-cube. We show an example of the beam smearing modelisation of NGC2403 in Fig. 5.4 at 3 different resolutions. The pixel size for this galaxy is 1"/pix. With an oversampling of four, it gives 4"/pix, leading to a resolution 3 times greater of 12" which is equivalent to 186 pc at galaxy distance (3.2 Mpc). The first column shows the beam smearing modelisation, the second one the dispersion from the mock cube and the last one the corrected dispersion. In the middle panel of the first row we give the celestial axis, to have the field-of-view which stays constant even when decreasing the resolution and for other resolutions we show the number of pixel to illustrate the binning process. On the first row, we have an oversampling of 4, which results in a linear resolution of 186 pc. The beam smearing is low and thus the correction is negligible. The second row has an oversampling parameter of 16 explaining that the size of the dispersion map is only 128 × 128 pixels and the spatial resolution is 4 times larger : 745 pc. The mock dispersion is smoother, and with a higher central dispersion due to the beam smearing. Finally, the last example is for an oversampling parameter of 32. The oversampling is twice larger than the second row, leading to a pixel size of 64 × 64 pixels and a resolution of 1489 pc on the mock galaxy. Those effects induce a high level of beam smearing which is corrected efficiently. The goal is to perform the same study of anisotropy on the corrected different maps to see up to which limit we can recover the results from the high resolution.

Finally, for each galaxy we have :

- A mock data-cube at the resolution of the THINGS data and the corresponding moment maps
- Four mocks data-cubes at low resolution, with their corresponding moment maps, in particular dispersion maps, corrected from the beam smearing effect.

We perform the anisotropy study described in the previous section in each of these

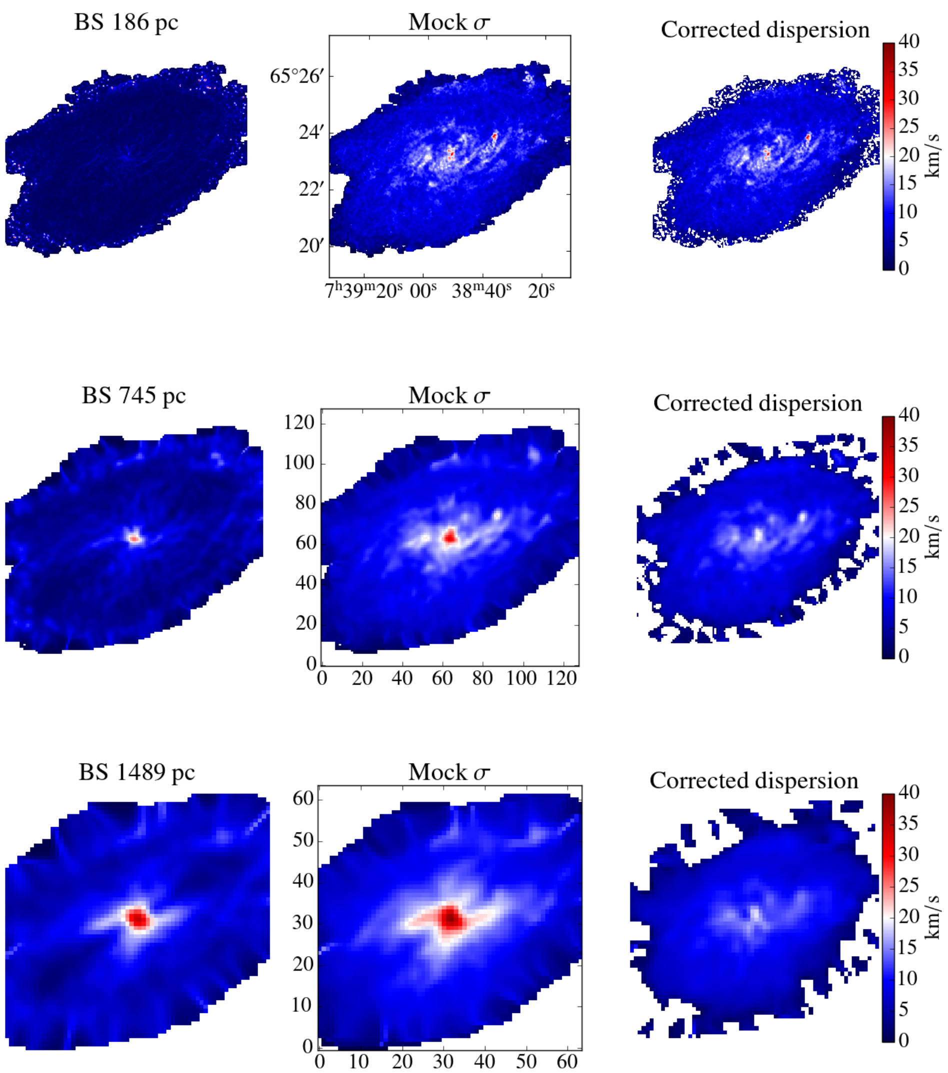

FIGURE 5.4. – Mock dispersion maps with beam smearing correction of NGC2403 at different spatial resolutions. Left : beam smearing correction map; middle : observed velocity dispersion in presence of beam smearing; right : corrected velocity dispersion map.

dispersion maps, compute the radial profile of β_θ and compare the results depending on the resolution. The methodology is different from before, since here our main focus is not on the anisotropy of each galaxies but on the variation of the anisotropy measurement with resolution. Therefore, in that case we fixed $\sigma_z = 7$ km/s and perform a single fit of the parameters σ_R and σ_θ for each ring. The result is presented in Fig. 5.5. On the left column, we have the anisotropy parameter β_θ calculated on the dispersion maps obtained using the second order moments of the low-resolution data-cubes and on the right column the same maps corrected from the beam smearing effect.

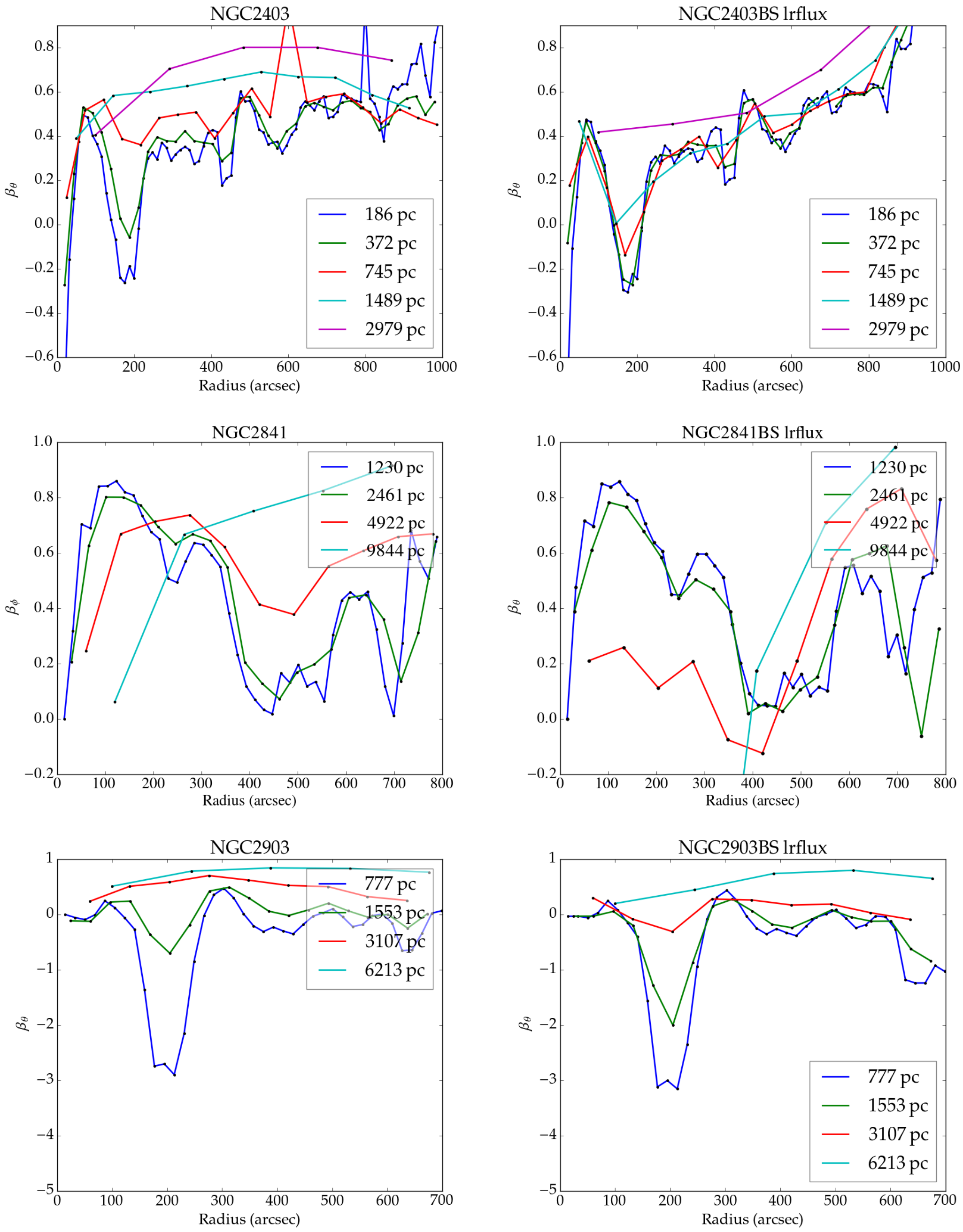

FIGURE 5.5. – Anisotropy for NGC2403, NGC2841, NGC2903 at different resolution on the beam smearing uncorrected (left column) and corrected (right column) dispersion maps.

A first look at the left column of Fig. 5.5 shows that the lower the resolution the higher the anisotropy parameter β_θ. The increase of beam smearing as well as the loss of resolution tends to make orbits appearing more radial (β_θ greater than 0 implies that $\sigma_R > \sigma_\theta$). Our goal is to use this figure is order to define a limit in resolution at which, by correcting from the beam smearing effect, we can recover the trend of β_θ at high resolution. Let's remind that our beam smearing correction only accounts for the unresolved velocity gradient. It does not account for the intrinsic local velocity dispersion. The beam spans hundreds of parcsecs in the galaxy, so that different regions, with their own kinematic properties, are mixed. With our modelisation, we can not recover the kinematic of each region.

For NGC2403, on the top left panel, we start losing information at a resolution of 745 pc. The increasing trend and the local variations of β_θ at 186 pc are lost, and at lower resolution it is even worse. By correcting the beam smearing effect, at a resolution of 745 pc, we can recover the information from high resolution, with a remarkable match between the blue, green and red curve. Even at 1500 pc, we can still observe the global increasing trend of β_θ. Nevertheless, at a resolution of 3 kpc, the anisotropy parameter stays above the high resolution one, and the sampling of the galaxy is too low to have a good match.

NGC2841, the most massive galaxy of our sample, is located at a distance almost five times larger than NGC2403, explaining why the physical scale is way larger than for NGC2403. At resolutions of 1230 and 2461 pc, the anisotropy parameter is equivalent, with only small variations at local scale. At resolution of 5 kpc, we have a sight of the global trend, but it is not accurate enough, and at a resolution of 10 kpc we lose all information about β_θ.

NGC2903 has a similar behaviour as NGC2403. β_θ is closer to 1 at lower resolution. Without beam smearing correction, at resolution of 3 kpc we have a constant anisotropy parameter around 0.4 or 0.5 which is not representative of the true anisotropy parameter art higher resolution. After the correction, except the loss of the local peak at 200 pc due to the lower resolution we recover the global trend of β_θ up to 3 kpc. But for an accurate description it is better to have a maximum resolution of 1.5 kpc.

Considering these results, we estimate that up to a resolution of 1.5 kpc, by modeling and correcting the beam smearing on the dispersion maps we can recover the anisotropy parameter that we would have obtained at higher resolution.

5.3.2. Analysis of the WHISP subsample

This preparatory work gives us a first insight at the type of analysis we can perform on the WHISP sample, especially which galaxies are adapted to this anisotropy/asymmetry study. If we apply this resolution criteria on the WHISP galaxies, this reduces the WHISP sample to 70 galaxies

As describe above, by correcting from beam smearing effects, the WHISP galaxies having a physical scale of 1.5 kpc should allow to recover the anisotropic parameter. In order to proceed to this correction we need the $H\alpha$ counterpart which is available for 150 galaxies amongst the 313 WHISP galaxies in order to have high resolution velocity fields. Combining this limitation to the previous one, the sample drops to 30 galaxies.

In the second chapter, to derive rotation curves with BBarolo we worked mainly with the 30" resolution data-cubes, due to the balance between resolution and sensitivity. In the present case we can not use these data, because it artificially creates beam smearing, which tends to dominate most galaxies. In conclusion we used the 15" resolution data-cubes. However, in several cases, the velocity dispersion maps at that resolution contains a large fraction of unaffected pixels as illustrated in the second line, middle column of Fig. 5.6. In addition, the beam smearing correction still reduces the number of independent velocity dispersion pixels as shown on the right column of Fig. 5.6. Furthermore, in order to fairly sample the radial distribution, we impose a lower limit of 4 beams for each galaxy (Bosma 1978). Applying those three last steps, 15 additional galaxies have been excluded. Because the excluded galaxies are the less resolved one, this is equivalent to redefine maximum physical scale of 1 kpc. The final sample is presented in Table 5.2.

Galaxy name	α(J2000) (hh mm ss)	δ(J2000) (dd mm ss)	Type	V_{sys} km/s	m_B mag	M_B mag	log(D_{25}) log(0.1')	Incl deg
UGC01256	01 47 53.9	+27 25 55	SBc	426	11.41	-18.94	1.85	69.6
UGC01913	02 27 16.9	+33 34 44	Scd	553	10.59	-20.05	2.03	58.7
UGC02455	02 59 42.5	+25 14 19	IB	373	12.07	-18.56	1.47	42.4
UGC03273	05 17 44.4	+53 33 05	SABm	616	14.95	-18.68	1.40	90.0
UGC04284	08 14 40.1	+49 03 42	SABc	547	12.25	-18.80	1.48	59.5
UGC04305	08 19 04.3	+70 43 18	I	158	11.16	-16.97	1.90	51.4
UGC04325	08 19 20.5	+50 00 35	SABm	506	12.69	-17.98	1.48	68.0
UGC04499	08 37 41.5	+51 39 09	Sd	687	15.36	-15.62	1.28	81.2
UGC05414	10 03 57.2	+40 45 27	IAB	604	13.81	-16.86	1.48	53.8
UGC05721	10 32 17.2	+27 40 08	Scd	532	13.21	-16.52	1.21	61.6
UGC05789	10 39 09.5	+41 41 13	SBc	738	11.77	-19.37	1.56	62.7
UGC05840	10 43 31.2	+24 55 20	Sbc	588	10.50	-19.64	1.83	18.7
UGC07323	12 17 30.2	+45 37 09	Sd	516	11.59	-17.46	1.58	51.5
UGC07766	12 35 57.7	+27 57 35	Sc	814	10.28	-19.67	2.02	64.8
UGC07831	12 39 59.3	+61 36 33	SBc	146	10.82	-18.65	1.77	70.1

Tableau 5.2. – Properties of the WHISP subsample used for the study of random motions.

In Fig. 5.6, we present the beam smearing modelisation (left column) and correction (right column) on the dispersion maps (middle column) of two WHISP galaxies : UGC7766 and UGC4325. UGC7766 is the "best" galaxy of the WHISP sample, therefore, the dispersion maps contains an important number of pixels, and the beam smearing correction doesn't impact significantly the number of pixel. On the opposite, UGC4325 represents an "average" WHISP galaxy. The galaxy is smaller, and the dispersion maps contains some holes. The beam smearing correction increase the number of holes in the galaxy.

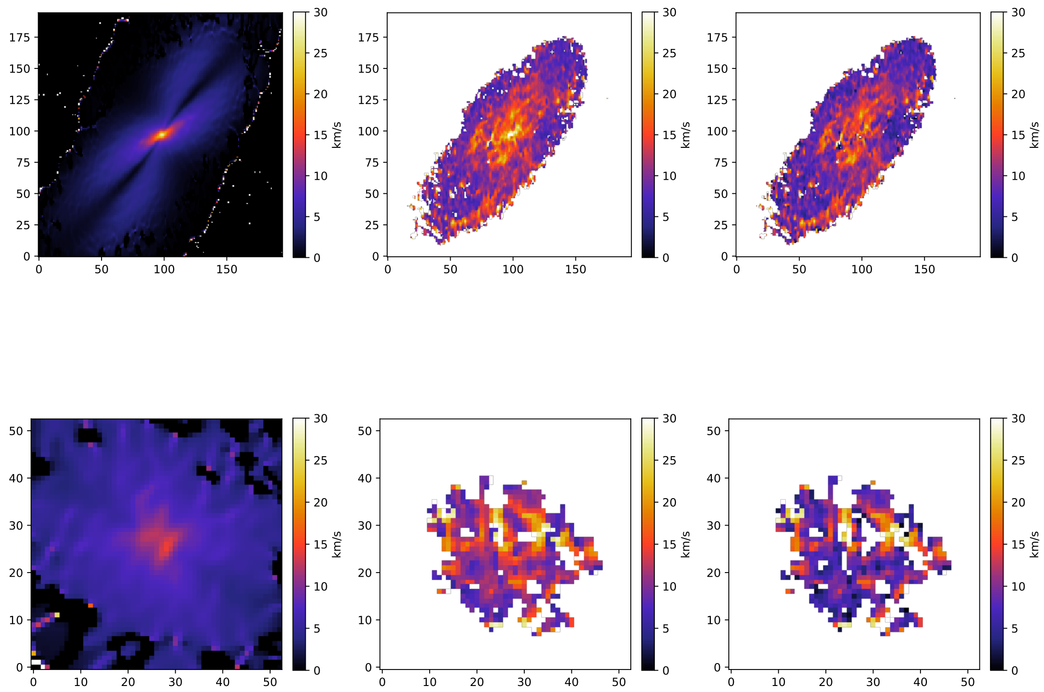

FIGURE 5.6. – Example of beam smearing modelisation for UGC7766 (first line) and UGC4325 (second second). On the left column, we have the beam smearing modelisation, on the middle one, the raw dispersion maps extracted with CAMEL and on the the right column the quadratical subtraction of the raw maps with the beam smearing model. Coordinates are given in pixels to give an idea of the number of pixels to sample the galaxy.

Dispersion maps are not given for the WHISP data. To derive the dispersion maps from the data-cube, we use the software CAMEL [1], a tool that fits Gaussian emission lines on data-cube to obtain kinematics. Actually, we perform this reduction on the entire WHISP sample presented in Chapter 2, for the data-cube at 15" and 30" resolution.

The methodology to fit the azimuthal variation is identical to the one used in the THINGS sample, except that for WHISP galaxies, we added an arbitrary limit of 40% of missing values in a ring to keep it for the study or not. Above 40%, the ring is discarded and the fit is not computed.

1. https ://gitlab.lam.fr/bepinat/CAMEL

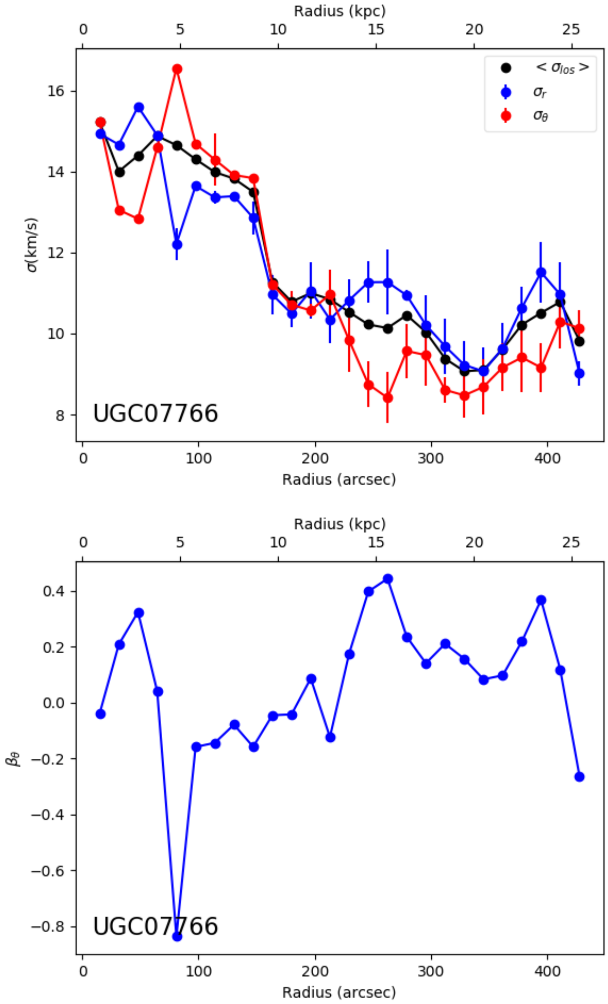

FIGURE 5.7. – Dispersion ellipsoid and anisotropy parameter β_θ calculated on the dispersion map corrected from the beam smearing of the galaxy UGC7766.

Result for the whole sample are presented in Appendix F. Without any surprise, once again we do not find a good agreement between the observed azimuthal variation and the variation expected in the case of an axisymmetric and anisotropic distribution. The number of pixels in a ring is much lower than for THINGS galaxies and the azimuthal sampling is not necessary continuous due to the beam smearing corrections, making the fit harder to adjust the data.

5.4. Conclusion

In this section, we studied the azimuthal variations of the velocity dispersion maps of galaxies from the THINGS and WHISP sample. To interpret those azimuthal variations, we worked in the simple case of an axi-symmetric system with anisotropy. This framework imposes to fit the data with Eq. 4.11, which is, assuming null cross-terms, composed by a constant value depending on the velocity ellipsoid component and a $\cos(2\theta)$ with its period linked with the sign of $\sigma_\theta^2 - \sigma_R^2$. This interpretation was motivated by the result obtained by Chemin et al. (2020) on M33. A first systematic study on 15 galaxies from the THINGS sample shows that this axisymmetric model is too restrictive to explain the azimuthal variation at all radii. Since the spatial resolution is crucial for this study, we used 3 galaxies from the THINGS sample, to create mock data at lower resolution. By correcting the beam smearing effect we conclude that up to a spatial resolution of 1.5 kpc, we can recover the anisotropy parameter β_θ as if it was obtained at higher resolution. Therefore, we were able to add 15 galaxies from the WHISP sample to our study. Similarly to the THINGS sample, the model doesn't reproduce the observed azimuthal variation of the velocity dispersion for galaxies of the WHISP sample. In general, these azimuthal variations are way more complex than a simple cosine function. Therefore, the values found for the anisotropy parameter β_θ could be due to asymmetries combined or not with anisotropies. Indeed this result doesn't rules out the anisotropy hypothesis. In order to investigate the possible anisotropy of the velocity dispersion ellipsoid, we need therefore a larger framework which includes the effect of non axi-symmetry on the azimuthal variation of the velocity ellipsoid.

6. Asymmetries in the HI random motions

Sommaire

6.1 Physical motivations 91
6.2 Asymmetry of the THINGS sample 92
  6.2.1 Method 1 : Rings study 92
  6.2.2 Method 2 : stacked galaxy 96
  6.2.3 Method 3 : Median values of radial distributions 107
6.3 Extension to the WHISP sample 108
6.4 Discussion 110
  6.4.1 Uncertainty in the beam shape 110
  6.4.2 Beam smearing and σ_4 112
  6.4.3 Multiple components and moments method compare with Gaussian fit 123
  6.4.4 Validity of the model and interpretation 124
6.5 Conclusion 127

6.1. Physical motivations

In the previous chapter, we saw that our axisymmetric-anisotropic model was too restrictive to explain the azimuthal variations in the rings. Following this model, the azimuthal variation of the line-of-sight velocity dispersion should be described by an order 2 with an angle phase aligned with the minor axis of the galaxy. Amongst all galaxies, some of them could be explained by an order 2, but with an angle phase different from $\pi/2$. In this chapter, we position ourselves in a larger framework, to quantify asymmetries in the distribution of HI random motion. For this purpose we are using the well-known technique of Fourier expansion which has been widely use to probe spiral arms or bars in flux distributions or to quantify non-circular motions in radial velocity distributions. This methodology is identical to the one presented in (Chemin et al. 2020), with a Fourier expansion up to the 4^{th} order of the HI velocity dispersion maps. On a large number of galaxies, the orientation of structures like spiral arms should be totally random. Therefore finding common asymmetric trends amongst various galaxies could be a sign of the presence of anisotropy in the velocity dispersion maps.

Our science objectives are manyfold :

- Measure asymmetries in high-resolution and high-sensitivity HI velocity dispersion maps. This will involve discrete Fourier Transforms of a cylindrical harmonics model $\sigma_{\rm asym} = \Sigma_k \sigma_k \cos k(\theta - \phi_k)$ (and squared values $\sigma_{\rm asym} = \Sigma_k \sigma_k^2 \cos k(\theta - \phi_k)$), where σ_k and ϕ_k are the amplitude and phase angle of the dispersion asymmetry of order k. Harmonic orders up to $k = 4$ will be probed, similarly to the M33 work (Chemin et al. 2020).
- Study the properties of the asymmetries. In particular, comparisons between the dominant perturbations with the axisymmetric mode will be done. The orientation of the phase angles will be investigated to detect possible alignments with major or minor axes of galaxies. Finding systematic alignments would argue in favour of gas being partly a collisionless medium, thus with an anisotropic velocity tensor.

6.2. Asymmetry of the THINGS sample

6.2.1. Method 1 : Rings study

Our goal is to study the asymmetry of the dispersion map for THINGS galaxies and look for systematic alignment of the phase angles. As exposed before, to perform this study we do a Fourier expansion of the dispersion maps, corrected from the beam smearing effect, up to the 4^{th} order. As we show later these first 4 orders describes dispersion maps very efficiently, and residuals are negligible.

Since we want to focus the study on the dispersion asymmetries due to gravitational effect, we do not use directly the observed dispersion. To account for instrumental effects, we subtract quadratically the instrumental dispersion σ_{LSF} of the Line Spread function (LSF). Moreover, the observed dispersion contains the information of the thermal component of the gas. The intrinsic temperature of the gas leads to isotropic random velocities σ_{th}. We want to get rid of this effect to focus on gravitational random motions. And as we mentioned in Section 4.3, we work with the dispersion squared. Chemin et al. (2020) showed that using dispersion or dispersion squared give the same result, and we also find the same behaviour in σ and σ^2 (cf Sect **??**). The final dispersion maps of the study are given by :

$$\sigma^2 = \sigma_{obs}^2 - \sigma_{LSF}^2 - \sigma_{th}^2 \tag{6.1}$$

Using the methodology defined in Sect. 4.3, we compute FFT for each ring in the galaxy, obtaining the radial variations of amplitudes and phases of modes 1 to 4. An example is given for the galaxy NGC3198 in Fig 6.1. At the end of this process, we can evaluate the level of asymmetries in each individual galaxy, the dominant modes, the evolution of the angle phases and so on.

To go further and look for eventual systematic in the orientation of the phase angles, we have to combine the information of the different galaxies of the sample. To do so, we focus on all the individual rings, independently of their galaxy. Among the 15 galaxies of our sample, we have 883 individual rings. Studying the distribution of the Fourier parameters (Fig 6.2) in these rings allows to point out possible systematic.

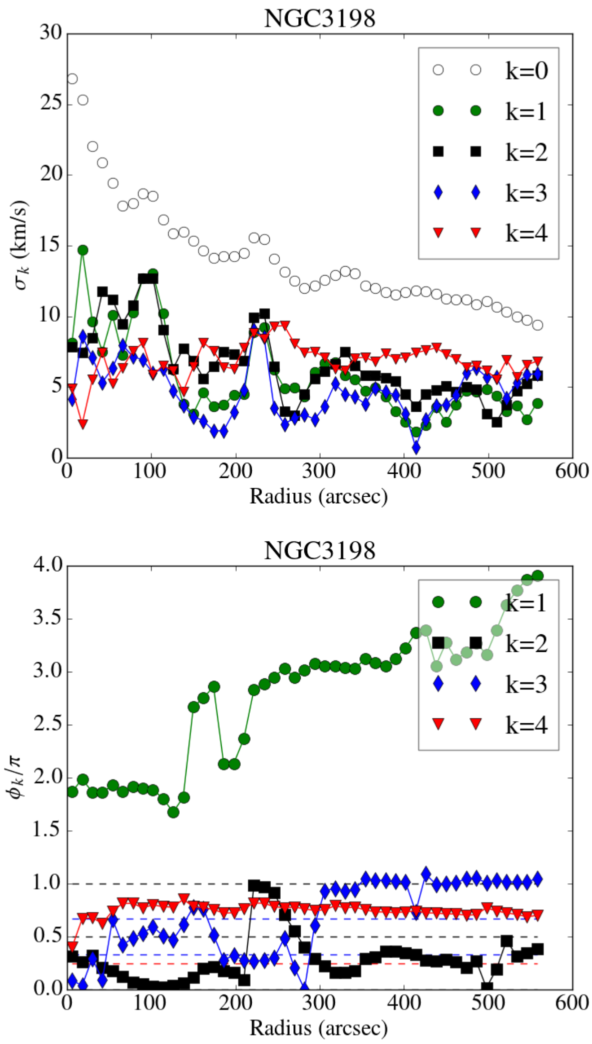

FIGURE 6.1. – Radial profiles of the FFT parameters for NGC3198. Top panel shows amplitudes σ_k while lower panel shows phases ϕ_k/π as a function of radius for modes 1 to 4.

Fig 6.1 presents the results of the FFT on the galaxy NGC3198. The top panel presents the amplitudes and the bottom panel the angle phases. The same plots are provided for every galaxies in Appendix X. A first result observed in Fig. 6.1 and in every other galaxy, is that the dispersion decreases with the radius as we can see with the mode k = 0, which corresponds to the mean value of the dispersion in a ring. For this particular galaxy, NGC3198, in the central part (up to 120 arcsec), amplitudes are dominated by orders k = 1 and k = 2. σ_4 stays at a constant level around 7 km/s at all radii and starts dominating other orders around 250 arcsec. Phases are periodic with a periodicity $2\pi/k$ (Fig. 6.1, bottom). For ϕ_2, around 200 arcsec, we observe a phase jump. In practice it's just the phase rolling up continuously so that's not a problem. Sometimes this can happen from ring-to-ring, and to keep the plot visible, we decided to limit the plot in a period as much as we could.

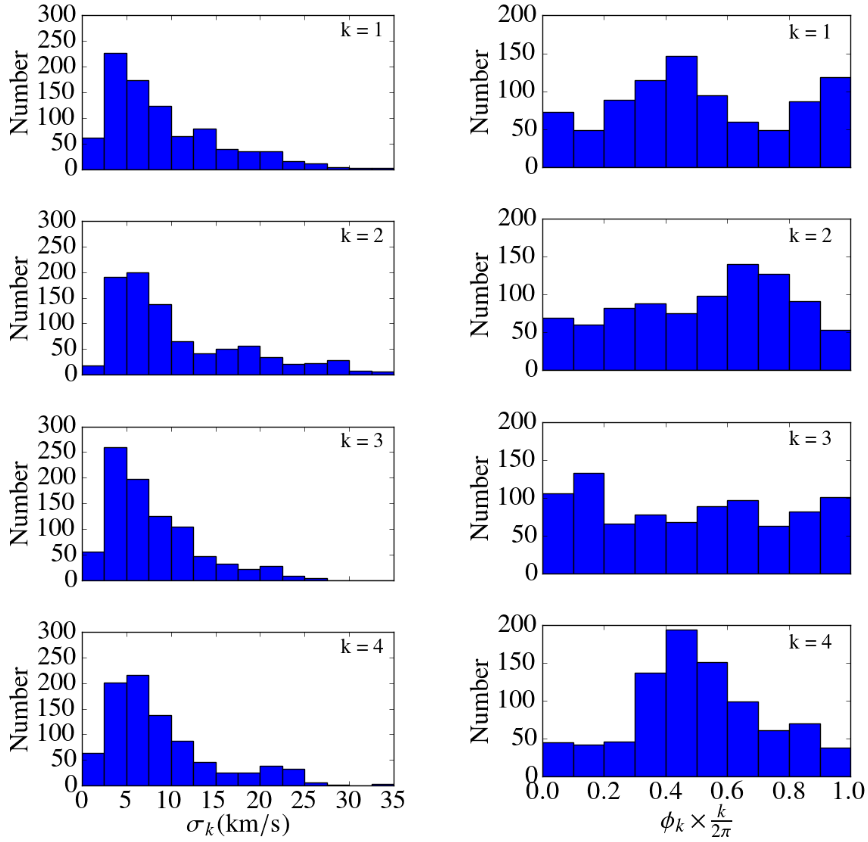

FIGURE 6.2. – Amplitude (left column) and phase (right column) distribution of the Fourier modes 1 to 4 in the 883 rings of the study. Phases are normalized such that 0.5 is the half period of the mode, and 1 is the full period. The period of the mode k is $\frac{2\pi}{k}$.

On Fig. 6.2, we present the distribution of the Fourier amplitudes (Fig. 6.2, left) and angle phases (Fig. 6.2, right) for the 883 rings of the study. To study these distributions in a more synthetic way, we reported mean, median and standard deviation values in Table 6.1. For all orders 1 to 4, the maximum of the distribution is located at amplitudes between 2.5 and 7.5 km/s and only few rings are described by amplitudes below 2.5 km/s. We observe similarities in the distributions of modes 1 and 3, with a faster decrease at high amplitudes for the 3^{rd} order. In the same way modes k = 2 and k = 4 are similar, with the maximum of the distribution between 5 and 7.5 km/s. The tail of σ_2 is also larger than the one of σ_4. From Table 6.1, we observe that the dominant amplitude is σ_2 with a median value of almost 8 km/s. Interestingly, median values for modes k = 1 and k = 4 are really close. Mode k = 3 has the lowest median and standard deviation indicating that in average amplitudes σ_3 are lower than amplitudes for other orders.

Concerning the phases, each modes exhibits a different distribution. For the mode k = 1, we observe a peak on the half period (0.5) and another peak on the entire period (1.0). The period of ϕ_1 is 2π, therefore the half period and the entire period corresponds respectively to π and 2π. Here both peaks are then located on the major axis of the galaxy. The majority of angle phases of the mode k = 1 in our 883 rings are distributed over the major axis. For ϕ_2, the distribution is flat, with a small bump at angle phases between 0.6 and 0.8. This bump does not coincides with any principal axis. Given the results from Chemin et al. (2020), we expected to observe a similar bump, maybe more significant at 0.5, which corresponds to the half period of mode k = 2, i.e. 0.5 π, the minor axis of the galaxy. The angle phase of the mode k = 3 is also flat, with a peak between 0.1 and 0.2. Finally, the mode k = 4 has a distribution centered on 0.5 which corresponds to the half period of ϕ_4 (0.25π). This distribution could be an hint for a possible systematic alignment of the angle phase of order 4, and we will study this result in more detail in the following parts.

Order Amplitude km/s	Mean km/s	Median km/s	Standard deviation km/s
σ_1	9.33	7.09	7.05
σ_2	10.9	7.96	7.67
σ_3	7.92	6.59	5.13
σ_4	8.82	7.02	6.06

Tableau 6.1. – Properties of the distributions of Fourier amplitudes in the 883 rings of the sample.

These first results are interesting but are nevertheless biased. Indeed, galaxies have different numbers of rings depending on their size and distance, see Fig. 6.3 . It varies from 7 rings for NGC3627 to more than 140 for NGC2403. We observe the same discrepancies in terms of pixel number (Fig. 6.3, bottom panel). Distributions are thus biased towards galaxies with higher number of sample elements like NGC2403 and NGC5055, and small galaxies like NGC3627 have only little importance in the result. Avoiding this bias is the main point of methods 2 and 3 in which we probe two different ways to mix the signal of all galaxies.

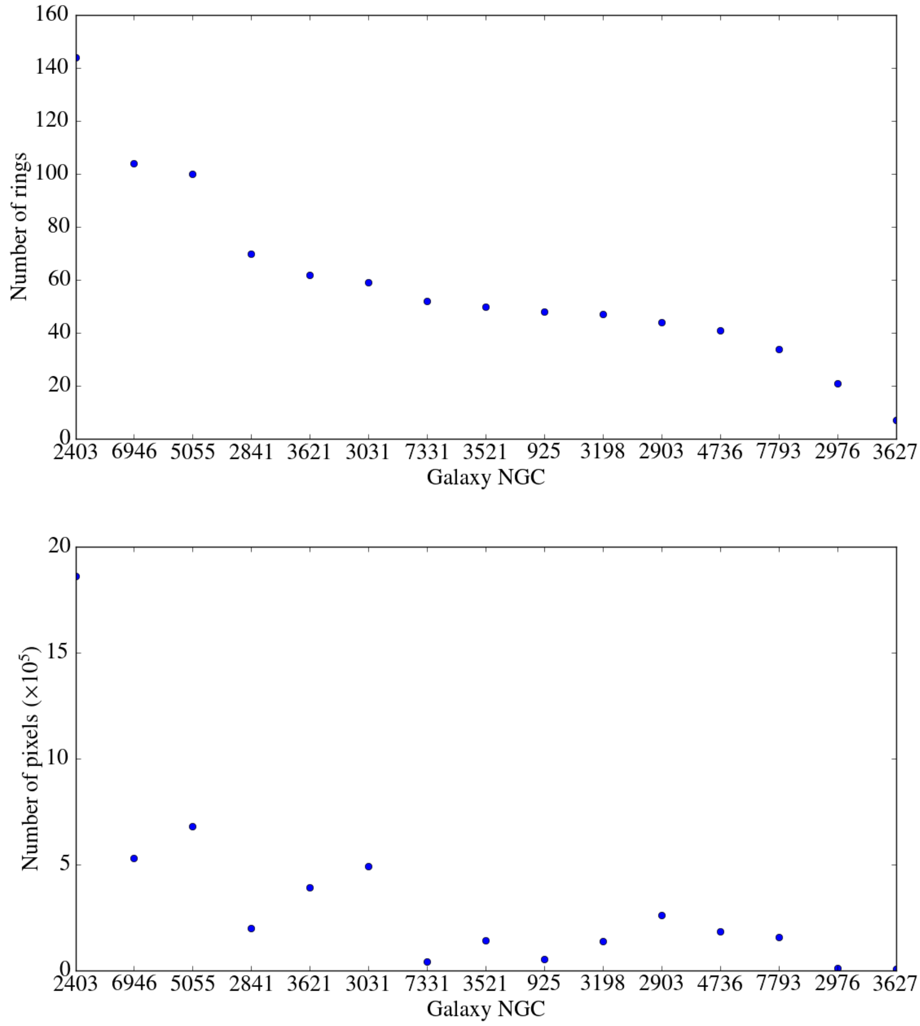

FIGURE 6.3. – Number of rings (top) and number of pixels (bottom) for each galaxy of our sample. Galaxies are sorted with decreasing number of radius.

6.2.2. Method 2 : stacked galaxy

In the previous section, we studied, for each galaxy, the variations of the amplitudes and phases of the velocity dispersion for the first four Fourier orders, as a function of the galacto-centric radius. The galaxies of the sample have nevertheless different surface brightnesses, different physical and projected sizes, making the comparison challenging. In the present section we aim to study trends coming for the whole sample in building a "stacked galaxy" and this requests a new method to analyse the data.

A bias of the study based on each galaxy using individual rings comes from the fact that each galaxy has a different number of rings and also that the number of pixels in each ring varies from galaxy to galaxy and from ring to ring. In this section, we introduce a normalisation to provide an equal weight for each galaxy.

The first step consists in reducing the velocity dispersion distribution of each galaxy, previously modelled by a suite of rings, to a single radius, in averaging all the radial contributions. The number of rings that varied from 7 to 144 in the previous method is now equal to unity for each galaxy making the comparison easier.

To minimize the bias due to the fact that the number of pixels varies from galaxy to galaxy and from sector to sector, we compute the average velocity dispersion within each angular sector, this provide a single value per sector as displayed in the left panel of figure 6.4.

On Fig. 6.4 we clearly see discrepancies in the level of asymmetries in the sample. As an illustration of these asymmetries, we show on Fig. 6.5 the observed squared dispersion map from THINGS of NGC2841 and its FFT modeling. NGC2841 corresponds to the light blue curve of Fig. 6.4 and its single-ring dispersion exhibits 2 peaks around 0.6π and 1.6π. By comparing this curve with the observed dispersion and the azimuthal map of the galaxy, we observe that these peaks are associated with two regions of high dispersion, respectively in the top right and bottom left part of the galaxy. As we can see on the 4 bottom panels of Fig. 6.5, which corresponds to the individual orders of the FFT from 1 to 4, asymmetries of NGC2841 are described by strong orders 2 and 4. Indeed, the observed dispersion map exhibits a symmetry along the major axis of the galaxy, explaining the presence of the order 4, with a X-shape in the dispersion. The third order is negligible in all the galaxy, and the first order has an impact lower than orders 2 and 4. The modelisation of the asymmetries with the orders 0 to 4 of the FFT is shown on the top right panel, next to the observed map. The residual map represents the observed map minus our modelisation. Its mean value is 26 $(\mathrm{km/s})^2$, and no obvious signal is observed, showing the consistency of our modeling.

The second step is made up in building the so-called "stacked"-galaxy. The previous plot shows that the amplitude of the velocity dispersion strongly differs from galaxy to galaxy, this trend is amplified since we work on the squared velocity dispersion (instead of the velocity dispersion). Thus we have to stack with caution the velocity dispersion of each galaxy to build the stacked-galaxy. Three galaxies shows tremendous velocity dispersion squared : NGC2841 (light blue curve), NGC3627 (red curve) and NGC3521(dark blue curve). Those galaxies should be discarded for the statistical analysis of the so-called "stacked"-galaxy. To reject further high amplitudes that could be due to some bins, instead of computing the mean velocity dispersion squared for each angular sector the velocity dispersion, we compute the median, as displayed on the bottom line of figure (6.4).

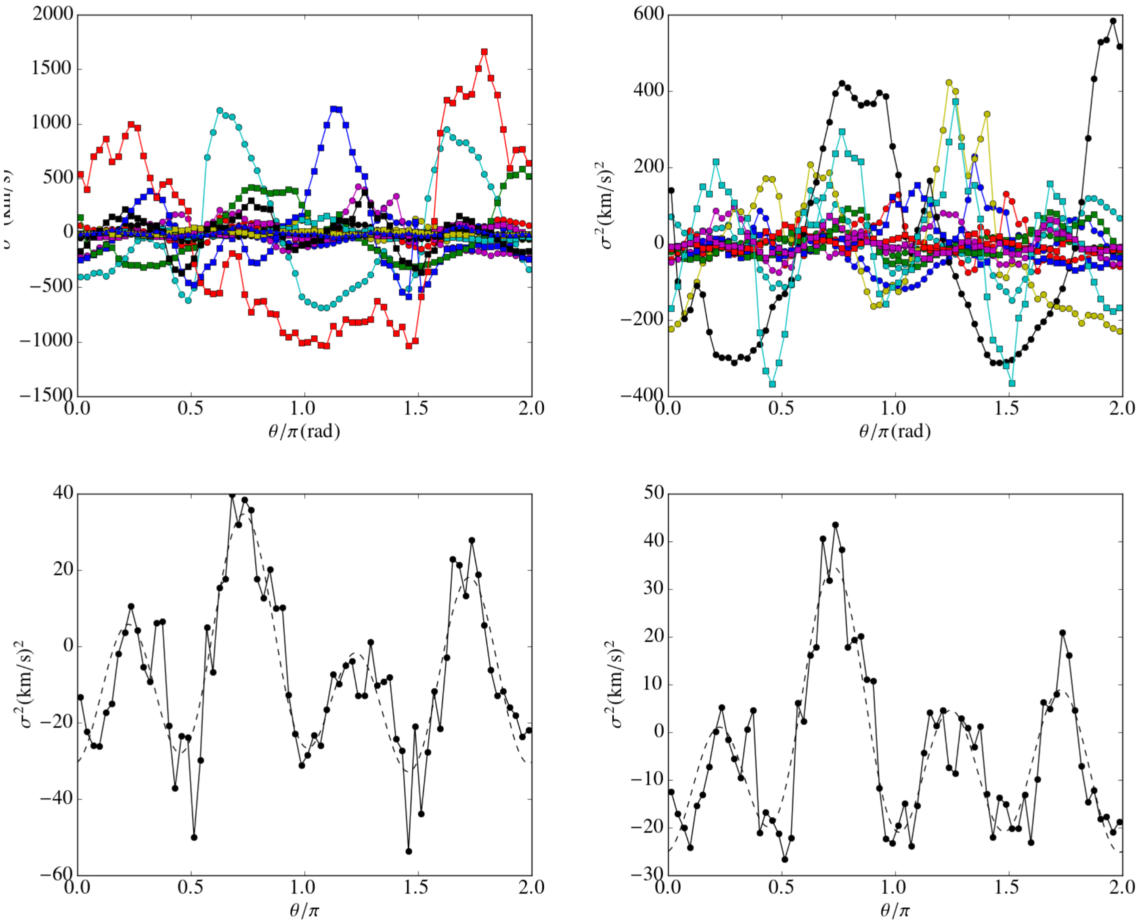

FIGURE 6.4. – Velocity dispersion squared σ^2 vs the angular sector θ for each galaxy. A bin step 5 degrees has been selected for each sector θ. (Upper left panel) For the whole sample of 15 galaxies. (Upper right panel) Same as the left panel but without galaxies NGC2841 (light blue curve), NGC3627 (red curve) and NGC3521(dark blue curve). (Bottom left panel) Stacked-galaxy computed using the mean velocity dispersion squared for each angular sector. (Bottom right) Stacked-galaxy using the median value instead of the mean.

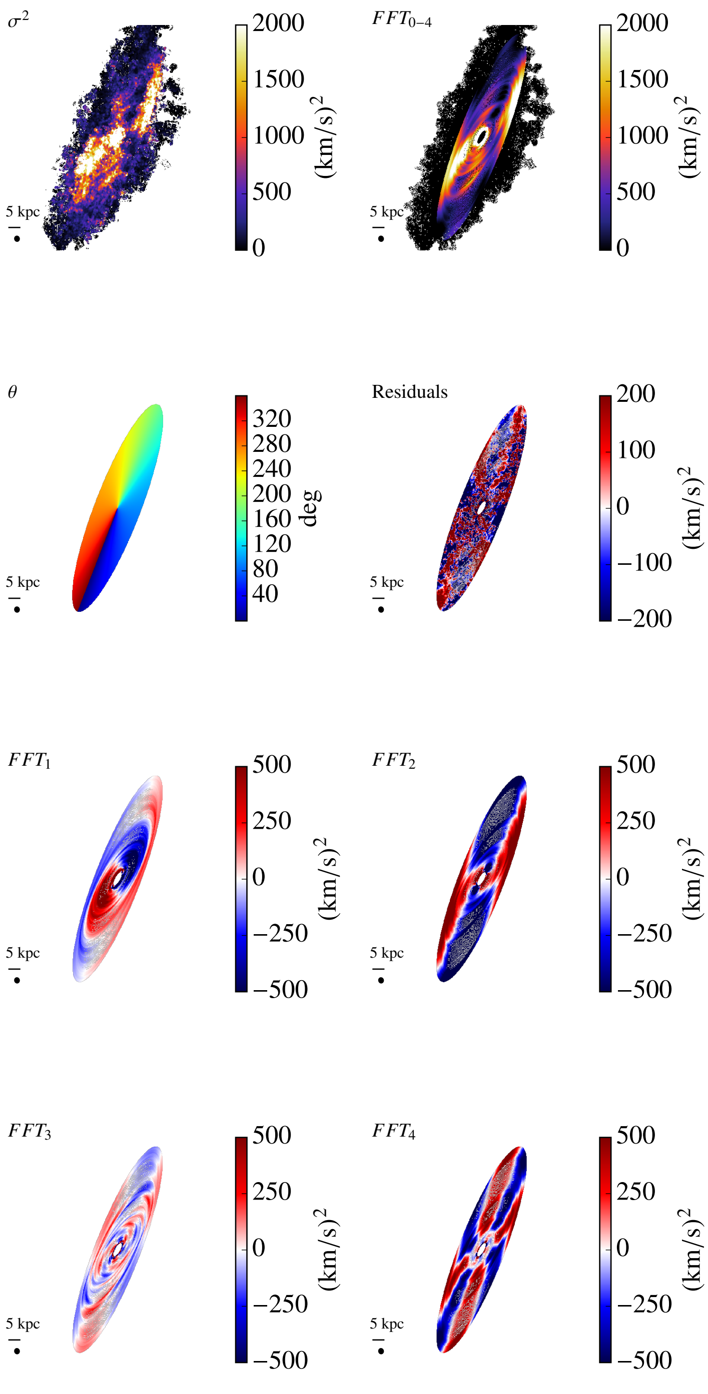

FIGURE 6.5. – THINGS dispersion map of NGC2841 (top left panel), projected result of the term of order 2 from the FFT (top right panel), azimuthal map (bottom left) and projected result of the FFT containing orders 0 to 4 (bottom right panel).

The third step comprises the FFT computation of the stacked-galaxy in order to study the amplitude and the phase of the different Fourier orders that will be analyse in the next section.

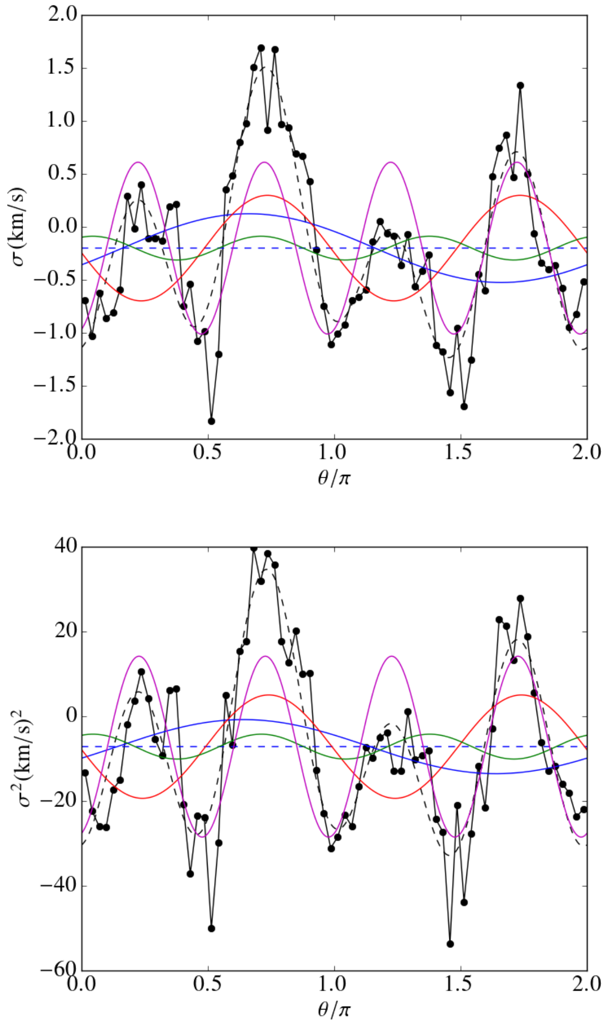

FIGURE 6.6. – σ vs θ (top panel) and σ^2 vs θ (bottom panel). Continuous black line with the black dots are the data points. Dashed black line is the FFT model of the data. Colored continuous lines represents individual orders 1 to 4.

In the present section we analyse the results of the FFT decomposition of the stacked-galaxy. Orders one to four are further considered. The zero order corresponds to the mean of the line-of-sight velocity dispersion $< \sigma_{\rm los} >$, it does not contain information on the azimuthal variation and has been subtracted from the velocity dispersion. Figure (6.6) shows the azimuthal dependence of the velocity dispersion, from which the mean velocity dispersion $< \sigma^2_{\rm los} >$ has been removed, and orders one to four. The median velocity dispersion has been computed in each azimuthal that has been sampled every 5°. The model (dashed line) fits the data (continuous line) with mean residual dispersion of $0.0004 \pm 9.6(\text{km/s})^2$.

For each pixel, the standard velocity dispersion σ has been used on the top panel while on the bottom panel, the square of the velocity dispersion σ^2 has been considered. This second choice is motivated by the FFT equation (4.9) that involves square of velocity dispersions rather velocity dispersion.

Apart from the amplitudes, trends for both signals are identical, for the direct signal as well as for the individual order of the FFT, with peaks located at the same positions.

Relative amplitudes between orders are well respected and we do not observe any change in the phase of individual orders, even for ϕ_3 which is likely to change due to the low amplitude of σ_3.[1] In conclusion, working directly with the σ or σ^2 is equivalent ; we make the choice to work with the σ^2 because it's easier to interpret results of the FFT with the equation (4.9).

Bottom panel of figure (6.6) exhibits strong oscillations in the velocity dispersion as a function of the phase θ, which are characterised by large FFT amplitudes for the order 2 and order 4, respectively ~12 and ~21$(\text{km/s})^2$. The first and the third order reach respectively the half and the fourth of the amplitude of order 2 ($\sim 6(\text{km/s})^2$ and $\sim 3(\text{km/s})^2$). The phase of the fourth order ϕ_4 is centred on 0.25 π, which is the half period of order 4, as we already observed on the previous histograms.

The phase of the second order ϕ_2 is equal to ~0.75 π, we indeed note that the first peak of the order 2 coincides with the second peak of order 4.

Surprisingly, the amplitude of order 4 is almost 50% larger than order 2 which is in turn larger than in the other orders. In addition the phase is $\phi_4 \sim \pi/4$. Is this phase due to a bias linked to an (un)lucky alignment of patterns in different galaxies, to noise, to instrumental finger print or is it a physical signature ? In the forthcoming paragraphs, we will test the robustness of the phase observed in the fourth order.

The first test to address these questions was to slit our sample into two randomly selected subsamples of same size. We have done 16 times a random selection, it was not necessary to make larger sample draw since we have a sample of 15 galaxies.

The results for six randomly selected sample draw are presented in Fig 6.7.

1. The amplitude factor between the upper and the lower plots is roughly ~20. It's not a direct transcription of the difference square factor due to all the processes needed to obtain this final signal (reducing the galaxy to one radius, taking the median values for all the bins).

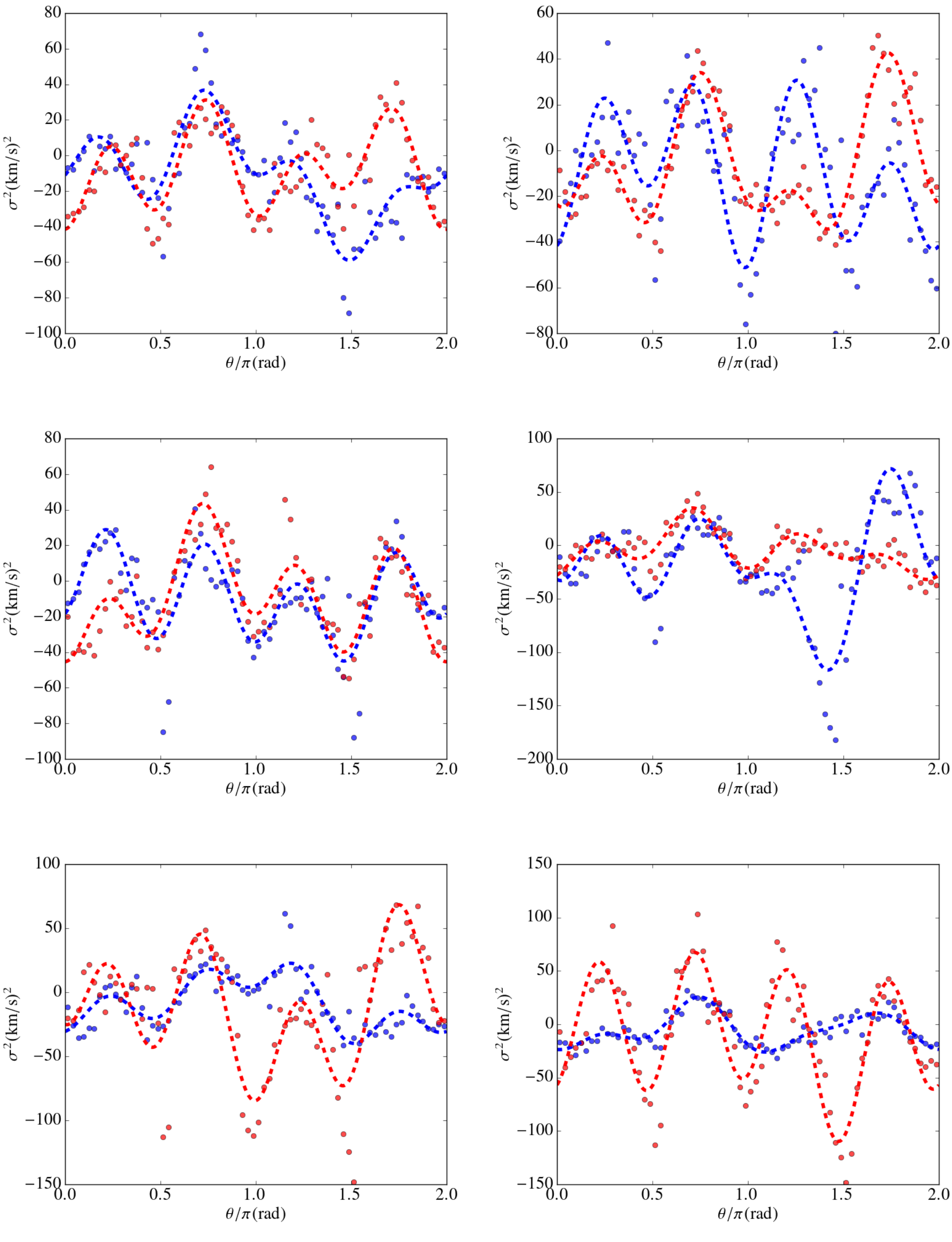

FIGURE 6.7. – The sample is randomly divided into 2 subsamples, in order to see if the trend observed in the global sample is due to a bias from some galaxies.

The visual comparison of the curves σ^2 versus θ for both subsamples for all the experiments show that the phase is basically conserved.

To quantify this agreement, Table 6.2 gives the mean, median and standard deviation values of FFT parameters computed for 30 randomly selected subsamples. Depending on the galaxies in the subsample, amplitudes vary considerably, inducing high values for standard deviation. As observed in Fig. 6.6, σ_2 and σ_4 tends to be have the largest amplitudes. A striking result appearing concerning the phases is the remarkably low spread of the value ϕ_4. The larger dispersions observed for amplitudes (σ_2, σ_4) correspond to the lower dispersion for phases (ϕ_2, ϕ_4).

Config Param	Mean	Median	Standard deviation
$\sigma_0^2 - <\sigma_0^2>$	-12.2	-7.2	10.9
$\sigma_1^2 (\mathrm{km/s})^2$	15.1	9.8	14.1
$\sigma_2^2 (\mathrm{km/s})^2$	19.5	14.7	16.2
$\sigma_3^2 (\mathrm{km/s})^2$	11.0	6.31	12.3
$\sigma_4^2 (\mathrm{km/s})^2$	30.3	24.8	20.8
ϕ_1/π	0.69	0.69	0.38
ϕ_2/π	0.75	0.77	0.12
ϕ_3/π	0.30	0.30	0.18
ϕ_4/π	0.23	0.23	0.02

Tableau 6.2. – FFT parameters for the 30 subsamples

Even with half the number of galaxies in each subsample, we still observe peaks at the same positions than the one observed in Fig 6.6, meaning that is probably not due to a chance alignment.

The second test consists in testing the probability to obtain an order 4 with such a high amplitude σ_4 for the total signal of the sample, as well as the velocity amplitudes σ_k and phases ϕ_k for the other order k? To test this probability, we introduce a random phase shift, constant along the radius, for each galaxy. In the galactic plane, the origin of the azimuth is not anymore aligned along the major axis, but distributed at any random azimuth, this arbitrary changes the location of the perturbations. We then follow the same methodology than the one used to obtain Fig 6.6 and compute the new velocity dispersion distribution of the new stacked galaxy. Since it is computationally expensive, we do 500 iterations of the mock sample and compute the FFT for every signal. The σ_k^2 and ϕ_k distribution are presented in Fig 6.8; a red dash line indicate the values found with the « real » stacked galaxy without phase shift.

The σ_1 and σ_3 random distribution peak at the value of the velocity dispersion computed on the stacked galaxy. For σ_2 the peak is slightly shifted towards smaller velocities dispersion but the observed value for σ_2 is still compatible with a random distribution. At the opposite, the square velocity dispersion σ_4 value observed for the stacked galaxy lies at the very bottom end of the distribution; values $\sigma_4^2 > 20(\mathrm{km/s})^2$ represents only 6 cases among the 500 mocks and σ_4 is larger than the observed value for one case only. This means that a random orientation for the phase is very unlikely to reproduce the large velocity dispersion observed for σ_4.

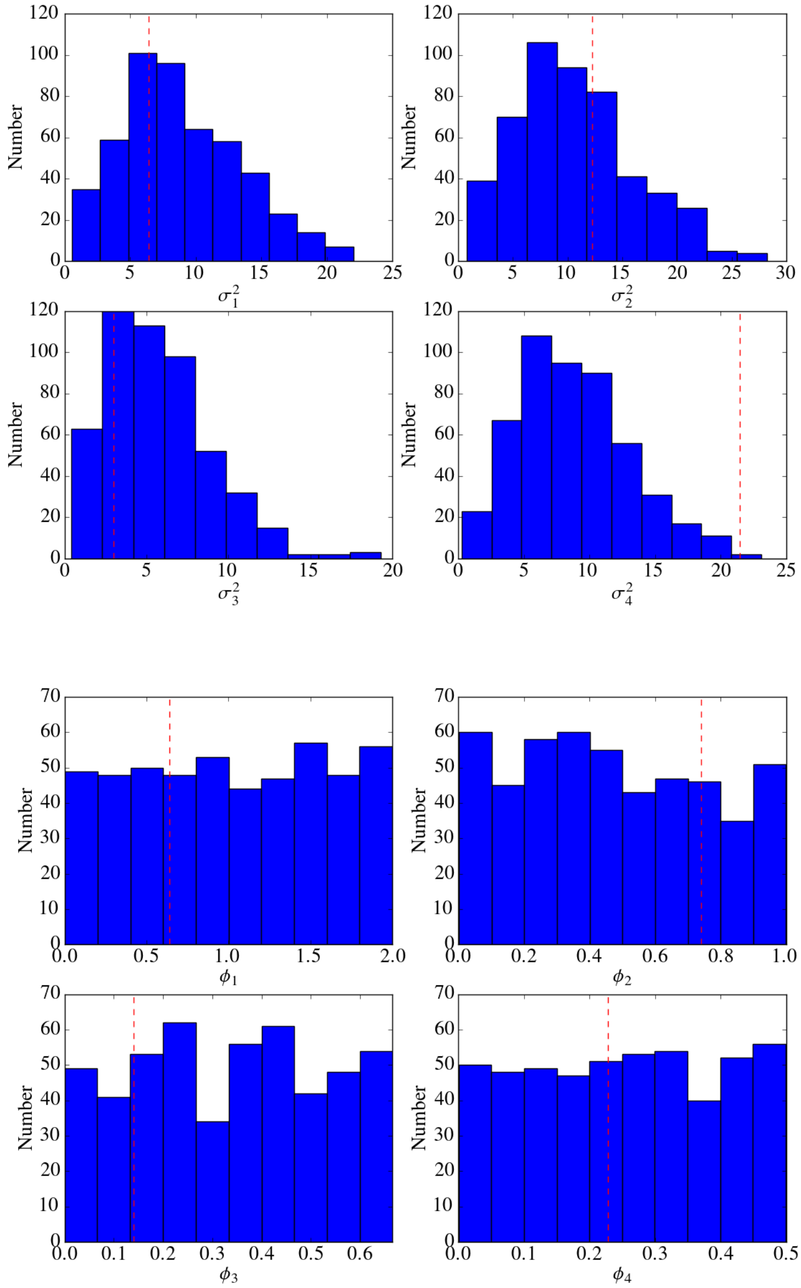

FIGURE 6.8. – Distribution of the order of the FFT for 500 iterations of the mock sample THINGS. The vertical lines corresponds to the reference value of the THINGS sample.

Before analysing the data, we probed the effect of the angular bin size in testing bins ranging from 2 to 20 degrees; we display the results of four different bins size (2, 5, 10 and 20 degrees) on Fig. 6.9. The FFT amplitudes moderately vary. σ_1 varies from 6.3 to 10.2 (km/s)^2, σ_2 stays roughly constant, between 11 and 12.4 (km/s)^2, σ_3 is negligible in all cases with amplitudes between 0.8 and 3.1 (km/s)^2 and finally σ_4 stays also constant with the bin size, with values between 19.9 and 21.4 (km/s)^2. Except for ϕ_3 which varies from 0.01 to 0.46 π, other orders have similar phases with dispersions lower than 0.02 π.

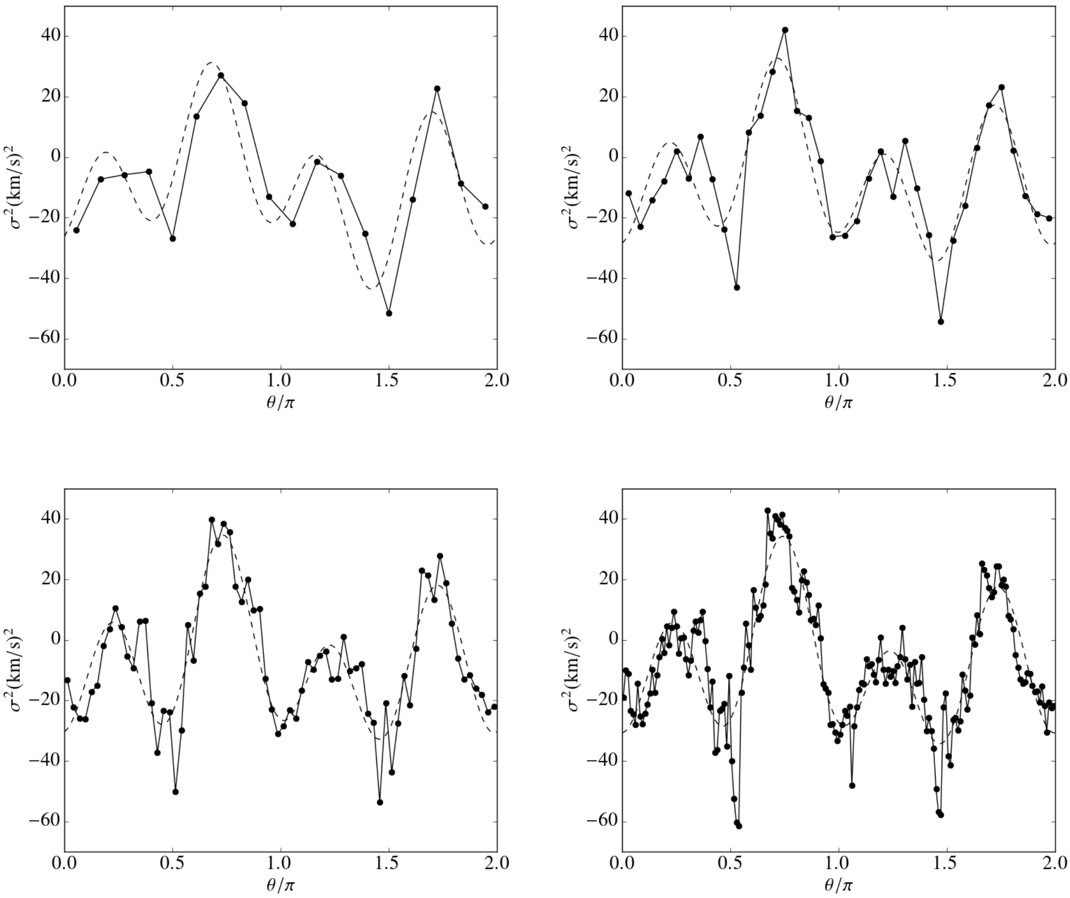

FIGURE 6.9. – σ^2 vs θ for the "super-galaxy" with various azimuthal bins sizes : 20 deg (top left), 10 deg (top right), 5 deg (bottom left), 2 deg (bottom right).

In this last section we discuss the method used in this section that consists in reducing the radial information to a single value. For this purpose, as a test bench, we use once again the galaxy NGC5055 for which we will compare the FFT computed without and with azimuthal binning.

Firstly, we study the distribution of the FFT parameters for 100 radii. For each radius, we compute the squared dispersion, subtract the instrumental dispersion and the mean squared velocity dispersion. This last operation only affects the 0^{th} order and allow to center the asymmetries around zero.

Each of the 100 radius depends on nine parameters : σ_0 (consistent with 0 due to the subtraction mentioned before), σ_k and ϕ_k, with k=1, 2, 3 and 4. We report the mean and median values of the radial distributions of σ_k in Column 1 and 2 of Table 6.3. For phases, due to the periodicity, we cannot compute the median value. This study annulus by annulus provides a description at local scale (down to the annulus scale), and allows to identify regions for which amplitudes of order σ_k are larger than a given threshold.

Secondly, we use the method previously described to reduce the galaxy to a single radius. We compute the signal for each annulus and subtract by the mean velocity dispersion for each radius and not for each annulus. We end up with a vector having the length equal to the total number of pixels (namely 680980 pixels) that contains the velocity dispersion and the azimuth of each pixel. We compute the FFT of this vector and we compare it to the FFT of the same signal but binned using azimuthal sector of 5°, for which we compute the mean dispersion values of all pixels within each bin range. By sampling every 5°, we obtain 72 data points to span the entire galaxy (360°). Result for these two configurations are shown in column 3 and 4 of Table 6.3.

Config Param	Mean Value	Median Value	Total Signal	Total signal binned
$\sigma_0^2 - <\sigma_0^2>$	$1e^{-7}$	$5e^{-8}$	$9e^{-9}$	0.95
σ_1^2(km/s)^2	53.9	27.0	12.9	12.4
σ_2^2(km/s)^2	72.9	53.1	39.6	43.3
σ_3^2(km/s)^2	46.2	20.3	2.91	2.76
σ_4^2(km/s)^2	55.0	41.8	22.6	24.1
ϕ_1/π	1.20	1.51	1.80	1.82
ϕ_2/π	0.63	0.73	0.77	0.73
ϕ_3/π	0.34	0.33	0.33	0.14
ϕ_4/π	0.25	0.24	0.31	0.28

Tableau 6.3. – FFT parameters of NGC5055 obtained using 4 different methods : the first column corresponds to the mean value of the FFT distributions among the 100 rings, the second one the median value of these distributions. Column 3 and 4 corresponds to the FFT parameters of the single radius velocity dispersion, before and after this dispersion within angular sector.

As we described many times, for each ring we subtract by the mean dispersion square value, explaining the values the first row consistent with 0 (km/s)^2. Averaging within angular sector changes slightly the value of the 0^{th} of the FFT. This is the reason why the "stacked" galaxy has a 0^{th} order different from 0. Depending on the method used, amplitudes of the FFT varies a lot. On the first column, corresponding to the mean value of the radial distribution of rings, all amplitudes are similar, with a factor 1.5 between the maximum amplitude σ_2 and the minimum one σ_3. Taking the median of the same distribution allows to have a better sight at the most dominant orders. We observe a decrease from column 1 to column 2 by a factor close to 2 for orders 1 and 3 while orders 2 and 4 decreased by 25%, indicating that in most rings amplitudes 2 and 4 tends to be higher. A similar phenomenon happens when performing the FFT on the single ring dispersion (column 3). All amplitudes decrease, due to the radial averaging, compared to column 2, but at a different rate. We also note that averaging the single ring dispersion within azimuthal sector does not change significantly the values of the FFT.

This single ring dispersion reinforce some signals in the galaxy (i.e. order 2 which dominates largely the single ring dispersion) and suppress others, such as σ_3 which becomes negligible. Compared to the mean value of the ring distribution, the median value of the distribution, and the FFT on the single ring dispersion are more appropriate to discriminate between orders. This last method seems to be the most efficient one, especially in order to combine the data to form the stacked galaxy. Nevertheless, there is a possibility that this single ring dispersion could enhance unreal signals such as remnant beam smearing. Indeed, the beam smearing creates a typical X-shape pattern, which increases the dispersion at given azimuths, at all radii. A deeper study of the link between the stacked galaxy and beam smearing will be discussed later. Therefore the last test we perform is the study of the median values of the ring distribution for each galaxy, because we expect a possible beam smearing remnant to be less important down to the annulus scale than on the galaxy reduced to a single ring.

6.2.3. Method 3 : Median values of radial distributions

In this section we study the FFT distributions of individual galaxies. Asymmetries are computed for each ring, to have the radial distribution of the FFT parameters. In the same spirit as before, to normalize the number of rings in each galaxy of the sample, only the median values of these FFT distribution are considered. Therefore, each galaxy is described by the 9 parameters of the FFT, σ_k and ϕ_k which are the median values of their own radial distributions. In Fig. 6.10 we present the median value of ϕ_k vs σ_k for each galaxy of the sample. Each point corresponds to a galaxy. Since all FFT are computed on projected galaxies, the minor and major axis corresponds to the same azimuthal values for all the sample. The blacked dashed lines represent the minor axis ($0.5\pi \mod \pi$) and the blue one the major axis ($0 \mod \pi$). Let's remind that the initial goal of this study was to search for systematic alignment of the phase ϕ_2 with the minor axis, similarly to the result from Chemin et al. (2020). Fig. 6.10 clearly shows that such result is not present in our sample of THINGS galaxies. The phase ϕ_2 has a large spread, with values from 0.1π to 0.9π. Only 6 galaxies have phases between 0.4 and 0.6π. Concerning the phase of order 1, ϕ_1, we observe, similarly to Fig. 6.2, that

10 out of 15 points are located at phases between 0.7π and π. For ϕ_3 the distribution is uniform, with a large spread, similar to ϕ_2. Finally, similarly to what was observed in Fig.6.2, the phase ϕ_4 is aligned close to 0.25π for 12 galaxies on the 15 in the sample.

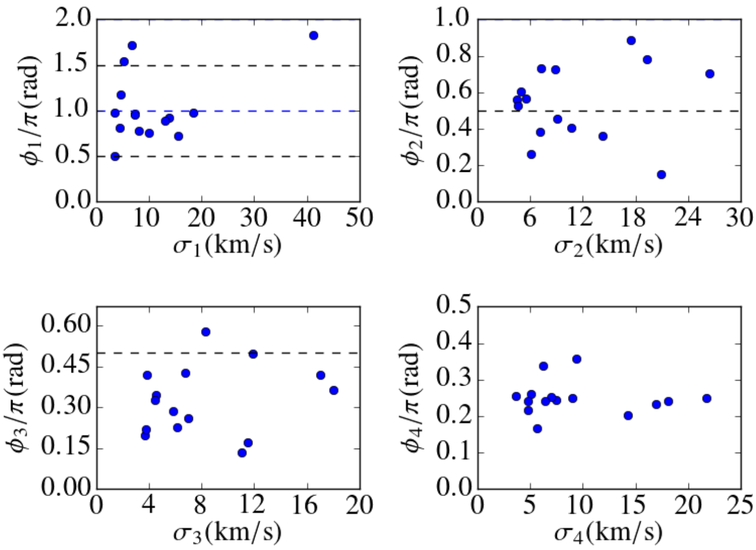

FIGURE 6.10. – Median phase ϕ_k vs velocity dispersion σ_k issued from FFT analysis of individual galaxies. Each point represents the median value of the radial distribution of the FFT parameters for a galaxy. Dashed horizontal line represents the minor (black) and major axis (blue) of galaxies.

6.3. Extension to the WHISP sample

In this section, we extend this analysis to the 15 galaxies from WHISP, carefully chosen in chapter 5 (see Table 5.2). Due to the lower resolution and larger distances of those objects, the 15 galaxies represents 154 independent rings, lower than the 883 rings obtained with THINGS. We apply the method described in Sect. 6.2.1. The FFT distribution for all rings is presented in Fig. 6.11, with the left panel dedicated to the amplitudes $\sigma_k, k \in 1...4$, and the right panel to the angle phases $\phi_k \times \frac{k}{2\pi}$. Considering the low number of rings, it's harder to obtain a true statistical information. We note that the distribution of ϕ_1, which was composed by two peaks for the THINGS ring distribution, is now flat. Concerning ϕ_2, the small bump in the distribution around 0.7π is still here, but with another bump around 0.25π. ϕ_3 does not exhibit any particular features, and finally ϕ_4 shows a similar peak as the one observed in Fig. 6.2, but less important.

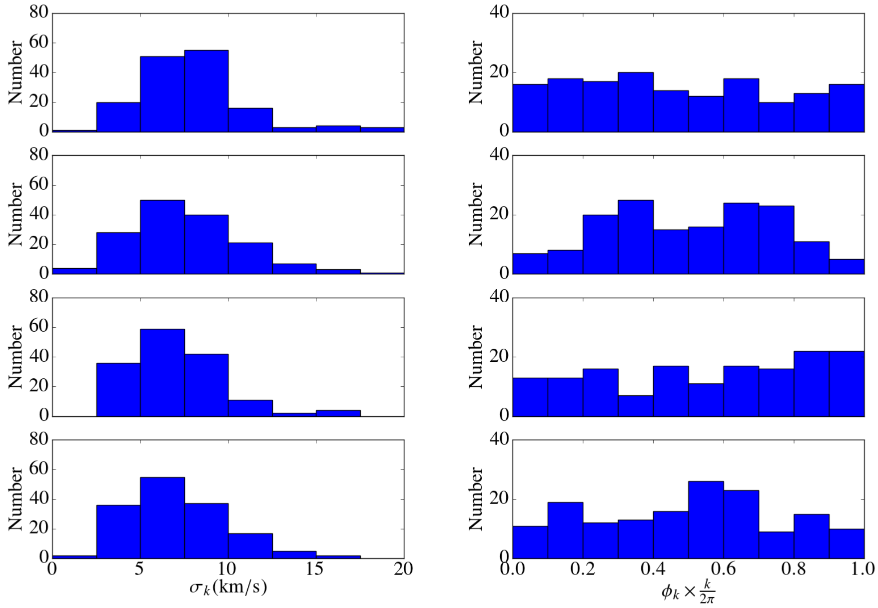

FIGURE 6.11. – Amplitude (left column) and phase (right column) distribution of the Fourier modes 1 to 4 in the 154 rings from the WHISP sample. Phases are normalized such that 0.5 is the half period of the mode, and 1 is the full period. The period of the mode k is $\frac{2\pi}{k}$.

We combine results from both samples, leading to a distribution of 1037 rings distributed over 30 galaxies from THINGS and WHISP. The result is presented in Fig. 6.12, with the ring distribution from THINGS in blue, and on top of this blue bars, the ring distribution from WHISP in green. Adding the WHISP galaxies doesn't break the shape observed for the THINGS galaxies.

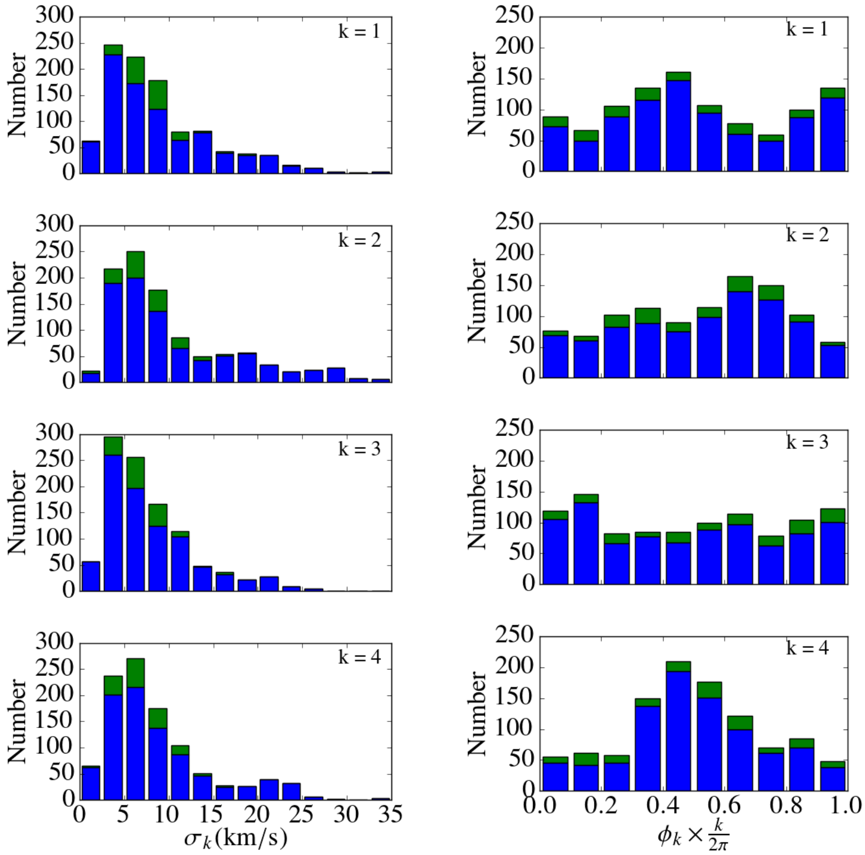

FIGURE 6.12. – Amplitude (left column) and phase (right column) distribution of the Fourier modes 1 to 4 in the (883 + 154) rings from the THINGS (blue) and WHISP (green) samples respectively. Phases are normalized such that 0.5 is the half period of the mode, and 1 is the full period. The period of the mode k is $\frac{2\pi}{k}$.

6.4. Discussion

6.4.1. Uncertainty in the beam shape

In previous sections, we exhibit strong asymmetries in the THINGS velocity dispersion maps for the FFT order 4 with a phase aligned on 0.25π. Using mocks we conclude that this signal was not the result of (un)lucky alignments. However, beam smearing fingerprint might provide a residual signature in the signal, in this section we aim to test this issue.

In others previous sections, we already describe the beam smearing modelling, but here we will specifically discuss here the possible links between the high amplitude of order 4 and the beam smearing that displays a cross shape, and thus could, for this reason, contribute to residual signal in the order 4, even on the highest resolution THINGS dataset.

To achieve this goal, we compared the difference between the beam smearing signature of a model datacube and the 2D moments computed from the same datacube. A good agreement between those two signatures would be a proof of the absence of residual beam smearing in the analysis; the method is described hereafter.

On the one hand, we created a model datacube, based on the different moment maps : a flux map, a velocity field and a velocity dispersion. We arbitrary chosen a galaxy disk inclination of 60 degrees. The axisymmetric velocity field is computed for an exponential disk, the maximum rotation velocity of 200 km/s is reached at a radius of 200 arcsec. The flux map is created using a decreasing exponential disk. In order to induce low variation of the flux values over the galaxy, we chose a disk scale length of 1000 arcsec, way above the radius where the maximum velocity is reached. In the sake of simplicity, the velocity dispersion is constant on the whole galaxy and equal to 10 km/s.

From these maps we create a high-resolution data-cube using Gaussian lines profile. The amplitude, center and velocity dispersion of the lines are respectively given by the value of the flux max, velocity field and velocity dispersion for each pixel. The spatial scale of the modelisation is 1 arcsec/pixel.

To model the instrumental radio beam, that we call hereafter the Point Spread Function (PSF), we use a 2D Gaussian function using a typical elliptical size and shape, namely a minor axis of BMIN = 10 arcsec, a major axis BMAJ =15 arcsec and a position angle orientation of the ellipse BPA = 30°. The next steps consists in convolving the high-resolution model datacube with this PSF in order to obtain a low-resolution datacube, mimicking the observations, from which the moment maps are extracted using the SpectralCube package. Since we did not introduce dispersion pattern in the high-resolution datacube but only a constant velocity dispersion for the whole galaxy, we expect that the spatial variations in the velocity dispersion map is only due to PSF beam smearing effect.

On the other hand, we compute the beam smearing map of the low-resolution datacube using the methodology defined in section 4.4.1. Next, we subtract quadratically this beam smearing map to the velocity dispersion map previously computed from the low-resolution datacube. The result of this subtraction looks very much as expected, like the initial dispersion map, with a constant velocity equal to 10 ± 0.001 km/s.

Thus we conclude that the beam smearing processing is correct. However, this does not mean that the PSF is correctly modelled. Indeed, beam smearing residual might remain in the data if the radio beam exhibits for instance asymmetries or a tail due to high frequencies that cannot be represented by a 2D Gaussian. In that case we would underestimate the contribution of the PSF.

6.4.2. Beam smearing and σ_4

In order to go further in the understanding of beam smearing contribution on the FFT fourth order 4, in this section we tackle this issue differently. Due to beam smearing effects, velocity gradient could be unresolved. To overcome this difficulty we used high-resolution $H\alpha$ velocity field (R = 1.6 x 1.6 arcsec^2) rather than the HI lower-resolution one (R = 8.66 x 10.06 arcsec^2). For the first part of the study, we focus on the test case galaxy NGC5055 ; in the second part, we will study how evolves the parameter of the FFT for the stacked galaxy.
a. The case of galaxy NGC 5055
(i) Azimuthal dependences

The THINGS beam shape of NGC 5055 is 8.66×10.06 arcsec^2, its inclination is 59^o in HI and 63^o in $H\alpha$.

For the beam smearing modelisation, we adopt the same methodology as presented in Sect. 4.4.1 for the SINGS data. The high resolution velocity field is created assuming a Courteau model of the $H\alpha$ rotation curve of NGC 5055. Using the THINGS flux map and PSF, we compute the corresponding beam map (Fig. 6.13).

We reduce the radial distribution of each azimuthal angle to a single value (see Sect. 6.2.2), and we compute the FFT as explained in method 1 (see figure 6.13, top-right panel) . Since the model is basic we work directly on the dispersion and not on the dispersion squared like we did previously. The top right panel of figure 6.13 shows that the beam smearing consists in a strong order 2, $\sigma_2 \sim 0.41$ km/s and phase $\phi_2 = 0.54\pi$ (low σ velocity dispersion along the major axis for $\theta \sim \pi$) and a high order 4 as well, $\sigma_4 \sim 0.33$ km/s and $\phi_4 = 0.21\pi$, which clearly appears with a X-shape of the beam smearing pattern (figure 6.13, top panel). Orders 1 and 3 are negligible, $\sigma_1 \approx \sigma_3 \approx 0.01$ km/s. In the case of NGC 5055, we clearly see that the beam smearing induces a strong fourth FFT order, which is aligned close to its half period. The second FFT order is not aligned exactly with 0.5π, and this could be explained by the non-axisymmetry of the beam. Indeed, assuming a circular beam of 10x10 arcsec^2 (Fig. 6.13, middle row), the phase ϕ_2 becomes exactly aligned with $0.5\,\pi$. Amplitudes are the same in the case of the circular beam with $\sigma_2 = 0.40$ km/s and $\sigma_=$0.34 km/s. Part of the discrepancy between the two first peaks are reduced using a circular beam. The residual difference is due to the combination of orders 2 and 4. If ϕ_4 was perfectly aligned with 0.25π, the peak of the order 2 would be at the exact center of the first peaks of the order 4. Here ϕ_4 is slightly lower inducing this amplitude difference.

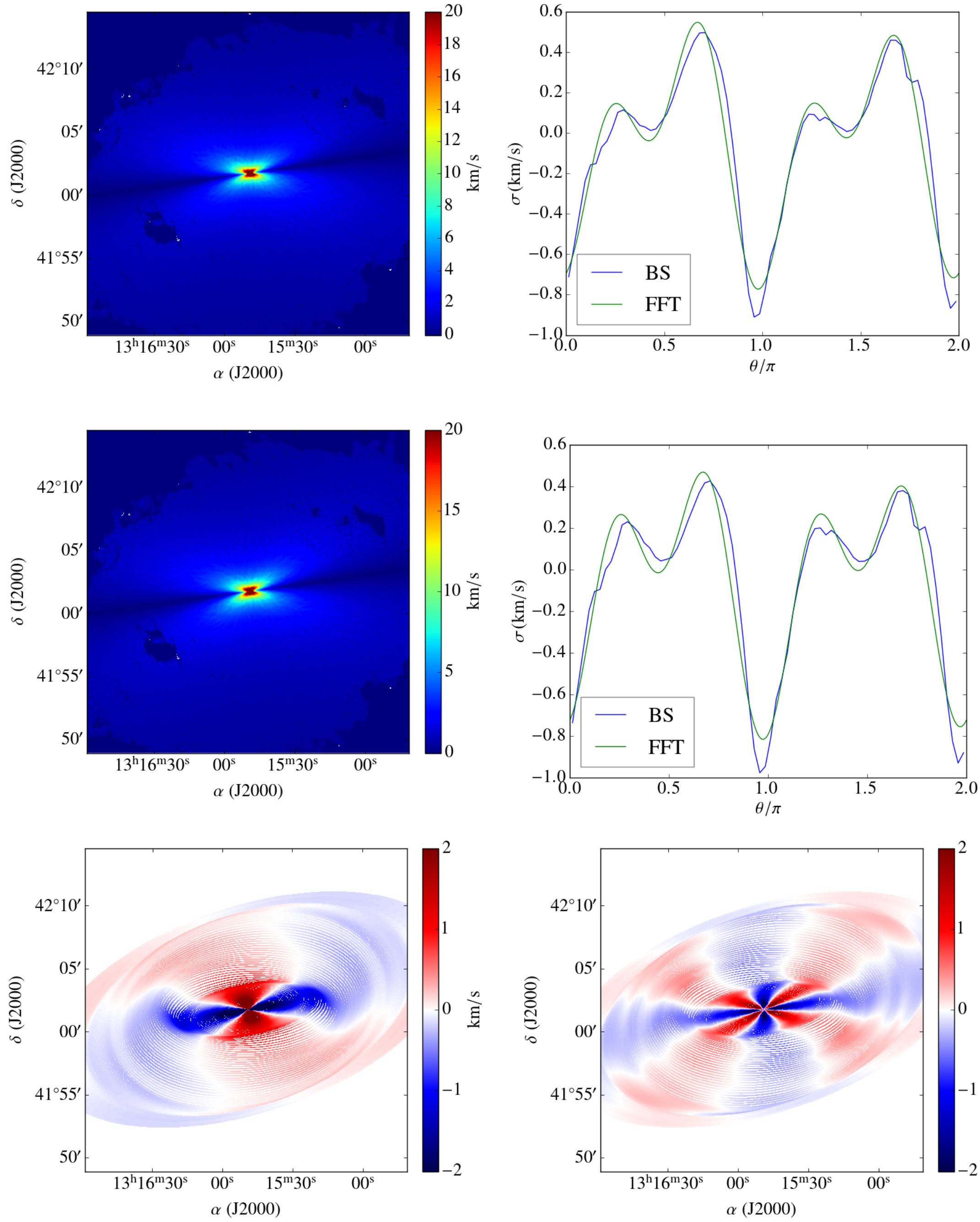

FIGURE 6.13. – Beam smearing modelisation of NGC5055 with the actual beam from THINGS(top left panel) and the corresponding FFT of this map reduced to a single radius (top right panel). Same plot with a circular beam of 10 arcsec^2 (middle row) and orders 2 (bottom left) and 4 (bottom right) of the FFT from top panel.

(ii) Radial dependences

In this paragraph we perform the FFT for each radius of the galaxy, mixing the azimuths, instead of studying each azimuth, mixing the radius, as we did in the previous section. The aim is to study the radial dependence of the different FFT parameters. The $H\alpha$ velocity field does not take warp into account, thus, in a first step, the position angle and the inclination, of each ring of the beam smearing map, are kept fixed. In the next step we include warps, by using the HI tilted-ring model's parameter.
(α) Without warp
On figure 6.14, we present the variation of amplitude of the velocity dispersions and of the phases, as a function of the radius. The FFT of the first four orders (k=1,2,3 and 4) for the velocity dispersion amplitude σ_k and the corresponding phase ϕ_k (only for k=2 and 4) are displayed in the top and bottom panel respectively. Concerning the amplitudes, we observe the same phenomenon than previously observed : σ_2 and σ_4 are by far larger than σ_1 and σ_3. Moreover, the decrease of amplitudes is fast, and at 200", the σ_2 and σ_4 represents only 1 km/s. Given the low values of σ_1 and σ_3, the corresponding phases ϕ_1 and ϕ_3 are meaningless, thus we only display ϕ_2 and ϕ_4 on the bottom panel. Those phases are roughly constant up to ~500 arcsec. In the range ~500–800 arcsec, small variations are observed, larger for ϕ_2 than for ϕ_4. After 800 arcsec, amplitudes are too low, therefore the results for the phase is not significant anymore.

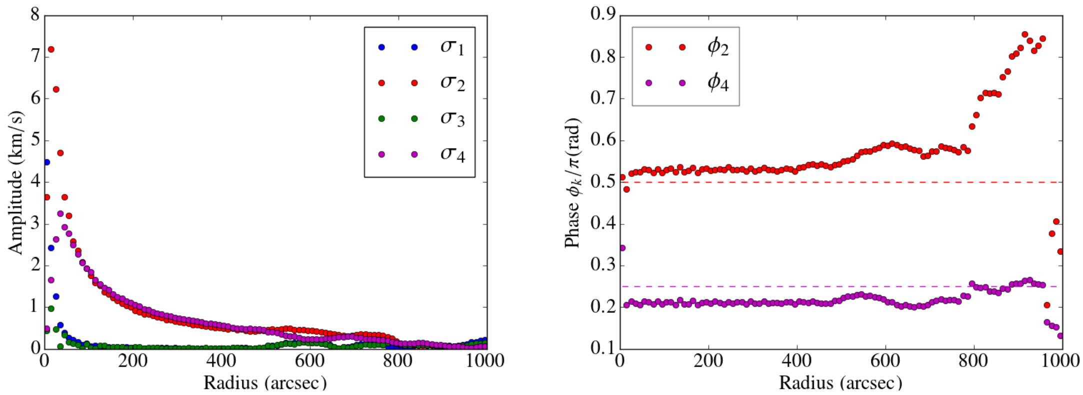

FIGURE 6.14. – Variations of the parameters of the FFT with the radius, amplitudes on top panel and phases on bottom panel.

(β) With warp
If we consider warps in taking the results of the tilted ring model, each radius has its own set of position angle and inclination, varying with the radius. On figure 6.15 we present the same plot as before, adding the radial variation of inclination.

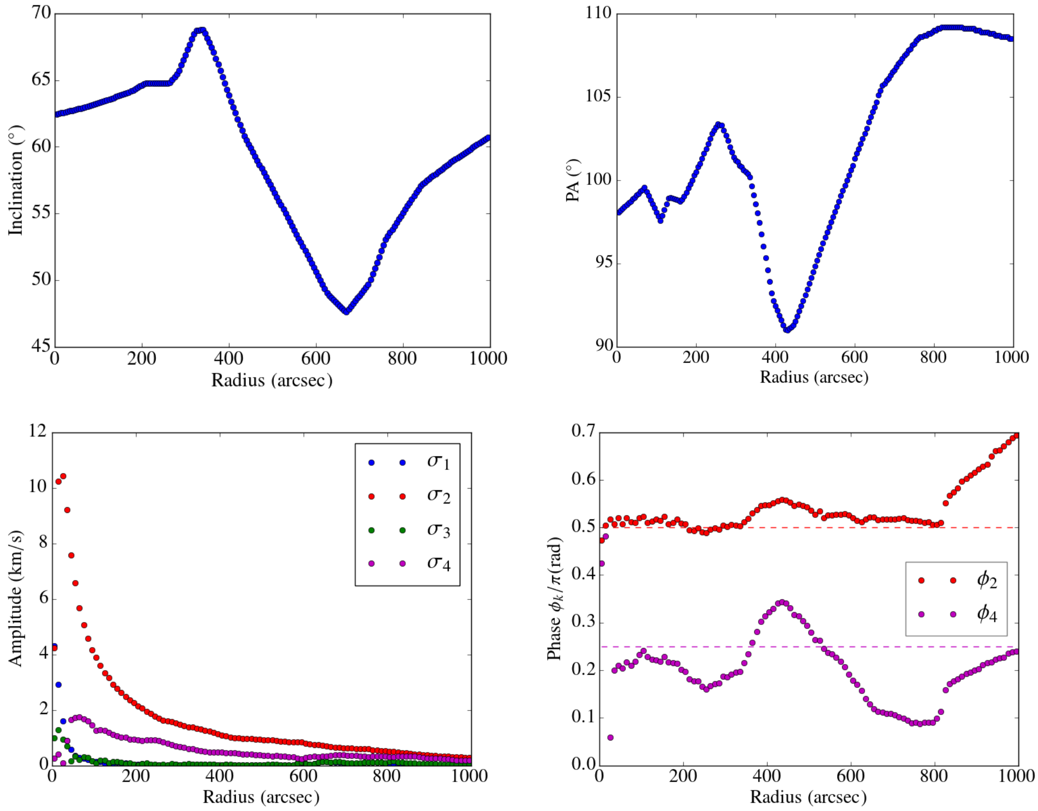

FIGURE 6.15. – Variations of the parameters of the FFT with the radius, amplitudes on top panel and phases on bottom panel.

Without warp, amplitudes σ_2 and σ_4 had similar behaviour. When accounting for the warp, amplitude σ_4 is greatly reduced, while σ_2 is stronger. Other amplitudes σ_1 and σ_3 are still negligible. First let's note that inclination varies from 45° to almost 70°, implying that the warp of NGC5055 is strong. The beam smearing model is calculated using the $H\alpha$ inclination of 63^o, meaning that locally the beam smearing is under/over-estimated depending if the actual inclination is greater/lower than the model inclination. Using HI data to compute the beam smearing suppress these effects, since the input radial velocity maps from THINGS already contains the signature of the warp.

Variations in position angles and inclinations induces variation of ϕ_2 and ϕ_4. A change in the position angle, i.e. in the initial starting azimuth, logically affect the phase. Between 450 and 650 arcsec, the increasing position angle leads to a decrease of ϕ_2. The influence of inclination on the phase is discussed in more detail in the next part.

(iii) Inclination dependences

In this section we study how the shape of the beam smearing pattern evolves with the inclination. As previously, NGC 5055 is still modelled using its $H\alpha$ rotation curve but we simulate three factice inclinations : 30°, 50°, 70°, instead of using only its actual inclination of 59°. The lowest inclination in the THINGS sample is 32.6° and the highest 75.8°, the median value being 64.5°. Those four inclinations allow to sample different configuration in our data. For each model, we compute the FFT of the map, by taking all pixels and reducing the galaxy to one radius as explained in section 6.2.2. Results for the parameters σ_k and ϕ_k are listed in Table 6.4. The maps showing the shape of the beam smearing as well as the corresponding FFT are displayed in figure 6.16.

Inclination Parameters	30°	50°	63°	70°
σ_1(km/s)	0.07	0.05	0.01	0.01
σ_2(km/s)	0.30	0.46	0.41	0.48
σ_3(km/s)	0.02	0.03	0.03	0.01
σ_4(km/s)	0.09	0.22	0.33	0.53
ϕ_1/π	0.54	0.65	0.35	0.05
ϕ_2/π	0.51	0.53	0.54	0.59
ϕ_3/π	0.59	0.00	0.03	0.10
ϕ_4/π	0.25	0.24	0.21	0.22

Tableau 6.4. – FFT parameters for the beam smearing model of NGC5055 at different inclinations.

Table 6.4 and Fig 6.16 show that the amplitude of the second and fourth orders grows with the inclination. For an inclination of 30°, the velocity dispersion due to the beam smearing is maximum along the minor axis and minimum along the major axis, characteristic of an order 2.The FFT displays a large amplitude of the velocity dispersion at a phase $\phi_2 \sim \pi/2$, because minor and major axis are orthogonal, this corresponds to a high value of $\sigma_2 \sim 0.30$ km/s, largely dominating the other orders. For the inclination 50°, high velocity dispersions are spread out over a larger area along the minor axis without affecting much the major axis direction.

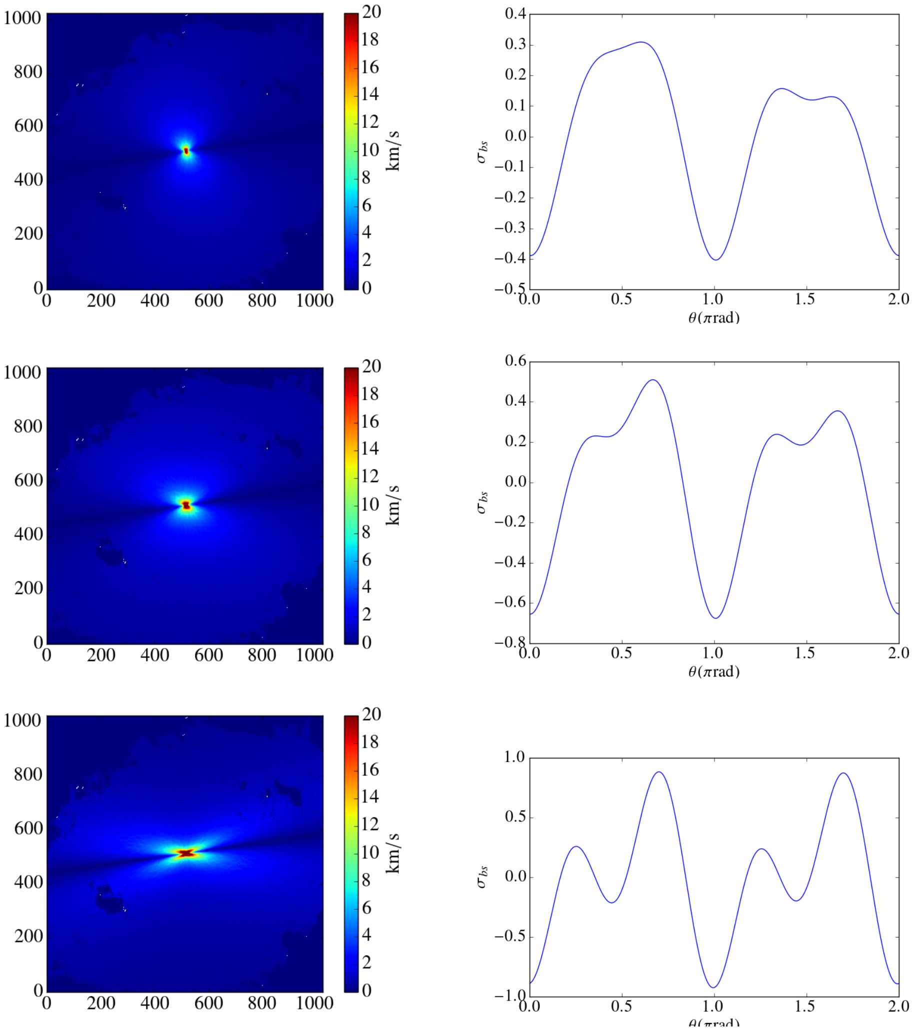

FIGURE 6.16. – Beam smearing model and corresponding FFT at different inclinations : 30°, 50° and 70° for the top, middle and bottom panel respectively.

Due to the higher values in the dispersion, order 2 increases by ~50%, but the amplitude of σ_4 grows even more by almost ~150%. Phases ϕ_2 and ϕ_4 doesn't change significantly. For an inclination of 70°, we observe a clear X-shape of the dispersion that was only weakly sketched for 50°. That X-shape, is more elongated on the major axis than for the previous inclination and gives a large velocity dispersion amplitude $\sigma_4 \sim 0.53$ km/s, which becomes more important than $\sigma_2 \sim 0.48$ km/s. On the corresponding FFT (bottom-right panel), the discrepancy between peaks of the order 4 increases. Part of this discrepancy is due to the asymmetry of the beam, and part of it is due to the asymmetry in the flux. As the inclination increases, the cross shape is more pronounced, making beam asymmetries more visible.

In conclusion, the beam smearing always creates an order 2, at any inclination, due to the minimum dispersion values along the major axis. Its phase ϕ_2 is directly link to the asymmetry of the beam. In the case of a perfectly circular beam, ϕ_2 is aligned with the minor axis (i.e. 0.5 π, half period of the order 2). Nevertheless, modelling the beam map with an inclination different than the one used to model the beam smearing drastically changes the result.

To this order 2 is superposed an order 4, the cross shape observed in the previous figures. At low inclination, this cross shape is reduced to a line, with maximum values of the dispersion being aligned on the minor axis. As we go towards higher inclination, the cross shape is more and more defined, inducing higher amplitudes σ_4. The phase ϕ_4 is also impacted, and going at higher inclination, the maximum values tends to be more and more aligned with the major axis leading to lower value ϕ_4 for NGC5055, while they were closer to the minor axis at lower inclination, $\phi_4 \approx 0.25\pi$. The beam smearing is more stronger at higher inclination. Therefore an increase of inclination induce an increase of both σ_2 and σ_4. Nevertheless, due to that cross shape, order 4 becomes more and more important relatively to the order 2. Furthermore, at high inclinations, an error of 7° in inclination leads to a difference of 60% in the value σ_4 (6.4).

b. The case of stacked galaxies

The goal of this section is to study how evolves the parameter of the FFT of the stacked galaxy when we exclude few annulus or some galaxies.

(i). Radial dependence

First we focus on the radii. As we observed in the previous section, the beam smearing is maximum in the central part of the galaxy and then becomes less important as we go towards the outer part of the galaxy. In order to observe the effect of beam smearing, we divide our sample into two subsamples : in the inner sample, we select only the inner part of each galaxy and in the outer subsample, the outer part. In other words, the inner and outer subsample contains all the points being below and above $r_{max}/2$ respectively, r_{max} being the last radius of each individual galaxy.

In order to check the beam smearing effect, both corrected and raw velocity dispersion maps are used and a stacked galaxy is created for each case : one using the corrected velocity dispersion maps and one using the raw map. For both subsamples and for both cases, we compute a stacked galaxy that contains the total signal for all galaxies, using the method described in the methodology section (6.2.2).

We thus end up with four configurations : a) using velocity dispersion maps corrected from beam smearing effects for the inner sample (refereed as « Corr Inner ») ; b) idem for the outer sample (refereed as « Corr Outer ») ; c) using velocity dispersion maps not corrected from beam smearing effects for the inner sample (refereed as « Raw Inner »), d) idem for the outer sample (refereed as « Raw Outer »). The result of the FFT parameters for each configurations are listed in Tab 6.5, and the total signal is shown in Fig 6.17. Contrarily to the study realised before on NGC5055 we used on the velocity dispersion squared.

Because we study the beam smearing effects, as a result of the previous sections, we are more concerned by the orders 2 and 4 than by the orders 1 and 3. We also expect that σ_2 and σ_4 decrease with the radius. Table 6.5 indeed indicates that σ_4 is

Model		(a) Corr inner	(b) Corr outer	(c) Raw inner	(d) Raw outer
Velocity dispersion		$(km/s)^2$	$(km/s)^2$	$(km/s)^2$	$(km/s)^2$
	$\sigma_0^2 - <\sigma_0^2>$	-7.4	-13.6	-7.8	-15.0
	σ_1^2	36.7	9.80	38.0	12.2
	σ_2^2	14.8	23.5	21.5	24.4
	σ_3^2	9.85	4.13	12.9	4.49
	σ_4^2	29.4	13.1	35.0	13.7
Phase	ϕ_1/π	0.04	0.79	0.06	0.81
	ϕ_2/π	0.39	0.58	0.41	0.58
	ϕ_3/π	0.47	0.30	0.45	0.31
	ϕ_4/π	0.23	0.22	0.23	0.22

(a) using velocity dispersion maps corrected from beam smearing effects for the inner subsample
(b) idem for the outer subsample
(c) using velocity dispersion maps not corrected from beam smearing effects for the inner subsample
(d) idem for the outer subsample.

Tableau 6.5. – FFT parameters for the total signal obtained in the 4 configurations describe in section 6.4.2.

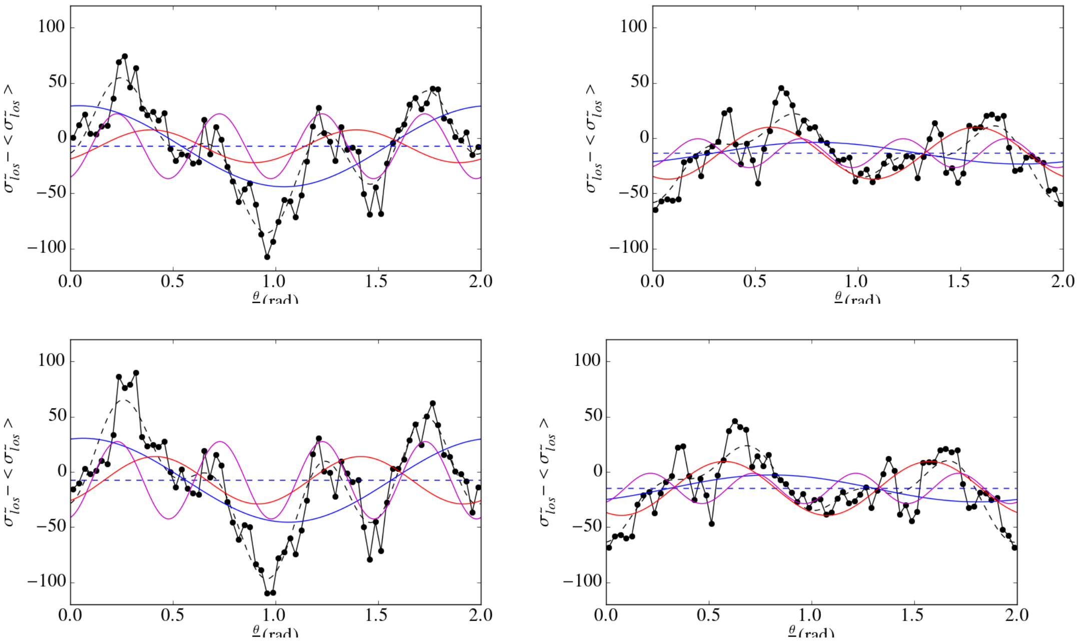

FIGURE 6.17. – Total signal and FFT orders superposed for the different cases mentioned before. a) top left, b) top right, c) bottom left, d) bottom right.

lower in the outer subsample (cases b and d) than in the inner one (cases a and c) but, surprisingly, σ_2 is higher.

Concerning the phases, ϕ_4 is not changing while ϕ_2 increases. As we mentioned it in the previous sections, phases are supposed to remain roughly constant with the radius, if we only consider beam smearing effects.

For both the inner and outer subsamples, the velocity dispersion amplitudes are lower when we correct for the beam smearing (cases a and b) than when we do not correct (cases c and d), but the phases do not change.

The beam smearing smearing correction has really few impact on the σ_2 (24.4 to 23.5 (km/s)^2) and σ_4 amplitudes (13.7 to 13.1 (km/s)^2) for the outer subsample.

For the inner subsample, the variation are larger, a shift from 21.5 (km/s)^2 to 14.8 (km/s)^2 is observed for σ_2^2 and from 35.0 to 29.4 (km/s)^2 for σ_4^2.
We conclude that the second order is probably associated to a dynamical process in galaxies, while the fourth order is more likely a residual of beam smearing that was poorly corrected during our process due to insufficient knowledge of the shape of the PSF.

(ii). Inclination dependence
In the previous paragraph we studied the radial dependence of the FFT second and fourth orders. In this section we focus on the effects of the inclination. We again split the sample into two subsamples, the pivot inclination being 64.5°, the median value of the inclination. Seven galaxies belong to the low-inclination subsample and eight in the high-inclination one. Once again we consider four configurations : a) using corrected velocity dispersion maps and galaxies from the low-inclinations subsample ; b) idem for the high-inclination subsample ; c) using raw velocity dispersion maps and galaxies from the low-inclinations subsample and d) idem the high-inclination subsample. The results of the FFT parameters for each configurations are listed in Tab 6.6, and the stacked galaxies for each configuration is shown in Fig 6.18.

Signatures of beam smearing effects are clearly identified on σ_4 which are by far larger when the velocity dispersion are not corrected. Table 6.6 indicates that, if one corrects the dispersion velocity field from beam-smearing effects, σ_2^2 is more than four times larger than σ_4^2 for the low-inclination subsample (case a), while σ_2^2 is similar to σ_4^2 for the high-inclination subsample (case b). In the low-inclination cases (a and c), velocity dispersions moderately vary, due to the fact that beam smearing is weaker at lower inclinations. In the high-inclination cases (b and d), the variations between corrected and raw velocity dispersion maps are not really larger except maybe for σ_4 that goes from 53.2 to 47.6 (km/s)^2 ; it is somehow surprising as we would expect beam smearing to be larger for higher inclination.
Whatever the case, σ_2 shows almost the same amplitudes but way above σ_1 and σ_3.

Case		(a)	(b)	(c)	(d)
Inclination		$< 64.5°$	$> 64.5°$	$< 64.5°$	$> 64.5°$
Beam smearing		Corrected	Corrected	Raw	Raw
Velocity Dispersion		$(km/s)^2$	$(km/s)^2$	$(km/s)^2$	$(km/s)^2$
	$\sigma_0^2 - <\sigma_0^2>$	-1.42	-20.7	-1.34	-21.6
	σ_1^2	12.5	16.3	12.9	17.3
	σ_2^2	44.9	49.5	46.9	49.1
	σ_3^2	11.6	10.8	11.1	11.5
	σ_4^2	8.98	47.6	8.38	53.2
Phase	ϕ_1/π	0.39	0.66	0.43	0.65
	ϕ_2/π	0.50	0.91	0.50	0.90
	ϕ_3/π	0.43	0.36	0.43	0.37
	ϕ_4/π	0.44	0.23	0.44	0.23

(a) using corrected velocity dispersion maps and galaxies from the low-inclinations subsample
(b) idem for the high-inclination subsample
(c) using raw velocity dispersion maps and galaxies from the low-inclinations subsample
(d) idem the high-inclination subsample

Tableau 6.6. – FFT parameters for the total signal obtained in the 4 configurations mentioned above.

Interestingly, none of those amplitudes vary considerably when subtracting the beam smearing. Concerning the phases, we observe that at low inclination ϕ_2 is equal to 0.5π, whereas for higher inclinations $\phi_2 \approx 0.9\pi$. A result from a previous analysis was that beam smearing effects induce a strong second order, aligned with 0.5π, this is confirmed by the present analysis.
In the other hand $\phi_4 \approx 0.44\pi$ at low inclination and $\phi_4 \approx 0.23\pi$ at high inclination. This is also consistent with what we previously conclude, i.e. that at low inclination the fourth order has a low amplitude and thus the phase has a « random value », while at higher inclination σ_4 becomes larger and is aligned close to $\approx 0.25\pi$.

To investigate the effect of inclination, we exclude the 4 highest inclined galaxies, NGC2841, NGC3198, NGC3521, NGC7331, which all have inclinations greater than 70°, and reproduce the plot of Fig. 6.2. By removing those galaxies, 664 independent rings remains, for which the distribution of FFT parameters are shown in Fig. 6.19. Concerning the phase angles ϕ_1, ϕ_2 and ϕ_3, the exclusion of 219 doesn't impact strongly the distributions. For ϕ_4, it has an important effect, since those rings had phase angles distributed mainly over the 3 central bins, between 0.3 and 0.6 π. Therefore the peak is much less pronounced than it was when computed using the entire sample.

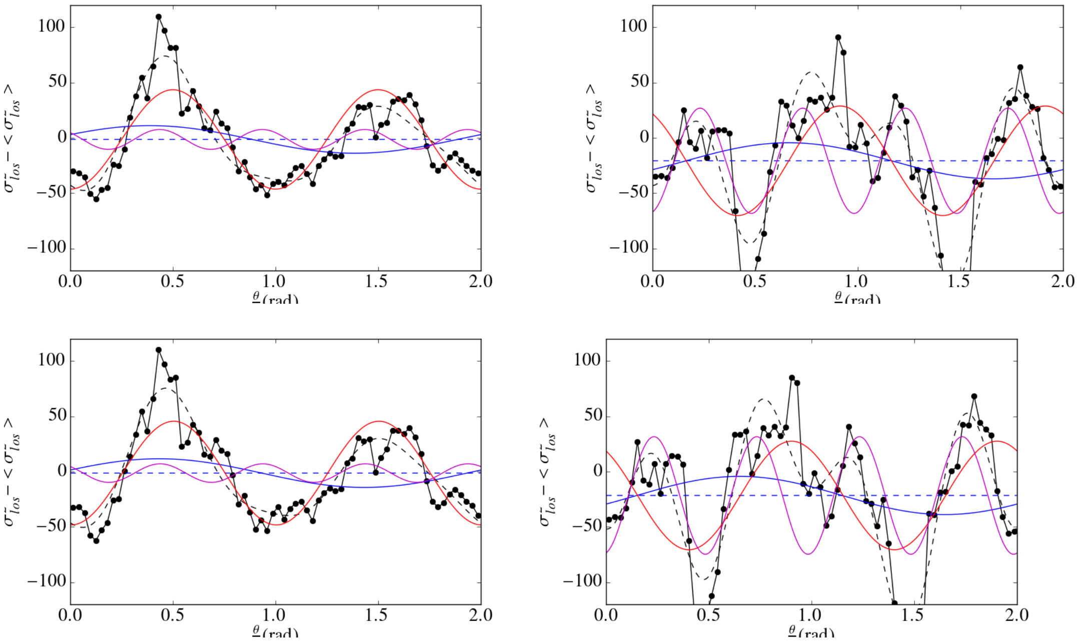

FIGURE 6.18. – Total signal and FFT orders superposed for the different cases mentioned before. a) top left, b) top right, c) bottom left, d) bottom right.

Furthermore, the other bins stays almost constant, confirming once again that the more inclined galaxies tends to have phase angles ϕ_4 close to the half period of the order 4.

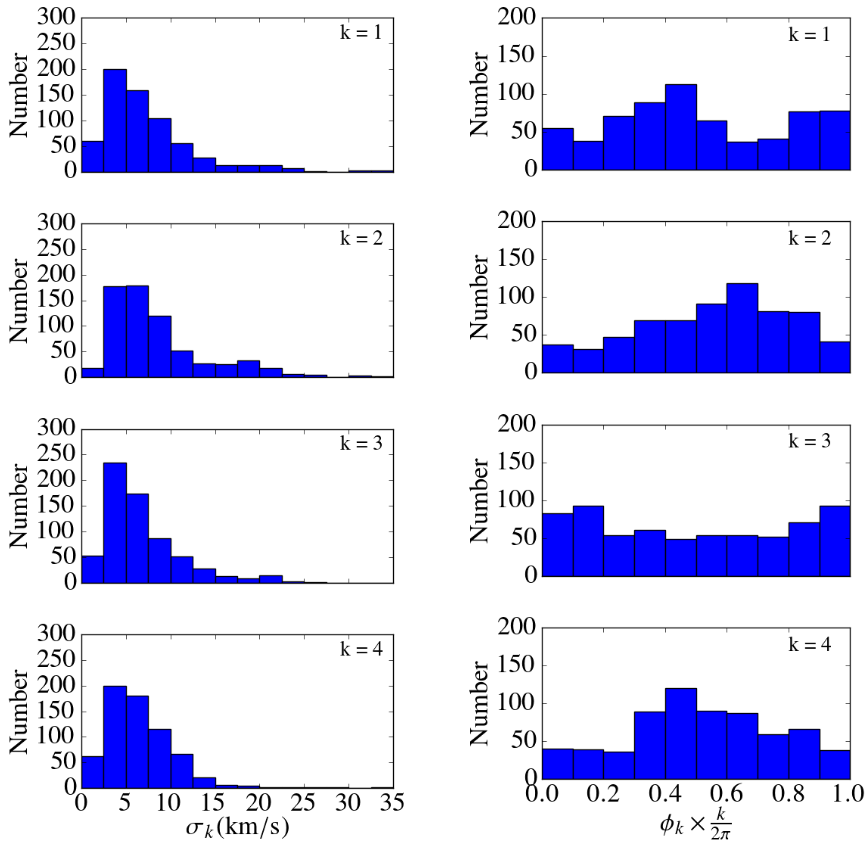

FIGURE 6.19. – Amplitude (left column) and phase (right column) distribution of the Fourier modes 1 to 4 in the 664 rings of the THINGS subsample, after exclusion of the 4 most inclined THINGS galaxies. Phases are normalized such that 0.5 is the half period of the mode, and 1 is the full period. The period of the mode k is $\frac{2\pi}{k}$.

6.4.3. Multiple components and moments method compare with Gaussian fit

A detailed inspection of data-cubes reveals that some galaxies contains multiple components, not only a well-defined gas disk, which rotates at different velocities. In some regions, flux is really low and we can hardly identify lines in the spectral profile of galaxies. For those two cases, tracing the dispersion using a second order moment maps from the observed data-cube might not the optimal method. On Fig. 6.20, we show the example of NGC2841, the galaxy which exhibits the largest dispersion of the entire THINGS sample. Using a region of 10 × 10 pixels, we were able to detect the presence of two distinct components, rotating at different velocities in the integrated spectrum (Fig. 6.20, left panel). For this type of spectrum, the method of the second order moments is not adapted, since it considers the two components as one, resulting in a larger dispersion velocity than in each individual components.

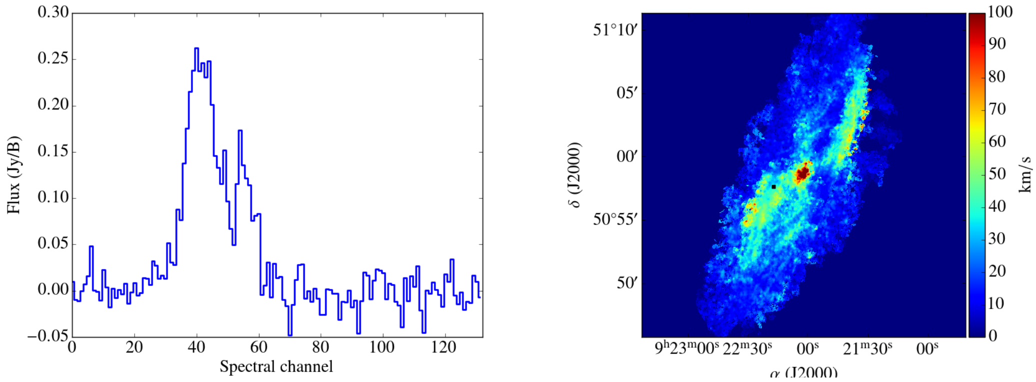

FIGURE 6.20. – Example of multiple components in the profiles of NGC2841 (left) and corresponding region in the dispersion map (right) indicated with the black square.

In Sect. 2.2.3, we described several papers focusing on the shape of the HI profiles in THINGS galaxies. In particular, Mogotsi et al. (2016) presented a comparison between the velocity dispersion values found using the second order moments and the Gaussian fit (Fig. 6.21). The main difference occurs in the inner part of galaxies, and authors argue that the profiles in the inner part tends to deviate more from Gaussianity than the outer parts. Therefore, the method used to trace the velocity dispersions has an effect on the derivation of the asymmetries.

6.4.4. Validity of the model and interpretation

In appendix H, we give an overview of the result of the asymmetry study on each individual THINGS galaxies. Here we show the result for the galaxy NGC2841 (Fig. 6.22). Left column, from top to bottom : (1) flux map from THINGS, (2) velocity map from THINGS, (3) dispersion map, (4) beam smearing modelisation and (5) dispersion map corrected from the beam smearing effect. Middle column : (1) Projected map of the 0^{th} order of the FFT, (2) map of order 1, (3) map of order 2, (4) map of order 3, (5) map of order 4 and (6) map of order 8. Right column : (1) Projected map containing all the FFT orders from 0 to N/2, N being the number of pixel in a ring, (2) dispersion maps corrected from the beam smearing subtracted by the FFT map containing all orders, (3) Projected map of the FFT containing orders 0 to 4, (4) Projected map of the FFT containing all orders subtracted by the map containing only orders 0 to 4, (5) Radial variation of the amplitudes σ_k of the FFT up to the order 20 and (6) Radial variation of the angle phases $\phi_k \times \frac{k}{2\pi}$ up to the order 20.

These maps contains a huge amount of information. In that part we highlight the main results.

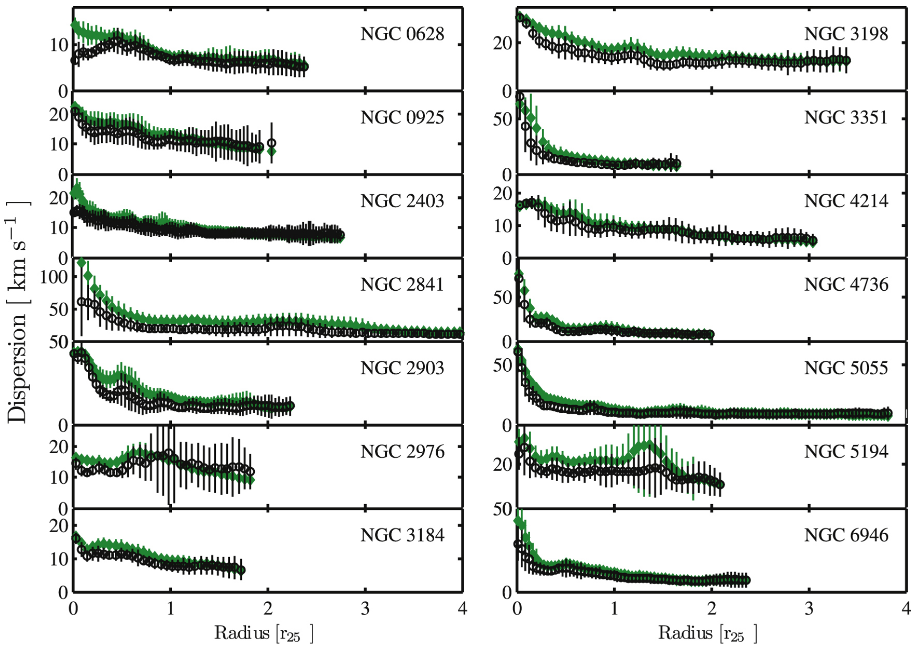

FIGURE 6.21. – Radial variation of the azimuthally averaged velocity dispersion in galaxies from the THINGS sample. The black circles represents the Gaussian fit and the green one the second-order moments. Figure from Mogotsi et al. (2016).

In a first time, these maps confirms the validity of cutting the FFT to the order 4 in our modelisation. By inspecting panels (3), (4) and (5) of the right column for all THINGS galaxies, we observe that :

- the projected map of the FFT containing orders 0 to 4 reflects fairly well the large-scale structures observed in the corrected dispersion maps.
- the comparison of the FFT maps containing all orders, subtracted by the FFT map containing only orders 0 to 4 shows no particular large-scale structures.
- the investigation of the amplitudes up to the order 20 shows that the highest amplitudes are confined in the first 4 orders.

The interpretation of the asymmetries in the dispersion maps is not trivial. Indeed, a visual comparison of the flux map and dispersion map from THINGS (left column, panel (1) and (3)) shows that the flux distribution is anti-correlated with the velocity dispersion. In other words, a general behaviour observed amongst the 15 THINGS galaxies is that the maximum values in the flux distribution corresponds to low values of dispersion velocities and on the opposite low flux regions corresponds to the most important values of the dispersion. For the most striking examples, see Fig.H.10, Fig.H.4, Fig.H.14. Therefore, it is not possible to associate immediately the asymmetries in the velocity dispersion maps with the structures that compose the galaxy, such as bars or spiral arms. For a further investigation, one needs to perform a similar work on the flux map and compare with the results found in the present work.

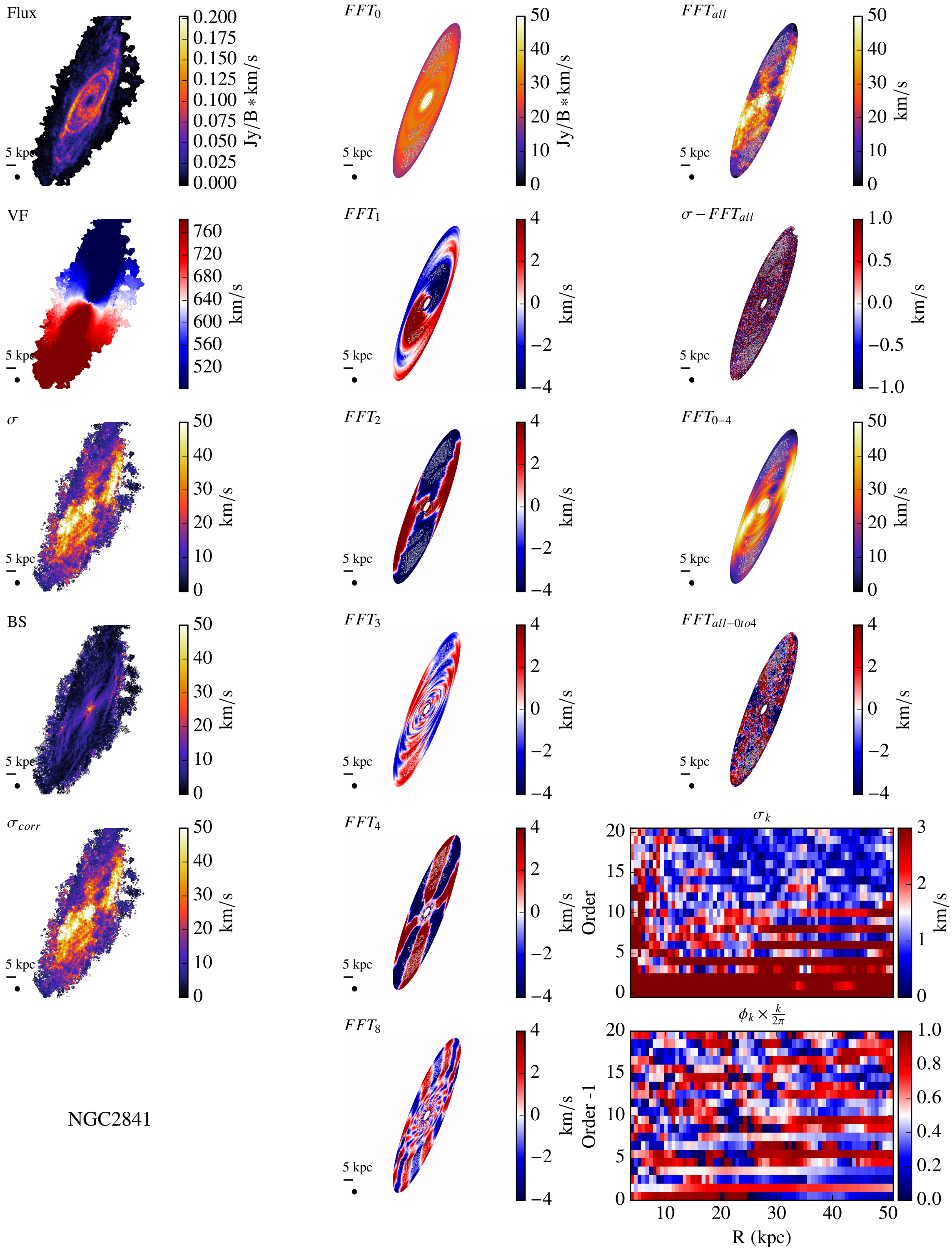

FIGURE 6.22. – Multiple plots of NGC2841

6.5. Conclusion

In this chapter, we perform a systematic study of the azimuthal variation of the velocity dispersion maps in the THINGS and WHISP samples. To describe those azimuthal variations at the local ring scale, we study the orders 0 to 4 of the FFT. First, we study the distribution of the FFT parameters σ_i and ϕ_i, $i \in (1,..,4)$, for each ring across all galaxies. Here we do not find a result similar to the one found in Chemin et al. (2020), with a phase ϕ_2 aligned systematically with the minor axis, but we find a random distributions of phases ϕ_2. This confirms the result found in the previous chapter that the velocity dispersion computed in the axi-symmetric and anisotropic case is not observed in the observational data. Nonetheless, an interesting result is found for the phase ϕ_4, which is aligned with the half period of order 4 (0.25π) for most rings of the study. To avoid bias due to the number of rings in each galaxy, we reduce the radial distribution of galaxies to a single ring, using to distinct methods : in the first one we average the radial distribution of the dispersion velocity and combine the signals for the entire sample creating a "stacked galaxy", in the second one, we compute the FFT on each ring and get the median value of the radial distribution of FFT parameters. Both methods show the order 4 aligned with 0.25π. In the case of the "stacked galaxy", the order 4 also became dominant in term of amplitude, becoming larger than σ_2 which generally dominates when we compute FFT at the local ring scale.

Considering the similarity of this observed order 4 with our beam smearing modelisation, an extensive discussion about its possible artificial nature is presented. From this discussion, the main uncertainty is that the real beam might deviates a simple Gaussian function, leading to possible incorrect beam smearing correction. An interesting part of the discussion is the study of distinct samples. In particular, separating samples depending on the galactic inclination (larger or smaller than 64.5° gives different trends in the velocity dispersion of the stacked galaxy. By combining data from galaxies at low inclination, velocity dispersion asymmetries tends to be dominated in amplitude by an order 2, while for the sample at high inclination, the amplitude of the order 4 is larger than the order 2. By excluding galaxies with inclinations higher than 70°, the peak observed in the distribution of phase angles ϕ_4 vanishes severely, indicating that some instrumental effects could still be an issue in our work. This systematic signal ϕ_4 associated with the variations of the asymmetries with the inclination could also be an indicator of anisotropy. Indeed, Eq. 4.9 shows a strong dependency with the inclination, and in the general case of non-axisymmetric systems, having a variation of the parameters σ_R, σ_θ and σ_z with the azimuth allows the possibility to have an order 4. This would also imply that the covariance terms are different from 0, and toy modeling using various values and function for this parameters could improve understanding the presence of this order 4 varying with the inclination. Then we discuss the choice of using the 2^{nd} order moment, rather than a Gaussian fit on the data-cube. The technique used has an impact on the dispersion maps, therefore a systematic comparison of dispersion maps using those two methods could allow us to evaluate the difference between those 2. In case of a major difference between the two outputs, a similar analysis on the dispersion maps obtained through Gaussian fit would be interesting.

Finally, the difficulties to interpret the asymmetries in the velocity dispersion are underlined. The fact that the velocity dispersion maps are anti-correlated with the dispersion maps complicate the analysis of asymmetries with structures in the galaxy. Therefore, a comparative study of the asymmetries in the flux distribution and velocity dispersion distribution would improve the understanding of the connection between those two.

Conclusion and perspectives

The core of this work is the study of the azimuthal variations in the velocity dispersion maps in nearby spiral galaxies. The velocity dispersion is a second order moment and therefore, it is much more complex to analyse than the flux and the radial velocity distributions of galaxies. Nevertheless, random motions gives tremendous information concerning the kinematics and the dynamics of galaxies.
Investing the collisional/collisionless nature of this gas is the main focus of this work. This nature is linked with the occupation fraction, defined by the volume filled by the gas over the total volume available in the disk. In case of collisionless objects, like stars, this ratio is close to 0, while for diffuse gas, this ratio is closer to 1. If the gas is made of extended tenuous clumps with a high velocity dispersion, the high frequency of collisions allows to dissipate energy isotropically, and the velocity dispersion ellipsoid is said isotropic. In the case more clumpy gaseous distribution, collisions should be less frequent, which makes the dissipation of the energy more difficult, and the gaseous clouds could behave like collisionless stars, that is showing an anisotropic velocity ellipsoid. In the first isotropic case, no projection effect on velocity dispersion within galaxies is expected, while in the second case the anisotropic velocity ellipsoid projects along the line-of-sight, and azimuthal variation of the dispersion are expected.
Therefore, the study of azimuthal variations of the velocity dispersion becomes important because it informs us on the collisional/collisionless nature of the gas, and on the shape of gas orbits in the plane of the galaxy (in the anisotropic case). In this framework, orbits can be radially biased (i.e. more radially directed) if the radial component of the velocity dispersion ellipsoid exceeds the tangential component. Such study has been carried out by Chemin et al. (2020) with the nearby galaxy Messier 33. For this galaxy, the azimuthal variations observed can be interpreted as an anisotropic and axisymmetric velocity ellipsoid. This model is characterised by a cosine function varying as 2θ, θ being the azimuth in the galactic plane and predicts a maximum velocity dispersion on the half period of this cosine. By initialising the azimuth on the major axis, this corresponds to a maximum velocity dispersion along a phase angle $\pi/2$, i.e. along the minor axis. The bisymmetry in the HI velocity dispersion seems to be linked to the presence of spiral arms of M33. It is thus possible that the minor axis coincidence with maximum dispersion is fortuitous. For a large sample of galaxies, the orientation of spiral arms is random, therefore studying the phase angle of asymmetric velocity dispersions is important. If the results found for M33 were observed in such other galaxies, that is if the HI velocity dispersion was observed always maximum along the minor axis, this would be a strong evidence for a generic anisotropic gas velocity ellipsoid in galactic disks (in this axisymmetric approach), and gas would thus

definitely need to be considered as a collisionless medium.

This is what we studied in the thesis, using a sample of 15 galaxies from THINGS, a HI survey of 34 galaxies observed at high spatial resolution, which was complemented with 15 galaxies from the WHISP sample, a larger sample of more than 300 galaxies observed at lower resolution. We first fit the azimuthal variation of the HI velocity dispersion in each galaxy. A general result was that the axisymmetric model used in Chemin et al. (2020) is too restrictive, and can not reproduce the complex shape of the azimuthal variations of the velocity dispersion. This is explained by the observations that the dispersion do not peak necessarily along the minor axis.
We then extended the modeling beyond the axisymmetric assumption, and measured the properties of the asymmetries in velocity dispersion maps through Fourier expansion up the 4th order. We showed that this method models the observed velocity dispersion maps very efficiently, since most of the power is contained in the first orders. Similarly to the previous conclusion concerning anisotropies, we do not reproduce the result obtained for M33 : the phase angles of the bisymmetric dispersion modes are not systematically aligned with the galaxy minor axes. We observe a random distribution of ϕ_2 in our sample. An important finding is however the observation that the phase angle of the 4th order dispersion mode ϕ_4 is systematically $\pi/4$. Although galaxies are different they all share this peculiarity in their velocity dispersion map. Using different methods, we confirmed the reality of this signal : we show that this is not due to noise, and that the probability to have such signal when combining all galaxies from the THINGS sample is lower than 1%.

In a next step, we thus investigated the impact of the beam smearing correction, since synthesized beam shapes draw a 4-order pattern. A weakness of the method is the lack of knowledge of the exact beam shape. For our model, we assumed an elliptical Gaussian beam, which is an approximation often done in HI studies, but which could bias the analysis since higher frequencies could be needed to model beam shapes more properly. Nevertheless, this effect only probably does not explain the feature observed in the 4-th order of the Fourier decomposition. Indeed, a comparative study of the inner and outer parts of each galaxy shows that this signal is as strong in the external part, affected only marginally by the beam smearing effect, as in the internal part, strongly affected by those instrumental effects. Another comparative study showed that dispersion maps of low inclination galaxies tend to be more dominated by a bisymmetry, while those of high inclination disks are dominated by 4-th order asymmetries. Finding $\phi_4 = \pi/4$ and amplitude variations of asymmetries with the inclination could indicate a strong projection effect in velocity dispersion maps of HI gas, therefore a hint for an anisotropic velocity ellipsoid.

In this thesis, we have initiated this modeling on a large sample, and keept the analysis as simple as possible. In the future, we will need to allow covariance terms in order to quantify the degree of correlation between the components of the velocity dispersion ellipsoid. The lack of knowledge about these terms, as well as the degeneracy between asymmetry and anisotropy, force us to remain cautious on the collisional/collisionless nature of HI gas. Another prospect to our work will be to measure the variation of velocity dispersions directly in the frame of the observed spiral arms. Another possibility to tackle this problem would be to use numerical hydrodynamical simulations and study the variations of σ_R, σ_θ and σ_z in and around spiral arms. All of these approaches would be helpful to disentangle effects of non-axisymmetry and of anisotropy, and help in understanding better the trends we observed in this thesis. These works were out of the scope of the present work, however. The upcoming generation of radio-telescopes like SKA will provide high-quality kinematics for thousands of galaxies. Our current analysis would thus surely benefit from such huge amount of data, and particularly in understanding better the impacts of effects like projection, asymmetric features, and beam smearing on the velocity dispersion.

The second important part of the thesis is the extraction of rotation curves for 313 galaxies from the WHISP sample, using the ^{3D}Barolo algorithm. This sample represents the entire set of data available for the WHISP survey. The strength of this tool is to fit tilted-ring model directly on 3D data-cubes, allowing to account for beam smearing effects, which have been a major issue for decades. Extracting rotation curves in an homogeneous way for a large sample requires a solid methodology is crucial for the analysis. Rotation curves allow to trace the potential of the galaxy. In particular, studying independently both sides of a galaxy is useful to evaluate the level of asymmetries between both sides : the kinematic lopsidedness. Quantifying and understanding the origin of those asymmetries is a key point for dynamical evolution of galaxy. Large samples are mandatory to investigate various environment and morphological types. This type of study is harder to perform with high-redshift galaxy, then spanning different morphological types allow to draw an evolutionary picture of those asymmetries. Nevertheless, in a near future, new spectroscopic survey of high redshift galaxies will be performed in optical (Harmoni), or in HI (SKA), and therefore an appropriate methodology must be prepared to use those data efficiently. This thesis provide an important amount of data reduced homogeneously, which can be used to quantify the kinematic lopsidedness for more than 250 galaxies. This would enhance by a factor five the classification first performed by Noordermeer et al. (2005). Another application for these rotation curves is illustrated in this thesis through the work of Korsaga et al. (2019). Mass modeling is a powerful tool to investigate the shape of dark matter halos. In that paper in which I participated, combined data from the sample WHISP and GHASP for 31 galaxies are presented, in order to evaluate the importance of the nature of data-sets in the mass modeling (using only the ionised gas component, only the cold gas or a mix of those two components). With the work I performed, extraction of rotation curves and $H\alpha$ observations of WHISP galaxies, the current common sample contains more than 200 galaxies, enhancing the sample used in Korsaga et al. (2019) by a factor seven. Indeed, the nature of the cusp/core controversy is based on statistical results, and a sample of 31 galaxies can't allow to have statistic while a sample of 200 galaxies is more representative. Finally, working with larger samples is a first step towards a new method for mass modeling directly on velocity fields.

Bibliographie

Abraham, R. G., Tanvir, N. R., Santiago, B. X., et al. 1996, MNRAS, 279, L47

Agertz, O., Lake, G., Teyssier, R., et al. 2009, MNRAS, 392, 294

Aguerri, J. A. L., Beckman, J. E., & Prieto, M. 1998, AJ, 116, 2136

Appleton, E. V. 1945, Nature, 156, 534

Baars, J. W. M., van der Brugge, J. F., Casse, J. L., et al. 1973, IEEE Proceedings, 61, 1258

Baldwin, J. E., Lynden-Bell, D., & Sancisi, R. 1980, MNRAS, 193, 313

Begeman, K. G. 1987, PhD thesis, -

Bender, R. 1990, A&A, 229, 441

Bershady, M. A., Verheijen, M. A. W., Swaters, R. A., et al. 2010, ApJ, 716, 198

Binney, J. & Tremaine, S. 2008, Galactic Dynamics : Second Edition

Blais-Ouellette, S., Amram, P., & Carignan, C. 2001, AJ, 121, 1952

Blandford, R. D. & Königl, A. 1979, ApJ, 232, 34

Boselli, A., Eales, S., Cortese, L., et al. 2010, PASP, 122, 261

Bosma, A. 1978, PhD thesis, -

Bosma, A. 1981a, AJ, 86, 1791

Bosma, A. 1981b, AJ, 86, 1825

Bosma, A. 2017, Astrophysics and Space Science Library, Vol. 434, HI in the Outskirts of Nearby Galaxies, ed. J. H. Knapen, J. C. Lee, & A. Gil de Paz, 209

Bottema, R. 1996, A&A, 306, 345

Bouché, N., Carfantan, H., Schroetter, I., Michel-Dansac, L., & Contini, T. 2015, AJ, 150, 92

Carignan, C. & Freeman, K. C. 1985, ApJ, 294, 494

Chabrier, G. 2003, PASP, 115, 763

Chemin, L., Braine, J., Combes, F., Kam, Z. S., & Carignan, C. 2020, A&A, 639, A145

Chemin, L., Huré, J.-M., Soubiran, C., et al. 2016, A&A, 588, A48

Christiansen, W. N. & Hindman, J. V. 1952, Australian Journal of Scientific Research A Physical Sciences, 5, 437

Combes, F. & Becquaert, J. F. 1997, A&A, 326, 554

Combes, F., Debbasch, F., Friedli, D., & Pfenniger, D. 1990, A&A, 233, 82

Combes, F. & Sanders, R. H. 1981, A&A, 96, 164

Conselice, C. J., Bershady, M. A., & Jangren, A. 2000, ApJ, 529, 886

Considere, S. & Athanassoula, E. 1982, A&A, 111, 28

Courteau, S. 1997, AJ, 114, 2402

Daigle, O., Carignan, C., Amram, P., et al. 2006, MNRAS, 367, 469

Dalcanton, J. J. & Stilp, A. M. 2010, ApJ, 721, 547

Davis, B. L., Berrier, J. C., Shields, D. W., et al. 2012, ApJS, 199, 33

de Blok, W. J. G. 2010, Advances in Astronomy, 2010, 789293

de Blok, W. J. G., Walter, F., Brinks, E., et al. 2008, AJ, 136, 2648

Di Teodoro, E. M. & Fraternali, F. 2014, A&A, 567, A68

Di Teodoro, E. M. & Fraternali, F. 2015, MNRAS, 451, 3021

Dicaire, I., Carignan, C., Amram, P., et al. 2008, MNRAS, 385, 553

Epinat, B., Amram, P., Balkowski, C., & Marcelin, M. 2010, MNRAS, 401, 2113

Epinat, B., Amram, P., & Marcelin, M. 2008a, MNRAS, 390, 466

Epinat, B., Amram, P., Marcelin, M., et al. 2008b, MNRAS, 388, 500

Ewen, H. I. & Purcell, E. M. 1951, Nature, 168, 356

Faber, S. M. & Gallagher, J. S. 1979, ARA&A, 17, 135

Field, G. B., Goldsmith, D. W., & Habing, H. J. 1969, ApJ, 155, L149

Franx, M., van Gorkom, J. H., & de Zeeuw, T. 1994, ApJ, 436, 642

Gaia Collaboration, Katz, D., Antoja, T., et al. 2018, A&A, 616, A11

Garcia-Gómez, C., Athanassoula, E., Barberà, C., & Bosma, A. 2017, A&A, 601, A132

García-Ruiz, I., Sancisi, R., & Kuijken, K. 2002, A&A, 394, 769

Garrido, O., Marcelin, M., & Amram, P. 2004, MNRAS, 349, 225

Garrido, O., Marcelin, M., Amram, P., et al. 2005, MNRAS, 362, 127

Garrido, O., Marcelin, M., Amram, P., & Boissin, O. 2003, A&A, 399, 51

Garrido, O., Marcelin, M., Amram, P., & Boulesteix, J. 2002, A&A, 387, 821

Gómez-López, J. A., Amram, P., Epinat, B., et al. 2019, A&A, 631, A71

Governato, F., Brook, C., Mayer, L., et al. 2010, Nature, 463, 203

Governato, F., Zolotov, A., Pontzen, A., et al. 2012, MNRAS, 422, 1231

Hewish, A., Bell, S. J., Pilkington, J. D. H., Scott, P. F., & Collins, R. A. 1968, Nature, 217, 709

Hindman, J. V., Kerr, F. J., & McGee, R. X. 1963, Australian Journal of Physics, 16, 570

Hogbom, J. A. & Brouw, W. N. 1974, A&A, 33, 289

Ianjamasimanana, R., de Blok, W. J. G., Walter, F., & Heald, G. H. 2012, AJ, 144, 96

Ianjamasimanana, R., de Blok, W. J. G., Walter, F., et al. 2015, AJ, 150, 47

Jansky, K. G. 1933, Popular Astronomy, 41, 548

Jog, C. J. & Combes, F. 2009, Phys. Rep., 471, 75

Józsa, G. I. G. 2007, A&A, 468, 903

Józsa, G. I. G., Kenn, F., Klein, U., & Oosterloo, T. A. 2007, A&A, 468, 731

Kalnajs, A. 1983, in IAU Symposium, Vol. 100, Internal Kinematics and Dynamics of Galaxies, ed. E. Athanassoula, 87–88

Kalnajs, A. J. 1975, in La Dynamique des galaxies spirales, ed. L. Weliachew, Vol. 241, 103

Kam, S. Z., Carignan, C., Chemin, L., et al. 2017, AJ, 154, 41

Kamphuis, J. J. 1993, PhD thesis, -

Kamphuis, J. J., Sijbring, D., & van Albada, T. S. 1996, A&AS, 116, 15

Kennicutt, Robert C., J., Armus, L., Bendo, G., et al. 2003, PASP, 115, 928

Kent, S. M. 1986, AJ, 91, 1301

Kerr, F. J., Hindman, J. F., & Robinson, B. J. 1954, Australian Journal of Physics, 7, 297

Kornreich, D. A., Haynes, M. P., Lovelace, R. V. E., & van Zee, L. 2000, AJ, 120, 139

Korsaga, M., Epinat, B., Amram, P., et al. 2019, MNRAS, 490, 2977

Koyama, H. & Ostriker, E. C. 2009, ApJ, 693, 1346

Krajnović, D., Cappellari, M., de Zeeuw, P. T., & Copin, Y. 2006, MNRAS, 366, 787

Kretschmer, M., Dekel, A., Freundlich, J., et al. 2020, arXiv e-prints, arXiv :2010.04629

Kroupa, P. 2001, MNRAS, 322, 231

Kuijken, K. & Garcia-Ruiz, I. 2001, in Astronomical Society of the Pacific Conference Series, Vol. 230, Galaxy Disks and Disk Galaxies, ed. J. G. Funes & E. M. Corsini, 401–408

Kuijken, K. & Gilmore, G. 1991, ApJ, 367, L9

Leroy, A. K., Walter, F., Brinks, E., et al. 2008, AJ, 136, 2782

Martinsson, T. P. K., Verheijen, M. A. W., Westfall, K. B., et al. 2013, A&A, 557, A130

Mogotsi, K. M., de Blok, W. J. G., Caldú-Primo, A., et al. 2016, AJ, 151, 15

Muller, C. A. & Oort, J. H. 1951, Nature, 168, 357

Muller, C. A. & Westerhout, G. 1957, Bull. Astron. Inst. Netherlands, 13, 151

Murugeshan, C., Kilborn, V., Jarrett, T., et al. 2020, MNRAS, 496, 2516

Navarro, J. F., Frenk, C. S., & White, S. D. M. 1996, ApJ, 462, 563

Navarro, J. F., Frenk, C. S., & White, S. D. M. 1997, ApJ, 490, 493

Nilson, P. 1973, Uppsala general catalogue of galaxies

Noordermeer, E., van der Hulst, J. M., Sancisi, R., Swaters, R. A., & van Albada, T. S. 2005, A&A, 442, 137

O'Brien, J. C., Freeman, K. C., & van der Kruit, P. C. 2010, A&A, 515, A62

Oh, S.-H., Brook, C., Governato, F., et al. 2011a, AJ, 142, 24

Oh, S.-H., de Blok, W. J. G., Brinks, E., Walter, F., & Kennicutt, Robert C., J. 2011b, AJ, 141, 193

Oh, S.-H., de Blok, W. J. G., Walter, F., Brinks, E., & Kennicutt, Robert C., J. 2008, AJ, 136, 2761

Ohta, K., Hamabe, M., & Wakamatsu, K.-I. 1990, ApJ, 357, 71

Olling, R. P. 1995, AJ, 110, 591

Oman, K. A., Marasco, A., Navarro, J. F., et al. 2019, MNRAS, 482, 821

Oort, J. H. 1932, Bull. Astron. Inst. Netherlands, 6, 249

Planck Collaboration, Aghanim, N., Akrami, Y., et al. 2020, A&A, 641, A6

Portinari, L., Sommer-Larsen, J., & Tantalo, R. 2004, MNRAS, 347, 691

Puerari, I. & Dottori, H. A. 1992, A&AS, 93, 469

Reber, G. 1940, ApJ, 91, 621

Reshetnikov, V. & Combes, F. 1998, A&A, 337, 9

Reshetnikov, V. & Combes, F. 1999, A&AS, 138, 101

Richter, O. G. & Sancisi, R. 1994, A&A, 290, L9

Rix, H.-W. & Zaritsky, D. 1995, ApJ, 447, 82

Roberts, M. S. 1967, in IAU Symposium, Vol. 31, Radio Astronomy and the Galactic System, ed. H. van Woerden, 189

Rogstad, D. H., Lockhart, I. A., & Wright, M. C. H. 1974, ApJ, 193, 309

Rogstad, D. H. & Shostak, G. S. 1971, A&A, 13, 99

Rogstad, D. H. & Shostak, G. S. 1972, ApJ, 176, 315

Ryle, M. 1972, Nature, 239, 435

Ryle, M., Elsmore, B., & Neville, A. C. 1965, Nature, 205, 1259

Ryle, M. & Vonberg, D. D. 1946, Nature, 158, 339

Saha, K., Pfenniger, D., & Taam, R. E. 2013, ApJ, 764, 123

Sancisi, R. 1976, A&A, 53, 159

Schoenmakers, R. H. M., Franx, M., & de Zeeuw, P. T. 1997, MNRAS, 292, 349

Shapiro, K. L., Gerssen, J., & van der Marel, R. P. 2003, AJ, 126, 2707

Smith, S. 1936, ApJ, 83, 23

Sofue, Y. & Rubin, V. 2001, ARA&A, 39, 137

Spano, M., Marcelin, M., Amram, P., et al. 2008, MNRAS, 383, 297

Swaters, R. A., Sancisi, R., van Albada, T. S., & van der Hulst, J. M. 2009, A&A, 493, 871

Swaters, R. A., van Albada, T. S., van der Hulst, J. M., & Sancisi, R. 2002, A&A, 390, 829

Tamburro, D., Rix, H. W., Leroy, A. K., et al. 2009, AJ, 137, 4424

Thompson, A. R., Clark, B. G., Wade, C. M., & Napier, P. J. 1980, ApJS, 44, 151

Thompson, A. R., Moran, J. M., & Swenson, George W., J. 2017, Interferometry and Synthesis in Radio Astronomy, 3rd Edition

Torres-Flores, S., Mendes de Oliveira, C., Amram, P., et al. 2010, A&A, 521, A59

Trachternach, C., de Blok, W. J. G., Walter, F., Brinks, E., & Kennicutt, R. C., J. 2008, AJ, 136, 2720

van Albada, T. S., Bahcall, J. N., Begeman, K., & Sancisi, R. 1985, ApJ, 295, 305

van de Hulst, H. C. 1957, in IAU Symposium, Vol. 4, Radio astronomy, ed. H. C. van de Hulst, 3

van de Hulst, H. C., Muller, C. A., & Oort, J. H. 1954, Bull. Astron. Inst. Netherlands, 12, 117

van der Hulst, J. M., van Albada, T. S., & Sancisi, R. 2001, in Astronomical Society of the Pacific Conference Series, Vol. 240, Gas and Galaxy Evolution, ed. J. E. Hibbard, M. Rupen, & J. H. van Gorkom, 451

van der Kruit, P. C. & Freeman, K. C. 2011, ARA&A, 49, 301

van der Marel, R. P. & Franx, M. 1993, ApJ, 407, 525

van Eymeren, J., Jütte, E., Jog, C. J., Stein, Y., & Dettmar, R. J. 2011a, A&A, 530, A29

van Eymeren, J., Jütte, E., Jog, C. J., Stein, Y., & Dettmar, R. J. 2011b, A&A, 530, A30

Walter, F., Brinks, E., de Blok, W. J. G., et al. 2008, AJ, 136, 2563

Wolfire, M. G., Hollenbach, D., McKee, C. F., Tielens, A. G. G. M., & Bakes, E. L. O. 1995, ApJ, 443, 152

Wong, T., Blitz, L., & Bosma, A. 2004, ApJ, 605, 183

Yim, K. & van der Hulst, J. M. 2016, MNRAS, 463, 2092

Zaritsky, D. & Rix, H.-W. 1997, ApJ, 477, 118

Zwicky, F. 1933, Helvetica Physica Acta, 6, 110

ANNEXES

A. Publication to be submitted January 6th, 2021.

Asymmetries in the HI random motions of nearby spiral galaxies

P. Adamczyk[1,⋆], B. Epinat[1], P. Amram[1] and L. Chemin[2]

[1] Aix-Marseille Univ., CNRS, CNES, LAM (France)
e-mail: paul.adamczyk@lam.fr
[2] Universidad de Antofagasta (Chili).

Received January xxx, 2021; accepted 2021

ABSTRACT

Context. The collisionless stellar component in disk galaxies is known to be anisotropic in response to non-axisymmetric perturbations (e.g. spiral arms, bars), whereas the uniformly distributed and highly collisional cold gas component should thus display isotropic random motions because it dissipates energy through collisions between clouds in all directions. However, if the cold gas is clumpy with a low collision rate as suggested by recent numerical simulations, gas clouds become a collisionless medium and its response to non-axisymmetric perturbations should also be anisotropic as it has observationally been observed in the galaxy M 33.
Aims. In studying the azimuthal dependences of the HI velocity dispersion fields, we aim to measure its (a)symmetries and/or (a)nisotropies in order to investigate the collisional/collisonless nature of the cold gas.
Methods. We perform the first systematic study of the HI random motions on a sample of 30 nearby galaxies selected from the THINGS and the WHISP surveys. We study asymmetries using Fourier decomposition of the HI velocity dispersion maps.
Results. We do not confirm the result found on M33 in Chemin et al. (2020) that showed a phase systematically matching the minor axis direction. At the opposite, we find a random phase distributions. The velocity dispersion computed in the axisymmetric and anisotropic case is not observed in the observational data. Nonetheless, we find a signature of an Fourier order four aligned with its half-period 0.25π for most cases. An extensive discussion is presented about the beam smearing and its possible link with this fourth order.
Conclusions. We describe possible issues, and suggest that those fourth-order asymmetries are probably not due to beam-smearing residual.

Key words. galaxies: fundamental parameters; galaxies: kinematics and dynamics; galaxies: spiral structure; galaxies: cold interstellar medium

1. Introduction

Non axisymmetric large-scale perturbations observed in HI disk galaxies like bars, spiral arms, warps, or lopsidedness induce perturbation in circular orbits. Those ruptures of axisymmetries in the density distribution are responsible for radial and streaming motions, thus the orbits become asymmetric (Kalnajs 1973; Visser 1980).

Observationally, only two kinematical components are accessible: the observed radial velocity V_{obs} and the observed radial velocity dispersions σ_{obs}. Those components are different from the line-of-sight velocities V_{los} and the line-of-sight velocity dispersions σ_{los} because spectroscopic observations give only access to the convolution of the line-of-sight velocity dispersions with the Line Spread Function σ_{lsf}. Moreover, part of the observational velocity dispersion is due to thermal processes in the gas σ_{th}, thus for instance the velocity dispersion writes :

$$\sigma_{obs} = \left(\sigma_{los}^2 + \sigma_{lsf}^2 + \sigma_{th}^2\right)^{1/2} \tag{1}$$

Thus V_{obs} and σ_{obs} are far to be sufficient to describe the motions. Firstly, the instrumental dispersion σ_{lsf}, including beam smearing effects, and the thermal enlargement σ_{th} should be taken into account to recover the line-of-sight velocity dispersions σ_{los} (idem for V_{los}). Secondly V_{los} and σ_{los} only provide two constrains amongst the three velocities components and the three velocity dispersion velocities, requested to describe 3D motions of a 3D cell, respectively named V_R, V_θ, V_z and σ_R, σ_θ, σ_z in cylindric coordinates, where R, θ and z are respectively the radial, azimutal and vertical components in the galactic midplane reference frame.

The shape of orbits V_R, V_θ, V_z can be modelled by the velocity dispersion ellipsoid. The random motion σ_R, σ_θ, σ_z for each point of a galaxy is called the velocity dispersion ellipsoid, it describes the scatter of orbital motions. The velocity dispersion ellipsoid is isotropic whether the three velocity dispersion components are identical ($\sigma_R = \sigma_\theta = \sigma_z$). This can be the case of the interstellar gas due to multi-directional collisions that isotropize the gas velocity tensor. In other words, the isotropic case correspond to a velocity dispersion ellipsoid locally spherical and in that case the three velocity dispersion components are given by the line-of-sight velocity dispersion ($\sigma_R = \sigma_\theta = \sigma_z = \sigma_{los}$). If those three velocity dispersions are not identical, the velocity dispersion ellipsoid is thus anisotropic. This is the case for instance if a star or a gas cloud rotates only in the disk plane but with different radial and azimutal velocity dispersions. Like any ellipsoid, a velocity dispersion ellipsoid is characterized by three axis ratios, among them the azimuthal-to-radial ratio, σ_θ/σ_R, traces the degree of anisotropy in the disk plane. This ratio could

⋆ xxx

be used to define by the anisotropic parameter $\beta_{\theta,R}$:

$$\beta_{\theta,R} = 1 - \left(\frac{\sigma_\theta}{\sigma_R}\right)^2 \quad (2)$$

for the collisionless component (Binney & Tremaine 2008), thus it could be used to measure the azimutal dependence at each radius. In case of isotropy, $\sigma_R = \sigma_\theta$ leads to $\beta_{\theta,R} = 0$. In case of anisotropy, $\beta_{\theta,R} < 0$ corresponds to $\sigma_\theta > \sigma_R$, meaning that, within an observed cell (bin) containing millions of stars or hundreds of gas clouds, the orbits are in average preferentially tangential and $\beta_{\theta,R} > 0$ that corresponds to $\sigma_\theta < \sigma_R$, the orbits are preferentially radial.

A proxy used to estimate the level of asymmetry or of anisotropy in the cold gas distribution is to measure the HI global profile of a galaxy. An asymmetric profile is the result of large-scale asymmetries in the galaxy. Axisymmetric motions do not depend on azimuth but only on the radius. However, on top of radial dependences, many line-of-sight velocity dispersion fields display azimuthal dependences (Walter et al. 2008). This could be interpreted as non-axisymmetric motions with isotropic velocity dispersion or alternatively, as axisymmetric motion with anisotropic velocity dispersion. Of course asymmetric motions and anisotropic velocity dispersion also provide a solution that is not excluded.

The degree of asymmetry and anisotropy of the gas component would allow determining the nature and the properties of the neutral gas. Indeed, in disk galaxies, the collisionless stellar component is known to be anisotropic in response to asymmetric perturbations (e.g. spiral arms, bars), whereas the uniformly distributed gas component is supposed to be highly collisional and thus may display an isotropic ellipsoid of random motions. However, if the gas is clumpy with a low collision rate, gas cloud could evolve in a collisionless medium that could leave fingerprints or (a)symmetries or (a)nisotropies in the gaseous velocity dispersion ellipsoid. Numerical models nevertheless indicate that the interstellar gas component behaved partly like a collisionless medium (Bottema 2003; Agertz et al. 2009). In that case, the azimuthal dependences of the velocity dispersion could be measured not only in the stellar component but using the gaseous component as well.

An anisotropic gaseous velocity dispersion ellipsoid would indicate that (part of) the gas behave like collisionless stars. That would have important implications in galactic dynamics; $\sigma_{\rm los}$ would no longer be the reference from which the velocity tensor can be measured directly (in the general case, $\sigma_R \neq \sigma_\theta \neq \sigma_z \neq \sigma_{los}$). For example, it would impact the study of the disk vertical equilibrium, which depends on σ_z, related to the history of the disk heating via secular and hierarchical processes, and to the mass distribution in the disk (Combes & Becquaert 1997; Koyama & Ostriker 2009; Bershady et al. 2010; Martinsson et al. 2013). It would also affect the study of the stability criterion, linearly depending on σ_r, which drives the possibility of star formation via the equilibrium of gas clouds against gravitational collapse (Leroy et al. 2008). Of particular interest for this study, it would also modify the study of the gas radial pressure support (also called 'gas asymmetric drift'), which depends on σ_r and on the radial derivative of σ_r. The radial pressure modifies the circular velocity curve into shallower velocity profiles (Dalcanton & Stilp 2010).

Chemin et al (2000) studied the HI velocity dispersion of the nearby galaxy Messier 33 (M 33) and found evidence for azimuthal variations of the velocity dispersion. They showed that the velocity dispersions are systematically larger along its minor axis, and lower along its major axis. This can be either interpreted as anisotropy or asymmetry. In the case where the system is both anisotropic and axi-symmetric, the radial component must be larger than the azimuthal one in the ellipsoid of random motions, or, in other words, the gaseous orbits are more numerous than radial one. In the case where the system is isotropic, it must be asymmetric and the asymmetries must lie along the minor axis. Given that, in M 33, $\sigma_R > \sigma_{\rm los}$ and $d\sigma_R > d\sigma_{\rm los}$, the isotropy assumption of $\sigma_R = \sigma_{\rm los}$ possibly underestimates the gas radial pressure in the disk, thus the inner slope of the gas rotation curve and the mass density profile. The HI spiral-like arm perturbation could be at the origin of the gas velocity asymmetries in M 33. Like other galaxies such as NGC 2403, the HI velocity field of M 33 shows anomalous velocities due to extra-planar HI layer lagging the rotation of the disk (Kam et al. 2017; Koch et al. 2018; Fraternali et al. 2001, 2002), which could lead to a singular dispersion velocity field.

M33 could constitute a singular case and it has not yet be attempted to study the azimuthal velocity anisotropy parameter on a sample of nearby galaxies, this is the goal of this paper. Using observed velocity dispersion fields to quantify the azimuthal HI velocity dispersion dependence we further aim to contraint velocity dispersion ellipsoid models, in order to determine whether collisional or collisionless models are appropriate to explain the observations and to probe the clumpiness nature of the of the cold gaseous interstellar medium. This problem will be investigated by performing the first large-scale study of random motions of gas in nearby galaxies from high-quality HI data. Velocity dispersion maps will be used to quantify asymmetries assuming an isotropic velocity model or alternatively to measure anisotropies in case of axisymmetric motions.

In section 2, we define our sample of 30 nearby galaxies selected from two nearby HI surveys. In section 3, we present the methodology to construct the velocity fields and the FFT analysis. In section 4 and 5 we study, respectively for the THINGS and the WHISP samples, the asymmetries of velocity dispersion maps, using different methodologies to account for method-dependent biases. Before concluding in section 7, we discuss our results in section 6. In a series of four Appendices A to D, the mathematical framework, mocks data and complementary information on the FFT are described.

2. Data Sample Selection

We present in this section the different samples used in this work. We describe the purpose of each survey, the targets as well as information linked to the observations.

Several factors limit the study of spatially resolved velocity dispersion on a large sample. For a given instrumental configuration, including a spatial and spectral sampling, beam smearing effects vary linearly with the distances for nearby galaxies. Among other consequences, beam smearing tend to produce artefacts like asymmetric signatures in the velocity dispersions. Thus spatial and spectral telescope resolutions of HI observations as well as the distance of the galaxies and their inclinations in the plane of the sky are key parameters to define a sample. Due to those limiting factors, systematic study of asymmetries and anisotropies in the velocity dispersion maps have not been performed yet on a sample of galaxies.

2.1. THINGS

The HI Nearby Galaxy Survey (THINGS, Walter et al. 2008) aimed to map the atomic gas ISM in nearby galaxies at high resolution. The main scientific goal was to study the links between HI gas, dust and star formation. Observations were led with the Very Large Array (VLA) of the National Radio Astronomy Observatory. Targets were mostly selected from the Spitzer Infrared Nearby Galaxy Survey (SINGS, Kennicutt et al. 2003), an infrared imaging and spectroscopic survey of 75 galaxies. Distances for these galaxies are between 2 and 15 Mpc. An angular resolution ∼ 10" corresponds to physical resolutions ranging between 150 and 800 pc. THINGS is the only survey to date made at such resolution for a few tens of galaxies. Its resolution is close to the native data from the Spitzer Space Telescope at 24 μm (≈ 6") and GALEX in the near UV (≈ 5"), which is suitable for multi-wavelength studies.

THINGS contains 34 galaxies spanning different properties such as the morphological type, the star formation rate, and gas metallicity. It nonetheless does not contain early-type galaxies (E/S0, owing to expected extremely low HI densities in those systems), and edge-on discs (to avoid important projection effects). Observations were reduced following the procedure described in Walter et al. (2008). Outputs for each galaxy consist in a masked, flux re-scaled data cube, with 3 moment maps for the integrated HI emission (0th moment), line-of-sight velocity (1st moment) and velocity dispersion (2nd moment). The data are available in free access on `https://www2.mpia-hd.mpg.de/THINGS/Data.html`.

de Blok et al. (2008) presented rotation curves and mass models for 19 of the 34 galaxies. Non-circular motions in velocity fields were corrected following a method introduced in Trachternach et al. (2008). de Blok et al. (2008) and Oh et al. (2011b) presented a new methodology dedicated to dwarf galaxies to extract the observed velocity from the HI cube. Strong feedback from supernovae events was found from Governato et al. (2012) and Oh et al. (2011a). THINGS data have also been used to study the velocity dispersion of the gaseous component in galactic disc. For 11 galaxies, Tamburro et al. (2009) investigated the main processes driving the dispersion (2^{nd} order moment maps derived from the THINGS data cubes). Ianjamasimanana et al. (2012) and Ianjamasimanana et al. (2015) investigated the HI profiles of THINGS galaxies.

The goal of the present work is to perform an exploratory study of asymmetries and anisotropies of THINGS HI velocity dispersions. To make it possible, robust constraints on the geometrical parameters of the galaxies are requested, namely the inclination and the position angle of the discs as a function of the galactocentric radius, which are provided in the THINGS subsample described in de Blok et al. (2008). This subsample consists of a selection of rotation-dominated galaxies with inclinations ranging between 40° and 80°. These criteria exclude dwarf, interacting and disturbed galaxies, namely galaxies NGC 2366, DDO 154, IC 2574 and NGC 4826. A summary of general properties of the 15 galaxies from my THINGS working subsample is given in Tab. 1.

2.2. $H\alpha$ follow-up of the SINGS and THINGS surveys

Daigle et al. (2006) and Dicaire et al. (2008) published $H\alpha$ datacube for respectively 28 and 37 galaxies from the SINGS sample. Those observations were led with a Fabry-Perot interferometer mainly at the Observatoire du mont Megantic, with 1.6m telescope but also at the 3.6m Canada-France-Hawaii Telescope and at the European Southern Observatory 3.6m-telescope located at La Silla, Chile.

Those kinematical $H\alpha$ datacube were observed to model of the galactic baryonic and dark matter mass distribution. High-resolution $H\alpha$ rotation curves in the inner regions of the galaxies combined to HI rotation curves allowed to discriminate cuspy and core-dominated mass profiles. In the present work, the high-resolution $H\alpha$ velocity fields have been used to estimated and corrected beam smearing effects on HI THINGS velocity fields.

2.3. WHISP

The need of larger HI samples spanning different morphologies, luminosities, and environments gave birth to the Westerbork HI Survey of Spiral and Irregular Galaxies (WHISP) (Kamphuis et al. 1996; van der Hulst et al. 2001). The initial aim of this survey was to map the HI emission in 500-1000 spiral and irregular galaxies in order to study of the properties of the HI gas in galaxies: content, distribution, kinematics, asymmetries and perturbations (such as lopsidedness, warps or extraplanar structures), galactic dynamics, mass distribution models, and structure of dark matter haloes, through HI mass surface density profiles and rotation curves.

Observations were done at the Westerbork Synthesis Radio Telescope (WSRT) from 1992 to 2005. Galaxies were selected from the UGC catalogue (Nilson 1973). The duration of an observation was typically 12h, and targets were selected (i) at galactic declination δ larger than 20°, (ii) with a lower limit of 1.5′ for the length of the photometric major axis of galaxies, and (iii) with HI flux densities greater than 100 mJy. The early WHISP observations, those between 1992 and 1998, were biased towards gas-rich galaxies (i.e types mostly later than Sc galaxies). Due to a sensitivity improvement of a factor two of the WSRT in 1998, which allowed to observe fainter galaxies, morphological type earlier than Sc galaxies were targeted in order to provide a more uniform distribution of galaxies versus the morphological types.

Observational data are reduced through a pipeline available on the WHISP homepage (`http://www.astro.rug.nl/~whisp`). This pipeline produces data cubes at 3 different resolutions: full resolution with a 14"×14"/ sin(δ) beam size, 30"×30", and 60" × 60" beams van der Hulst et al. (2001) and Swaters et al. (2002). All the data are available for download on the website `http://wow.astron.nl/`. The catalog of observed galaxies that is available on the WHISP homepage contains 383 entries but some data are missing. In the end, the working sample is made of 313 galaxies [1]

We made some statistics on the whole sample. About two thirds of the WHISP galaxy sample have a distance lower than 30 Mpc. A distance of 30 Mpc implies a FWHM beam resolution of 30", corresponding to a linear scale of 4.3 kpc. The galaxies span a broad range of absolute $B-$magnitude, from −12 to −23, with a distribution centered on −20. Most of galaxies have typical inclinations between 50° and 70°, and ∼ 20% of them are more inclined than ∼ 80°. A wide distribution optical galaxy size is observed, with a scaling factor of 100 between the smallest and the largest ones.

Various studies have been published from WHISP observations. The kinematics of late-type dwarf galaxies was studied, yielding integrated and radially dependent properties (HI mass,

[1] Among the 375 galaxies with reduced data, about 40 of them are referred as being galactic companions, with no UGC number. Thus, the main WHISP galaxy sample is made of 342 UCG galaxies. Data for the ∼ 40 galaxies are missing. Pr. Van der Hulst, who is warmly thank, help us to recover some of the missing data cubes.

Galaxy name	α(J2000) (hh mm ss)	δ(J2000) (dd mm ss)	D Mpc	log(D_{25}) log(0.1')	m_B mag	M_B mag	Incl deg	Δv km/s
NGC 925	02 27 16.5	+33 34 44	9.2	2.03	9.77	-20.04	66	2.6
NGC 2403	07 36 51.1	+65 36 03	3.2	2.20	8.11	-19.43	63	5.2
NGC 2841	09 22 02.6	+50 58 35	14.1	1.84	9.54	-21.21	74	5.2
NGC 2903	09 32 10.1	+21 30 04	8.9	2.07	8.82	-20.93	65	5.2
NGC 2976	09 47 15.3	+67 55 00	3.6	1.86	9.98	-17.78	65	5.2
NGC 3031	09 55 33.1	+69 03 55	3.6	2.33	7.07	-20.73	59	2.6
NGC 3198	10 19 55.0	+45 32 59	13.8	1.81	9.95	-20.75	72	5.2
NGC 3521	11 05 48.6	-00 02 09	10.7	1.92	9.21	-20.94	73	5.2
NGC 3621	11 18 16.5	-32 48 51	6.6	1.99	9.06	-20.05	65	5.2
NGC 3627	11 20 15.0	+12 59 30	9.3	2.01	9.09	-20.74	62	5.2
NGC 4736	12 50 53.0	+41 07 13	4.7	1.89	8.54	-19.80	41	5.2
NGC 5055	13 15 49.2	+42 01 45	10.1	2.07	8.90	-21.12	59	5.2
NGC 6946	20 34 52.2	+60 09 14	5.9	2.06	8.24	-20.61	33	1.3
NGC 7331	22 37 04.1	+34 24 57	14.7	1.96	9.17	-21.67	76	5.2
NGC 7793	23 57 49.7	-32 35 28	3.9	2.02	9.17	-18.79	50	2.6

Table 1. Subsample of THINGS data use in this work

surface density profiles) for 73 galaxies (Swaters et al. 2002), and rotation curves for 62 galaxies (Swaters et al. 2009). This analysis was extended to earlier morphological types (from S0 to Sab) in Noordermeer et al. (2005) (68 galaxies), though without measuring the rotation curves. The study of the physical properties of HI discs such as warps (García-Ruiz et al. 2002), and lopsidedness (van Eymeren et al. 2011a,b). García-Ruiz et al. (2002) were performed a study on 26 edge-on galaxies from WHISP using HI and optical R-band data to study the HI disc morphologies. van Eymeren et al. (2011a) and van Eymeren et al. (2011b) performed respectively a kinematical and a morphological analysis of the disc lopsidedness in 70 WHISP galaxies. WHISP has been used to address questions about the environment of galaxies, and gas accretion from mergers. For example, Di Teodoro & Fraternali (2014) found that minor mergers can not sustain the process of star formation in spiral discs. Yim & van der Hulst (2016) investigated the Kennicutt–Schmidt law in different types of galaxies to probe different environments. Murugeshan et al. (2020) studied the relation between angular momentum, environment, star formation and morphology for 114 WHISP galaxies.

2.4. $H\alpha$ follow-up of WHISP : GHASP

Galaxies from the GHASP sample, a $H\alpha$ survey of galaxies was used to model the beam smearing of WHISP galaxies. The Gassendi $H\alpha$ survey of SPirals (GHASP) is a project conducted at Observatoire de Haute Provence (OHP), with a goal to study $H\alpha$ velocities in nearby spiral galaxies (Garrido et al. 2002, 2003, 2004, 2005; Epinat et al. 2008a,b,a; Spano et al. 2008; Korsaga et al. 2019). The GHASP sample consisted in 203 nearby spiral galaxies. Those galaxies were selected from the initial WHISP target list, in order to have for each galaxy the $H\alpha$ and the HI kinematics. Nevertheless, not all galaxies have been observed from WHISP, leaving only $\approx$ 130 galaxies in common between both samples. Observations were performed at OHP on the 193cm telescope, with a Fabry-Perot interferometer and a 512×512 Imaging Photon Counting System (IPCS) with a pixel size of 0.68 arcsec, a field-of-view (FoV) of 5.8 arcmin^2. The angular resolution of the data is limited by the seeing at OHP, between 1.5 and 3 arcsec. The spectral resolution is $\sim$ 30 km/s (FWHM). The typical duration of an observation is 2 hours.

2.5. Connecting the samples

Following the evidence of strongly asymmetric velocity random motions of the HI gas in M 33, as possible hint of anisotropy in the gas velocity ellipsoid (Chemin et al. 2020), we aim to perform the same analysis on the largest possible sample of high-spatial resolution galaxies in the HI. Thus we selected our galaxy sample among two distinct but complementary HI sample available from the literature and the archives: 15 galaxies among the 34 galaxies of the THINGS survey characterised by the high spatial resolution of the observation (150 to 800 pc) and 15 targets from the WHISP survey. The WHISP survey contains 313 galaxies, a much larger sample than the THINGS one allowing to better control selection effects, but its spatial resolution is lower by a factor xxx, thus only a few galaxies could have been selected. High-resolution $H\alpha$ velocity fields are used to account for beam smearing effects in the HI data.

3. Methodology

3.1. WHISP

Tilted-ring models on 2D velocity fields have been performed by de Blok et al. (2008) for 19 of the 34 THINGS galaxies. Among the different methods to obtain the velocity field from the data-cube, they have chosen to use Hermite h3 polynomials, due its stability in low S/N regions. To filter low-quality regions of the galaxy, two masks were successively applied on the velocity field. The first one consisted in rejecting profiles (i) for which the fitted maximum intensity was lower than $3\sigma_{ch}$, with σ_{ch} being the average noise in the profile out of the line region, and (ii) for which the dispersion of the fitted function was lower than the channel separation. The second mask consisted of a sigma-clipping on the HI column density maps to suppress noise pixels and to exclude regions inside r_{min} and outside r_{max}, which are respectively the innermost and outermost radii of the tilted-ring models fitted on the final velocity fields in order to obtain rotation curves. The sampling of the rotation curve has been fixed at 2 velocity points per beam. In the present work, we recomputed the maps using the same method to build the mask. However, we note that for some galaxies like NGC3031 (Fig **??**), NGC3627 (Fig **??**), the velocity field model could be extended further away. Nevertheless, to be conservative and consistent with their analysis, we kept the parameters of the tilted-ring model determined by de Blok et al. (2008).

To calculate the deprojected cylindrical coordinate on the dispersion maps we use the tilted-ring model described above and values are reported in Table 1. Knowing the radial variation of the position angle and inclination allows to take the warp into account. In our study we considered only one data-point per beam to minimize the correlation between adjacent rings.

We aim at measuring anisotropy directly at the local annulus scale. For this purpose each galaxy is decomposed into rings, and the azimuthal variation of the dispersion velocity is fitted by the combination of Eqs. 1 and A.12, and with cross-terms equal to zero:

$$\sigma^2_{\rm obs} = \sigma^2_\theta \cos^2\theta \sin^2 i + \sigma^2_R \sin^2\theta \sin^2 i + \sigma^2_z \cos^2 i + \sigma^2_{th} + \sigma^2_{LSF} \quad (3)$$

Components σ_{th} and σ_{LSF} are considered as fixed parameters in the fit. The interstellar neutral gas could be cold or warm. In the case of a cold component the temperature is around 100 K which leads to $\sigma_{th} < 1$ km/s while in the case of a warm component the temperature of the gas is around 5500 K leading to dispersion of 6-7 km/s (Field et al. 1969; Wolfire et al. 1995). In our study we consider a cold gas for which σ_{th} is negligible compared to the observed dispersion, thus we fix $\sigma_{th} = 0$ km/s. We already discussed in the previous chapter the degeneracy of the parameters $\sigma_R, \sigma_\theta, \sigma_z$. We probed different ways to reduce the number of free parameters :

- fixing $\sigma_z = 0.5\ (\sigma^2_R + \sigma^2_\theta)$.
- fixing σ_z to a fixed value spanning between 6 and 10 km/s.
- fixing $\sigma_z = \left\langle \left(\sigma^2_{\rm los} - \sigma^2_{th} - \sigma^2_{LSF}\right)^{1/2} \right\rangle$ on a ring.

The choice of reducing the degeneracy could artificially bias the result toward anisotropy, hence we focus here on the last configuration, which corresponds to the most isotropic configuration. With this model the only two free parameters of the fit are σ_R and σ_θ. For the fitting process we use the routine mpfit, a code which performs a Levenberg-Marquardt least-squares minimization. Results can be sensitive to the initial conditions. To obtain a robust results, we perform 1000 fits for each ring, starting with random values between 0 and 50 km/s for σ_R and σ_θ. The final values are chosen as the mean of the distributions of σ_R and σ_θ.

In Fig. 1, we show two examples of fit. The azimuthal variation of the ring located at a radius R = 564" for the galaxy NGC 2403 is displayed on the top panel. We observe that the period of the cosine in the fit is $\pi/2$. By identification to Eq. A.12, we conclude that we are in the case $\sigma_R > \sigma_\theta$, equivalent to $\beta_\theta > 0$. Let's remind that this equation shows that the period of the $\cos(2\theta)$ is ruled by the sign $\sigma^2_\theta - \sigma^2_R$. The bottom panel shows the fit of the ring at a radius R = 150" for the galaxy NGC 3521. By opposition to the upper panel, the period is π, indicating that $\sigma_\theta > \sigma_R$.

For each galaxy, we plot :

- the radial variation of the dispersion ellipsoid, σ_R, σ_θ, σ_z, the mean value of $\sigma_{\rm los}$ in a ring, and the mean value $\sigma_{los,mod}$ of the modeled line-of-sight dispersion.
- the radial variation of the anisotropy parameter defined in relation (2).

An example is given for NGC2403 in Fig. 2, with the dispersion ellipsoid on the left panel, σ_R, σ_θ and the mean value of $\sigma_{\rm los}$ in the ring. σ_z is fixed equal to $< \sigma_{\rm los} >$ so we do not plot it. Errorbars correspond to the 1σ of the distributions from the 1000 results. On the right panel we have the corresponding anisotropy

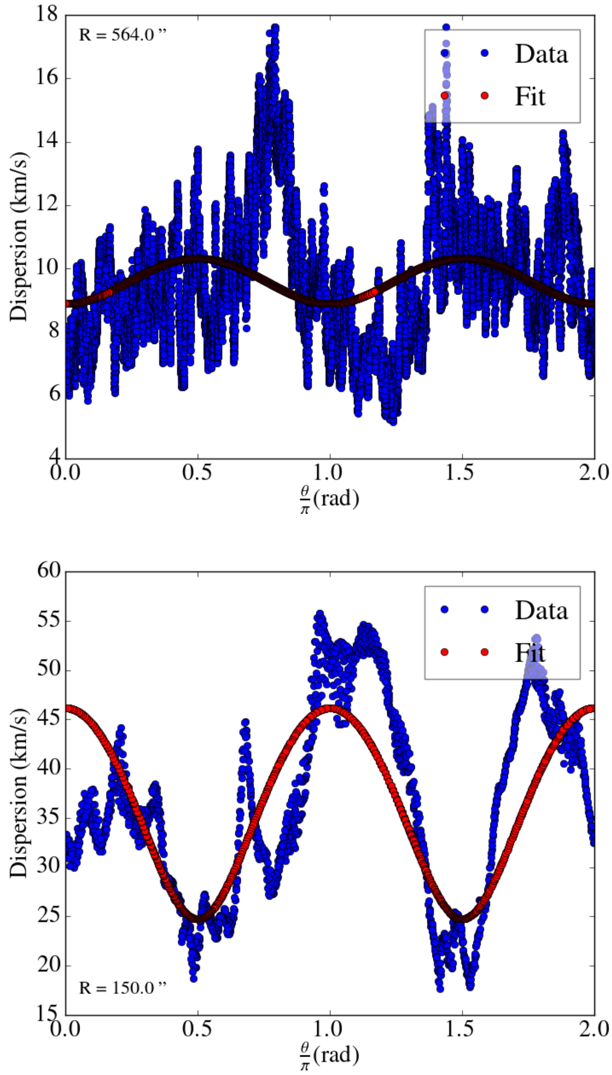

Fig. 1. Example of fit of the azimuthal variations in the case $\sigma_R > \sigma_\theta$ (left, NGC 2403 at R = 564") and in the case $\sigma_\theta > \sigma_R$ (right, NGC 3521 at R = 150").

parameter, which is another way to visualize the first plot. In the inner 200 pc, in average β_θ is close to 0, and the isotropic configuration is consistent within the uncertainties if we look at the dispersion ellipsoid. At larger radii the radial component tends to dominate the azimuthal one, increasing the value of β_θ.

Results for the whole sample are presented in Appendix **??**. We note that the results obtained by the fit (for σ_R and σ_θ) are not reliable for most radii. It's a general result across a majority of the ring studied : the azimuthal variations at a given rings are often more complex than a simple function in $\cos 2\theta$. The strong order 2 aligned with the minor axis obtained in Chemin et al. (2020) is not found in other galaxies. Nevertheless for some galaxies the $\cos 2\theta$ seems to fit approximately the azimuthal variation, but the stron hypothesis of our model, i.e. null cross-terms, does not allow any change in the angle phase.

3.2. FFT

In order to quantify asymmetries in the distribution of HI random motion we use Fast Fourier Transform (FFT) expansion which has been widely use to probe spiral arms or bars in flux distribu-

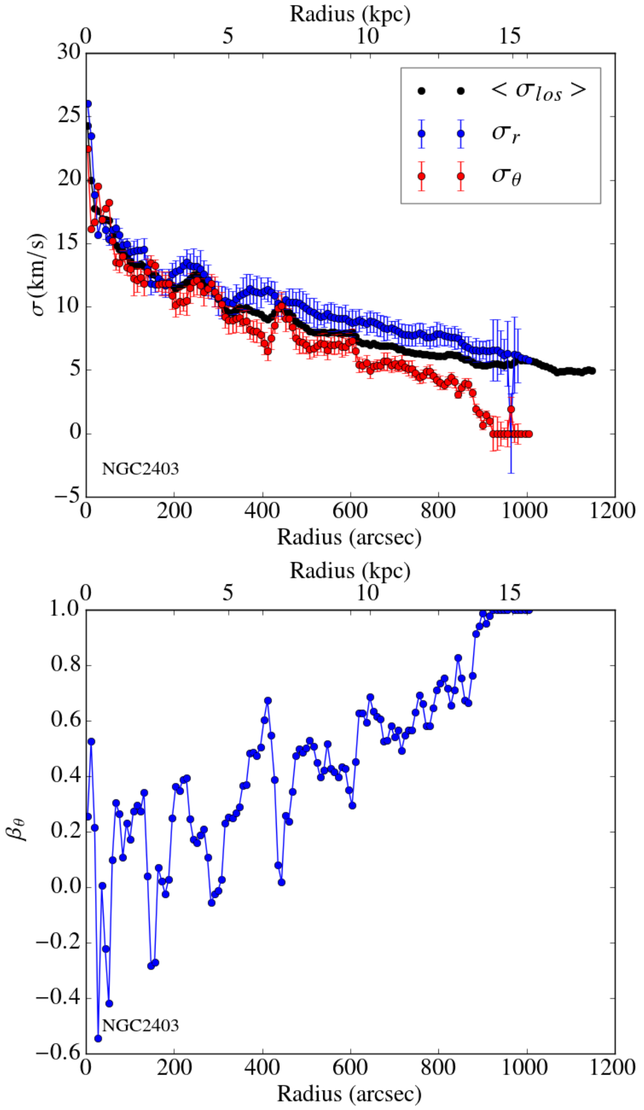

Fig. 2. Radial variation of the dispersion ellipsoid and anisotropy parameter β_θ of the galaxy NGC2403.

tions or to quantify non-circular motions in radial velocity distributions, we refer to those work in Appendix (D). The methodology we use here is identical to the one presented in Chemin et al. (2020). We will show that a Fourier expansion up to the 4^{th} order of the HI velocity dispersion maps is sufficient to describe the observations, indeed reconstruction processes bases of FFT coefficient up to the fourth order match fairly well the data, showing negligible residuals. On a large number of galaxies, the orientation of the structures like spiral arms or arms should be totally random and this random distribution must be found in the FFT coefficients. On the other hand, finding similar FFT coefficient in a sample of galaxies could be the signature presence of anisotropic velocity dispersion maps or/and instrumental fingerprint.

Our goal is thus to measure and study the asymmetries in the high-resolution and high-sensitivity HI velocity dispersion maps. Asymmetries are measured using discrete FFT. For a cylindrical model, harmonics are given by $\sigma_{\rm asym} = \Sigma_k \sigma_k \cos k(\theta - \phi_k)$ (and squared values $\sigma_{\rm asym} = \Sigma_k \sigma_k^2 \cos k(\theta - \phi_k)$), where σ_k and ϕ_k are the amplitude and phase angle of the dispersion asymmetry of order k. A more detailed description is given in Appendix (D). Asymmetry properties are analysed in comparing the dominant perturbations with the axisymmetric mode. The orientation of the phase angles are investigated to detect possible alignments with major or minor axes of galaxies. Finding systematic alignments would argue in favour of gas being (partly) a collisionless medium, thus with an anisotropic velocity tensor.

4. Asymmetries in the THINGS sample

The goal of the two following sections is to study the asymmetry of the velocity dispersion map for THINGS galaxies (this section) and for the WHISP galaxies (in the next section) in order to possible detect systematic alignments in the phase angles.

To perform this study, we use FFT expansion of the velocity dispersion maps, corrected from the beam smearing effects, up to the 4^{th} order.

Since we focus to the dispersion asymmetries due to gravitational effect, we do not use directly the observed dispersion. To account for instrumental effects, we subtract quadratically the instrumental dispersion σ_{LSF} of the Line Spread function (LSF). Moreover, the observed dispersion contains the information of the thermal component of the gas. The intrinsic temperature of the gas leads to isotropic random velocities σ_{th}. We want to get rid of this effect to focus on gravitational random motions. The final dispersion maps are thus obtained using relation (1).

And as we mentioned in Appendix D, we use the dispersion squared. Chemin et al. (2020) showed that using dispersion or dispersion squared give the same result, and we also find the same behaviour in σ and σ^2 (cf Sect **??**).

4.1. Method 1 : Rings study

Using the methodology defined in Sect. D, we compute FFT for each ring in the galaxy, obtaining the radial variations of amplitudes and phases of modes 1 to 4. An example is given for the galaxy NGC3198 in Fig. 3. At the end of this process, we evaluate the level of asymmetries in each individual galaxy, the dominant modes and the evolution of the angle phase angle.

To study possible systematics in the orientation of the phase angles, we have combined the information from the different galaxies of the sample. To achieve this goal, we combine all the individual rings, independently of their galaxy. Among the 15 galaxies forming our sample, we cumulate 883 individual rings. Studying the distribution of the Fourier parameters (see Fig. 4) in these rings allows to point out possible systematic.

Fig. 3 presents the results of the FFT on the galaxy NGC3198. The top panel presents the amplitudes and the bottom panel the angle phases. The same plots are provided for every galaxies in Appendix X. A first result observed in Fig. 3 and in every other galaxy, is that the dispersion decreases with the radius as we can see with the mode k = 0, which corresponds to the mean value of the dispersion in a ring. For this particular galaxy, NGC3198, in the central part (up to 120 arcsec), amplitudes are dominated by orders k = 1 and k = 2. σ_4 stays at a constant level around 7 km/s at all radii and starts dominating other orders around 250 arcsec. Phases are periodic with a periodicity $2\pi/k$ (Fig. 3, bottom). For ϕ_2, around 200 arcsec, we observe a phase jump. In practice it's just the phase rolling up continuously so that's not a problem. Sometimes this can happen from ring-to-ring, and to keep the plot visible, we decided to limit the plot in a period as much as we could.

On Fig. 4, we present the distribution of the Fourier amplitudes (Fig. 4, left) and angle phases (Fig. 4, right) for the 883

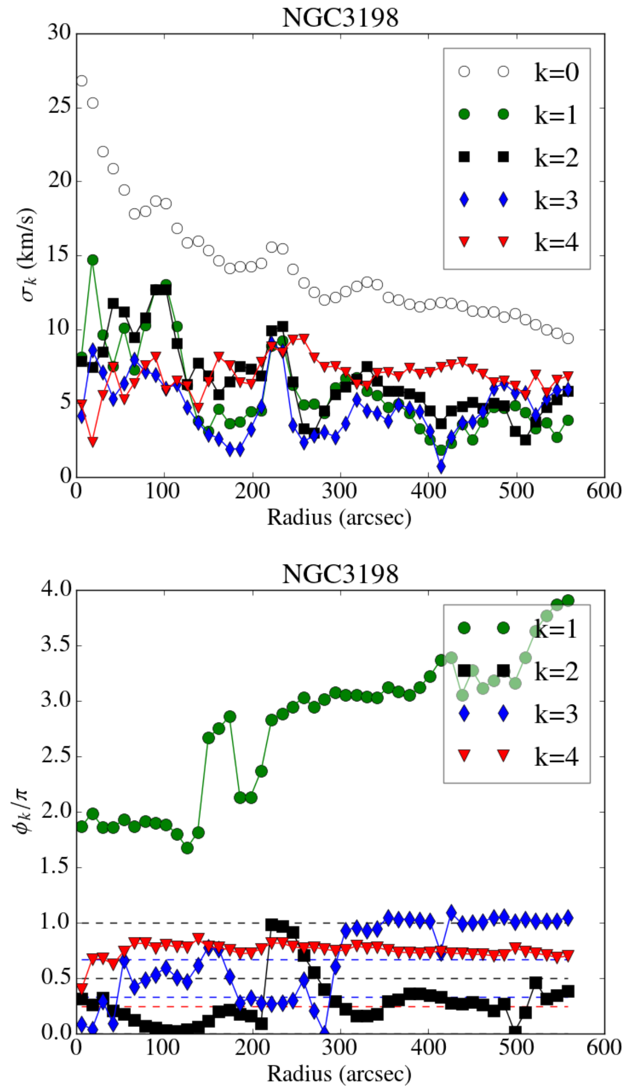

Fig. 3. Radial profiles of the FFT parameters for the galaxy NGC 3198. The top panel shows amplitudes σ_k whereas the lower panel shows phases ϕ_k/π as a function of radius for modes 0 to 4 (0-mode has no phase). Each point represent a circular ring in the galaxy plane. The horizontal dash-lines in the bottom plot represent the XXX

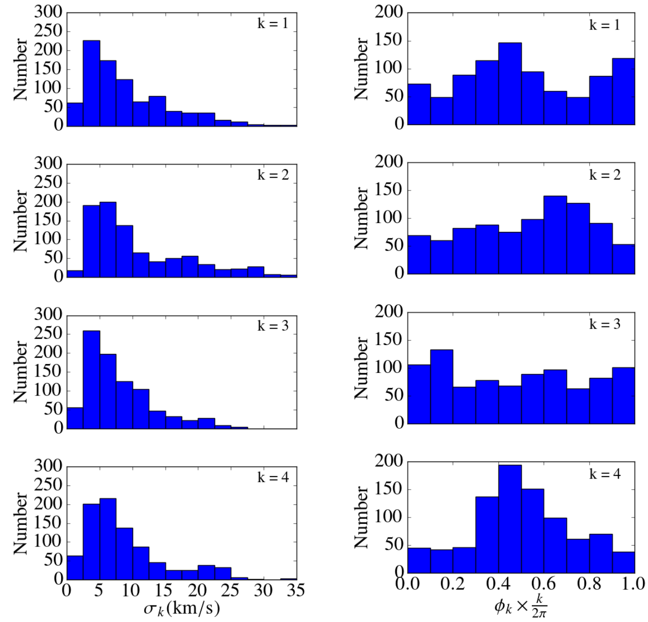

Fig. 4. Amplitude (left column) and phase (right column) distribution of the Fourier modes k=1 to 4 for the 883 rings of the study. Phases are normalized such that 0.5 is the half period of the mode, and 1 is the full period. The period of the mode k is $\frac{2\pi}{k}$.

rings of the study. To study these distributions in a more synthetic way, we reported mean, median and standard deviation values in Table 2. For all orders 1 to 4, the maximum of the distribution is located at amplitudes between 2.5 and 7.5 km/s and only few rings are described by amplitudes below 2.5 km/s. We observe similarities in the distributions of modes 1 and 3, with a faster decrease at high amplitudes for the 3^{rd} order. In the same way modes k = 2 and k = 4 are similar, with the maximum of the distribution between 5 and 7.5 km/s. The tail of σ_2 is also larger than the one of σ_4. From Table 2, we observe that the dominant amplitude is σ_2 with a median value of almost 8 km/s. Interestingly, median values for modes k = 1 and k = 4 are really close. Mode k = 3 has the lowest median and standard deviation indicating that in average amplitudes σ_3 are lower than amplitudes for other orders. Concerning the phases, each modes exhibits a different distribution. For the mode k = 1, we observe a peak on the half period (0.5) and another peak on the entire period (1.0). The period of ϕ_1 is 2π, therefore the half period and the entire period corresponds respectively to π and 2π. Here both peaks are then located on the major axis of the galaxy. The majority of angle phases of the mode k = 1 in our 883 rings are distributed over the major axis. For ϕ_2, the distribution is flat, with a small bump at angle phases between 0.6 and 0.8. This bump does not coincides with any principal axis. Given the results from Chemin et al. (2020), we expected to observe a similar bump, maybe more significant at 0.5, which corresponds to the half period of mode k = 2, i.e. 0.5 π, the minor axis of the galaxy. The angle phase of the mode k = 3 is also flat, with a peak between 0.1 and 0.2. Finally, the mode k = 4 has a distribution centered on 0.5 which corresponds to the half period of ϕ_4 (0.25π). This distribution could be an hint for a possible systematic alignment of the angle phase of order 4, and we will study this result in more detail in the following parts.

Order Amplitude km/s	Mean km/s	Median km/s	Standard deviation km/s
σ_1	9.33	7.09	7.05
σ_2	10.9	7.96	7.67
σ_3	7.92	6.59	5.13
σ_4	8.82	7.02	6.06

Table 2. Properties of the distributions of Fourier amplitudes in the 883 rings of the sample.

These first results are interesting but are nevertheless biased. Indeed, galaxies have different numbers of rings depending on their size and distance (see Fig. 5). It varies from 7 rings for NGC3627 to more than 140 for NGC2403. We observe the same broad dynamics in terms of pixel number (see Fig. 5, bottom panel). Distributions are thus biased towards galaxies with higher number of sample elements like NGC2403 and NGC5055, and small galaxies like NGC3627 have only little importance in the result. Avoiding this bias is the main point of methods 2 and 3 in which we probe two different ways to mix the signal from all galaxies.

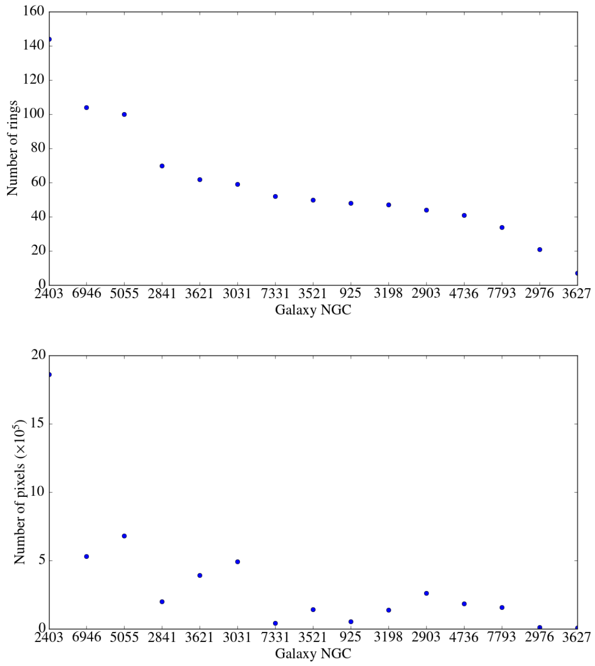

Fig. 5. Number of rings (top) and number of pixels (bottom) as a function of the NGC name for each galaxy of our sample. NGC galaxy names are sorted with decreasing number of rings. XXX FAUDRAIT REFAIRE CE PLOT AVEC LES MEMES POLICES QUE LES AUTRES ET DECALER LES X VERS LA DROITE ET LA GAUCHE POUR NE PAS QUE LES 2 POINTS SOIENT SUR LES AXES.

4.2. Method 2 : stacked galaxy

In the previous section, we studied, for each galaxy, the variations of the amplitudes and phases of the velocity dispersion for the first four Fourier orders, as a function of the galacto-centric radius. The galaxies of the sample have nevertheless different surface brightnesses, different physical and projected sizes, making the comparison challenging. In the present section we aim to study trends coming for the whole sample in building a "stacked galaxy" and this requests a new method to analyse the data.

A bias of the study based on each galaxy using individual rings comes from the fact that each galaxy has a different number of rings and also that the number of pixels in each ring varies from galaxy to galaxy and from ring to ring. In this section, we introduce a normalisation to provide an equal weight for each galaxy.

The first step consists in reducing the velocity dispersion distribution of each galaxy, previously modelled by a suite of rings, to a single radius, in averaging all the radial contributions. The number of rings that varied from 7 to 144 in the previous method is now equal to unity for each galaxy making the comparison easier.

To minimize the bias due to the fact that the number of pixels varies from galaxy to galaxy and from sector to sector, we compute the average velocity dispersion within each angular sector, this provide a single value per sector as displayed in the left panel of Fig. 6.

On Fig. 6 we clearly see discrepancies in the level of asymmetries in the sample. As an illustration of these asymmetries, we show on Fig. 7 the observed squared dispersion map from THINGS of NGC2841 and its FFT modeling. NGC2841 corresponds to the light blue curve of Fig. 6 and its single-ring dispersion exhibits 2 peaks around 0.6π and 1.6π. By comparing this curve with the observed dispersion and the azimuthal map of the galaxy, we observe that these peaks are associated with two regions of high dispersion, respectively in the top right and bottom left part of the galaxy. As we can see on the 4 bottom panels of Fig. 7, which corresponds to the individual orders of the FFT from 1 to 4, asymmetries of NGC2841 are described by strong orders 2 and 4. Indeed, the observed dispersion map exhibits a symmetry along the major axis of the galaxy, explaining the presence of the order 4, with a X-shape in the dispersion. The third order is negligible in all the galaxy, and the first order has an impact lower than orders 2 and 4. The modelisation of the asymmetries with the orders 0 to 4 of the FFT is shown on the top right panel, next to the observed map. The residual map represents the observed map minus our modelisation. Its mean value is 26 $(\mathrm{km/s})^2$, and no obvious signal is observed, showing the consistency of our modeling.

The second step is made up in building the so-called "stacked"-galaxy. The previous plot shows that the amplitude of the velocity dispersion strongly differs from galaxy to galaxy, this trend is amplified since we work on the squared velocity dispersion (instead of the velocity dispersion). Thus we have to stack with caution the velocity dispersion of each galaxy to build the stacked-galaxy. Three galaxies shows tremendous velocity dispersion squared: NGC2841 (light blue curve), NGC3627 (red curve) and NGC3521(dark blue curve). Those galaxies should be discarded for the statistical analysis of the so-called "stacked"-galaxy. To reject further high amplitudes that could be due to some bins, instead of computing the mean velocity dispersion squared for each angular sector the velocity dispersion, we compute the median, as displayed on the bottom line of Fig. (6).

The third step comprises the FFT computation of the stacked-galaxy in order to study the amplitude and the phase of the different Fourier orders that will be analyse in the next section.

In the present section we analyse the results of the FFT decomposition of the stacked-galaxy. Orders one to four are further considered. The zero order corresponds to the mean of the line-of-sight velocity dispersion $< \sigma_{\mathrm{los}} >$, it does not contain information on the azimuthal variation and has been subtracted from the velocity dispersion.Fig. 8 shows the azimuthal dependence of the velocity dispersion, from which the mean velocity dispersion $< \sigma^2_{\mathrm{los}} >$ has been removed, and orders one to four. The median velocity dispersion has been computed in each azimuthal that has been sampled every 5°. The model (dashed line) fits the data (continuous line) with mean residual dispersion of $0.0004 \pm 9.6(\mathrm{km/s})^2$.

For each pixel, the standard velocity dispersion σ has been used on the top panel while on the bottom panel, the square of the velocity dispersion σ^2 has been considered. This second choice is motivated by the FFT equation (A.10) that involves square of velocity dispersions rather velocity dispersion.

Apart from the amplitudes, trends for both signals are identical, for the direct signal as well as for the individual order of the FFT, with peaks located at the same positions.

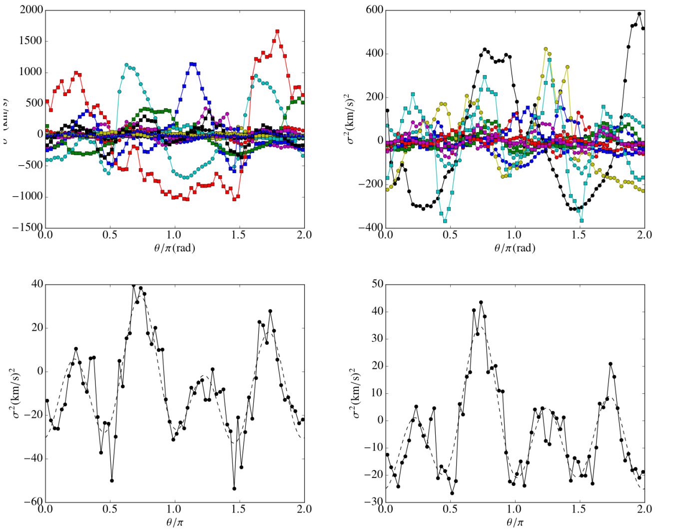

Fig. 6. Velocity dispersion squared σ^2 vs the angular sector θ for each galaxy. A bin step 5 degrees has been selected for each sector θ. (Upper left panel) For the whole sample of 15 galaxies. (Upper right panel) Same as the left panel but without galaxies NGC2841 (light blue curve), NGC3627 (red curve) and NGC3521(dark blue curve). (Bottom left panel) Stacked-galaxy computed using the mean velocity dispersion squared for each angular sector. (Bottom right) Stacked-galaxy using the median value instead of the mean. REFAIRE LES PLOTS POUR NE PAS COUPER LES LABELS EN Y ET AVOIR LES MEMES TAILLES DE POLICE QU'AILLEURS.

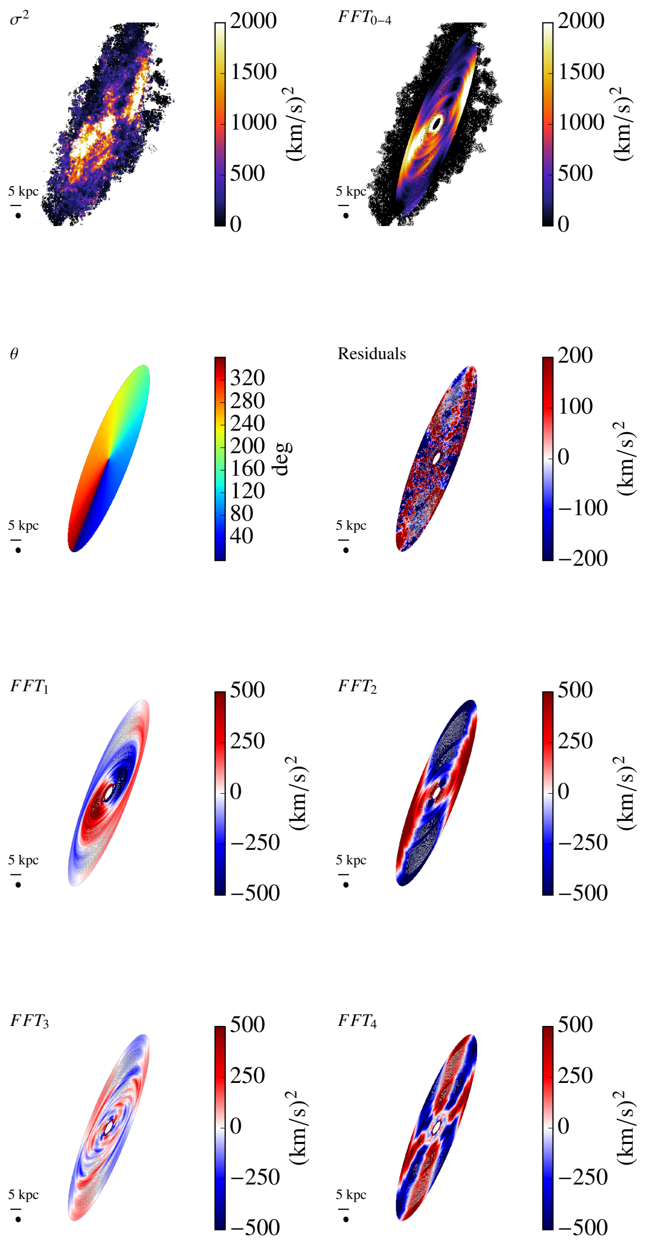

Fig. 7. THINGS dispersion map of NGC2841 (top left panel), projected result of the term of order 2 from the FFT (top right panel), azimuthal map (bottom left) and projected result of the FFT containing orders 0 to 4 (bottom right panel).

Relative amplitudes between orders are well respected and we do not observe any change in the phase of individual orders, even for ϕ_3 which is likely to change due to the low amplitude of σ_3. [2] In conclusion, working directly with the σ or σ^2 is equivalent; we make the choice to work with the σ^2 because it's easier to interpret results of the FFT with the equation (A.10).

Bottom panel of Fig. (8) exhibits strong oscillations in the velocity dispersion as a function of the phase θ, which are characterised by large FFT amplitudes for the order 2 and order 4, respectively $\sim$12 and $\sim$21(km/s)^2 . The first and the third order reach respectively the half and the fourth of the amplitude of order 2 ($\sim$ 6(km/s)^2 and $\sim$ 3(km/s)^2). The phase of the fourth order ϕ_4 is centred on 0.25 π, which is the half period of order 4, as we already observed on the previous histograms.

The phase of the second order ϕ_2 is equal to $\sim$0.75 π, we indeed note that the first peak of the order 2 coincides with the second peak of order 4.

Surprisingly, the amplitude of order 4 is almost 50% larger than order 2 which is in turn larger than in the other orders. In addition the phase is $\phi_4 \sim \pi/4$. Is this phase due to a bias linked to an (un)lucky alignment of patterns in different galaxies, to noise, to instrumental finger print or is it a physical signature ? In the forthcoming paragraphs, we will test the robustness of the phase observed in the fourth order.

The first test to address these questions was to slit our sample into two randomly selected subsamples of same size. We have done 16 times a random selection, it was not necessary to make larger sample draw since we have a sample of 15 galaxies.

The results for six randomly selected sample draw are presented in Fig. 9.

The visual comparison of the curves σ^2 versus θ for both subsamples for all the experiments show that the phase is basically conserved. To quantify this agreement, Table 3 gives the mean, median and standard deviation values of FFT parameters computed for 30 randomly selected subsamples. Depending on the galaxies in the subsample, amplitudes vary considerably, inducing high values for standard deviation. As observed in Fig. 8, σ_2

[2] The amplitude factor between the upper and the lower plots is roughly $\sim$20. It's not a direct transcription of the difference square factor due to all the processes needed to obtain this final signal (reducing the galaxy to one radius, taking the median values for all the bins).

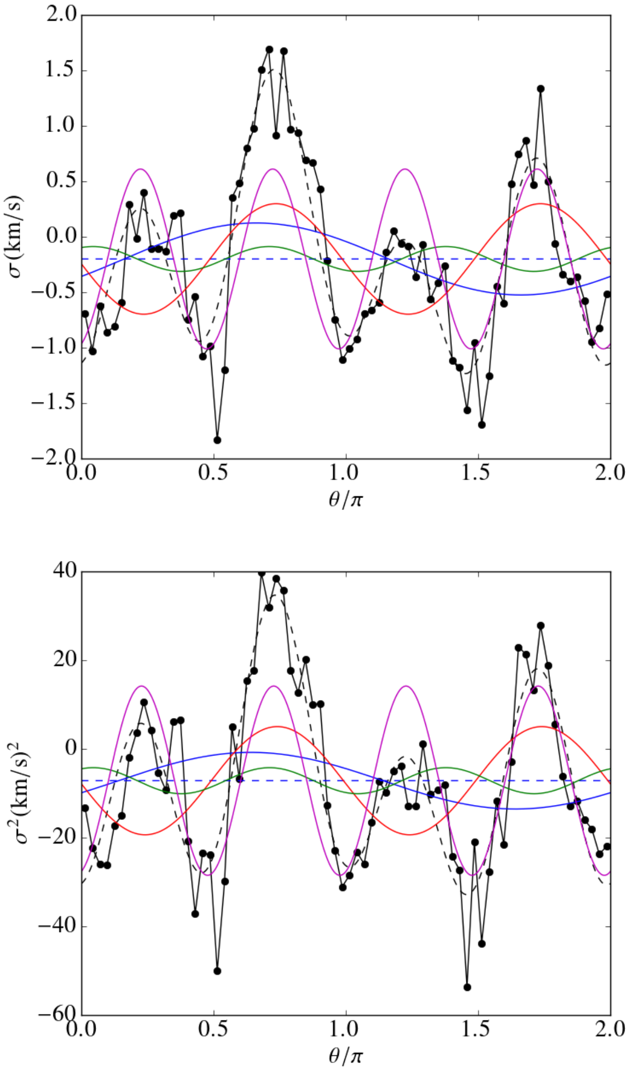

Fig. 8. σ vs θ (top panel) and σ^2 vs θ (bottom panel). Continuous black line with the black dots are the data points. Dashed black line is the FFT model of the data. Colored continuous lines represents individual orders 1 to 4.

and σ_4 tends to be have the largest amplitudes. A striking result appearing concerning the phases is the remarkably low spread of the value ϕ_4. The larger dispersions observed for amplitudes (σ_2, σ_4) correspond to the lower dispersion for phases (ϕ_2, ϕ_4).

Config Param	Mean	Median	Standard deviation
$\sigma_0^2 - < \sigma_0^2 >$	-12.2	-7.2	10.9
$\sigma_1^2 (km/s)^2$	15.1	9.8	14.1
$\sigma_2^2 (km/s)^2$	19.5	14.7	16.2
$\sigma_3^2 (km/s)^2$	11.0	6.31	12.3
$\sigma_4^2 (km/s)^2$	30.3	24.8	20.8
ϕ_1/π	0.69	0.69	0.38
ϕ_2/π	0.75	0.77	0.12
ϕ_3/π	0.30	0.30	0.18
ϕ_4/π	0.23	0.23	0.02

Table 3. FFT parameters for the 30 subsamples

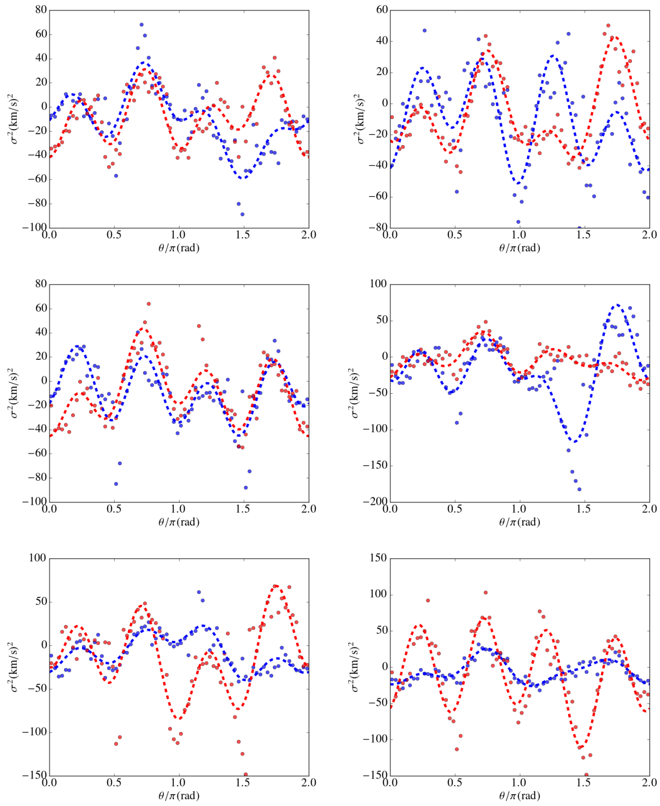

Fig. 9. The sample is randomly divided into 2 subsamples, represented by red and blue colours, in order to study whether the trend observed in the global sample is due to a bias due to peculiar galaxies. XXX C'EST QUOI LA DIFFERENCE ENTRE LES POINTS QUI SUIVENT LES COURBES ET LES AUTRES ?

Even with half the number of galaxies in each subsample, we still observe peaks at the same positions than the one observed in Fig. 8, meaning that is probably not due to a chance alignment.

The second test consists in testing the probability to obtain an order 4 with such a high amplitude σ_4 for the total signal of the sample, as well as the velocity amplitudes σ_k and phases ϕ_k for the other order k ? To test this probability, we introduce a random phase shift, constant along the radius, for each galaxy. In the galactic plane, the origin of the azimuth is not anymore aligned along the major axis, but distributed at any random azimuth, this arbitrary changes the location of the perturbations. We then follow the same methodology than the one used to obtain Fig. 8 and compute the new velocity dispersion distribution of the new stacked galaxy. Since it is computationally expensive, we do 500 iterations of the mock sample and compute the FFT for every signal. The σ_k^2 and ϕ_k distribution are presented in Fig. 10; a red dash line indicate the values found with the 'real' stacked galaxy without phase shift.

The σ_1 and σ_3 random distribution peak at the value of the velocity dispersion computed on the stacked galaxy. For σ_2 the peak is slightly shifted towards smaller velocities dispersion but the observed value for σ_2 is still compatible with a random distribution. At the opposite, the square velocity dispersion σ_4 value observed for the stacked galaxy lies at the very bottom end of the distribution; values $\sigma_4^2 > 20(\mathrm{km/s})^2$ represents only 6 cases among the 500 mocks and σ_4 is larger than the observed value for one case only. This means that a random orientation for the phase is very unlikely to reproduce the large velocity dispersion observed for σ_4.

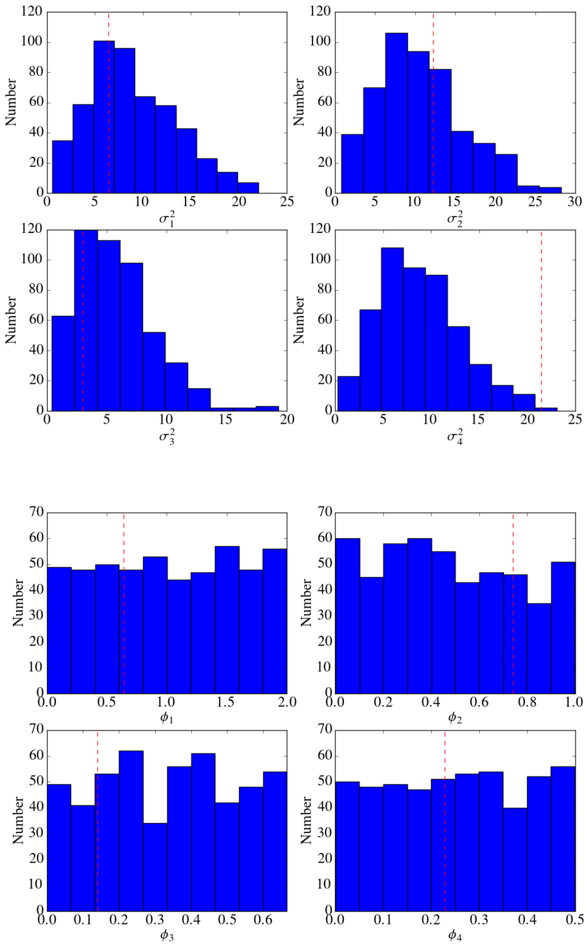

Fig. 10. Distribution of the FFT four orders for 500 iterations for the THINGS mock sample. Amplitudes are shown in the two first lines and phases in the two last ones. The red vertical lines correspond to the reference value of the THINGS sample. METTRE LA LIGNE ROUGE EN PLUS ÉPAIS.

Before analysing the data, we probed the effect of the angular bin size in testing bins ranging from 2 to 20 degrees; we display the results of four different bins size (2, 5, 10 and 20 degrees) on Fig. 11. The FFT amplitudes moderately vary. σ_1 varies from 6.3 to 10.2 (km/s)^2, σ_2 stays roughly constant, between 11 and 12.4 (km/s)^2, σ_3 is negligible in all cases with amplitudes between 0.8 and 3.1 (km/s)^2 and finally σ_4 stays also constant with the bin size, with values between 19.9 and 21.4 (km/s)^2. Except for ϕ_3 which varies from 0.01 to 0.46 π, other orders have similar phases with dispersions lower than 0.02 π.

In this last section we discuss the method used in this section that consists in reducing the radial information to a single value. For this purpose, as a test bench, we use once again the galaxy NGC5055 for which we will compare the FFT computed without and with azimuthal binning.

Firstly, we study the distribution of the FFT parameters for 100 radii. For each radius, we compute the squared dispersion, subtract the instrumental dispersion and the mean squared velocity dispersion. This last operation only affects the 0^{th} order and allow to center the asymmetries around zero.

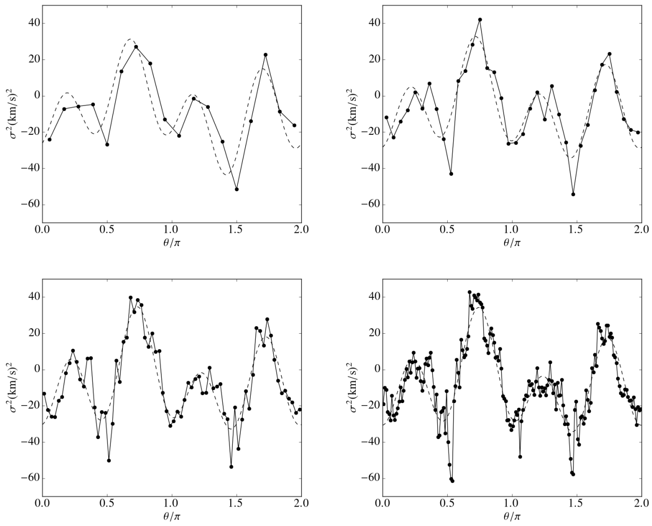

Fig. 11. Squared velocity dispersion σ^2 vs the azimuthal angle θ for the mock-galaxy for different azimuthal bins sizes: 20 deg (top left), 10 deg (top right), 5 deg (bottom left) and 2 deg (bottom right).

Each of the 100 radius depends on nine parameters: σ_0 (consistent with 0 due to the subtraction mentioned before), σ_k and ϕ_k, with k=1, 2, 3 and 4. We report the mean and median values of the radial distributions of σ_k in Column 1 and 2 of Table 4. For phases, due to the periodicity, we cannot compute the median value. This study annulus by annulus provides a description at local scale (down to the annulus scale), and allows to identify regions for which amplitudes of order σ_k are larger than a given threshold.

Secondly, we use the method previously described to reduce the galaxy to a single radius. We compute the signal for each annulus and subtract by the mean velocity dispersion for each radius and not for each annulus. We end up with a vector having the length equal to the total number of pixels (namely 680980 pixels) that contains the velocity dispersion and the azimuth of each pixel. We compute the FFT of this vector and we compare it to the FFT of the same signal but binned using azimuthal sector of 5°, for which we compute the mean dispersion values of all pixels within each bin range. By sampling every 5°, we obtain 72 data points to span the entire galaxy (360°). Result for these two configurations are shown in column 3 and 4 of Table 4.

As we described many times, for each ring we subtract by the mean dispersion square value, explaining the values the first row consistent with 0 (km/s)^2. Averaging within angular sector changes slightly the value of the 0^{th} of the FFT. This is the reason why the "stacked" galaxy has a 0^{th} order different from 0. Depending on the method used, amplitudes of the FFT varies a lot. On the first column, corresponding to the mean value of the radial distribution of rings, all amplitudes are similar, with a factor 1.5 between the maximum amplitude σ_2 and the minimum one σ_3. Taking the median of the same distribution allows to have a better sight at the most dominant orders. We observe a decrease from column 1 to column 2 by a factor close to 2 for orders 1 and 3 while orders 2 and 4 decreased by 25%, indicating that in most rings amplitudes 2 and 4 tends to be higher. A similar phenomenon happens when performing the FFT on the single ring dispersion (column 3). All amplitudes decrease, due to the radial averaging, compared to column 2, but at a different rate. We also note that averaging the single ring dispersion

Config Param	Mean Value	Median Value	Total Signal	Total signal binned
$\sigma_0^2 - < \sigma_0^2 >$	$1e^{-7}$	$5e^{-8}$	$9e^{-9}$	0.95
$\sigma_1^2 (\mathrm{km/s})^2$	53.9	27.0	12.9	12.4
$\sigma_2^2 (\mathrm{km/s})^2$	72.9	53.1	39.6	43.3
$\sigma_3^2 (\mathrm{km/s})^2$	46.2	20.3	2.91	2.76
$\sigma_4^2 (\mathrm{km/s})^2$	55.0	41.8	22.6	24.1
ϕ_1/π	1.20	1.51	1.80	1.82
ϕ_2/π	0.63	0.73	0.77	0.73
ϕ_3/π	0.34	0.33	0.33	0.14
ϕ_4/π	0.25	0.24	0.31	0.28

Table 4. FFT parameters of NGC5055 obtained using 4 different methods : the first column corresponds to the mean value of the FFT distributions among the 100 rings, the second one the median value of these distributions. Column 3 and 4 corresponds to the FFT parameters of the single radius velocity dispersion, before and after this dispersion within angular sector.

within azimuthal sector does not change significantly the values of the FFT.

This single ring dispersion reinforce some signals in the galaxy (i.e. order 2 which dominates largely the single ring dispersion) and suppress others, such as σ_3 which becomes negligible. Compared to the mean value of the ring distribution, the median value of the distribution, and the FFT on the single ring dispersion are more appropriate to discriminate between orders. This last method seems to be the most efficient one, especially in order to combine the data to form the stacked galaxy. Nevertheless, there is a possibility that this single ring dispersion could enhance unreal signals such as remnant beam smearing. Indeed, the beam smearing creates a typical X-shape pattern, which increases the dispersion at given azimuths, at all radii. A deeper study of the link between the stacked galaxy and beam smearing will be discussed later. Therefore the last test we perform is the study of the median values of the ring distribution for each galaxy, because we expect a possible beam smearing remnant to be less important down to the annulus scale than on the galaxy reduced to a single ring.

4.3. Method 3 : Median values of radial distributions

In this section we study the FFT distributions of individual galaxies. Asymmetries are computed for each ring, to have the radial distribution of the FFT parameters. In the same spirit as before, to normalize the number of rings in each galaxy of the sample, only the median values of these FFT distribution are considered. Therefore, each galaxy is described by the 9 parameters of the FFT, σ_k and ϕ_k which are the median values of their own radial distributions. In Fig. 12 we present the median value of ϕ_k vs σ_k for each galaxy of the sample. Each point corresponds to a galaxy. Since all FFT are computed on projected galaxies, the minor and major axis corresponds to the same azimuthal values for all the sample. The blacked dashed lines represent the minor axis ($0.5\pi \mod \pi$) and the blue one the major axis ($0 \mod \pi$). Let's remind that the initial goal of this study was to search for systematic alignment of the phase ϕ_2 with the minor axis, similarly to the result from Chemin et al. (2020). Fig. 12 clearly shows that such result is not present in our sample of THINGS galaxies. The phase ϕ_2 has a large spread, with values from 0.1π to 0.9π. Only 6 galaxies have phases between 0.4 and 0.6π. Concerning the phase of order 1, ϕ_1, we observe, similarly to Fig. 4, that 10 out of 15 points are located at phases between 0.7π and π. For ϕ_3 the distribution is uniform, with a large spread, similar to ϕ_2. Finally, similarly to what was observed in Fig. 4, the phase ϕ_4 is aligned close to 0.25π for 12 galaxies on the 15 in the sample.

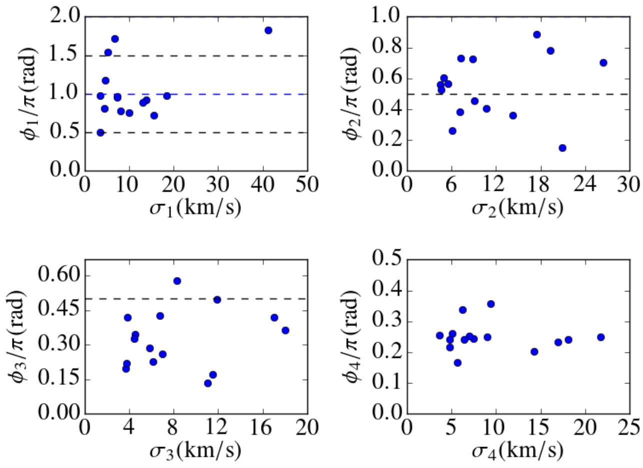

Fig. 12. Median phase ϕ_k vs velocity dispersion σ_k issued from FFT analysis of individual galaxies, for order k=1 to 4. Each point represents the median value of the radial distribution of the FFT parameters for a galaxy. Dashed horizontal line represents the minor (black) and major axis (blue) of galaxies.

5. Extension to the WHISP sample

TBD

6. Discussion

6.1. Uncertainty in the beam shape

In previous sections, we exhibit strong asymmetries in the THINGS velocity dispersion maps for the FFT order 4 with a phase aligned on 0.25π. Using mocks we conclude that this signal was not the result of (un)lucky alignments. However, beam smearing fingerprint might provide a residual signature in the signal, in this section we aim to test this issue.

In others previous sections, we already describe the beam smearing modelling, but here we will specifically discuss here the possible links between the high amplitude of order 4 and the beam smearing that displays a cross shape, and thus could, for this reason, contribute to residual signal in the order 4, even on the highest resolution THINGS dataset.

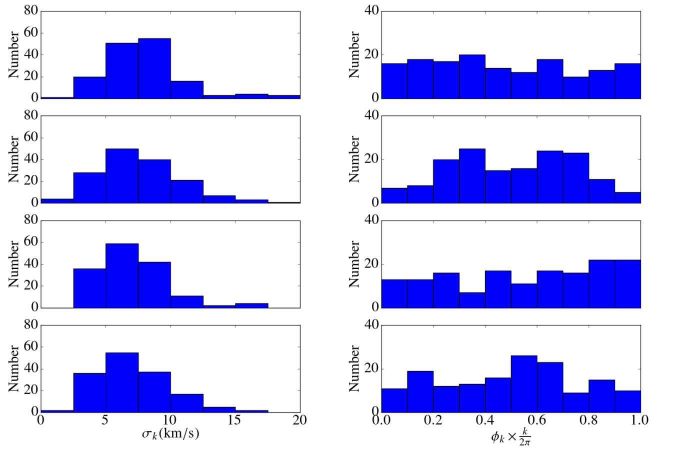

Fig. 13. Amplitude (left column) and phase (right column) distribution of the Fourier modes 1 to 4 for the 154 rings of this study. Phases are normalized such as 0.5 is the half period of the mode, and 1 is the full period. The period of the mode k is $\frac{2\pi}{k}$. CHOISIR UNE FOIS POUR TOUTE LA TAILLE DE LA POLICE DE LA FIGURE 12 POUR LES LABELS

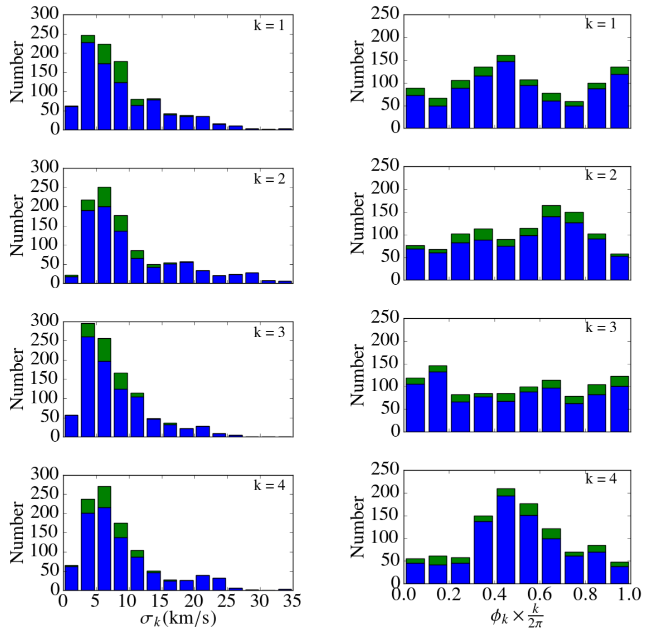

Fig. 14. Amplitude (left column) and phase (right column) distribution of the Fourier modes k=1 to 4 for the 883 rings from the THINGS sample (blue) plus the 154 rings WHISP sample (green). Phases are normalized such that 0.5 is the half period of the mode, and 1 is the full period. The period of the mode k is $\frac{2\pi}{k}$.

To achieve this goal, we compared the difference between the beam smearing signature of a model datacube and the 2D moments computed from the same datacube. A good agreement between those two signatures would be a proof of the absence of residual beam smearing in the analysis; the method is described hereafter.

On the one hand, we created a model datacube, based on the different moment maps: a flux map, a velocity field and a velocity dispersion. We arbitrary chosen a galaxy disk inclination of 60 degrees. The axisymmetric velocity field is computed for an exponential disk, the maximum rotation velocity of 200 km/s is reached at a radius of 200 arcsec. The flux map is created using a decreasing exponential disk. In order to induce low variation of the flux values over the galaxy, we chose a disk scale length of 1000 arcsec, way above the radius where the maximum velocity is reached. In the sake of simplicity, the velocity dispersion is constant on the whole galaxy and equal to 10 km/s.

From these maps we create a high-resolution data-cube using Gaussian lines profile. The amplitude, center and velocity dispersion of the lines are respectively given by the value of the flux max, velocity field and velocity dispersion for each pixel. The spatial scale of the modelisation is 1 arcsec/pixel.

To model the instrumental radio beam, that we call hereafter the Point Spread Function (PSF), we use a 2D Gaussian function using a typical elliptical size and shape, namely a minor axis of $BMIN$ = 10 arcsec, a major axis $BMAJ$ = 15 arcsec and a position angle orientation of the ellipse BPA = 30°. The next steps consists in convolving the high-resolution model datacube with this PSF in order to obtain a low-resolution datacube, mimicking the observations, from which the moment maps are extracted using the SpectralCube package. Since we did not introduce dispersion pattern in the high-resolution datacube but only a constant velocity dispersion for the whole galaxy, we expect that the spatial variations in the velocity dispersion map is only due to PSF beam smearing effect.
On the other hand, we compute the beam smearing map of the low-resolution datacube using the methodology defined in section E. Next, we subtract quadratically this beam smearing map to the velocity dispersion map previously computed from the low-resolution datacube. The result of this subtraction looks very much as expected, like the initial dispersion map, with a constant velocity equal to 10 ± 0.001 km/s.

Thus we conclude that the beam smearing processing is correct. However, this does not mean that the PSF is correctly modelled. Indeed, beam smearing residual might remain in the data if the radio beam exhibits for instance asymmetries or a tail due to high frequencies that cannot be represented by a 2D Gaussian. In that case we would underestimate the contribution of the PSF.

6.2. Beam smearing and σ_4

In order to go further in the understanding of beam smearing contribution on the FFT fourth order 4, in this section we tackle this issue differently. Due to beam smearing effects, velocity gradient could be unresolved. To overcome this difficulty we used high-resolution $H\alpha$ velocity field (R = 1.6 x 1.6 arcsec^2) rather than the HI lower-resolution one (R = 8.66 x 10.06 arcsec^2). For the first part of the study, we focus on the test case galaxy NGC5055; in the second part, we will study how evolves the parameter of the FFT for the stacked galaxy.

6.2.1. The case of galaxy NGC 5055

(a) Azimuthal dependences

The THINGS beam shape of NGC 5055 is 8.66×10.06 arcsec^2, its inclination is 59^o in HI and 63^o in $H\alpha$. For the beam smearing modelisation, we adopt the same methodology as presented in Sect. E for the SINGS data. The high resolution velocity field is created assuming a Courteau model of the $H\alpha$ rotation curve of NGC 5055. Using the THINGS flux map and PSF, we compute the corresponding beam map (Fig. 15).

We reduce the radial distribution of each azimuthal angle to a single value following method 2, and we compute the FFT as explained in method 1 (see Fig. 15, top-right panel) . Since the mod el is basic we work directly on the dispersion and not on the dispersion squared like we did previously. The top right panel of Fig. 15 shows that the beam smearing consists in a strong order 2, $\sigma_2 \sim 0.41$ km/s and phase $\phi_2 = 0.54\pi$ (low σ velocity dispersion along the major axis for $\theta \sim \pi$) and a high order 4 as well, $\sigma_4 \sim 0.33$ km/s and $\phi_4 = 0.21\pi$, which clearly appears with a X-shape of the beam smearing pattern (Fig. 15, top panel). Orders 1 and 3 are negligible, $\sigma_1 \approx \sigma_3 \sim 0.01$ km/s. In the case of NGC 5055, we clearly see that the beam smearing induces a strong fourth FFT order, which is aligned close to its half period. The second FFT order is not aligned exactly with 0.5π, and this could be explained by the non-axisymmetry of the beam. Indeed, assuming a circular beam of 10x10 arcsec^2 (Fig. 15, middle row), the phase ϕ_2 becomes exactly aligned with 0.5 π. Amplitudes are the same in the case of the circular beam with $\sigma_2 = 0.40$ km/s and $\sigma_=0.34$ km/s. Part of the discrepancy between the two first peaks are reduced using a circular beam. The residual difference is due to the combination of orders 2 and 4. If ϕ_4 was perfectly aligned with 0.25π, the peak of the order 2 would be at the exact center of the first peaks of the order 4. Here ϕ_4 is slightly lower inducing this amplitude difference.

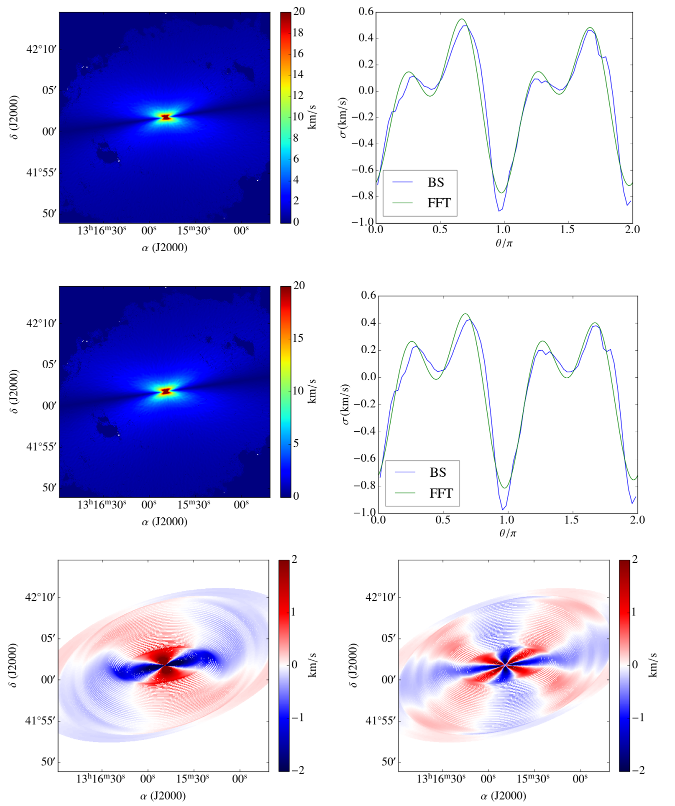

Fig. 15. Beam smearing modelisation of NGC5055 using different beam sizes. (Top panels) Using the actual beam from THINGS. The left panels displays the reconstructed image and the right one, the corresponding FFT of this map reduced to a single radius. (Middle panel) Same as the top panel but using a circular beam of 10 arcsec^2. (Bottom panel) Reconstructed orders 2 (left panel) and 4 (right panel) of the FFT from top panel.

(b) Radial dependences

In this paragraph we perform the FFT for each radius of the galaxy, mixing the azimuths, instead of studying each azimuth, mixing the radius, as we did in the previous section. The aim is to study the radial dependence of the different FFT parameters. The $H\alpha$ velocity field does not take warp into account, thus, in a first step, the position angle and the inclination, of each ring of the beam smearing map, are kept fixed. In the next step we include warps, by using the HI tilted-ring model's parameter.

(b.1) Without warp

On Fig. 16, we present the variation of amplitude of the velocity dispersions and of the phases, as a function of the radius. The FFT of the first four orders (k=1,2,3 and 4) for the velocity dispersion amplitude σ_k and the corresponding phase ϕ_k (only for k=2 and 4) are displayed in the top and bottom panel respectively. Concerning the amplitudes, we observe the same phenomenon than previously observed: σ_2 and σ_4 are by far larger than σ_1 and σ_3. Moreover, the decrease of amplitudes is fast, and at 200", the σ_2 and σ_4 represents only 1 km/s. Given the low values of σ_1 and σ_3, the corresponding phases ϕ_1 and ϕ_3 are meaningless, thus we only display ϕ_2 and ϕ_4 on the bottom panel. Those phases are roughly constant up to ~500 arcsec. In the range ~500–800 arcsec, small variations are observed, larger for ϕ_2 than for ϕ_4. After 800 arcsec, amplitudes are too low, therefore the results for the phase is not significant anymore.

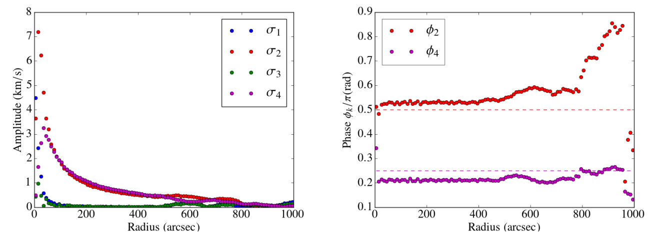

Fig. 16. Variations of the parameters of the FFT with the radius for the galaxy NGC 5055, amplitudes on the left panel and phases on right one. The inclination and the position angle do not vary with the radius.

(b.2) With warp

If we consider warps in taking the results of the tilted ring model, each radius has its own set of position angle and inclination, varying with the radius. On Fig. 17 we present the same plot as before, adding the radial variation of inclination.

Without warp, amplitudes σ_2 and σ_4 had similar behaviour. When accounting for the warp, amplitude σ_4 is greatly reduced, while σ_2 is stronger. Other amplitudes σ_1 and σ_3 are still negligible. First let's note that inclination varies from 45° to almost 70°, implying that the warp of NGC5055 is strong. The beam smearing model is calculated using the $H\alpha$ inclination of 63^o, meaning that locally the beam smearing is under/over-estimated depending if the actual inclination is greater/lower than the model inclination.

Variations in position angles and inclinations induces variation of ϕ_2 and ϕ_4. A change in the position angle, i.e. in the initial starting azimuth, logically affect the phase. Between 450 and 650 arcsec, the increasing position angle leads to a decrease of ϕ_2. The influence of inclination on the phase is discussed in more detail in the next part.

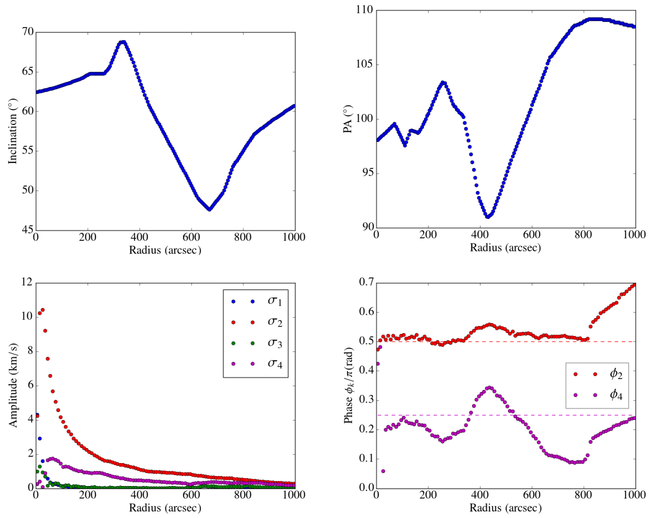

Fig. 17. Same as Fig. 16 but modelling the warp of NGC 5055. The inclination and position angle variations as a function of the radius are given on the top line. Variations of the parameters of the FFT amplitude and phase with the radius are displayed on the bottom line.

(c) Inclination dependences

In this section we study how the shape of the beam smearing pattern evolves with the inclination. As previously, NGC 5055 is still modelled using its $H\alpha$ rotation curve but we simulate three factice inclinations: 30°, 50°, 70°, instead of using only its actual inclination of 59°. The lowest inclination in the THINGS sample is 32.6° and the highest 75.8°, the median value being 64.5°. Those four inclinations allow to sample different configuration in our data. For each model, we compute the FFT of the map, by taking all pixels and reducing the galaxy to one radius as explained in section 4.2. Results for the parameters σ_k and ϕ_k are listed in Table 5. The maps showing the shape of the beam smearing as well as the corresponding FFT are displayed in Fig. 18.

Inclination Parameters	30°	50°	63°	70°
σ_1(km/s)	0.07	0.05	0.01	0.01
σ_2(km/s)	0.30	0.46	0.41	0.48
σ_3(km/s)	0.02	0.03	0.03	0.01
σ_4(km/s)	0.09	0.22	0.33	0.53
ϕ_1/π	0.54	0.65	0.35	0.05
ϕ_2/π	0.51	0.53	0.54	0.59
ϕ_3/π	0.59	0.00	0.03	0.10
ϕ_4/π	0.25	0.24	0.21	0.22

Table 5. FFT parameters for the beam smearing model of NGC5055 at different inclinations.

Table 5 and Fig. 18 show that the amplitude of the second and fourth orders grows with the inclination. For an inclination of 30°, the velocity dispersion due to the beam smearing is maximum along the minor axis and minimum along the major axis, characteristic of an order 2.The FFT displays a large amplitude of the velocity dispersion at a phase $\phi_2 \sim \pi/2$, because minor and major axis are orthogonal, this corresponds to a high value of $\sigma_2 \sim 0.30$ km/s, largely dominating the other orders. For the inclination 50°, high velocity dispersions are spread out over a larger area along the minor axis without affecting much the major axis direction.

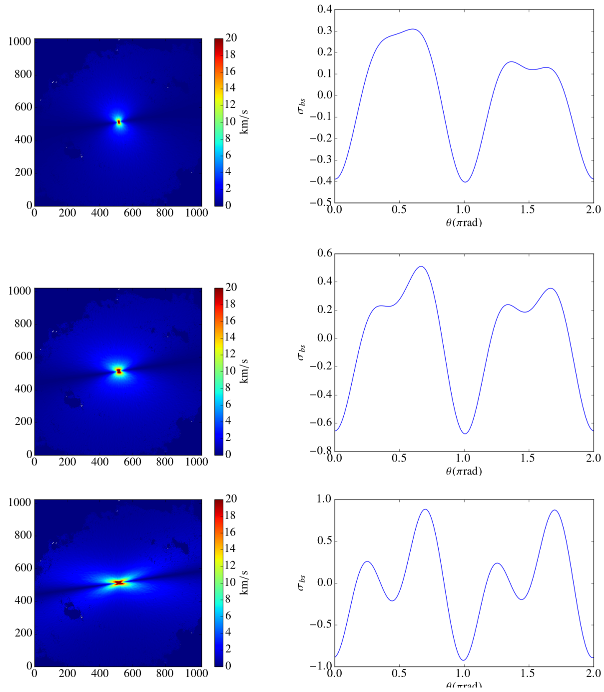

Fig. 18. Beam smearing model (left panels) and corresponding FFT (right panels) for the galaxy NGC 5055 for different inclinations: 30°, 50° and 70° for the top, middle and bottom panel respectively. LA TAILLE DES PANNEAUX DE DROITE N'EST PAS TOUJOURS LA MEME ET LES LABELS SONT COUPÉS.

Due to the higher values in the dispersion, order 2 increases by ~50%, but the amplitude of σ_4 grows even more by almost ~150%. Phases ϕ_2 and ϕ_4 doesn't change significantly. For an inclination of 70°, we observe a clear X-shape of the dispersion that was only weakly sketched for 50°. That X-shape, is more elongated on the major axis than for the previous inclination and gives a large velocity dispersion amplitude $\sigma_4 \sim 0.53$ km/s, which becomes more important than $\sigma_2 \sim 0.48$ km/s. On the corresponding FFT (bottom-right panel), the discrepancy between peaks of the order 4 increases. Part of this discrepancy is due to the asymmetry of the beam, and part of it is due to the asymmetry in the flux. As the inclination increases, the cross shape is more pronounced, making beam asymmetries more visible.

In conclusion, the beam smearing always creates an order 2, at any inclination, due to the minimum dispersion values along the major axis. Its phase ϕ_2 is directly link to the asymmetry of the beam. In the case of a perfectly circular beam, ϕ_2 is aligned with the half period of the order 2 (i.e. 0.5 π). Nevertheless, modelling the beam map with an inclination different than the one used to model the beam smearing drastically changes the result. To this order 2 is superposed an order 4, the cross shape observed in the previous figures. At low inclination, this cross shape is reduced to a line, with maximum values of the dispersion being aligned on the minor axis. As we go towards higher inclination, the cross shape is more and more defined, inducing higher amplitudes σ_4. The phase ϕ_4 is also impacted, and going at higher inclination, the maximum values tends to be more and more aligned with the major axis leading to lower value ϕ_4 for NGC5055, while they were closer to the minor axis at lower inclination, $\phi_4 \approx 0.25\pi$. The beam smearing is more stronger at higher inclination. Therefore an increase of inclination induce an increase of both σ_2 and σ_4. Nevertheless, due to that cross shape, order 4 becomes more and more important relatively to the order 2. Furthermore, at high inclinations, an error of 7° in inclination leads to a difference of 60% in the value σ_4 (5).

6.2.2. The case of stacked galaxies

The goal of this section is to study how evolves the parameter of the FFT of the stacked galaxy when we exclude few annulus or some galaxies.

*(*a) Radial dependence

First we focus on the radii. As we observed in the previous section, the beam smearing is maximum in the central part of the galaxy and then becomes less important as we go towards the outer part of the galaxy. In order to observe the effect of beam smearing, we divide our sample into two subsamples: in the inner sample, we select only the inner part of each galaxy and in the outer subsample, the outer part. In other words, the inner and outer subsample contains all the points being below and above $r_{max}/2$ respectively, r_{max} being the last radius of each individual galaxy.
In order to check the beam smearing effect, both corrected and raw velocity dispersion maps are used and a stacked galaxy is created for each case: one using the corrected velocity dispersion maps and one using the raw map. For both subsamples and for both cases, we compute a stacked galaxy that contains the total signal for all galaxies, using the method described in the methodology section (4.2).
We thus end up with four configurations : a) using velocity dispersion maps corrected from beam smearing effects for the inner sample (refereed as 'Corr Inner'); b) idem for the outer sample (refereed as 'Corr Outer'); c) using velocity dispersion maps not corrected from beam smearing effects for the inner sample (refereed as 'Raw Inner'), d) idem for the outer sample (refereed as 'Raw Outer'). The result of the FFT parameters for each configurations are listed in Tab 6, and the total signal is shown in Fig. 19. Contrarily to the study realised before on NGC5055 we used on the velocity dispersion squared.

Because we study the beam smearing effects, as a result of the previous sections, we are more concerned by the orders 2 and 4 than by the orders 1 and 3. We also expect that σ_2 and σ_4 decrease with the radius. Table 6 indeed indicates that σ_4 is lower in the outer subsample (cases b and d) than in the inner one (cases a and c) but, surprisingly, σ_2 is higher.

Concerning the phases, ϕ_4 is not changing while ϕ_2 increases. As we mentioned it in the previous sections, phases are supposed to remain roughly constant with the radius, if we only consider beam smearing effects.

For both the inner and outer subsamples, the velocity dispersion amplitudes are lower when we correct for the beam smearing (cases a and b) than when we do not correct (cases c and d), but the phases do not change.

The beam smearing smearing correction has really few impact on the σ_2 (24.4 to 23.5 $(km/s)^2$) and σ_4 amplitudes (13.7 to 13.1 $(km/s)^2$) for the outer subsample.

For the inner subsample, the variation are larger, a shift from 21.5 $(km/s)^2$ to 14.8 $(km/s)^2$ is observed for σ_2^2 and from 35.0 to 29.4 $(km/s)^2$ for σ_4^2.

We conclude that the second order is probably associated to a dynamical process in galaxies, while the fourth order is more likely a residual of beam smearing that was poorly corrected during our process due to insufficient knowledge of the shape of the PSF.

(b) Inclination dependence

In the previous paragraph we studied the radial dependence of the FFT second and fourth orders. In this section we focus on the effects of the inclination. We again split the sample into two subsamples, the pivot inclination being 64.5°, the median value of the inclination. Seven galaxies belong to the low-inclination subsample and eight in the high-inclination one. Once again we consider four configurations : a) using corrected velocity dispersion maps and galaxies from the low-inclinations subsample; b) idem for the high-inclination subsample; c) using raw velocity dispersion maps and galaxies from the low-inclinations subsample and d) idem the high-inclination subsample. The results of the FFT parameters for each configurations are listed in Tab 7, and the stacked galaxies for each configuration is shown in Fig. 20.

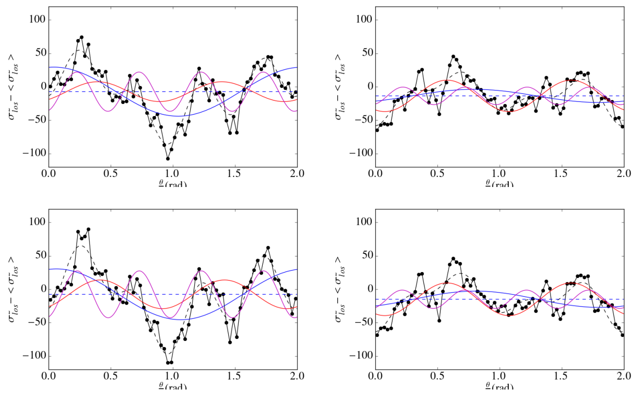

Fig. 19. Total signal and FFT orders superposed for the different cases mentioned before. a) top left, b) top right, c) bottom left, d) bottom right. EXPLICITER LE BEFORE

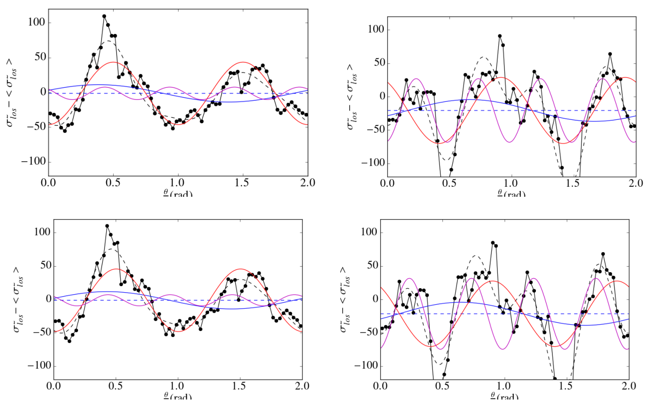

Fig. 20. Total signal and FFT orders superposed for the different cases mentioned before. a) top left, b) top right, c) bottom left, d) bottom right. EXPLICITER LE BEFORE

Signatures of beam smearing effects are clearly identified on σ_4 which are by far larger when the velocity dispersion are not corrected. Table 7 indicates that, if one corrects the dispersion velocity field from beam-smearing effects, σ_2^2 is more than four times larger than σ_4^2 for the low-inclination subsample (case

Model		(a) Corr inner	(b) Corr outer	(c) Raw inner	(d) Raw outer
Velocity dispersion		$(km/s)^2$	$(km/s)^2$	$(km/s)^2$	$(km/s)^2$
	$\sigma_0^2 - <\sigma_0^2>$	-7.4	-13.6	-7.8	-15.0
	σ_1^2	36.7	9.80	38.0	12.2
	σ_2^2	14.8	23.5	21.5	24.4
	σ_3^2	9.85	4.13	12.9	4.49
	σ_4^2	29.4	13.1	35.0	13.7
Phase	ϕ_1/π	0.04	0.79	0.06	0.81
	ϕ_2/π	0.39	0.58	0.41	0.58
	ϕ_3/π	0.47	0.30	0.45	0.31
	ϕ_4/π	0.23	0.22	0.23	0.22

Table 6. FFT parameters for the total signal obtained in the 4 configurations describe in section xxx.

Case		(a)	(b)	(c)	(d)
Inclination		$< 64.5°$	$> 64.5°$	$< 64.5°$	$> 64.5°$
Beam smearing		Corrected	Corrected	Raw	Raw
Velocity Dispersion		$(km/s)^2$	$(km/s)^2$	$(km/s)^2$	$(km/s)^2$
	$\sigma_0^2 - <\sigma_0^2>$	-1.42	-20.7	-1.34	-21.6
	σ_1^2	12.5	16.3	12.9	17.3
	σ_2^2	44.9	49.5	46.9	49.1
	σ_3^2	11.6	10.8	11.1	11.5
	σ_4^2	8.98	47.6	8.38	53.2
Phase	ϕ_1/π	0.39	0.66	0.43	0.65
	ϕ_2/π	0.50	0.91	0.50	0.90
	ϕ_3/π	0.43	0.36	0.43	0.37
	ϕ_4/π	0.44	0.23	0.44	0.23

Table 7. FFT parameters for the total signal obtained in the 4 configurations mentioned above.

a), while σ_2^2 is similar to σ_4^2 for the high-inclination subsample (case b). In the low-inclination cases (a and c), velocity dispersions moderately vary, due to the fact that beam smearing is weaker at lower inclinations. In the high-inclination cases (b and d), the variations between corrected and raw velocity dispersion maps are not really larger except maybe for σ_4 that goes from 53.2 to 47.6 $(km/s)^2$; it is somehow surprising as we would expect beam smearing to be larger for higher inclination. Whatever the case, σ_2 shows almost the same amplitudes but way above σ_1 and σ_3. Interestingly, none of those amplitudes vary considerably when subtracting the beam smearing. Concerning the phases, we observe that at low inclination ϕ_2 is equal to 0.5π, whereas for higher inclinations $\phi_2 \approx 0.9\pi$. A result from a previous analysis was that beam smearing effects induce a strong second order, aligned with 0.5π, this is confirmed by the present analysis.

In the other hand $\phi_4 \approx 0.44\pi$ at low inclination and $\phi_4 \approx 0.23\pi$ at high inclination. This is also consistent with what we previously conclude, i.e. that at low inclination the fourth order has a low amplitude and thus the phase has a 'random value', while at higher inclination σ_4 becomes larger and is aligned close to $\approx 0.25\pi$.

6.3. Validity of the model and interpretation

Fig. 21 provides an overview of the result of the asymmetry study for the galaxy NGC2841. In appendix **??**, we show the results each individual THINGS galaxies. These maps contain a large amount of information. In this section, we highlight the main results.

First of all, these maps confirms the validity of limiting the FFT analysis to the orders 0 to 4 in our modelisation. By inspecting panels (3), (4) and (5) of the right column for all THINGS galaxies, we observe that :

- the projected maps of the FFT containing orders 0 to 4 reflect fairly well the large-scale structures observed in the corrected dispersion maps.
- the comparison of the FFT maps containing all orders, subtracted by the FFT maps containing only orders 0 to 4 shows no particular large-scale structures.
- the investigation of the amplitudes up to the order 20 shows that the highest amplitudes are confined in the first 4 orders.

The interpretation of the asymmetries in the dispersion maps is not strait-forward. Indeed, a visual comparison of the flux map and dispersion map from THINGS (left column, panel (1) and (3)) shows that the flux distribution is anti-correlated with the velocity dispersion. In other words, a general behaviour observed amongst the 15 THINGS galaxies is that the maximum values in the flux distribution corresponds to low values of dispersion velocities and on the opposite low flux regions corresponds to the most important values of the dispersion. For the most striking examples, see Fig. **??**, Fig. **??**, Fig. **??** in Appendix XXX. Therefore, it is not possible to associate immediately the asymmetries in the velocity dispersion maps with the structures that compose the galaxy, such as bars or spiral arms. For a further investigation, one needs to perform a similar work on the flux map and compare with the results found in the present work.

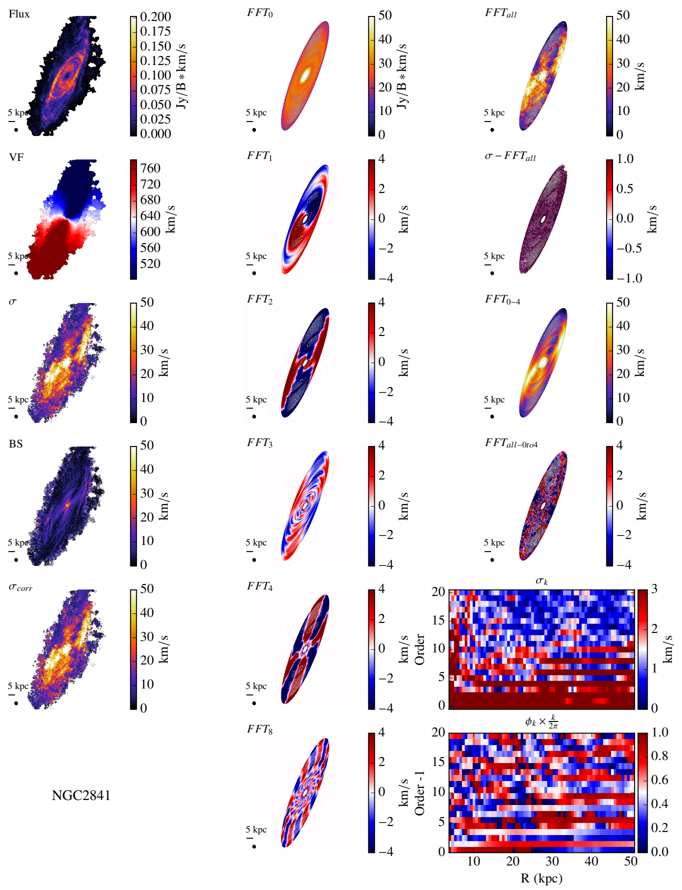

Fig. 21. Results of the FFT analysis for the galaxie NGC 2841. (Left column, from top to bottom) : (1) flux map from THINGS, (2) velocity map from THINGS, (3) dispersion map, (4) beam smearing modelisation and (5) dispersion map corrected from the beam smearing effect. (Middle column from top to bottom) : (1) Projected map of the 0^{th} order of the FFT, (2) map of order 1, (3) map of order 2, (4) map of order 3, (5) map of order 4 and (6) map of order 8. (Right column, from top to bottom) : (1) Projected map containing all the FFT orders from 0 to N/2, N being the number of pixel in a ring, (2) dispersion maps corrected from the beam smearing subtracted by the FFT map containing all orders, (3) Projected map of the FFT containing orders 0 to 4, (4) Projected map of the FFT containing all orders subtracted by the map containing only orders 0 to 4, (5) Radial variation of the amplitudes σ_k of the FFT up to the order 20 and (6) Radial variation of the angle phases $\phi_k \times \frac{k}{2\pi}$ up to the order 20.

7. Conclusions.

Frequent cloud-cloud gas collisions tend to make the random motions spatially uniform. At the opposite, if the gas is even partly collisionless, each cloud keeps its own orbital dynamic like stars do. Those motions, mainly circular may nevertheless be perturbed by non-axisymmetric disk structures like bars and spiral arms, therefore azimuthal variation of the velocity dispersion provides hits on the orbital motions in the galactic plane of the galaxy.

In this work, we performed a systematic study of random motions in the cold gas component for a sample of nearby spiral galaxies. We have studied these random motions using radial velocity dispersions, i.e. second order moments, more complex to manipulate than fluxes and the radial velocities, but which provide tremendous, but degenerate, kinematic information allowing to probing, for instance, the possible clumpiness nature of the cold gas component. Indeed, if the random motions are anisotropic, this could mean that at least part of the cold gas consists of low density dense clouds, which would thus follow a collisionless behaviour, like the stellar disk component.

Such study has already been carried out by Chemin et al. (2020) on the nearby galaxy M 33 for which the observed azimuthal variations have be interpreted as the result of anisotropic cold gas motions. However, it was important to extend this analysis to a sample of galaxies in order to check if this effect is not a particularity of M 33 or if it is not related to projection effects. A difficulty of this project was to select galaxies observed at high HI spatial resolution. To achieve this, we needed to select nearby resolved galaxies. Indeed, if the resolution is not sufficient, the global rotation of the galaxy will add artificial enlargements on the velocity dispersion profiles, which it will not be possible to get rid of. Additionally, the velocity dispersion is a local indicator and if too large regions are embedded in the beam, the local motions will be spread out and and it will net be possible to trace them back. For this purpose, we selected 15 galaxies from the HI high-resolution THINGS survey, which consists of 34 galaxies in total, and we add another set of 15 galaxies selected from the larger WHISP survey, which includes 313 galaxies but at lower resolution, so only the closest and largest galaxies were suitable. Together, those two samples gave rise to the largest dataset of 30 galaxies never used to perform this dynamical analysis, highly demanding in spatial resolution.

Thanks to some hypothesis and with the help of 3D or 2D-velocity dispersion ellipsoid models, projected line-of-sight velocity dispersion fields allow to deduce the gas azimuthal dependency. We started the study assuming that an axisymmetric but anisotropic velocity ellipsoid could describe the observed velocity dispersion fields. Using this model we fit the azimuthal variation of each galaxy, using titled-ring models to master the axisymmetries. We concluded that this approach was too restrictive to reproduce the complex shape of the azimuthal variations of the observed velocity dispersion fields. Therefore we modify the framework in order to be able to study non-axisymmetric structures using FFT tools. We thus described azimuthal variations at the local ring scale. Using FFT expansion, we fit models that satisfactorily reproduce and quantify the non-axisymmetries in the observed velocity dispersion fields. We demonstrated that the FFT analysis could be limited to expansion only up to the fourth order. We studied the distribution of the FFT velocity dispersion amplitudes σ_i and phases ϕ_i, $i \in (1, .., 4)$, for each ring across all galaxies and we do not find a result similar to the one found in Chemin et al. (2020), who found a second-order phase ϕ_2 aligned systematically with the minor axis, but we find a random distributions of phases ϕ_2. This study also confirms that the velocity dispersion computed in the axisymmetric and anisotropic case do not reproduce the observational data.

Nonetheless, an interesting result is found for the phase ϕ_4, which is almost systematically aligned with the half period of the fourth order (0.25π) for most of the 883 rings that this study contains. To avoid bias due to the wide variation in the number of rings for each galaxy, ranging from 7 to 144 rings depending on the galaxy, we model the radial distribution of galaxies over a single ring, using two distinct methods. In the first one, we average the radial distribution of the dispersion velocity and combine the signals for the entire sample, creating a "stacked galaxy". In the second one, we calculate the FFT on each ring to compute the median value of the radial distribution of FFT parameters. Both methods show a fourth-order aligned with 0.25π. In the case of the "stacked galaxy", the fourth-order turn into a term of greater amplitude, becoming larger than σ_2, which generally dominates when we compute the FFT at the local ring scale. We conclude that this fourth-order signal is not due to artefacts: it is not due to noise, and the probability to introduce it when combining all galaxies from the THINGS sample is lower than 1%. This fourth-order is probably not due to beamsmearing effects. Indeed, a strong argument is given the comparison of the fourth-order distribution between the inner and the outer regions of each galaxy, which shows that this signal is as strong in the outskirts than in the central regions; while only the center is strongly affected by beam smearing effects. Thus the fourth-order signal could be an indicator of anisotropy but at this point, it is not possible to state if the cold gas is collisional or not. Indeed, to interpret this order 4 as an anisotropies, one needs to consider the covariance terms which are set to zero, i.e. to quantify the degree of correlation between all the components of the velocity dispersion ellipsoid. The lack of knowledge of these terms, as well as the degeneracy between asymmetry and anisotropy, force us to remain cautious.

Considering the similarity of this observed order four with our beam smearing modelisation, an extensive discussion about its possible artificial nature is led. Alternatives explanations should be more widely explored for quantifying this fourth order. In our study, for the sake of simplicity and by lack of information, we assume a Gaussian beam, the actual beam may deviates from it, specially if it contains higher frequencies as expected in interferometric beam recombinaison, leading to insufficient beam smearing correction. In the other hand, our beam smearing modelisation doesn't account for warps, i.e. the inclination used for the beam smearing correction is an average value and not the inclination at each ring. In case of strong warps, the beam smearing could be locally under or over-estimated. More generally, errors in determining the position angle of the major axis of the galaxy, the position of its center and its inclination, induce errors on the azimuthal angles and probably introduce higher FFT orders. We also discuss the choice of using the 2^{nd} order moment to fit the datacube, rather than a Gaussian fit. Indeed, the technique used to fit the data impacts the dispersion maps, therefore a systematic comparison of dispersion maps using those two methods should allow us to evaluate the difference between those two methods. Finally, the difficulties to interpret the asymmetries in the velocity dispersion field are underlined. In isotropic or/and non-axisymmetric models, we do not expect to observe a fixed phase. Degeneracies between axisymmetric-anisotropic models and a non-axisymmetric isotropic model complicate the task and should be further explored. On the other hand, we have noted that the velocity dispersion maps are widely anti-correlated with the flux distribution (0th-order momentum) maps, which provides new hits for the asymmetry analysis. Taking into account the large-scale rotation and the deviations from this rotation in using the velocity fields (1st-order momentum) should also improve the model. Therefore, a comparative study of the asymmetries in the light, velocity dispersion and velocity distributions would improve our understanding of anisotropies. In particular studying the anisotropies along a non axisymmetric structure like arms or bars should be interesting. It should be possible to isolate a spiral arm in a velocity dispersion maps and to study the variation of the velocity dispersion in the spiral arm.

Appendix A: Geometrical and mathematical framework

In this Appendix, we introduce the mathematical tools requested to describe asymmetries in the neutral gas velocity dispersion fields. We introduce and discuss the geometrical and mathematical framework used to study spatially resolved velocity dispersion. Velocity dispersion is a second order moment, and therefore is a more complex quantity to study than flux and radial velocity which are respectively the zero and first moment order.

Due to its hydrodynamical properties, the gas basically lies one a plane. The velocity vector in the frame of the galactic plane is described by two components lying in the plane of the galaxy. Thus, in the cylindrical frame:

$$V_{\rm los} = V_{\rm sys} + V_\theta \cos\theta \sin i + V_R \sin\theta \sin i + V_z \cos i \tag{A.1}$$

Whereas,

1. V_θ: the tangential velocity, i.e. the rotation motion;
2. V_R: the radial velocity, that is the inward or outward motion;

and one component perpendicular to this plane:

3. V_z: the vertical velocity.

The observed velocity $V_{\rm los}$ (los for line-of-sight) is linked to the projection of V_θ, V_R and V_z along the line of sight through 5 additional parameters:

4. PA: the position angle of the major axis of the galaxy (measured counterclockwise from the North to the direction of receding side of the galaxy);
5. i: the inclination of the galactic disk with respect to the sky plane;
6. $V_{\rm sys}$: the systemic velocity of the galaxy;
7. x_c and y_c: coordinates of the rotation center in cartesian coordinates (sky projection)

Both the radial, tangential, and vertical components can vary with R and θ, which are the polar coordinates in the plane of the galaxy with respect to the center, choosing the major axis as reference $\theta = 0$. The azimuth in the plane of the galaxy, θ, is linked to the position angle PA, the inclination i, the position x (east-west),y (north-south) and center x_c, y_c in the sky by the set of equations A.2 to A.7:

$$R\cos\theta = r\cos\psi \tag{A.2}$$

$$R\sin\theta = r\frac{\sin\psi}{\cos i} \tag{A.3}$$

$$\cos\psi = \frac{(y-y_c)\cos PA - (x-x_c)\sin PA}{r} \tag{A.4}$$

$$\sin\psi = -\frac{(x-x_c)\cos PA + (y-y_c)\sin PA}{r} \tag{A.5}$$

$$r = \sqrt{(x-x_c)^2 + (y-y_c)^2} \tag{A.6}$$

$$R = r\sqrt{\cos^2\psi + \frac{\sin^2\psi}{\cos^2 i}} \tag{A.7}$$

ψ being the counterclockwise angle in the plane of the sky from the North.

Using the same formalism, it is possible to define:

$$\sigma_{ab} = \overline{V_a V_b} - \overline{V_a}\;\overline{V_b} \tag{A.8}$$

where a and b denote the different coordinate direction : radial (r), azimuthal (θ) and vertical (z) and V_a and V_b gives the corresponding velocities. When $a \neq b$, the term is the covariance between V_a and V_b, whereas in the specific case of a = b, the term is the variance of V_a and we note $\sigma_{aa} = \sigma_a^2$. The line-of-sight velocity dispersion of a single particle is thus defined as in equation A.1 by

$$\sigma_{\rm los}^2 = \overline{V_{\rm los}^2} - \overline{V_{\rm los}}^2 \tag{A.9}$$

As $V_{\rm sys}$ is constant, we deduce that:

$$\begin{aligned}\sigma_{\rm los}^2 = {} & \sigma_\theta^2\cos^2\theta\sin^2 i + \sigma_R^2\sin^2\theta\sin^2 i + \sigma_z^2\cos^2 i \\ & +2(\sigma_{R\theta}\cos\theta\sin\theta\sin^2 i + \sigma_{\theta z}\sin\theta\cos i\sin i \\ & +\sigma_{Rz}\cos\theta\cos i\sin i)\end{aligned} \tag{A.10}$$

where $\sigma_{R\theta}, \sigma_{Rz}, \sigma_{\theta z}$ are the covariance terms of Eq. A.8. A null value $\sigma_{R\theta}$ is equivalent to state that σ_R and σ_θ are independent. This equation is the most generic form to express the velocity dispersion along the line-of-sight. Since we observe galaxies with a finite resolution, individual pixel/spaxels of 3D spectroscopy instruments observe at a given position the motions of hundreds or thousands of stars or tens of gaseous clouds, all of them following their own orbit with different radial, vertical and tangential velocities. The random motion thus describes the scatter of orbital motions in each direction at the given position, called the velocity dispersion ellipsoid (Fig. A.1). It is characterized by the three axis ratios, $\sigma_\theta/\sigma_R, \sigma_\theta/\sigma_z, \sigma_z/\sigma_R$. For collisionless tracers, like stellar populations, the axis ratios are not equal. Indeed, stellar orbits are not perfectly circular, and the presence of large-scale asymmetries, like bars and spiral arms creates streaming and radial motions.

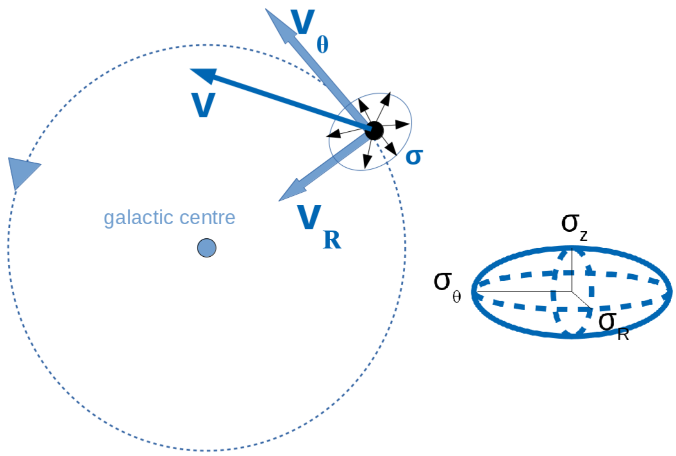

Fig. A.1. Velocity ellipsoid, in cylindrical coordinates. To the left, illustration of a group of stars or gaseous clouds travelling along an orbit in the mid-plane ($z = 0$) at mean radial and rotational velocities V_R and V_θ, and with a r.m.s. planar velocity of V and random motion σ. The blue dashed circle corresponds to an orbit of purely circular motions. To the right, the 3 components of the random motion describe the so-called velocity ellipsoid.

We can recast the equation A.10 in a sum of trigonometric polynomials of degree 2 :

$$\begin{aligned}\sigma_{\rm los}^2 = {} & \left(\frac{\sigma_\theta^2 - \sigma_R^2}{2}\cos 2\theta + \sigma_{R\theta}\sin 2\theta\right)\sin^2 i \\ & + (\sigma_{Rz}\cos\theta + \sigma_{\theta z}\sin\theta)\sin 2i \\ & +\sigma_z^2\cos^2 i + \frac{\sigma_\theta^2 + \sigma_R^2}{2}\sin^2 i\end{aligned} \tag{A.11}$$

We can formulate differently this equation to match better the formalism introduced with Fourier Transforms (see Section D). To do so, we write $a = \frac{\sigma_\theta^2 - \sigma_R^2}{2}$ and $b = \sigma_{R\theta}$, and define $\alpha_2 = \sin^2 i \sqrt{a^2 + b^2}$, and ϕ_2 such that $\cos 2\phi_2 = a/\alpha_2$ and $\sin 2\phi_2 = b/\alpha_2$.

Hence, we get for the second degree term of Eq. A.11:

$$\left(\frac{\sigma_\theta^2 - \sigma_R^2}{2} \cos 2\theta + \sigma_{R\theta} \sin 2\theta\right) \sin^2 i = \alpha_2 \cos\left(2(\theta - \phi_2)\right)$$

Similarly, we can introduce $\alpha_1 = \sin 2i \sqrt{\sigma_{Rz}^2 + \sigma_{\theta z}^2}$ and ϕ_1 such that $\cos \phi_1 = \sigma_{Rz}/\alpha_1$ and $\sin \phi_1 = \sigma_{\theta z}/\alpha_1$. We thus get for the term of degree 1 in Eq. A.11:

$$(\sigma_{Rz} \cos \theta + \sigma_{\theta z} \sin \theta) \sin 2i = \alpha_1 \cos(\theta - \phi_1)$$

Finally, defining $\alpha_0 = \sigma_z^2 \cos^2 i + \frac{\sigma_\theta^2 + \sigma_R^2}{2} \sin^2 i$ for the 0^{th} degree amplitude, which corresponds to the average value of $\sigma_{\rm los}^2$, we obtain:

$$\sigma_{\rm los}^2 = \alpha_0 + \alpha_1 \cos(\theta - \phi_1) + \alpha_2 \cos\left(2(\theta - \phi_2)\right) \quad \text{(A.12)}$$

As this relation is deduced from relation A.1 and the conditions underlying its expression, these expressions are only valid for motions observed in the galactic plane. They are not valid for spheroidal objects, like stellar bulges or halos. As described before, terms α_0, α_1 and α_2 depend on $\sigma_R, \sigma_\theta, \sigma_z, \sigma_{R\theta}, \sigma_{Rz}, \sigma_{\theta z}$. In a general case, those parameters are dependent on the radius and the azimuth. Therefore, the azimuthal variations of $\sigma_{\rm los}$ are complex to analyse because $\alpha_0, \alpha_1, \alpha_2, \phi_1, \phi_2$ are all dependent on azimuth, combined with the variation in $\cos\theta$ and $\cos 2\theta$. In practice, for reasons of simplicity, in the following the cross-terms $\sigma_{R\theta}, \sigma_{Rz}, \sigma_{\theta z}$ are set to zero, implying $\alpha_1 = 0$. Nevertheless, the azimuthal dependence of Eq. A.12 is still degenerated.

In practice, we do not observe directly $\sigma_{\rm los}$, because spectroscopic observations are a convolution of the physical dispersion with a Line Spread Function (LSF) with a finite instrumental resolution σ_{LSF}. Moreover, part of the physical dispersion is due to thermal processes in the gas. The observed velocity dispersion is thus given by relation (1)

To express σ_{obs} following a similar polynomial decomposition as of Eq. A.12, the term $\sigma_{\rm LSF}$ is a 0^{th} degree term, because the line spread function is roughly constant on the field. The thermal dispersion $\sigma_{\rm th}$ depends on the temperature of gas and is supposed isotropic. It therefore also fits in the 0^{th} degree. However, since it is linked to the temperature, and therefore to the local density of gas, which is clearly not axi-symmetric due to features like bars and spiral arms, it could contain a non axisymmetric modulation. In the case of bars and 2 spiral arms, the asymmetric terms are dominated by the degree 2, they are antisymmetric with respect to the minor axis (mirrored symmetry). Since the problem is highly degenerated, we assume a constant gas temperature on the galaxy. Indeed, random motions are due to different causes, mainly the thermic motions of the gas and the gravitational force exerted by the surroundings of the cloud. In this thesis we focus on the random motions caused by gravitational effects.

Appendix B: Mathematical framework: (a)symmetries and (an)isotropies

Velocity ellipsoids and velocity dispersion ellipsoids formally introduced in equation A.10, attempt to determining the shape and orientation of the three-dimensional distribution of velocities and velocity dispersions respectively from the point of view of the observer who is usually not located in the center of the system but who sees for instance a galaxy disk in projection under a certain inclination and position angle. Modelling in 3D the spatial distribution of velocities and velocity dispersion is a longstanding problem in galactic dynamics. Velocity ellipsoids comes up in the kinematics modelling of N-body systems. They are theoretical mathematical objects that must account for the velocity and velocity dispersion maps, that are observational quantities. Those ellipsoids model three-dimensional distributions whereas one-dimensional quantities only are observed, the line-of-sight velocities and line-of-sight velocity dispersions. The velocity dispersion tensor describes the local distribution of velocities at each point. This velocity ellipsoid is directly related to the symmetry and the shape of the galactic potential (e.g. Kuijken & Gilmore 1991) and non-axisymmetric structures such as bars and spiral arms in disk galaxies impact velocity ellipsoids, as shown by N-body simulations that indicate that the tilt of the stellar velocity ellipsoid is a signature of a bar in a disk (Saha et al. 2013).

Equation A.10 or A.11 show that six parameters are needed to describe this ellipsoid, σ_R, σ_θ, σ_z, $\sigma_{R\theta}$, σ_{Rz}, $\sigma_{\theta z}$. Since we only have access to σ_{los}, all parameters are strongly degenerated and therefore some hypothesis are mandatory to simplify this issue. Some hypotheses concern the geometrical properties of the velocity ellipsoid components, i.e. hypothesis about symmetry and some others concerns the axis ratio of the ellipsoid, i.e. hypothesis about isotropy.

To clarify the terminology, we precise in these two paragraphs the notions of (a)symmetry and (an)isotropy. Symmetry refers to a system that is invariant under some transformations: translation, reflection, rotation, scaling, helical transformation, etc. The type of symmetry is determined by the type of the transformation. The overall shape is changed after a reflectional symmetry (or mirror symmetry), in that case, there exists an axis or a plane which divides the system into two pieces that are mirror images of each other. The overall shape does not change in case of:

(1) A translational symmetry.

(2) A scale symmetry when it is expanded or contracted.

(3) A rotational symmetry around a fixed point in the three angles defining any rotation or about a line. Rotational symmetry around a point is also called central symmetry. A galaxy with a bar or an even number of spiral arms displays a rotational symmetry around an axis. It finds the same geometry/properties after a rotation of an angle π. Rotational symmetry based on comparing a source image with its rotated counterpart has been widely used in the literature (e.g. Abraham et al. 1996; Conselice et al. 2000).

(4) A cylindrical symmetry around an axis, that is also called axisymmetric, which is different from the rotational symmetry around an axis. In case of a cylindrical symmetry, the only dependence is radial, whatever the value of the azimuth angle, the system has the same properties at a given radius. For a planar system like the disk of a galaxy, this results in losing one of the two dimensions, the angular one. In the context of our study, axisymmetry is the symmetry that will hold our attention. When we mention a symmetric system, we mean an axisymmetric distribution, in which there are no azimuthal variations of the velocity dispersion components, while the asymmetric case describes all the distribution which deviates from axisymmetry. Structures like spiral arms or bars are rotationally symmetric but are not axisymmetric thus we consider them as asymmetric.

A general tool for studying an ellipsoid is given by a cosine decomposition as the one given in relation A.12 but harmonic decomposition will also be used later. So, by analogy we will call axisymmetric a symmetry of 0^{th} order while any symmetry of orders $m \geq 1$ is considered as an asymmetry.

Isotropy refers to a system that is invariant under all direction. For instance, around a point, which is for a galaxy its center of mass, at the same distance from that point, all the different directions are all equivalent and the potential energy at given distance is the same, as all directions are equivalent. More generally, a system is isotropic if none of its macroscopic properties have directional dependence. Links exist between isotropy and rotational symmetry: an isotropic system is rotationally symmetric and reciprocally. By consequence, anisotropy is the characteristic of a system in which certain physical properties vary with direction. An anisotropic medium has different properties depending on the direction in which it is studied.

If no further hypothesis is made, all those dispersion terms in equations A.10 and A.11 (σ_R, σ_θ, σ_z, $\sigma_{R\theta}$, σ_{Rz}, $\sigma_{\theta z}$) can vary with both radius (R) and azimuth (θ). This translates in terms α_i and ϕ_i also possibly varying with both coordinates in equation A.12. This complex general case corresponds to the **anisotropic-asymmetric** case.

An assumption that can be made is the one where the ellipsoid is isotropic. This can be motivated by the fact that interstellar gas is a medium in which multi-directional collisions are thought to isotropize the gas velocity tensor. This is the reason why the ellipsoid of random motions of gas is often considered isotropic in galactic disks, equivalent to:

$$\begin{aligned} \sigma_{\mathrm{los}} = \sigma_R = \sigma_\theta = \sigma_z = \alpha_0 \\ \sigma_{R\theta} = \sigma_{Rz} = \sigma_{\theta z} = 0 \end{aligned} \tag{B.1}$$

In other words, in the isotropic case the velocity ellipsoid is locally spherical. There is no geometrical projection modulation anymore (and cross-terms are all null) and one thus does not need to deproject σ_{los} to study the random motions of gas. However, in the general **isotropic-non axi-symmetric** case, relation B.1 is only valid locally, i.e. the isotropic dispersion amplitude itself can still vary as a function of position, with both R and θ. The amplitude of these variations with the azimuth θ quantifies in that case the degree of asymmetry, i.e. the deviation from axi-symmetry. One has to add an hypothesis of axi-symmetry of the system to remove the dependency with the azimuth. In that **isotropic-axi-symmetric** case, the line-of-sight dispersion can only vary with radius.

On the other side, non-collisional particles, which describe stellar systems, but eventually also gas if the collisional efficiency is smaller than unity, correspond to an **axisymmetric and anisotropic** velocity dispersion ellipsoid. In that case, the parameters of the ellipsoid do not longer depend on the azimuth and a single value could be used to model a axisymmetric ring at a given radius. A useful parameter to quantify the level of anisotropy in the plane of the galaxy is β_θ defined by relation (2). In the case of isotropy, $\sigma_\theta = \sigma_R$ leading to $\beta_\theta = 0$. In an anisotropic distribution of gas, this parameter can be negative, $\beta_\theta < 0$ corresponds to $\sigma_\theta > \sigma_R$ meaning that the gas particles move in tangential orbits or positive $\beta_\theta > 0$ because $\sigma_R > \sigma_\theta$, in other words orbits of the gas are more radial.

The terms α_0, α_1 and α_2 in equation A.12 describe the order 0, 1 and 2 respectively. The 0^{th} order depends on the dispersion vector components σ_R, σ_θ and σ_z. The first order term is composed only by cross-terms σ_{Rz} and $\sigma_{\theta z}$. The second order term is composed by the difference $\sigma_\theta^2 - \sigma_R^2$ and a cross-term $\sigma_{R\theta}$. However, it is worth to notice that this problem remains degenerated, since only five independent parameters are necessary in relation **??**. Within this assumption, some hypotheses can be made in order reduce the number of free parameters. By assuming a disk transparent and a symmetry with respect to the galactic plan, we can approximate that $\overline{V_z} = 0$. The assumption that rotation motions are preponderant is used to compute rotation curves and implies $\overline{V_r} = 0$.

However, the problem is more difficult for the velocity dispersion. For a stellar population distributed symmetrically, $\sigma_{R\theta}$ and σ_{Rz} are equal to zero (Shapiro et al. 2003). One solution to further reduce the number of free parameters is to constrain the ratio of planar component σ_R and σ_θ. This can be done by using the epicycle approximation:

$$\frac{\sigma_\theta^2}{\sigma_R^2} = \frac{1}{2}\left(1 + \frac{\partial \ln V_\theta}{\partial \ln R}\right) \tag{B.2}$$

R being the radius in the plane of the galaxy.

Within this approximation, the anisotropy parameter can be inferred at any radius. For a flat rotation curve, according to equation B.2, $\sigma_R^2 = 2\sigma_\theta^2$ and $\beta_\theta = 0.5$, whereas for a solid body rotation curve $\sigma_R^2 = \sigma_\theta^2$ and $\beta_\theta = 0$. In absence of asymmetry, the dispersion component corresponding to vertical velocity dispersion does not depend on the azimuth. In face-on systems $\sigma_{\mathrm{los}} = \sigma_z$. Studies of such systems led to values of the vertical dispersion σ_z between 6 and 10 km/s (Combes & Becquaert 1997). Fixing σ_z to this value further enables to reduce the number of free parameters. If one only makes the assumption that the cross terms are null, we see from equation A.11 that depending on the sign of $\sigma_\theta^2 - \sigma_R^2$, we have either a phase of 0 ($\sigma_\theta^2 - \sigma_R^2 > 0$) or $\pi/2$ ($\sigma_\theta^2 - \sigma_R^2 < 0$) for the line-of-sight dispersion as a function of the azimuth.

Making the distinction between isotropic-non-axi-symmetric and anisotropic-axi-symmetric cases is not trivial, especially if cross terms can differ from zero. However, in the anisotropic-symmetric case, only orders 0, 1 and 2 are expected for the azimuthal variations (i.e. Eq. A.12), whereas asymmetries could be more complex. In practice, the study of the anisotropic-asymmetric case, which is not a simple task could eventually be achieved by making assumptions on the nature of the asymmetries. For instance, one could consider that along an asymmetric structure (e.g. a spiral arm), the amplitudes of the ellipsoid terms are constant. If the asymmetry has a shape that varies with both radius and azimuth, in theory, one could therefore deproject equation A.10 along the asymmetry. This is beyond the scope of this thesis.

Appendix C: (A)symmetries and (an)isotropies: examples of mock galaxies

To illustrate the (an)isotropic and (a)symmetric considerations, we created a mock galaxy with controlled values $\sigma_R, \sigma_\theta, \sigma_z$, constant at all radii. The inclination is set to 60°, and the PA to 30°. All cross-terms are set equal to 0 in the following.

- In the first scenario, we create an isotropic symmetrical model (Fig. C.1, top left). In the isotropic case $\sigma_{\mathrm{los}} = \sigma_R = \sigma_\theta = \sigma_z$, and we fix $\sigma_{los1} = 12$ km/s.

– The second scenario is an isotropic and asymmetrical model (Fig. C.1, top right). We add an azimuthal modulation, with an arbitrary phase of 0.7π which could be associated with spiral arms features on a real galaxy : $\sigma_{los2}(\theta) = \sigma_{los1}(1 + 0.2\cos 2(\theta - 0.7\pi))$
– The third scenario is an anisotropic and axi-symmetrical model (Fig. C.1, bottom left). In this case we compute the value σ_{los3} using Eq. A.10. We fix the value σ_{z3} = 6 km/s, $\sigma_{\theta 3}$ = 12 km/s and σ_{R3} = 16 km/s constant with the radius. We observe on the bottom left panel of Fig. C.2 that the dispersion is maximum along the minor axis because of the sign of $\sigma_\theta - \sigma_R$ as it was discussed for Eq. A.11.
– The last model is the most degenerated one, anisotropic and asymmetric (Fig. C.1, bottom right). For this model we keep the same value σ_z and add the same modulation as in the second model for both planar terms $\sigma_{R4} = \sigma_{R3}(1 + 0.2\cos 2(\theta - 0.7\pi))$ and $\sigma_{\theta 4} = \sigma_{\theta 3}(1+0.2\cos 2(\theta - 0.7\pi))$. In that case the dispersion doesn't peak on the minor axis nor at a phase of 0.7π which is the maximum of the azimuthal modulation, but between those two values.

This previous set of models is very basic. In order to mimic the methodology that will be used in the next two chapters and to be closer from real galaxies, we perform a second set of models. Parameters $\sigma_{\rm los}$, σ_R, σ_θ and σ_z are not constant anymore with the radius. We keep the same inclination and set the PA to 30°. All cross-terms are set to zero. To simulate a tilted-ring model, we decompose the galactic disk into 10 concentric rings.

– Isotropic and axi-symmetrical model (Fig. C.2, top left) : like above, the isotropic case $\sigma_{\rm los} = \sigma_R = \sigma_\theta = \sigma_z$ We set a radial decrease of σ_{los1} from 14 to 10 km/s. In a given ring, the value of the dispersion stays constant with the azimuth : $\sigma_{los1} = 14 - 0.4R$.
– Isotropic and non-axi-symmetrical model (Fig. C.2, top right) : we keep the same radial decrease of σ_{los1} and add a second order modulation with an arbitrary phase, which could be associated with spiral arms features on a real galaxy : $\sigma_{los2}(R,\theta) = \sigma_{los1}(R)(1 + 0.2\cos 2(\theta - 0.7\pi))$
– Anisotropic and axi-symmetrical model (Fig. C.2, bottom left) : in this case we compute the value σ_{los3} using Eq. A.10. We fix the value σ_z = 6 km/s and keep it constant for all rings. This is a reasonable value that has been observed on face-on systems. Since the vertical dispersion is roughly constant in a galaxy, we use the previously described anisotropy parameter β_θ (Eq. **??**). In our case, we create a vector σ_R of dispersion with a radial decrease from 18 to 13 km/s, and a similar vector for σ_θ, with a faster decrease to increase the anisotropy with the radius : $\sigma_R = 18 - 0.5R$ and $\sigma_\theta = \sigma_R(1 - 0.05R)$. We observe on the bottom left panel of Fig. C.2 that the dispersion is maximum along the minor axis because of the sign of $\sigma_\theta - \sigma_R$ as it was discussed for Eq. A.11.
– Anisotropic and asymmetric model (Fig. C.2, bottom right) : For this model we keep the same value of σ_z and same variation with radius of σ_θ and σ_r as for the anisotropic and axi-symmetric model for which we add the same modulation as in the second model. In that case the dispersion doesn't peak on the minor axis nor at a phase of 0.7π which is the maximum of the azimuthal modulation, but between those two values.
These figures illustrate the complexity of the problem and the difficulty to discriminate between the different model.

Appendix D: Fast Fourier Transform (FFT)

Fourier analysis are frequently used to probe spiral structures in galaxies (e.g. Puerari & Dottori 1992; Davis et al. 2012) and to study stellar bars (e.g. Combes & Sanders 1981; Combes et al. 1990; Garcia-Gómez et al. 2017). Harmonic expansion has been widely used to describe non-axisymmetry in velocity fields of galaxies (e.g. Franx et al. 1994; Schoenmakers et al. 1997; Wong et al. 2004; Trachternach et al. 2008), in particular with tools like kinemetry (Krajnović et al. 2006), which perform harmonic expansion of 2D maps of observed moments of the line-of-sight velocity distribution (surface brightness, velocity, velocity dispersion). The first harmonic decomposition of HI dispersion maps was performed on M33 by Chemin et al. (2020).

In this work, we use the following parametrisation of the line-of-sight velocity dispersion in order to investigate asymmetries of the dispersion maps:

$$\sigma_{obs}^2 = \sigma_0^2 + \sigma_1^2\cos(\theta - \phi_1) + \sigma_2^2\cos(2(\theta - \phi_2)) + \sigma_3^2\cos(3(\theta - \phi_3)) + \sigma_4^2\cos(4(\theta - \phi_4)) \quad \text{(D.1)}$$

This corresponds to the analytical expression of the FFT on σ^2 maps up to the fourth order. We use the dispersion squared, because it's easier to express the dispersion as a quadratic sum of the dispersion ellipsoid component(cf. Eq. A.10) rather than a square root of quadratic terms.

In practice, we decompose the galactic disk in a series of concentric rings (we detail this in Sect. 4.1). For each ring, we have N pixels with associated values of the velocity dispersion σ^2 and azimuth θ. To make asymmetries more visible, we subtract the mean value of σ^2 in the corresponding ring which just centers values of σ^2 on 0. This affects only the 0^{th} order term of the FFT and does not change the asymmetries in the ring. We sort the velocity dispersion values with increasing values of azimuth and apply the FFT, using the routine scipy.fftpack.fft, leading to a decomposition with N/2 terms. Ordered values of azimuth at a given radius vary linearly whatever the inclination value, if no value is missing. A ring-by-ring study of the entire sample showed that missing values represents most of the time less than 1% of the total number of pixel in a ring as we can see on Fig. D.1. We performed a similar study on WHISP data and observed that the result of the FFT is less robust when the number of missing values is important. Indeed, radius to radius, the phase is less continuous, we observe frequent phase jumps which are not physical. Even if it's not crucial here, we replaced the missing values by the average values in the ring, which is equivalent to adding zeros since we subtract by this mean value.

Because we only consider the five first terms of the FFT (from 0 to 4), each ring is described by 9 parameters : σ_0, σ_1, σ_2, σ_3, σ_4, ϕ_1, ϕ_2, ϕ_3, ϕ_4. We compute the FFT (i.e. Eq. D.1) on each radius for each galaxy, obtaining the radial variation of these parameters.

To study asymmetries of the dispersion maps, Chemin et al. (2020) used both a least square fit and the FFT methodology described above, on the σ rather than σ^2:

$$\sigma_{obs} = \sigma_0 + \sigma_1\cos(\theta - \phi_1) + \sigma_2\cos(2(\theta - \phi_2)) + \sigma_3\cos(3(\theta - \phi_3)) + \sigma_4\cos(4(\theta - \phi_4)) \quad \text{(D.2)}$$

Both methods turn out to give similar results for the four first orders. The main difference between the 2 methods is that the least square stops by construction at the order 4 while the FFT goes up to the order N/2 (N being the number of points) and is computationally faster. Another difference is that uncertainties

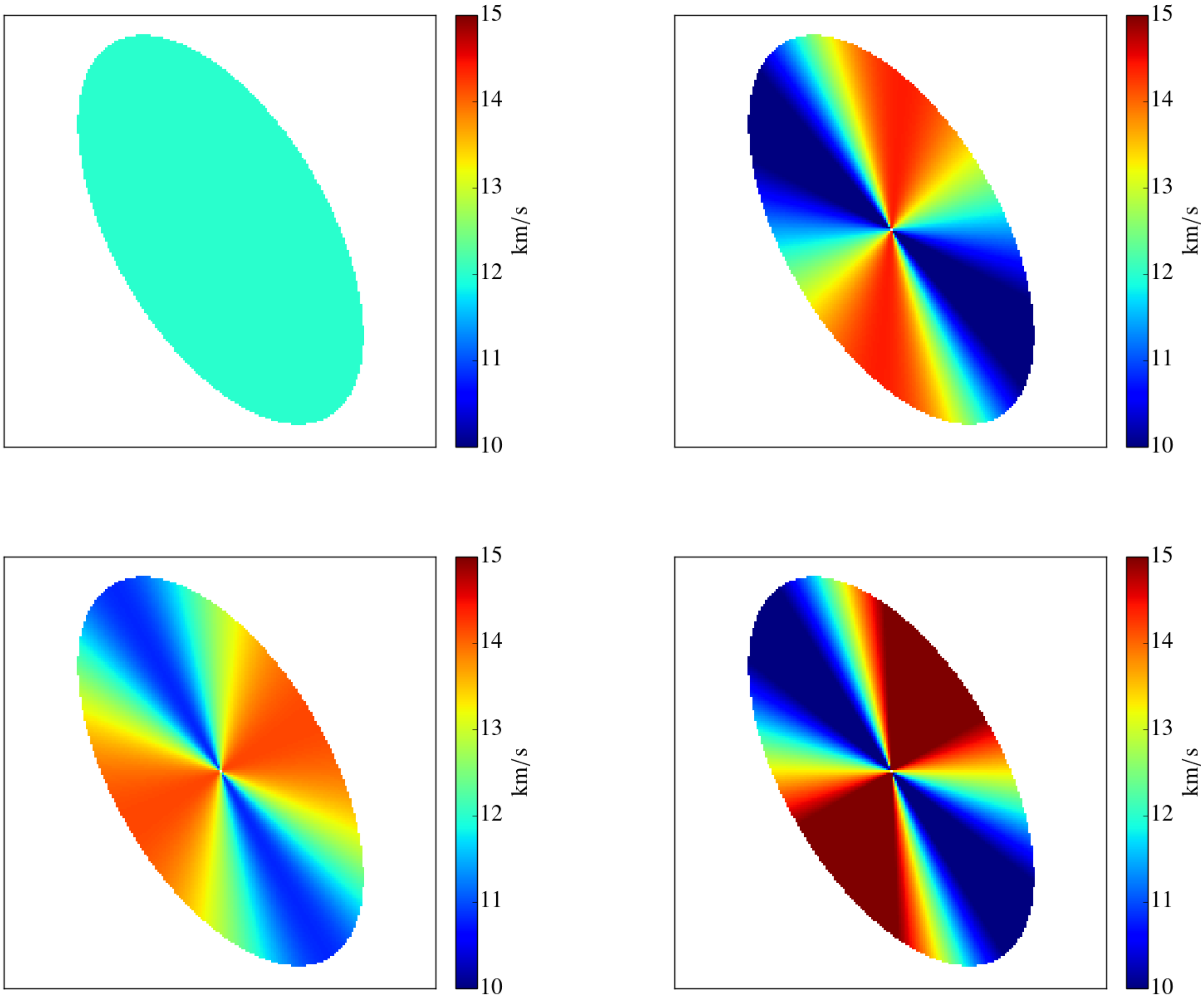

Fig. C.1. Mock $\sigma_{\rm los}$ galaxy to illustrate the different case : isotropic and symmetric (top left), isotropic and asymmetric (top right), anisotropic and symmetric (bottom left), anisotropic and asymmetric (bottom right).

are better handled in the least square fit. In addition, when some data is missing, the linearity between the index along the ring and the corresponding value of theta is partially lost, whereas the fit takes the sampling into account, as explained above. However, the work of Chemin et al. (2020) shows similar results between the two methods. In appendix **??** we show the residuals between the FFT containing all the orders minus the first 4 orders of the FFT and observe that higher orders are negligible.

Appendix E: Systematic biases: beam smearing effect

The first systematic we need to get rid of is the beam smearing. We already presented several times this issue in the introduction and in the study of the WHISP sample. Beam smearing impacts the various kinematic maps extracted from datacubes (flux map, velocity field and velocity dispersion), but in a different way. de Blok et al. (2008) showed that the beam smearing is not important on THINGS data, by comparing an observed rotation curve derived from a cube smoothed at the THINGS resolution with a modeled rotation curve created using galaxy's parameters. Both curves behave similarly with differences below 1km/s except around two positions where they observed a more significant variation, but only due to the unrealistic shape of their model. They concluded that the beam smearing was not a serious problem. Nevertheless, the beam smearing pattern is not unidirectional: to derive the rotation curve, we focus mainly on positions close to the major axis, where the rotational velocity dominates, rather than on the minor axis where we expect more radial motions. This excludes or reduces the importance of velocities along the minor axis where the beam smearing can be important in 2D maps due to the azimuthal variations of the line-of-sight velocities (cf. equation A.1), and due to the smaller apparent size of the minor axis. Therefore, using the rotation curve to evaluate the importance of beam smearing may minimize its impact. To avoid this, a 2D modeling is more appropriate, and in our case mandatory to determine the beam smearing component on velocity dispersion. Indeed, the beam smearing effect on the dispersion map is larger across the minor axis due to the strongest variation of $\cos(\theta)$ at a given rotation velocity. We thus need to take into account the 2D velocity field to compute the beam smearing induced on the dispersion map. Since we want to study azimuthal variations of the dispersion, we need to make

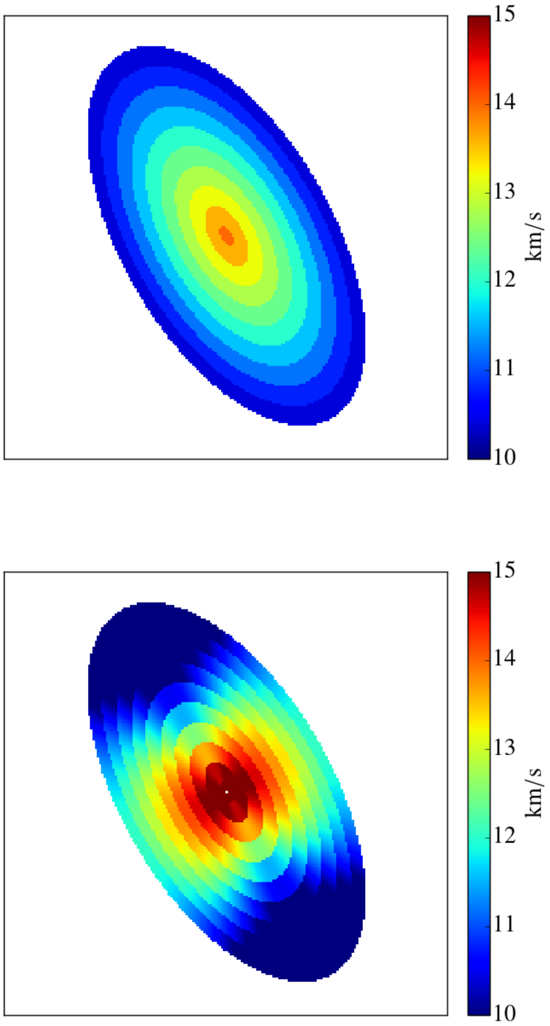

Fig. C.2. Mock $\sigma_{\rm los}$ galaxy to illustrate the different case : isotropic and symmetric (top left), isotropic and asymmetric (top right), anisotropic and symmetric (bottom left), anisotropic and asymmetric (bottom right).

a proper beam smearing correction. As we will show in the next sections, we observe a possible beam smearing remnant in the THINGS dispersion maps. For the moment let's focus on the methodology used for the modeling of the beam smearing effect.

To model the beam smearing effect on our data, we use the tool MocKing (Modeling Kinematics of Galaxies [3]) based on an analytical formula presented in Epinat et al. (2010) who derived the observed dispersion velocity in a galaxy in terms of the real dispersion and an instrumental dispersion (Eq. E.1).

$$\sigma_1^2 = \sigma^2 + \frac{\int_{pix}\left[\overline{V}^2 M\right] \otimes_{xy} \mathrm{PSF}_{xy} dxy}{M_1} - \left(\frac{\int_{pix}\left[\overline{V} M\right] \otimes_{xy} \mathrm{PSF}_{xy} dxy}{M_1}\right)^2 \tag{E.1}$$

with σ the local velocity dispersion, assumed constant to derive this equation. For the complete derivation of this equation, we refer the reader to the Appendices A3 and A4 of their paper. Using an appropriate velocity model, one can subtract quadratically the dispersion induced by the unresolved velocity gradients in the dispersion maps. MocKing handles velocity field and flux map at high resolution to compute this instrumental dispersion. It allows to define your own PSF, from a model or from a 2D map directly. MocKing also allows to compute velocity field from different rotation curve model already prepared, making the code very easy to adapt and use. We apply this method using two different approaches.

As we mentioned in section **??**, THINGS targets were selected from the SINGS survey. Thus the THINGS survey also has a $H\alpha$ follow-up which allows us to have the kinematic of the ionised gas at really high resolution (Daigle et al. 2006; Dicaire et al. 2008). Thus, to model the beam smearing effect for our sample, we can use the data from SINGS or directly use the THINGS data. As we mentioned before, a flux map and a velocity field are needed to estimate the beam smearing contribution in the data. Using THINGS data is then really straightforward since we have those maps as well as the properties of the radio beam, given in Table E.1. Using SINGS data for this purpose is more complex because we first need to compute a $H\alpha$ velocity field. Indeed, due to the holes in the observed velocity map of the SINGS data (see Fig. E.1), we can't use them directly, and then we have to create a model map. We fit a Courteau model on the

[3] https://gitlab.lam.fr/bepinat/MocKinG

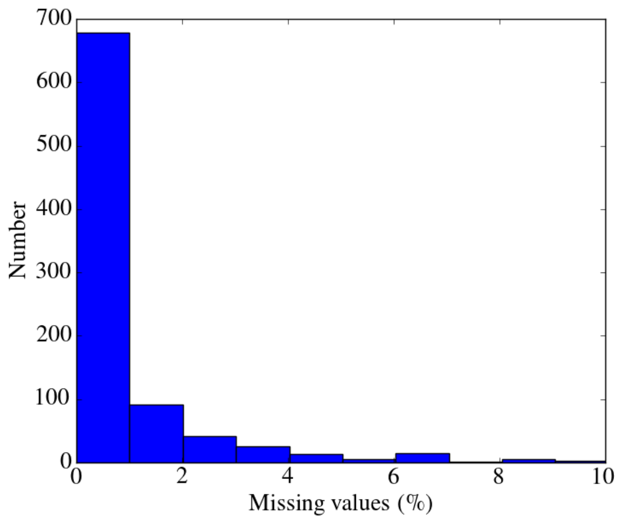

Fig. D.1. Fraction of missing values in each of the 883 rings of the 15 THINGS galaxies.

rotation velocities (Courteau 1997), and compute the 2D velocity field from this model, assuming the $H\alpha$ geometrical parameters listed in Table E.2 are also valid for the HI gas, which may not be the case, in particular at large radii. A comparison of inclinations between optical and HI data (Table E.2 and Table E.1) show that on average the difference of inclination is less than 5 degrees. The most striking issue comes from galaxy NGC 925 for which HI inclination is 66 degrees, compared to the optical one which is 50 degrees. A modelisation using SINGS data would underestimate the beam smearing. Due to the higher resolution of the $H\alpha$ data, we have a better estimation of the correction in the inner part of the galaxy. The main drawback is that the 2D model is computed from a 1D rotation curve, and then does not contain any information on possible azimuthal deviations from axisymmetric rotation. Signatures like spiral arms and bars also induce beam smearing and are not taken into account with this method.

Fig E.1 shows the difference between the observed radial velocity map from THINGS, the one from SINGS and the one modeled with SINGS for the galaxy NGC5055. We can observe that both maps are relatively close from each other on large scales, with a velocity model from $H\alpha$ data which is similar to the HI map from THINGS. Nevertheless, this galaxy seems to have a warp in HI. Our $H\alpha$ velocity model is constructed in excluding the possibility to have a warp, i.e. with fixed position angle and inclination for reasons explained in Epinat et al. (2008b), and thus in the outer part of the galaxy, we observe a discrepancy in the velocity fields. This is also due to the fact that the Courteau model at large radius is an extrapolation of the $H\alpha$ velocity field in the inner part. This is not crucial, because the beam smearing effect is dominant in the center, where both models are in agreement, and the beam smearing corrections in the outer part are negligible (see Fig. E.2). Since the HI beam has a really complex shape, and we do not have any beam map from THINGS data, we approximate the beam by a 2D Gaussian function, created using parameters BMIN, BMAJ and BPA, which are respectively the minor and major axis and the orientation of the beam, showed in Table E.1. Finally, the beam smearing modeling is shown in Fig E.2 for NGC5055. A central peak and a X-shape pattern are the dominant features present in both maps. Fine structures are only present in the beam smearing map inferred from the THINGS velocity field and correspond to small scale deviations to rotation. In velocity fields, the impact of beam smearing is dominant in the center, which is not necessary the case for the dispersion. The amplitude of the central peak and the X-shape is slightly higher using SINGS data, due to the better resolution, but without a significant difference. Thus, we decided to use the model derived using THINGS data because we can account for local features at large radii and still having a robust description in the inner part of the galaxy.

Appendix F: Systematic biases – noise in the FFT

Before applying FFT on real data, we need to understand in a first step how evolves the results of the FFT with the noise in the data, and to which limits we can recover the real signal. In other words, if the uncertainties on the dispersion are greater than the true signal, can we recover the true signal, and with which accuracy ? To do so, we create a toy model from the equation D.1, with phases $\phi_k = 0$ and in adding noise. The noise we add corresponds roughly to the uncertainties on the instrumental resolution that we will first estimate. The uncertainties on σ^2 are linked to the amplitude of the mean value σ_0 of the model and the intrinsic dispersion $d\sigma$ following the differential :

$$d(\sigma^2) = 2 \times \sigma_0 \times d\sigma \tag{F.1}$$

in which $\sigma = \sigma_0$ because in a ring all higher orders are on average zero and then $<\sigma>=\sigma_0$. Since we do not have uncertainty maps due to the processing techniques (moments method) on THINGS data, $d\sigma$ is not known precisely. By inspecting residual maps from WHISP, we estimate that the uncertainty on the dispersion velocity is typically $d\sigma = 1$ km/s. Thus, we define the noise δ on σ^2_{obs}, as a Gaussian distribution centered on 0 and with a standard deviation of $\sigma_{Gauss} = d\sigma^2$.

Finally, the equation of the toy model is given by :

$$\sigma^2_{obs} = \sigma^2_0 + \sigma^2_1 \cos(\theta) + \sigma^2_2 \cos(2\theta) + \sigma^2_3 \cos(3\theta) + \sigma^2_4 \cos(4\theta) + \delta \tag{F.2}$$

With δ a random value in the noise distribution. In order to investigate the impact of the noise on the uncertainty of measured amplitudes $\sigma_{out,k}$, we first set the amplitude of one order $\sigma_{in,k}$ to 0, 1, 2 and 4 km s^{-1}, all other orders having their amplitude set to zero, except order zero. For each value of the amplitude $\sigma_{in,k}$, we realise $M = 1000$ iterations of the noise distribution and evaluate the FFT coefficients to measure the mean uncertainty on $\sigma_{out,k}$. We show the results in Fig. F.1, with two values adopted for both σ_0 and σ_{Gauss}. This study clearly shows that the uncertainties do not depend on the order, nor on the amplitude of $\sigma_{in,k}$, and then, as expected, these uncertainties are proportional to σ_0. The difference between input and output amplitudes is larger when the amplitude is low, because amplitudes in the FFT decomposition cannot be negative.

We then create toy models with $\sigma_{in,k} = 0$ except for $k = 0$, and input a noise δ by spanning different values for $d\sigma$, in order to find a function that describes the uncertainties depending on the main parameters : σ_0, $d\sigma$ and N the number of points in the FFT. Indeed, N varies from one ring to another and from one galaxy to another. We do 1000 iterations of the FFT and analyse the amplitudes for orders 1 to 4, which are 0 in our model (see Fig. F.2). By varying parameters defined before, we observe that amplitudes of order $\sigma_k, k = 1, ..., 4$ vary with $\sqrt{2\sigma_0 d\sigma}$ and with $N^{-1/4}$, as expected, since the noise is supposed to vary as $N^{-1/2}$ on σ^2_k, and because we provide here the result on σ_k. That gives

Galaxy name	D Mpc	V_{sys} km/s	Incl deg	PA deg	B_{maj} arcsec	B_{min} arcsec	B_{pa} deg
NGC925	9.2	546.3	66.0	286.6	5.9	5.7	31
NGC2403	3.2	132.8	62.9	123.7	8.8	7.7	25
NGC2841	14.1	633.7	73.7	152.6	11.1	9.4	-12
NGC2903	8.9	555.6	65.2	204.3	15.3	13.3	-51
NGC2976	3.6	1.1	64.5	334.5	7.4	6.4	72
NGC3031	3.6	-39.8	59.0	330.2	12.9	12.4	80
NGC3198	13.8	660.7	71.5	215.0	13.0	11.6	-59
NGC3521	10.7	803.5	72.7	339.8	14.1	11.2	-62
NGC3621	6.6	728.5	64.7	345.4	15.9	10.2	4
NGC3627	9.3	708.2	61.8	173.0	10.6	8.9	-48
NGC4736	4.7	306.7	41.4	296.1	10.2	9.1	-23
NGC5055	10.1	496.8	59.0	101.8	10.1	8.7	-40
NGC6946	5.9	43.7	32.6	242.7	6.0	5.6	7
NGC7331	14.7	818.3	75.8	167.7	6.1	5.6	34
NGC7793	3.9	226.2	49.6	290.1	15.6	10.9	11

Table E.1. Beam parameters for the THINGS data

Galaxy name	α(J2000) (hh mm ss)	δ(J2000 (dd mm ss)	V_{sys} km/s	PA deg	Incl deg	V_{court} km/s	r_{court} arcsec	index
NGC0925	02 27 16.8	+33 34 41	554	105	50	132	187.0	5.13
NGC2403	07 36 54.5	+65 35 58	132	125	60	10000	0.3	0.10
NGC2841	09 22 02.6	+50 58 35	638	150	70	327	27.4	2.04
NGC2903	09 32 10.1	+21 30 04	556	212	64	197	79.2	299.70
NGC2976	09 47 15.4	+67 54 59	3	323.5	70.2	66	84.5	243.80
NGC3031	09 55 33.2	+69 03 55	-34	332.9	62.4	279	89.3	1.06
NGC3198	10 19 54.9	+45 33 09	660	33.9	69.8	170	50.5	1.54
NGC3521	11 05 48.6	-00 02 09	805	342	66.7	225	22.5	3.24
NGC3621	11 18 16.3	-32 48 45	727	342.5	65.2	10000	2.7	0.12
NGC3627	11 20 15.0	+12 59 30	727	170	65	1440	0.2	0.17
NGC4736	12 50 53.0	+41 07 14	308	292	36	169	0.0	1.88
NGC5055	13 15 49.3	+42 01 45	504	98.0	63	225	3.6	0.79
NGC6946	20 34 52.0	+60 09 15	46	239	38.4	223	7.7	0.50
NGC7331	22 37 04.1	+34 24 56	816	165	78.1	231	15.7	120.0
NGC7793	23 57 49.8	-32 35 28	230	277	47	287	39.9	0.42

Table E.2. SINGS parameters to model the beam smearing effect

us the following equation for the noise :

$$d\sigma_{out,k}(\sigma_0, d\sigma, N) = \frac{\sqrt{2\sigma_0 d\sigma}}{0.75N^{1/4}} \tag{F.3}$$

The coefficient 0.75 was necessary to scale correctly the curves.

This formula (Eq. F.3) allows us to have a robust estimation of the noise in a ring containing N pixels and with an average dispersion σ_0.

References

Abraham, R. G., Tanvir, N. R., Santiago, B. X., et al. 1996, MNRAS, 279, L47
Bershady, M. A., Verheijen, M. A. W., Swaters, R. A., et al. 2010, ApJ, 716, 198
Chemin, L., Braine, J., Combes, F., Kam, Z. S., & Carignan, C. 2020, A&A, 639, A145
Combes, F. & Becquaert, J. F. 1997, A&A, 326, 554
Combes, F., Debbasch, F., Friedli, D., & Pfenniger, D. 1990, A&A, 233, 82
Combes, F. & Sanders, R. H. 1981, A&A, 96, 164
Conselice, C. J., Bershady, M. A., & Jangren, A. 2000, ApJ, 529, 886
Courteau, S. 1997, AJ, 114, 2402
Daigle, O., Carignan, C., Amram, P., et al. 2006, MNRAS, 367, 469
Dalcanton, J. J. & Stilp, A. M. 2010, ApJ, 721, 547
Davis, B. L., Berrier, J. C., Shields, D. W., et al. 2012, ApJS, 199, 33
de Blok, W. J. G., Walter, F., Brinks, E., et al. 2008, AJ, 136, 2648
Di Teodoro, E. M. & Fraternali, F. 2014, A&A, 567, A68
Dicaire, I., Carignan, C., Amram, P., et al. 2008, MNRAS, 385, 553
Epinat, B., Amram, P., Balkowski, C., & Marcelin, M. 2010, MNRAS, 401, 2113
Epinat, B., Amram, P., & Marcelin, M. 2008a, MNRAS, 390, 466
Epinat, B., Amram, P., Marcelin, M., et al. 2008b, MNRAS, 388, 500
Field, G. B., Goldsmith, D. W., & Habing, H. J. 1969, ApJ, 155, L149
Franx, M., van Gorkom, J. H., & de Zeeuw, T. 1994, ApJ, 436, 642
Garcia-Gómez, C., Athanassoula, E., Barberà, C., & Bosma, A. 2017, A&A, 601, A132
García-Ruiz, I., Sancisi, R., & Kuijken, K. 2002, A&A, 394, 769
Garrido, O., Marcelin, M., & Amram, P. 2004, MNRAS, 349, 225
Garrido, O., Marcelin, M., Amram, P., et al. 2005, MNRAS, 362, 127
Garrido, O., Marcelin, M., Amram, P., & Boissin, O. 2003, A&A, 399, 51
Garrido, O., Marcelin, M., Amram, P., & Boulesteix, J. 2002, A&A, 387, 821
Governato, F., Zolotov, A., Pontzen, A., et al. 2012, MNRAS, 422, 1231
Ianjamasimanana, R., de Blok, W. J. G., Walter, F., & Heald, G. H. 2012, AJ, 144, 96
Ianjamasimanana, R., de Blok, W. J. G., Walter, F., et al. 2015, AJ, 150, 47
Kamphuis, J. J., Sijbring, D., & van Albada, T. S. 1996, A&AS, 116, 15
Kennicutt, Robert C., J., Armus, L., Bendo, G., et al. 2003, PASP, 115, 928
Korsaga, M., Epinat, B., Amram, P., et al. 2019, MNRAS, 490, 2977
Koyama, H. & Ostriker, E. C. 2009, ApJ, 693, 1346
Krajnović, D., Cappellari, M., de Zeeuw, P. T., & Copin, Y. 2006, MNRAS, 366, 787
Kuijken, K. & Gilmore, G. 1991, ApJ, 367, L9
Leroy, A. K., Walter, F., Brinks, E., et al. 2008, AJ, 136, 2782
Martinsson, T. P. K., Verheijen, M. A. W., Westfall, K. B., et al. 2013, A&A, 557, A130
Murugeshan, C., Kilborn, V., Jarrett, T., et al. 2020, MNRAS, 496, 2516
Nilson, P. 1973, Uppsala general catalogue of galaxies

Noordermeer, E., van der Hulst, J. M., Sancisi, R., Swaters, R. A., & van Albada, T. S. 2005, A&A, 442, 137
Oh, S.-H., Brook, C., Governato, F., et al. 2011a, AJ, 142, 24
Oh, S.-H., de Blok, W. J. G., Brinks, E., Walter, F., & Kennicutt, Robert C., J. 2011b, AJ, 141, 193
Puerari, I. & Dottori, H. A. 1992, A&AS, 93, 469
Saha, K., Pfenniger, D., & Taam, R. E. 2013, ApJ, 764, 123
Schoenmakers, R. H. M., Franx, M., & de Zeeuw, P. T. 1997, MNRAS, 292, 349
Shapiro, K. L., Gerssen, J., & van der Marel, R. P. 2003, AJ, 126, 2707
Spano, M., Marcelin, M., Amram, P., et al. 2008, MNRAS, 383, 297
Swaters, R. A., Sancisi, R., van Albada, T. S., & van der Hulst, J. M. 2009, A&A, 493, 871
Swaters, R. A., van Albada, T. S., van der Hulst, J. M., & Sancisi, R. 2002, A&A, 390, 829
Tamburro, D., Rix, H. W., Leroy, A. K., et al. 2009, AJ, 137, 4424
Trachternach, C., de Blok, W. J. G., Walter, F., Brinks, E., & Kennicutt, R. C., J. 2008, AJ, 136, 2720
van der Hulst, J. M., van Albada, T. S., & Sancisi, R. 2001, in Astronomical Society of the Pacific Conference Series, Vol. 240, Gas and Galaxy Evolution, ed. J. E. Hibbard, M. Rupen, & J. H. van Gorkom, 451
van Eymeren, J., Jütte, E., Jog, C. J., Stein, Y., & Dettmar, R. J. 2011a, A&A, 530, A29
van Eymeren, J., Jütte, E., Jog, C. J., Stein, Y., & Dettmar, R. J. 2011b, A&A, 530, A30
Walter, F., Brinks, E., de Blok, W. J. G., et al. 2008, AJ, 136, 2563
Wolfire, M. G., Hollenbach, D., McKee, C. F., Tielens, A. G. G. M., & Bakes, E. L. O. 1995, ApJ, 443, 152
Wong, T., Blitz, L., & Bosma, A. 2004, ApJ, 605, 183
Yim, K. & van der Hulst, J. M. 2016, MNRAS, 463, 2092

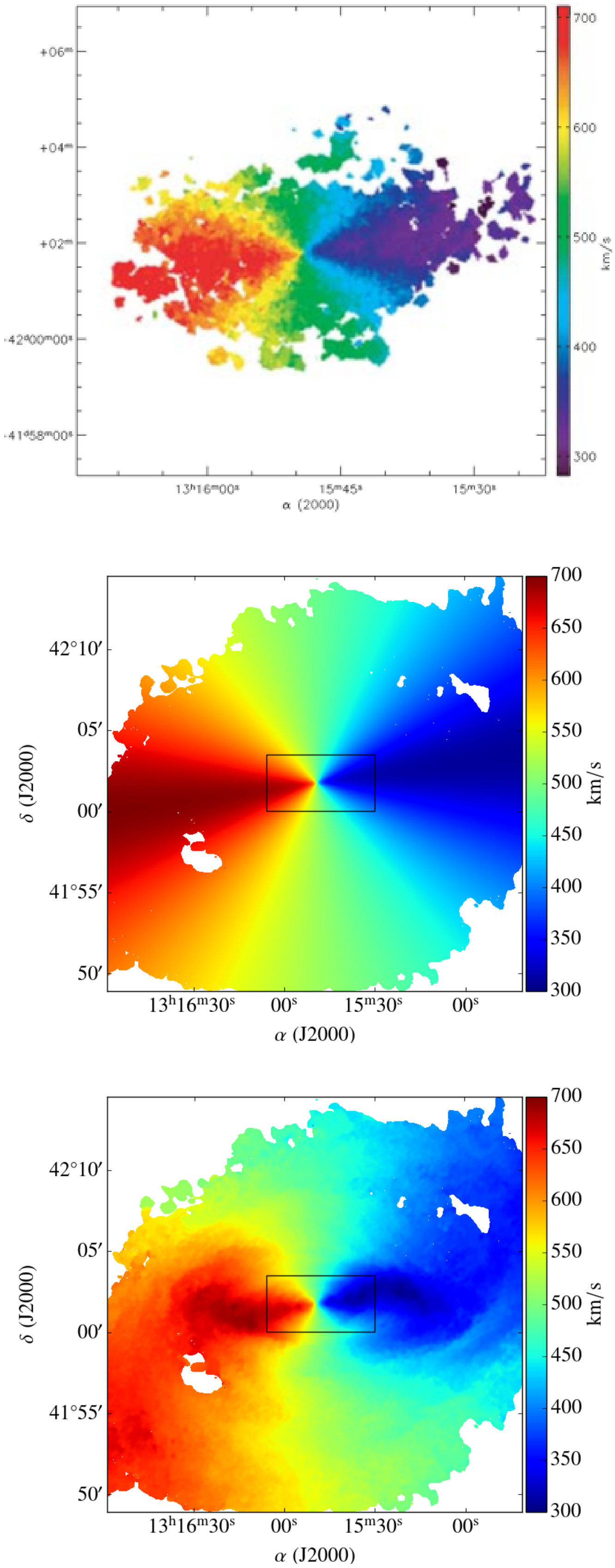

Fig. E.1. Observed radial velocity map of NGC5055 from SINGS (Fig. from Daigle et al. 2006, top panel), radial velocity map modeled using Courteau rotation curves from SINGS data (middle panel), and radial velocity map observed with THINGS (bottom panel). Black rectangle on the middle and bottom panel indicates the size of the galaxy in $H\alpha$.

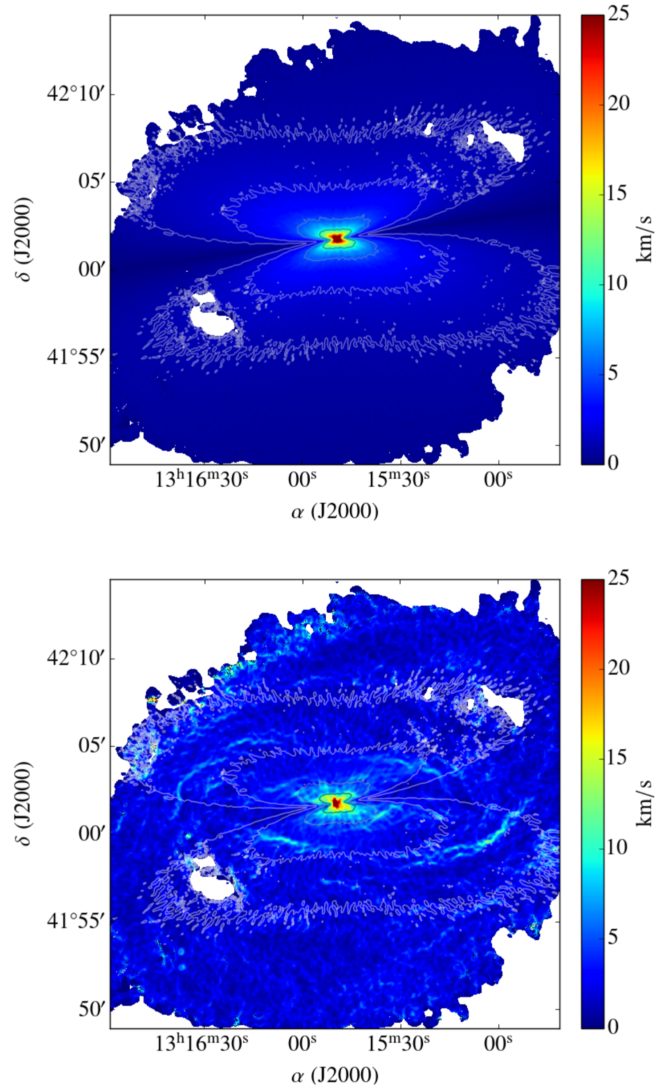

Fig. E.2. Beam smearing modeling using SINGS (top panel) and THINGS data of NGC5055. We overplot contours at 1-2-5-10 km/s in gray to highlight the fast decrease of the beam smearing effect in the outer part of the galaxy.

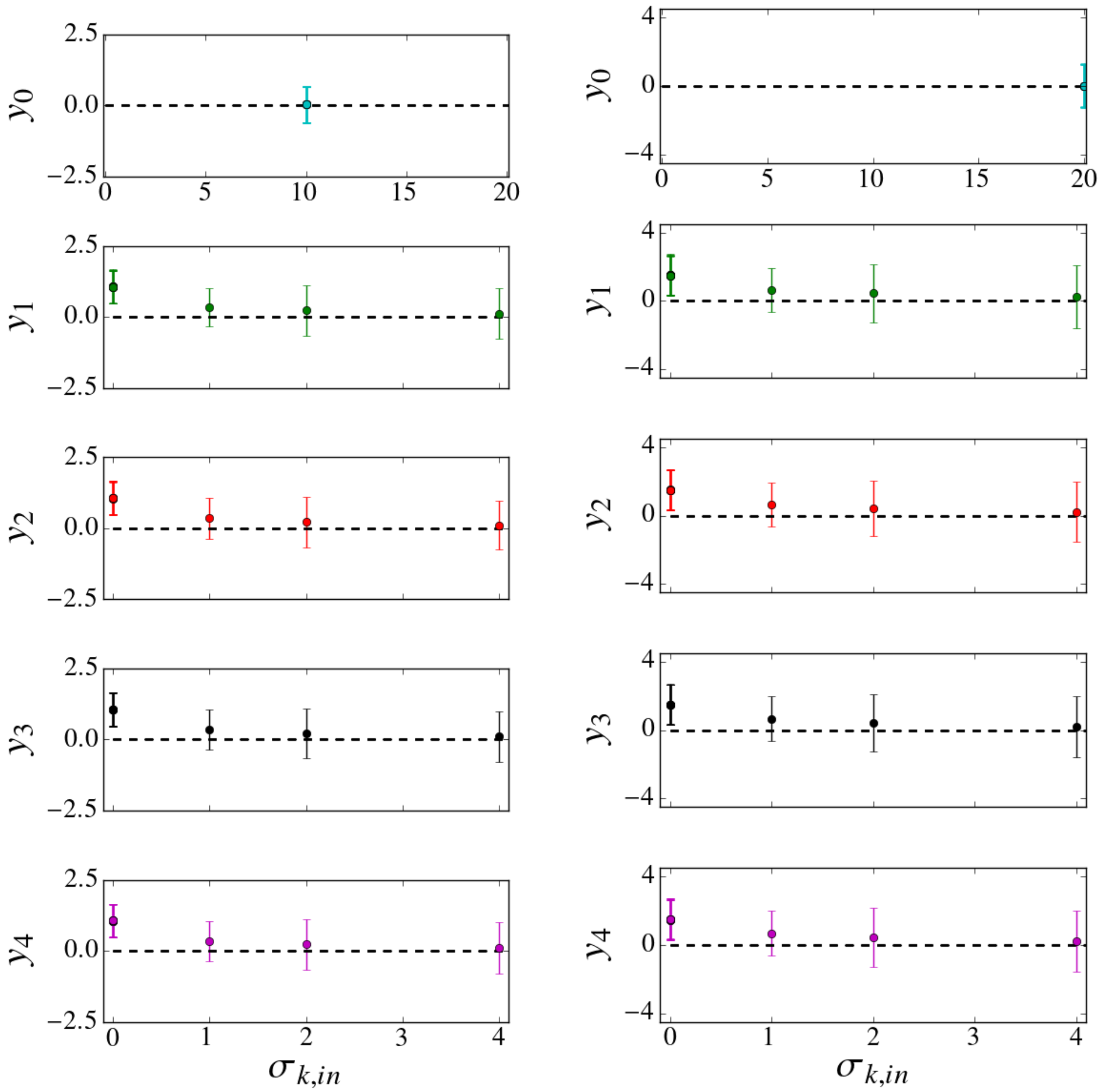

Fig. F.1. Mean difference between the input $\sigma_{k,in}$ of the toy model and the FFT output $\sigma_{k,out}$ following the relation $y_k = \sqrt{\frac{\sum(\sigma_{k,out}-\sigma_{k,in})^2}{M}}$, where M is the number of iterations of the noise, as a function of $\sigma_{k,in}$. Errorbars are the 1σ uncertainties of the distributions. Each quadrant shows an order of the FFT. Left/right column represents models with $\sigma_0 = 10/20$ km s^{-1} and $\sigma_{Gauss} = 20/40$ km s^{-1}.

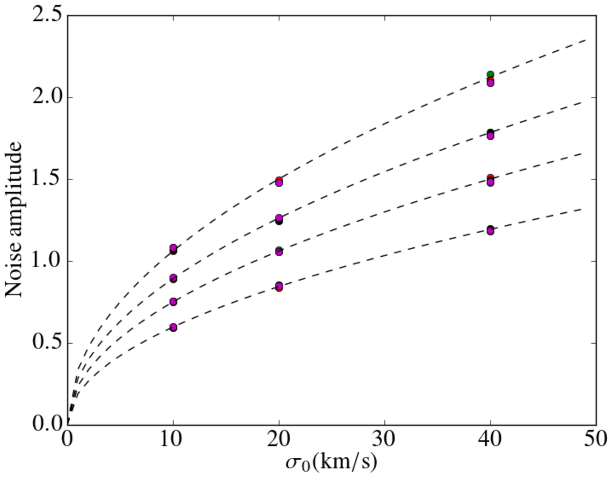

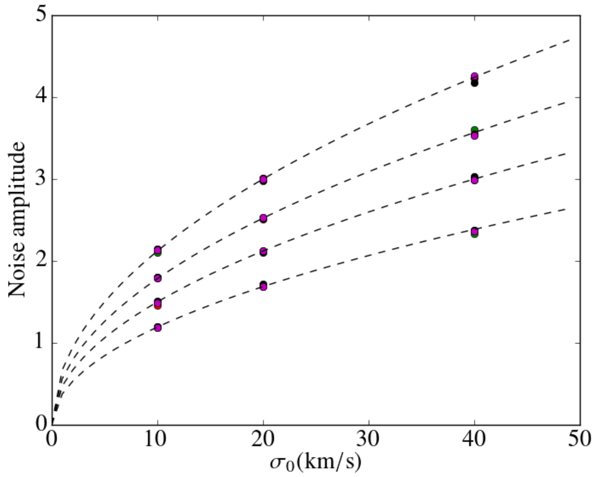

Fig. F.2. Noise on the dispersion amplitude for orders 1 to 4 of the FFT vs σ_0 for two distinct values of $d\sigma$ (top panel : $d\sigma$ = 1 km/s, bottom panel : $d\sigma$ = 4 km/s) and various number of points in the FFT N. The dashed lines correspond to Eq. F.3, each curve corresponding to a different value of N (from top to bottom : 1000, 2000, 4000 and 10000). Dots corresponds to different orders (order 1 : green, order 2 : red, order 3 : black, order 4 : magenta). The similar behaviour of orders leads to superposed points.

B. Parameters of the WHISP sample presented in the thesis

Galaxy name	α(J2000) (hh mm ss)	δ(J2000) (dd mm ss)	Type	V_{sys} km/s	m_B mag	M_B mag	log(D_{25}) log(0.1')	Incl deg
UGC00079	00 09 04.4	+25 37 06	Sc	4338	15.66	-18.82	0.94	43.7
UGC00089	00 09 53.3	+25 55 25	Sa	4561	12.84	-21.45	1.19	40.5
UGC00094	00 10 25.9	+25 49 54	Sab	4592	13.84	-20.77	1.05	49.9
UGC00192	00 20 23.1	+59 17 35	IB	-345	11.78	0.00	1.83	31.1
UGC00232	00 24 38.7	+33 15 22	Sa	4841	14.64	-20.09	1.02	54.7
UGC00485	00 47 08.3	+30 20 27	Sc	5247	14.77	-21.36	1.36	90.0
UGC00499	00 48 47.1	+31 57 25	S0-a	4526	14.24	-20.26	1.07	68.0
UGC00508	00 49 47.8	+32 16 39	Sab	4653	12.65	-21.91	1.45	15.9
UGC00528	00 52 04.3	+47 33 02	SABb	639	11.49	-19.55	1.37	12.8
UGC00622	01 00 28.1	+47 59 43	Sc	2715	14.16	-19.86	1.07	54.9
UGC00623	01 00 32.5	+30 47 50	Sa	4840	14.93	-20.12	1.09	85.0
UGC00624	01 00 36.5	+30 40 07	Sab	4779	13.56	-21.53	1.24	75.6
UGC00625	01 00 55.4	+47 40 55	Sbc	2618	13.60	-20.45	1.41	79.7
UGC00655	01 04 01.4	+41 50 30	Sm	828	15.08	-15.99	1.40	0.0
UGC00690	01 07 32.8	+39 24 00	SBc	5868	13.71	-21.52	1.23	47.3
UGC00718	01 09 27.0	+35 43 04	E-S0	-52	11.19	-16.43	1.53	10.4
UGC00731	01 10 44.0	+49 36 07	I	641	15.13	-15.92	1.27	21.1
UGC00798	01 15 11.8	+30 11 41	Sa	4898	14.52	-20.38	1.00	69.2
UGC01013	01 26 21.8	+34 42 10	Sb	5189	13.22	-21.54	1.47	62.8
UGC01249	01 47 29.9	+27 19 59	SBm	338	12.08	-18.32	1.81	90.0
UGC01256	01 47 53.9	+27 25 55	SBc	426	11.41	-18.94	1.85	69.6
UGC01281	01 49 31.6	+32 35 20	Sd	143	13.08	-16.94	1.71	90.0
UGC01437	01 57 42.2	+35 54 57	SABc	4902	13.07	-21.98	1.14	52.5
UGC01501	02 01 16.9	+28 50 14	SBd	189	12.22	-17.76	1.62	90.0
UGC01541	02 03 27.9	+38 07 01	SABa	5663	13.58	-21.41	1.08	30.3
UGC01550	02 03 45.0	+38 15 32	Sc	5762	13.94	-21.87	1.44	84.8
UGC01633	02 08 44.5	+38 46 38	Sbc	4244	13.18	-21.73	1.34	74.0
UGC01810	02 21 28.7	+39 22 32	SABb	7559	13.61	-22.56	1.24	74.4
UGC01856	02 24 31.6	+31 36 55	Scd	4803	14.79	-21.19	1.33	90.0
UGC01886	02 26 00.5	+39 28 15	SABb	4853	13.10	-21.72	0.72	47.1

UGC01913	02 27 16.9	+33 34 44	Scd	553	10.59	-20.05	2.03	58.7
UGC01993	02 31 40.0	+39 22 42	Sb	8022	14.20	-22.24	1.25	90.0
UGC02023	02 33 18.1	+33 29 27	I	603	13.97	-16.40	1.41	15.0
UGC02034	02 33 42.9	+40 31 43	IAB	578	13.69	-16.76	1.48	36.8
UGC02045	02 34 13.4	+29 18 40	Sab	1518	12.16	-19.66	1.52	65.8
UGC02053	02 34 29.2	+29 44 59	IB	1026	15.21	-16.77	1.27	66.3
UGC02065	02 35 22.5	+37 29 09	Sm	3890	14.56	-19.60	0.95	38.0
UGC02067	02 35 29.4	+37 31 08	Sab	3884	14.71	-20.01	1.24	90.0
UGC02069	02 35 37.3	+37 38 20	Scd	3774	13.13	-21.25	1.09	56.0
UGC02080	02 36 27.8	+38 58 08	SABc	903	11.89	-19.34	1.63	19.7
UGC02082	02 36 16.1	+25 25 26	Sc	707	13.70	-19.09	1.72	87.6
UGC02141	02 39 15.0	+30 09 06	S0-a	986	12.99	-18.78	1.32	68.0
UGC02183	02 42 48.3	+28 34 27	Sa	1542	13.40	-19.78	1.27	46.7
UGC02193	02 43 30.1	+37 20 28	Sc	518	11.96	-18.89	1.39	58.5
UGC02455	02 59 42.5	+25 14 19	IB	373	12.07	-18.56	1.47	42.4
UGC02459	03 00 36.8	+49 02 38	Sd	2464	18.00	-18.32	1.37	90.0
UGC02487	03 01 42.4	+35 12 20	S0	4950	13.46	-21.71	1.26	49.0
UGC02491	03 01 53.8	+35 44 00	Sa	4872	14.69	-20.80	1.13	60.5
UGC02503	03 03 34.8	+46 23 10	Sb	2387	12.35	-21.78	1.52	57.2
UGC02800	03 40 02.4	+71 24 21	I	1177	15.78	-18.62	1.37	72.6
UGC02855	03 48 20.7	+70 07 58	SABc	1202	14.45	-20.02	1.55	68.2
UGC02866	03 50 14.8	+70 05 41	Sc	1280	15.45	-18.75	1.02	36.7
UGC02916	04 02 33.8	+71 42 21	Sab	4519	14.83	-20.62	1.12	25.4
UGC02941	04 03 44.0	+22 09 32	SBb	6260	14.60	-21.86	0.97	52.5
UGC02953	04 07 46.9	+69 48 45	Sb	895	11.56	-21.90	1.60	22.4
UGC03013	04 23 27.1	+75 17 44	SBb	2464	12.50	-20.32	1.26	58.3
UGC03137	04 46 13.6	+76 25 06	Sbc	992	15.16	-18.17	1.58	90.0
UGC03205	04 56 14.8	+30 03 08	Sab	3589	16.00	-20.47	1.12	72.9
UGC03273	05 17 44.4	+53 33 05	SABm	616	14.95	-18.68	1.40	90.0
UGC03326	05 39 37.1	+77 18 45	Sc	4106	15.45	-20.98	1.52	90.0
UGC03334	05 42 04.8	+69 22 43	SABb	3935	11.79	-22.92	1.64	47.0
UGC03344	05 44 56.6	+69 09 34	SABb	4282	14.63	-20.33	1.13	54.4
UGC03354	05 47 18.2	+56 06 45	Sab	3088	15.21	-19.54	1.22	78.6
UGC03371	05 56 36.5	+75 18 59	I	815	14.39	-18.08	1.58	46.1
UGC03382	05 59 47.7	+62 09 29	Sa	4497	14.73	-20.26	1.10	20.6
UGC03384	06 01 37.2	+73 07 01	Sm	1089	15.64	-16.90	0.62	44.9
UGC03407	06 09 08.1	+42 05 07	Sa	3606	14.54	-20.10	1.05	48.3
UGC03422	06 15 08.1	+71 08 12	SABb	4060	14.40	-20.95	1.26	66.2
UGC03426	06 15 36.4	+71 02 15	S0	4009	13.95	-20.86	1.23	35.7
UGC03546	06 50 08.7	+60 50 45	Sa	1840	12.62	-20.29	1.36	57.4
UGC03574	06 53 10.4	+57 10 40	Sc	1441	13.82	-17.81	1.17	21.9
UGC03580	06 55 30.8	+69 33 47	SABa	1206	12.79	-19.61	1.33	62.2
UGC03642	07 04 20.3	+64 01 13	S0	4494	13.31	-21.14	1.18	39.0

UGC03660	07 06 34.8	+63 50 56	Sa	4268	13.51	-21.05	1.25	63.8
UGC03685	07 09 05.9	+61 35 44	Sb	1796	13.00	-19.88	1.28	55.4
UGC03698	07 09 18.3	+44 22 48	I	423	15.73	-15.34	0.98	57.4
UGC03711	07 10 13.6	+44 27 26	IB	436	13.02	-17.87	1.34	47.7
UGC03734	07 12 28.6	+47 10 01	SABb	970	12.89	-18.67	1.32	26.0
UGC03740	07 27 12.9	+85 45 05	SABc	2416	11.99	-21.61	1.35	39.8
UGC03759	07 16 03.9	+64 42 39	Sb	4424	13.31	-21.60	1.22	45.4
UGC03817	07 22 44.5	+45 06 31	I	437	16.48	-14.16	1.24	70.8
UGC03826	07 24 27.9	+61 41 38	SABc	1733	14.86	-17.81	1.51	29.8
UGC03851	07 28 54.0	+69 12 54	IB	100	11.57	-17.06	1.64	90.0
UGC03965	07 41 18.1	+34 13 56	Sab	4641	15.35	-19.14	0.95	24.1
UGC03966	07 41 25.9	+40 06 43	I	362	14.44	-15.91	1.23	19.9
UGC03992	07 53 34.7	+84 37 07	Sab	0	16.00	0.00	1.14	0.0
UGC03993	07 55 43.8	+84 55 35	S0	4365	14.34	-20.14	0.92	22.3
UGC04036	07 51 54.7	+73 00 57	SABb	3465	13.00	-20.14	1.30	24.5
UGC04165	08 01 53.2	+50 44 14	Scd	500	12.22	-17.94	1.39	18.7
UGC04173	08 07 11.0	+80 07 34	I	860	15.68	-16.15	0.80	75.8
UGC04256	08 10 15.2	+33 57 24	SABc	5248	13.06	-21.79	1.22	36.0
UGC04273	08 12 57.9	+36 15 17	Sb	2471	13.08	-20.24	1.38	66.4
UGC04274	08 13 14.7	+45 59 25	SBm	452	12.27	-17.20	1.32	20.9
UGC04278	08 13 58.9	+45 44 31	SBc	558	12.45	-19.40	1.46	90.0
UGC04284	08 14 40.1	+49 03 42	SABc	547	12.25	-18.80	1.48	59.5
UGC04305	08 19 04.3	+70 43 18	I	158	11.16	-16.97	1.90	51.4
UGC04325	08 19 20.5	+50 00 35	SABm	506	12.69	-17.98	1.48	68.0
UGC04458	08 32 11.3	+22 33 38	Sa	4757	13.19	-21.30	1.19	34.4
UGC04483	08 37 03.4	+69 46 35	I	157	15.13	-13.23	1.05	67.4
UGC04499	08 37 41.5	+51 39 09	Sd	687	15.36	-15.62	1.28	81.2
UGC04543	08 43 21.8	+45 44 10	SABd	1960	15.08	-17.69	1.10	45.3
UGC04605	08 49 11.8	+60 13 16	SBab	1340	12.67	-20.74	1.65	90.0
UGC04637	08 55 38.4	+78 13 25	S0-a	1385	10.98	-21.22	1.59	66.2
UGC04666	08 55 34.7	+58 44 04	S0-a	877	12.16	-19.15	1.64	68.4
UGC04806	09 09 33.7	+33 07 25	Sc	1947	12.76	-20.56	1.54	82.4
UGC04838	09 12 14.5	+44 57 18	SABc	2622	12.20	-21.53	1.33	67.4
UGC04862	09 14 05.1	+40 06 50	SABa	2623	12.32	-20.91	1.51	45.2
UGC05060	09 30 16.9	+29 32 24	S0-a	1701	13.86	-18.39	1.01	39.1
UGC05079	09 32 10.1	+21 30 06	Sbc	555	9.53	-21.02	2.08	67.1
UGC05251	09 48 35.6	+33 25 18	Sbc	1480	12.25	-20.30	1.68	87.0
UGC05253	09 50 22.1	+72 16 45	Sab	1323	11.22	-20.85	1.56	37.9
UGC05272	09 50 22.4	+31 29 16	IB	520	14.46	-16.06	1.21	90.0
UGC05351	09 58 21.1	+32 22 12	SABa	1457	12.73	-19.24	1.31	81.6
UGC05414	10 03 57.2	+40 45 27	IAB	604	13.81	-16.86	1.48	53.8
UGC05446	10 06 30.9	+32 56 49	SABc	1365	15.32	-17.50	1.12	80.3
UGC05452	10 07 11.5	+33 01 39	Sbc	1337	14.31	-18.91	1.32	90.0

UGC05459	10 08 10.1	+53 05 01	SBc	1111	13.19	-19.57	1.58	90.0
UGC05532	10 16 53.7	+73 24 03	Sbc	2814	11.26	-21.92	1.61	31.2
UGC05556	10 17 47.9	+21 52 24	SBc	1583	13.76	-19.08	1.35	74.6
UGC05557	10 18 16.9	+41 25 28	SABc	592	10.41	-20.01	1.87	14.4
UGC05559	10 18 06.3	+21 49 58	Sa	1317	11.88	-20.53	1.56	87.8
UGC05582	10 21 49.0	+74 10 37	SBbc	3092	12.67	-21.32	1.35	53.7
UGC05614	10 23 44.6	+57 01 37	Sb	1165	13.91	-18.26	1.07	70.4
UGC05685	10 29 20.1	+29 29 31	Sbc	1367	12.29	-21.11	1.37	64.4
UGC05717	10 32 34.9	+65 02 28	SABb	1678	12.97	-20.00	1.24	61.1
UGC05721	10 32 17.2	+27 40 08	Scd	532	13.21	-16.52	1.21	61.6
UGC05786	10 38 45.9	+53 30 12	SABb	990	11.28	-20.08	1.25	16.1
UGC05789	10 39 09.5	+41 41 13	SBc	738	11.77	-19.37	1.56	62.7
UGC05829	10 42 42.3	+34 26 56	I	629	13.73	-16.73	1.65	24.6
UGC05840	10 43 31.2	+24 55 20	Sbc	588	10.50	-19.64	1.83	18.7
UGC05846	10 44 30.2	+60 22 04	I	1020	15.34	-16.02	1.21	0.0
UGC05906	10 48 12.2	+28 36 07	SBa	1596	13.45	-16.71	1.19	27.7
UGC05909	10 48 24.8	+34 42 41	SBbc	1628	12.89	-19.34	1.30	26.3
UGC05918	10 49 37.0	+65 31 53	I	339	15.16	-14.24	1.39	11.3
UGC05927	10 49 25.1	+32 46 22	SBm	1630	14.86	-17.47	1.07	32.6
UGC05935	10 49 55.1	+32 59 27	Sm	1694	12.55	-20.39	1.49	90.0
UGC05960	10 51 20.7	+32 45 59	S0-a	635	13.12	-18.04	1.30	90.0
UGC05982	10 52 11.4	+32 57 02	Sc	1584	12.19	-20.67	1.60	58.0
UGC05997	10 53 54.8	+73 41 26	Sbc	1262	13.02	-20.14	1.44	72.1
UGC06001	10 53 08.1	+33 54 37	Sab	1730	13.82	-18.65	0.74	52.4
UGC06016	10 54 12.9	+54 17 14	I	1512	16.10	-16.25	1.26	50.6
UGC06024	10 54 39.4	+54 18 19	S?	1372	12.41	-20.26	1.47	79.2
UGC06118	11 03 11.2	+27 58 21	Sab	1539	11.62	-20.48	1.39	26.4
UGC06126	11 03 43.4	+28 53 14	SBm	708	13.49	-18.39	1.19	78.1
UGC06128	11 04 03.0	+28 02 13	Sc	1372	13.00	-18.94	1.20	31.7
UGC06161	11 06 49.1	+43 43 23	Sd	749	15.66	-15.79	0.92	90.0
UGC06225	11 11 30.9	+55 40 28	Sc	698	10.70	-20.00	1.60	67.5
UGC06251	11 13 26.0	+53 35 41	SABm	926	15.32	-16.20	0.91	51.7
UGC06263	11 14 10.9	+48 19 07	Sb	2111	12.17	-20.76	1.35	58.7
UGC06283	11 15 52.0	+41 35 28	SBa	703	12.98	-18.18	1.27	87.7
UGC06446	11 26 40.5	+53 44 48	Scd	650	13.61	-17.94	1.15	44.2
UGC06456	11 27 59.7	+78 59 38	I	-107	15.25	-13.75	0.90	69.8
UGC06537	11 33 21.2	+47 01 45	Sc	864	10.67	-20.37	1.75	50.5
UGC06621	11 39 42.4	+31 54 26	SABa	2701	13.42	-20.18	1.29	65.1
UGC06628	11 40 06.7	+45 56 35	Sm	849	13.23	-17.96	1.33	33.2
UGC06713	11 44 24.9	+48 50 08	SABm	900	15.03	-16.34	1.08	41.4
UGC06733	11 45 35.6	+55 53 13	Sc	1155	14.47	-17.85	1.23	68.9
UGC06742	11 45 56.6	+50 12 00	S0-a	745	13.49	-17.38	1.02	49.7
UGC06778	11 48 38.2	+48 42 39	SABc	962	10.82	-21.03	1.43	59.9

UGC06786	11 49 09.5	+27 01 20	S0-a	1798	12.29	-20.21	1.41	70.6
UGC06787	11 49 15.3	+56 05 04	Sab	1173	11.26	-20.67	1.54	56.3
UGC06791	11 49 23.6	+26 44 30	Sc	1844	14.99	-18.86	1.32	87.5
UGC06797	11 49 40.5	+48 25 34	SBcd	964	13.52	-18.15	1.14	52.3
UGC06813	11 50 38.9	+55 21 14	Scd	951	13.36	-18.08	1.22	32.4
UGC06815	11 50 45.5	+51 49 28	Sc	965	12.53	-19.82	1.67	82.1
UGC06816	11 50 47.4	+56 27 23	I	888	14.26	-18.04	1.21	44.0
UGC06817	11 50 53.0	+38 52 50	I	248	13.46	-14.51	1.60	90.0
UGC06833	11 51 45.9	+38 00 54	Sc	921	13.51	-17.46	1.42	43.0
UGC06840	11 52 07.1	+52 06 29	SBm	1032	14.45	-17.57	1.22	75.0
UGC06869	11 53 41.7	+47 51 32	Sbc	800	11.37	-20.44	1.35	56.0
UGC06870	11 53 49.0	+52 19 36	Sbc	1051	10.49	-20.60	1.79	62.3
UGC06880	11 54 33.7	+58 22 02	Sa	3320	13.81	-20.20	1.10	75.1
UGC06884	11 54 58.7	+58 29 37	Sbc	3184	12.60	-21.10	1.40	28.9
UGC06921	11 56 42.1	+48 20 02	Sm	983	13.12	-18.41	1.05	56.2
UGC06930	11 57 17.4	+49 17 00	Scd	784	12.72	-18.37	1.15	26.5
UGC06937	11 57 36.0	+53 22 28	Sbc	1047	10.48	-21.85	1.85	47.4
UGC06944	11 57 44.1	+32 17 39	SABm	3315	12.68	-21.73	1.41	90.0
UGC06956	11 58 25.6	+50 55 02	SBm	916	15.34	-16.18	0.87	48.5
UGC06964	11 58 37.8	+47 15 41	SBcd	905	13.17	-19.39	1.49	82.2
UGC07030	12 03 09.7	+44 31 53	SABb	704	10.77	-19.84	1.77	48.7
UGC07047	12 04 02.0	+52 35 21	I	210	13.07	-15.64	1.28	61.3
UGC07075	12 05 22.7	+50 21 11	SABc	784	12.30	-20.18	1.35	81.2
UGC07081	12 05 33.9	+50 32 20	SABc	749	11.35	-20.27	1.74	71.3
UGC07094	12 06 10.8	+42 57 21	Sd	772	15.27	-15.73	1.09	90.0
UGC07095	12 06 08.6	+49 34 58	Sbc	1115	11.71	-20.74	1.66	79.5
UGC07125	12 08 42.1	+36 48 10	SBm	1070	14.48	-18.75	1.32	90.0
UGC07151	12 09 58.5	+46 27 27	SABc	265	12.04	-18.45	1.72	85.6
UGC07154	12 10 01.5	+39 53 02	Scd	1011	11.78	-19.50	1.66	64.3
UGC07166	12 10 32.6	+39 24 21	Sab	989	11.36	-17.30	1.46	42.0
UGC07183	12 11 04.3	+50 29 06	SABb	778	12.09	-20.13	1.82	90.0
UGC07199	12 12 09.1	+36 10 07	I	164	13.70	-14.08	1.22	54.3
UGC07204	12 12 20.8	+29 12 34	SBcd	1126	13.59	-18.44	1.37	90.0
UGC07222	12 13 16.9	+43 41 55	Sc	920	12.84	-19.75	1.63	90.0
UGC07232	12 13 44.5	+36 38 00	IB	158	13.85	-13.61	1.18	25.4
UGC07256	12 15 05.0	+33 11 50	E-S0	1071	11.72	-19.23	1.53	90.0
UGC07261	12 15 14.5	+20 39 32	SBd	855	12.89	-18.13	1.61	0.0
UGC07278	12 15 39.4	+36 19 35	I	292	10.21	-17.46	1.83	43.7
UGC07321	12 17 34.0	+22 32 25	Scd	411	13.79	-20.14	1.68	90.0
UGC07323	12 17 30.2	+45 37 09	Sd	516	11.59	-17.46	1.58	51.5
UGC07353	12 18 57.6	+47 18 14	Sbc	454	9.12	-20.94	2.23	68.3
UGC07399	12 20 38.2	+46 17 30	SBcd	531	13.30	-18.90	1.23	42.1
UGC07408	12 21 15.2	+45 48 43	I	459	13.55	-16.50	1.30	84.2

UGC07483	12 24 11.1	+31 31 19	SBc	1251	13.65	-18.36	1.14	54.5
UGC07490	12 24 24.9	+70 20 03	Sm	466	13.42	-17.30	1.06	62.8
UGC07506	12 25 11.9	+54 30 23	Sa	2499	13.52	-18.77	1.11	41.7
UGC07524	12 25 48.9	+33 32 49	Sm	318	10.84	-18.50	1.62	90.0
UGC07559	12 27 05.2	+37 08 34	I	217	14.18	-14.71	1.55	56.7
UGC07577	12 27 41.4	+43 29 45	I	199	12.90	-14.62	1.59	57.4
UGC07584	12 28 02.8	+22 35 17	Sd	606	15.70	-15.02	0.78	54.9
UGC07592	12 28 11.1	+44 05 37	IB	204	9.50	-19.17	1.67	63.5
UGC07599	12 28 28.1	+37 14 06	Sm	292	14.92	-14.03	1.27	68.8
UGC07603	12 28 44.1	+22 49 15	SBcd	643	13.12	-17.92	1.21	90.0
UGC07608	12 28 44.5	+43 13 28	I	537	13.70	-16.76	1.54	30.5
UGC07651	12 30 36.4	+41 38 39	SBcd	587	9.76	-21.49	1.83	90.0
UGC07690	12 32 26.9	+42 42 15	I	531	13.13	-17.40	1.14	32.3
UGC07704	12 33 06.5	+32 05 28	Sb	917	14.08	-17.48	0.82	59.8
UGC07766	12 35 57.7	+27 57 35	Sc	814	10.28	-19.67	2.02	64.8
UGC07774	12 36 22.7	+40 00 19	Sc	531	14.80	-18.71	1.30	90.0
UGC07831	12 39 59.3	+61 36 33	SBc	146	10.82	-18.65	1.77	70.1
UGC07853	12 41 32.9	+41 09 04	SBm	538	11.31	-19.44	1.55	57.6
UGC07861	12 41 52.7	+41 16 26	SABm	609	13.03	-17.78	1.15	46.1
UGC07866	12 42 15.1	+38 30 10	IAB	354	13.75	-14.70	1.52	25.0
UGC07916	12 44 25.1	+34 23 10	I	607	16.50	-14.22	1.36	46.8
UGC07917	12 44 26.2	+37 07 17	Sbc	6976	13.53	-21.86	1.26	37.7
UGC07949	12 46 59.9	+36 28 35	I	332	16.06	-11.57	1.26	39.2
UGC07971	12 48 22.7	+51 09 56	Sm	468	13.46	-15.73	1.34	26.2
UGC08146	13 02 07.7	+58 41 57	Sc	663	14.47	-18.13	1.38	78.7
UGC08188	13 05 49.3	+37 36 17	Sm	314	12.59	-15.74	1.78	25.7
UGC08201	13 06 24.9	+67 42 25	I	31	12.93	-16.14	1.52	71.2
UGC08246	13 10 04.5	+34 10 52	SBc	808	14.98	-17.65	1.39	79.9
UGC08254	13 10 38.3	+36 38 04	Sm	1064	14.65	-16.64	1.14	71.3
UGC08271	13 11 31.3	+36 16 55	Sa	1133	13.48	-16.49	1.32	83.1
UGC08286	13 12 11.7	+44 02 16	Sc	407	12.82	-17.87	1.79	90.0
UGC08303	13 13 17.6	+36 13 00	IAB	945	13.66	-17.91	1.16	53.6
UGC08314	13 14 01.0	+36 19 09	IAB	935	18.19	-13.14	0.95	32.1
UGC08331	13 15 29.8	+47 29 59	I	265	14.62	-14.49	1.41	90.0
UGC08396	13 21 25.0	+38 32 13	SBcd	945	13.75	-18.62	1.23	75.5
UGC08403	13 21 56.4	+38 44 05	SBc	973	12.63	-18.98	1.48	53.6
UGC08490	13 29 36.6	+58 25 14	Sm	202	11.73	-17.00	1.65	58.8
UGC08508	13 30 44.4	+54 54 41	I	60	14.01	-13.53	1.24	61.2
UGC08550	13 34 02.9	+47 54 56	SBcd	392	14.51	-16.68	1.36	76.9
UGC08651	13 39 53.8	+40 44 21	I	202	14.65	-13.32	1.36	66.0
UGC08683	13 42 32.5	+39 39 31	IAB	663	15.70	-15.03	1.27	0.0
UGC08699	13 45 08.7	+41 30 12	SABa	2519	13.94	-19.86	1.37	85.3
UGC08700	13 45 19.2	+41 42 45	Sbc	2559	13.28	-20.36	1.51	80.6

UGC08709	13 46 23.7	+43 52 20	Sc	2406	12.40	-21.26	1.57	82.2
UGC08711	13 46 24.7	+46 06 26	SBc	1506	13.33	-19.49	1.60	90.0
UGC08805	13 53 17.8	+33 29 27	Sab	2371	13.44	-19.75	1.21	45.3
UGC08837	13 54 45.8	+53 54 09	IB	142	13.78	-16.53	1.60	90.0
UGC08863	13 56 16.7	+47 14 09	Sa	1796	12.17	-20.60	1.56	77.2
UGC08900	13 58 38.0	+37 25 28	SABb	3469	12.28	-21.94	1.40	66.1
UGC09018	14 05 33.3	+54 27 39	Sm	315	14.37	-15.11	1.04	51.7
UGC09128	14 15 56.5	+23 03 20	IAB	153	14.56	-12.71	1.02	58.7
UGC09133	14 16 07.7	+35 20 38	SABa	3863	12.68	-21.47	1.46	60.3
UGC09211	14 22 32.3	+45 23 00	I	686	15.63	-15.95	0.80	90.0
UGC09242	14 25 21.0	+39 32 22	Scd	1467	14.11	-19.87	1.62	90.0
UGC09366	14 32 46.9	+49 27 28	Sc	2104	11.87	-21.51	1.55	66.2
UGC09431	14 38 11.5	+46 38 18	SBc	2238	14.10	-20.12	1.45	90.0
UGC09632	14 57 56.4	+53 47 06	Scd	3177	15.15	-18.73	1.08	46.3
UGC09642	14 58 39.8	+53 53 10	S0	3331	13.21	-20.54	1.22	56.3
UGC09644	14 59 34.3	+27 06 59	Sa	6657	15.37	-19.94	1.06	28.6
UGC09648	14 58 59.7	+53 55 24	Sc	3348	14.71	-19.47	1.17	60.5
UGC09649	14 57 45.7	+71 40 57	Sb	447	13.51	-17.12	1.27	69.5
UGC09753	15 09 46.8	+57 00 01	Sbc	763	12.12	-19.62	1.58	72.7
UGC09797	15 15 23.4	+55 31 02	Sb	3391	13.30	-20.57	1.51	37.5
UGC09805	15 16 43.2	+55 24 34	SBb	3333	12.81	-21.35	1.53	65.3
UGC09858	15 26 41.5	+40 33 53	Sbc	2616	13.88	-20.21	1.59	90.0
UGC09969	15 39 37.1	+59 19 55	Sb	2519	11.95	-22.09	1.60	63.3
UGC09992	15 41 47.9	+67 15 14	I	428	15.41	-15.41	1.16	60.3
UGC10227	16 08 58.3	+36 36 39	Sc	9031	15.40	-21.84	1.30	90.0
UGC10310	16 16 17.9	+47 02 43	Sm	717	13.69	-17.41	1.41	41.7
UGC10359	16 20 57.9	+65 23 25	Sc	907	12.25	-19.23	1.32	32.2
UGC10445	16 33 47.5	+28 59 04	Sc	960	13.77	-17.89	1.29	45.8
UGC10448	16 34 25.5	+21 32 27	Sa	2936	14.23	-19.67	1.20	71.0
UGC10470	16 32 39.3	+78 11 54	Sbc	1368	11.89	-20.50	1.35	44.8
UGC10497	16 36 47.9	+72 24 14	Sc	4295	14.34	-20.83	1.07	74.8
UGC10502	16 37 37.7	+72 22 29	Sc	4300	12.99	-21.55	1.30	40.0
UGC10546	16 44 34.8	+70 46 49	SABc	1280	12.60	-19.77	1.26	55.2
UGC10564	16 46 22.0	+70 21 32	SBc	1132	14.03	-18.28	1.09	52.7
UGC10757	17 10 13.2	+72 24 38	Sc	1170	14.33	-19.54	1.08	59.3
UGC10769	17 11 33.5	+72 24 07	Sb	1205	15.11	-17.23	0.96	56.5
UGC10791	17 14 38.7	+72 23 56	Sm	1328	15.40	-17.37	1.27	0.0
UGC11124	18 07 27.5	+35 33 50	SBc	1610	13.79	-18.66	1.35	22.5
UGC11218	18 19 46.4	+74 34 06	Sc	1484	11.76	-20.66	1.52	62.7
UGC11269	18 30 39.9	+67 59 13	SABa	2585	13.60	-20.17	1.27	60.1
UGC11283	18 33 52.6	+49 16 43	Sd	1964	13.61	-19.37	1.12	34.2
UGC11300	18 34 50.3	+70 31 26	SABc	489	13.05	-18.84	1.52	77.1
UGC11429	19 20 57.4	+43 07 57	SBb	4641	13.29	-21.92	1.32	61.0

UGC11466	19 42 58.8	+45 17 53	Sbc	820	13.42	-18.74	1.17	55.1
UGC11496	19 53 01.9	+67 39 54	Sm	2115	17.00	-16.95	1.28	0.0
UGC11557	20 24 00.7	+60 11 41	SABd	1388	14.40	-18.68	1.30	28.8
UGC11670	21 03 33.6	+29 53 50	Sa	778	12.37	-19.75	1.62	90.0
UGC11852	21 55 59.3	+27 53 54	SBa	5849	14.96	-20.27	0.96	46.7
UGC11861	21 56 24.2	+73 15 39	Sd	1479	15.10	-19.28	1.25	75.0
UGC11864	21 57 54.8	+42 18 22	Sd	4328	15.60	-20.08	1.29	57.1
UGC11891	22 03 33.7	+43 44 56	I	461	15.36	-16.04	1.52	43.3
UGC11909	22 06 16.2	+47 15 04	Sc	1105	13.19	-19.86	1.30	90.0
UGC11914	22 07 52.4	+31 21 33	Sab	951	11.03	-20.57	1.65	33.4
UGC11951	22 12 30.1	+45 19 41	SBa	1086	13.91	-18.75	1.23	81.0
UGC11994	22 20 53.1	+33 17 43	Sbc	4879	14.89	-20.78	1.32	90.0
UGC12043	22 27 50.5	+29 05 45	S0-a	1008	13.30	-18.39	1.26	90.0
UGC12060	22 30 33.9	+33 49 12	IB	884	15.44	-16.56	1.04	73.9
UGC12082	22 34 10.8	+32 51 40	SABm	803	14.16	-17.14	1.43	28.7
UGC12212	22 50 30.2	+29 08 18	Sm	893	16.00	-16.62	1.29	70.7
UGC12276	22 58 32.6	+35 48 08	Sa	5663	14.42	-20.86	1.06	38.9
UGC12554	23 22 06.6	+40 50 43	Sc	372	11.61	-19.66	1.91	85.7
UGC12632	23 29 58.7	+40 59 25	SABm	422	12.88	-17.69	1.63	37.3
UGC12693	23 35 43.6	+32 23 06	Sc	4955	15.54	-20.33	1.04	85.0
UGC12713	23 38 14.4	+30 42 29	Sa	288	14.81	0.00	0.98	70.6
UGC12732	23 40 39.8	+26 14 10	SABm	747	14.47	-16.45	1.44	19.5
UGC12754	23 43 54.5	+26 04 31	SBc	752	11.82	-19.53	1.56	50.1
UGC12808	23 51 04.0	+20 09 01	Sb	4221	12.50	-22.42	1.26	73.2
UGC12815	23 51 24.9	+20 06 43	Sa	4292	12.94	-21.72	1.40	66.7

Tableau B.1. – Properties of the WHISP subsample used in this thesis

C. Comparison with the literature

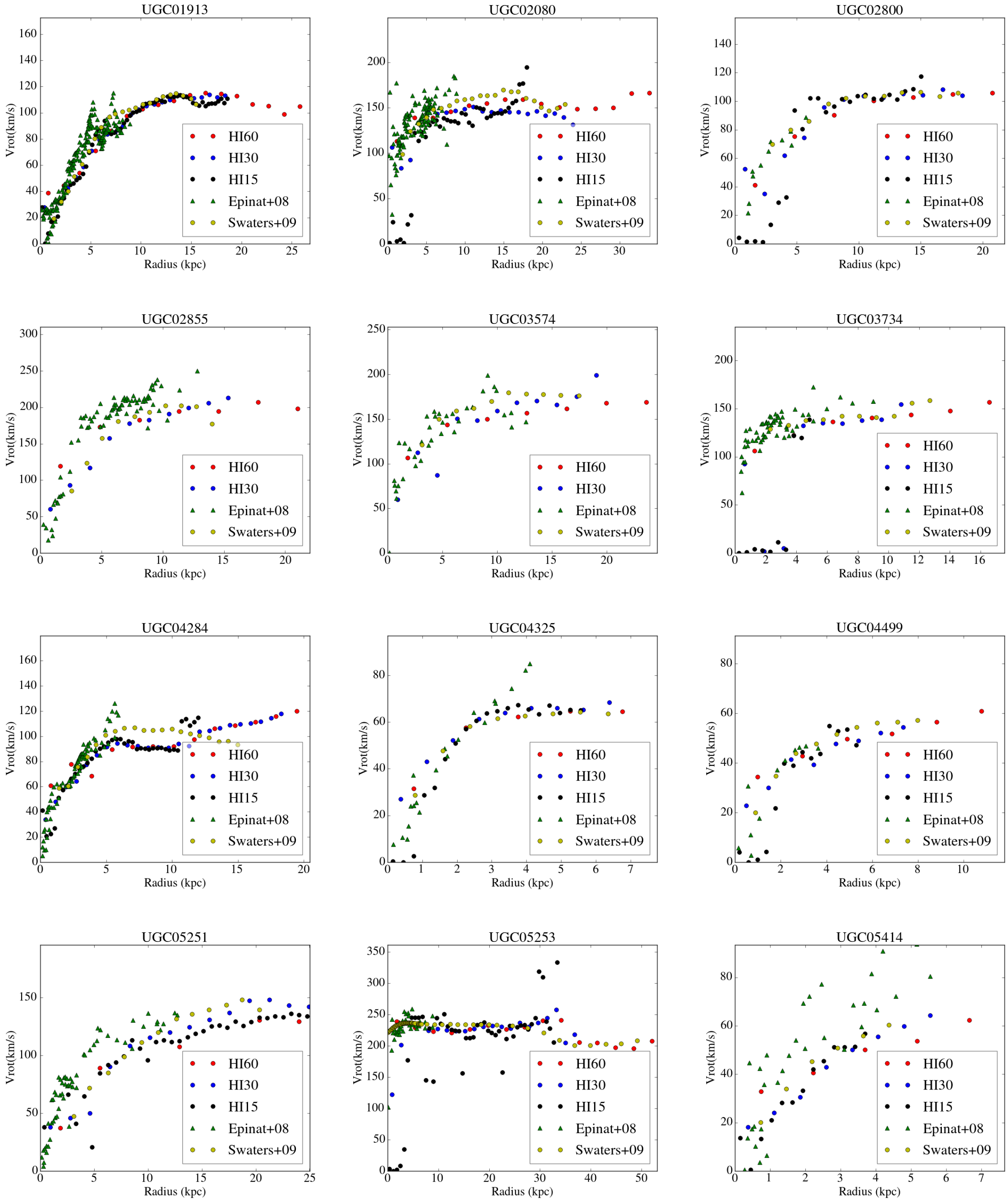

FIGURE C.0. – Comparison of the rotation curves obtained using ^{3D}Barolo with HI data and $H\alpha$ data available in the literature.

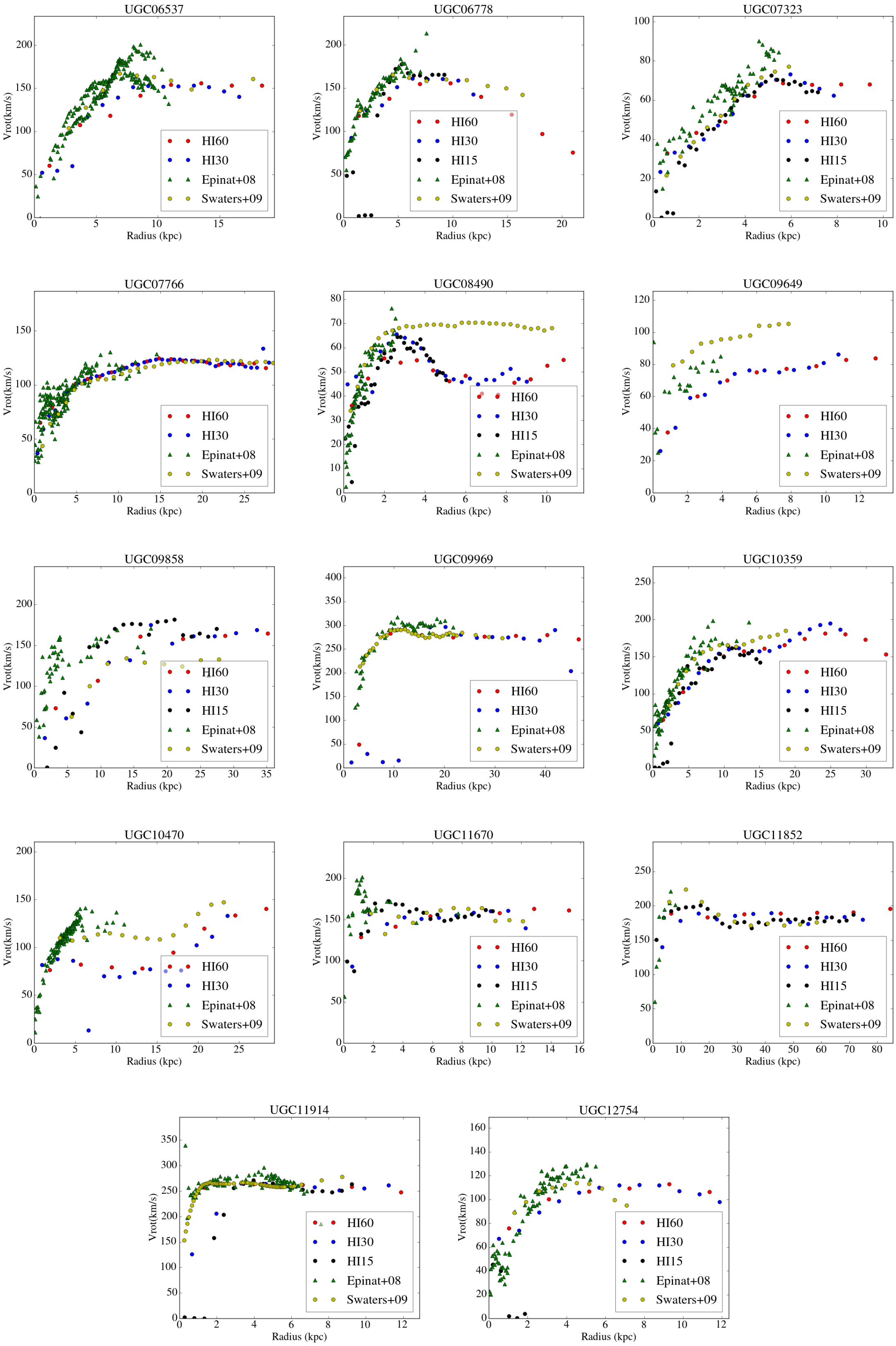

FIGURE C.0. – Continued

D. Outputs from ^{3D}Barolo

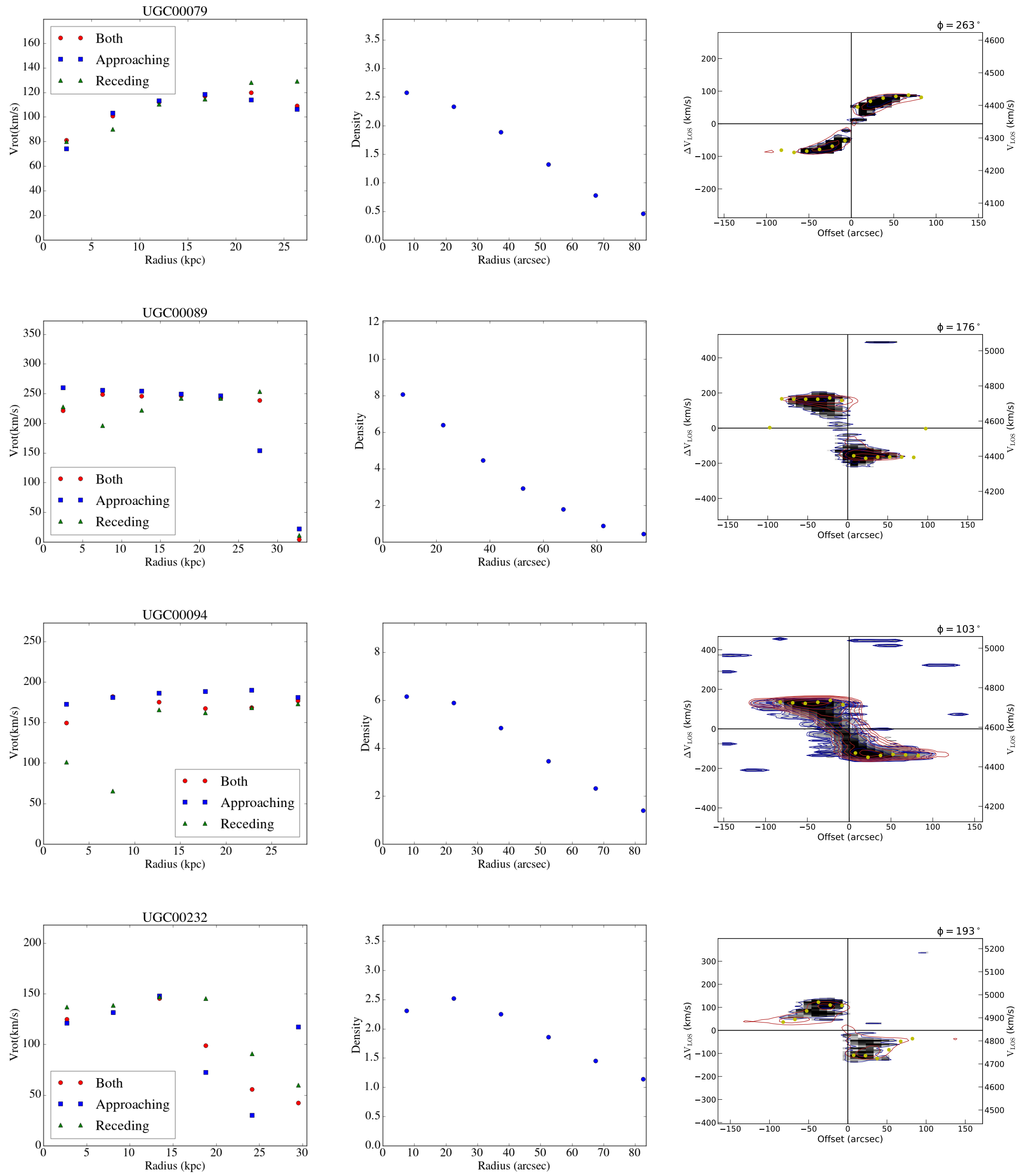

Figure 0: Rotation curves, mass density profiles in $M_{\odot}/\mathrm{pc}^2$ and position-velocity diagram obtained with ^{3D}Barolo for each indivual galaxy.

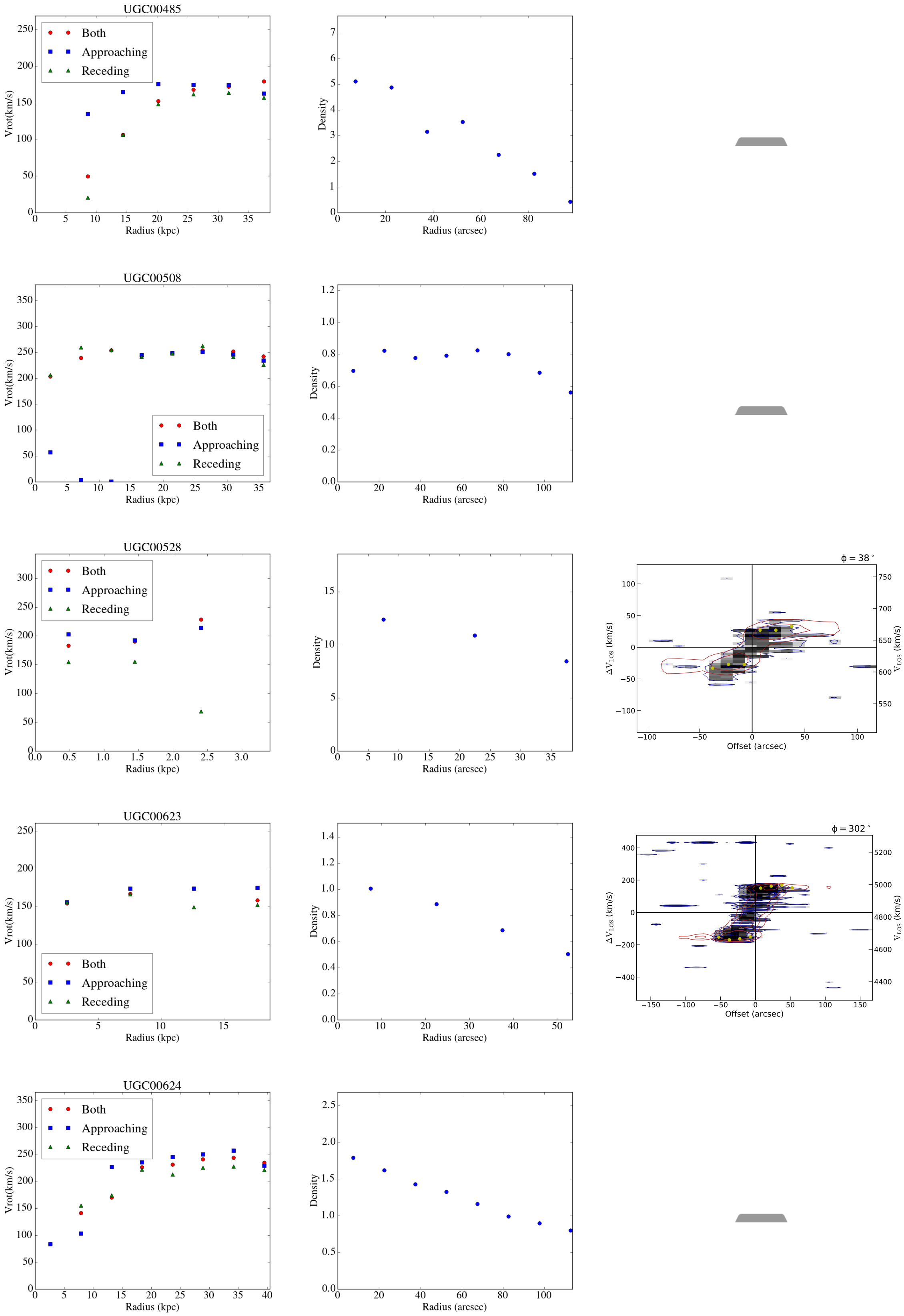

Figure 0: Continued

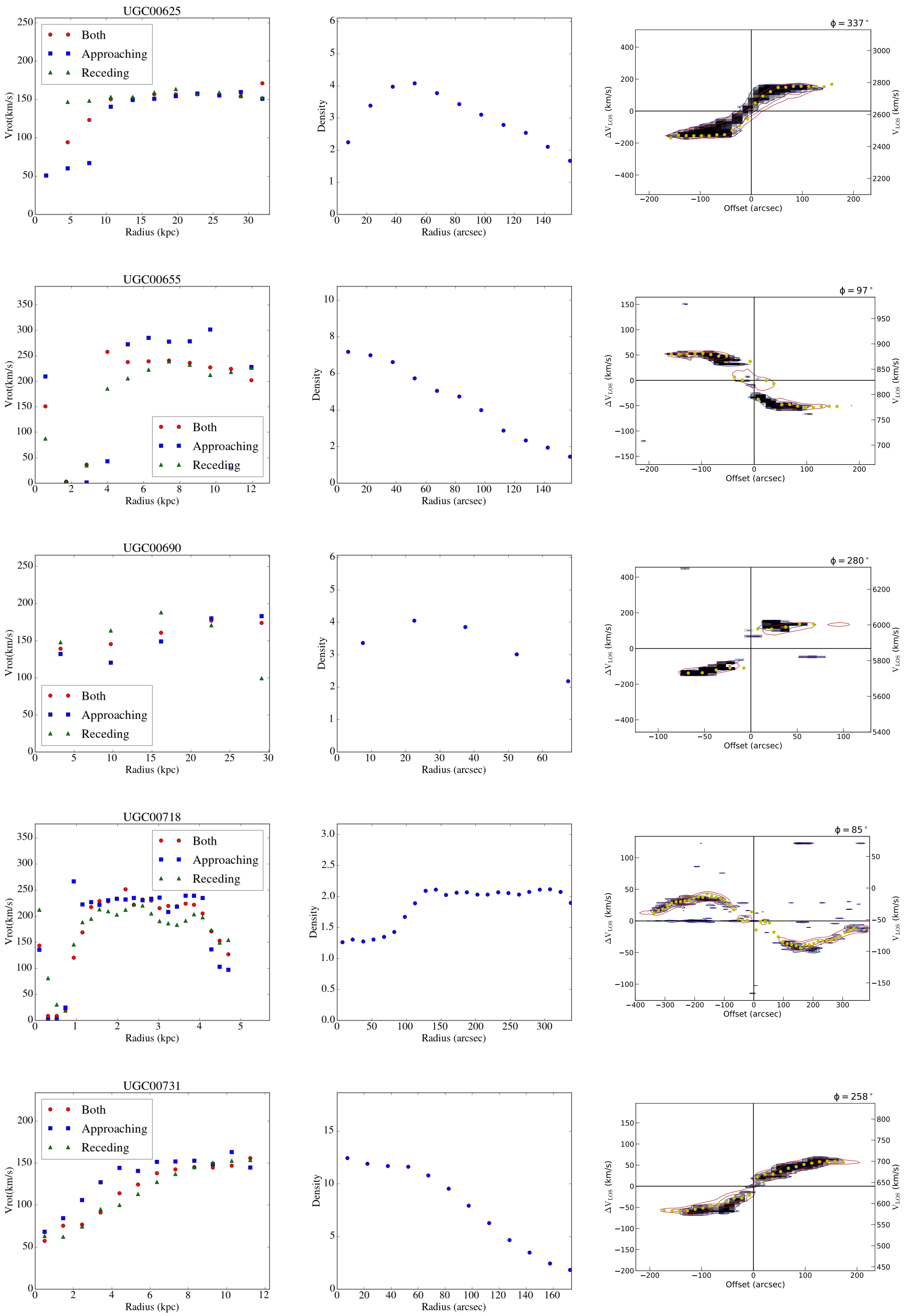

Figure 0: Continued

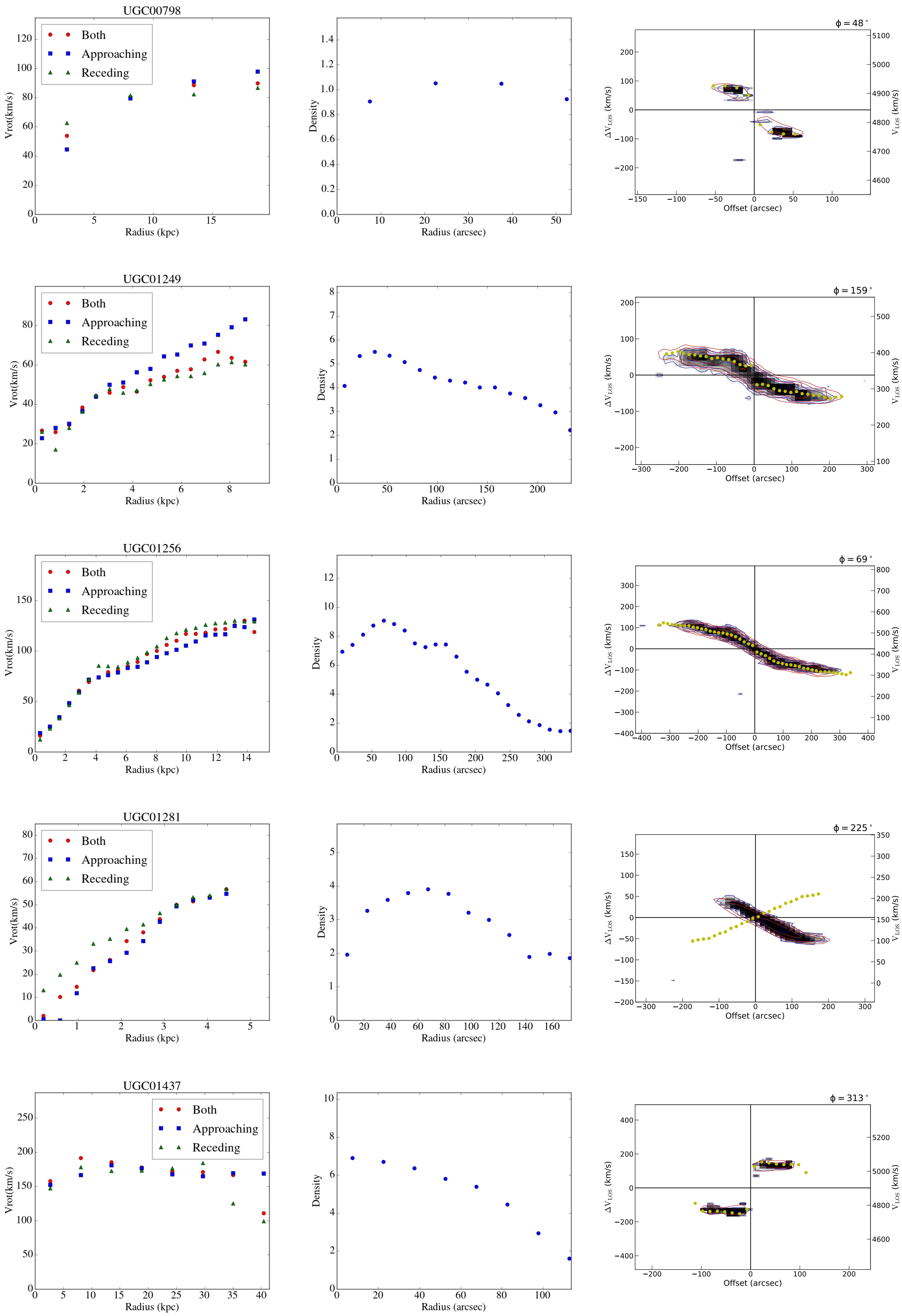

Figure 0: Continued

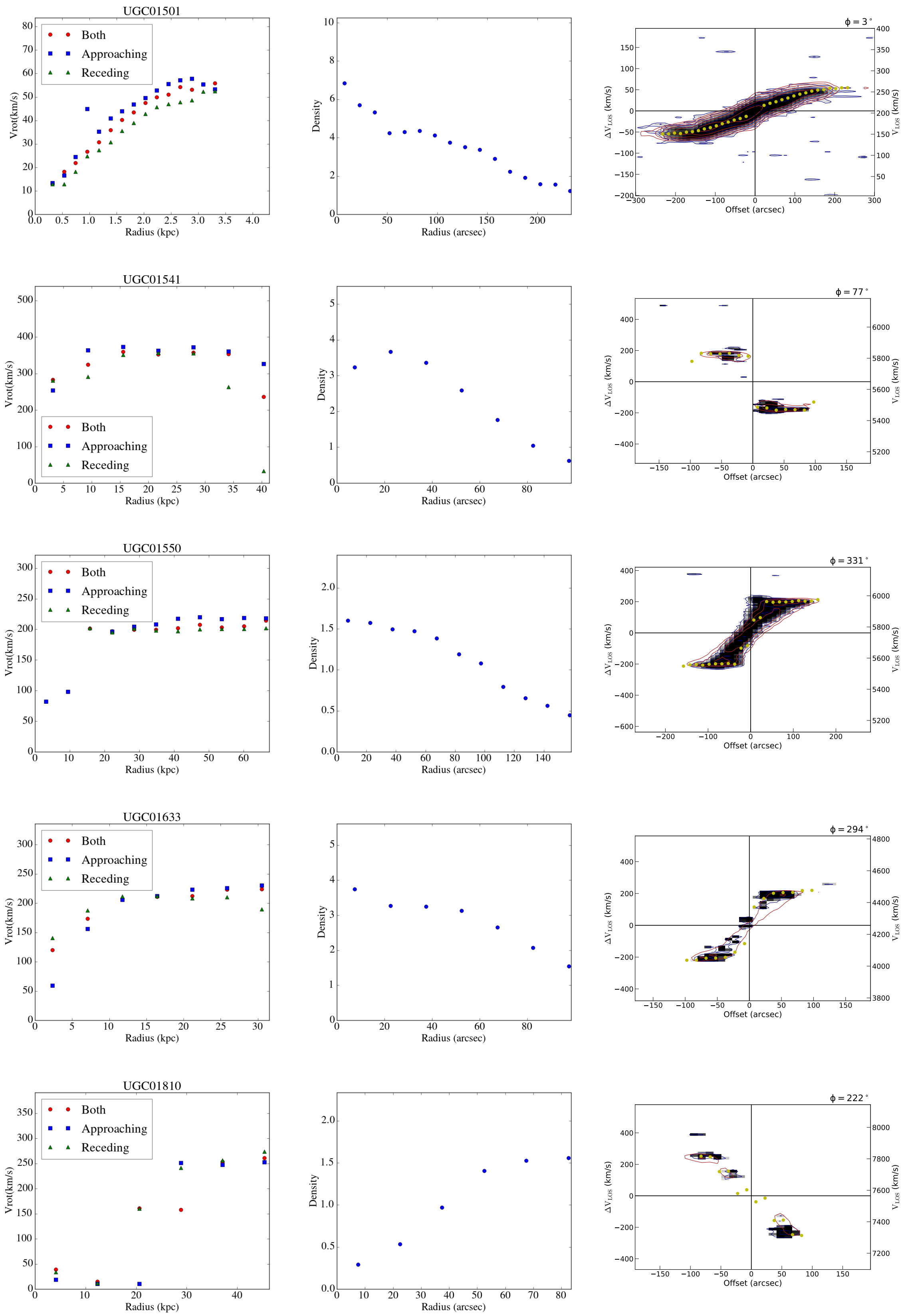

Figure 0: Continued

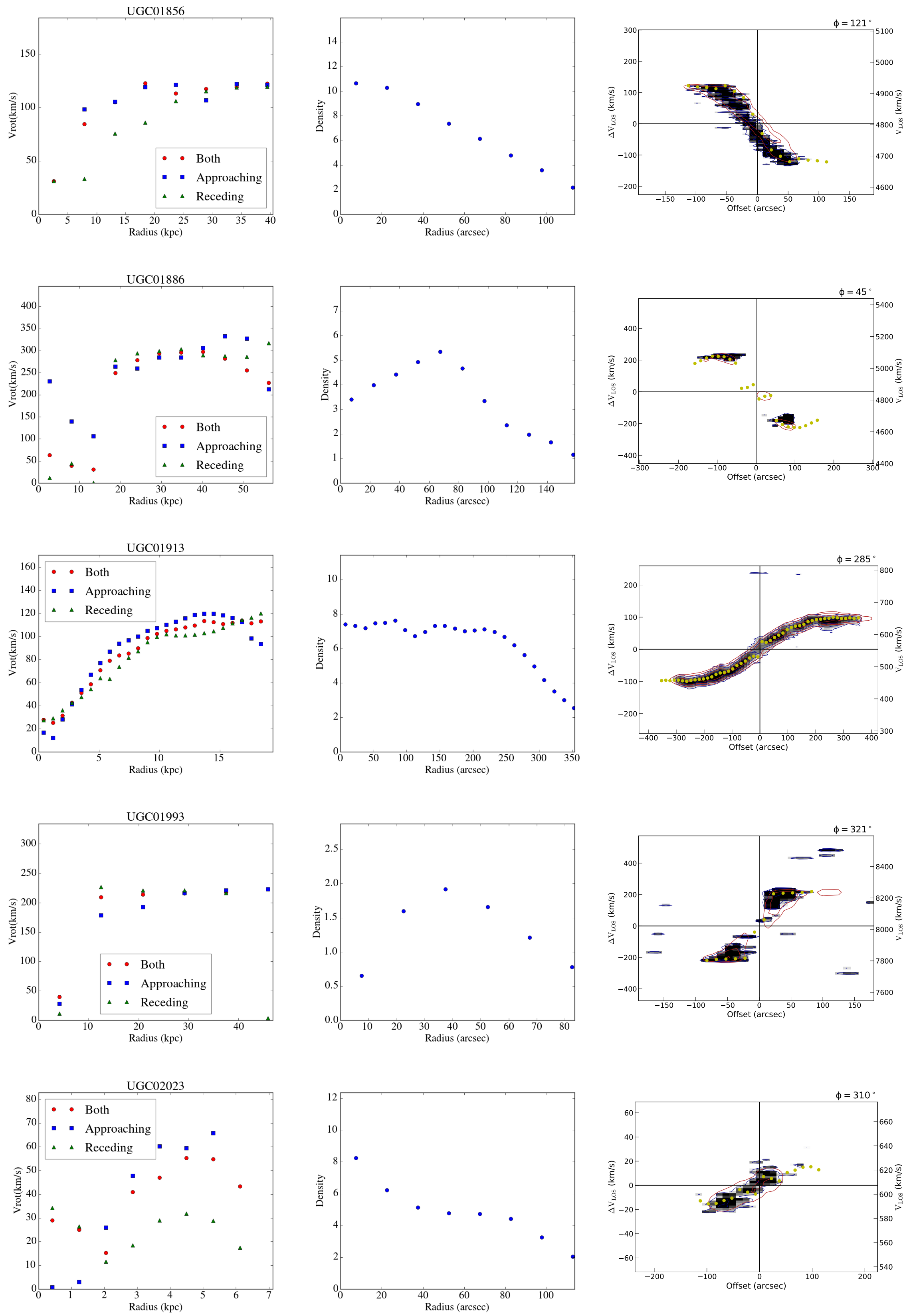

Figure 0: Continued

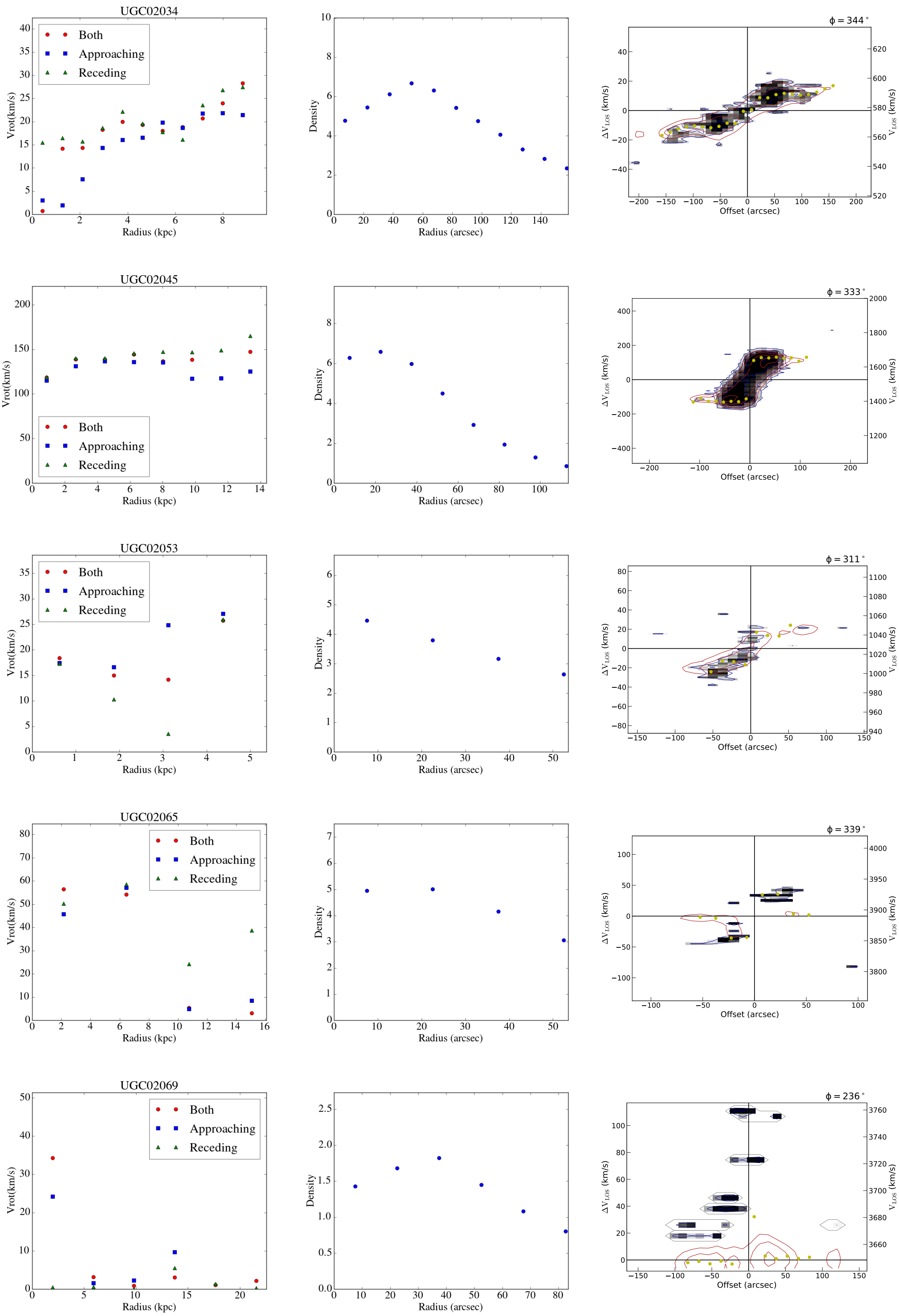

Figure 0: Continued

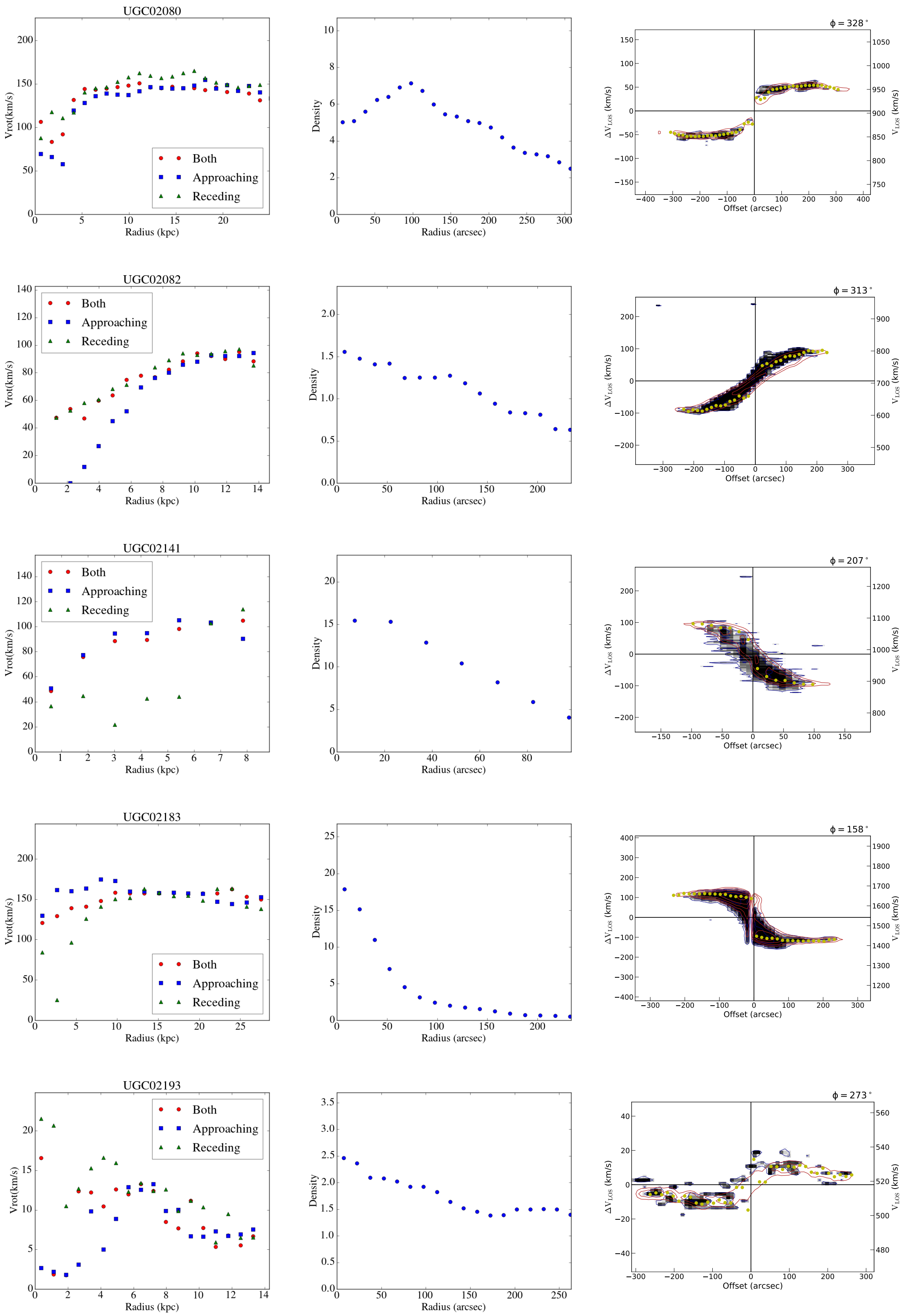

Figure 0: Continued

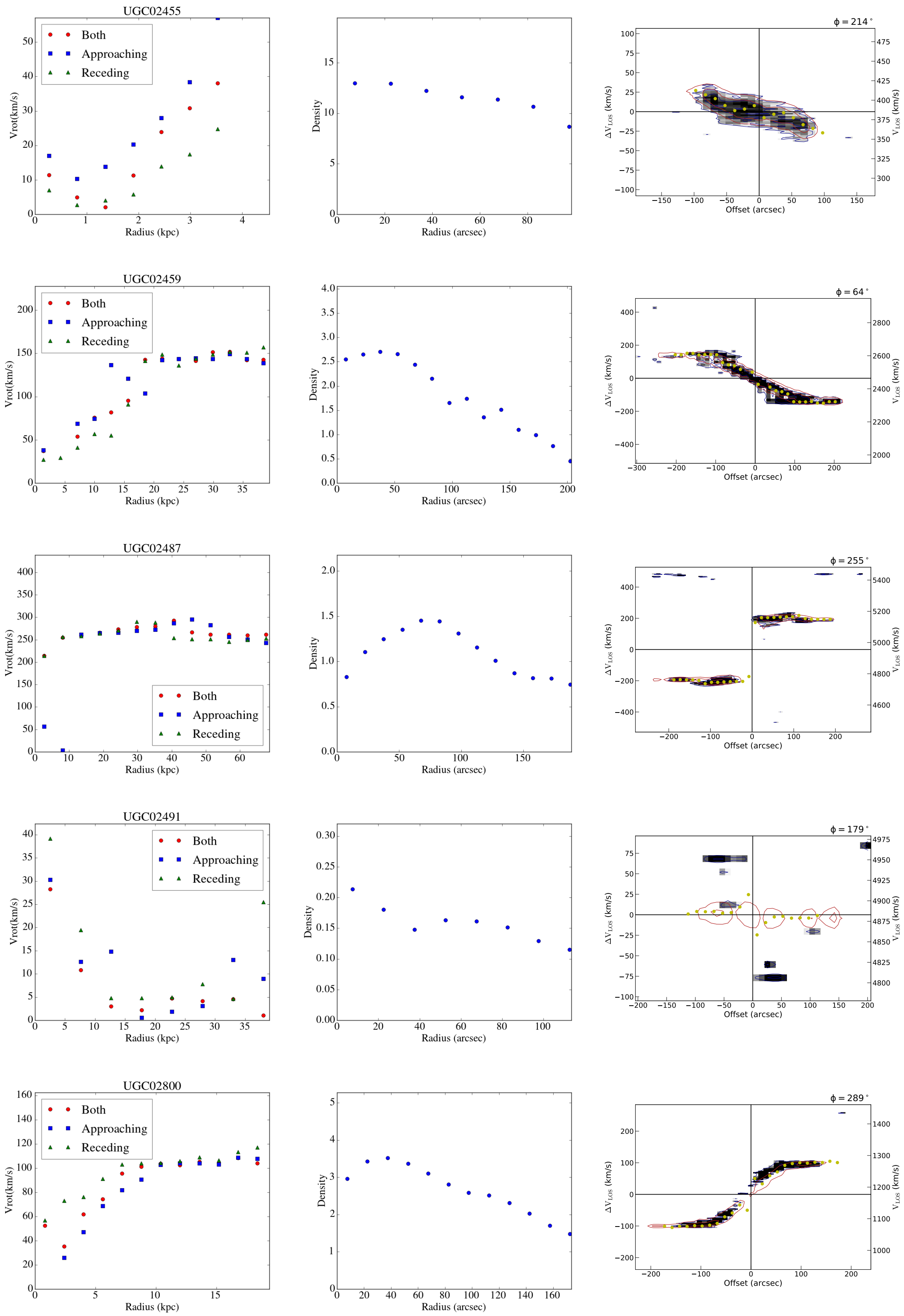

Figure 0: Continued

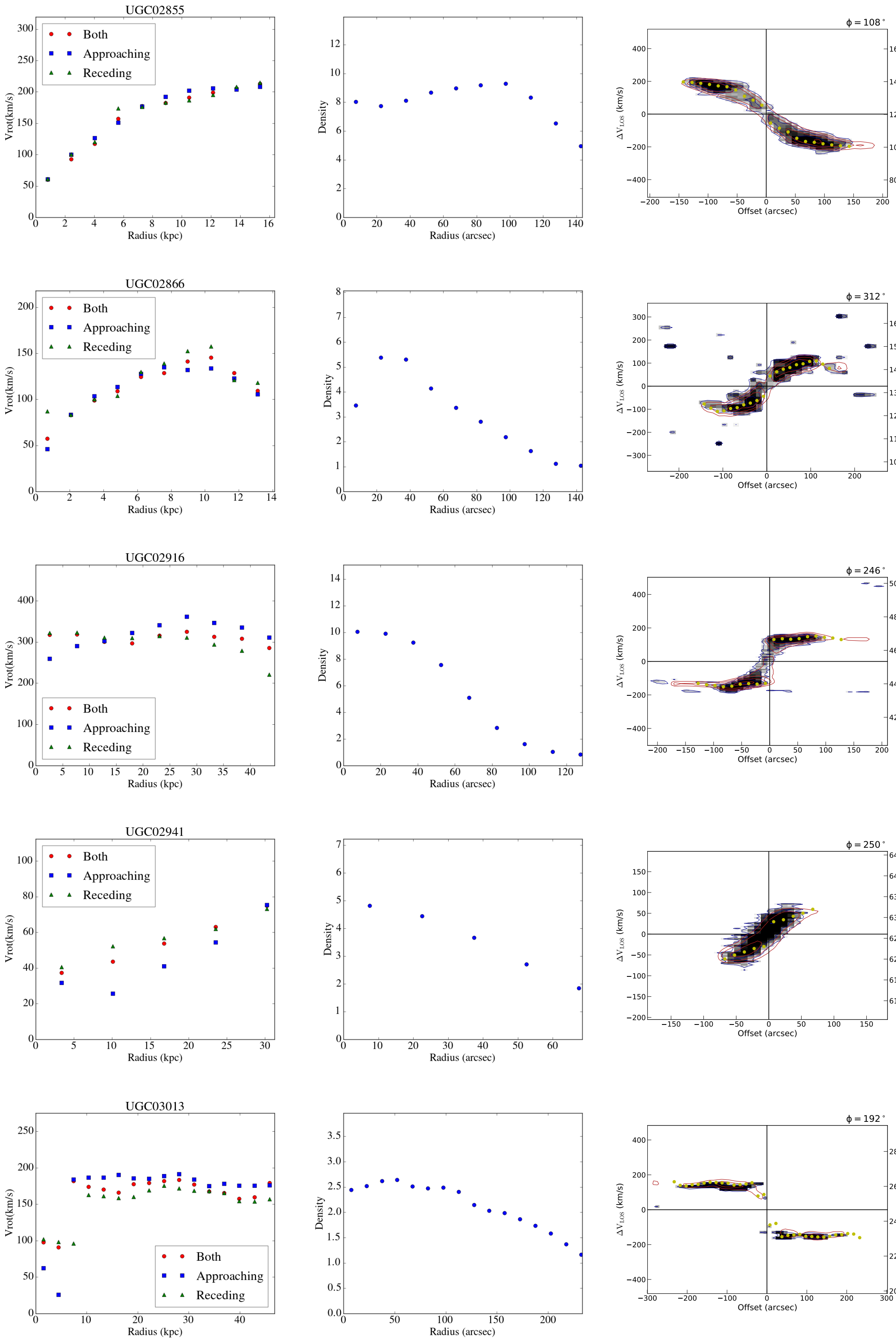

Figure 0: Continued

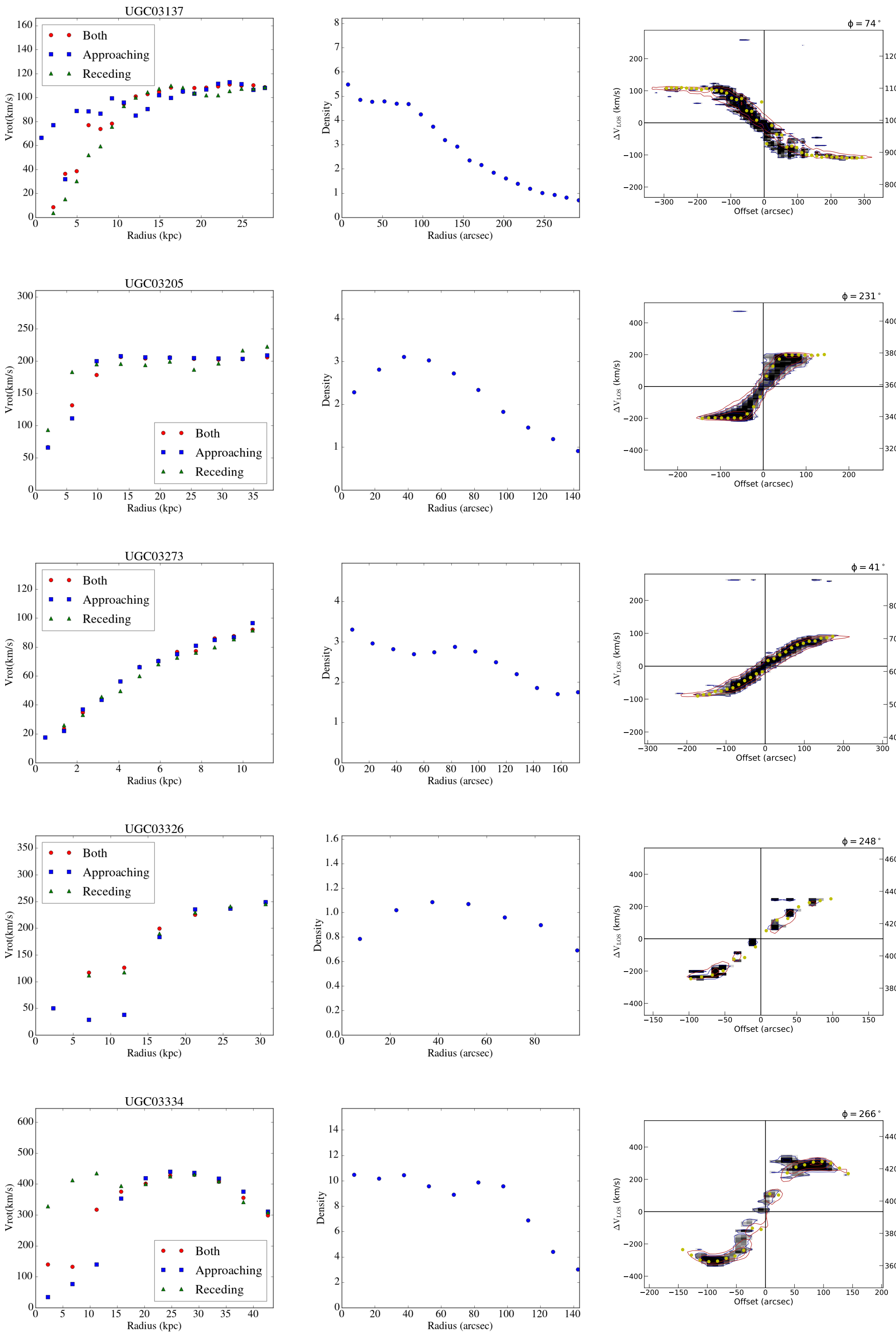

Figure 0: Continued

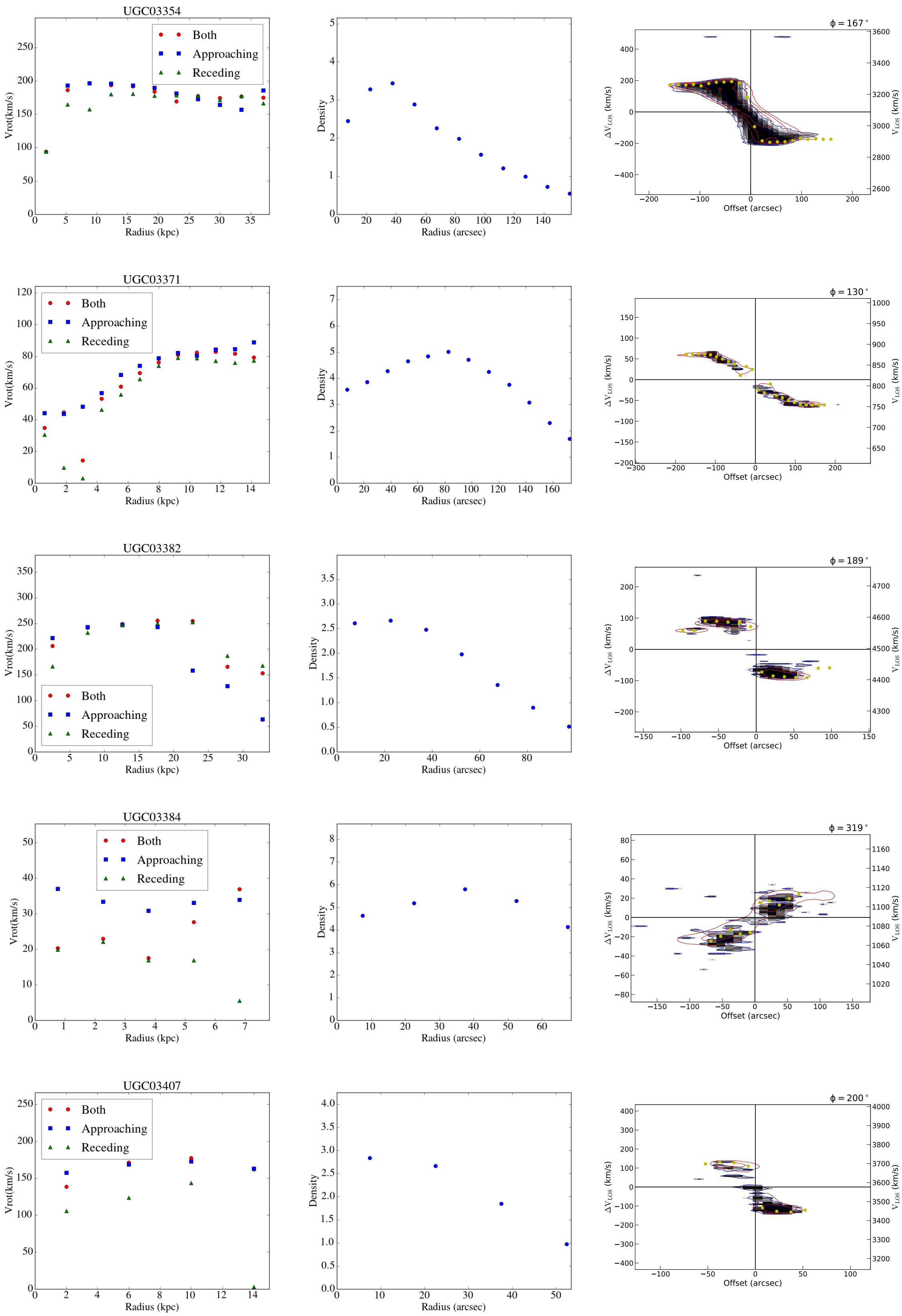

Figure 0: Continued

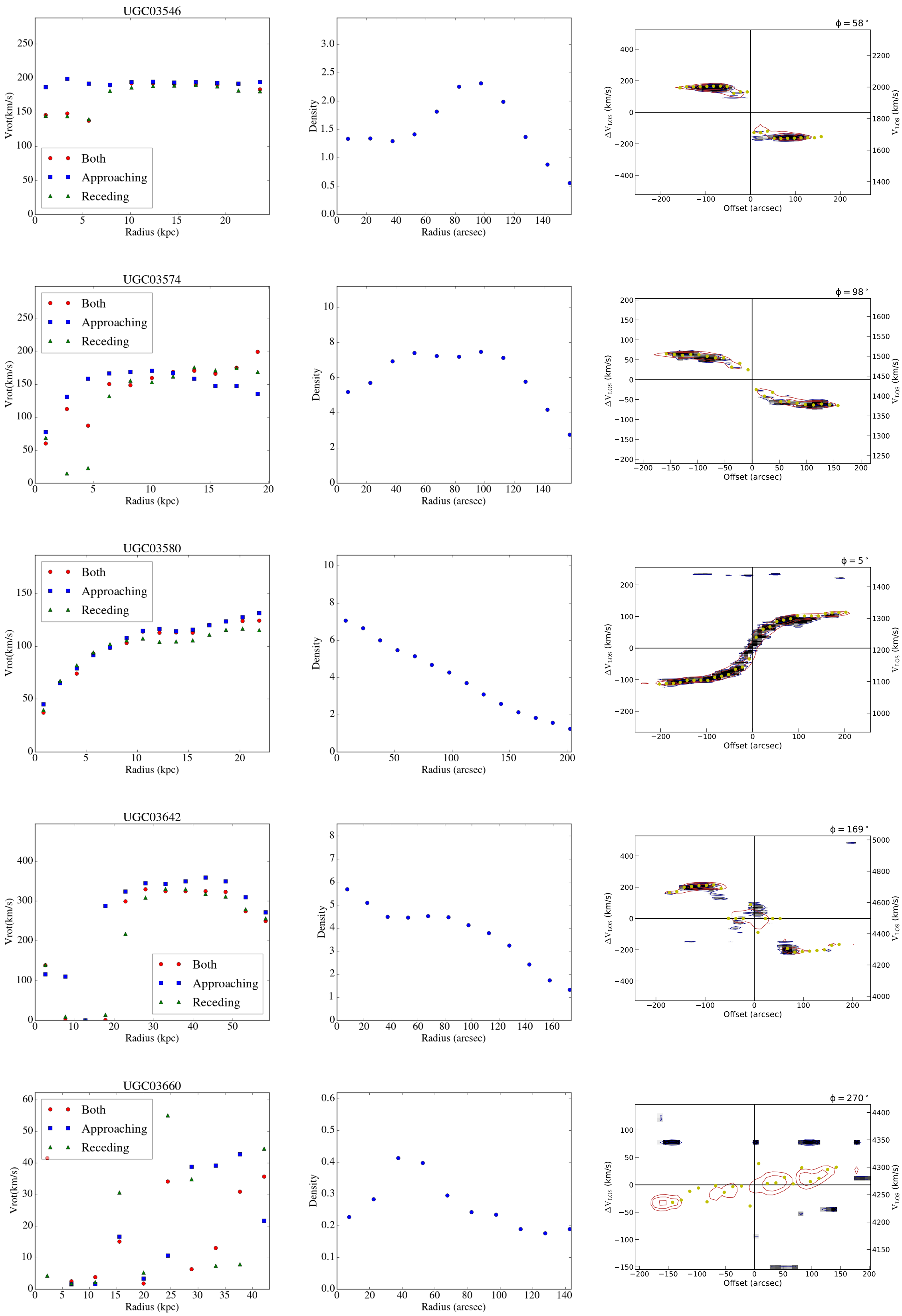

Figure 0: Continued

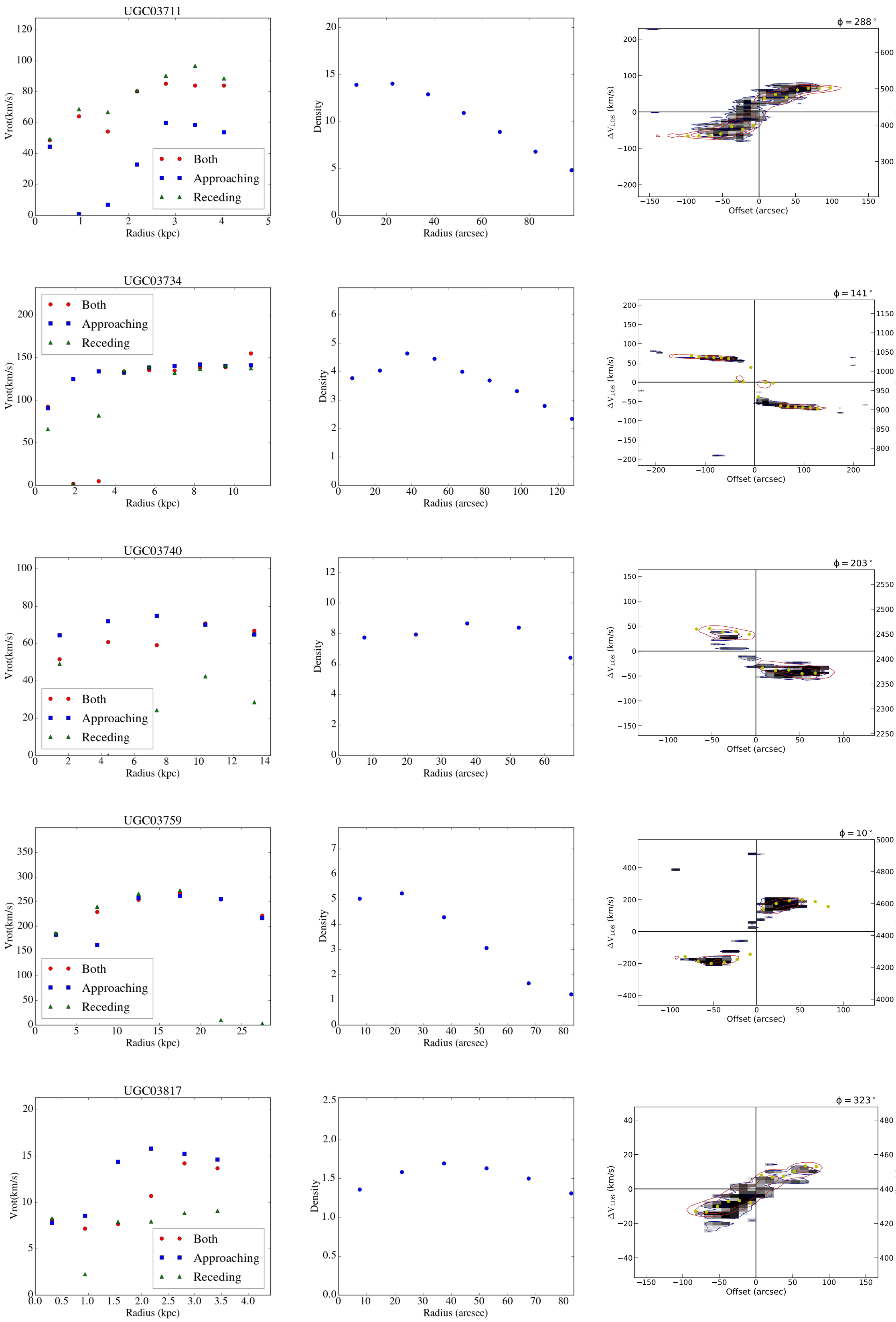

Figure 0: Continued

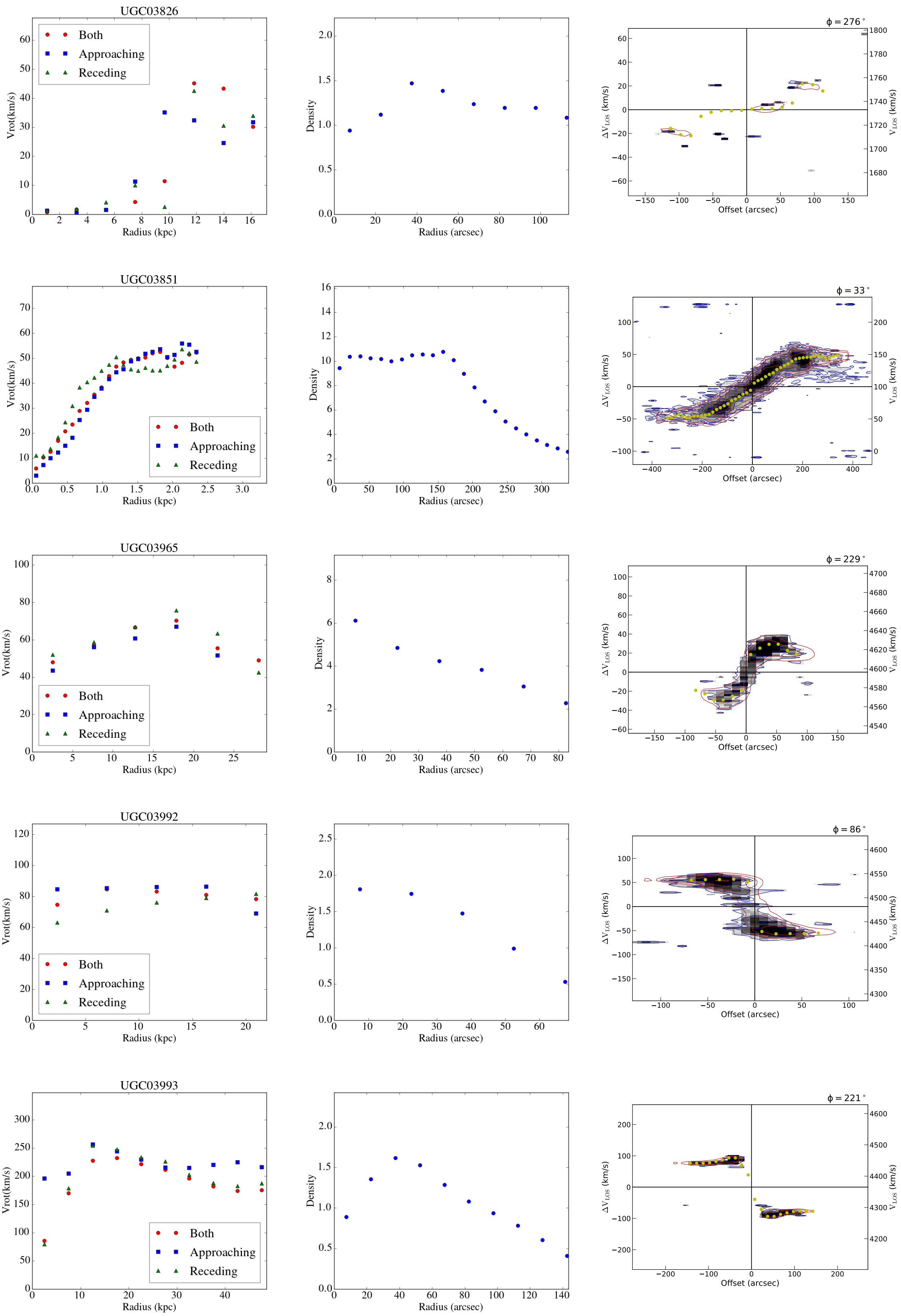

Figure 0: Continued

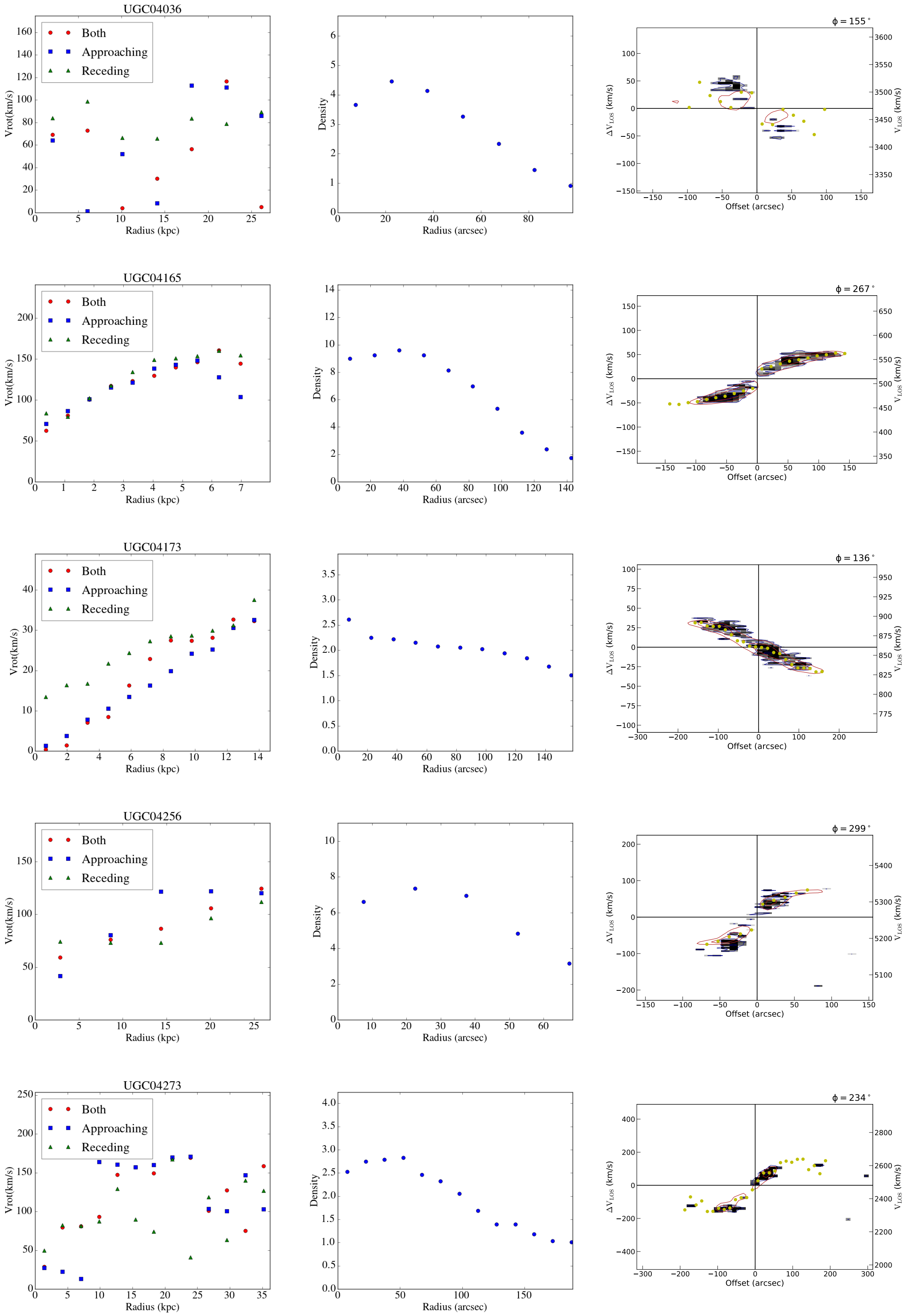

Figure 0: Continued

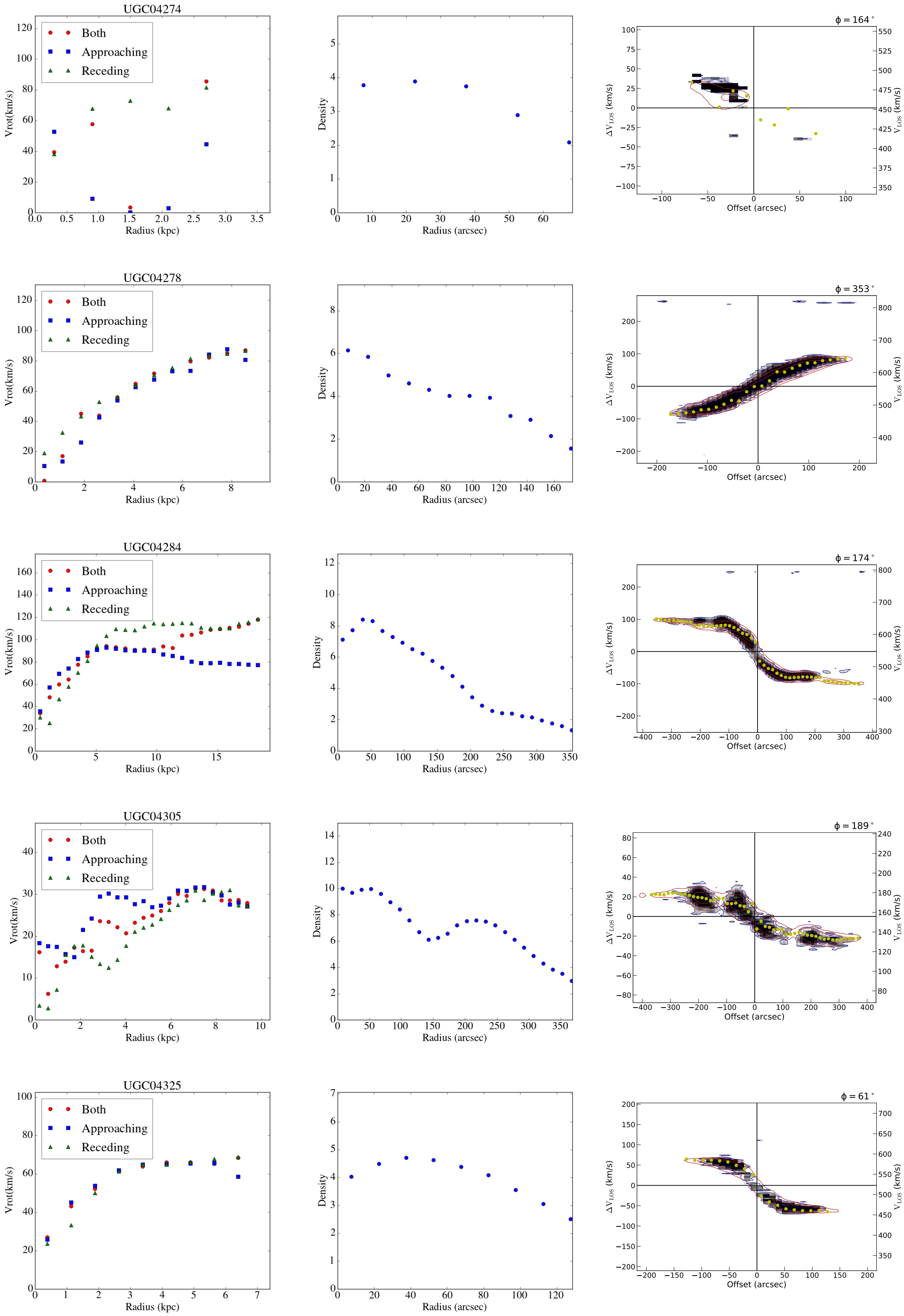

Figure 0: Continued

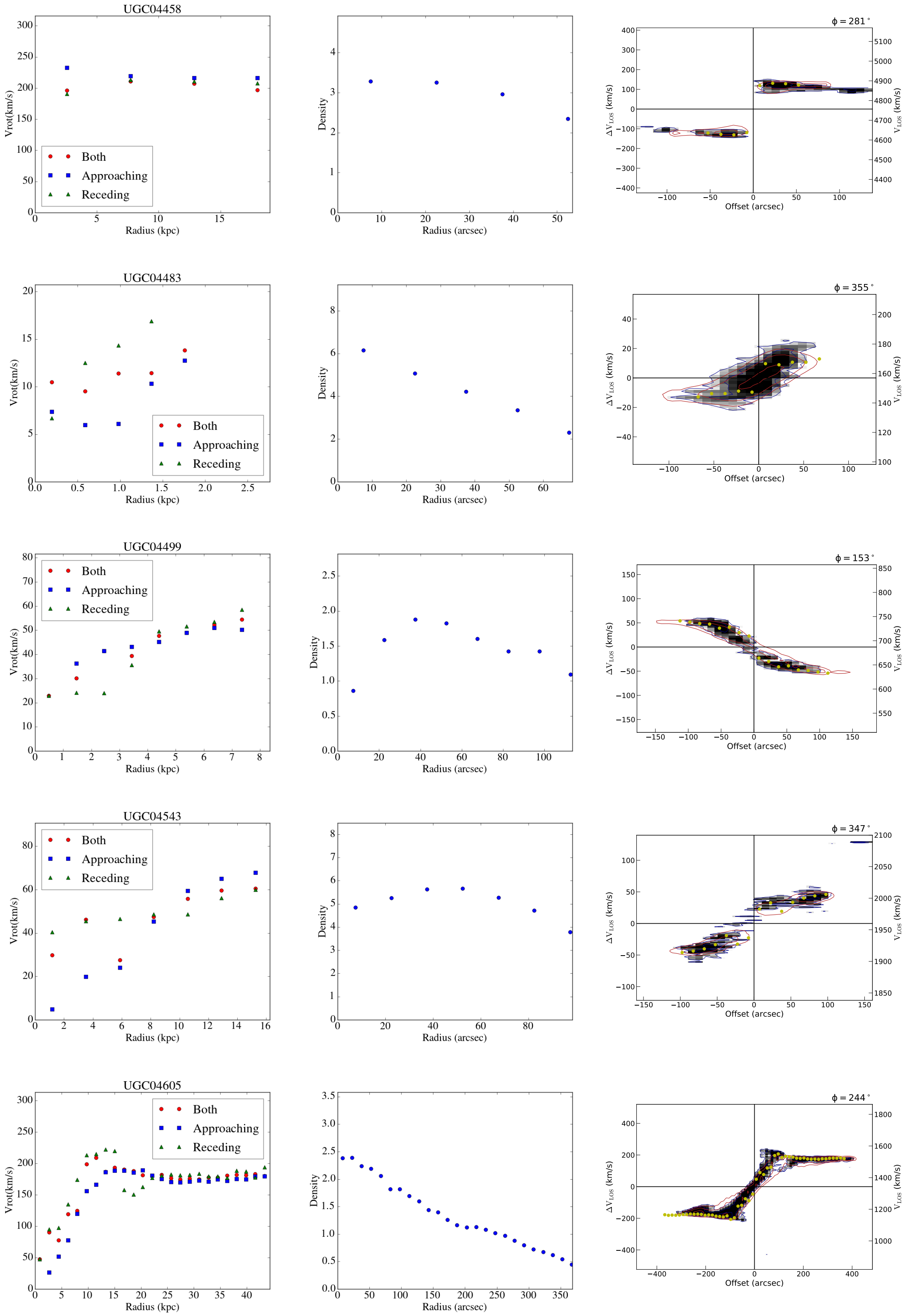

Figure 0: Continued

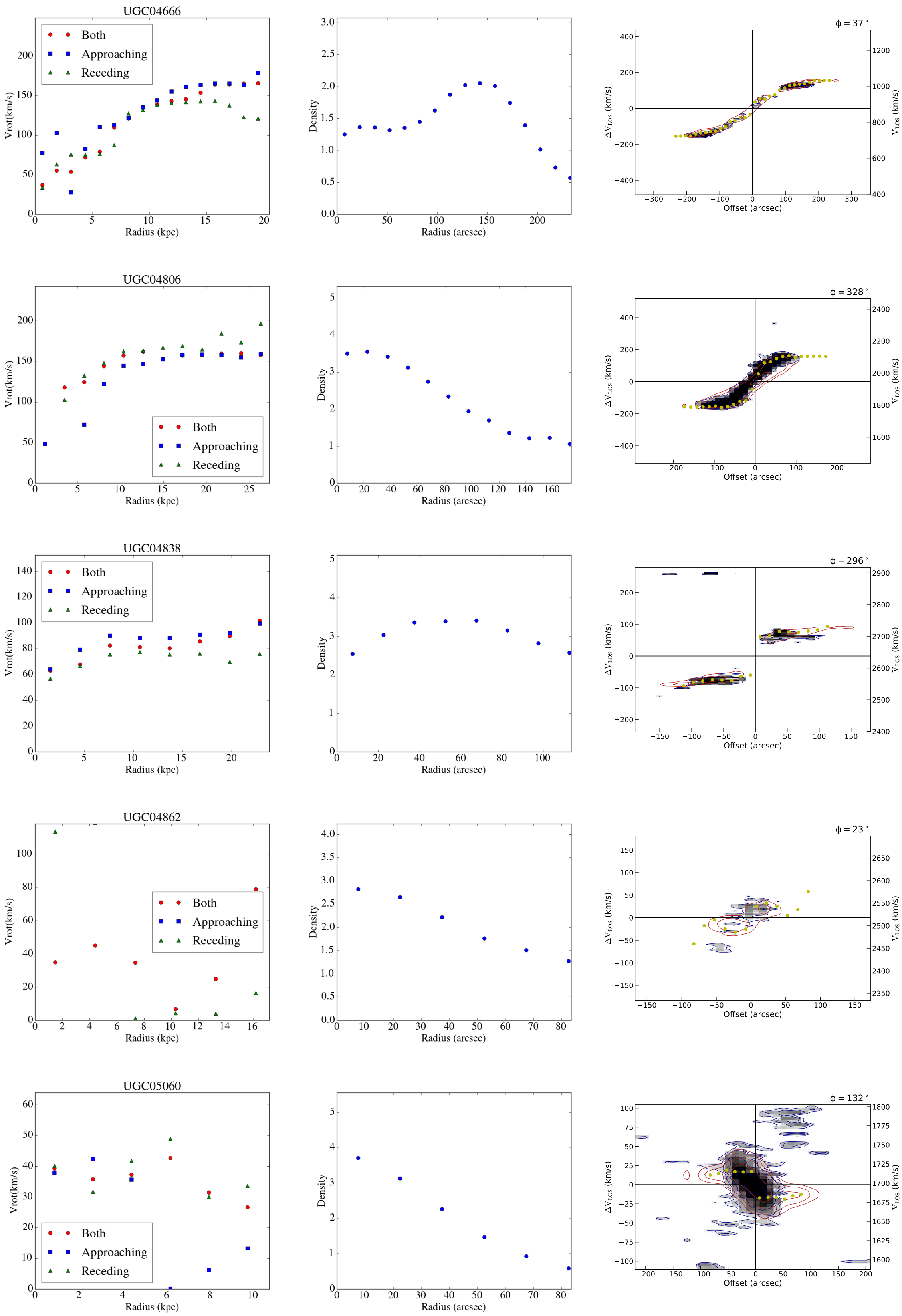

Figure 0: Continued

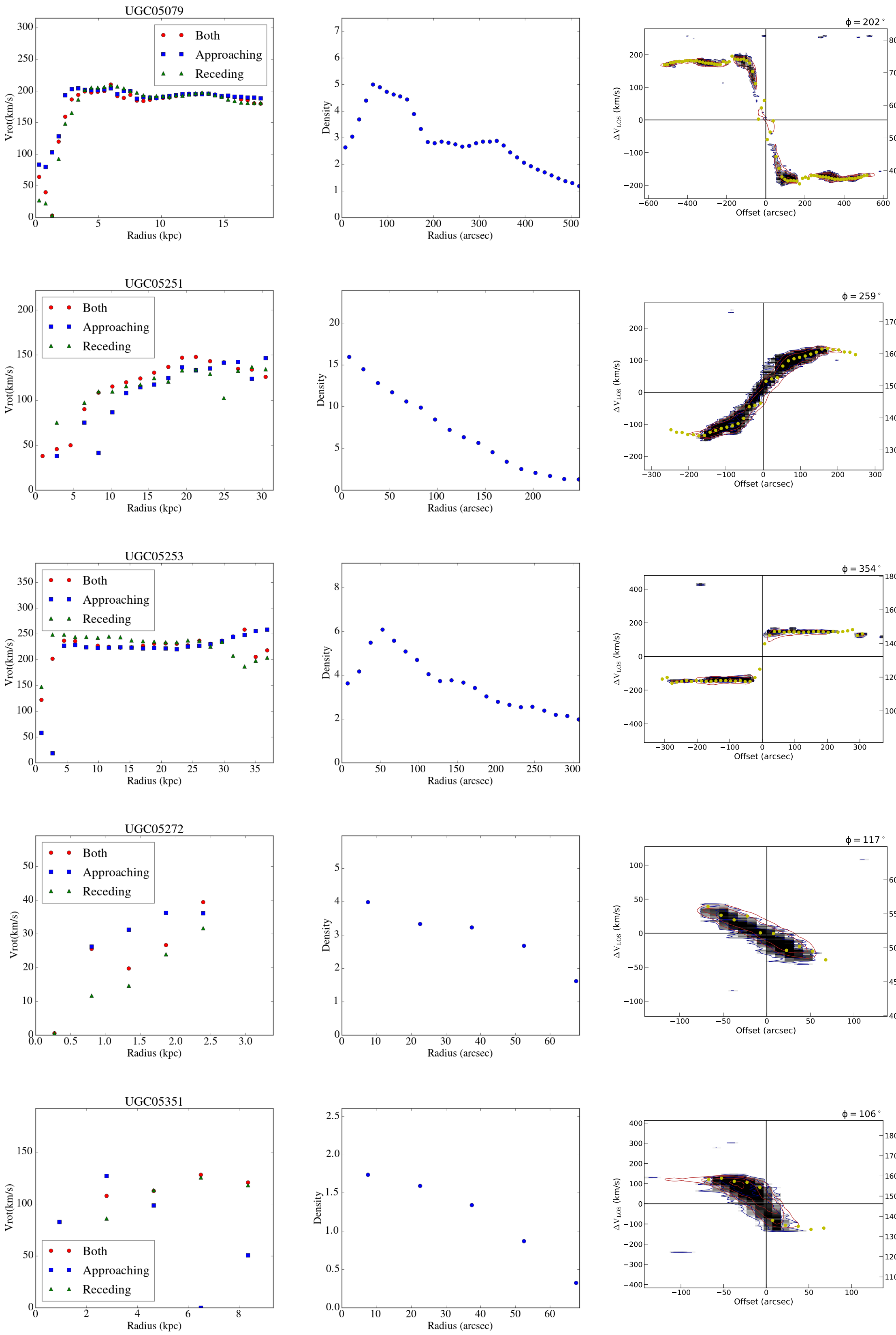

Figure 0: Continued

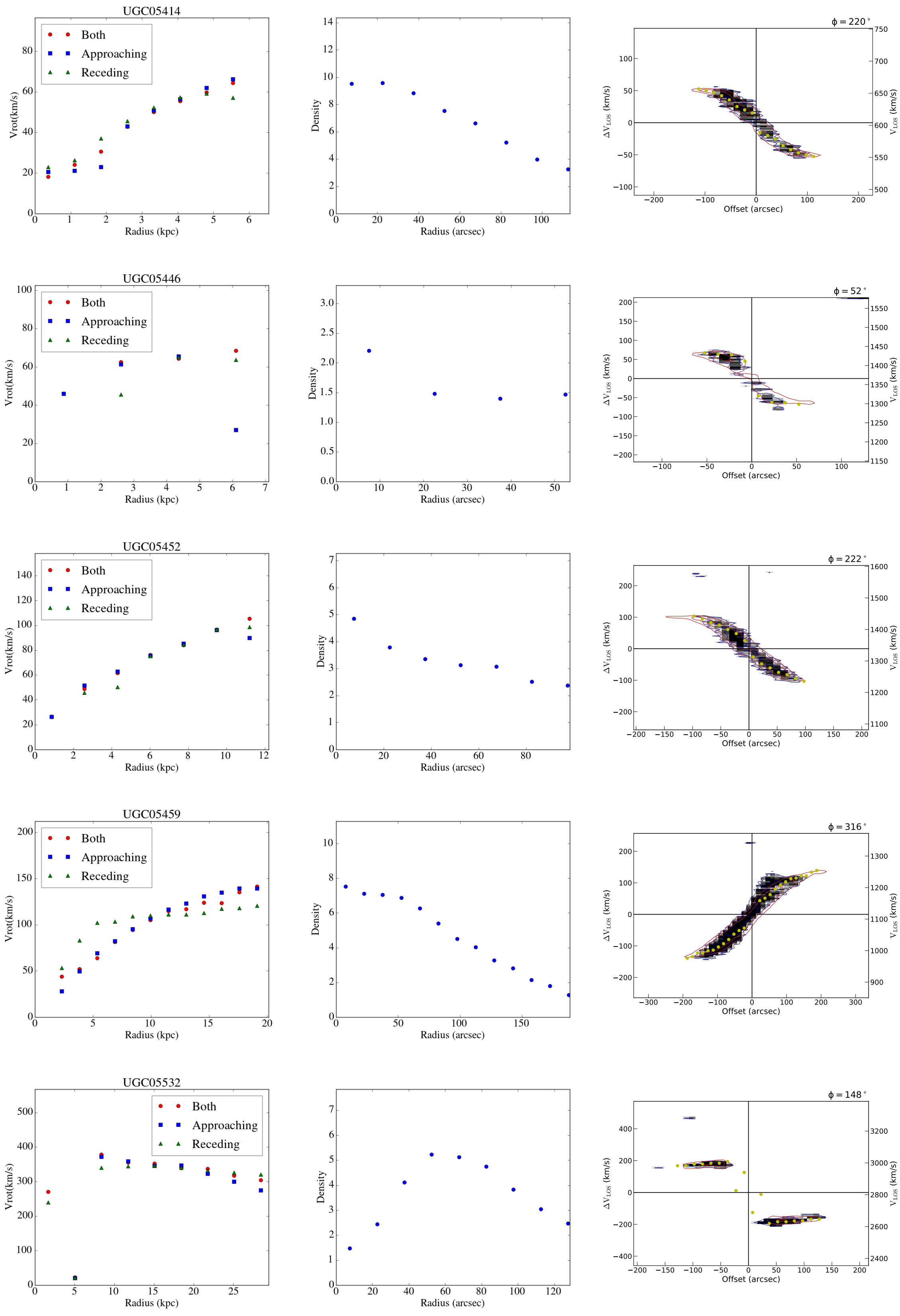

Figure 0: Continued

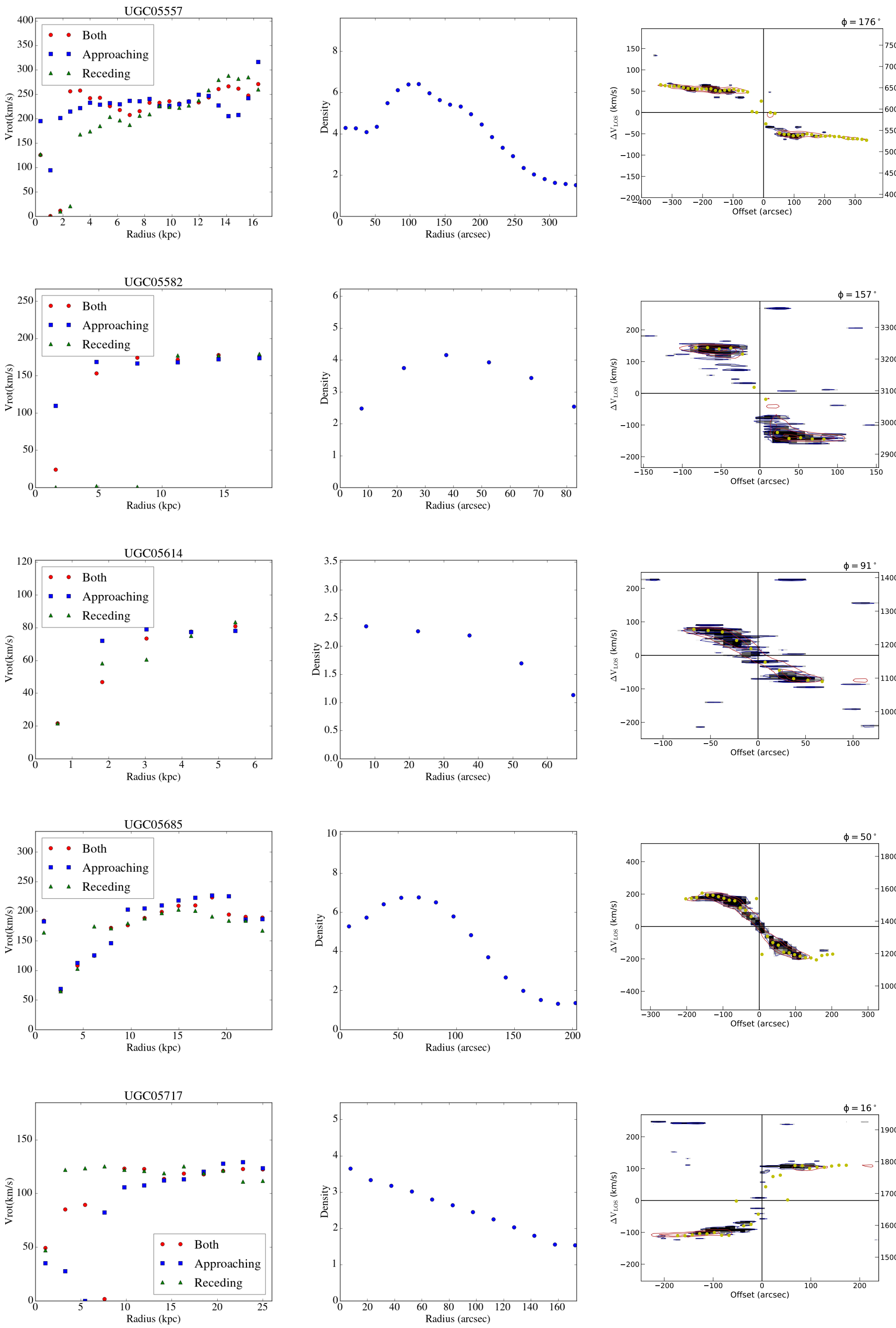

Figure 0: Continued

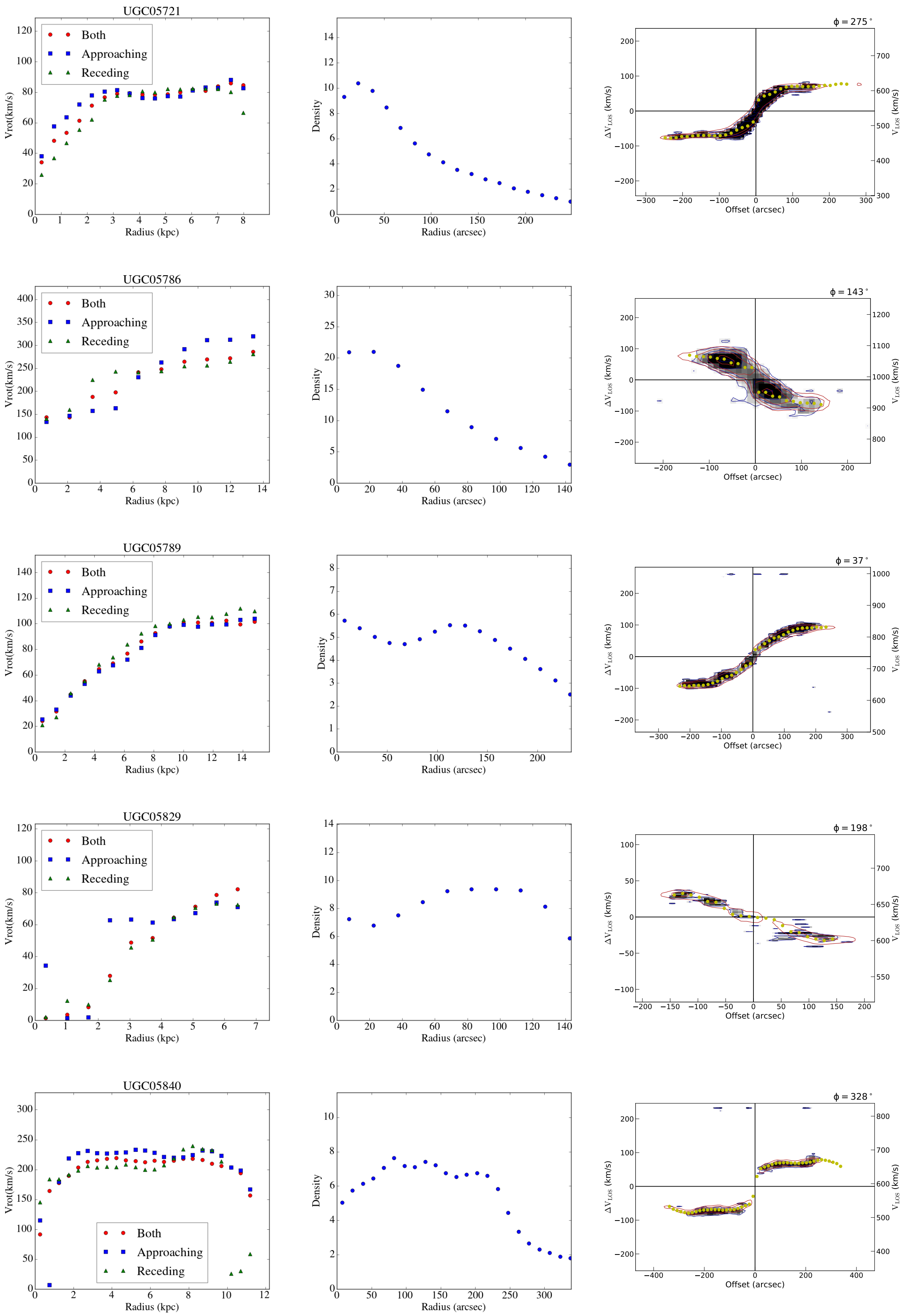

Figure 0: Continued

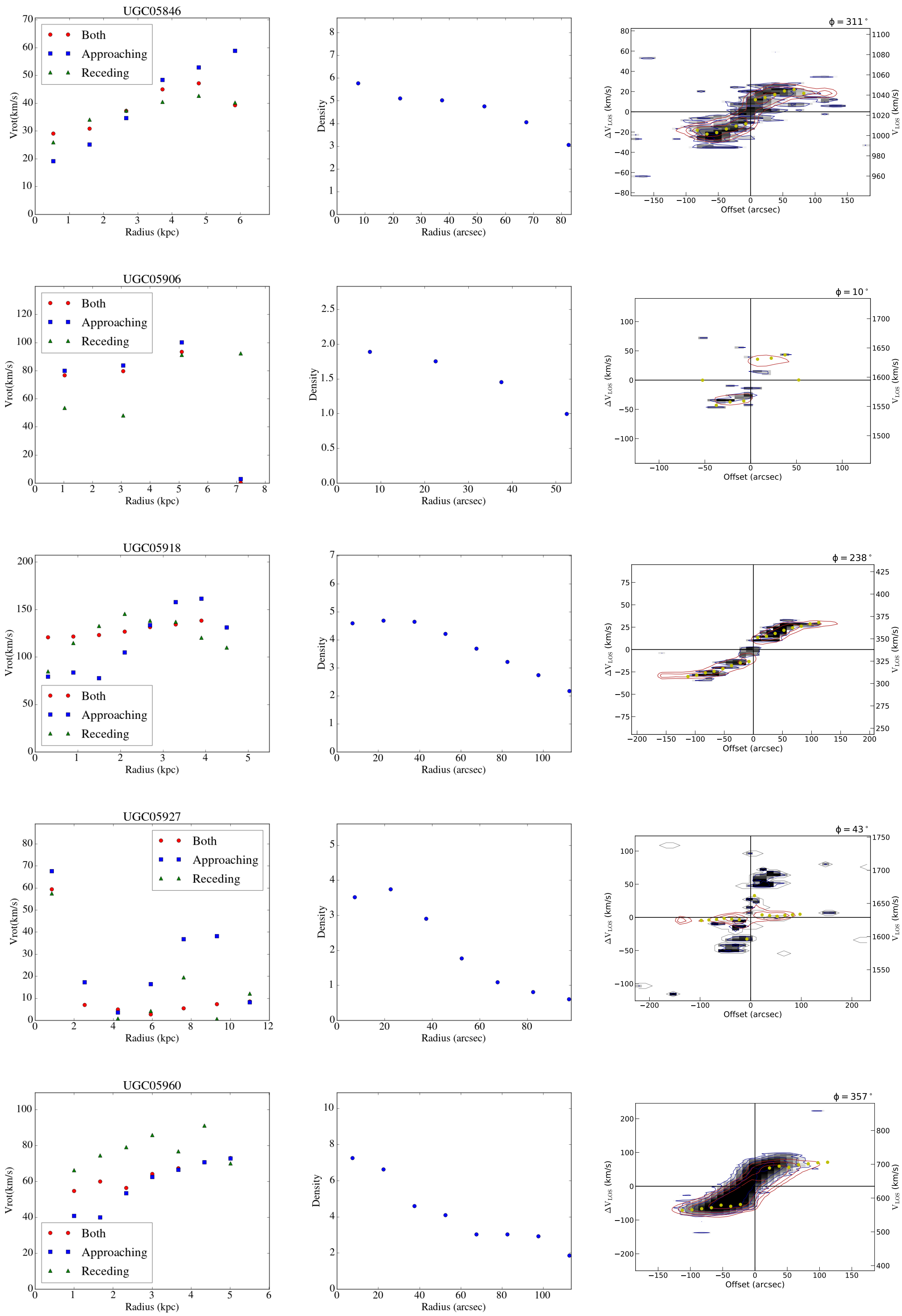

Figure 0: Continued

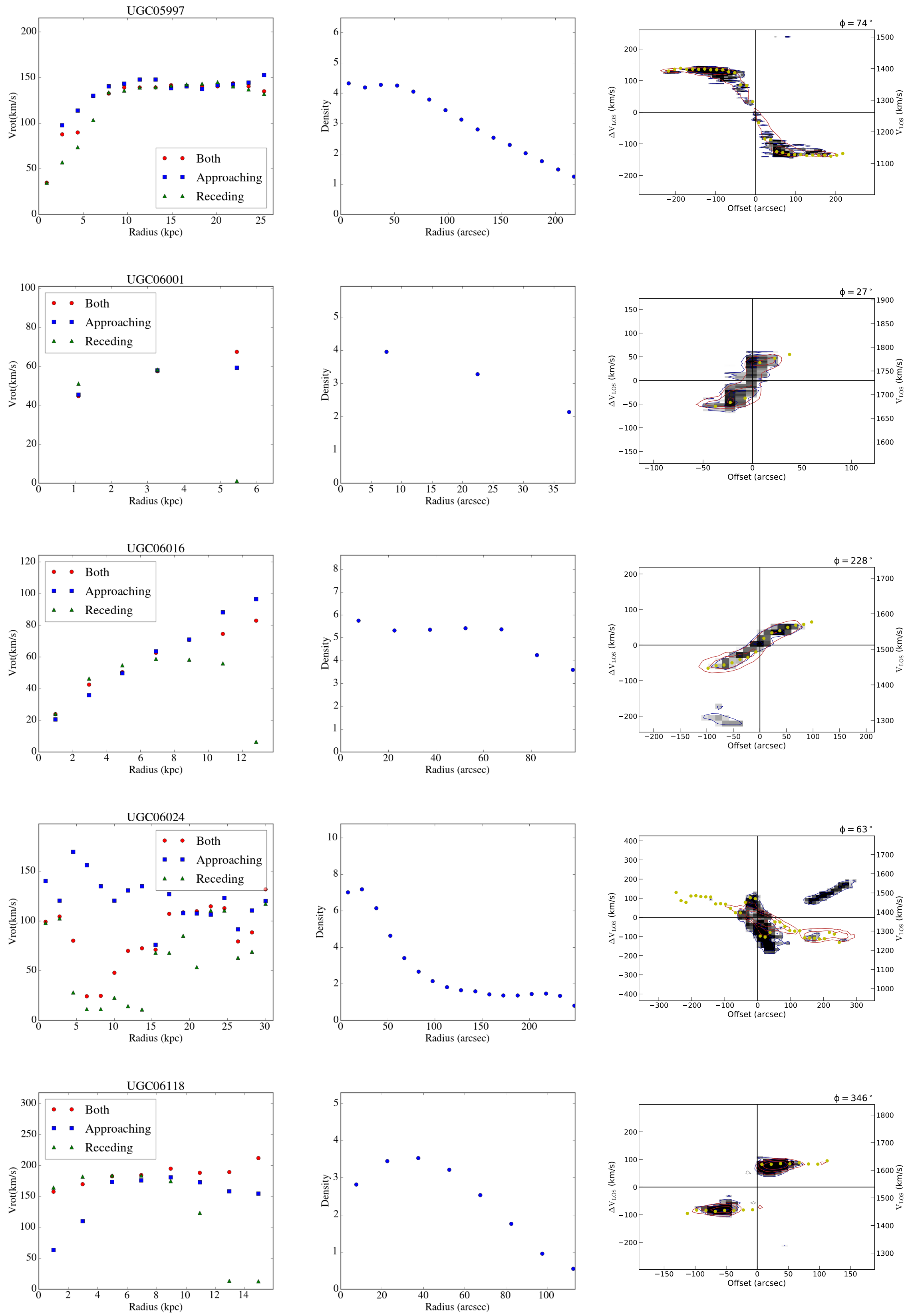

Figure 0: Continued

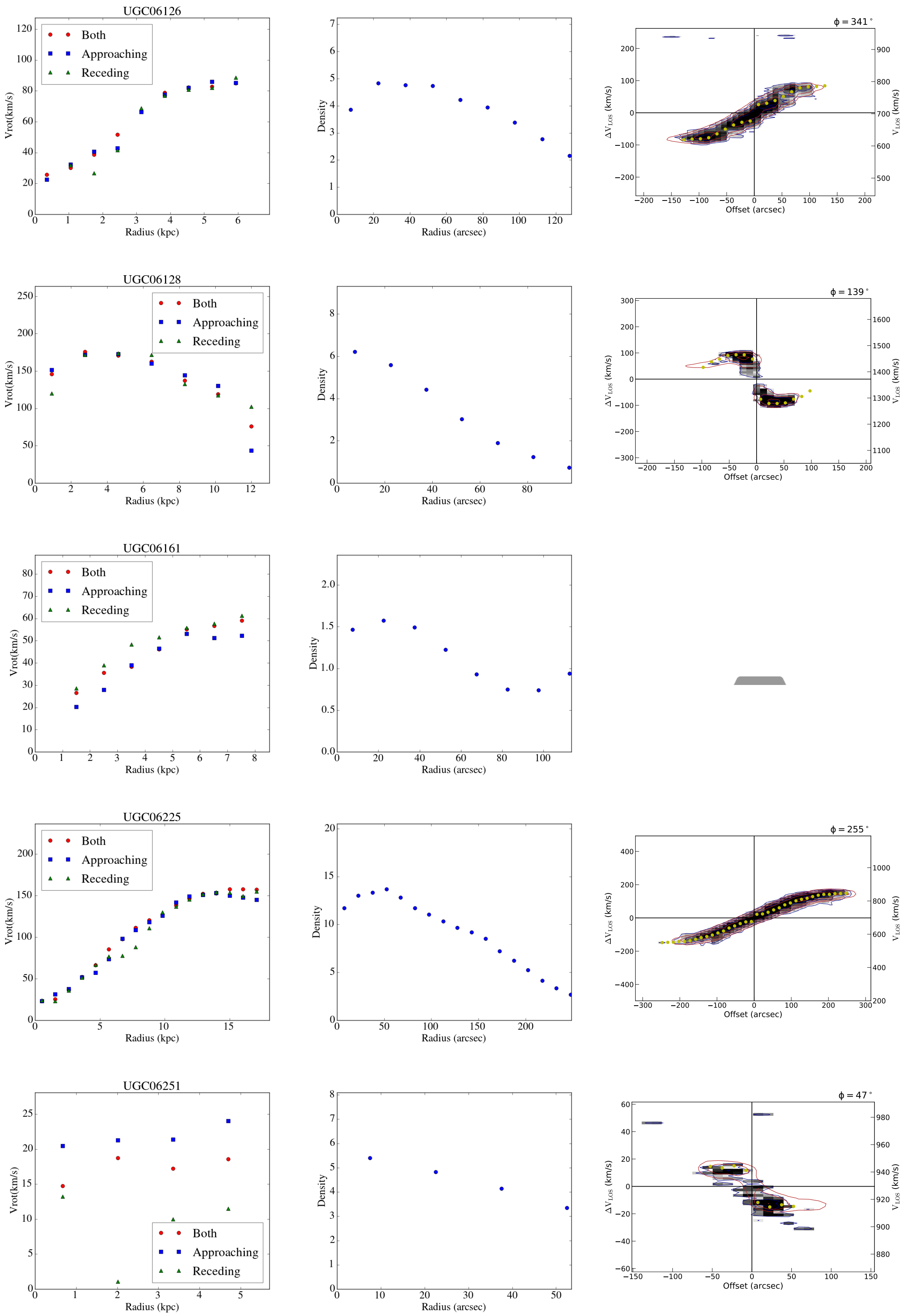

Figure 0: Continued

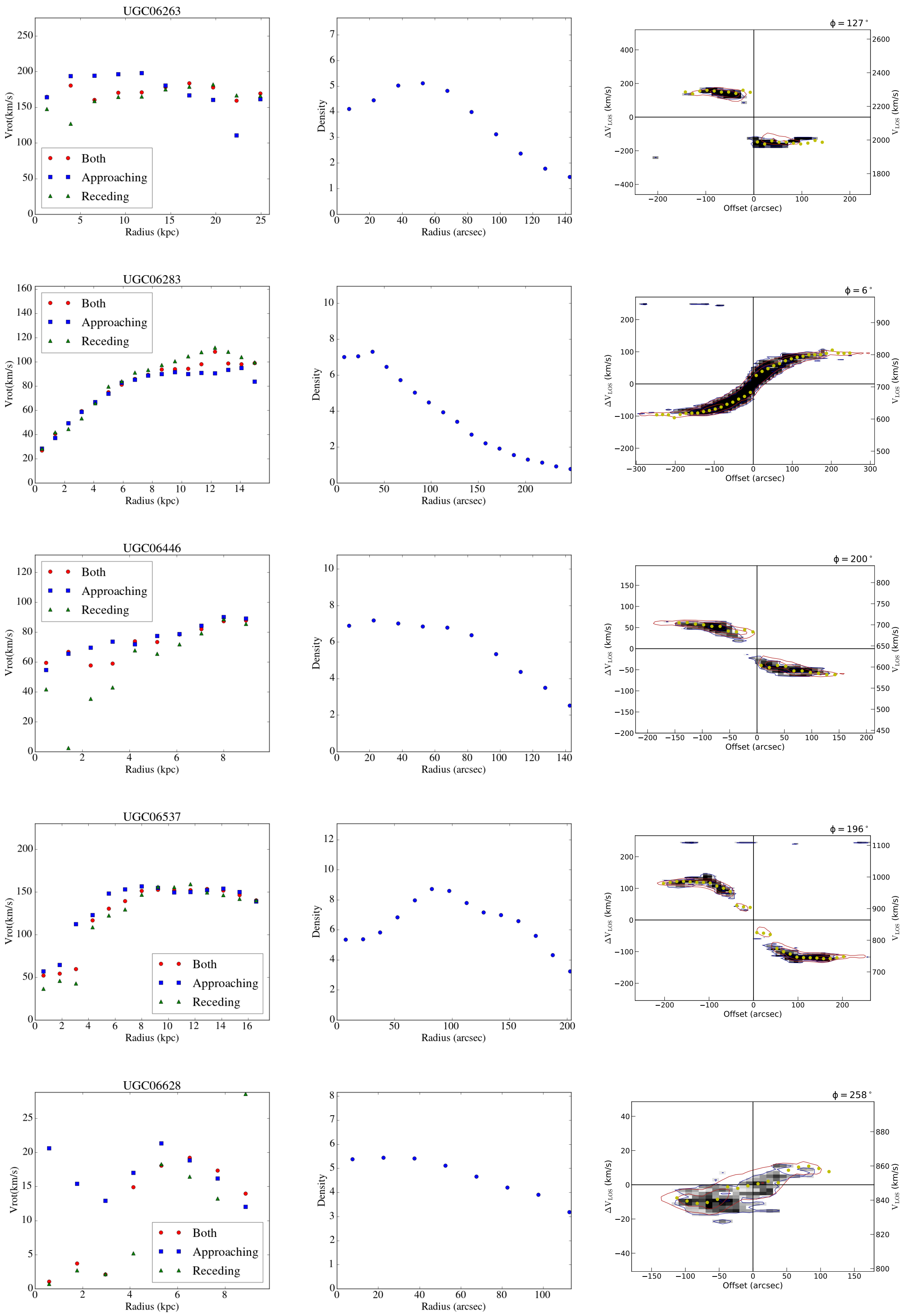

Figure 0: Continued

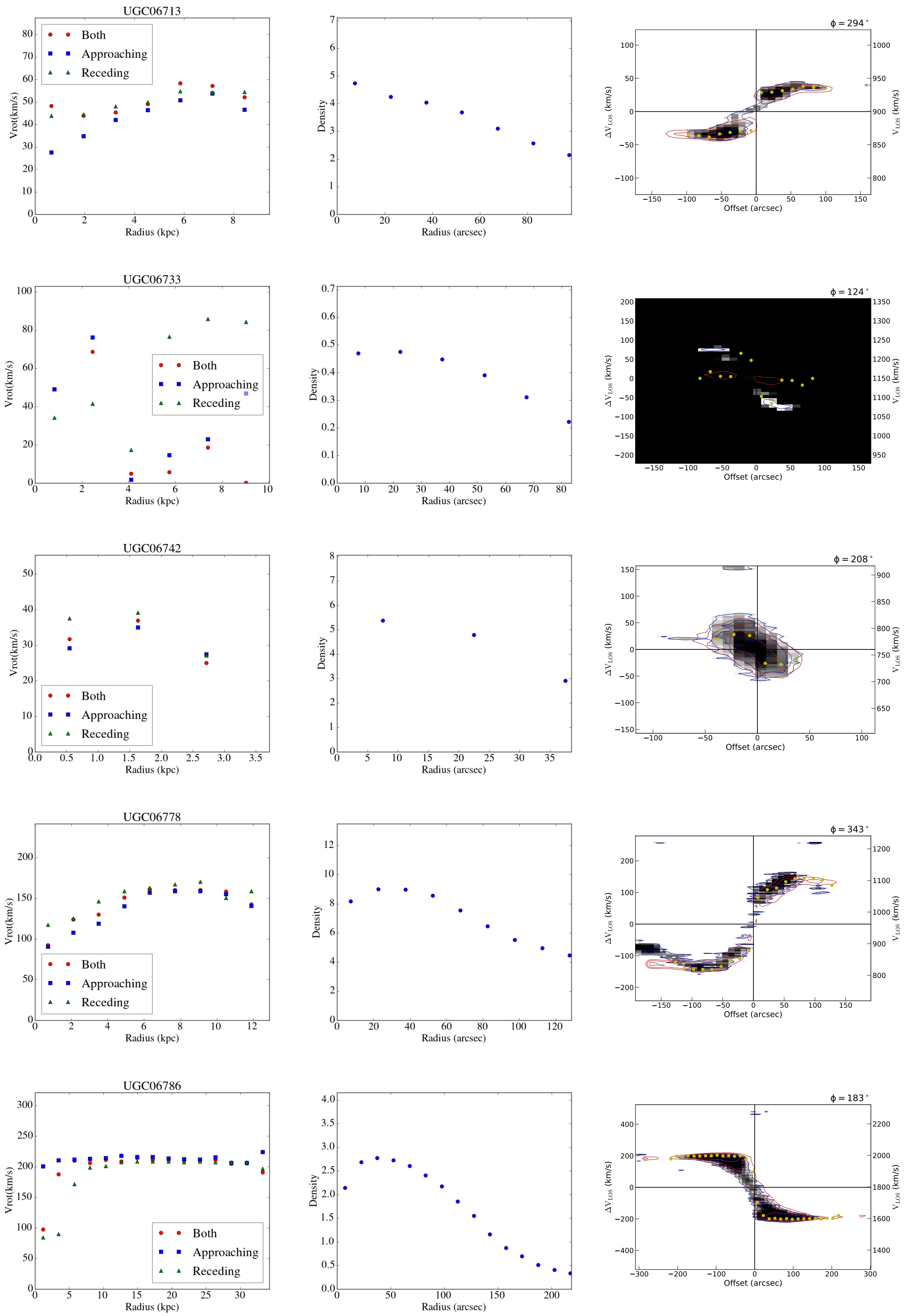

Figure 0: Continued

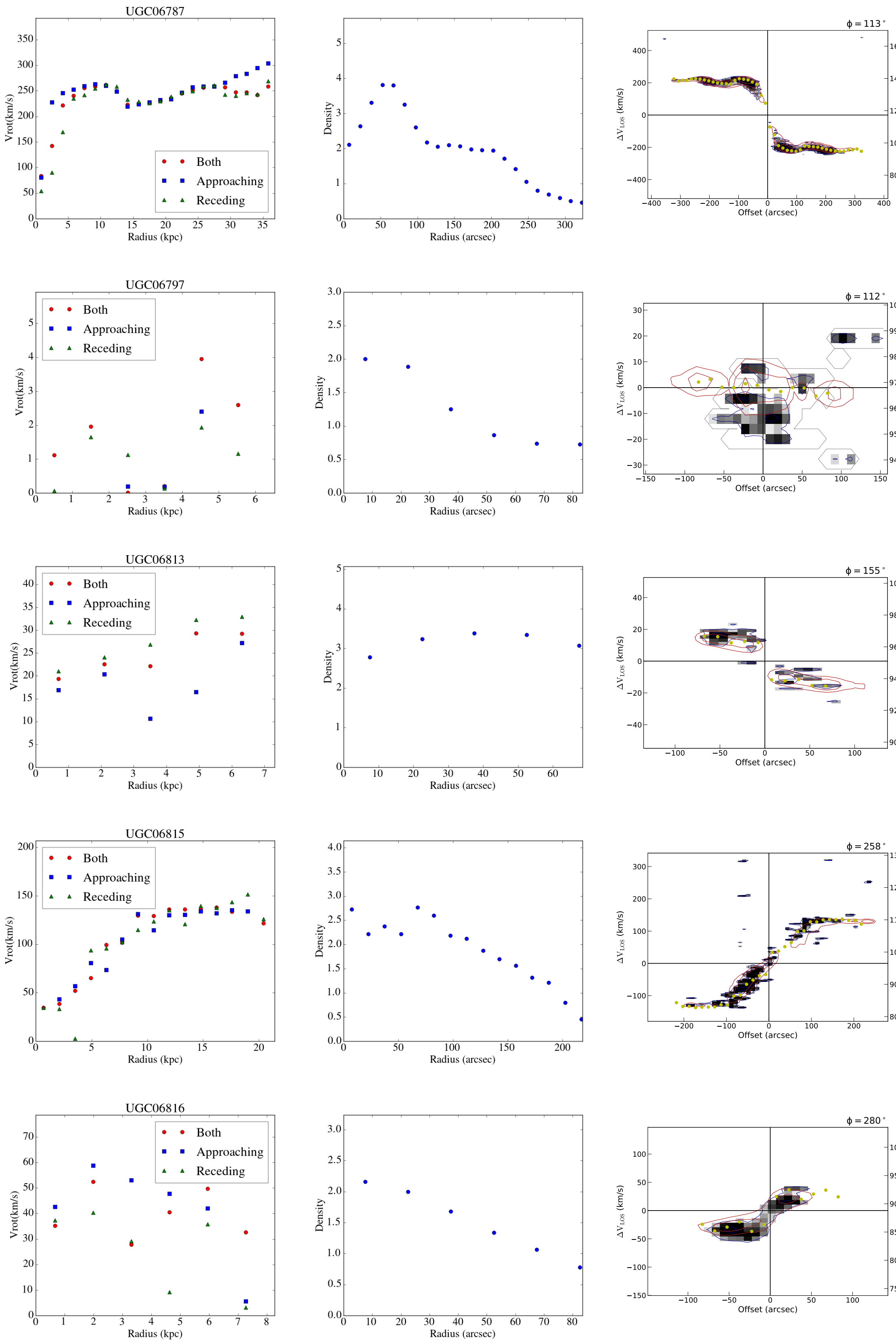

Figure 0: Continued

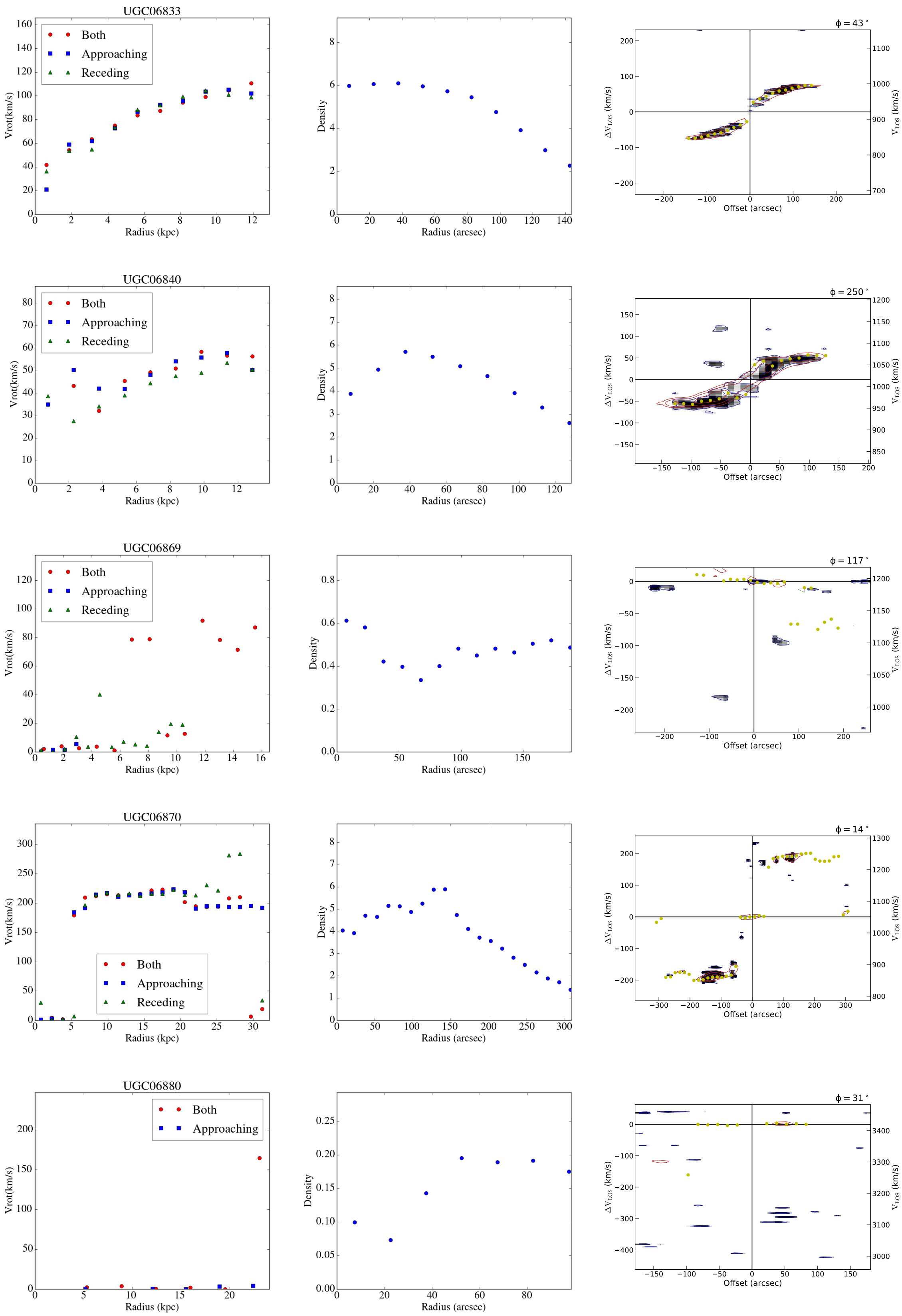

Figure 0: Continued

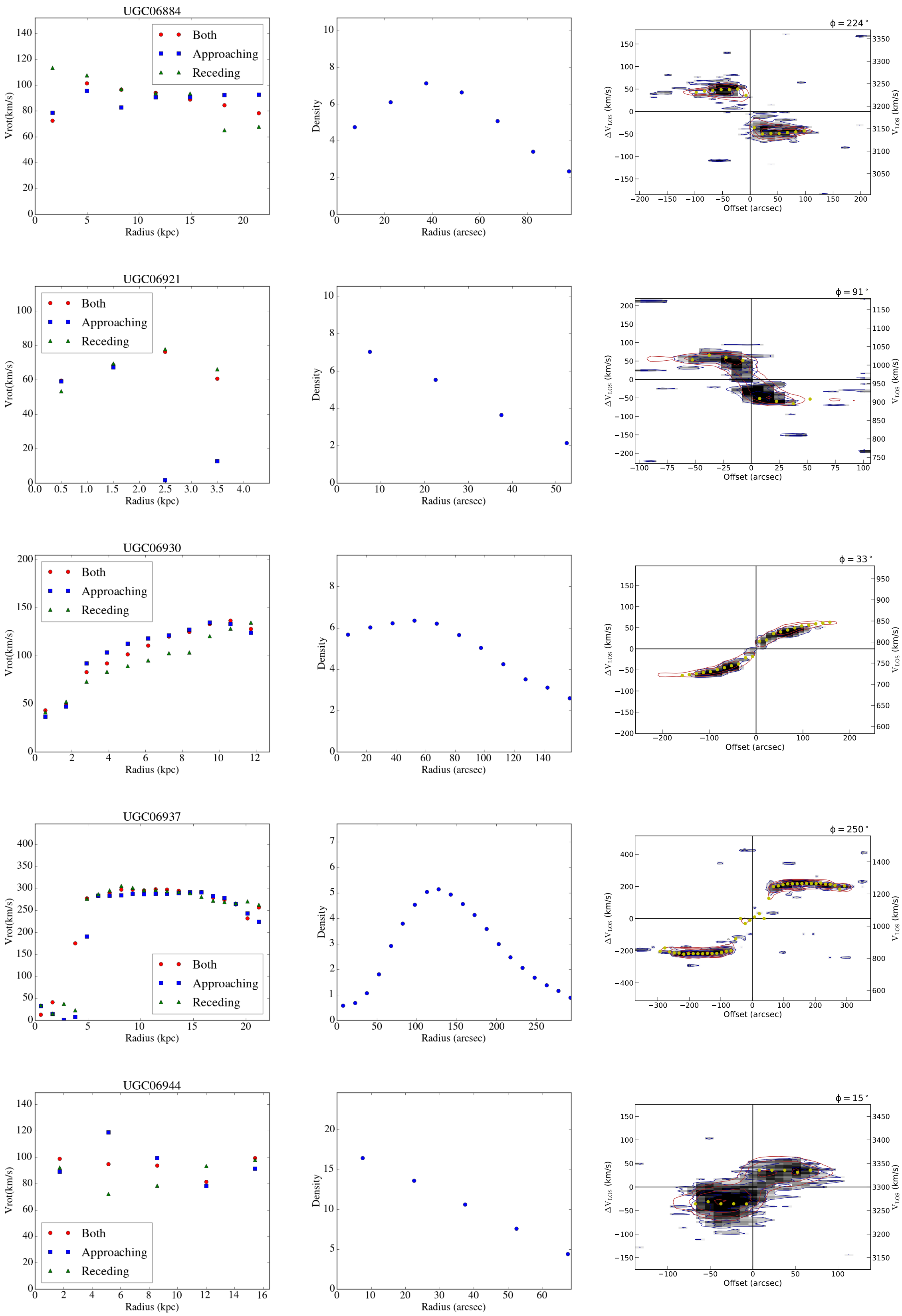

Figure 0: Continued

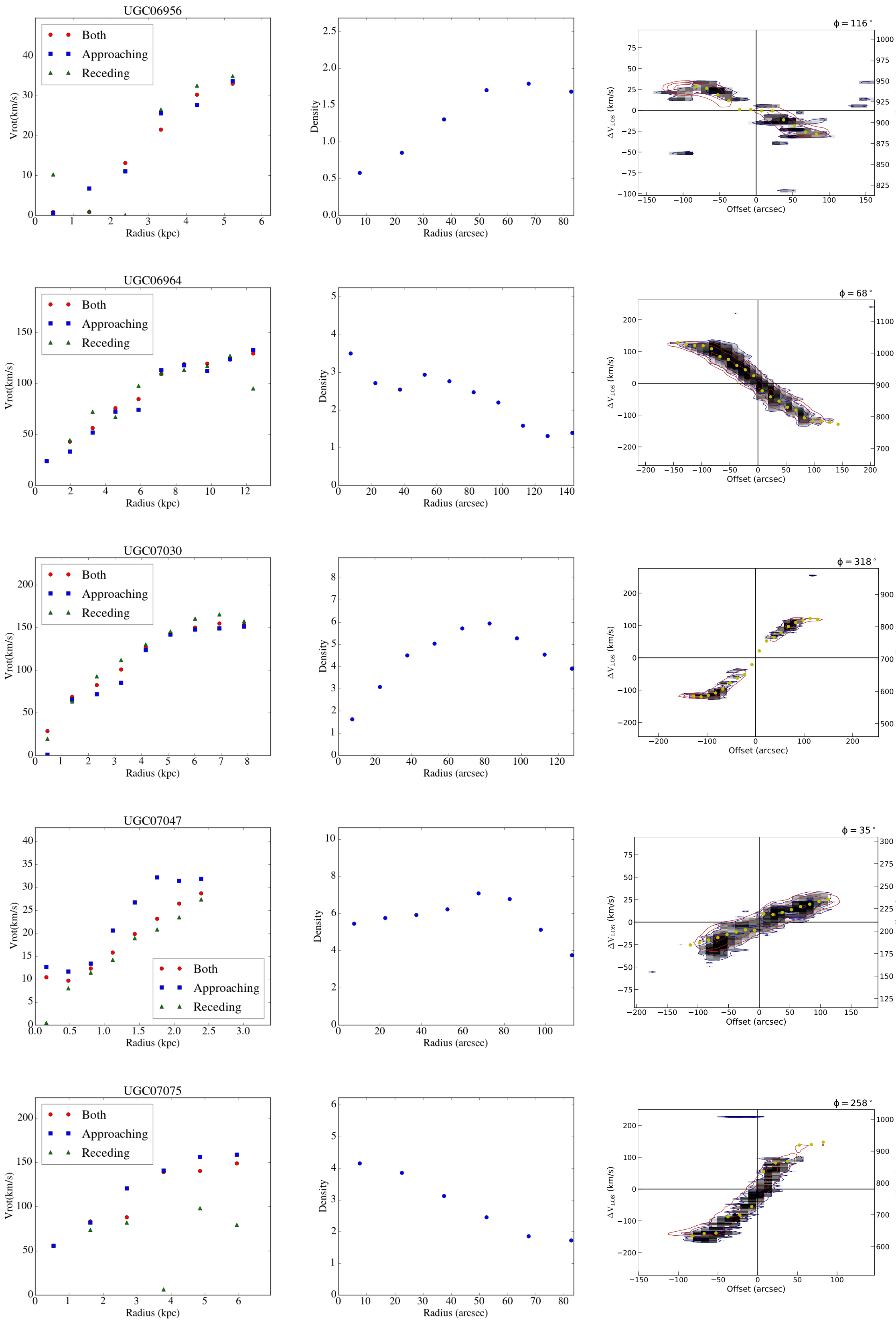

Figure 0: Continued

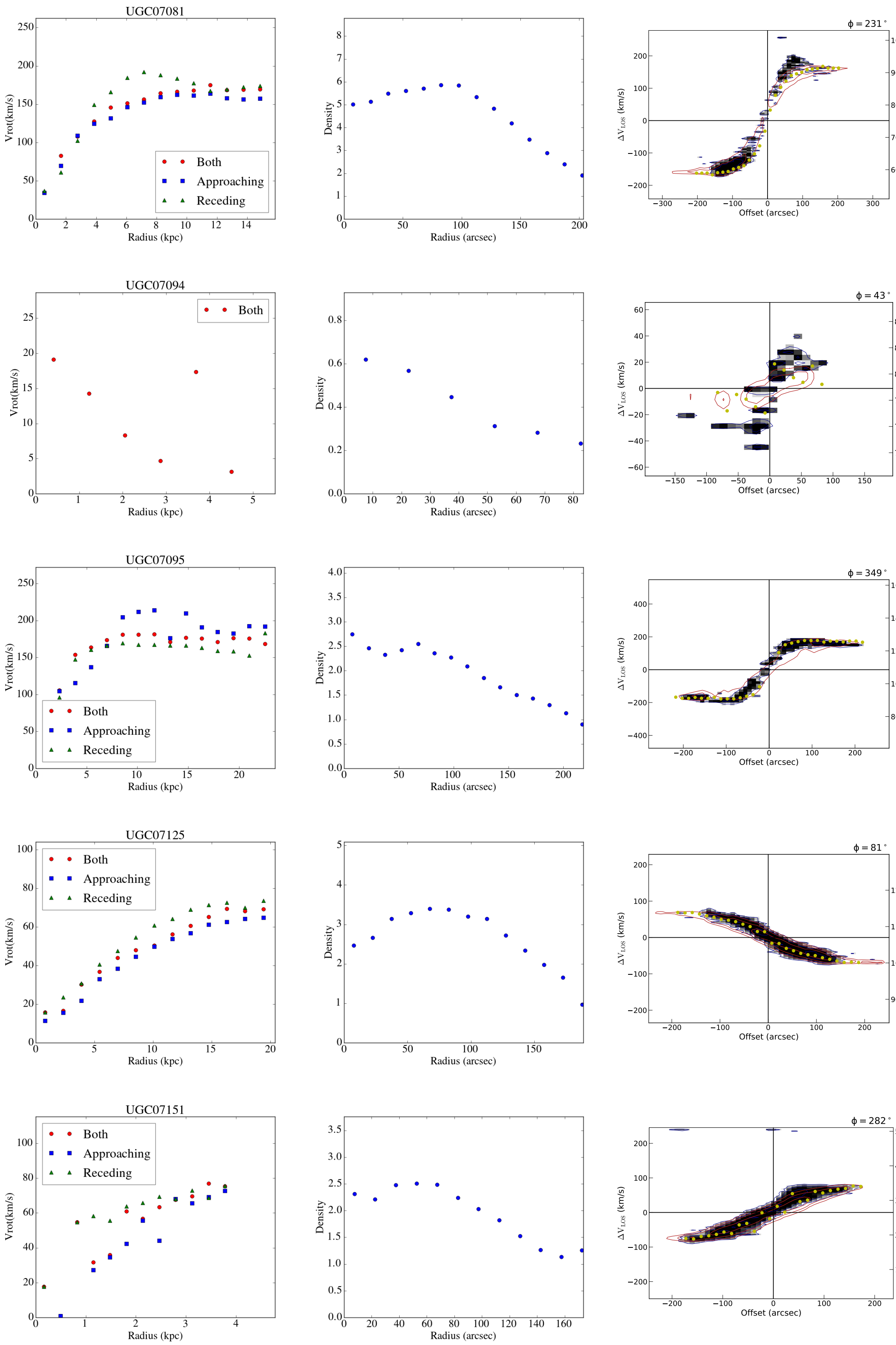

Figure 0: Continued

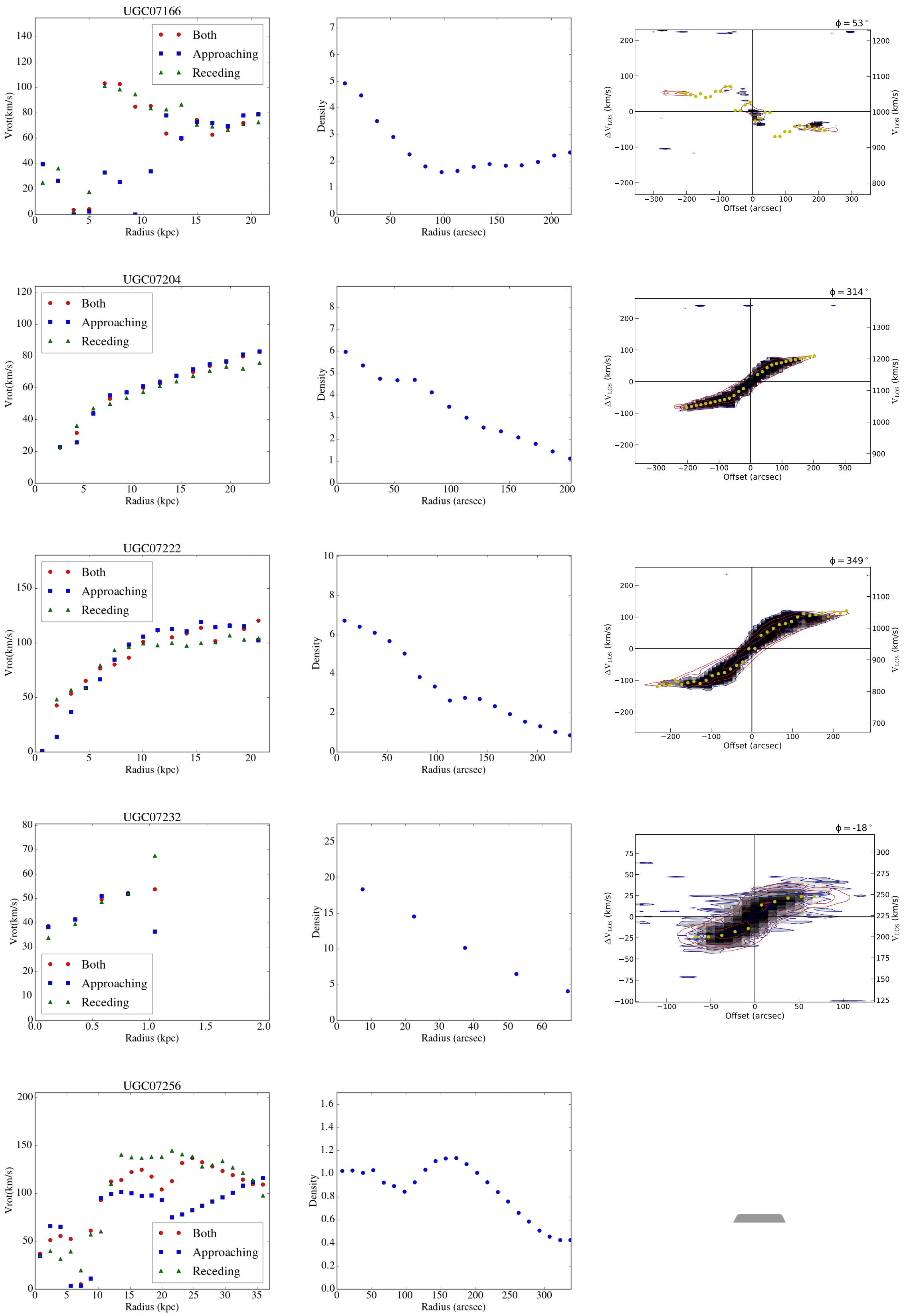

Figure 0: Continued

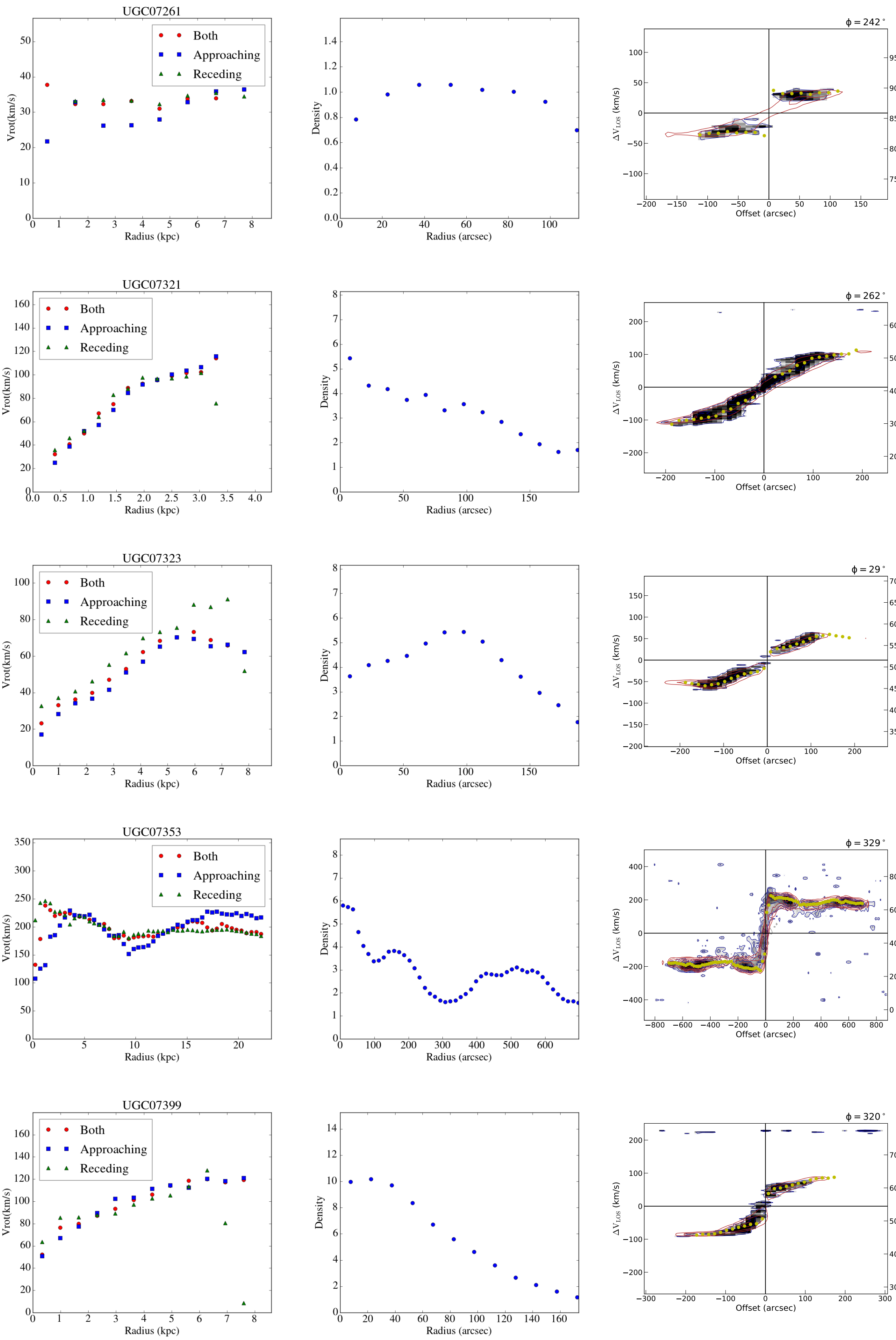

Figure 0: Continued

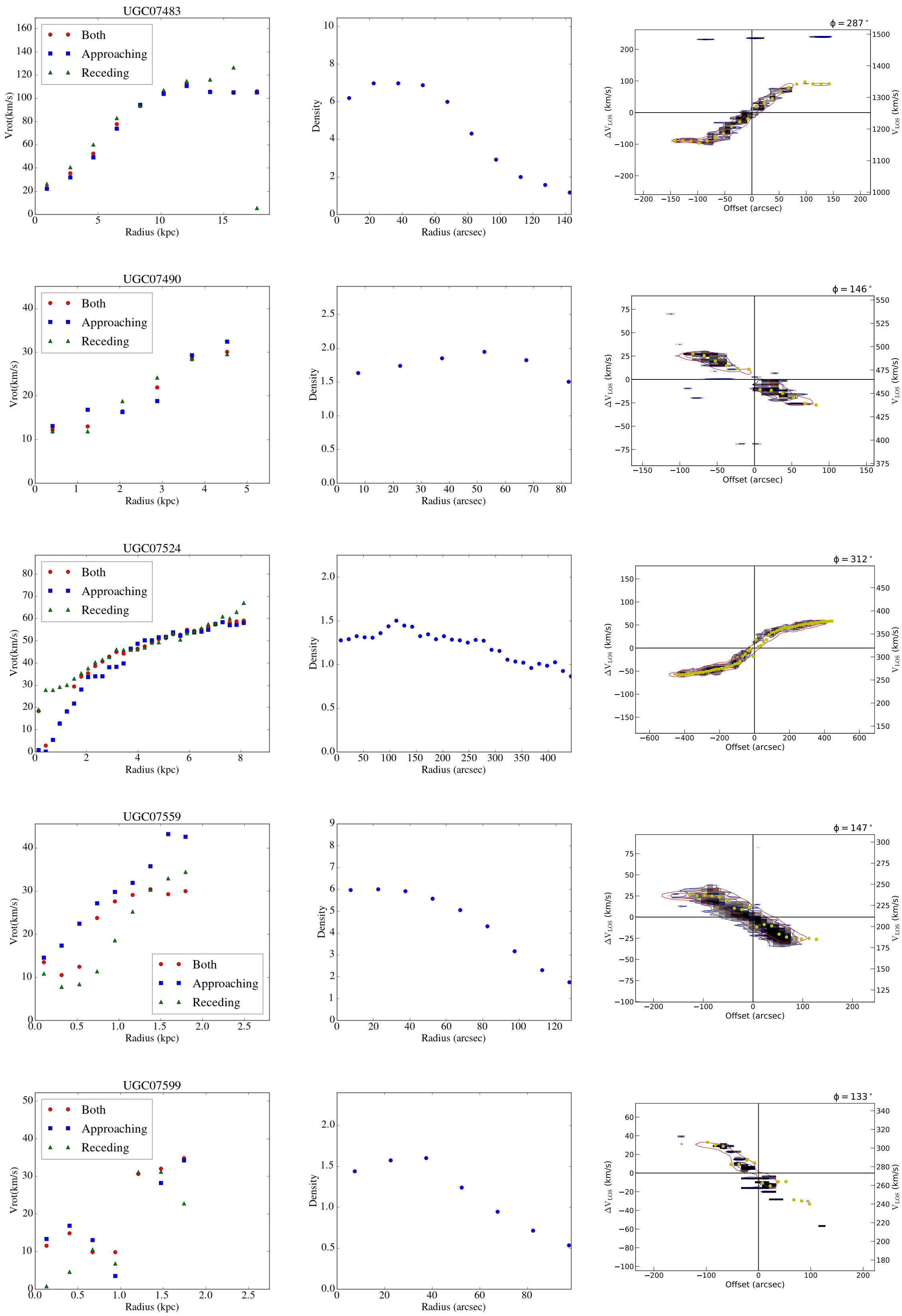

Figure 0: Continued

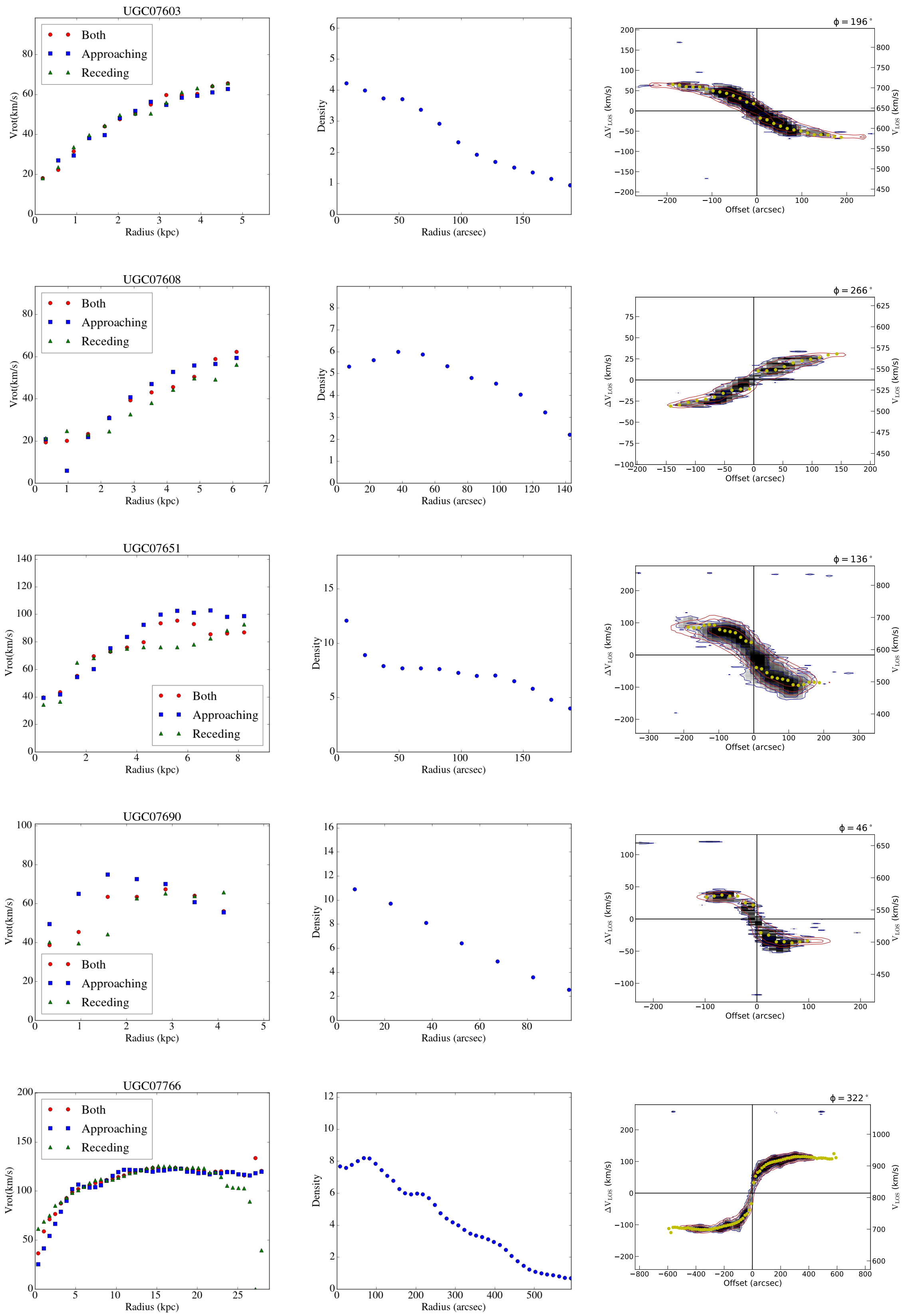

Figure 0: Continued

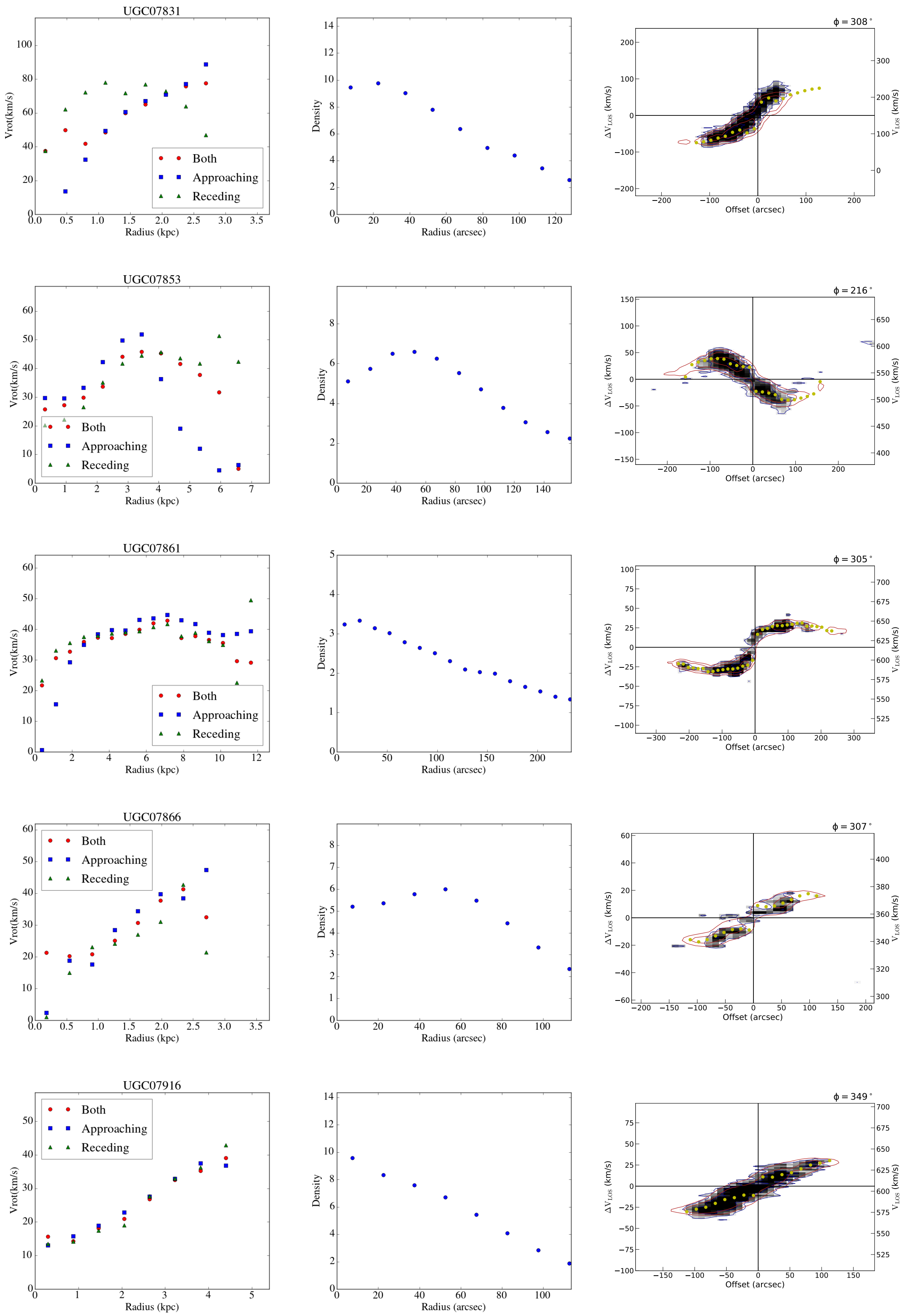

Figure 0: Continued

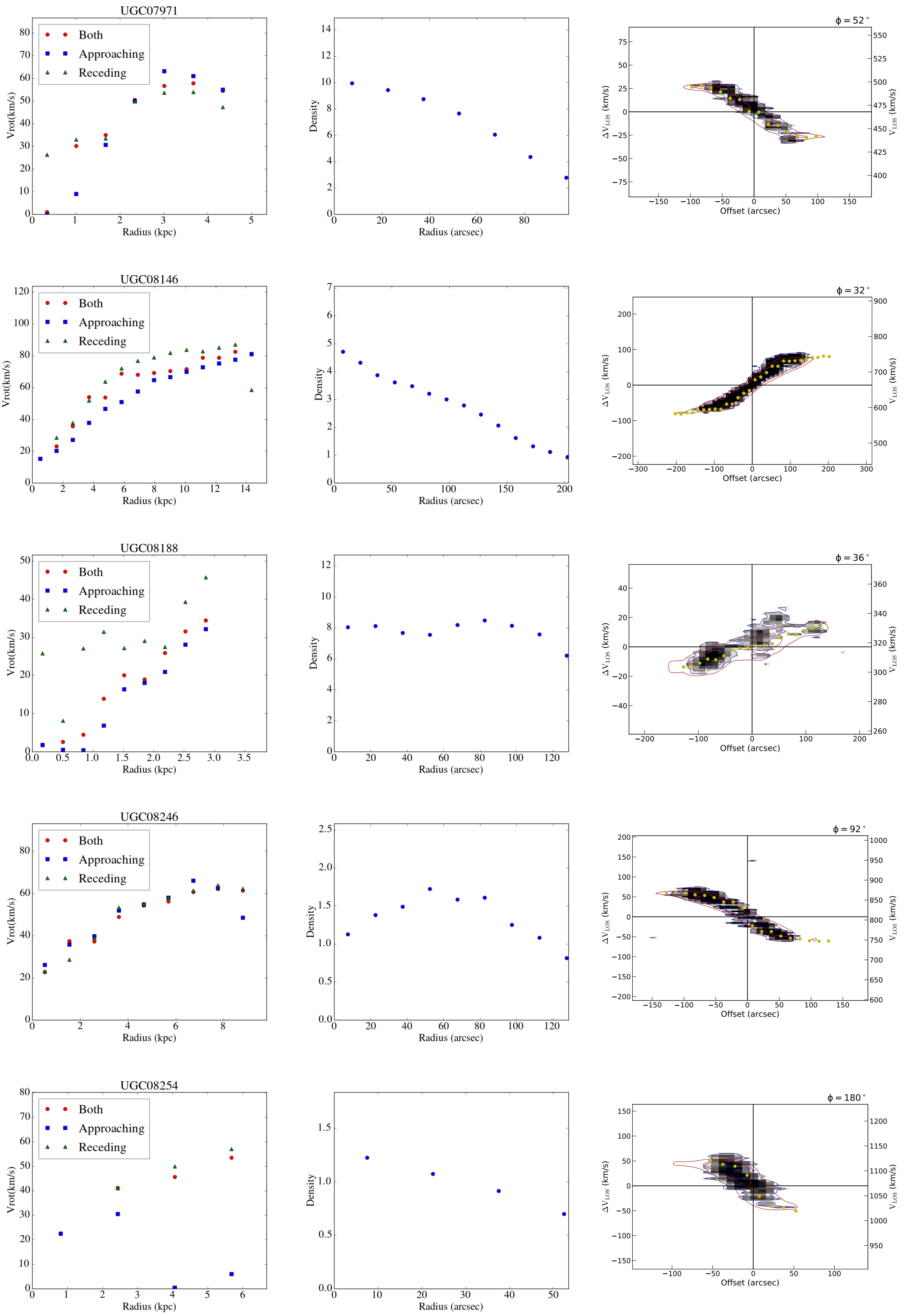

Figure 0: Continued

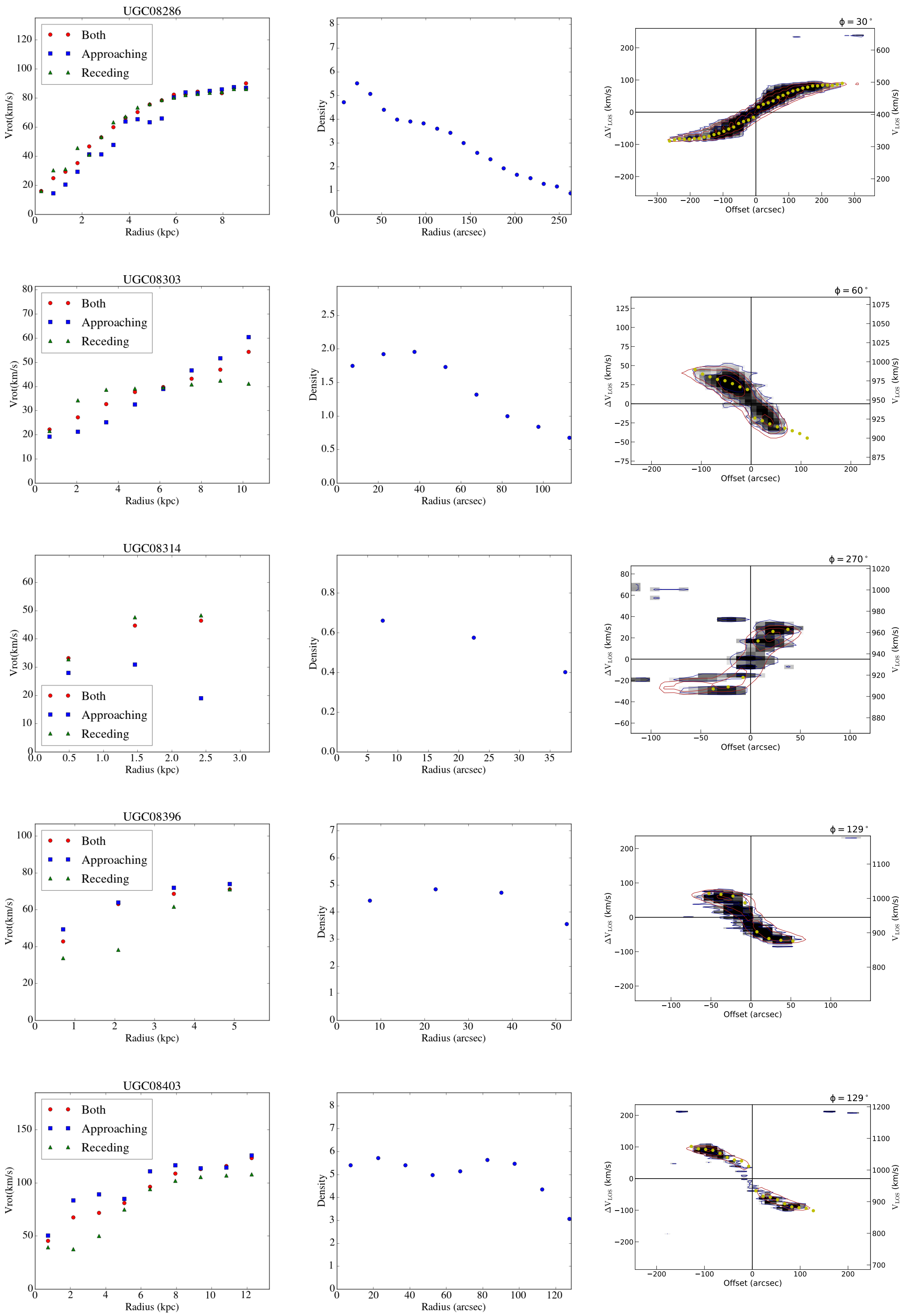

Figure 0: Continued

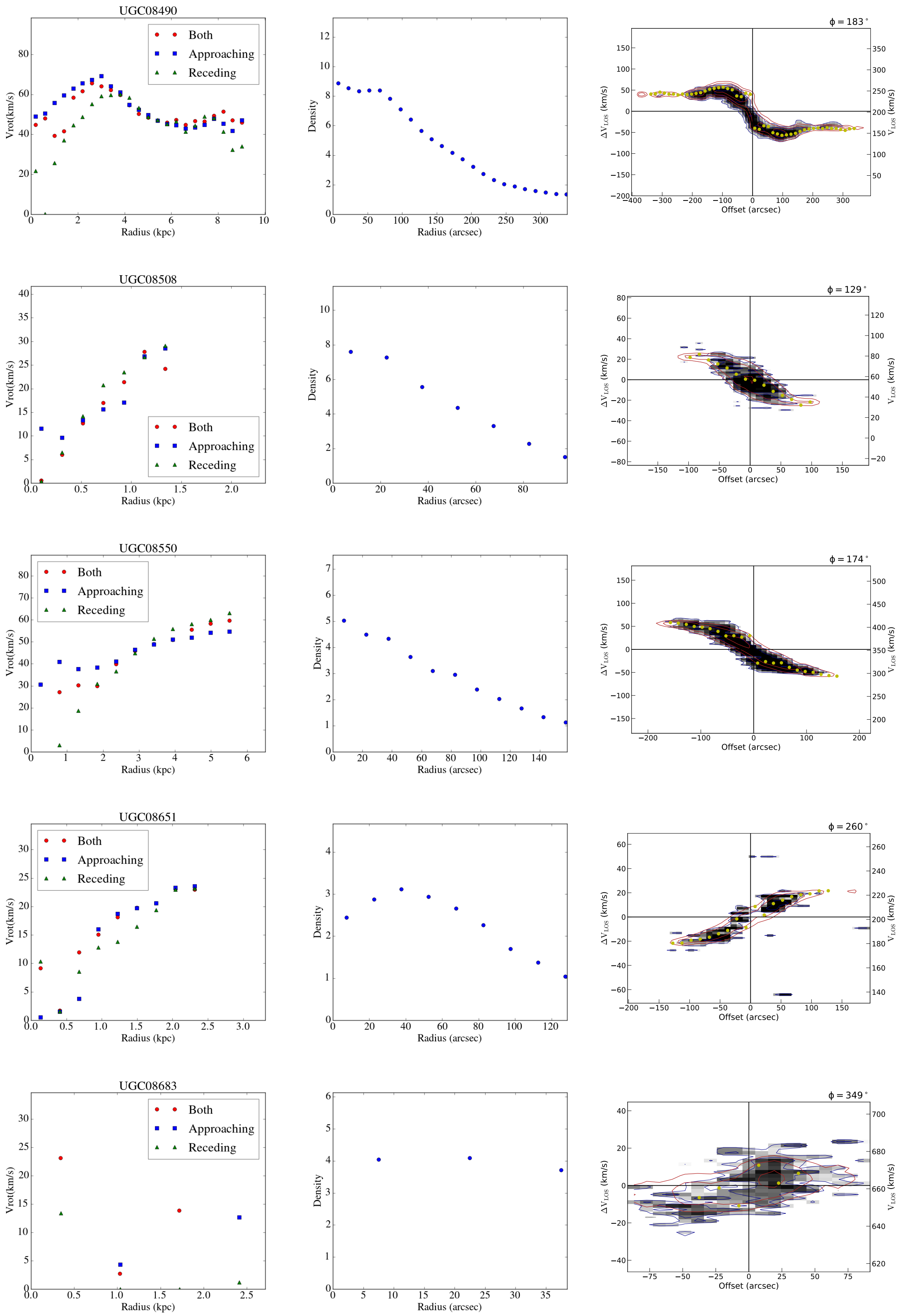

Figure 0: Continued

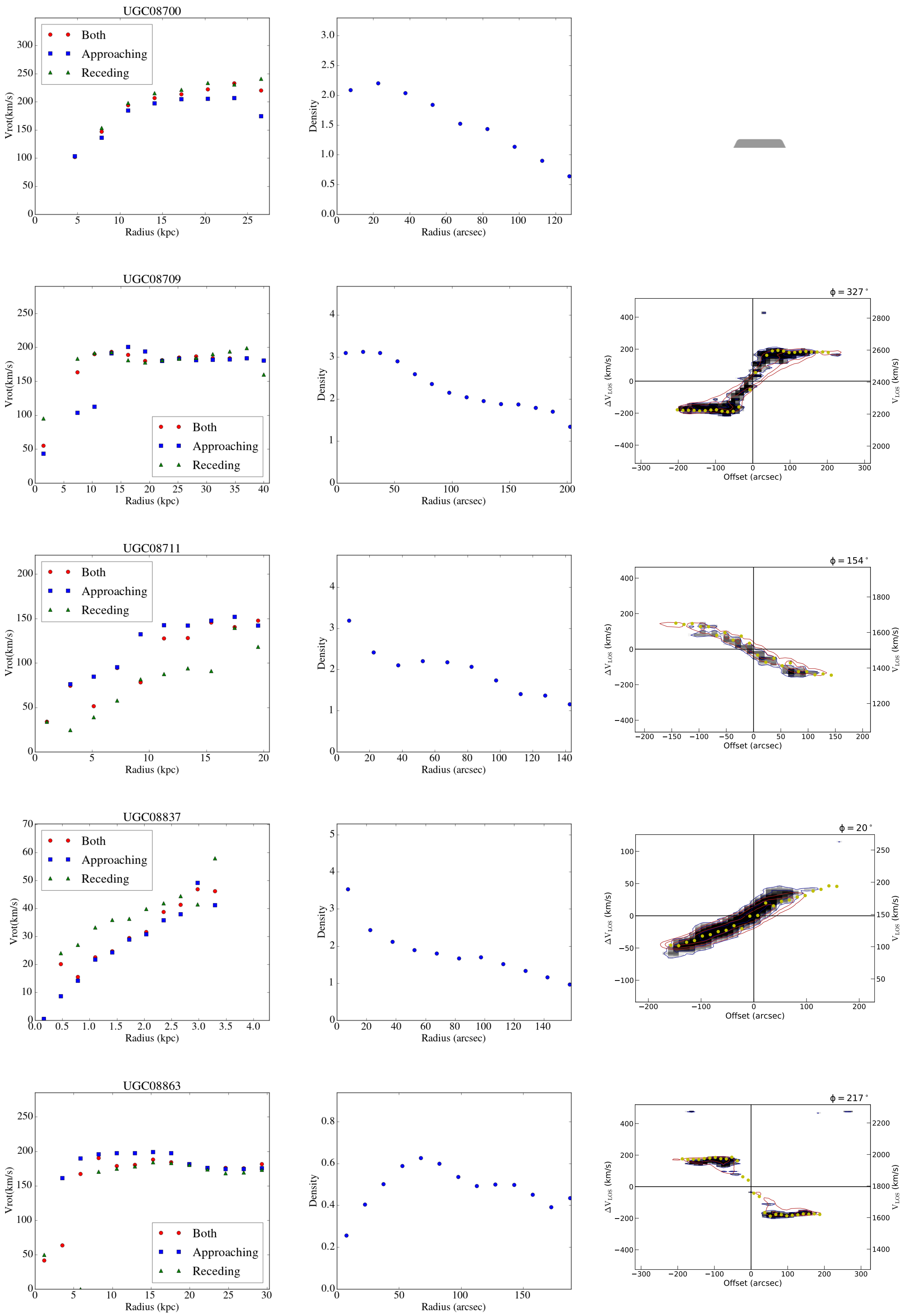

Figure 0: Continued

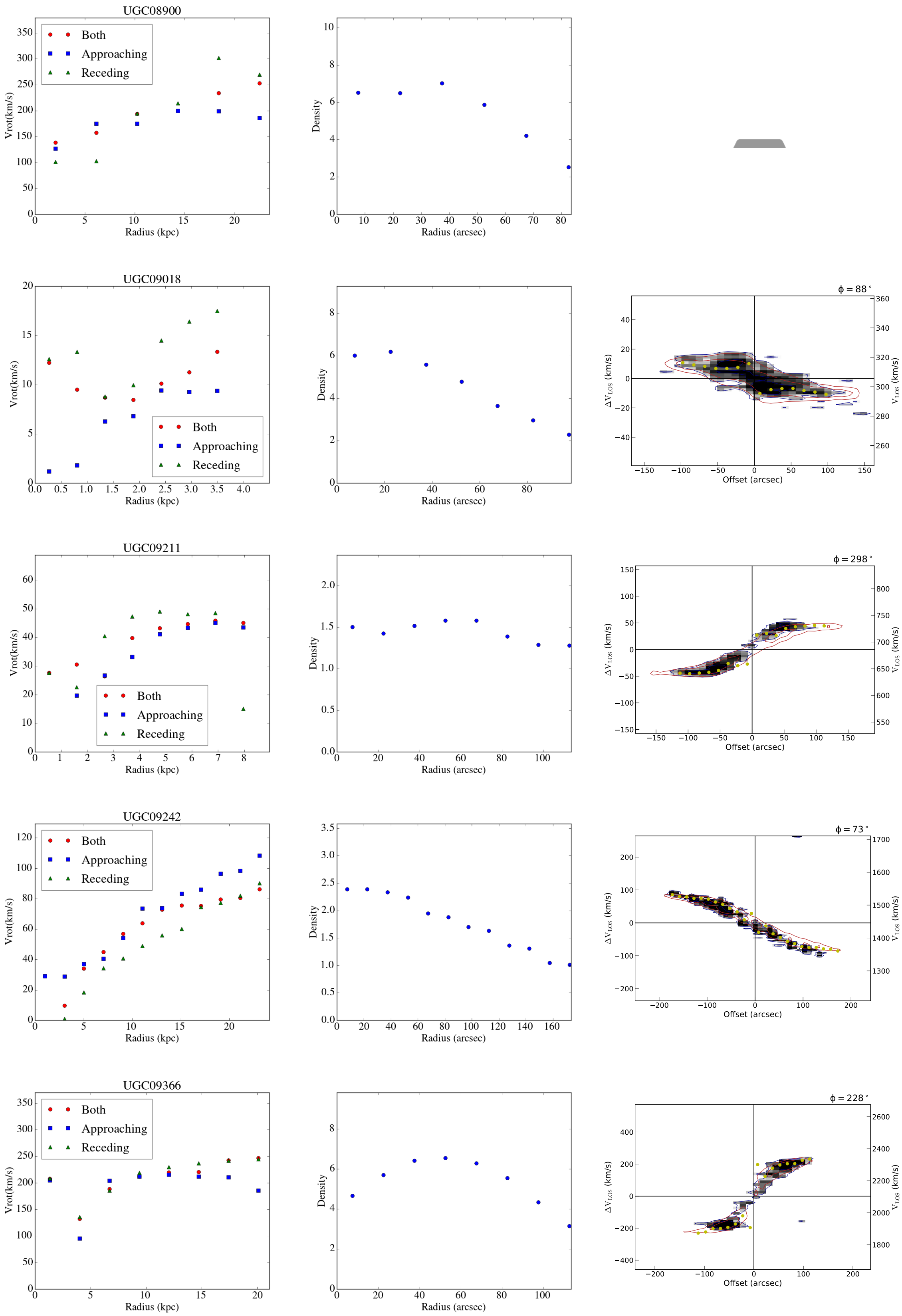

Figure 0: Continued

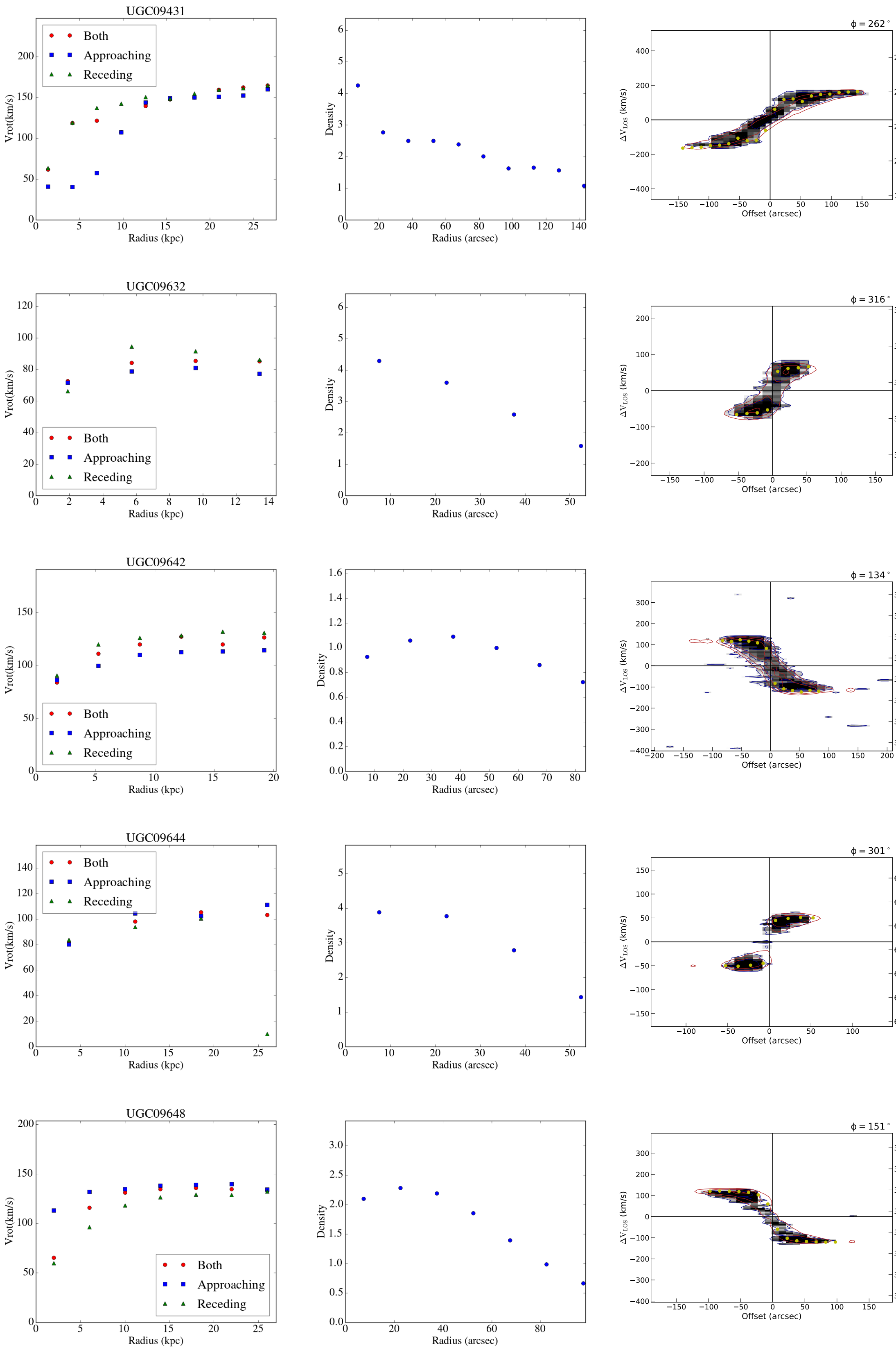

Figure 0: Continued

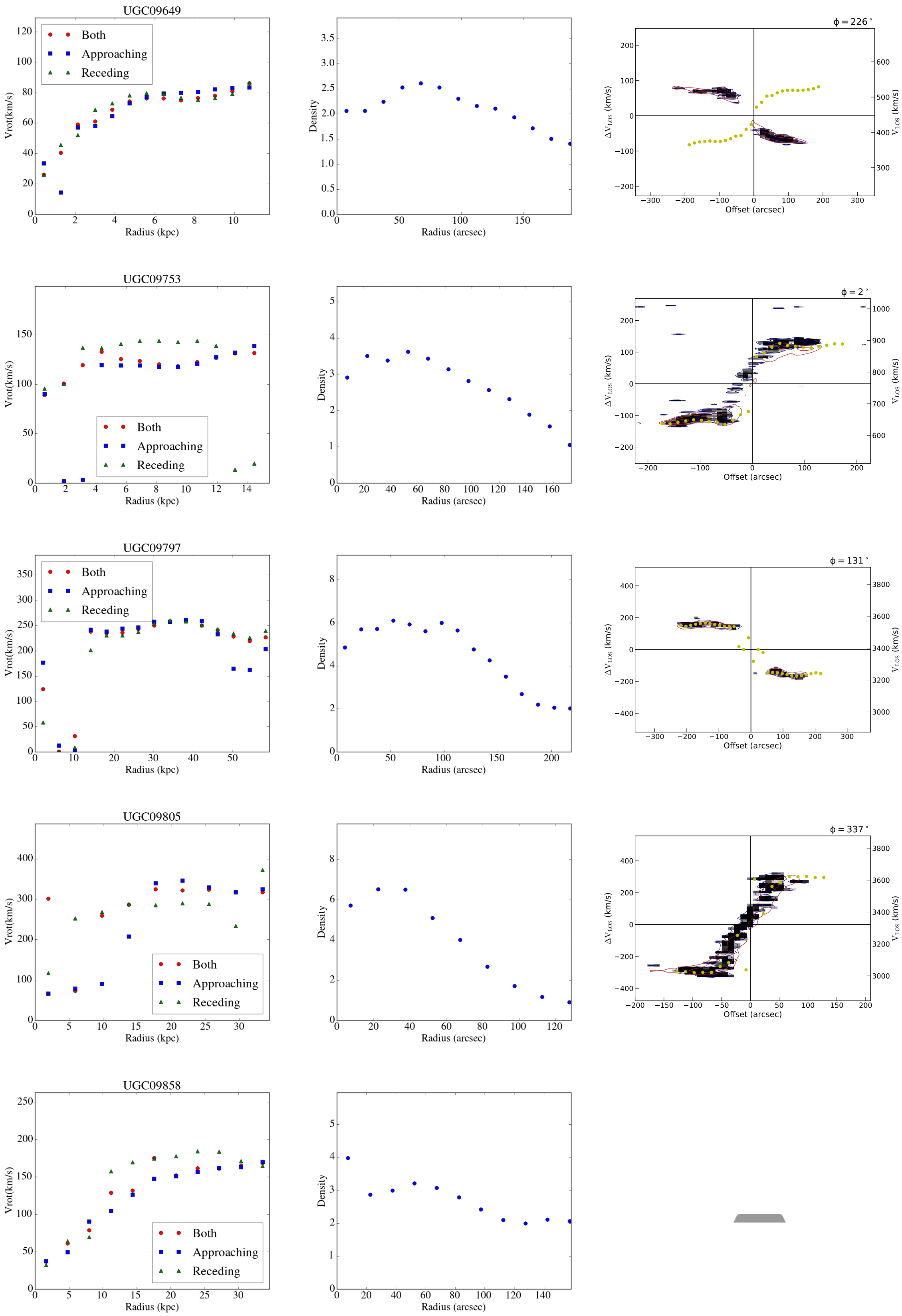

Figure 0: Continued

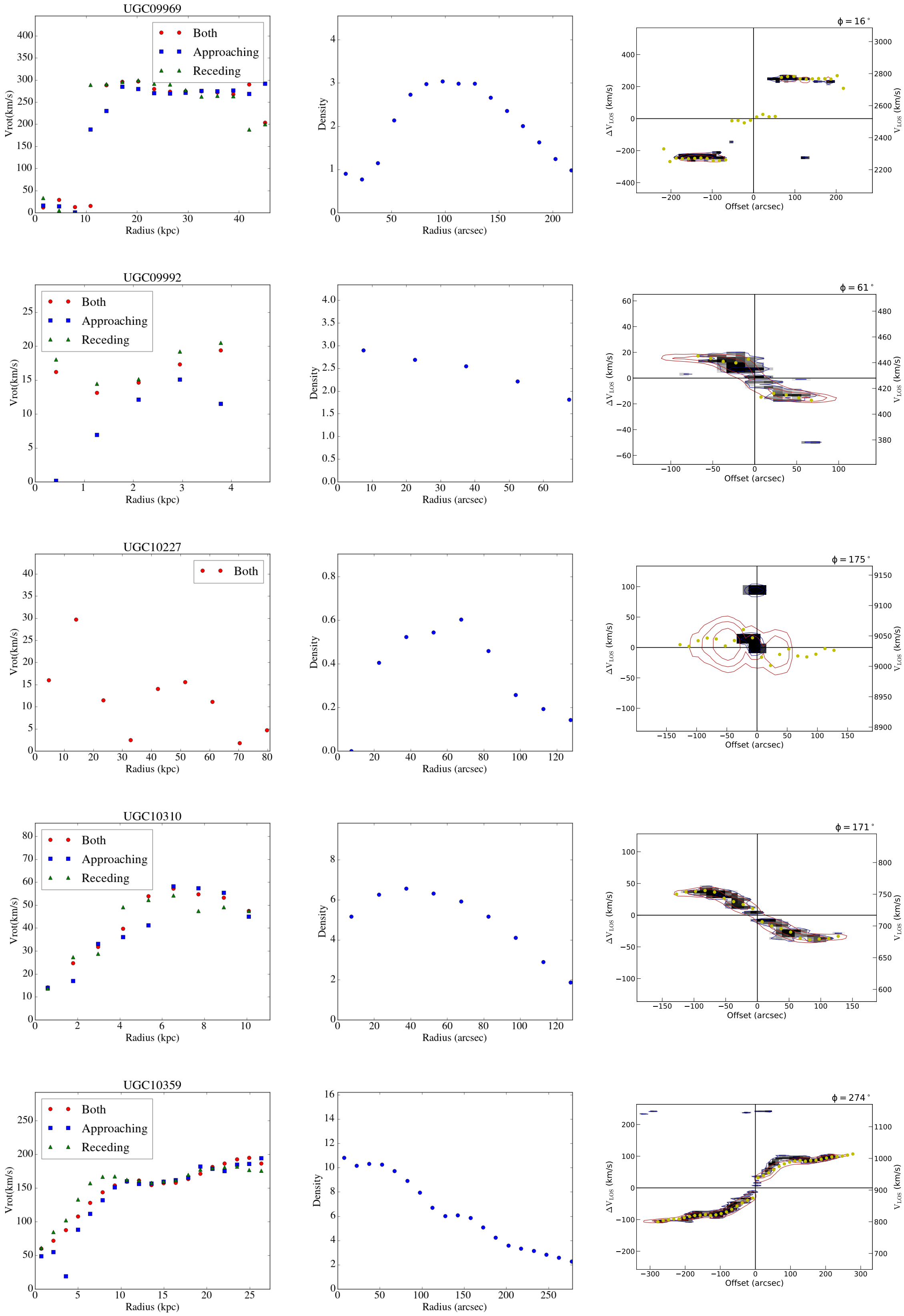

Figure 0: Continued

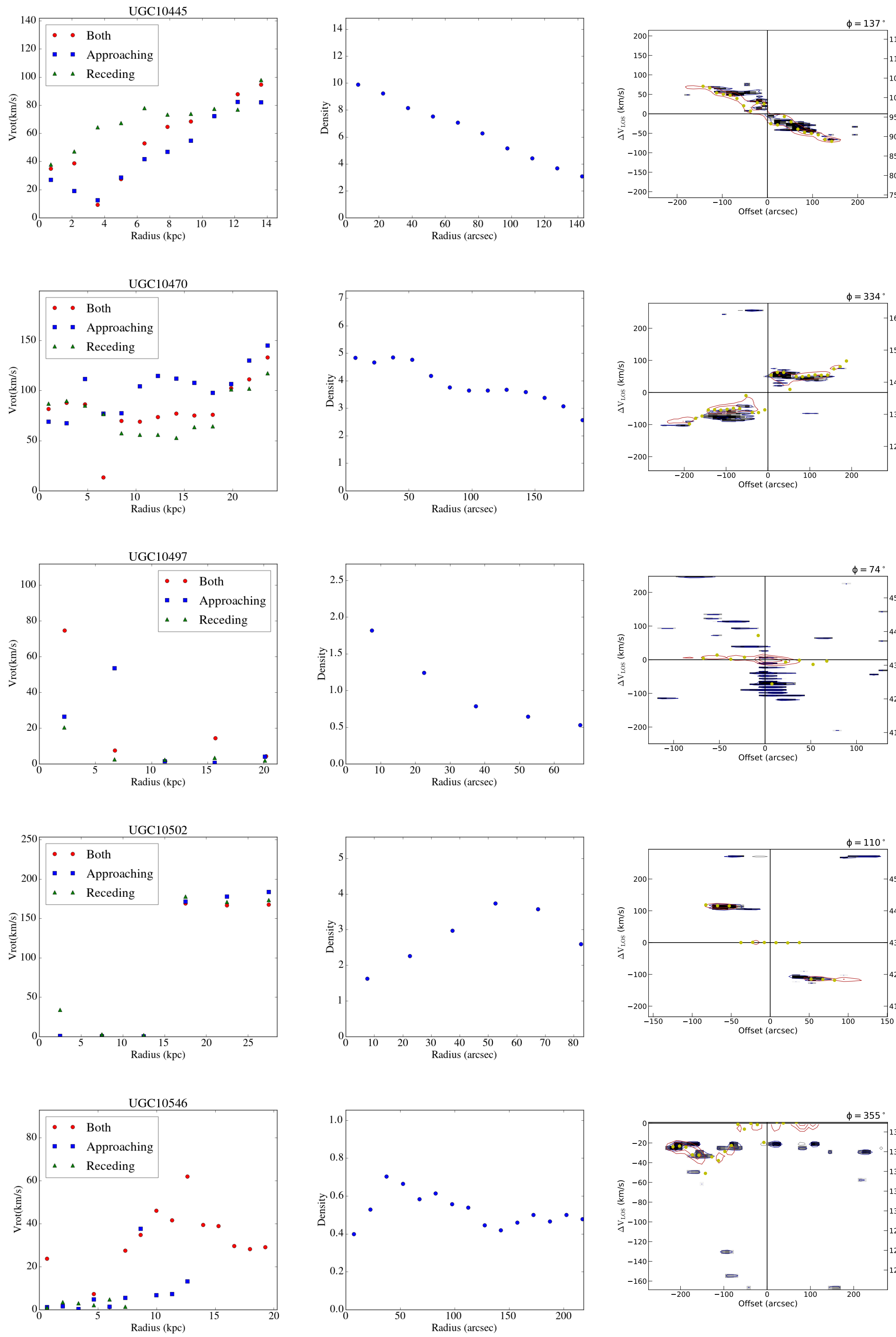

Figure 0: Continued

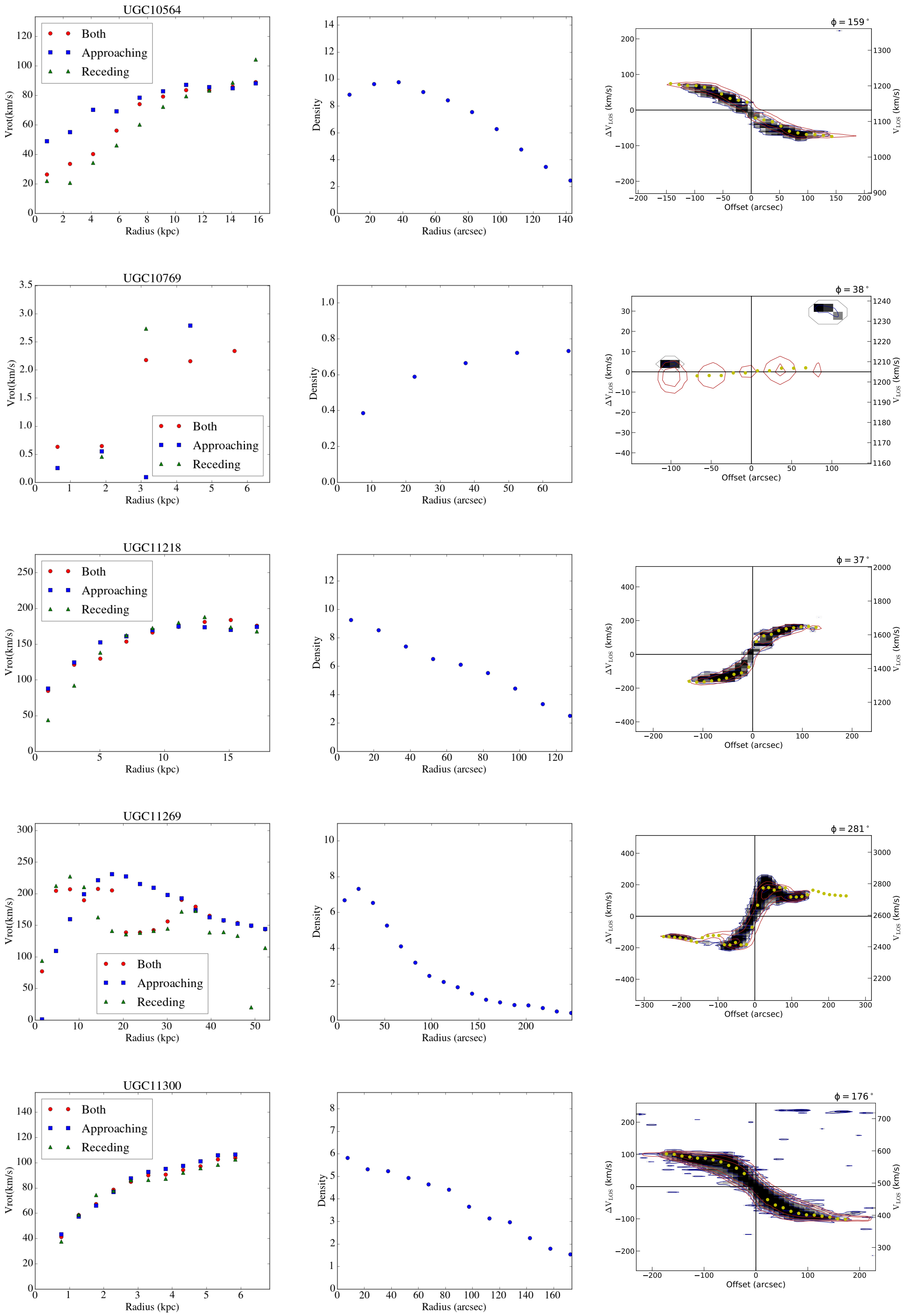

Figure 0: Continued

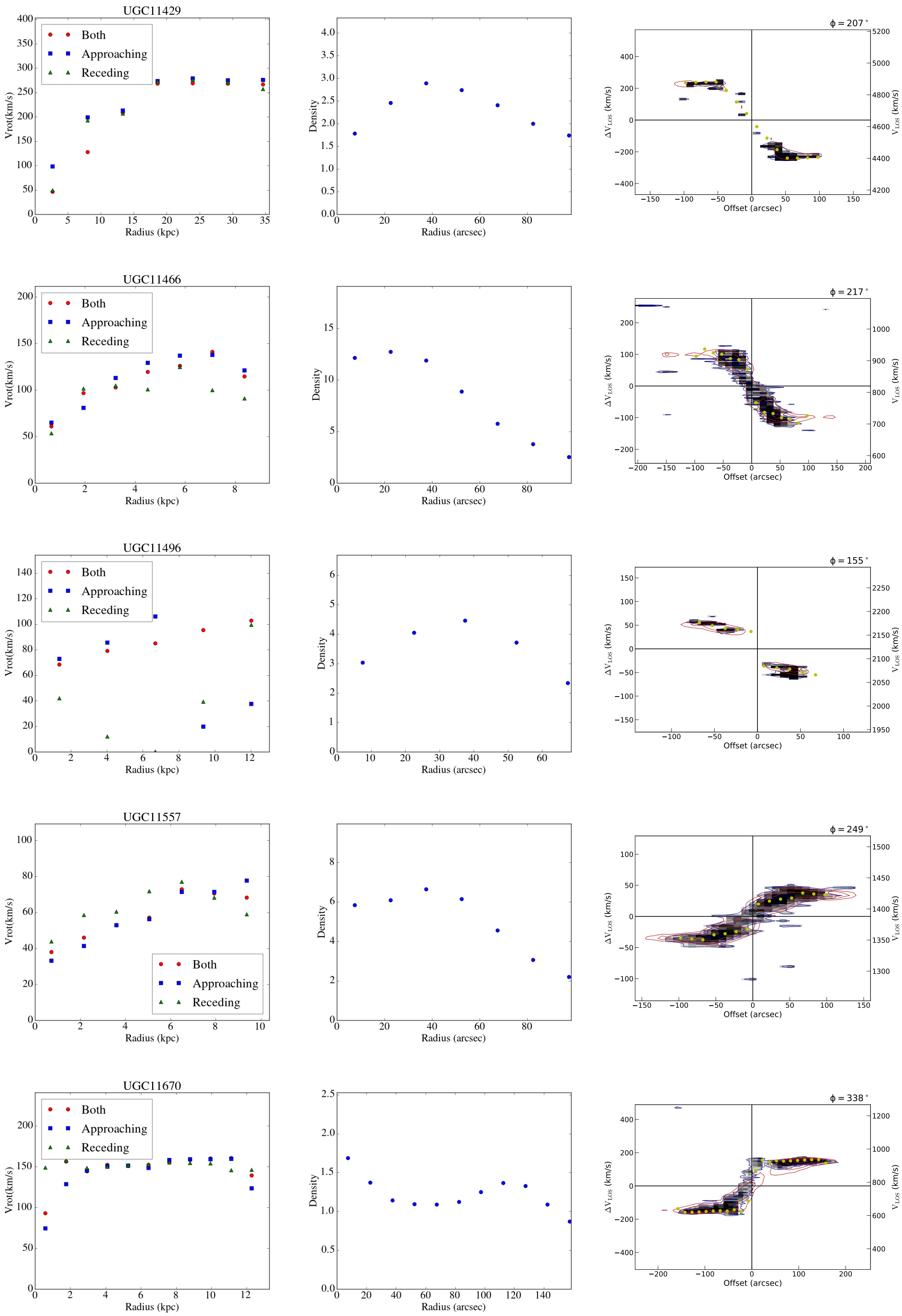

Figure 0: Continued

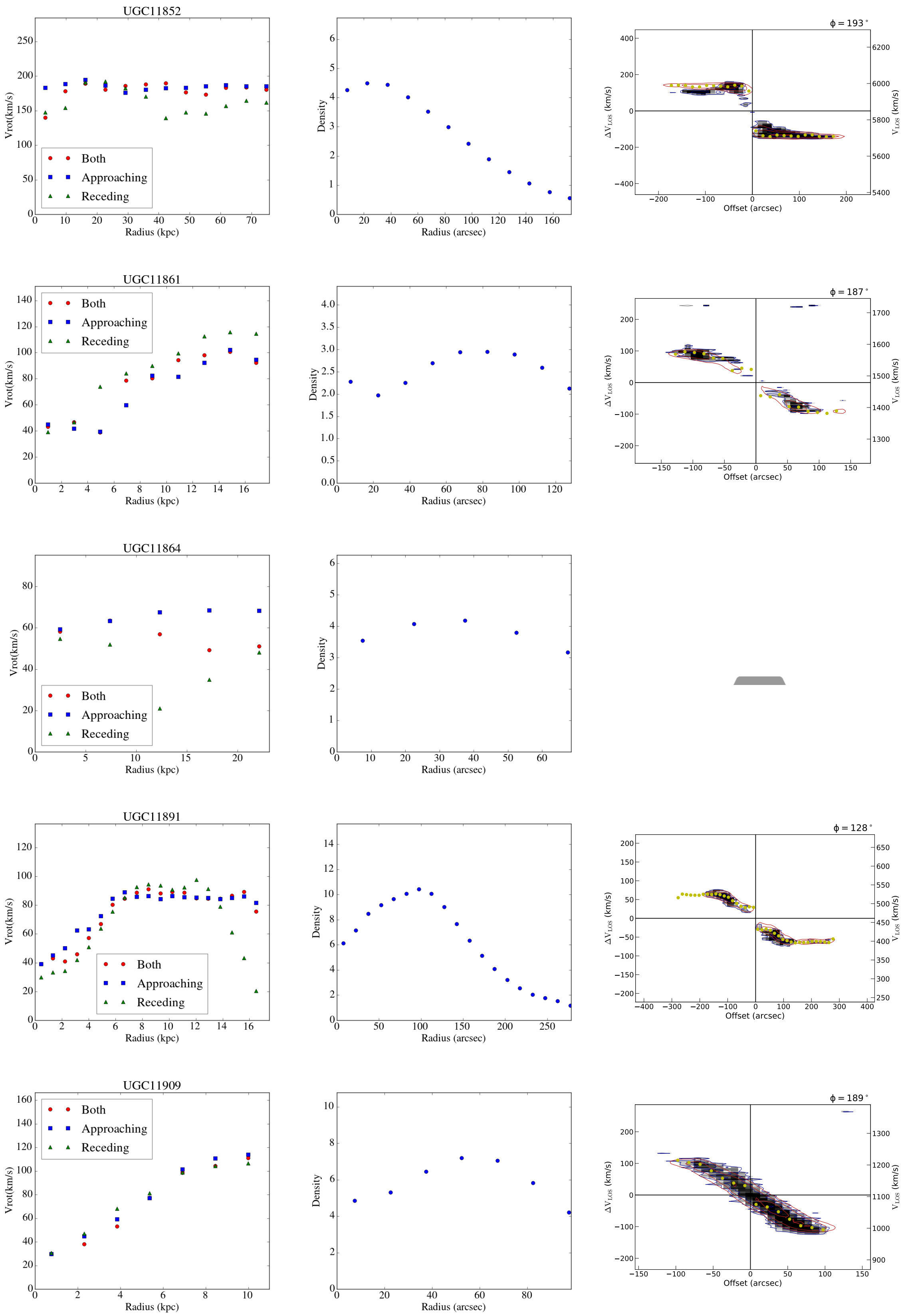

Figure 0: Continued

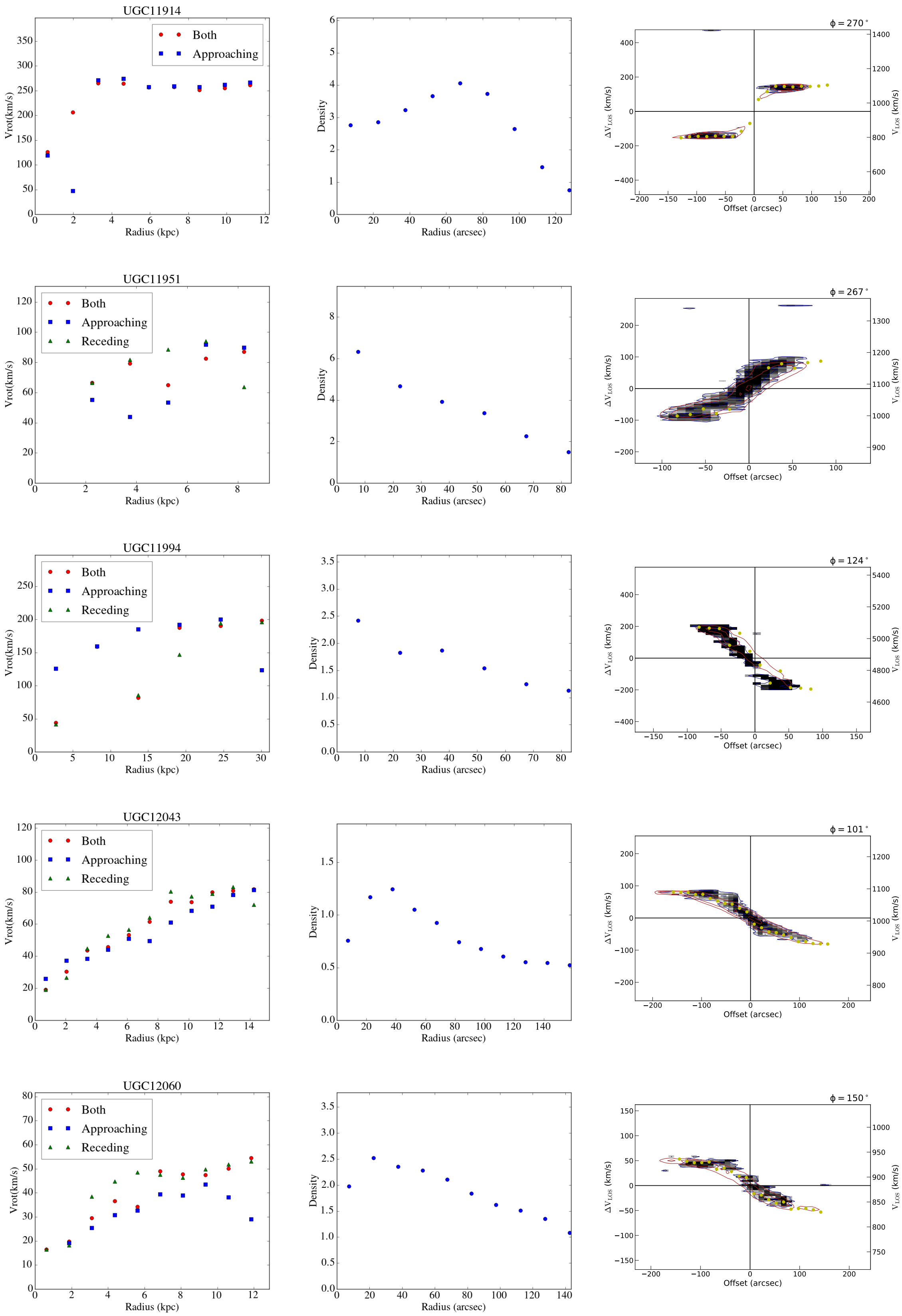

Figure 0: Continued

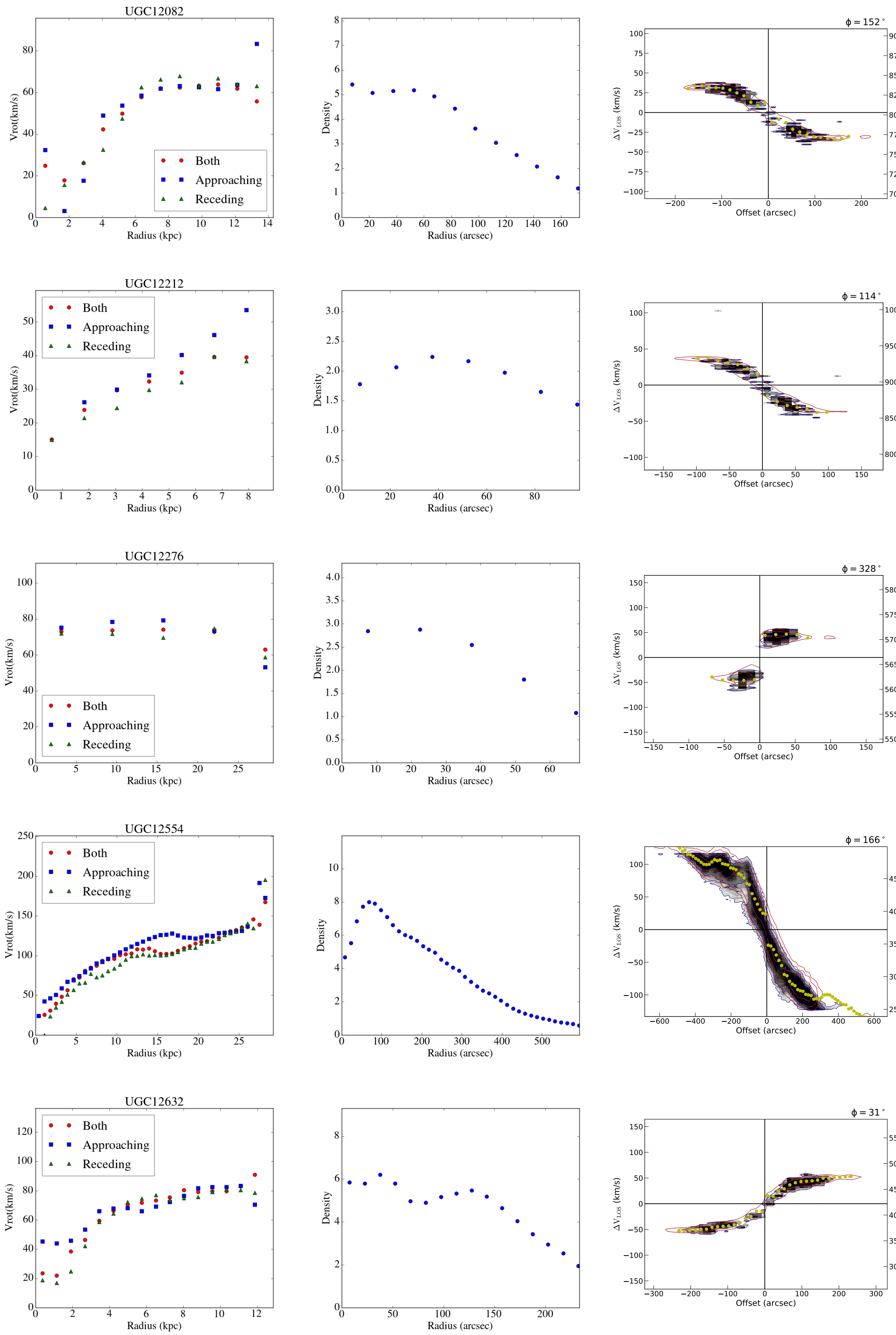

Figure 0: Continued

E. Anisotropy result for the THINGS sample

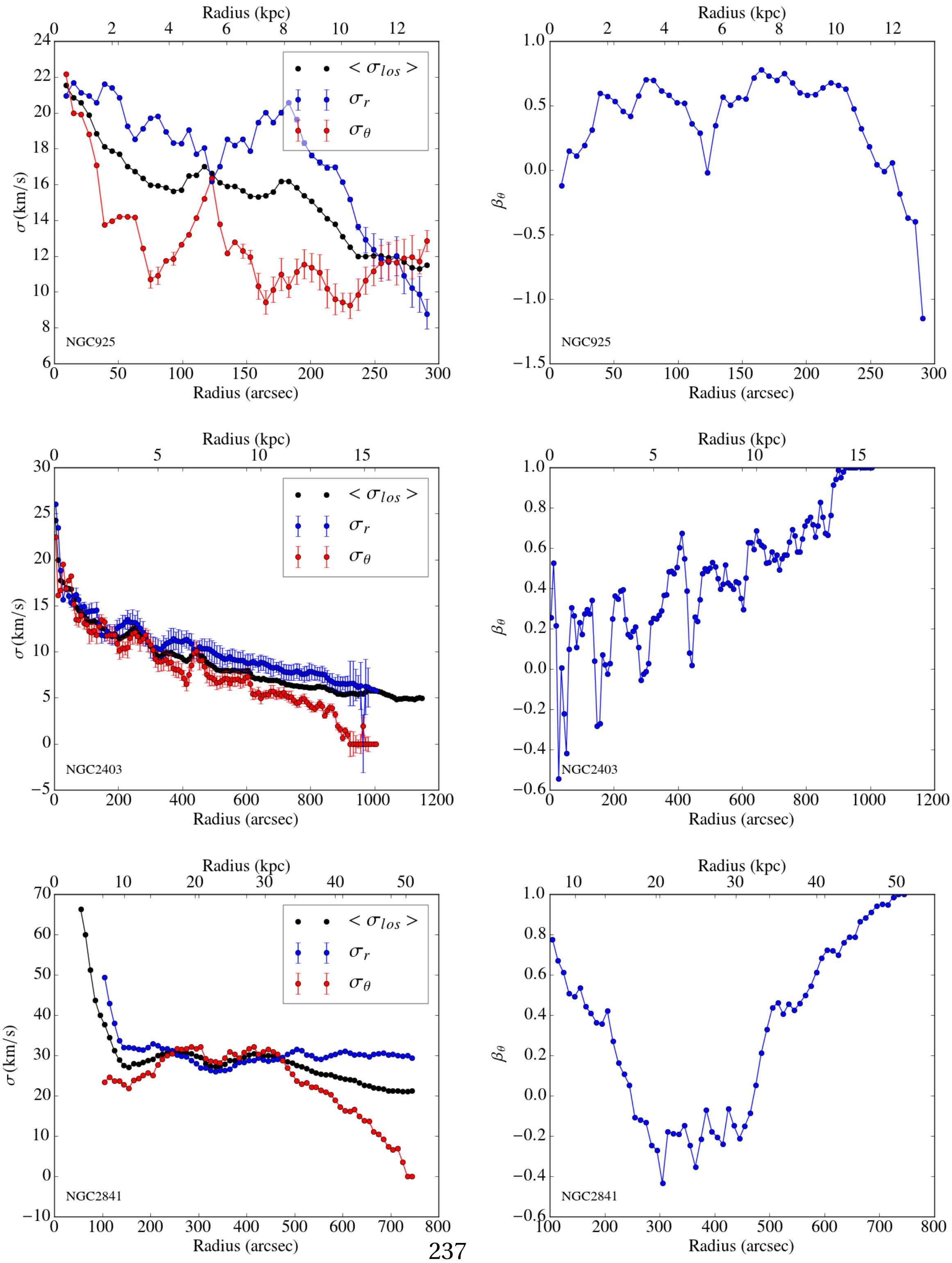

FIGURE E.0. – Radial variation of the dispersion ellipsoid (left) and β_θ (right)

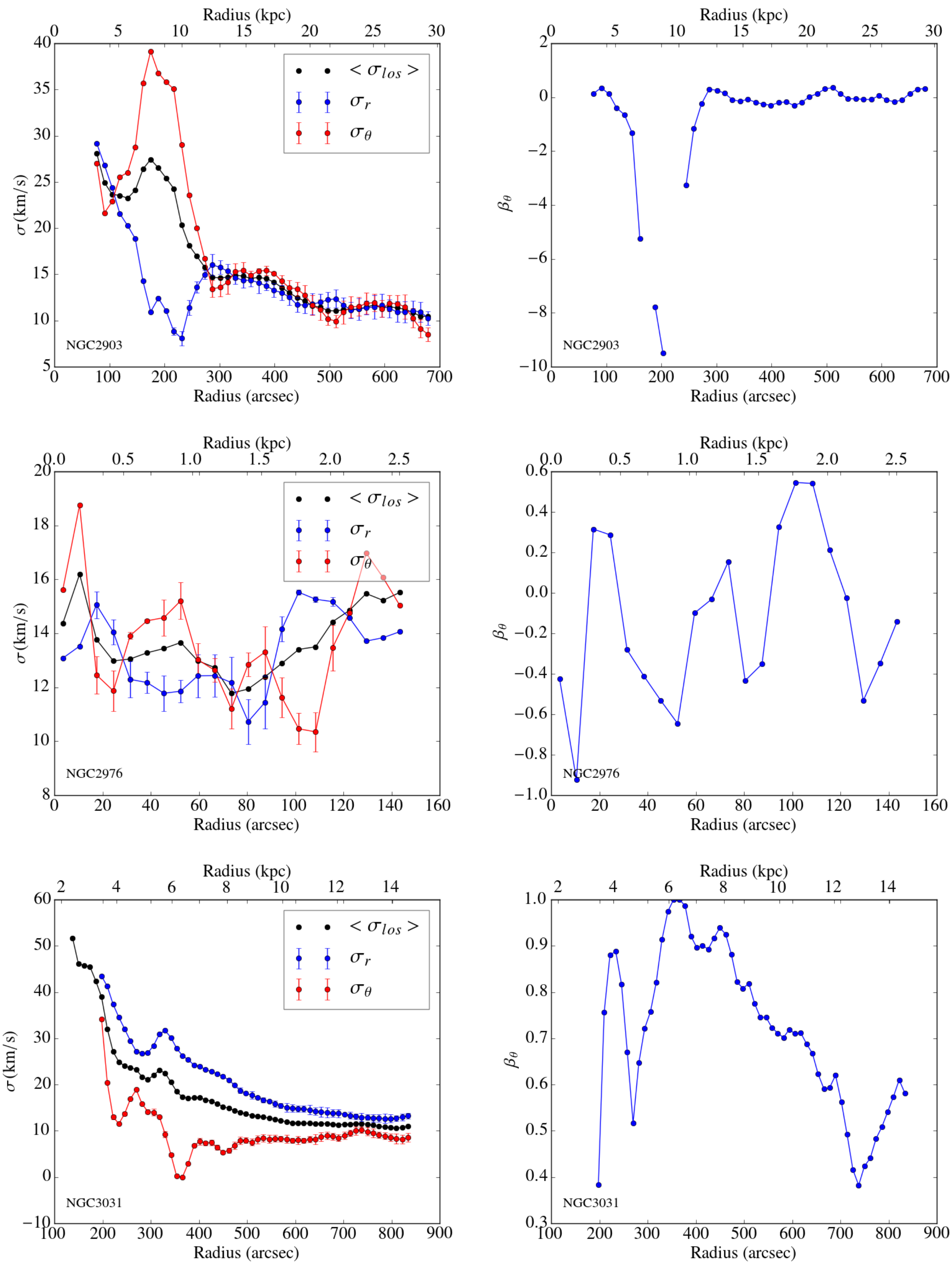

FIGURE E.0. – Continued

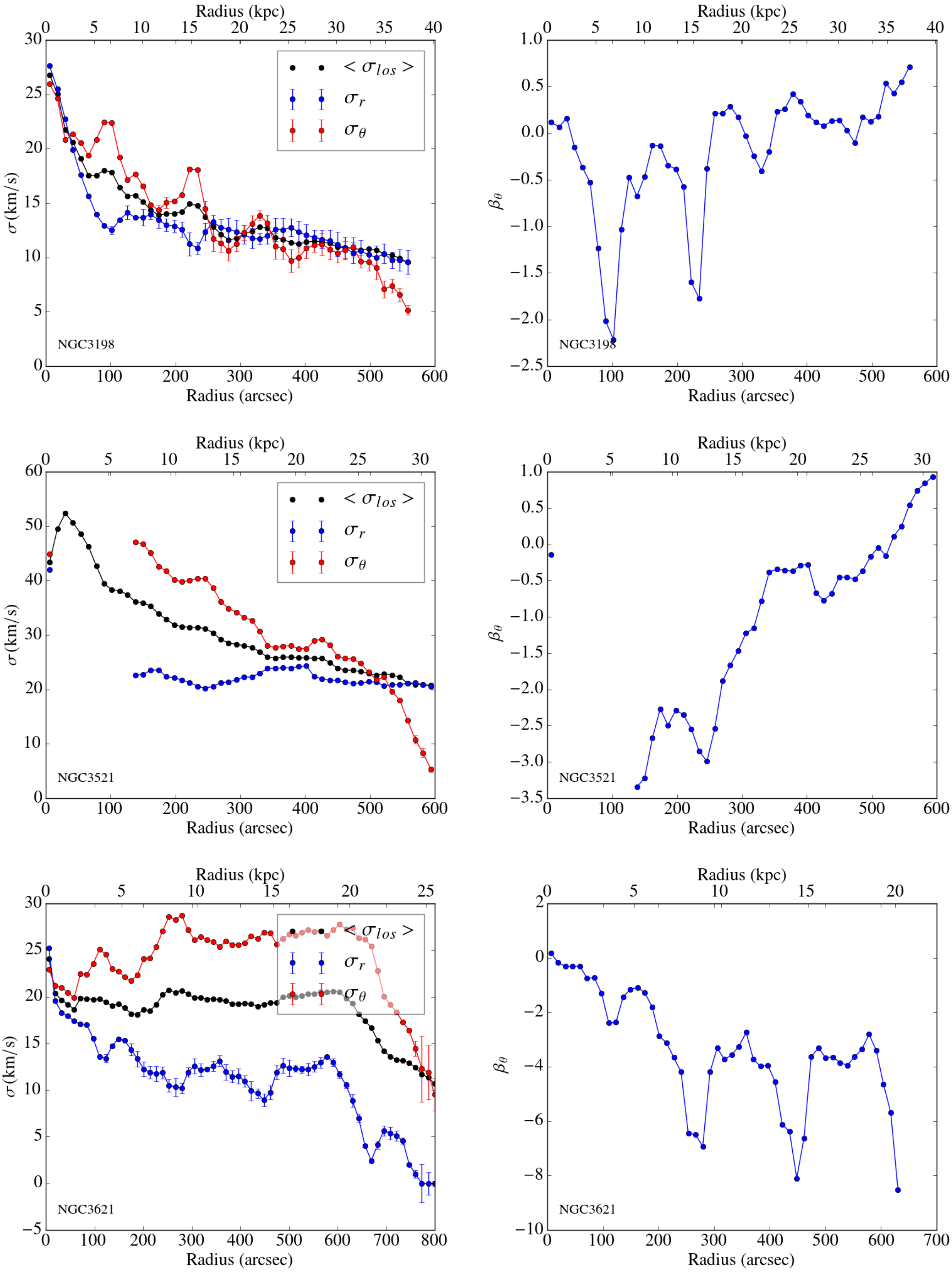

FIGURE E.0. – Continued

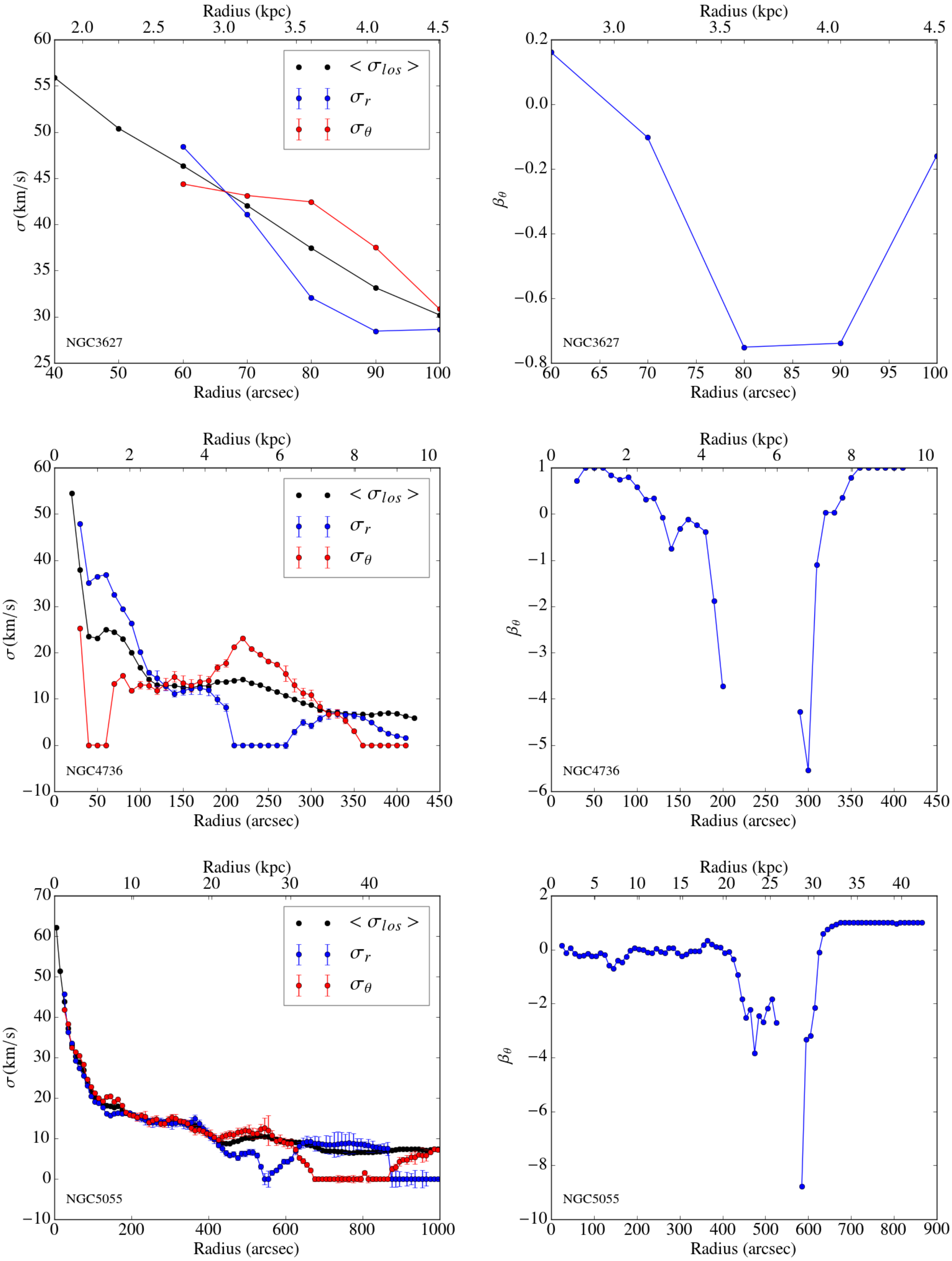

FIGURE E.0. – Continued

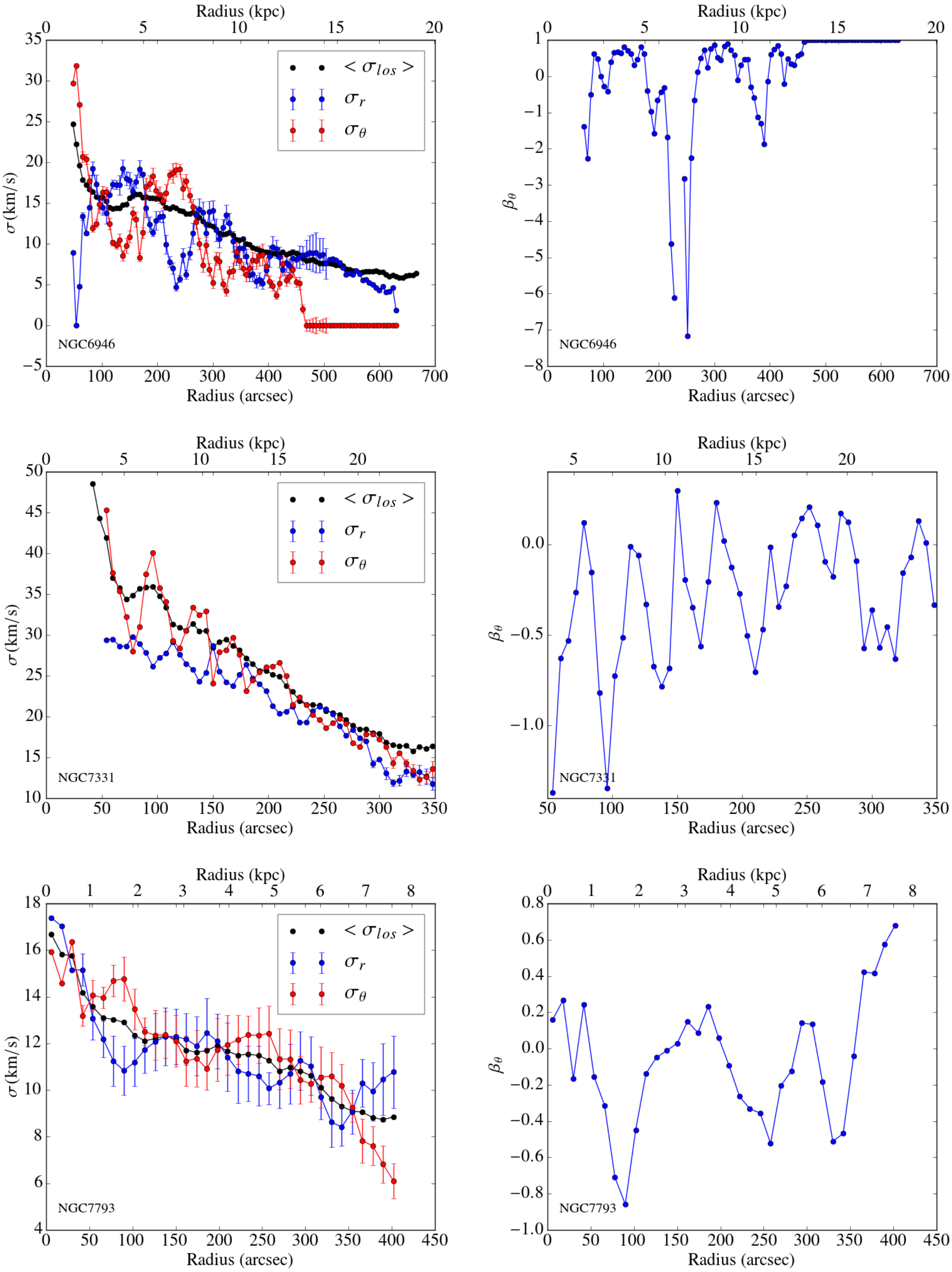

FIGURE E.0. – Continued

F. Anisotropy result for the WHISP sample

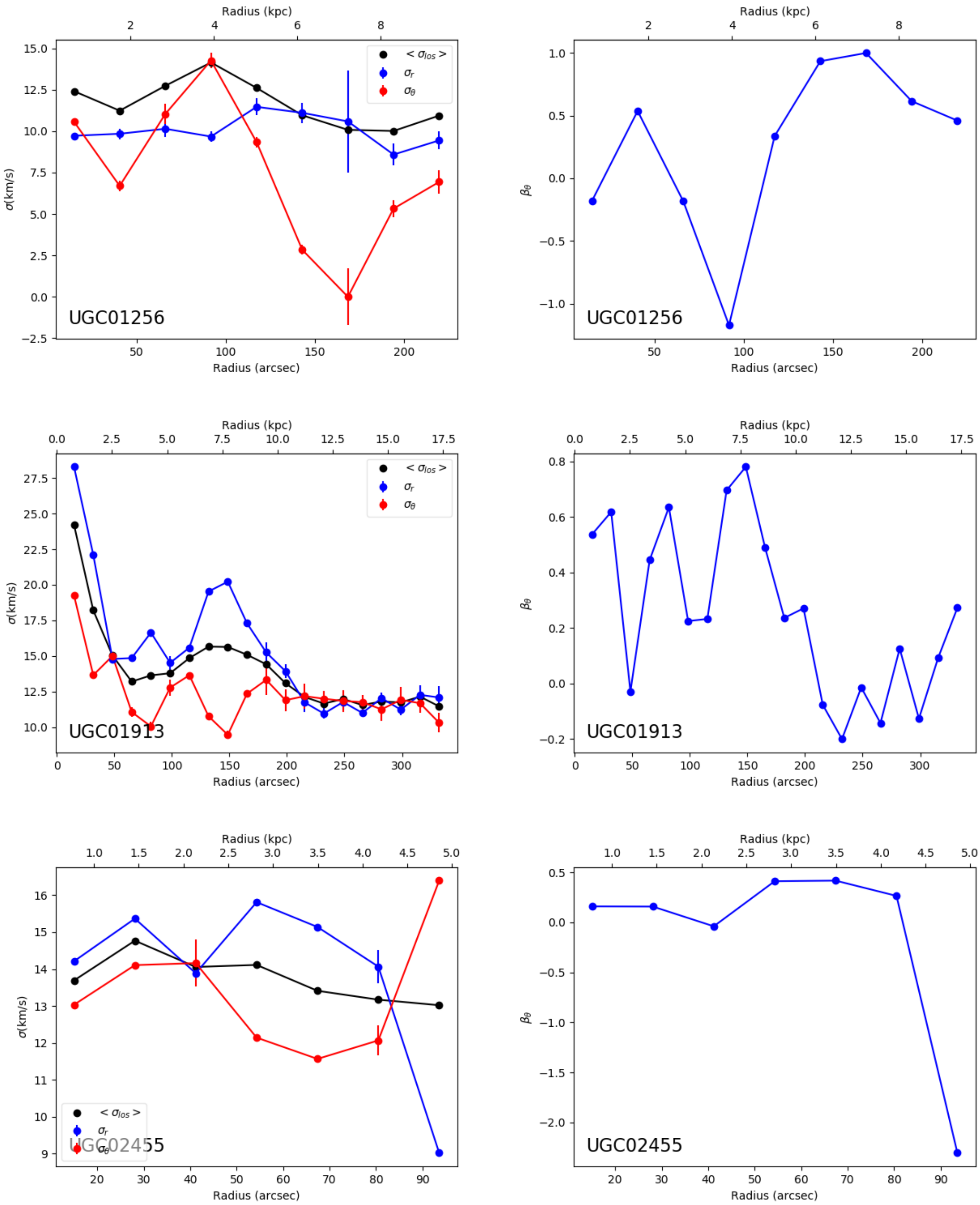

FIGURE F.0. – Radial variation of the dispersion ellipsoid (left) and β_θ (right)

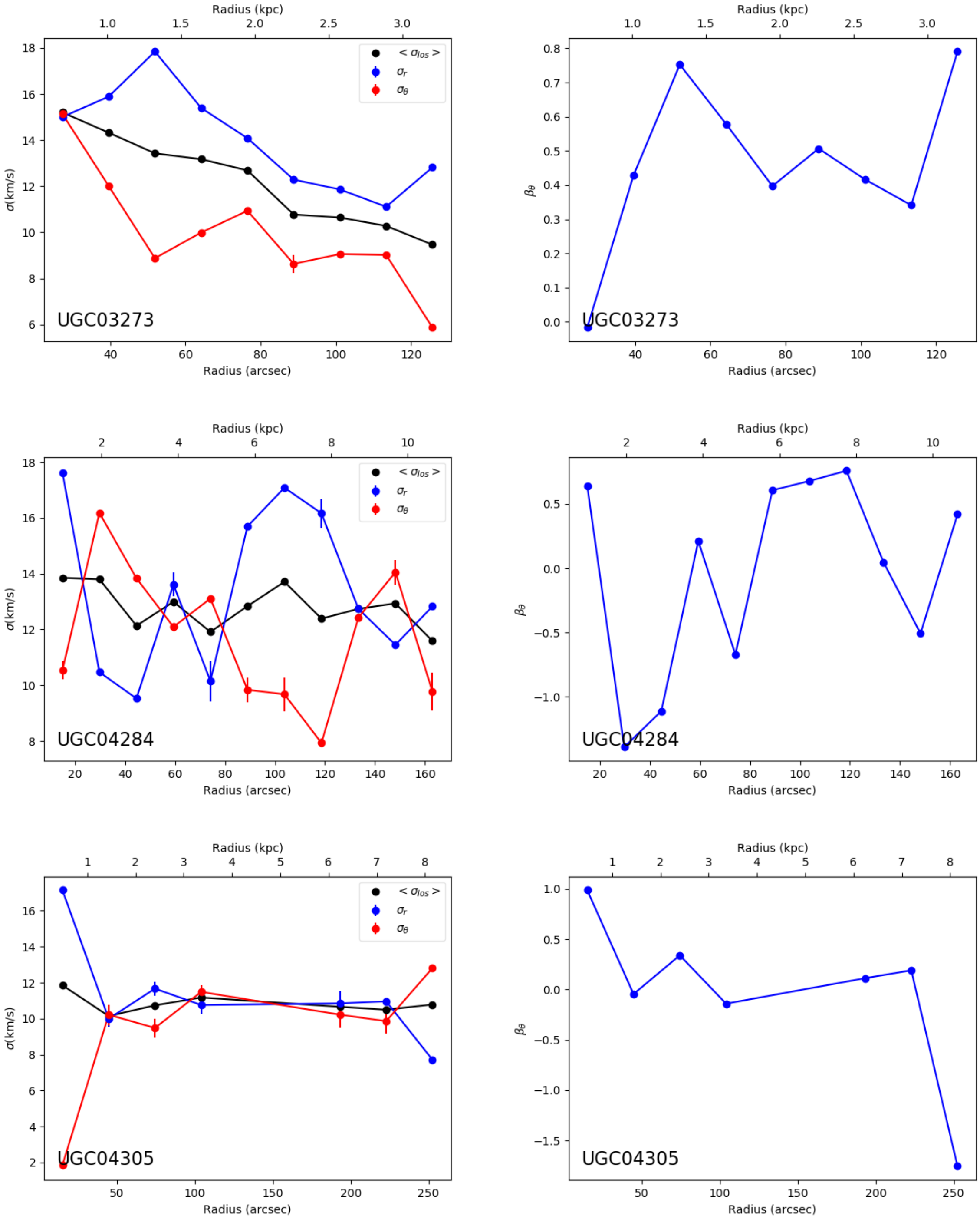

FIGURE F.0. – Continued

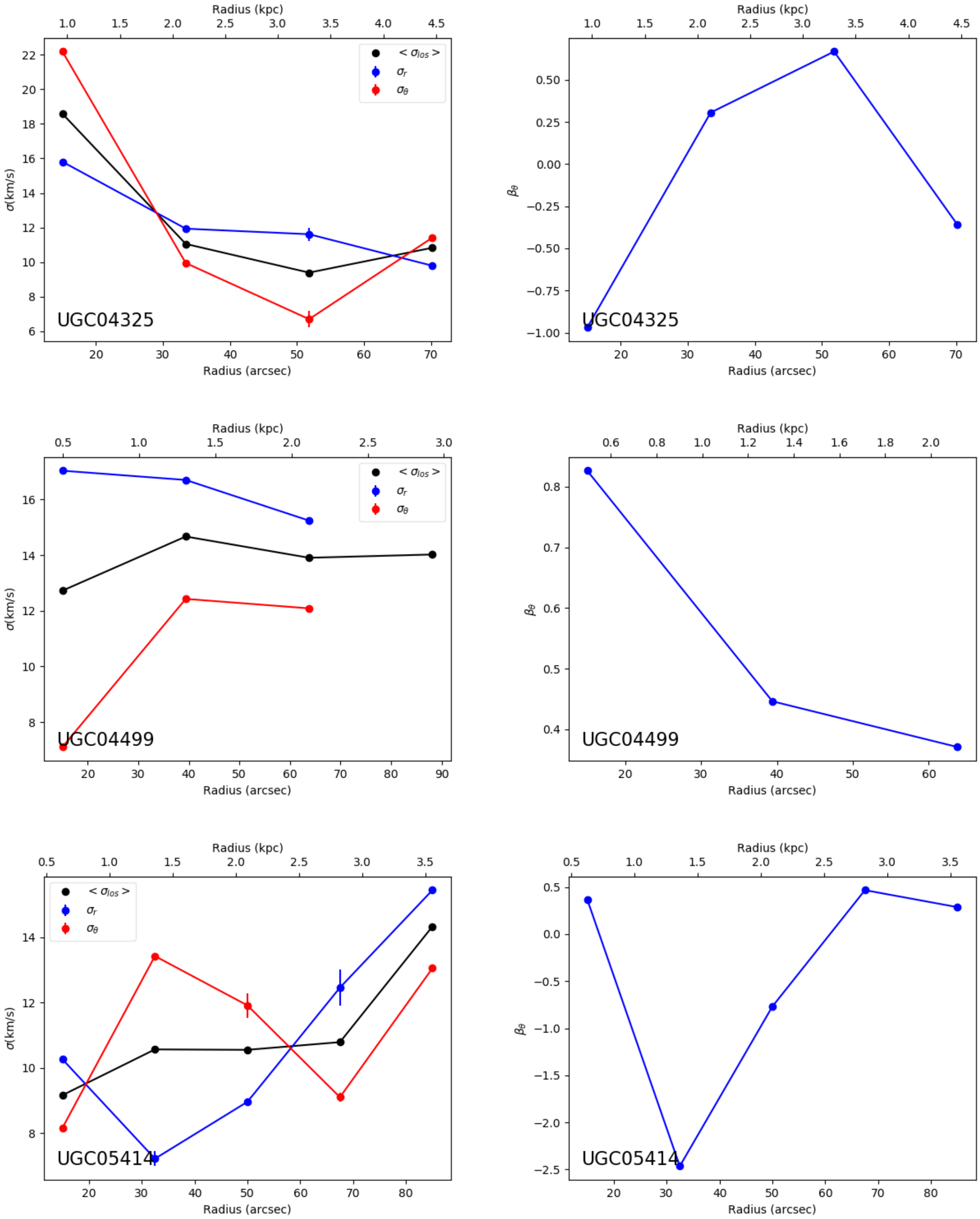

FIGURE F.0. – Continued

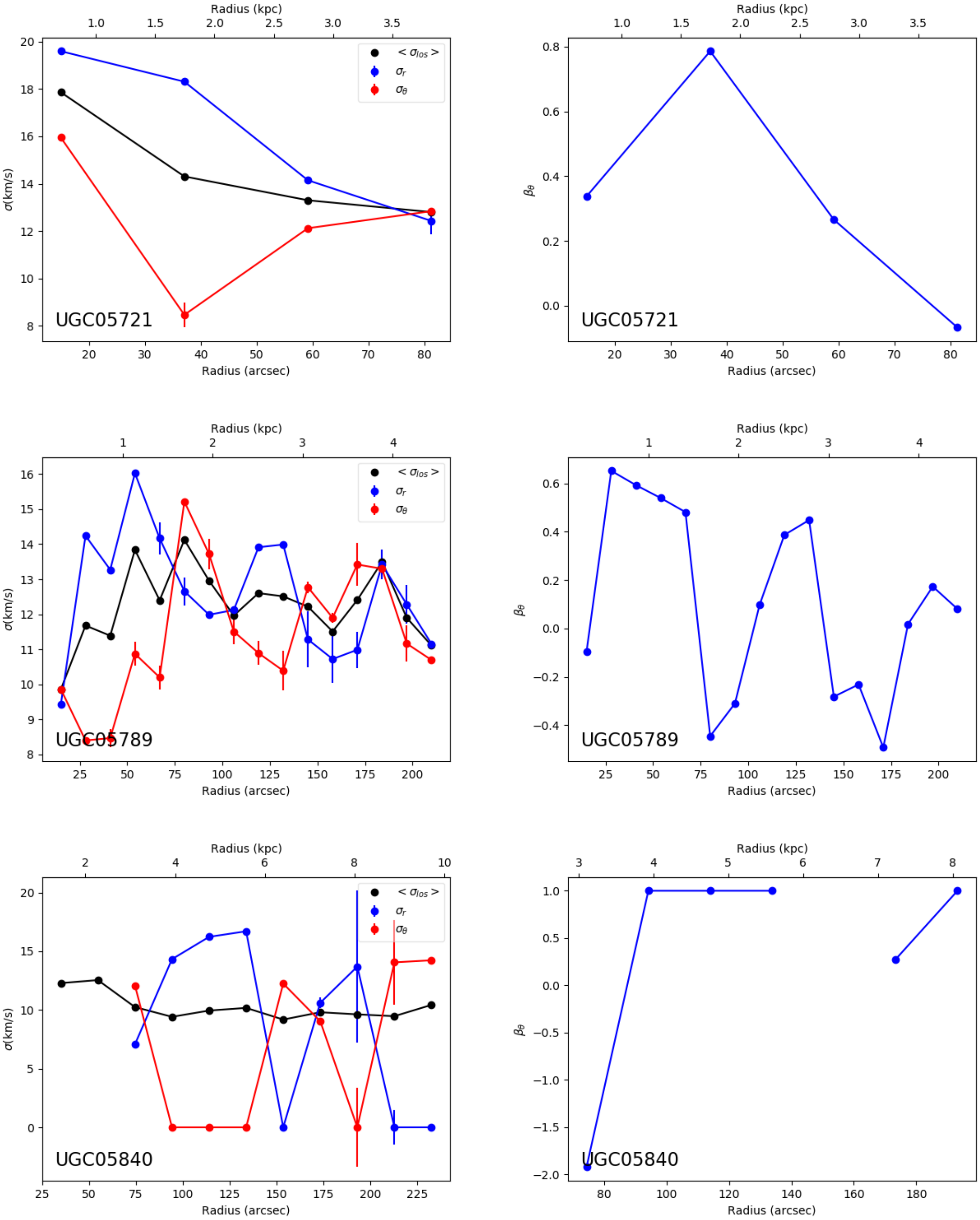

FIGURE F.0. – Continued

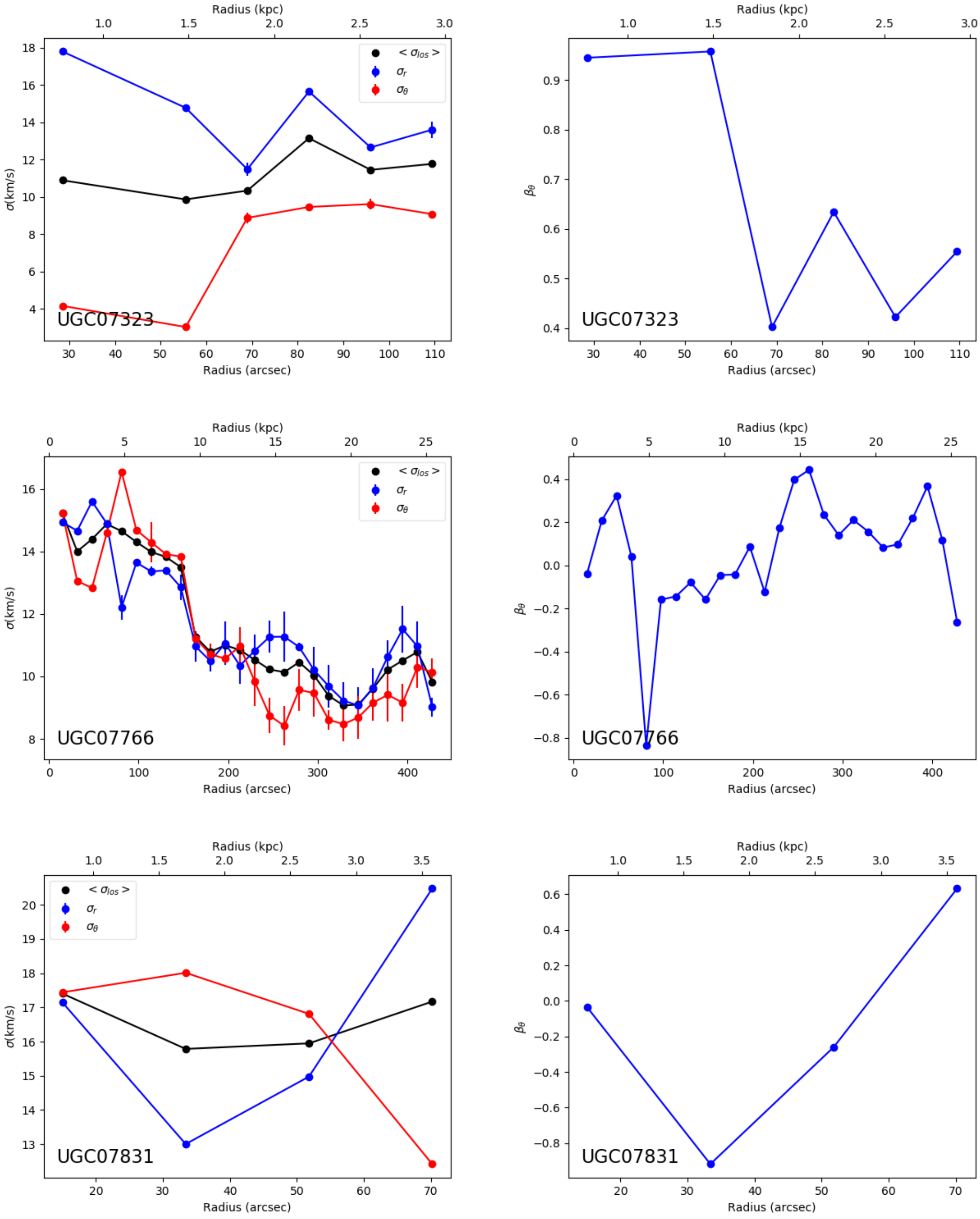

FIGURE F.0. – Continued

G. Asymmetry results for the THINGS sample

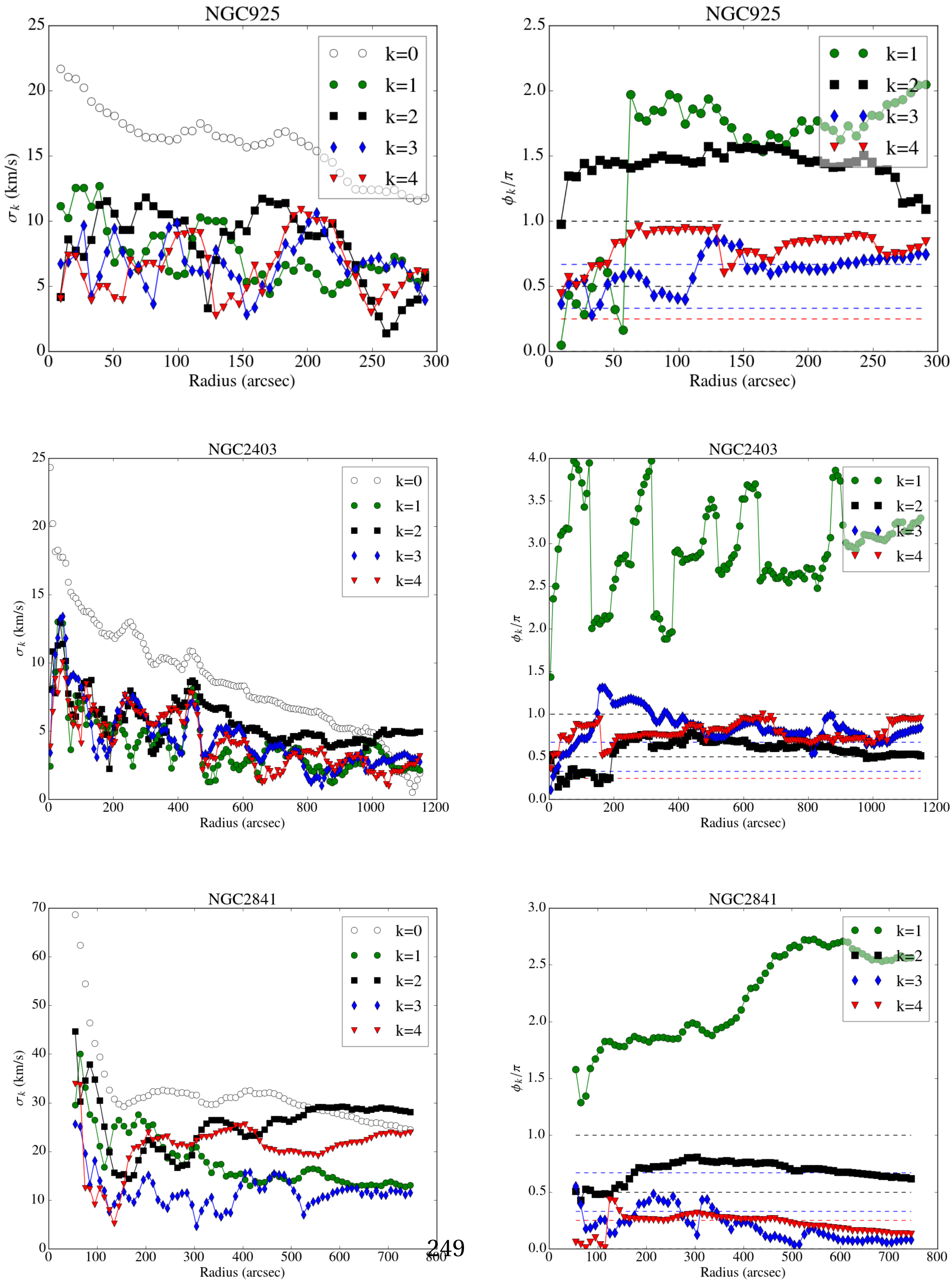

FIGURE G.0. – Radial variation of the FFT parameters : amplitudes on the left panel, and angle phases on the right panel.

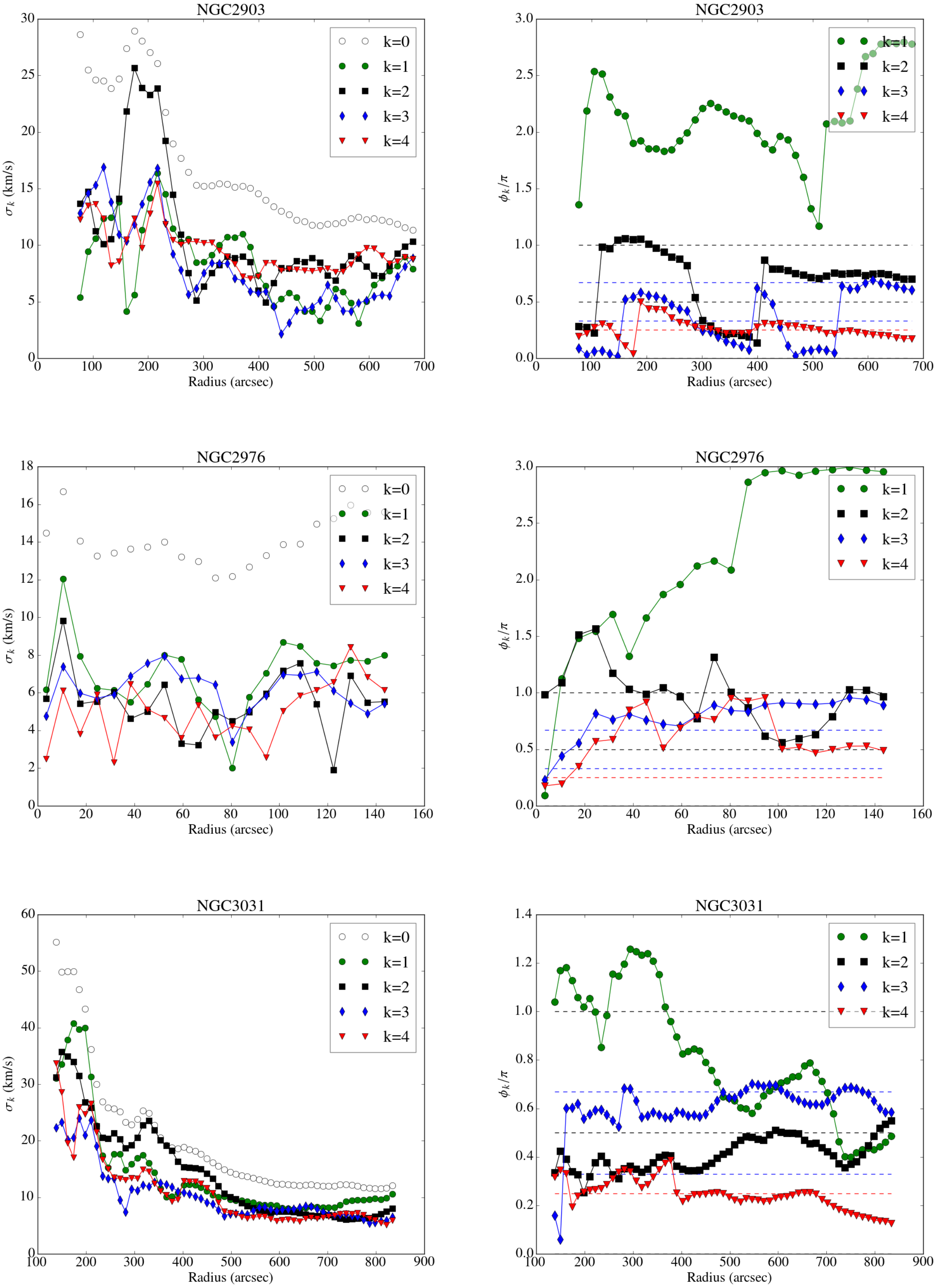

FIGURE G.0. – Continued

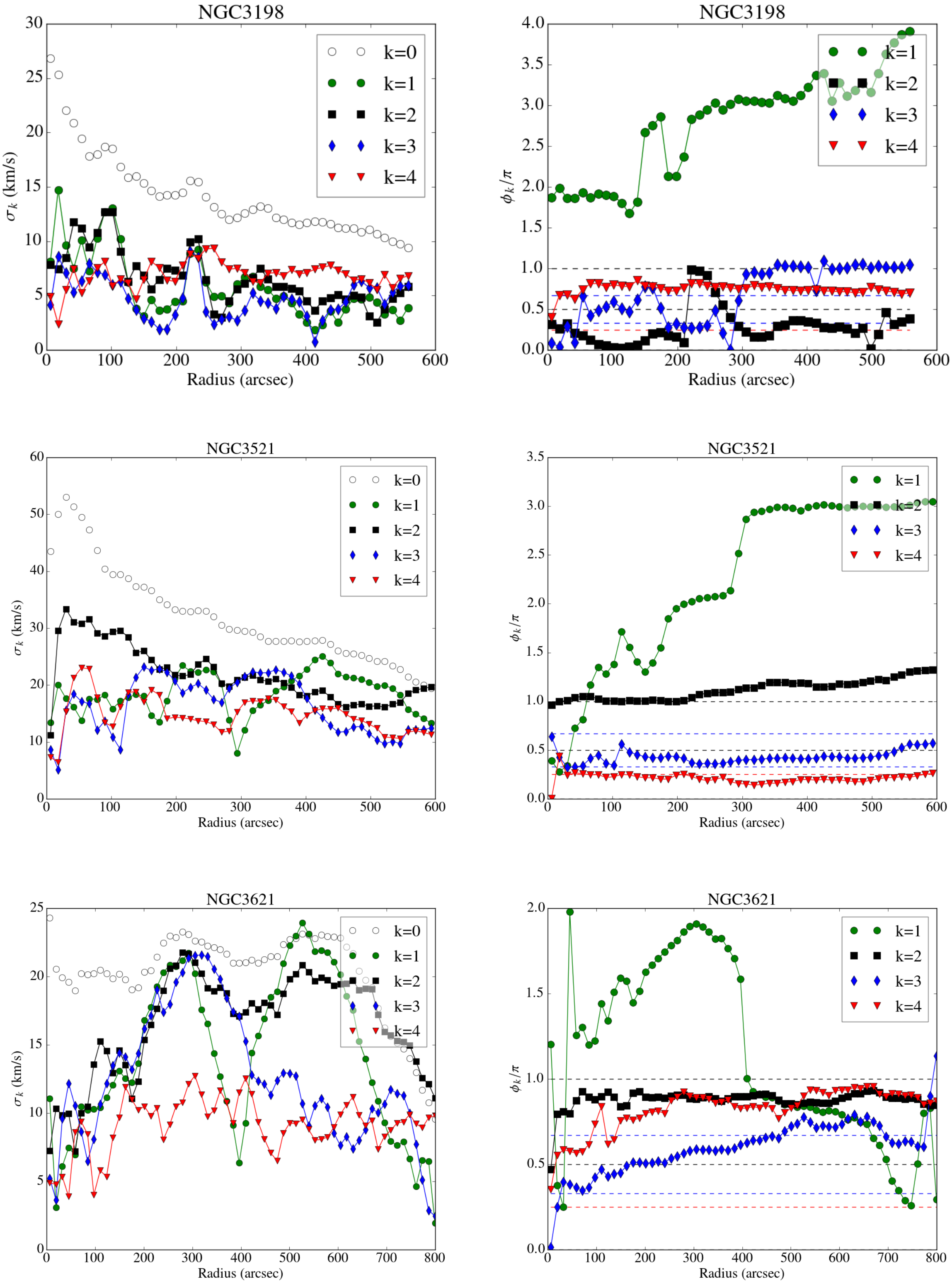

FIGURE G.0. – Continued

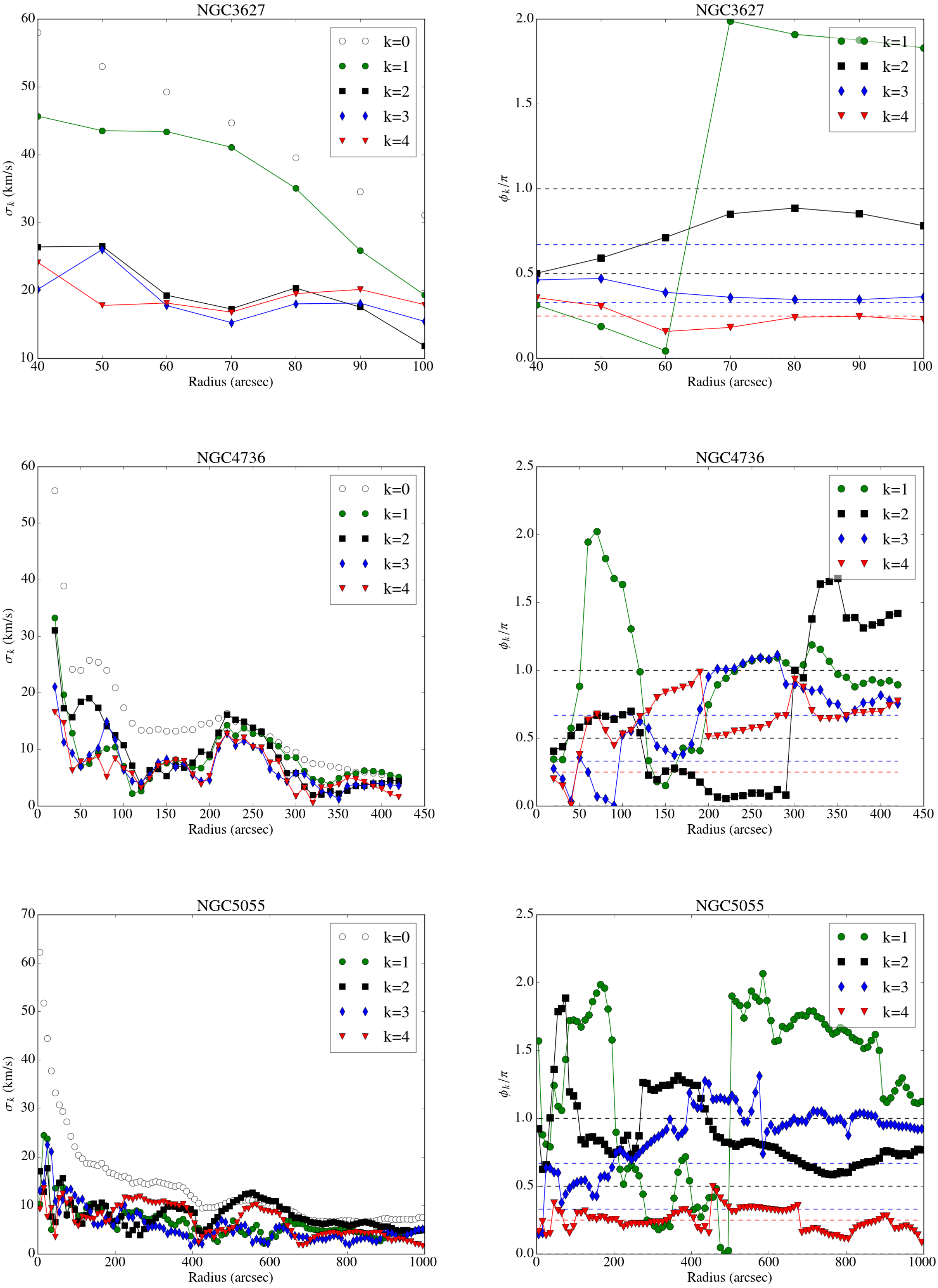

FIGURE G.0. – Continued

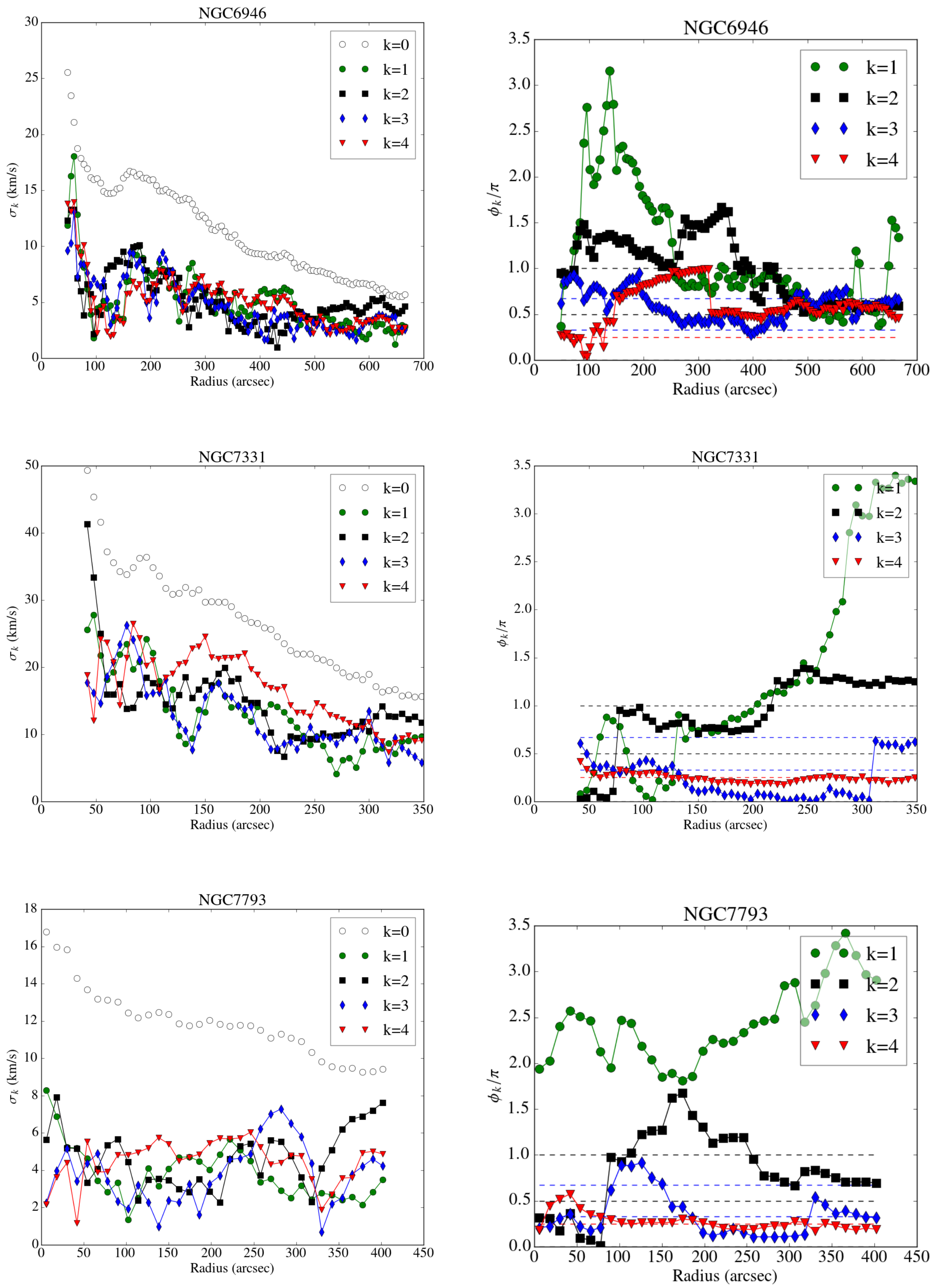

FIGURE G.0. – Continued

H. Detail of individual galaxy

For a complete description of each panel, see Sect. 6.4.4.

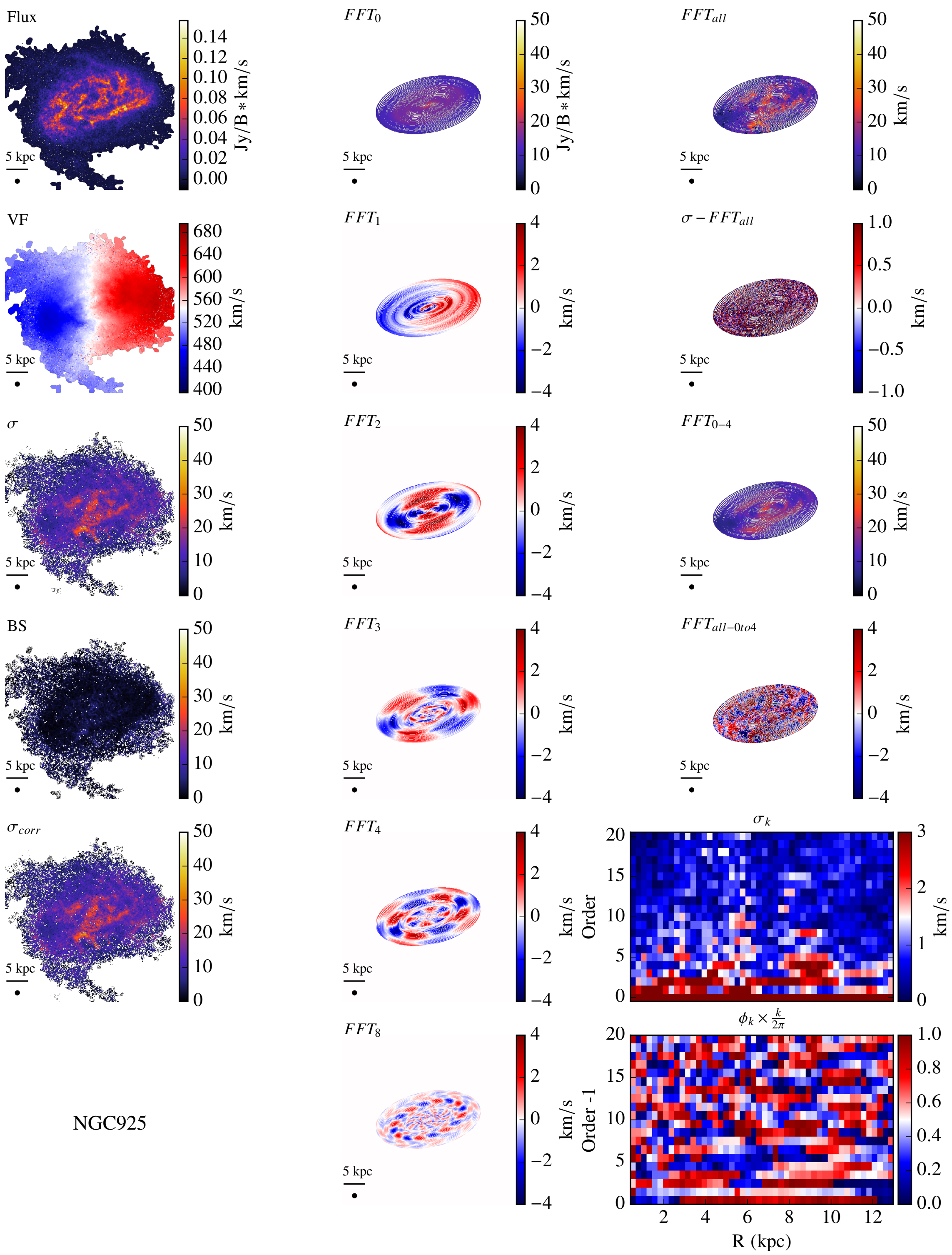

FIGURE H.1. – Overview of NGC925

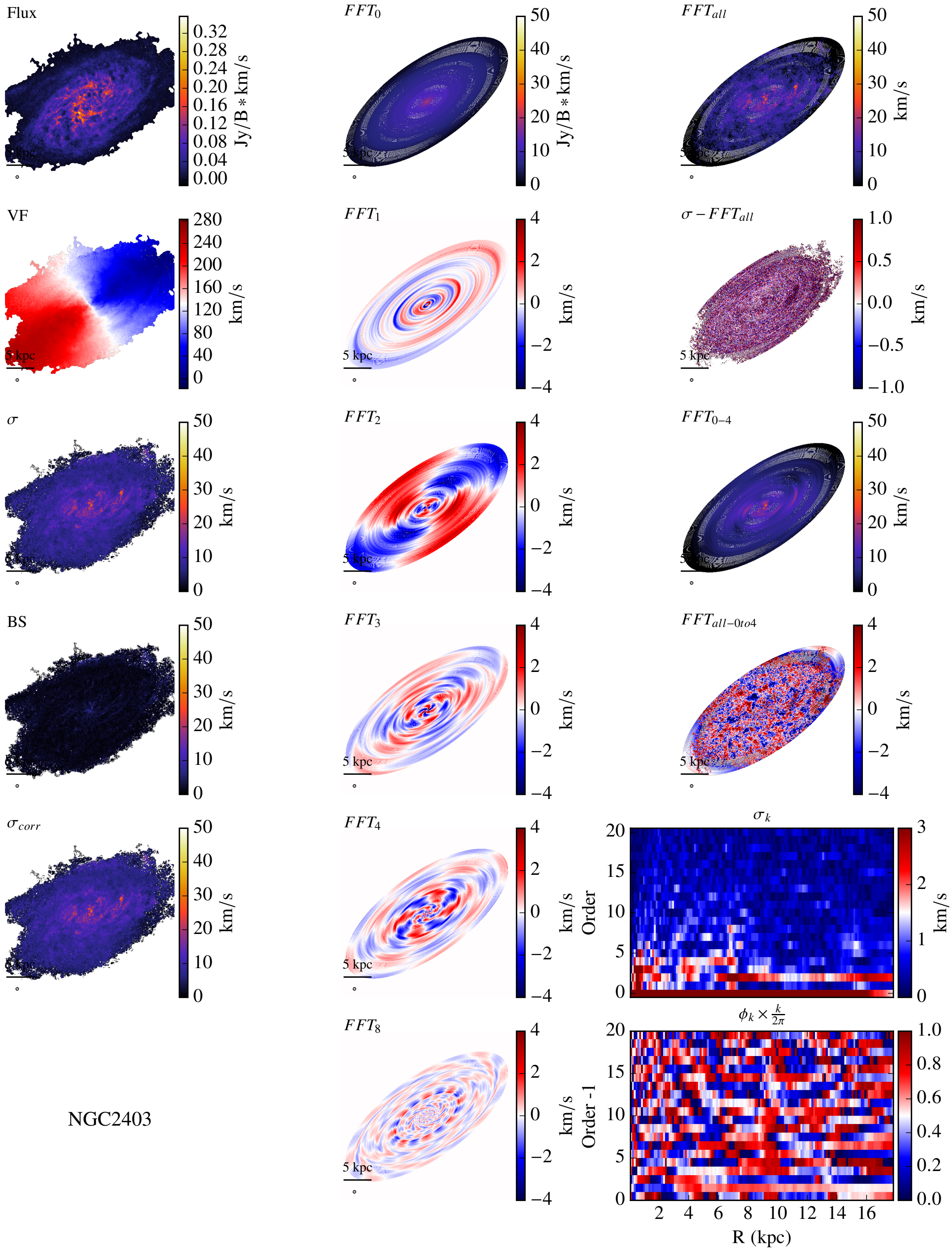

FIGURE H.2. – Overview of NGC2403

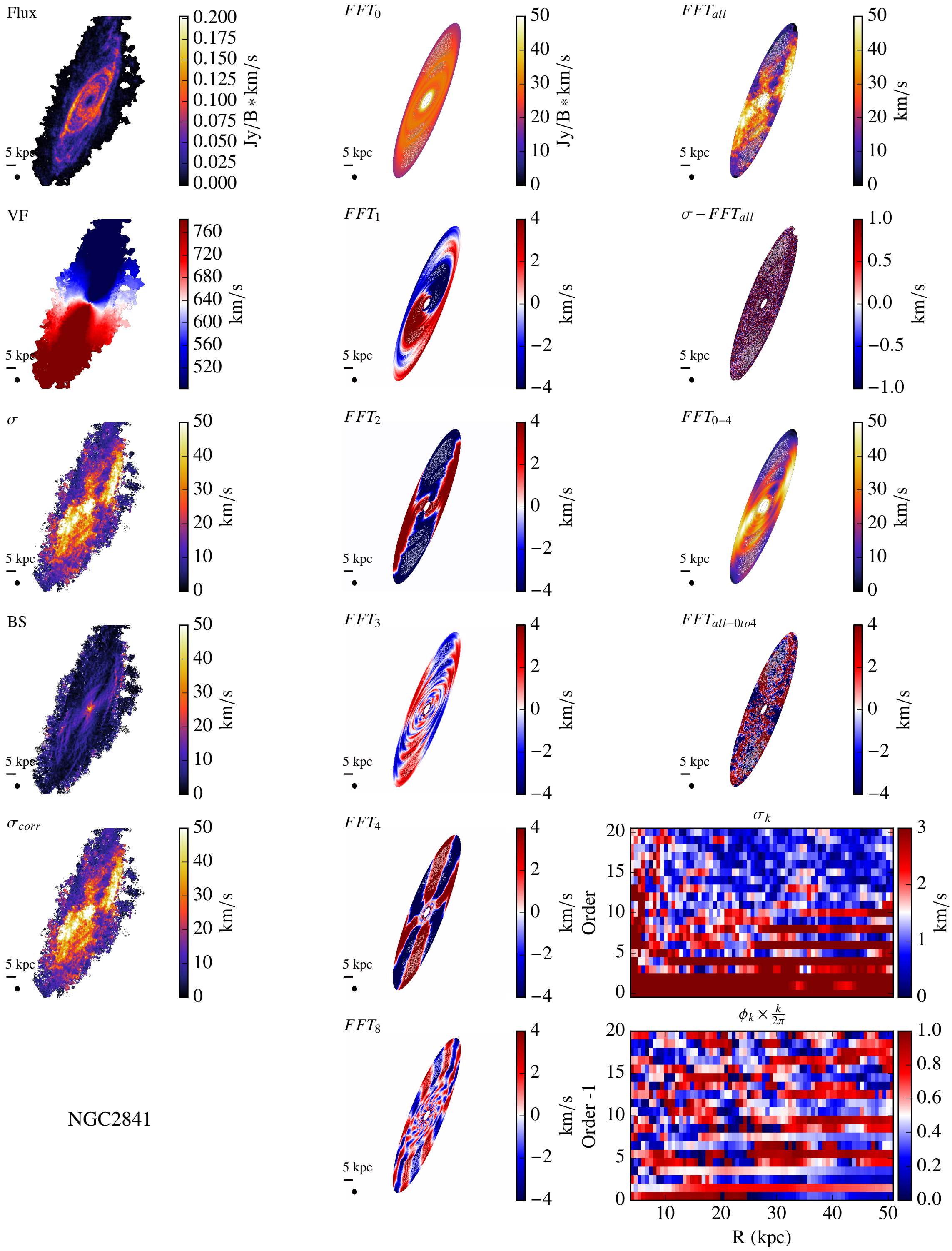

FIGURE H.3. – Overview of NGC2841

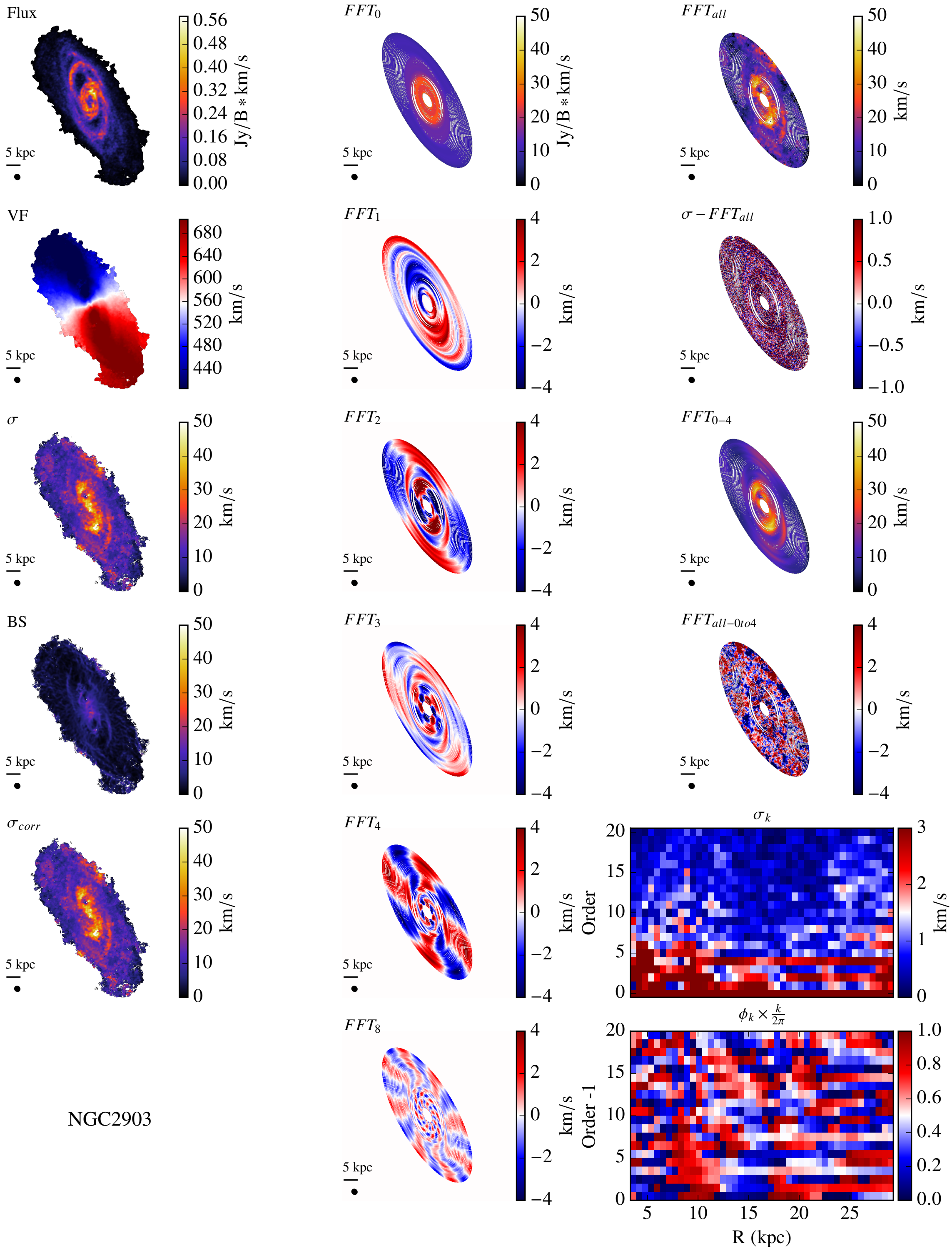

FIGURE H.4. – Overview of NGC2903

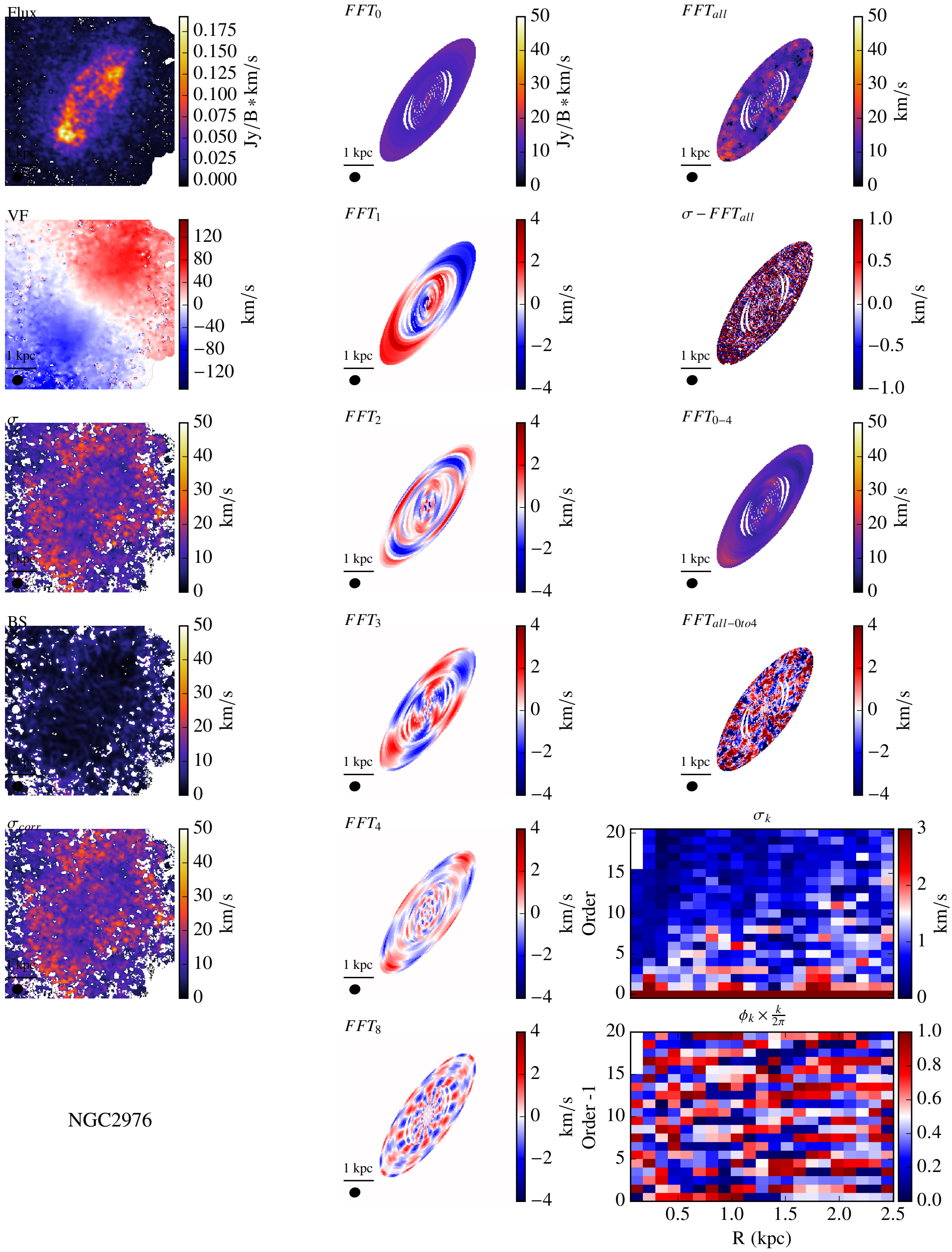

FIGURE H.5. – Overview of NGC2976

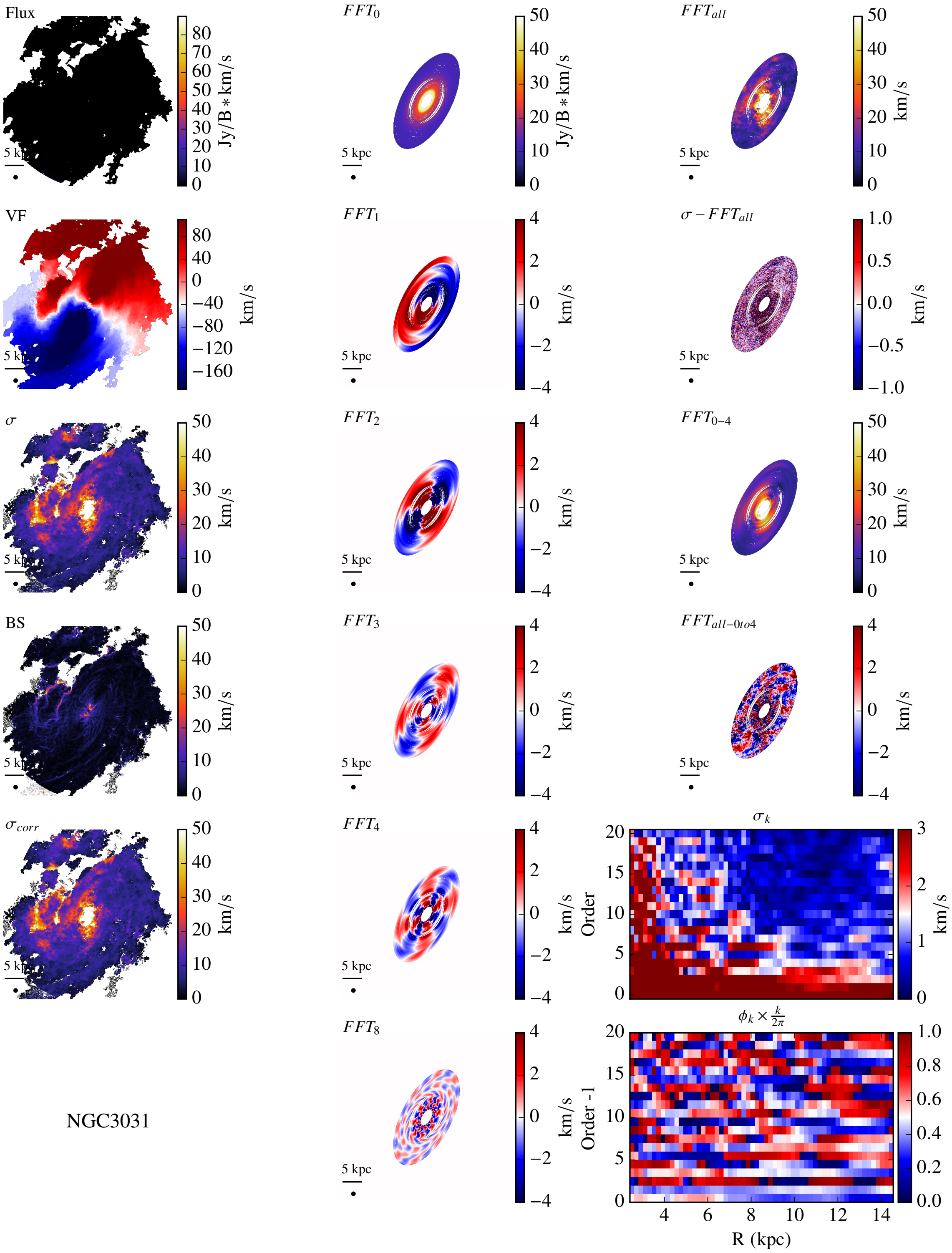

FIGURE H.6. – Overview of NGC3031

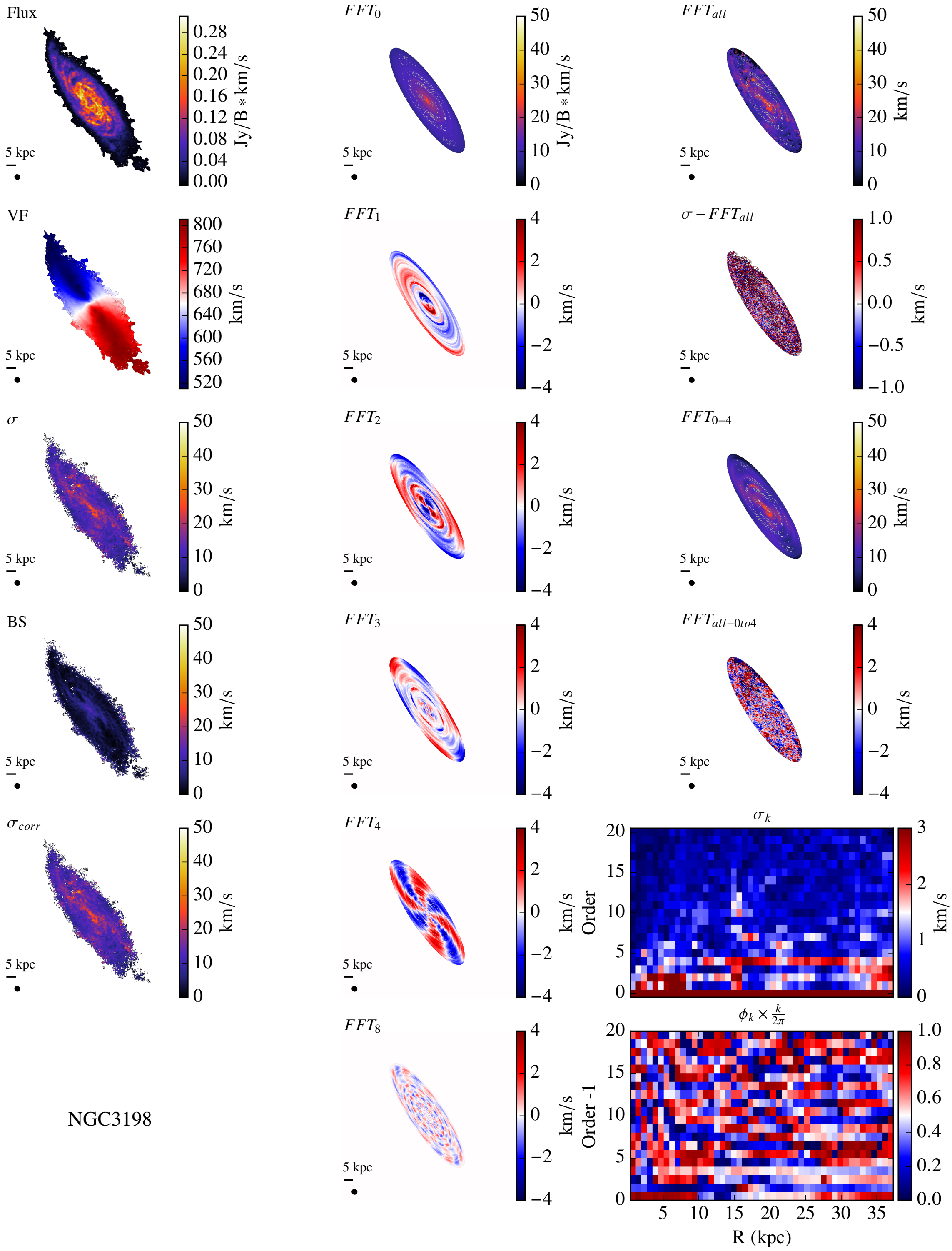

FIGURE H.7. – Overview of NGC3198

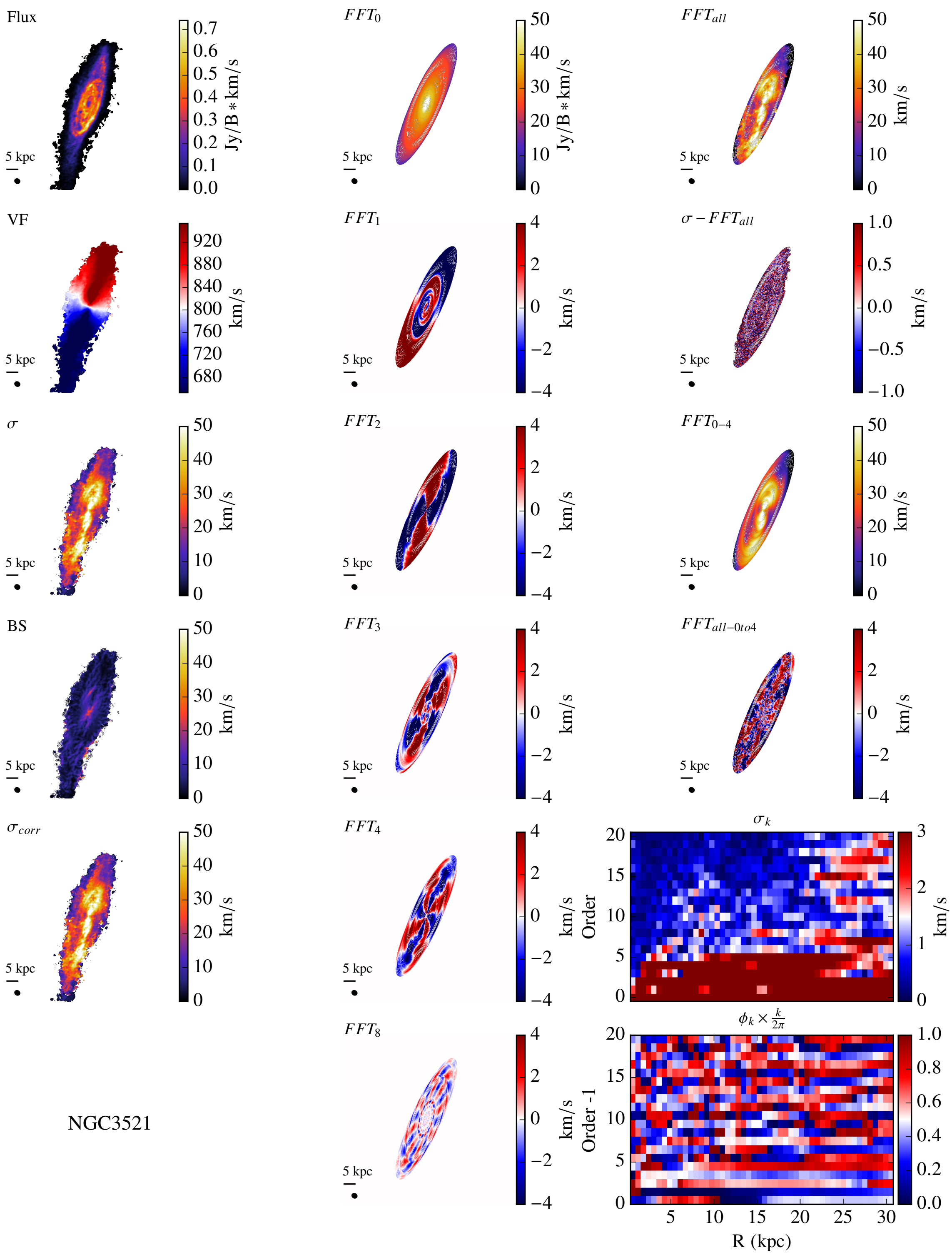

FIGURE H.8. – Overview of NGC3521

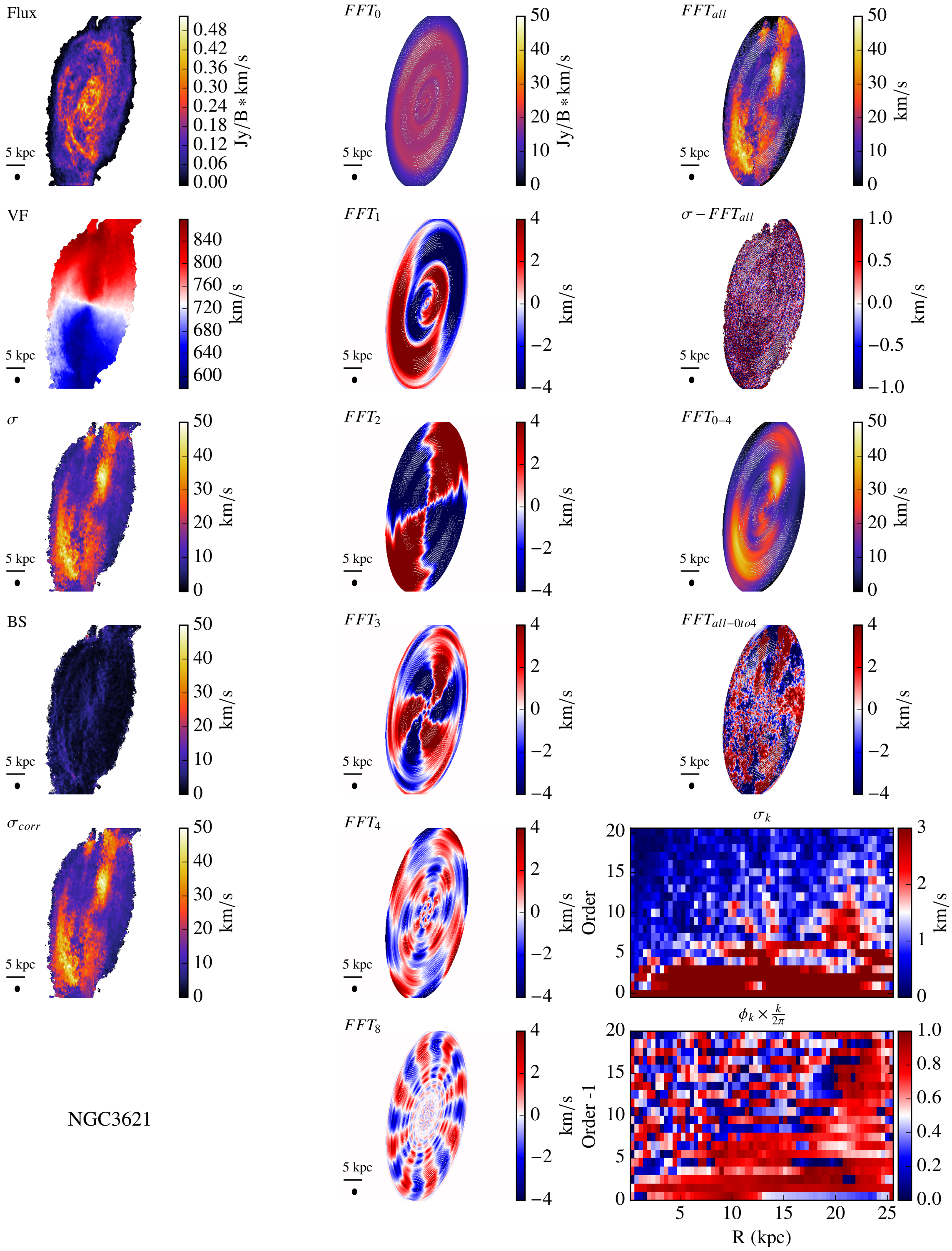

FIGURE H.9. – Overview of NGC3621

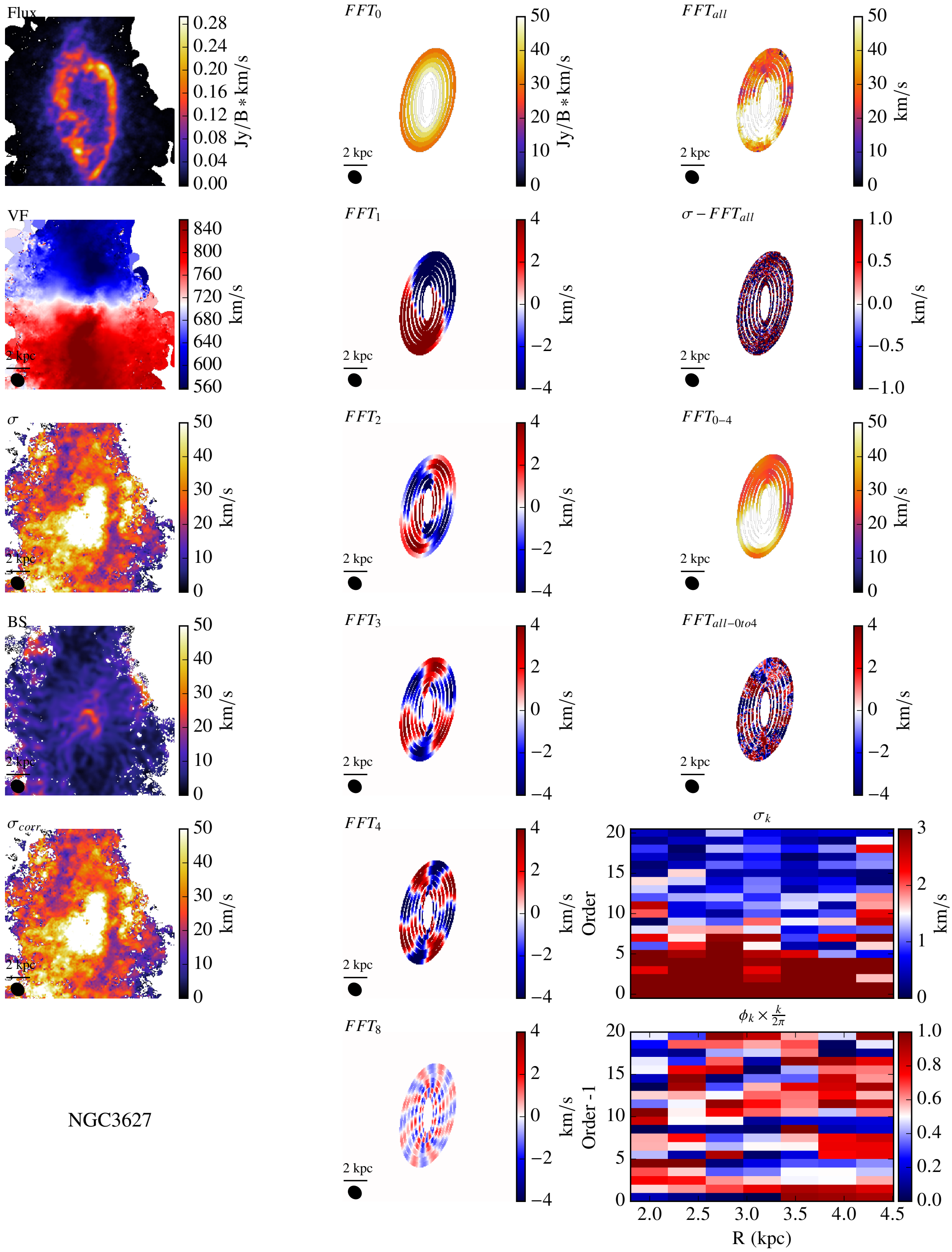

FIGURE H.10. – Overview of NGC3627

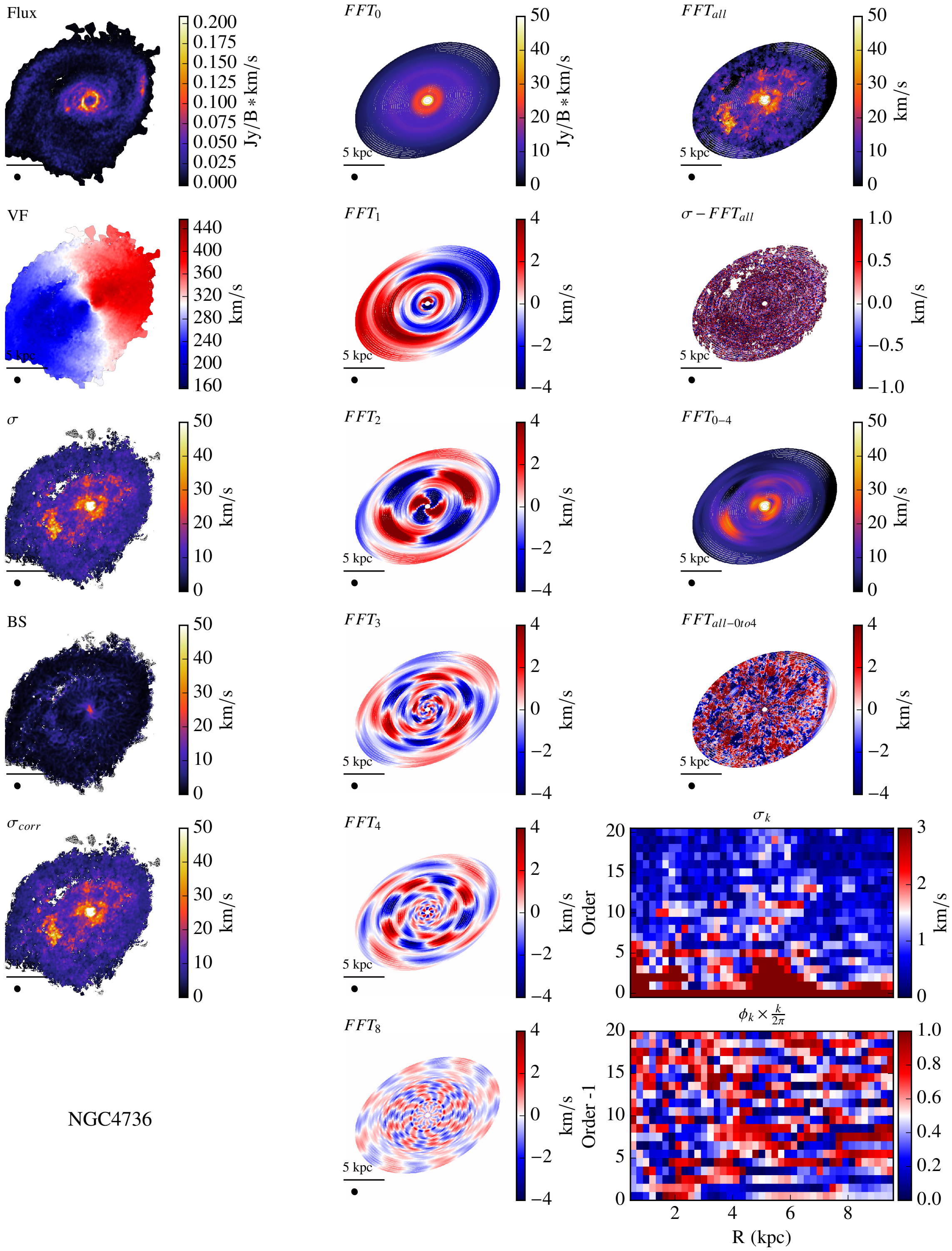

FIGURE H.11. – Overview of NGC4736

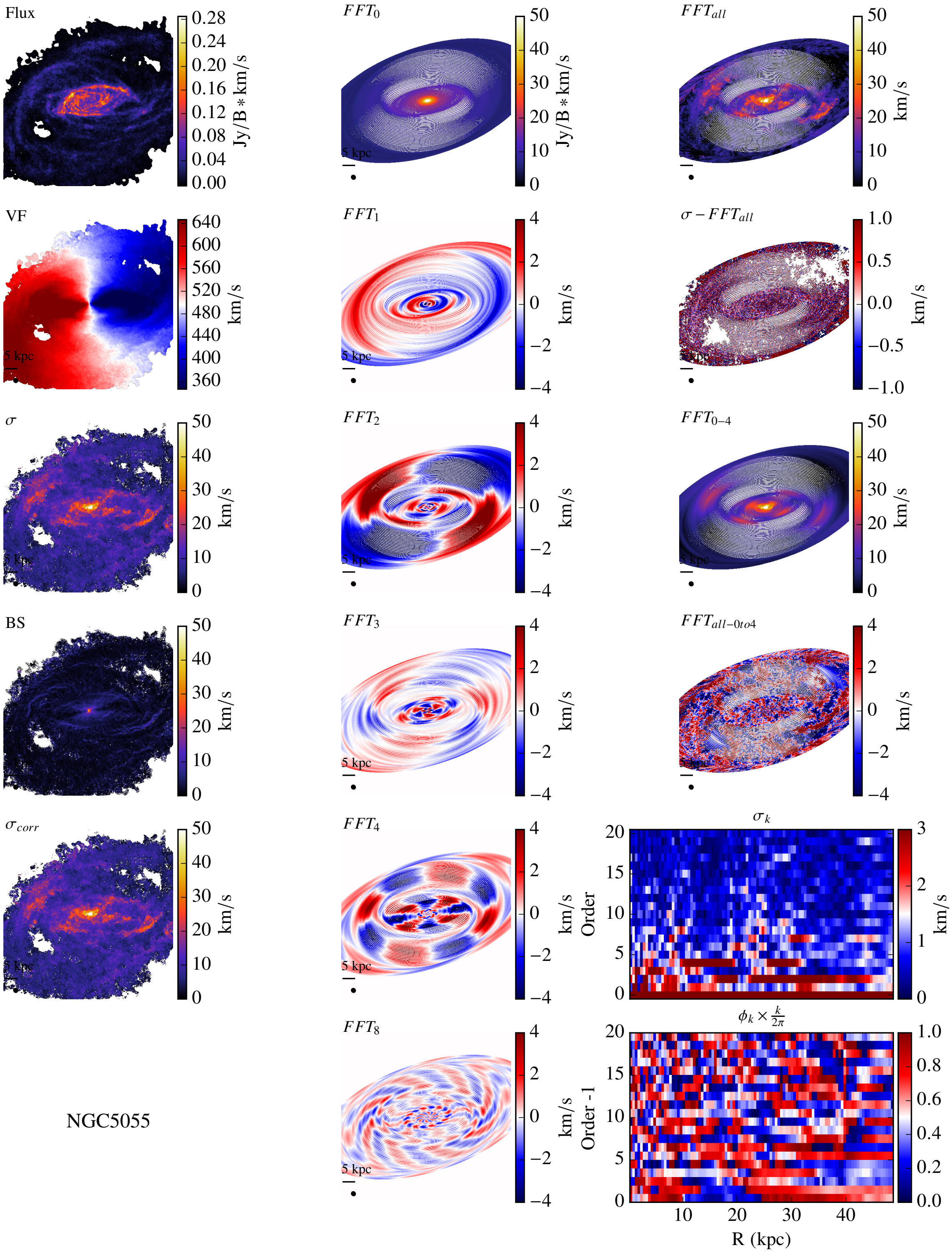

FIGURE H.12. – Overview of NGC5055

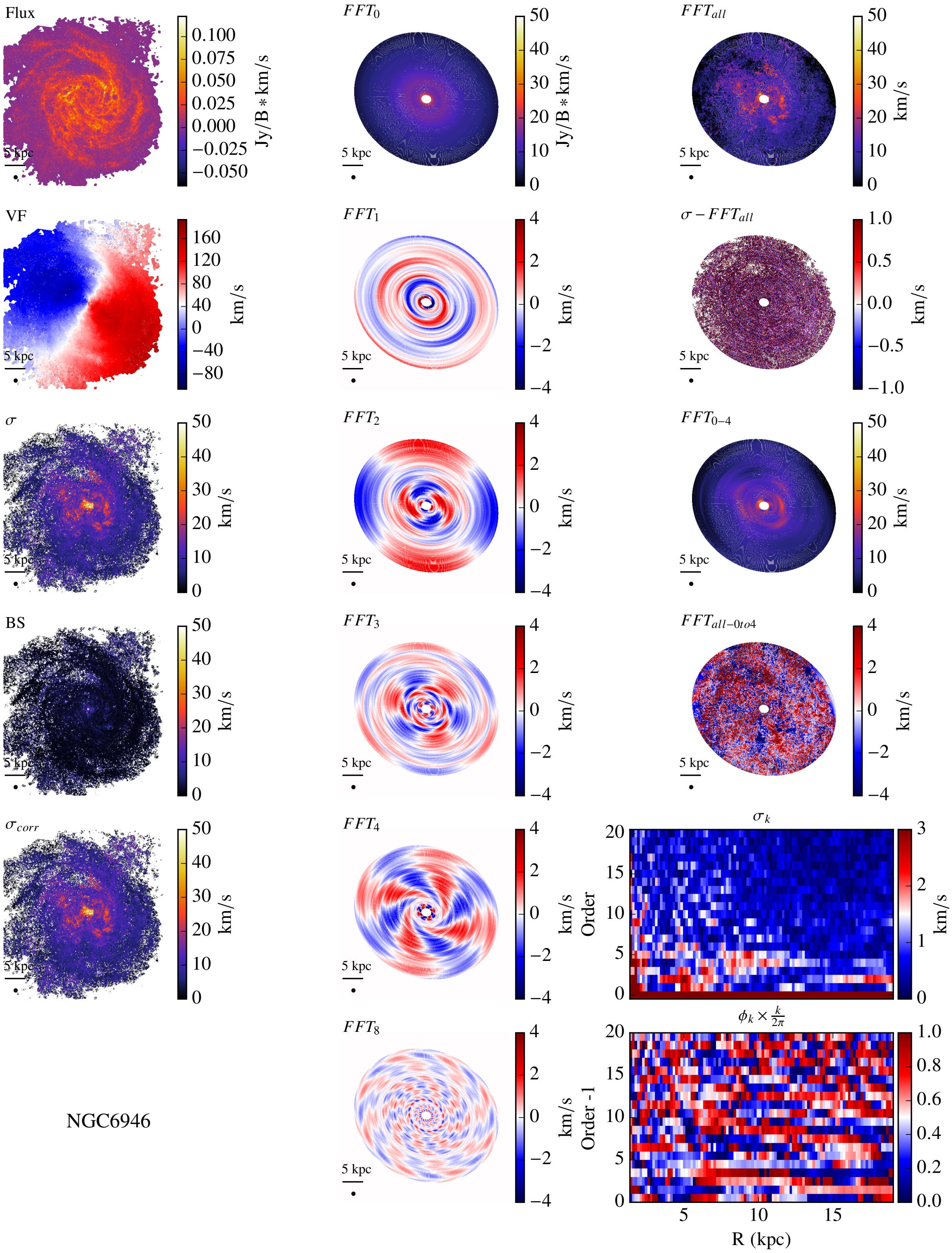

FIGURE H.13. – Overview of NGC6946

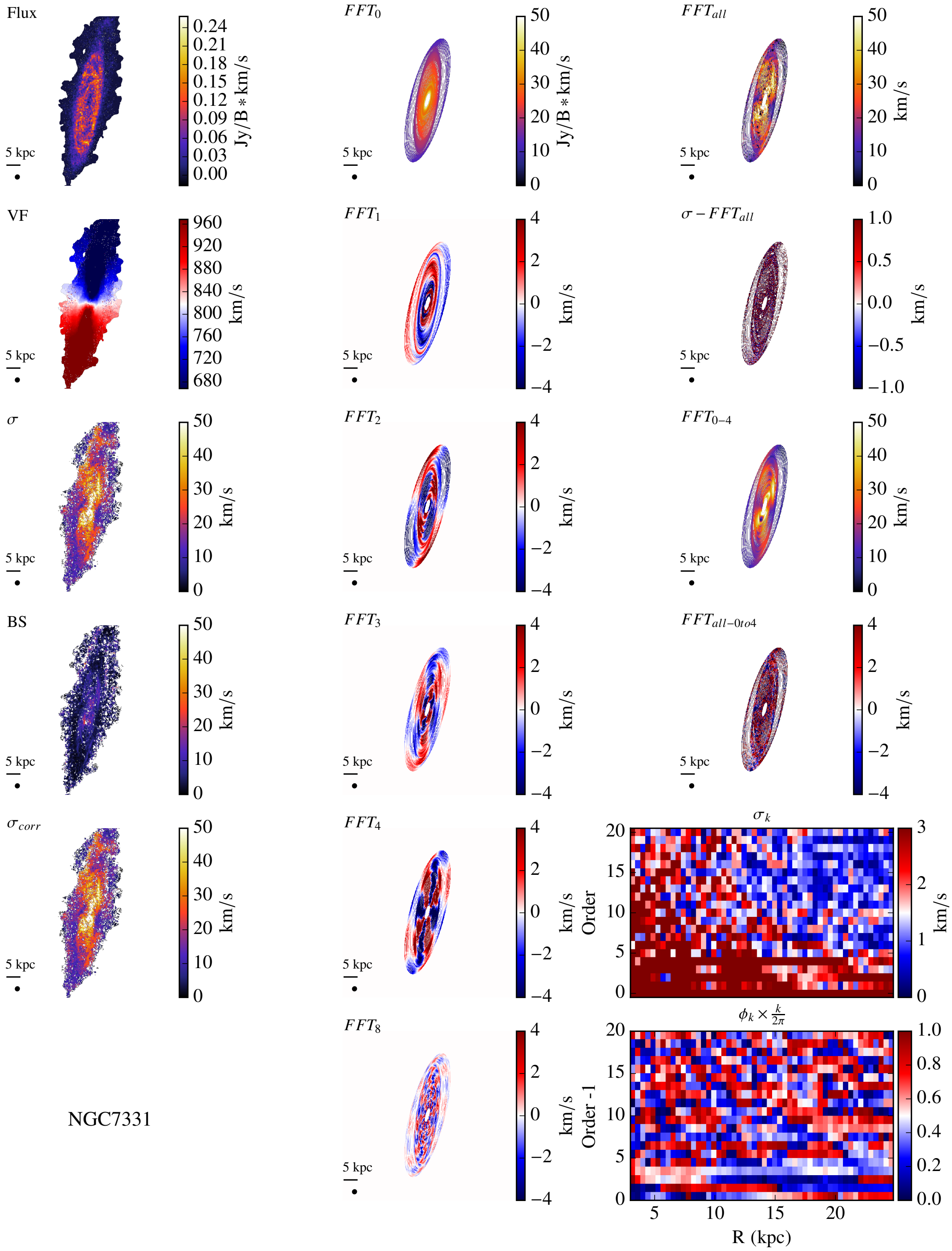

FIGURE H.14. – Overview of NGC7331

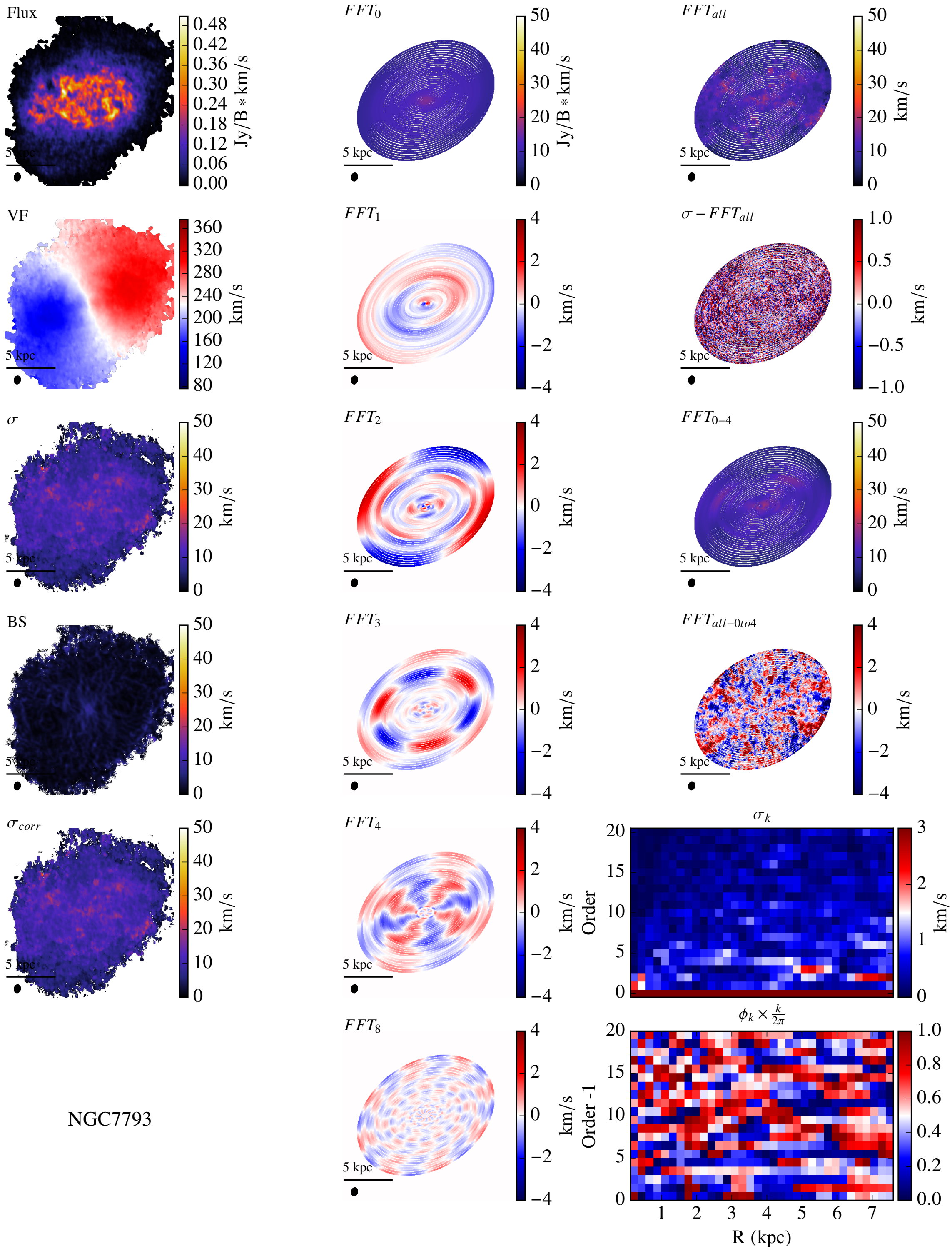

FIGURE H.15. – Overview of NGC7793

I. THINGS maps superposed with B-band contours

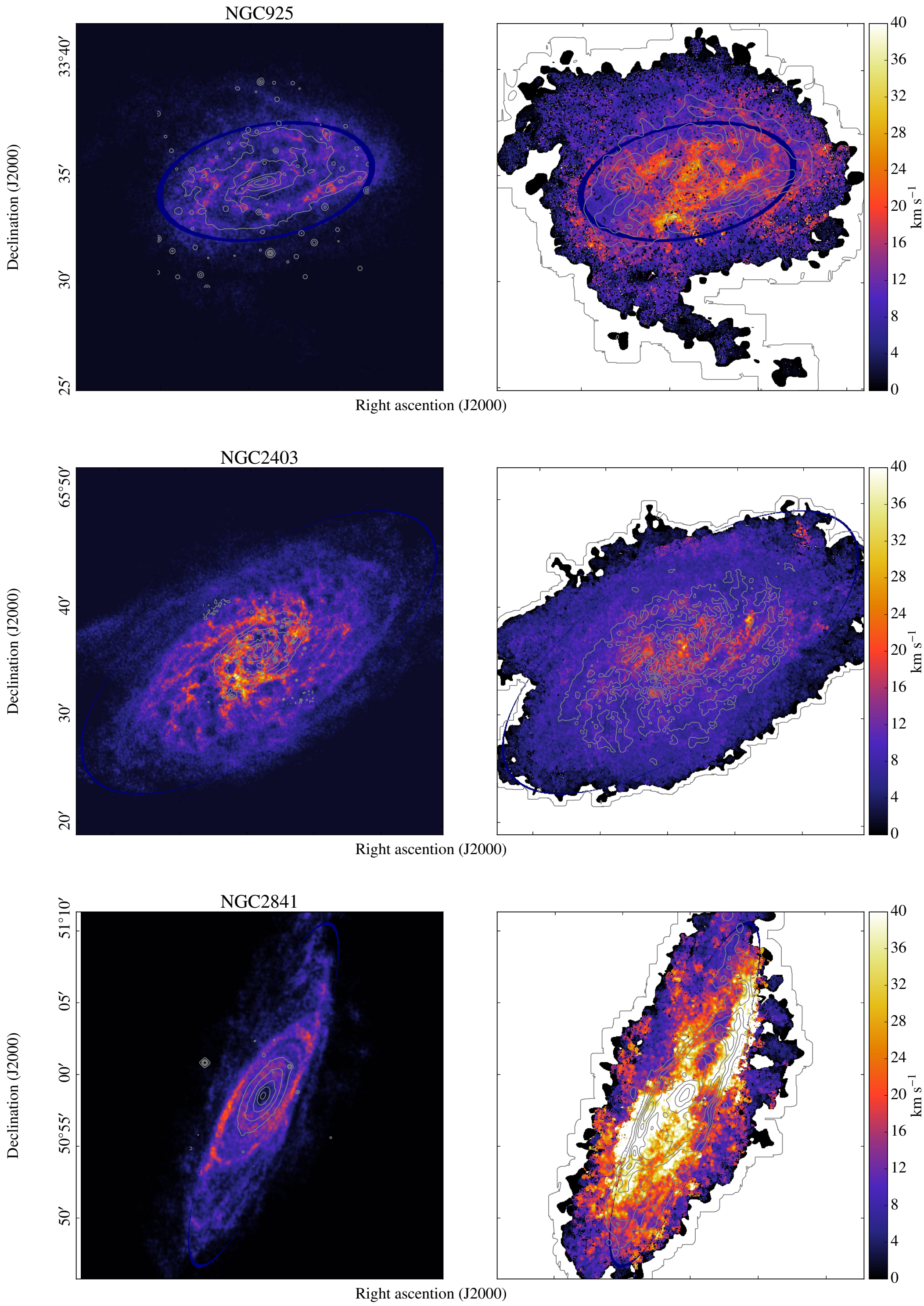

FIGURE I.0. – Flux map from THINGS with B-band contours superposed in gray (left), and dispersion maps from THINGS superposed with the flux contours (right). The blue ellipse corresponds to the last radius of each galaxy.

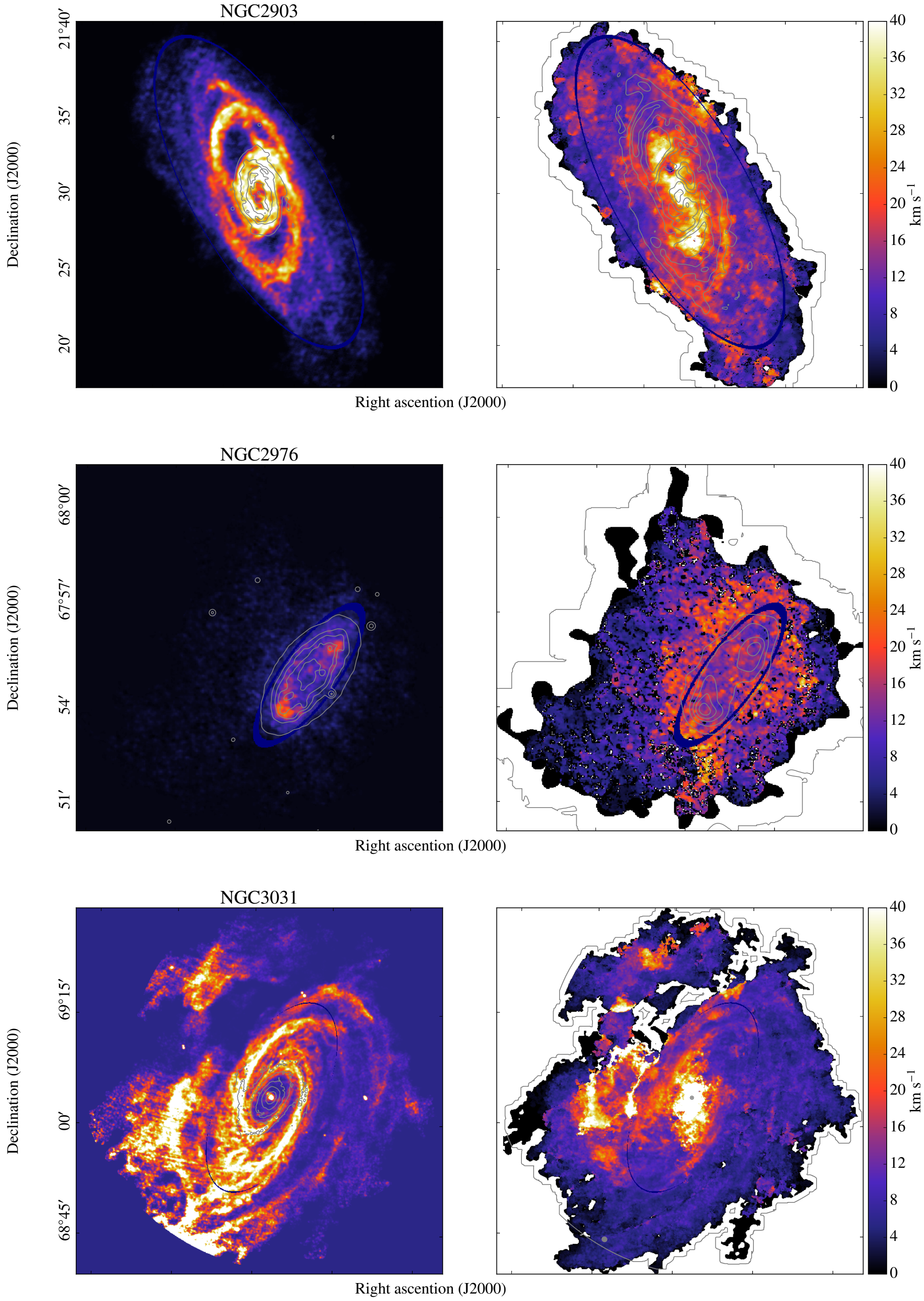

FIGURE I.0. – Continued

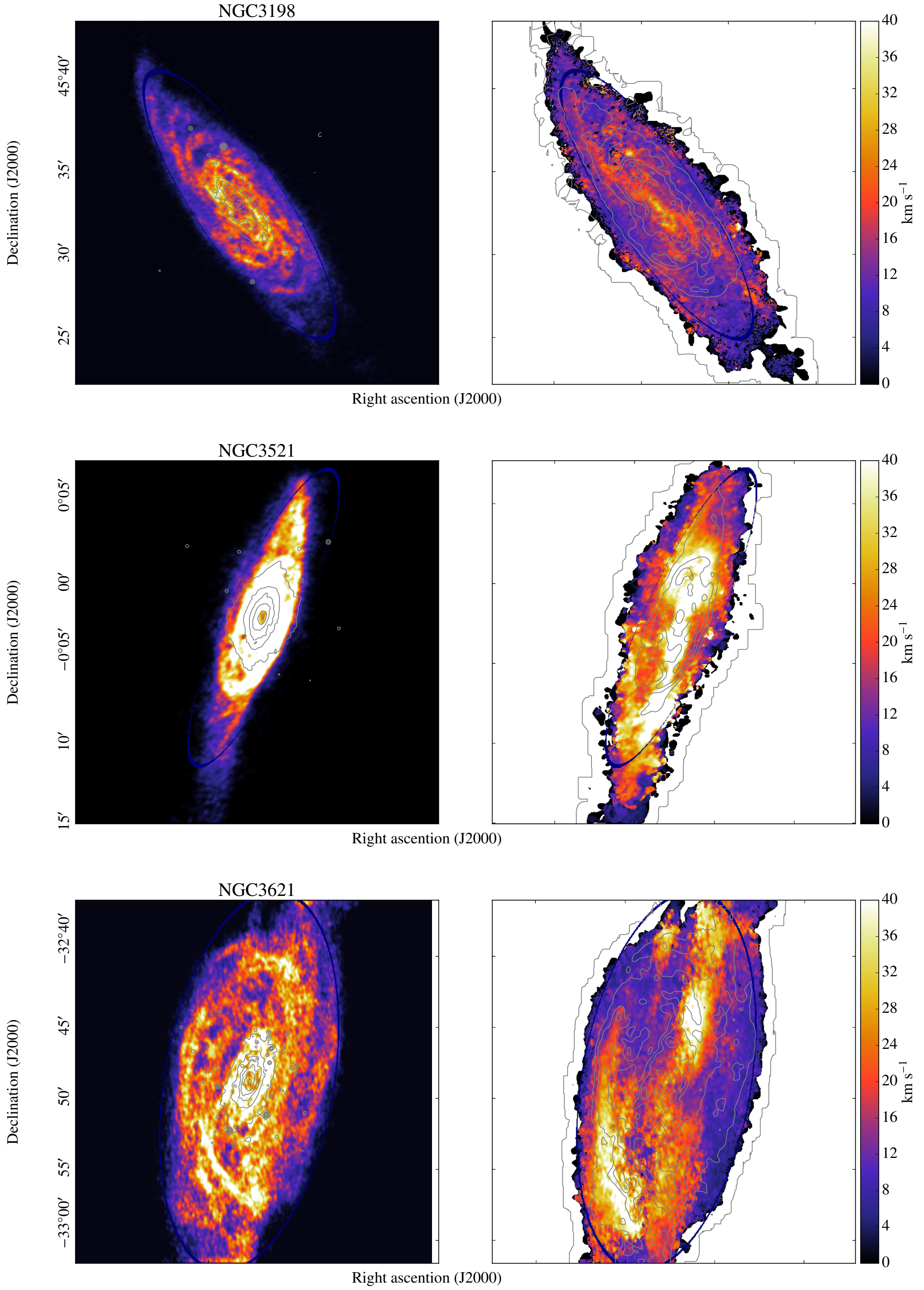

FIGURE I.0. – Continued

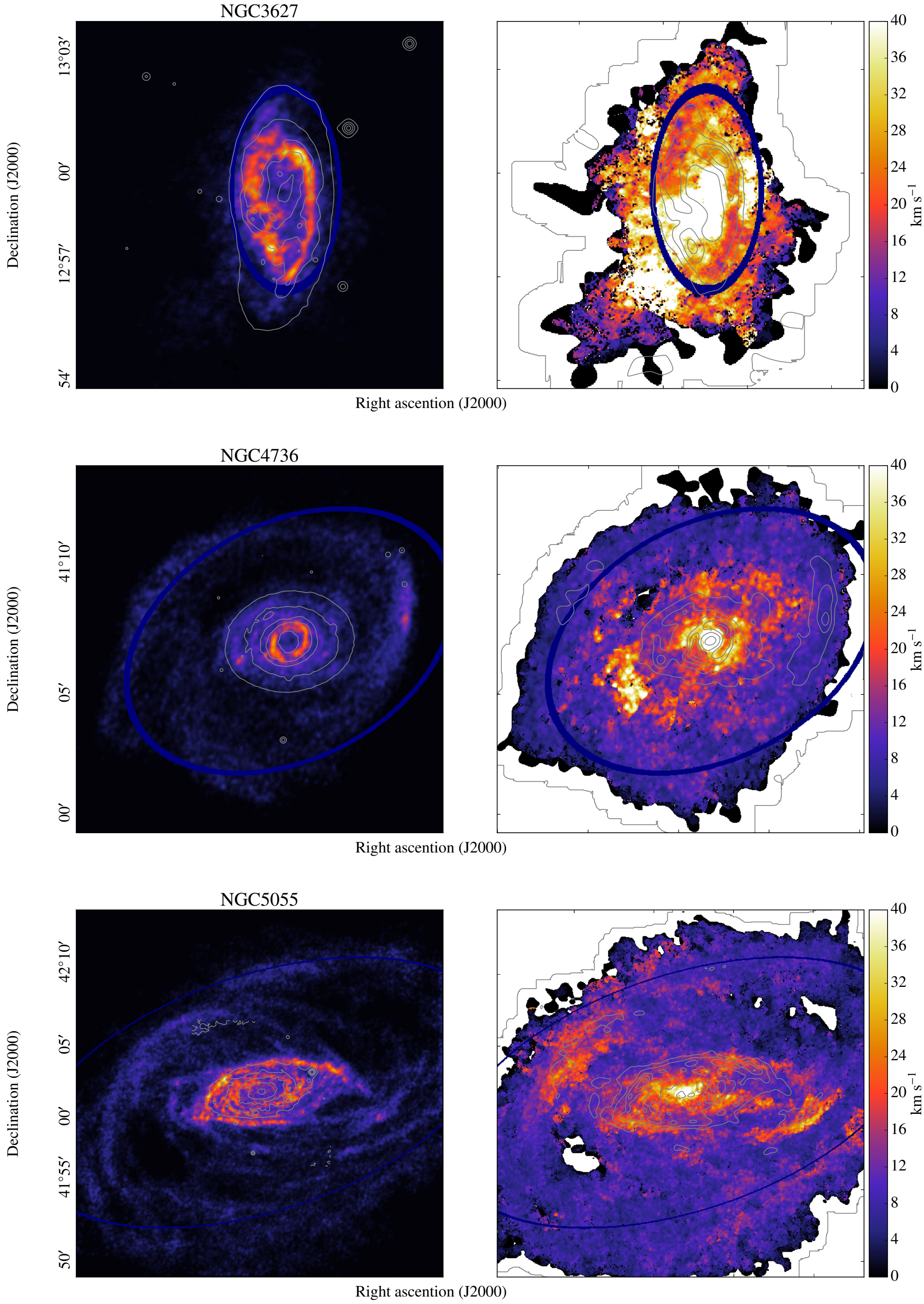

FIGURE I.0. – Continued

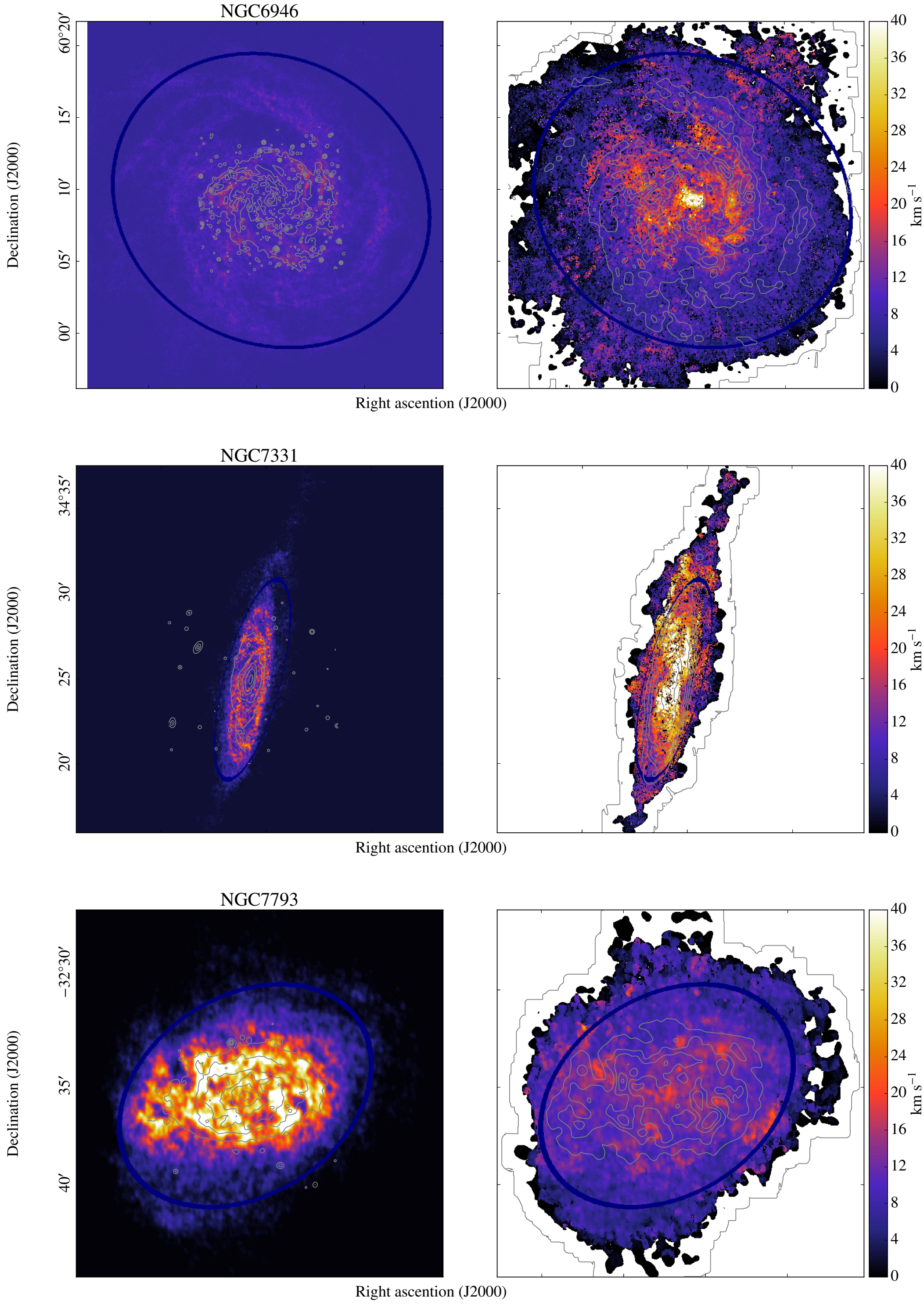

FIGURE I.0. – Continued

Le coeur de cette thèse porte sur l'étude des asymétries et des anisotropies dans les distributions de dispersion de vitesses radiales du gaz neutre dans un échantillon de galaxies spirales proches.
Dans un premier temps, afin d'extraire des courbes de rotation de manière homogène du sondage HI WHISP, j'ai constitué un échantillon de 313 galaxies spirales et irrégulières. J'ai ensuite utilisé l'algorithme 3DBarolo permettant de calculer les courbes de rotation en ajustant un modèle dit d'anneaux inclinés sur chaque cube de données et non pas sur les champs de vitesses. Cette méthode novatrice, comparée aux méthodes utilisées traditionnellement, permet de s'affranchir d'effets instrumentaux bien connus liés à la résolution spatiale finie des observations.
Dans un second temps, j'ai réalisé la toute première étude systématique des mouvements aléatoires du gaz froid sur un échantillon soigneusement sélectionné de 15 galaxies spirales extraites de l'échantillon HI THINGS et de 15 autres galaxies spirales de l'échantillon HI WHISP. Cette étude est motivée par la recherche systématique d'anisotropies dans les champs de dispersions de vitesses, comme cela a été découvert dans la galaxie Messier 33 (M33). Cette anisotropie indiquerait que le gaz neutre et froid du milieu interstellaire serait distribué en amas dense et qu'il serait par conséquent moins sujet aux collisions qu'escompté, ce qui limiterait la dissipation de son énergie. Je montre dans cette thèse que le résultat découvert dans M33 n'est pas confirmé pour d'autres galaxies de même nature et que cette particularité de M33 est probablement liée à un effet de projection. Néanmoins, en analysant ces champs de dispersion de vitesse à l'aide de transformées de Fourier, j'ai découvert la présence d'un signal d'ordre 4, présentant un alignement systématique de pi / 4 par rapport au grand axe. A travers deux différentes méthodes, je confirme la réalité physique de ce signal, et je propose différentes pistes pour l'interpréter. Parmi celles-ci, une discussion sur les effets instrumentaux est détaillée, ainsi qu'une possible explication par des effets d'anisotropies d'une nature différente.

The core of this thesis concerns the study of asymmetries and anisotropies in the radial velocity dispersion distributions of neutral gas in a sample of nearby spiral galaxies.
First, in order to extract rotation curves in a homogeneous way from the HI WHISP survey, I constituted a sample of 313 spiral and irregular galaxies. I then used the 3DBarolo algorithm to calculate the rotation curves by fitting a model called tilted-ring on each data-cube and not on the velocity fields. This innovative method, compared to the methods traditionally used, accounts for the well-known instrumental effects linked to the finite spatial resolution of the observations.
Secondly, I carried out the very first systematic study of the random movements of cold gas on a carefully selected sample of 15 spiral galaxies extracted from the sample HI THINGS and 15 other spiral galaxies from the sample HI WHISP. This study is motivated by the systematic search for anisotropies in the velocity dispersions fields, as was discovered in the galaxy Messier 33 (M33). This anisotropy would indicate that the neutral and cold gas of the interstellar medium would be distributed in dense clusters and that it would therefore be less subject to collisions than expected, which would limit the dissipation of its energy. I show in this thesis that the result discovered in M33 is not confirmed for other galaxies of the same nature and that this particularity of M33 is probably linked to a projection effect. However, by analyzing these velocity dispersion fields using Fourier transforms, I discovered the presence of a 4th order signal, exhibiting a systematic alignment of pi / 4 with respect to the major axis . Through two different methods, I confirm the physical reality of this signal, and I suggest different ways to interpret it. Among these, a discussion of instrumental effects is detailed, as well as a possible explanation by anisotropy effects of a different nature.